

Copyright
by
Brady Ray Cox
2006

**The Dissertation Committee for Brady Ray Cox Certifies that this is the approved
version of the following dissertation:**

**Development of a Direct Test Method for Dynamically Assessing the
Liquefaction Resistance of Soils In Situ**

Committee:

Kenneth H. Stokoe II, Supervisor

Ellen M. Rathje

John L. Tassoulas

Clark R. Wilson

T. Leslie Youd

**Development of a Direct Test Method for Dynamically Assessing the
Liquefaction Resistance of Soils In Situ**

by

Brady Ray Cox, M.S.

Dissertation

Presented to the Faculty of the Graduate School of

The University of Texas at Austin

in Partial Fulfillment

of the Requirements

for the Degree of

Doctor of Philosophy

The University of Texas at Austin

May 2006

Dedication

To my lovely wife Audrey and my two beautiful daughters Kayla and Savannah

To my steadfast parents Clayton and Jerri Lynn

To all my family

Acknowledgements

I express my deepest gratitude to my advisor, Dr. Kenneth H. Stokoe II. I could not have asked to work with a more talented and enthusiastic individual. He has involved me on many interesting and challenging projects that have allowed me to travel, to meet people in the profession, and to gain knowledge and expertise outside the bounds of my dissertation research. I will forever benefit from these experiences. It has been an honor and a privilege to not only work for a great professor, but also a great man.

I am grateful for the help and guidance provided to me by my advisory committee members, Dr. Ellen Rathje, Dr. John L. Tassoulas, Dr. Clark R. Wilson, and Dr. T. Leslie Youd. I have learned a great deal from each of these individuals.

I acknowledge and give thanks to the other geotechnical engineering faculty members at The University of Texas, Dr. Gilbert, Dr. Olson, Dr. Tonon, Dr. Wright and Dr. Zornberg. They have made, and will continue to make, this program one of the best in the country.

There have been many students and other individual who have helped me during my time at The University of Texas. In particular, I give thanks to Min Jae Jung for keeping me laughing on many long field excursions, to Cecil Hoffpaur for his hard work and expertise in working with the vibroseis trucks, to Dr. Farn-Yuh Menq and Dr. Brent Rosenblad for hands on training in many soil dynamics related issues, to Dr. Wen-Jong Chang for teaching me about his liquefaction

research, to Frank Wise for his tutelage on electronics and circuitry, to Jeffery Lee, Asli Kurtulus and Yin-Cheng Lin for sharing an office and advice, to Wayne Fontenot, Max Trevino and Gonzalo Zapata for helping my to blow off steam and refine my ping-pong skills during lunch, and to Teresa Tice-Boggs, Chris Trevino and Alicia Zapata for their administrative support.

I am most grateful to my dear wife, and eternal companion, Audrey. Her strength and support in my life cannot be quantified. She is such a wonderful mother to our two daughters, Kayla and Savannah. They have been understanding and extremely patient with me during the writing of this dissertation and my research related travels. I love them with all of my heart and cannot imagine a life without them. I also give thanks to my parents, Clayton and Jerri Lynn Cox. They set my feet on the path that has brought me to this point in my life. I am grateful for the principles they instilled in me as a young man and for their continued support, guidance and love for our family. I am also thankful for my parents-in-law, Curtis and Catherine Steele. In addition to their support and concern for us, their biannual trips to Austin have been especially enjoyable for Audrey, the girls and me.

Development of a Direct Test Method for Dynamically Assessing the Liquefaction Resistance of Soils In Situ

Publication No. _____

Brady Ray Cox, Ph.D.

The University of Texas at Austin, 2006

Supervisor: Kenneth H. Stokoe, II

This dissertation details work conducted by researchers from the University of Texas at Austin aimed toward the development and implementation of a new in-situ liquefaction testing technique. This technique is an active method that may be used to directly evaluate the liquefaction resistance of soils in place. The test is based on the premise of dynamically loading a native soil deposit in a manner similar to an earthquake while simultaneously measuring its response with embedded instrumentation. Dynamic loading is performed via a large, truck-mounted hydraulic shaker (vibroiseis) that is used to excite the ground surface and generate stress waves of varying amplitudes within an instrumented portion of the soil mass. The embedded sensors consist of instrumentation to measure the coupled response of soil particle motion and pore water pressure generation.

The validity of this new test method has been demonstrated by conducting field experiments at the Wildlife Liquefaction Array (WLA) in Imperial Valley, California. The extensive site characterization, the documented occurrence of earthquake-induced soil liquefaction at the site twice in the 1980's, and the likelihood for re-liquefaction of the site during subsequent earthquakes make the WLA an ideal location for verifying the proposed in-situ dynamic liquefaction test method.

In-situ liquefaction tests were carried out at three separate locations at the WLA. The tests were successful at measuring: (1) excess pore water pressure generation, and (2) nonlinear shear modulus behavior in the native silty-sand deposits as a function of induced cyclic shear strain and number of loading cycles. These results are compared to pore pressure generation curves and nonlinear shear modulus curves previously developed for WLA soils from laboratory testing methods. Variations in the dynamic soil response across the site are also discussed and the importance of evaluating liquefaction from direct in-situ measurements is emphasized. These accomplishments represent a large step forward in the ability to accurately evaluate the susceptibility of a soil deposit to earthquake-induced liquefaction.

Table of Contents

| | |
|---|---------|
| List of Figures | xiv |
| List of Tables..... | xxxviii |
| Chapter 1 | 1 |
| Introduction | 1 |
| 1.1 Earthquake-Induced Soil Liquefaction..... | 1 |
| 1.2 Research Significance | 2 |
| 1.3 Scope of Research | 4 |
| 1.4 Organization of Dissertation | 6 |
| Chapter 2 | 11 |
| Soil Liquefaction Background | 11 |
| 2.1 Introduction | 11 |
| 2.2 Liquefaction – A Complicated Phenomenon | 11 |
| 2.3 Liquefaction Evaluation Procedures | 20 |
| 2.4 In-Situ Soil Liquefaction Measurements..... | 34 |
| 2.5 Need For A Dynamic In-Situ Liquefaction Test..... | 37 |
| 2.6 Summary | 38 |
| Chapter 3 | 40 |
| In-Situ Dynamic Liquefaction Test..... | 40 |
| 3.1 Introduction | 40 |

| | |
|--|-----|
| 3.2 First-Generation In-Situ Liquefaction Test | 41 |
| 3.3 Second-Generation In-Situ Liquefaction Test..... | 45 |
| 3.4 Summary | 48 |
| Chapter 4 | 50 |
| In-Situ Liquefaction Test Instrumentation | 50 |
| 4.1 Introduction | 50 |
| 4.2 Liquefaction Sensor..... | 50 |
| 4.3 Data Acquisition..... | 80 |
| 4.4 Summary | 86 |
| Chapter 5 | 88 |
| Generalized In-Situ Liquefaction Test Procedure..... | 88 |
| 5.1 Introduction | 88 |
| 5.2 Sensor Installation | 88 |
| 5.3 Staged Dynamic Loading..... | 101 |
| 5.4 Sensor Extraction | 103 |
| 5.5 Summary | 104 |
| Chapter 6 | 106 |
| In-Situ Liquefaction Test Data Analysis..... | 106 |
| 6.1 Introduction | 106 |
| 6.2 Recorded Raw Data..... | 106 |
| 6.3 Shear Strain Evaluation..... | 112 |
| 6.4 Pore Pressure Ratio Evaluation | 134 |

| | |
|--|-----|
| 6.5 Nonlinear Shear Modulus Evaluation | 139 |
| 6.6 Summary | 147 |
| Chapter 7 | 148 |
| The Wildlife Liquefaction Array; Imperial Valley, California | 148 |
| 7.1 Introduction | 148 |
| 7.2 Imperial Valley, California | 149 |
| 7.3 Wildlife Liquefaction Array (WLA) | 149 |
| 7.4 The 1987 Elmore Ranch and Superstition Hills Earthquakes | 170 |
| 7.5 WLA Re-Instrumented as a NEES Site..... | 177 |
| 7.6 Generalized WLA Liquefiable Soil Layer Properties | 183 |
| 7.7 In-Situ Liquefaction Tests at the Wildlife Site..... | 192 |
| 7.8 Summary | 192 |
| Chapter 8 | 194 |
| In-Situ Liquefaction Test Results: Test Location C, WLA..... | 194 |
| 8.1 Introduction | 194 |
| 8.2 Test C: Array Location and Pre-Dynamic Loading Information | 194 |
| 8.3 Test C: Staged Dynamic Loading Series 1..... | 211 |
| 8.4 Test C: Staged Dynamic Loading Series 2..... | 252 |
| 8.5 General Comparison of Results for Series 1 and Series 2..... | 294 |
| 8.6 Summary | 297 |

| | |
|--|-----|
| Chapter 9 | 299 |
| In-Situ Liquefaction Test Results: Test Location B, WLA..... | 299 |
| 9.1 Introduction | 299 |
| 9.2 Test B: Array Location and Pre-Dynamic Loading Information | 299 |
| 9.3 Test B: Staged Dynamic Loading Series 1..... | 316 |
| 9.4 Test B: Staged Dynamic Loading Series 2..... | 342 |
| 9.5 General Comparison of Results for Series 1 and Series 2..... | 369 |
| 9.6 Summary | 370 |
| Chapter 10 | 373 |
| In-Situ Liquefaction Test Results: Test Location A, WLA | 373 |
| 10.1 Introduction | 373 |
| 10.2 Test A: Array Location and Pre-Dynamic Loading Information | 373 |
| 10.3 Test A: Staged Dynamic Loading Series 1 | 404 |
| 10.4 Test A: Staged Dynamic Loading Series 2 | 427 |
| 10.5 General Comparison of Results for Series 1 and Series 2..... | 445 |
| 10.6 Summary | 447 |
| Chapter 11 | 450 |
| Comparison of Pore Pressure Generation Results: Test Locations A, B and C; WLA..... | 450 |
| 11.1 Introduction | 450 |
| 11.2 Comparison of In-Situ Pore Pressure Generation Results | 450 |
| 11.3 General Site Comparison | 460 |

| | |
|---|-----|
| 11.4 Summary | 469 |
| Chapter 12 | 471 |
| Summary, Conclusions, Recommendations and Future Work | 471 |
| 12.1 Summary | 471 |
| 12.2 Conclusions | 474 |
| 12.3 Recommendations | 479 |
| 12.4 Future Work | 488 |
| References | 491 |
| Vita | 498 |

List of Figures

| | | |
|------------|--|----|
| Figure 2-1 | Liquefaction-induced differential settlement between a row of buildings and a sidewalk in Adapazari following the 1999 Kocaeli, Turkey earthquake (Cox, 2001)..... | 18 |
| Figure 2-2 | Liquefaction-induced bearing capacity failure of a 5-story building in Adapazari following the 1999 Kocaeli, Turkey earthquake (from www.eerc.berkeley.edu/turkey/adapazari). | 19 |
| Figure 2-3 | Liquefaction-induced lateral spreading and settlement, coupled with tectonic subsidence, carried Hotel Sapanca partially into Lake Sapanca following the 1999 Kocaeli, Turkey earthquake (from www.eerc.berkeley.edu/turkey/adapazari). | 20 |
| Figure 2-4 | Empirical relationship between cyclic resistance ratio and stress-corrected shear wave velocity for M=7.5 earthquakes (from Andrus and Stokoe, 2000)..... | 25 |
| Figure 2-5 | Ratio of cyclic strength between partially and fully saturated sand as a function of measured P-wave velocity (from Ishihara, 2001)..... | 27 |
| Figure 2-6 | Pore pressure generation curve developed from strain-controlled cyclic triaxial tests on various sands with different specimen preparation techniques and confining pressures (modified from Dobry et al., 1982)..... | 28 |
| Figure 3-1 | Picture of the vibroseis truck used as a dynamic source in the first-generation in-situ liquefaction tests (from Stokoe et al., 2004)..... | 42 |
| Figure 3-2 | Schematic layout of vibroseis truck location, reconstituted soil test pit, and associated instrumentation used in the first-generation in-situ liquefaction test (from Chang, 2002). | 42 |
| Figure 3-3 | Liquefaction sensor used in the first-generation in-situ liquefaction test (from Chang, 2002). | 43 |
| Figure 3-4 | Shearing strain and excess pore water pressure time histories obtained from a first-generation in-situ liquefaction test (from Chang, 2002)..... | 44 |

| | | |
|------------|--|----|
| Figure 3-5 | Pore pressure generation curves for different numbers of loading cycles evaluated from a first-generation in-situ liquefaction test series (from Chang, 2002)..... | 45 |
| Figure 3-6 | Simplified schematic of first- and second-generation in-situ liquefaction testing configurations (from Stokoe et al., 2004)..... | 47 |
| Figure 3.7 | Picture of T-Rex, the new triaxial vibroseis truck used as a dynamic source for second-generation liquefaction tests (from Stokoe et al., 2004)..... | 48 |
| Figure 4-1 | Picture of an in-situ liquefaction sensor and its associated cables. ... | 52 |
| Figure 4-2 | Schematic detailing the dimensions and components of the in-situ liquefaction sensor..... | 52 |
| Figure 4-3 | Picture of a triaxial (3D) MEMS accelerometer used as the vibration-sensing component of the in-situ liquefaction sensors (from www. silicondesigns.com). | 55 |
| Figure 4-4 | Picture of the compound sine plate used to calibrate the 3D-MEMS accelerometers for tilt. | 57 |
| Figure 4-5 | Tilt calibration results for a 3D-MEMS accelerometer rotated about its x-axis. | 59 |
| Figure 4-6 | Tilt calibration results for a 3D-MEMS accelerometer rotated about its y-axis. | 59 |
| Figure 4-7 | Picture of the modal shaker used to dynamically calibrate the 3D-MEMS accelerometers installed in each in-situ liquefaction sensor..... | 62 |
| Figure 4-8 | Dynamic amplitude calibration results for a single component of a 3D-MEMS accelerometer displayed on: a) a linear-frequency scale, and b) a log-frequency scale..... | 64 |
| Figure 4-9 | Dynamic phase calibration results between two y-components of two 3D-MEMS accelerometers displayed on: a) a linear-frequency scale, and b) a log-frequency scale..... | 67 |

| | | |
|-------------|---|----|
| Figure 4-10 | Picture of an Entran model EPX-V02-25P miniature pore water pressure transducer (PPT) used in each in-situ liquefaction sensor..... | 71 |
| Figure 4-11 | Picture of the standpipe used for calibration of the pore pressure transducer (PPT) in each liquefaction sensor during field testing. .. | 72 |
| Figure 4-12 | Linear calibration results for a typical pore pressure transducer (PPT) used during dynamic in-situ liquefaction tests. | 73 |
| Figure 4-13 | Picture of the Druck PDCR 35/D pressure transducer in its acrylic case. | 77 |
| Figure 4-14 | Picture of a liquefaction sensor prior to pore pressure transducer cavity saturation and filter installation. | 79 |
| Figure 4-15 | Picture of a saturated liquefaction sensor with its protective rubber membrane..... | 79 |
| Figure 4-16 | Picture of the connector box used to rout individual conductors from the liquefaction sensor cables to their appropriate inputs and outputs. | 81 |
| Figure 4-17 | Picture of the system used to provide power to the in-situ liquefaction sensors. | 84 |
| Figure 4-18 | Picture of the data acquisition system used for dynamic in-situ liquefaction tests..... | 87 |
| Figure 5-1 | Picture of an in-situ liquefaction sensor and its associated cables. .. | 89 |
| Figure 5-2 | Picture of the hydraulic cylinder on the rear bumper of T-Rex used with push rods to install the liquefaction sensors in the field. .. | 90 |
| Figure 5-3 | Picture of the pushing and pulling connections that couple the hydraulic cylinder on the rear bumper of T-Rex to the push rods. .. | 91 |
| Figure 5-4 | Picture of the two pilot cones used to help install the liquefaction sensors in the field..... | 93 |
| Figure 5-5 | Picture of the rubber gasket used to seal the hollow section of the steel push rods. | 94 |

| | | |
|-------------|---|-----|
| Figure 5-6 | Picture of a liquefaction sensor and the pilot that enables it to be lowered to the ground water level. | 95 |
| Figure 5-7 | Picture of the installed liquefaction sensor array and crosshole source rods. | 97 |
| Figure 5-8 | Cross-sectional schematic of the trapezoidal sensor array used for in-situ liquefaction tests. | 97 |
| Figure 5-9 | Picture of the backfilled liquefaction sensor trench. | 100 |
| Figure 5-10 | Picture of the base plate of T-Rex centered over the top of the liquefaction sensor array. | 100 |
| Figure 5-11 | Calibration results for the base plate hold-down force of T-Rex. ... | 102 |
| Figure 5-12 | Schematic showing the location and mode of operation of T-Rex during staged dynamic loading of the instrumented liquefiable layer. | 102 |
| Figure 5-13 | Picture detailing the simultaneous withdrawal of the push rods and wire rope during liquefaction sensor extraction. | 105 |
| Figure 6-1 | Raw output signals from the x-, y-, and z-components of a 3D-MEMS accelerometer during dynamic in-situ liquefaction testing. | 108 |
| Figure 6-2 | Raw output signal from a single component of a 3D-MEMS accelerometer during dynamic in-situ liquefaction testing; displayed in the: a) time domain, and b) frequency domain. | 110 |
| Figure 6-3 | Velocity signal obtained from integrating a single component of a 3D-MEMS accelerometer recorded during dynamic in-situ liquefaction testing; displayed in the: a) time domain, and b) frequency domain. | 113 |
| Figure 6-4 | Displacement signal obtained from double integration of a single component of a 3D-MEMS accelerometer recorded during dynamic in-situ liquefaction testing; displayed in the: a) time domain, and b) frequency domain. | 114 |

| | | |
|-------------|---|-----|
| Figure 6-5 | Representation of 4-node element in (a) the global coordinate system and (b) the natural coordinate system (from Chang, 2002)..... | 117 |
| Figure 6-6 | Schematic detailing the liquefaction sensor array, the direction of dynamic excitation, the primary components of particle displacement, and the equation used to calculate the strain vector at the center of the element using a 4-node, finite element formulation. | 122 |
| Figure 6-7 | Example of a shear strain time history calculated at the center of the in-situ liquefaction sensor array using a 4-node, finite element strain formulation. | 122 |
| Figure 6-8 | Comparisons between in-plane shear strains (γ_{yz}) calculated using the 4-node displacement-based (DB) method and the 2-node DB method..... | 125 |
| Figure 6-9 | In-plane shear strains (γ_{yz}) predicted by the 2-node DB method, as percentages of the shear strains calculated using the 4-node DB method. | 125 |
| Figure 6-10 | Comparisons between in-plane shear strains (γ_{yz}) calculated using the 4-node displacement-based (DB) method, the 4-node DB method with only y-component particle displacements, and the 2-node DB method. | 127 |
| Figure 6-11 | Comparisons between in-plane shear strains (γ_{yz}) calculated using the 4-node displacement-based (DB) method and the out-of-plane shear strains (γ_{xz}) calculated using the 2-node DB method..... | 130 |
| Figure 6-12 | Out-of-plane shear strains (γ_{xz}) predicted by the 2-node DB method, as percentages of the shear strains calculated using the 4-node DB method. | 130 |
| Figure 6-13 | Comparisons between in-plane shear strains (γ_{yz}) calculated using the 4-node displacement-based (DB) method, the 4-node DB method with only y-component particle displacements, and the wave based (WB) method. | 133 |

| | | |
|-------------|---|-----|
| Figure 6-14 | In-plane shear strains (γ_{yz}) predicted by the wave-based (WB) method, and the 4-node displacement-based (DB) method with only y-component particle displacements, as percentages of the shear strains calculated using the traditional 4-node DB method. . | 133 |
| Figure 6-15 | Examples of pore pressure time histories obtained during in-situ liquefaction testing in which: a) induced shear strains were not large enough to generate excess pore water pressure, and b) induced shear strains were large enough to generate excess pore water pressure..... | 135 |
| Figure 6-16 | Example of an excess pore water pressure time history obtained during in-situ liquefaction testing: a) prior to frequency-domain filtering, and b) after frequency domain filtering to separate the hydrodynamic and residual portions of the signal. | 137 |
| Figure 6-17 | Mean modulus reduction curve for sands proposed by Seed et al., (1986). | 141 |
| Figure 6-18 | Schematic detailing the liquefaction sensor array and the components of particle motion used to calculate the strain dependent shear wave velocity of the instrumented soil mass..... | 142 |
| Figure 6-19 | Cycle-by-cycle shear wave velocities from an in-situ liquefaction test with relatively moderate induced shear strains ($\gamma \sim 0.009\%$).. | 144 |
| Figure 6-20 | Cycle-by-cycle shear wave velocities from an in-situ liquefaction test with relatively large induced shear strains ($\gamma \sim 0.045\%$)..... | 144 |
| Figure 6-21 | Comparison between the amplitudes and phase of two separate receivers located at the same depth on either side of the base plate centerline during an in-situ dynamic liquefaction test. | 146 |
| Figure 7-1 | Map showing the location of the Wildlife Liquefaction Array (WLA) and the epicenters for the 1981 Westmorland earthquake ($M_w = 5.9$), the 1987 Elmore Ranch earthquake ($M_w = 6.2$), and the 1987 Superstition Hills ($M_w = 6.6$) earthquake (after Holzer et al., 1989)..... | 151 |
| Figure 7-2 | Plan view and cross section of the Wildlife Liquefaction Array (WLA) showing sediment stratigraphy and locations of accelerometers and piezometers installed by USGS personnel (from Bennett et al., 1984): a) plan view, and b) cross section..... | 152 |

| | | |
|-------------|---|-----|
| Figure 7-3 | Plan view of the Wildlife Liquefaction Array (WLA) showing the locations of instrumentation and tests performed by various researchers (from Bennett et al., 1984). | 155 |
| Figure 7-4 | Average sediment properties and test parameters for the soil layers at the Wildlife Liquefaction Array (WLA) (after Bennett et al., 1984)..... | 155 |
| Figure 7-5 | Shear wave velocity profiles obtained from SASW and crosshole tests performed at the Wildlife Liquefaction Array (from Bierschwale and Stokoe, 1984)..... | 159 |
| Figure 7-6 | Range in modulus reduction curves for upper liquefiable layer (A) Wildlife Site specimens tested in the resonant column device (from Haag and Stokoe, 1985). | 164 |
| Figure 7-7 | Range in modulus reduction curves for lower liquefiable layer (B) Wildlife Site specimens tested in the resonant column device (from Haag and Stokoe, 1985). | 164 |
| Figure 7-8 | Comparison between the range in modulus reduction curves for upper (A) and lower (B) liquefiable layer Wildlife Site specimens tested in the resonant column device by Haag and Stokoe (1985). | 165 |
| Figure 7-9 | Comparison between the range in modulus reduction curves for liquefiable Wildlife Site soils and clean sands..... | 165 |
| Figure 7-10 | Dobry's pore pressure generation model (Vucetic and Dobry, 1986) for the Wildlife Site liquefiable soil layer..... | 169 |
| Figure 7-11 | Acceleration (a) and pore pressure time histories (b) recorded at the Wildlife Liquefaction Array during the 1987 Superstition Hills earthquake ($M_w = 6.6$) (from Holzer et al., 1989). | 172 |
| Figure 7-12 | Wildlife Site shear moduli values estimated from the 1987 Elmore Ranch (ER) and Superstition Hills (SH) earthquakes using shear stress-strain loops obtained from surface and downhole accelerometer records (from Zeghal and Elgamal, 1994)..... | 174 |

| | | |
|-------------|--|-----|
| Figure 7-13 | Comparison between the range in modulus reduction curves obtained from resonant column tests performed on liquefiable soils from the Wildlife Site with in-situ estimates obtained from the 1987 Elmore Ranch and Superstition Hills earthquakes. | 176 |
| Figure 7-14 | Relative locations of the 1982 (old) and 2004 (new) Wildlife Liquefaction Array (WLA) instrumentation sites (after http://nees.ucsb.edu). | 178 |
| Figure 7-15 | CPT soundings from the: a) old Wildlife Liquefaction Array (WLA) site, and b) new WLA site including the approximate locations of the upper and lower liquefiable soil layers proposed by Bennett et al. (1984) (raw CPT data from http://nees.ucsb.edu). | 179 |
| Figure 7-16 | Locations of the in-situ soil characterization tests performed, and instrumentation installed, at the 2004 (new) Wildlife Liquefaction Array (WLA) instrumentation site (after http://nees.ucsb.edu). | 181 |
| Figure 7-17 | Tip resistance (q_c), friction ratio, and apparent fines content values obtained from CPT 43 (http://nees.ucsb.edu) at the Wildlife Site. | 189 |
| Figure 7-18 | Deep shear wave velocity profiles obtained from SASW testing and P-S logger measurements (http://nees.ucsb.edu) at the Wildlife Site. | 191 |
| Figure 7-19 | Approximate locations of the three in-situ dynamic liquefaction tests that were carried out at the Wildlife Liquefaction Array (WLA) (after http://nees.ucsb.edu). | 193 |
| Figure 8-1 | Approximate location of the in-situ liquefaction sensor array installed at Test Location C, Wildlife Liquefaction Array (WLA) (after http://nees.ucsb.edu). | 195 |
| Figure 8-2 | Picture of an installed liquefaction sensor array as seen from the ground surface. | 196 |
| Figure 8-3 | Cross-sectional schematic of an embedded liquefaction sensor array. | 196 |

| | | |
|-------------|--|-----|
| Figure 8-4 | Position of the liquefaction sensor array at Test Location C, shown with respect to the general soil layering at the Wildlife Site as proposed by Bennett et al. (1984)..... | 201 |
| Figure 8-5 | Depth range of the liquefaction sensor array at Test Location C, shown with respect to the tip resistance (q_c) and friction ratio (F_r) values obtained from CPT 47 and the upper and lower liquefiable soil layers proposed by Bennett et al. (1984) (raw CPT data from http://nees.ucsb.edu)..... | 203 |
| Figure 8-6 | Cross-sectional schematic of the liquefaction sensor array, the crosshole source rods, and the base plate of T-Rex. | 207 |
| Figure 8-7 | Crosshole waveforms recorded by the: a) horizontal, in-line components (P_h -waves identified on), and b) vertical components (S_{hv} -waves identified on) of sensors No. 2 (near) and No. 1 (far) at Test Location C. | 208 |
| Figure 8-8 | Illustration of how cyclic shear strains are averaged over various numbers of loading cycles..... | 214 |
| Figure 8-9 | Force applied at the ground surface by T-Rex, shear strain induced at the center of the instrumented soil mass, and pore pressure ratios generated at each sensor location during Series 1, loading stage No. 1; Test Location C, Wildlife Liquefaction Array..... | 216 |
| Figure 8-10 | Force applied at the ground surface by T-Rex, shear strain induced at the center of the instrumented soil mass, and pore pressure ratios generated at each sensor location during Series 1, loading stage No. 2; Test Location C, Wildlife Liquefaction Array..... | 219 |
| Figure 8-11 | Force applied at the ground surface by T-Rex, shear strain induced at the center of the instrumented soil mass, and pore pressure ratios generated at each sensor location during Series 1, loading stage No. 3; Test Location C, Wildlife Liquefaction Array..... | 220 |

| | | |
|-------------|--|-----|
| Figure 8-12 | Force applied at the ground surface by T-Rex, shear strain induced at the center of the instrumented soil mass, and pore pressure ratios generated at each sensor location during Series 1, loading stage No. 4; Test Location C, Wildlife Liquefaction Array..... | 222 |
| Figure 8-13 | Force applied at the ground surface by T-Rex, shear strain induced at the center of the instrumented soil mass, and pore pressure ratios generated at each sensor location during Series 1, loading stage No. 5; Test Location C, Wildlife Liquefaction Array..... | 224 |
| Figure 8-14 | Force applied at the ground surface by T-Rex, shear strain induced at the center of the instrumented soil mass, and pore pressure ratios generated at each sensor location during Series 1, loading stage No. 6; Test Location C, Wildlife Liquefaction Array..... | 225 |
| Figure 8-15 | Force applied at the ground surface by T-Rex, shear strain induced at the center of the instrumented soil mass, and pore pressure ratios generated at each sensor location during Series 1, loading stage No. 7; Test Location C, Wildlife Liquefaction Array..... | 227 |
| Figure 8-16 | Pore pressure ratios generated at each sensor location during Series 1, loading stage No. 7; Test Location C, Wildlife Liquefaction Array..... | 228 |
| Figure 8-17 | Force applied at the ground surface by T-Rex, shear strain induced at the center of the instrumented soil mass, and pore pressure ratios generated at each sensor location during Series 1, loading stage No. 8; Test Location C, Wildlife Liquefaction Array..... | 230 |
| Figure 8-18 | Pore pressure ratios generated at each sensor location during Series 1, loading stage No. 8; Test Location C, WLA..... | 232 |
| Figure 8-19 | Pore pressure generation curves obtained from in-situ liquefaction tests conducted during staged dynamic loading Series 1 at Test Location C, Wildlife Liquefaction Array..... | 233 |

| | | |
|-------------|--|-----|
| Figure 8-20 | Comparison between Dobry's pore pressure generation model (Vucetic and Dobry, 1986) and pore pressure generation curves obtained from in-situ liquefaction tests conducted during staged dynamic loading Series 1 at Test Location C, Wildlife Liquefaction Array. | 234 |
| Figure 8-21 | Full pore pressure ratio scale comparison between Dobry's pore pressure generation model (Vucetic and Dobry, 1986) and pore pressure generation curves obtained from in-situ liquefaction tests conducted during staged dynamic loading Series 1 at Test Location C, Wildlife Liquefaction Array. | 236 |
| Figure 8-22 | Cycle-by-cycle shear wave velocities from loading stage No. 1 ($\gamma \sim 0.0010\%$) of staged dynamic loading Series 1 at Test Location C, Wildlife Liquefaction Array. | 238 |
| Figure 8-23 | Cycle-by-cycle shear wave velocities from loading stage No. 7 ($\gamma \sim 0.0234\%$) of staged dynamic loading Series 1 at Test Location C, Wildlife Liquefaction Array. | 238 |
| Figure 8-24 | Cycle-by-cycle shear wave velocities from loading stage No. 8 ($\gamma \sim 0.0451\%$) of staged dynamic loading Series 1 at Test Location C, Wildlife Liquefaction Array. | 240 |
| Figure 8-25 | Shear modulus values (G) calculated from the data collected during staged dynamic loading Series 1 at Test Location C, Wildlife Liquefaction Array. | 243 |
| Figure 8-26 | Normalized shear modulus (G/G_{\max}) – $\log \gamma$ relationship calculated from the data collected during staged dynamic loading Series 1 at Test Location C, Wildlife Liquefaction Array. | 244 |
| Figure 8-27 | Normalized shear modulus values (G/G_{\max}) resulting from the combined effects of modulus nonlinearity and modulus degradation due to excess pore water pressure generation during loading stage No. 8 of Series 1 at Test Location C, Wildlife Liquefaction Array. | 246 |
| Figure 8-28 | Illustration of the process used to try to predict the 100-cycle normalized shear modulus value obtained during loading stage No.8 from the 10-cycle normalized shear modulus value obtained during loading stage No. 8. | 247 |

| | | |
|-------------|---|-----|
| Figure 8-29 | Pore pressure generation curves and nonlinear soil shear modulus values obtained during Series 1 staged dynamic loading at Test Location C, Wildlife Liquefaction Array (WLA). | 251 |
| Figure 8-30 | Force applied at the ground surface by T-Rex, shear strain induced at the center of the instrumented soil mass, and pore pressure ratios generated at each sensor location during Series 2, loading stage No. 9; Test Location C, Wildlife Liquefaction Array..... | 256 |
| Figure 8-31 | Force applied at the ground surface by T-Rex, shear strain induced at the center of the instrumented soil mass, and pore pressure ratios generated at each sensor location during Series 2, loading stage No. 10; Test Location C, Wildlife Liquefaction Array..... | 258 |
| Figure 8-32 | Force applied at the ground surface by T-Rex, shear strain induced at the center of the instrumented soil mass, and pore pressure ratios generated at each sensor location during Series 2, loading stage No. 11; Test Location C, Wildlife Liquefaction Array..... | 260 |
| Figure 8-33 | Force applied at the ground surface by T-Rex, shear strain induced at the center of the instrumented soil mass, and pore pressure ratios generated at each sensor location during Series 2, loading stage No. 12; Test Location C, Wildlife Liquefaction Array..... | 262 |
| Figure 8-34 | Force applied at the ground surface by T-Rex, shear strain induced at the center of the instrumented soil mass, and pore pressure ratios generated at each sensor location during Series 2, loading stage No. 13; Test Location C, Wildlife Liquefaction Array..... | 263 |
| Figure 8-35 | Force applied at the ground surface by T-Rex, shear strain induced at the center of the instrumented soil mass, and pore pressure ratios generated at each sensor location during Series 2, loading stage No. 14; Test Location C, Wildlife Liquefaction Array..... | 265 |

| | | |
|-------------|---|-----|
| Figure 8-36 | Force applied at the ground surface by T-Rex, shear strain induced at the center of the instrumented soil mass, and pore pressure ratios generated at each sensor location during Series 2, loading stage No. 15; Test Location C, Wildlife Liquefaction Array..... | 266 |
| Figure 8-37 | Pore pressure ratios generated at each sensor location during Series 2, loading stage No. 15; Test Location C, Wildlife Liquefaction Array. | 268 |
| Figure 8-38 | Force applied at the ground surface by T-Rex, shear strain induced at the center of the instrumented soil mass, and pore pressure ratios generated at each sensor location during Series 2, loading stage No. 16; Test Location C, Wildlife Liquefaction Array..... | 270 |
| Figure 8-39 | Pore pressure ratios generated at each sensor location during Series 2, loading stage No. 16; Test Location C, Wildlife Liquefaction Array. | 272 |
| Figure 8-40 | Horizontal, in-line component (y-component) particle displacements recorded at each of the liquefaction sensor location during Series 2, loading stage No. 16; Test Location C, Wildlife Liquefaction Array..... | 274 |
| Figure 8-41 | Pore pressure generation curves obtained from in-situ liquefaction tests conducted during staged dynamic loading Series 2 at Test Location C, Wildlife Liquefaction Array. | 276 |
| Figure 8-42 | Comparison between Dobry's pore pressure generation model (Vucetic and Dobry, 1986) and pore pressure generation curves obtained from in-situ liquefaction tests conducted during staged dynamic loading Series 2 at Test Location C, Wildlife Liquefaction Array. | 277 |
| Figure 8-43 | Full pore pressure ratio scale comparison between Dobry's pore pressure generation model (Vucetic and Dobry, 1986) and pore pressure generation curves obtained from in-situ liquefaction tests conducted during staged dynamic loading Series 2 at Test Location C, Wildlife Liquefaction Array..... | 278 |

| | | |
|-------------|--|-----|
| Figure 8-44 | Cycle-by-cycle shear wave velocities from loading stage No. 9 ($\gamma \sim 0.0012\%$) of staged dynamic loading Series 2 at Test Location C, Wildlife Liquefaction Array. | 280 |
| Figure 8-45 | Cycle-by-cycle shear wave velocities from loading stage No. 15 ($\gamma \sim 0.0287\%$) of staged dynamic loading Series 2 at Test Location C, Wildlife Liquefaction Array. | 280 |
| Figure 8-46 | Cycle-by-cycle shear wave velocities from Load No. 16 ($\gamma \sim 0.0754\%$) of staged dynamic loading Series 2 at Test Location C, Wildlife Liquefaction Array. | 283 |
| Figure 8-47 | Shear modulus values (G) calculated from the data collected during staged dynamic loading Series 2 at Test Location C, Wildlife Liquefaction Array. | 285 |
| Figure 8-48 | Normalized shear modulus (G/G_{max}) – $\log \gamma$ relationship calculated from the data collected during staged dynamic loading Series 1 at Test Location C, Wildlife Liquefaction Array. | 287 |
| Figure 8-49 | Normalized shear modulus values (G/G_{max}) resulting from the combined effects of modulus nonlinearity and modulus degradation due to excess pore water pressure generation during loading stage No. 16 of Series 2 at Test Location C, Wildlife Liquefaction Array. | 289 |
| Figure 8-50 | Illustration of the process used to try to predict the 100-cycle normalized shear modulus value obtained during loading stage No.16 from the 10-cycle normalized shear modulus value obtained during loading stage No. 16. | 290 |
| Figure 8-51 | Pore pressure generation curves and nonlinear soil shear modulus values obtained during Series 2 staged dynamic loading at Test Location C, Wildlife Liquefaction Array (WLA). | 293 |
| Figure 8-52 | Comparison of the pore pressure generation curves and nonlinear soil shear modulus values obtained during Series 1 and Series 2 staged dynamic loading at Test Location C, Wildlife Liquefaction Array (WLA). | 296 |

| | | |
|------------|---|-----|
| Figure 9-1 | Approximate location of the in-situ liquefaction sensor array installed at Test Location B, Wildlife Liquefaction Array (WLA) (after http://nees.ucsb.edu)..... | 300 |
| Figure 9-2 | Picture of a liquefaction sensor array as seen from the ground surface. | 301 |
| Figure 9-3 | Cross-sectional schematic of an embedded liquefaction sensor array..... | 301 |
| Figure 9-4 | Position of the liquefaction sensor array at Test Location B, shown with respect to the general soil layering at the Wildlife Site as proposed by Bennett et al. (1984)..... | 305 |
| Figure 9-5 | Depth range of the liquefaction sensor array at Test Location B, shown with respect to the tip resistance (q_c) and friction ratio (F_r) values obtained from CPT 5Cg and the upper and lower liquefiable soil layers proposed by Bennett et al. (1984) (raw CPT data from http://nees.ucsb.edu)..... | 308 |
| Figure 9-6 | Cross-sectional schematic of the liquefaction sensor array, crosshole source rods, and the base plate of T-Rex at Test Location B. | 311 |
| Figure 9-7 | Crosshole waveforms recorded by the: a) horizontal, in-line components (P_h -waves identified on), and b) vertical components (S_{hv} -waves identified on) of sensors No. 3 (near) and No. 4 (far) at Test Location B. | 312 |
| Figure 9-8 | Force applied at the ground surface by T-Rex, shear strain induced at the center of the instrumented soil mass, and pore pressure ratios generated at each sensor location during Series 1, loading stage No. 1; Test Location B, Wildlife Liquefaction Array..... | 321 |
| Figure 9-9 | Force applied at the ground surface by T-Rex, shear strain induced at the center of the instrumented soil mass, and pore pressure ratios generated at each sensor location during Series 1, dynamic Load No. 5; Test Location B, Wildlife Liquefaction Array..... | 323 |

| | | |
|-------------|---|-----|
| Figure 9-10 | Force applied at the ground surface by T-Rex, shear strain induced at the center of the instrumented soil mass, and pore pressure ratios generated at each sensor location during Series 1, loading stage No. 6; Test Location B, Wildlife Liquefaction Array..... | 325 |
| Figure 9-11 | Force applied at the ground surface by T-Rex, shear strain induced at the center of the instrumented soil mass, and pore pressure ratios generated at each sensor location during Series 1, loading stage No. 7; Test Location B, Wildlife Liquefaction Array..... | 327 |
| Figure 9-12 | Force applied at the ground surface by T-Rex, shear strain induced at the center of the instrumented soil mass, and pore pressure ratios generated at each sensor location during Series 1, loading stage No. 8; Test Location B, Wildlife Liquefaction Array..... | 328 |
| Figure 9-13 | Force applied at the ground surface by T-Rex, shear strain induced at the center of the instrumented soil mass, and pore pressure ratios generated at each sensor location during Series 1, loading stage No. 9; Test Location B, Wildlife Liquefaction Array..... | 330 |
| Figure 9-14 | Force applied at the ground surface by T-Rex, shear strain induced at the center of the instrumented soil mass, and pore pressure ratios generated at each sensor location during Series 1, loading stage No. 10; Test Location B, Wildlife Liquefaction Array..... | 331 |
| Figure 9-15 | Pore pressure ratios generated at each sensor location during Series 1, loading stage No. 10; Test Location B, Wildlife Liquefaction Array..... | 333 |
| Figure 9-16 | Force applied at the ground surface by T-Rex, shear strain induced at the center of the instrumented soil mass, and pore pressure ratios generated at each sensor location during Series 1, loading stage No. 11; Test Location B, Wildlife Liquefaction Array..... | 335 |
| Figure 9-17 | Pore pressure ratios generated at each sensor location during Series 1, loading stage No. 11; Test Location B, Wildlife Liquefaction Array..... | 337 |

| | | |
|-------------|--|-----|
| Figure 9-18 | Horizontal, in-line component (y-component) particle displacements recorded at each of the liquefaction sensor location during Series 1, dynamic Load No. 11; Test Location B, Wildlife Liquefaction Array..... | 338 |
| Figure 9-19 | Pore pressure generation curves obtained from in-situ liquefaction tests conducted during staged dynamic loading Series 1 at Test Location B, Wildlife Liquefaction Array. | 340 |
| Figure 9-20 | Comparison between Dobry's pore pressure generation model (Vucetic and Dobry, 1986) and pore pressure generation curves obtained from in-situ liquefaction tests conducted during staged dynamic loading Series 1 at Test Location B, Wildlife Liquefaction Array. | 341 |
| Figure 9-21 | Full pore pressure ratio scale comparison between Dobry's pore pressure generation model (Vucetic and Dobry, 1986) and pore pressure generation curves obtained from in-situ liquefaction tests conducted during staged dynamic loading Series 1 at Test Location B, Wildlife Liquefaction Array. | 342 |
| Figure 9-22 | Force applied at the ground surface by T-Rex, shear strain induced at the center of the instrumented soil mass, and pore pressure ratios generated at each sensor location during Series 2, dynamic Load No. 12; Test Location B, Wildlife Liquefaction Array..... | 346 |
| Figure 9-23 | Force applied at the ground surface by T-Rex, shear strain induced at the center of the instrumented soil mass, and pore pressure ratios generated at each sensor location during Series 2, loading stage No. 13; Test Location B, Wildlife Liquefaction Array..... | 349 |
| Figure 9-24 | Force applied at the ground surface by T-Rex, shear strain induced at the center of the instrumented soil mass, and pore pressure ratios generated at each sensor location during Series 2, loading stage No. 14; Test Location B, Wildlife Liquefaction Array..... | 351 |

| | | |
|-------------|---|-----|
| Figure 9-25 | Force applied at the ground surface by T-Rex, shear strain induced at the center of the instrumented soil mass, and pore pressure ratios generated at each sensor location during Series 2, loading stage No. 15; Test Location B, Wildlife Liquefaction Array..... | 353 |
| Figure 9-26 | Force applied at the ground surface by T-Rex, shear strain induced at the center of the instrumented soil mass, and pore pressure ratios generated at each sensor location during Series 2, loading stage No. 16; Test Location B, Wildlife Liquefaction Array..... | 354 |
| Figure 9-27 | Force applied at the ground surface by T-Rex, shear strain induced at the center of the instrumented soil mass, and pore pressure ratios generated at each sensor location during Series 2, loading stage No. 17; Test Location B, Wildlife Liquefaction Array..... | 356 |
| Figure 9-28 | Force applied at the ground surface by T-Rex, shear strain induced at the center of the instrumented soil mass, and pore pressure ratios generated at each sensor location during Series 2, loading stage No. 18; Test Location B, Wildlife Liquefaction Array..... | 357 |
| Figure 9-29 | Pore pressure ratios generated at each sensor location during Series 2, loading stage No. 18; Test Location B, Wildlife Liquefaction Array..... | 359 |
| Figure 9-30 | Horizontal, in-line component (y-component) particle displacements recorded at each of the liquefaction sensor locations during Series 2, loading stage No. 18; Test Location B, Wildlife Liquefaction Array..... | 360 |
| Figure 9-31 | Force applied at the ground surface by T-Rex, shear strain induced at the center of the instrumented soil mass, and pore pressure ratios generated at each sensor location during Series 2, loading stage No. 19; Test Location B, Wildlife Liquefaction Array..... | 362 |
| Figure 9-32 | Pore pressure ratios generated at each sensor location during Series 2, loading stage No. 19; Test Location B, Wildlife Liquefaction Array..... | 364 |

| | | |
|-------------|--|-----|
| Figure 9-33 | Horizontal, in-line component (y-component) particle displacements recorded at each of the liquefaction sensor locations during Series 2, loading stage No. 19; Test Location B, Wildlife Liquefaction Array..... | 365 |
| Figure 9-34 | Pore pressure generation curves obtained from in-situ liquefaction tests conducted during staged dynamic loading Series 2 at Test Location B, Wildlife Liquefaction Array. | 366 |
| Figure 9-35 | Comparison between Dobry's pore pressure generation model (Vucetic and Dobry, 1986) and pore pressure generation curves obtained from in-situ liquefaction tests conducted during staged dynamic loading Series 2 at Test Location B, Wildlife Liquefaction Array. | 368 |
| Figure 9-36 | Full pore pressure ratio scale comparison between Dobry's pore pressure generation model (Vucetic and Dobry, 1986) and pore pressure generation curves obtained from in-situ liquefaction tests conducted during staged dynamic loading Series 2 at Test Location B, Wildlife Liquefaction Array. | 369 |
| Figure 9-37 | Comparison of the pore pressure generation curves obtained during Series 1 and Series 2 staged dynamic loading at Test Location B, Wildlife Liquefaction Array (WLA). | 371 |
| Figure 10-1 | Approximate location of the in-situ liquefaction sensor array installed at Test Location A, Wildlife Liquefaction Array (WLA) (after http://nees.ucsb.edu). | 374 |
| Figure 10-2 | Picture of a liquefaction sensor array as seen from the ground surface. | 375 |
| Figure 10-3 | Cross-sectional schematic of an embedded liquefaction sensor array..... | 375 |
| Figure 10-4 | Position of the liquefaction sensor array at Test Location A, shown with respect to the general soil layering at the Wildlife Site as proposed by Bennett et al. (1984)..... | 379 |

| | | |
|--------------|--|-----|
| Figure 10-5 | Depth range of the liquefaction sensor array at Test Location A, shown with respect to the tip resistance (q_c) and friction ratio (F_r) values obtained from CPT 43 and the upper and lower liquefiable soil layers proposed by Bennett et al. (1984) (raw CPT data from http://nees.ucsb.edu)..... | 381 |
| Figure 10-6 | Cross-sectional schematic of the liquefaction sensor array, crosshole source rods, and the base plate of T-Rex at Test Location A. | 385 |
| Figure 10-7 | Typical crosshole waveforms recorded by the: a) horizontal, in-line components (P-waves identified on), and b) vertical components (S_{hv} -waves identified on) of sensors No. 2 (near) and No. 1 (far) at Test Location A, Wildlife Liquefaction Array (WLA)..... | 388 |
| Figure 10-8 | Typical crosshole waveforms recorded by the: a) horizontal, in-line components (P-waves identified on), and b) vertical components (S_{hv} -waves identified on) of sensors No. 3 (near) and No. 4 (far) at Test Location A, Wildlife Liquefaction Array (WLA)..... | 393 |
| Figure 10-9 | Relative locations of the liquefaction sensor array at Test Location A and the area where a separate crosshole P-wave velocity survey was conducted; Wildlife Liquefaction Array (WLA) (after http://nees.ucsb.edu)..... | 399 |
| Figure 10-10 | Waterfall plot of waveforms recorded by the horizontal, in-line component (P_h -waves identified on) of a sensor during crosshole tests conducted approximately 6 ft south of the liquefaction sensor array at Test Location A, Wildlife Liquefaction Array (WLA)..... | 400 |
| Figure 10-11 | P_h -wave velocities obtained from crosshole tests between sensors in the liquefaction sensor array (August 10-11, 2005) and from a separate set of crosshole tests (August 19, 2005) conducted approximately 6 ft south of the liquefaction sensor array at Test Location A, Wildlife Liquefaction Array (WLA). .. | 401 |

| | |
|--|-----|
| Figure 10-12 Force applied at the ground surface by T-Rex, shear strain induced at the center of the instrumented soil mass, and pore pressure ratios generated at each sensor location during Series 1, loading stage No. 4; Test Location A, Wildlife Liquefaction Array..... | 411 |
| Figure 10-13 Force applied at the ground surface by T-Rex, shear strain induced at the center of the instrumented soil mass, and pore pressure ratios generated at each sensor location during Series 1, loading stage No. 6; Test Location A, Wildlife Liquefaction Array..... | 412 |
| Figure 10-14 Force applied at the ground surface by T-Rex, shear strain induced at the center of the instrumented soil mass, and pore pressure ratios generated at each sensor location during Series 1, loading stage No. 11; Test Location A, Wildlife Liquefaction Array..... | 414 |
| Figure 10-15 Force applied at the ground surface by T-Rex, shear strain induced at the center of the instrumented soil mass, and pore pressure ratios generated at each sensor location during Series 1, loading stage No. 15; Test Location A, Wildlife Liquefaction Array..... | 415 |
| Figure 10-16 Force applied at the ground surface by T-Rex, shear strain induced at the center of the instrumented soil mass, and pore pressure ratios generated at each sensor location during Series 1, loading stage No. 16; Test Location A, Wildlife Liquefaction Array..... | 417 |
| Figure 10-17 Pore pressure ratios generated at each sensor location during Series 1, loading stage No. 16; Test Location A, Wildlife Liquefaction Array..... | 418 |
| Figure 10-18 Force applied at the ground surface by T-Rex, shear strain induced at the center of the instrumented soil mass, and pore pressure ratios generated at each sensor location during Series 1, loading stage No. 17; Test Location A, Wildlife Liquefaction Array..... | 420 |
| Figure 10-19 Pore pressure ratios generated at each sensor location during Series 1, loading stage No. 17; Test Location A, Wildlife Liquefaction Array..... | 422 |

| | | |
|--------------|--|-----|
| Figure 10-20 | Pore pressure generation curves obtained from in-situ liquefaction tests conducted during staged dynamic loading Series 1 at Test Location A, Wildlife Liquefaction Array..... | 424 |
| Figure 10-21 | Comparison between Dobry's pore pressure generation model (Vucetic and Dobry, 1986) and pore pressure generation curves obtained from in-situ liquefaction tests conducted during staged dynamic loading Series 1 at Test Location A, Wildlife Liquefaction Array..... | 425 |
| Figure 10-22 | Full pore pressure ratio scale comparison between Dobry's pore pressure generation model (Vucetic and Dobry, 1986) and pore pressure generation curves obtained from in-situ liquefaction tests conducted during staged dynamic loading Series 1 at Test Location A, Wildlife Liquefaction Array. | 427 |
| Figure 10-23 | Force applied at the ground surface by T-Rex, shear strain induced at the center of the instrumented soil mass, and pore pressure ratios generated at each sensor location during Series 2, loading stage No. 23; Test Location A, Wildlife Liquefaction Array. | 431 |
| Figure 10-24 | Force applied at the ground surface by T-Rex, shear strain induced at the center of the instrumented soil mass, and pore pressure ratios generated at each sensor location during Series 2, loading stage No. 24; Test Location A, Wildlife Liquefaction Array. | 433 |
| Figure 10-25 | Force applied at the ground surface by T-Rex, shear strain induced at the center of the instrumented soil mass, and pore pressure ratios generated at each sensor location during Series 2, loading stage No. 26; Test Location A, Wildlife Liquefaction Array. | 434 |
| Figure 10-26 | Force applied at the ground surface by T-Rex, shear strain induced at the center of the instrumented soil mass, and pore pressure ratios generated at each sensor location during Series 2, loading stage No. 27; Test Location A, Wildlife Liquefaction Array. | 436 |
| Figure 10-27 | Pore pressure ratios generated at each sensor location during Series 2, loading stage No. 27; Test Location A, Wildlife Liquefaction Array..... | 438 |

| | | |
|--------------|---|-----|
| Figure 10-28 | Horizontal, in-line component (y-component) particle displacements recorded at each of the liquefaction sensor locations during Series 2, loading stage No. 27; Test Location B, Wildlife Liquefaction Array..... | 439 |
| Figure 10-29 | Force applied at the ground surface by T-Rex, shear strain induced at the center of the instrumented soil mass, and pore pressure ratios generated at each sensor location during Series 2, loading stage No. 30; Test Location A, Wildlife Liquefaction Array..... | 440 |
| Figure 10-30 | Pore pressure ratios generated at each sensor location during Series 2, loading stage No. 30; Test Location A, Wildlife Liquefaction Array..... | 442 |
| Figure 10-31 | Pore pressure generation curves obtained from in-situ liquefaction tests conducted during staged dynamic loading Series 1 at Test Location A, Wildlife Liquefaction Array..... | 443 |
| Figure 10-32 | Comparison between Dobry's pore pressure generation model (Vucetic and Dobry, 1986) and pore pressure generation curves obtained from in-situ liquefaction tests conducted during staged dynamic loading Series 2 at Test Location A, Wildlife Liquefaction Array..... | 444 |
| Figure 10-33 | Full pore pressure ratio scale comparison between Dobry's pore pressure generation model (Vucetic and Dobry, 1986) and pore pressure generation curves obtained from in-situ liquefaction tests conducted during staged dynamic loading Series 2 at Test Location A, Wildlife Liquefaction Array..... | 446 |
| Figure 10-34 | Comparison of the pore pressure generation curves obtained during Series 1 and Series 2 staged dynamic loading at Test Location A, Wildlife Liquefaction Array (WLA). | 447 |
| Figure 11-1 | Approximate locations of the three in-situ dynamic liquefaction tests that were carried out at the Wildlife Liquefaction Array (WLA) (after http://nees.ucsb.edu)..... | 451 |
| Figure 11-2 | Comparison of the pore pressure generation curves obtained from staged loading Series 1 in-situ liquefaction tests at Test Locations C, B and A, Wildlife Liquefaction Array (WLA)..... | 453 |

| | | |
|-------------|--|-----|
| Figure 11-3 | Comparison between Dobry's pore pressure generation model (Vucetic and Dobry, 1986) and the pore pressure generation curves obtained from staged loading Series 1 in-situ liquefaction tests at Test Locations C, B and A, Wildlife Liquefaction Array. . | 455 |
| Figure 11-4 | Comparison of the pore pressure generation curves obtained from staged loading Series 2 in-situ liquefaction tests at Test Locations C, B and A, Wildlife Liquefaction Array (WLA). | 457 |
| Figure 11-5 | Comparison between Dobry's pore pressure generation model (Vucetic and Dobry, 1986) and the pore pressure generation curves obtained from staged loading Series 2 in-situ liquefaction tests at Test Locations C, B and A, Wildlife Liquefaction Array. . | 459 |
| Figure 11-6 | Depth ranges of the liquefaction sensor arrays at Test Locations A, B and C, shown with respect to the general soil layering at the Wildlife Site, as proposed by Bennett et al. (1984). | 462 |
| Figure 11-7 | Depth range of the liquefaction sensor arrays at Test Locations A, B and C, shown with respect to the tip resistance (q_c) and friction ratio (F_r) values obtained from the closest CPT sounding at each test location, and the upper and lower liquefiable soil layers proposed by Bennett et al. (1984) (raw CPT data from http://nees.ucsb.edu)..... | 464 |
| Figure 11-8 | Comparison between shear wave and P-wave velocities obtained from performing crosshole tests between in-situ liquefaction sensors in the arrays installed at Test Locations A, B and C, Wildlife Liquefaction Array (WLA). | 466 |

List of Tables

| | | |
|-----------|---|-----|
| Table 2-1 | Select summary of some previous in situ liquefaction measurements (from Chang, 2002) | 35 |
| Table 4-1 | VXI dynamic signal analyzer recording channels assigned to the instrumentation components of each in-situ liquefaction sensor | 57 |
| Table 4-2 | Tilt calibration results for the 3D-MEMS accelerometer installed in each in-situ liquefaction sensor | 60 |
| Table 4-3 | Dynamic amplitude calibration factors for the 3D-MEMS accelerometer installed in each in-situ liquefaction sensor | 66 |
| Table 4-4 | Calibration results for EPX-VO2-25P miniature PPT #34 | 74 |
| Table 4-5 | Mean slope values and associated standard deviations for the miniature pore pressure transducer (PPT) installed in each liquefaction sensor..... | 75 |
| Table 4-6 | Calibration results for the Druck PDCR 35/D pressure transducer.. | 77 |
| Table 4-7 | Input or output associated with each colored conductor pair of the liquefaction sensor cable | 82 |
| Table 6-1 | Tabulated values of in-plane shear strains predicted using the 4-node displacement-based (DB) method, the 4-node DB method without vertical particle motions, the 2-node DB method, and the wave-based (WB) method; Wildlife Liquefaction Array (WLA) Test Location C | 128 |
| Table 7-1 | Summary of the field tests performed at the Wildlife Site by Bennett et al. (1984)..... | 154 |
| Table 7-2 | Summary of the grain size characteristics for all of the samples obtained from the upper (B1) and lower (B2) units of the liquefiable layer at the Wildlife Site as reported by Bennett et al. (1984) | 157 |

| | | |
|-----------|---|-----|
| Table 7-3 | Summary of the soil properties of specimens from upper (A) and lower (B) portions of the liquefiable layer at the Wildlife Site that were tested in consolidated-drained (CU) triaxial tests by Haag and Stokoe (1985)..... | 161 |
| Table 7-4 | Summary of the soil properties of specimens from upper (A) and lower (B) portions of the liquefiable layer at the Wildlife Site that were tested in the resonant column device by Haag and Stokoe (1985)..... | 163 |
| Table 7-5 | Summary of the numbers and types of laboratory tests conducted on specimens from the Wildlife Site liquefiable soil layer at Rensselaer Polytechnic Institute (RPI) and Woodward-Clyde (WC) Laboratory (after Vucetic and Dobry, 1986)..... | 167 |
| Table 7-6 | Summary of the soil properties determined from SPT split-spoon samples obtained from the upper liquefiable layer at the 2004 (new) Wildlife Liquefaction Array (WLA) (data from http://nees.ucsb.edu) | 182 |
| Table 7-7 | Summary of the soil properties determined from SPT split-spoon samples obtained from the lower liquefiable layer at the 2004 (new) Wildlife Liquefaction Array (WLA) (data from http://nees.ucsb.edu) | 184 |
| Table 7-8 | Summary of the grain size characteristics obtained by various researchers for soil samples obtained from the upper liquefiable layer at the 1982 (old) and 2004 (new) WLA instrumentation sites..... | 186 |
| Table 7-9 | Summary of the grain size characteristics obtained by various researchers for soil samples obtained from the lower liquefiable layer at the 1982 (old) and 2004 (new) WLA instrumentation sites..... | 187 |
| Table 8-1 | Coordinates and tilt angles for the sensors installed in the liquefaction sensor array at Test Location C, Wildlife Liquefaction Array (WLA) | 198 |

| | | |
|------------|---|-----|
| Table 8-2 | Estimates for the effective overburden stress, increase in vertical stress due to the vibroseis base plate load, and total vertical effective stress at the approximate depth of each sensor in the liquefaction sensor array at Test Location C, Wildlife Liquefaction Array (WLA) | 205 |
| Table 8-3 | Results from three separate sets of crosshole tests performed between the top (sensors No. 3 and No. 4) and bottom (sensors No. 2 and No. 1) sensor pairs in the liquefaction sensor array at Test Location C, Wildlife Liquefaction Array (WLA) | 210 |
| Table 8-4 | Details of the Series 1 staged dynamic loading sequence conducted at Test Location C, Wildlife Liquefaction Array (WLA) | 213 |
| Table 8-5 | Pore pressure ratios and average shear strains at the center of the liquefaction sensor array for different numbers of loading cycles; Series 1, Test Location C, Wildlife Liquefaction Array (WLA) ... | 217 |
| Table 8-6 | Average 100-cycle shear strains, shear wave velocities and shear moduli obtained from loading stages No. 1 through No. 7 of staged loading Series 1 at Test Location C, Wildlife Liquefaction Array..... | 240 |
| Table 8-7 | Shear strains, shear wave velocities and shear moduli obtained from averaging over various numbers of cycles during loading stage No. 8 of staged loading Series 1 at Test Location C, Wildlife Liquefaction Array | 241 |
| Table 8-8 | Measure G/G_{\max} values and predicted G/G_{\max} values obtained from taking into account the combined effects of modulus degradation and nonlinearity after 20, 50, 100, 150 and 200 cycles of loading during stage No. 8 of staged loading Series 1 at Test Location C, Wildlife Liquefaction Array | 250 |
| Table 8-9 | Details of the Series 2 staged dynamic loading sequence conducted at Test Location C, Wildlife Liquefaction Array (WLA) | 253 |
| Table 8-10 | Pore pressure ratios and average shear strains at the center of the liquefaction sensor array for different numbers of loading cycles; Series 2, Test Location C, Wildlife Liquefaction Array | 257 |

| | | |
|------------|---|-----|
| Table 8-11 | Average 100-cycle shear strains, shear wave velocities and shear moduli obtained from loading stages No. 9 through No. 15 of staged loading Series 2 at Test Location C, Wildlife Liquefaction Array..... | 282 |
| Table 8-12 | Shear strains, shear wave velocities and shear moduli obtained from averaging over various numbers of cycles during loading stage No. 16 of staged loading Series 2 at Test Location C, Wildlife Liquefaction Array..... | 284 |
| Table 8-13 | Measure G/G_{\max} values and predicted G/G_{\max} values obtained from taking into account the combined effects of modulus degradation and nonlinearity after 20, 50 and 100 cycles of loading during stage No. 16 of staged loading Series 2 at Test Location C, Wildlife Liquefaction Array..... | 292 |
| Table 9-1 | Coordinates and tilt angles for the sensors installed in the liquefaction sensor array at Test Location B, Wildlife Liquefaction Array (WLA) | 303 |
| Table 9-2 | Estimates for the effective overburden stress, increase in vertical stress due to the vibroseis base plate load, and total vertical effective stress at the approximate depth of each sensor in the liquefaction sensor array at Test Location B, Wildlife Liquefaction Array (WLA) | 309 |
| Table 9-3 | Results from three separate sets of Crosshole tests performed between the top (sensors No. 3 and No. 4) and bottom (sensors No. 2 and No. 1) sensor pairs in the liquefaction sensor array at Test Location B, Wildlife Liquefaction Array (WLA) | 314 |
| Table 9-4 | Details of the Series 1 staged dynamic loading sequence conducted at Test Location B, Wildlife Liquefaction Array (WLA) | 318 |
| Table 9-5 | Pore pressure ratios and average shear strains at the center of the liquefaction sensor array for different numbers of loading cycles; Series 1, Test Location B, Wildlife Liquefaction Array | 322 |
| Table 9-6 | Details of the Series 2 staged dynamic loading sequence conducted at Test Location B, Wildlife Liquefaction Array (WLA) | 344 |

| | | |
|------------|---|-----|
| Table 9-7 | Pore pressure ratios and average shear strains at the center of the liquefaction sensor array for different numbers of loading cycles; Series 2, Test Location B, Wildlife Liquefaction Array | 348 |
| Table 10-1 | Coordinates and tilt angles for the sensors installed in the liquefaction sensor array at Test Location A, Wildlife Liquefaction Array (WLA) | 377 |
| Table 10-2 | Estimates for the effective overburden stress, increase in vertical stress due to the vibroseis base plate load, and total vertical effective stress at the approximate depth of each sensor in the liquefaction sensor array at Test Location B, Wildlife Liquefaction Array (WLA) | 383 |
| Table 10-3 | P_h -wave velocity results from three separate sets of crosshole tests performed between the bottom sensor pair (sensors No. 2 and No. 1) in the liquefaction sensor array at Test Location A, Wildlife Liquefaction Array (WLA) | 390 |
| Table 10-4 | Shear wave velocity results from three separate sets of crosshole tests performed between the bottom sensor pair (sensors No. 2 and No. 1) in the liquefaction sensor array at Test Location A, Wildlife Liquefaction Array (WLA) | 392 |
| Table 10-5 | P_h -wave velocity results from three separate sets of crosshole tests performed between the top sensor pair (sensors No. 3 and No. 4) in the liquefaction sensor array at Test Location A, Wildlife Liquefaction Array (WLA) | 395 |
| Table 10-6 | Shear wave velocity results from three separate sets of crosshole tests performed between the top sensor pair (sensors No. 3 and No. 4) in the liquefaction sensor array at Test Location A, Wildlife Liquefaction Array (WLA) | 397 |
| Table 10-7 | P_h -wave velocities obtained from crosshole tests conducted approximately 6 ft south of the liquefaction sensor array at Test Location A, Wildlife Liquefaction Array (WLA) | 403 |
| Table 10-8 | Details of the Series 1 staged dynamic loading sequence conducted at Test Location A, Wildlife Liquefaction Array (WLA) | 406 |

| | | |
|-------------|--|-----|
| Table 10-9 | Pore pressure ratios and average shear strains at the center of the liquefaction sensor array for different numbers of loading cycles; Series 1, loading stages No. 1 through No. 11, Test Location A, Wildlife Liquefaction Array | 409 |
| Table 10-10 | Pore pressure ratios and average shear strains at the center of the liquefaction sensor array for different numbers of loading cycles; Series 1, loading stages No. 12 through Load No. 17, Test Location A, Wildlife Liquefaction Array | 410 |
| Table 10-11 | Details of the Series 2 staged dynamic loading sequence conducted at Test Location A, Wildlife Liquefaction Array (WLA)..... | 429 |
| Table 10-12 | Pore pressure ratios and average shear strains at the center of the liquefaction sensor array for different numbers of loading cycles; Series 2, Test Location A, Wildlife Liquefaction Array (WLA)..... | 430 |

Chapter 1

Introduction

1.1 EARTHQUAKE-INDUCED SOIL LIQUEFACTION

The diverse and devastating nature of earthquake-induced soil liquefaction was powerfully confirmed in the minds of civil engineers through the occurrence of two large earthquakes in 1964. While the effects of soil liquefaction had been observed in large earthquakes prior to this time, little effort had been devoted to the detailed and systematic study of the phenomenon of earthquake-induced soil liquefaction (Vucetic and Dobry, 1986). In the 1964 Good Friday Alaska earthquake, extensive damage was done to a wide variety of bridge foundations as liquefied soils spread laterally toward stream channels. Earthquake-weakened soils also triggered large landslides in the cities of Anchorage, Seward, and Valdez. In the 1964 Niigata, Japan earthquake, thousands of buildings were damaged when their foundation soils liquefied. Many of these buildings settled more than a meter and tilted severely due to differential movement (Seed and Idriss, 1982). Following these two events, researchers realized that while the major outward manifestations of the soil failures varied between earthquakes, the triggering mechanism (the cyclic buildup of excess pore water pressure) was the same.

The 1964 earthquakes spawned research interest centered on the phenomenon of earthquake-induced soil liquefaction that still continues today.

Much progress has been made over the past four decades. These research efforts have focused on: (1) field observations of liquefaction during and after earthquakes, (2) field testing to determine the characteristics of liquefiable soil deposits, (3) laboratory sample testing to simulate soil liquefaction via cyclic pore pressure generation, (4) laboratory model (centrifuge) testing to simulate pore pressure generation, dissipation and the complex response of soil-structure interaction, and (5) analytical studies designed to help predict pore pressure generation and associated deformations (Vucetic and Dobry, 1986). Despite all that has been learned, much progress still remains to be made. For verification of this fact, one need not look any further than the substantial, widespread liquefaction damage caused by the recent 1999 Kocaeli, Turkey earthquake (EERI, 2000; Cox, 2001) and the 1999 Chi-Chi, Taiwan earthquake (EERI, 2001).

1.2 RESEARCH SIGNIFICANCE

It is well established that loose, dry, granular soils tend to densify under both static and cyclic loadings. If these same soils are saturated and then subjected to undrained loading, the tendency to densify causes a buildup of pore water pressure, which in turn reduces the contact stresses between individual soil particles, thus reducing the strength of the soil mass. Excess pore water pressures can be induced in saturated soil deposits by rapid earthquake loading. During an earthquake, vertically propagating shear waves tend to shake loosely packed soil particles into a denser configuration. However, this densification cannot take place until the water that occupies the voids between particles is forced out. Earthquake-induced cyclic loading occurs so rapidly that even highly permeable

sands and gravels cannot dispel water quick enough to stop the buildup of excess pore water pressure. When the pore water pressure approaches a value equal to the effective overburden pressure, large deformations take place and the soil weakens to a point where it is said to have liquefied (Seed and Idriss, 1982).

Earthquake-induced soil liquefaction can cause untold amounts of damage. Diverse problems include differential settlement and bearing capacity failures of buildings, movements and failures of earth dams, lateral spreads and landslides, and floatation of buried pipes and tanks (Dobry et al., 1982). Since all of these failures result in the loss of money, and potentially lives, predicting the risk of earthquake-induced soil liquefaction is one of the most important tasks with which a geotechnical engineer is faced when working in seismically active regions.

The state of the practice for evaluating the susceptibility of soil deposits to liquefaction is centered around simplified procedures based either on direct measurements of pore pressure generation in cyclic laboratory tests (Dobry et al., 1982) or indirect empirical correlations derived from various in-situ tests (Youd et al., 2001). Unfortunately, these procedures have disadvantages related to their indirect nature when empiricism is used, and sample disturbance when laboratory testing is involved. A much more robust approach to the problem of evaluating liquefaction susceptibility would involve directly measuring the pore pressure generation characteristics of the soil in situ.

During an earthquake, the generation of excess pore water pressure in a soil mass is a direct function of the level of cyclic shear strain induced in the soil

(Dobry et al., 1982; Vucetic and Dobry, 1986). Therefore, the ability to evaluate the potential of a soil to strain, and hence build up excess pore pressure, is of great importance. However, at this time, no active field test methods are available to the earthquake engineering profession that can be used to determine directly the liquefaction resistance (i.e. excess pore pressure generation as a function of induced cyclic shear strain) of soil deposits in situ. A few passive in-situ measurements of both dynamic response and pore pressure generation have been reported (Ishihara et al., 1981; Ishihara et al., 1989; Shen et al., 1991; Holzer et al., 1989; Youd and Holzer, 1994). In these studies classified as passive measurements, instrumentation was installed and researchers waited for an earthquake to load the site. Surface and downhole accelerometers were used to monitor the ground response and pressure transducers were utilized to measure pore water pressure generation. Although these measurements are the ultimate field investigation of liquefaction, they have several key limitations. These limitations include: (1) the unknown recurrence of earthquakes (hence, potentially decades of waiting), (2) durability of the sensors after long waiting periods, and (3) the inability to perform parametric studies. Hence, the need to develop a direct, active, field test method to evaluate liquefaction resistance.

1.3 SCOPE OF RESEARCH

This dissertation details work conducted by researchers from the University of Texas at Austin (UT) aimed toward the development and implementation of a new in-situ liquefaction testing technique. This technique is an active method that may be used to directly evaluate the liquefaction resistance of soils in place. The

test is based on the premise of dynamically loading a native soil deposit in a manner similar to an earthquake while simultaneously measuring its response with embedded instrumentation. Dynamic loading is performed via a large, truck-mounted hydraulic shaker (vibroiseis) that is used to excite the ground surface and generate stress waves of varying amplitudes within an instrumented portion of the soil mass. The embedded sensors consist of instrumentation to measure the coupled response of soil particle motion and pore water pressure generation.

Work on this new in-situ liquefaction test is currently in its second stage of development. In the first stage, liquefaction of a large-scale, reconstituted, test specimen was successfully accomplished in the field (Chang, 2002; Rathje et al., 2004). Building on the success of the first-generation testing, it was desired to advance the technique to a second-generation level by enabling testing of native soil deposits at greater depths using vertically propagating shear waves to strain the soil. The development of the second-generation testing equipment, field technique and resulting measurements obtained from its implementation comprise the bulk of this research.

The validity of this new test method has been demonstrated by conducting field experiments at the Wildlife Liquefaction Array (WLA) in Imperial Valley, California. WLA has been intensely studied over the past 25 years (Bennett et al., 1984; Bierschwale and Stokoe, 1984; Hagg and Stokoe, 1985; Vucetic and Dobry, 1986; Youd and Bartlett, 1988; Holzer et al., 1989; Dobry et al., 1992; Youd and Holzer, 1994; Zeghal and Elgamal, 1994). It has also recently been designated as a Network for Earthquake Engineering Simulation (NEES) site for the study of

soil liquefaction (<http://nees.ucsb.edu>). The extensive site characterization, the documented occurrence of earthquake-induced soil liquefaction at the site twice in the 1980's (1981, $M_w = 5.9$ Westmorland earthquake; and 1987, $M_w = 6.6$ Superstition Hills earthquake) and the likelihood for re-liquefaction of the site during subsequent earthquakes make WLA an ideal location for verifying the proposed in-situ dynamic liquefaction test method.

In-situ liquefaction tests were carried out at three separate locations at WLA. The tests were successful at measuring: (1) excess pore water pressure generation, and (2) nonlinear shear modulus behavior in the native silty-sand deposits as a function of induced cyclic shear strain. These results are compared to pore pressure generation curves and nonlinear shear modulus curves previously developed for WLA soils from laboratory testing methods. Variations in the dynamic soil response across the site are also discussed. These accomplishments represent a large step forward in the ability to accurately evaluate the susceptibility of a soil deposit to earthquake-induced liquefaction.

1.4 ORGANIZATION OF DISSERTATION

This research consists of four main topics: (1) the generalized in-situ liquefaction testing procedure, (2) the instrumentation developed to monitor soil response during testing, (3) the data collection and analysis techniques, and (4) the results obtained from field studies at the WLA. The dissertation contains 12 chapters as follows:

In Chapter 1, the phenomenon of earthquake-induced soil liquefaction is briefly introduced, the need for an in-situ dynamic liquefaction test is presented,

and WLA is introduced as the area where field verification of the new test method has been conducted. A chapter-by-chapter organizational outline of the dissertation is also given.

Background information on earthquake-induced soil liquefaction is provided in Chapter 2. State-of-the-practice soil liquefaction evaluation procedures are discussed. The need for an active, direct test method to dynamically evaluate the liquefaction resistance of soil deposits in-situ is presented.

The accomplishments made during first-generation in-situ liquefaction tests and briefly summarized in Chapter 3. The need to advance this technique beyond its current capabilities is discussed. The second-generation in-situ liquefaction test is proposed as a viable method to quantify the pore pressure generation characteristics and nonlinear soil shear modulus behavior of native liquefiable soil deposits. Hereafter, the second-generation in-situ liquefaction test is simply referred to as the in-situ liquefaction test.

In Chapter 4, the instrumentation that was developed for dynamic in-situ liquefaction testing is described. The major components of the in-situ liquefaction instrumentation system are: (1) the liquefaction sensors, and (2) the data acquisition system used to power and record their output signals. The liquefaction sensors are composed of a sealed, miniature pore water pressure transducer and a three-component (3D) Micro-Electrical Mechanical Systems (MEMS) accelerometer. Their output signals are captured using a 72-channel dynamic signal analyzer that has VXI hardware and Data Physics software.

The generalized dynamic in-situ liquefaction test procedure is described in Chapter 5. The generalized in-situ liquefaction test procedure may be subdivided into three basic categories. They are: (1) sensor installation, (2) staged dynamic loading, and (3) sensor extraction. Each of these procedural categories is addressed.

In Chapter 6, the data analysis procedures used to process the raw data recorded during dynamic in-situ liquefaction tests are described. The main raw data recorded during an in-situ dynamic liquefaction test are the acceleration and pore water pressure time histories generated at multiple sensor locations beneath the loaded surface area. The processed data desired from an in-situ dynamic liquefaction test are: (1) induced cyclic shear strain, (2) excess pore water pressure ratio as a function of induced cyclic shear strain and number of loading cycles, and (3) nonlinear soil shear modulus as a function of induced cyclic shear strain. The analysis techniques used to take the data from its raw state to its desired processed form are presented.

In Chapter 7, background information on the Wildlife Liquefaction Array (WLA) in Imperial Valley, California is presented. WLA has been an intensely studied soil liquefaction site since 1981. The extensive site characterization, the documented occurrence of earthquake-induced soil liquefaction at the site twice in the 1980's (1981, $M_w = 5.9$ Westmorland earthquake; and 1987, $M_w = 6.6$ Superstition Hills earthquake) and the likelihood for re-liquefaction of the site during subsequent earthquakes make WLA an ideal location for verifying the proposed in-situ dynamic liquefaction test method. In-situ liquefaction tests were

carried out at three separate locations at WLA. The areas that were tested are referred to as Test Location A, Test Location B and Test Location C.

The results obtained from performing in-situ liquefaction tests at Test Location C at WLA are contained in Chapter 8. Specifically, this chapter presents and discusses the in-situ pore pressure generation characteristics and nonlinear soil shear modulus behavior measured in the liquefiable soil layer at this location. Results obtained from two staged loading series at Test Location C are also compared.

The results obtained from performing in-situ liquefaction tests at Test Location B at WLA are contained in Chapter 9. Specifically, this chapter presents and discusses the pore pressure generation characteristics measured in the liquefiable soil layer at this location. Results obtained from two staged loading series at Test Location B are also compared.

The results obtained from performing in-situ liquefaction tests at Test Location A at WLA are contained in Chapter 10. Specifically, this chapter presents and discusses the pore pressure generation characteristics measured in the liquefiable soil layer at this location. Results obtained from two staged loading series at Test Location A are also compared.

In Chapter 11, the pore pressure generation characteristics obtained from conducting in-situ liquefaction tests at all three test locations at WLA are compared. The pore pressure generation characteristics measured at Test Location A do not agree well with the in-situ pore pressure generation curves obtained at Test Locations B and C. In general, the pore pressure generation data

collected at Test Location A indicates a higher threshold shear strain and significantly lower pore pressure ratios than expected for a given shear strain amplitude and number of loading cycles. It is hypothesized that this odd behavior was caused by partially saturated soil in the upper-portion of the liquefiable soil layer in the vicinity of Test Location A. Evidence to support this hypothesis is presented.

In Chapter 12, the work discussed in this dissertation is summarized. Future recommendations and refinements for the proposed dynamic in-situ liquefaction test method are discussed. Applications of the proposed dynamic in-situ liquefaction test in geotechnical earthquake engineering practice are also set forth.

Chapter 2

Soil Liquefaction Background

2.1 INTRODUCTION

In this chapter, some of the general concepts related to earthquake-induced soil liquefaction and its evaluation via current state-of-the-practice methods are briefly discussed. The strengths and weaknesses of these methods are reviewed. Previous measurements of pore water pressure generation and dynamic soil motions measured at instrumented sites during earthquakes are discussed. Justification for the need of a systematic test method to evaluate pore pressure generation characteristics and nonlinear shear modulus behavior of soil in situ is presented. The proposed in-situ dynamic liquefaction test is presented as a powerful new tool for evaluating the susceptibility of a soil deposit to earthquake-induced liquefaction.

2.2 LIQUEFACTION – A COMPLICATED PHENOMENON

Earthquake-induced soil liquefaction is a very complicated phenomenon. Its complexity is derived from the simultaneous interaction of several components, which even addressed separately are poorly understood. Firstly, seismic loads are three-directional, cyclic, highly irregular and difficult to predict (Vucetic and Dobry, 1986). Secondly, while often assumed so for simplicity, soil is not a homogeneous, isotropic, linearly elastic half space. It is a highly variable material that is extremely difficult to characterize properly. Soil characterization

is further complicated by the fact that its properties change substantially as it is seismically loaded. The complexities involved with seismic loading and soil response leading to liquefaction failure are further discussed below.

2.2.1 Seismic Loading

Intensity and duration of shaking are the two principle components of seismic loading that influence soil liquefaction (Seed and Idriss, 1971). Duration of shaking is primarily a function of the earthquake magnitude and is important because it reflects the number of cycles of shear strain and shear stress applied to the soil. Intensity is of concern because it represents the magnitude of the applied shear strains and shear stresses. Generally speaking, sites closer to the zone of seismic energy release tend to experience higher ground shaking intensities. However, ground motion intensity at a site is also strongly influenced by local soil/rock conditions, topography effects, and location with respect to both distance and direction from the zone of energy release (Kramer, 1996). In geotechnical earthquake engineering, the intensity of shaking is most often expressed as peak ground acceleration (PGA). However, it should be noted that PGA is not the best indicator of intensity for liquefaction studies. Ground velocity and ground displacement more explicitly reflect the frequency content of the ground motion and are better indicators of strain induced in the soil. Moss et al. (2005) report a liquefaction case history from the River Park location in Imperial Valley, California where a soft soil site experienced very similar PGA's in three separate earthquakes yet only liquefied in one of them. Even after accounting for the differences in duration of shaking (magnitude based), the events were predicted to

have nearly identical cyclic stress ratios. However, by examining the velocity and displacement records, it is clear that the event that liquefied the site had a lower frequency content and substantially higher ground velocities and displacements.

2.2.2 Dynamic Soil Response

When considering the response of a potentially liquefiable soil deposit to seismic loading, one must also explicitly consider the extent (vertically and horizontally) over which the estimated response may be assumed to apply. Natural liquefiable soils have often been formed in very complex depositional environments (Bennett et al., 1984). As a result, the factors influencing seismic soil response, as discussed below, may vary substantially across any given site.

Part of the complexity involved with understanding liquefaction comes from the fact that these types of soil deposits are at least two-phase (soil particles and water when fully saturated), and sometimes three-phase (with the addition of air if not fully saturated), materials. It is well established that loose, dry, granular soils tend to densify under both static and cyclic loadings. If these same soils are saturated and then subjected to undrained loading, the tendency to densify causes a buildup of pore water pressure, which in turn reduces the contact stresses between individual soil particles, thus reducing the strength and stiffness of the soil mass. Sustained loading, and its associated rise in pore pressure, may transform the initially stable solid soil state into an unstable almost liquid state (Vucetic and Dobry, 1986). If the soil is only partially saturated, the rise in excess pore water pressure is somewhat retarded, thus increasing the liquefaction resistance of the deposit (Chaney, 1978; Ishihara et al., 2001).

Excess pore water pressures can be induced in saturated soil deposits by rapid earthquake loading. During an earthquake, vertically propagating shear waves tend to shake loosely packed soil particles into a denser configuration. However, this densification cannot take place until the water that occupies the voids between particles is forced out. Earthquake-induced cyclic loading occurs so rapidly that even highly permeable sands and gravels cannot dispel water quick enough to stop the buildup of excess pore water pressure. When the pore water pressure approaches a value equal to the effective overburden pressure, large deformations take place and the soil weakens to a point where it is said to have liquefied (Seed and Idriss, 1982).

In regards to evaluating soil liquefaction, pore water pressure data are typically quantified in terms of a pore pressure ratio (r_u) (De Alba et al., 1975; Seed et al., 1975; Kramer, 1996). Pore pressure ratio values are obtained by normalizing the excess pore water pressure generated during dynamic loading by the initial effective confining pressure acting on the soil. In field studies, the normalizing stress is the initial vertical effective stress (i.e. $r_u = \Delta u / \sigma_v'$, where Δu is excess pore water pressure and σ_v' is initial vertical effective stress). The r_u value helps one visualize how close the buildup in residual pressure has come to completely liquefying the soil. A r_u value equal to 1.0 (or 100%) means that the excess pore pressure has built to the point where it is equal to the initial vertical effective stress, and the soil is said to have fully liquefied

Laboratory testing has revealed that a single soil may have drastically varying pore pressure responses during dynamic loading based on its: (1) relative

density, (2) soil fabric (primarily a function of the sample preparation method in laboratory studies), (3) prior seismic straining, (4) stress history (i.e. overconsolidation ratio and lateral earth pressure coefficient), and (5) aging effects (Seed, 1979). While for many years it was believed that relative density was the primary controlling factor affecting pore pressure generation for a given soil, later research showed that in laboratory testing the other four factors could affect pore pressure generation even more significantly than large variations in density (Dobry, 1982).

2.2.3 Types of Soil Liquefaction

The cyclic loading of an earthquake can cause various degrees of soil liquefaction in saturated, cohesionless soils. These degrees have been referred to as cyclic mobility, limited liquefaction, and flow liquefaction, among others (Robertson et al., 1992). Despite the wide array of terms, liquefaction phenomena may generally be categorized as either flow liquefaction or cyclic mobility (Kramer, 1996). Vucetic and Dobry (1986) referred to these same two phenomena as liquefaction flow failure and liquefaction deformation failure, respectively. The main difference between these two types of soil liquefaction is the initial state of stress acting on the soil mass prior to dynamic loading. Liquefaction flow failures occur at locations where substantial static shear stresses already exist in the soil mass before dynamic loading. Such conditions exist in soils beneath large buildings, bridge piers or retaining walls, and in sloping ground and earth dams. In such cases, large displacements occur when the earthquake-induced pore pressure has increased enough to lower the shear

strength of the soil below the limit needed to support the pre-existing static shear stresses in the soil mass. These types of failures are triggered by excess pore pressure generation, yet the associated large displacements are driven by static shear stresses. Flow failures are in fact triggered when the pore pressure ratio of the soil is still less than one ($r_u < 1.0$).

Deformation failures typically occur at level ground or gently sloping sites with limited static shear stresses. Deformation failures may be partially driven by static shear stresses, but are primarily driven by seismic shear stresses. The displacements associated with deformation failures are typically much smaller than those associated with flow failures. Additionally, deformation failures require that the pore pressure ratio of the soil mass approach a value much closer to one for displacements to occur. While flow failures represent dramatic events, often with catastrophic consequences, it is estimated that more damage during earthquakes is caused by deformation failures (Vucetic and Dobry, 1986). Liquefaction deformation failures are associated with lateral spreading and damage done to roadways, railroads, pipelines and single-family homes.

It should be emphasized here that two sites with identical soil conditions, excited by the same seismic motions, might experience very different manifestations of soil liquefaction. For example, a site with a six-story apartment complex built on a mat foundation could experience a liquefaction flow failure (i.e. complete bearing capacity failure) triggered by an $r_u < 1.0$, while an empty lot across the road may show no visible signs of soil liquefaction despite the fact that the soil experienced nearly identical pore pressure generation.

2.2.4 Liquefaction Failures

Earthquake-induced soil liquefaction can cause untold amounts of damage. Diverse problems include differential settlement and bearing capacity failures of buildings, movements and failures of earth dams, lateral spreads and landslides, and floatation of buried pipes and tanks. Liquefaction failures continue to be a problem during major earthquakes. For verification of this fact, one need not look any further than the substantial, widespread liquefaction damage caused by the recent 1999 Kocaeli, Turkey earthquake (EERI, 2000; Cox, 2001) and the 1999 Chi-Chi, Taiwan earthquake (EERI, 2001). For illustrative purposes, a variety of liquefaction-induced failures caused by the Kocaeli earthquake are discussed below.

The city of Adapazari, located approximately 7 km north of the 1999 Kocaeli earthquake fault rupture, suffered the highest degree of property damage and life loss of any city affected by the earthquake. Turkish federal government data indicates that 27% of the buildings in Adapazari were either severely damaged or destroyed. Literally thousands of people lost their lives. The city also experienced one of the most spectacular and extensive occurrences of soil liquefaction ever documented, as hundreds of buildings settled, tilted, or translated excessively (EERI, 2000). A picture illustrating the liquefaction-induced settlement that was so pervasive throughout the city of Adapazari is shown in Figure 2-1. In addition to the obvious distress inflicted on structures, differential settlements of this nature also wreak havoc on underground utilities and lifelines, often severing every connection that spans between buildings and



Figure 2-1 Liquefaction-induced differential settlement between a row of buildings and a sidewalk in Adapazari following the 1999 Kocaeli, Turkey earthquake (Cox, 2001).

adjacent sidewalks or roads. Multiple tall, slender buildings in Adapazari also experienced bearing capacity failures such as the one shown in Figure 2-2. While the building appears to have performed well structurally, its foundation failed, thereby causing it to tip over.

The 1999 Kocaeli earthquake also caused large numbers of liquefaction induced lateral spreads along the shores of Lake Sapanca and Izmit Bay. Lateral spreading commonly occurs along shorelines and river channels where the liquefied soil is unconfined and can easily flow toward these open areas. A



Figure 2-2 Liquefaction-induced bearing capacity failure of a 5-story building in Adapazari following the 1999 Kocaeli, Turkey earthquake (from www.eerc.berkeley.edu/turkey/adapazari).

particularly dramatic failure occurred along the southern shore of Lake Sapanca, where tectonic subsidence, coupled with liquefaction-induced lateral spreading and settlement, caused Hotel Sapanca to be partially carried into the lake. A picture of the Hotel Sapanca failure is shown in Figure 2-3. Lateral movements at the site were on the order of 2 meters and the hotel settled between 20 to 50 cm. These two phenomena, coupled with tectonic subsidence, resulted in movement of the shoreline inward by 30 to 50 meters. People fleeing the hotel after the earthquake reported water and soil “boiling out of the ground” (EERI, 2000).



Figure 2-3 Liquefaction-induced lateral spreading and settlement, coupled with tectonic subsidence, carried Hotel Sapanca partially into Lake Sapanca following the 1999 Kocaeli, Turkey earthquake (from www.eerc.berkeley.edu/turkey/adapazari).

While not a direct type of failure, liquefaction of subsurface sediment also leads to modifications in both the amplitude and frequency content of seismic waves propagating toward the ground surface. These modifications may affect the spectral accelerations used for design of bridges, buildings, pipelines, and other structures (Youd et al., 2004a), and should not be neglected when considering the potential consequences of earthquake-induced soil liquefaction.

2.3 LIQUEFACTION EVALUATION PROCEDURES

Currently, the two most common methods used for evaluating earthquake-induced soil liquefaction are: (1) the cyclic stress approach, and (2) the cyclic

strain approach (Kramer, 1996). Of these two methods, the cyclic stress approach is far more commonly used in earthquake engineering practice today. However, the cyclic strain approach is considered by many to have a more robust theoretical basis for predicting pore water pressure generation. While not as commonly used in engineering practice, modeling soil liquefaction response using cyclic nonlinear stress-strain behavior shows promise for moving toward deformation-based analyses.

2.3.1 Cyclic Stress Approach

The cyclic stress approach was the first systematic analytical procedure used for evaluating soil liquefaction susceptibility during earthquakes (Seed and Idriss, 1967). The cyclic stress approach evaluates the susceptibility of a soil to liquefaction by comparing the cyclic stress resistance of the soil (i.e. cyclic strength of the soil) to the expected cyclic stress induced in the soil by an earthquake. The cyclic stress induced in the soil by an earthquake can either be calculated from a fully nonlinear or equivalent linear ground response analysis, or estimated from a simplified formula proposed by Seed and Idriss (1971). The simplified earthquake-induced cyclic stress calculation is widely used in engineering practice and is most often expressed as a cyclic stress ratio (CSR):

$$CSR = \frac{\tau_{av}}{\sigma'_{vo}} = 0.65 \frac{a_{max}}{g} \frac{\sigma'_{vo}}{\sigma'_{vo}} r_d \dots\dots\dots(2-1)$$

where τ_{av} is the equivalent uniform cyclic shear stress; σ'_{vo} and σ_{vo} are the initial

effective and total vertical stresses, respectively; a_{\max} is the peak horizontal acceleration at the ground surface; g is the acceleration of gravity; and r_d is the stress reduction factor at the depth of interest. This simple equation allows one to estimate an “average” earthquake-induced cyclic shear stress at any depth in the soil column as a simple function of the horizontal ground surface acceleration generated (or predicted to be generated) by an earthquake. Issues related to the use of acceleration as an intensity descriptor for liquefaction studies have already been addressed (see Section 2.2.1).

In the original cyclic stress approach, the liquefaction resistance of a soil subjected to cyclic stresses was evaluated in the laboratory using undrained, stress-controlled, cyclic triaxial tests. Realizing the futile nature of trying to obtain undisturbed samples of potentially liquefiable material, researchers originally proposed that the cyclic strength of these soils could be evaluated from tests on reconstituted specimens by replicating their in situ relative density and confining pressure. However, it later became apparent that the cyclic strength of the soil, as determined from laboratory testing, was unreliable due to the fact that reconstituting specimens erased many of the factors that strongly influenced the liquefaction resistance of soils (see Section 2.2.2). Peck (1979) concluded that: “(1) unless the cyclic loading tests used to evaluate liquefaction potential can be performed on absolutely undisturbed samples, which is manifestly impossible, the results will probably indicate too great a likelihood of liquefaction; and (2) in many instances the resistance to liquefaction in the field may be appreciably, even spectacularly, greater than that determined on the basis of conventional cyclic

laboratory tests on reconstituted or even “undisturbed” samples if no allowances are made for various possible beneficial effects such as time, repeated small shearing forces, and stress history.” These revelations eventually led to the abandonment of laboratory testing as a method for obtaining the liquefaction resistance of soils in terms of cyclic strength. As a result, researchers began to estimate liquefaction resistance based on empirical correlations with field test parameters (Seed et al., 1983).

Liquefaction case histories have been used as tools to help characterize liquefaction resistance in terms of various in-situ test parameters. The most widely used empirical correlations are based on the Standard Penetration Test (SPT) blow count (Seed et al., 1985), the Cone Penetration Test (CPT) tip resistance (Robertson and Wride, 1998), and shear wave velocity measurements (Andrus and Stokoe, 2000). These relationships were developed from previous liquefaction case histories by combining an estimate of the earthquake loading parameter (i.e. CSR) with a measured in-situ test parameter representing soil resistance (i.e. blow count, tip resistance or shear wave velocity). After plotting these points on a graph, a threshold line, which represents the cyclic stress ratio needed to trigger liquefaction, was drawn at the boundary between points denoting liquefaction and non-liquefaction. This boundary represents the cyclic resistance ratio (CRR) of a soil with the given in-situ test parameter value. Traditionally, different boundaries are given for soils with varying fines content. A detailed description for each of the three empirical correlations listed above may be found in Youd et al. (2001).

Figure 2-4 shows the empirical curves used to determine the CRR of soils using in-situ shear wave velocity measurements. Different curves exist for different magnitude earthquakes. The CRR obtained from one of these relationships may be compared to the CSR estimated for the site in order to predict if liquefaction is expected. If the CRR is less than the predicted CSR, then one would expect the site to liquefy during the anticipated ground motions. Conversely, if the CRR is greater than the predicted CSR, then one would expect the site to resist liquefaction during the anticipated ground motions. Empirical correlations based on the cyclic stress approach are widely used in engineering practice today and are great screening tools for evaluating sites that are predicted to definitely liquefy (i.e. $CSR \gg CRR$) or definitely not liquefy (i.e. $CSR \ll CRR$). However, they are not well suited for predicting the liquefaction potential of borderline cases.

When using empirical correlations one should be aware of their potential shortcomings. Firstly, surface evidence of soil liquefaction was used to characterize a site as either fully liquefied or non-liquefied. However, surface expressions of liquefaction may not occur at all sites that experience a complete reduction of effective stress (i.e. $r_u = 1.0$) within a soil layer at depth. This is especially true for level ground sites with no man-made structures on them (see Section 2.2.3). Conversely, surface expressions of liquefaction may occur at sites that experience pore pressure ratios of less than 1.0. This is especially true for sites with substantial, pre-existing shear stresses in the soil due to sloping ground or large man-made structures. As a result, some of the data points do not agree

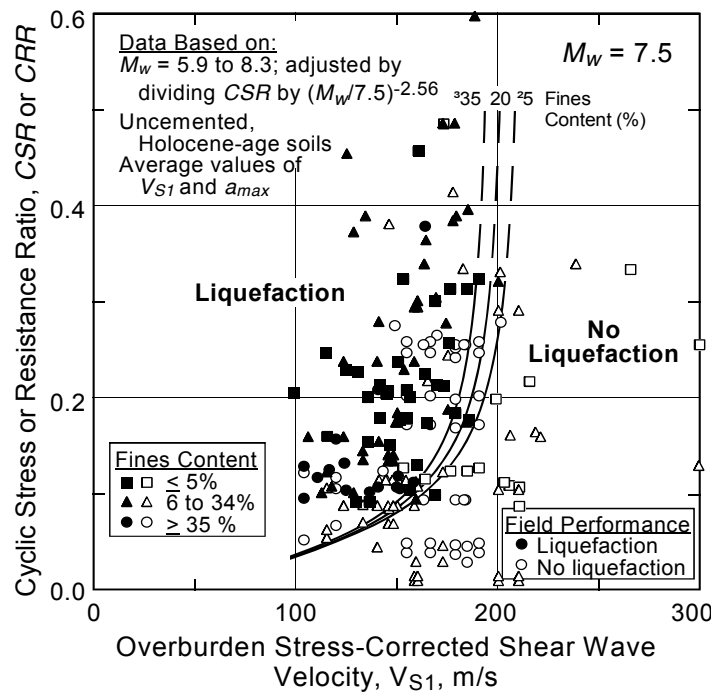


Figure 2-4 Empirical relationship between cyclic resistance ratio and stress-corrected shear wave velocity for $M=7.5$ earthquakes (from Andrus and Stokoe, 2000).

with the empirical boundary lines because case histories with a wide range of induced pore pressure ratios have all been lumped into categories as either fully liquefied or non-liquefied. Additionally, correlation procedures cannot evaluate cases where partial pore water pressure generation (i.e. $0 < r_u < 1$) occurs and therefore cannot predict the strain potential of liquefiable soils.

A separate, and often ignored problem with correlation procedures arises from the fact that the in-situ saturation level at case history sites has rarely been verified. It is not uncommon for potentially liquefiable soil deposits to be slightly unsaturated at depths below the static ground water level (Ishihara, 2001). The

cyclic resistance of slightly unsaturated soil can be substantially greater than the cyclic resistance of fully saturated soil. In-situ saturation may readily be verified by measuring the compression wave (P-wave) velocity of a soil deposit. Completely saturated soil has a P-wave velocity of approximately 1500 m/s (i.e. the velocity of a compression wave traveling through water). A drastic decrease in P-wave propagation velocity occurs when a soil deposit is only slightly unsaturated. Figure 2-5 shows a relationship reported by Ishihara (2001) that correlates the cyclic strength of partially saturated sand with P-wave propagation velocity. Indeed, these results show that the cyclic strength of slightly unsaturated sand with a P-wave velocity of 500 m/s may be as much as 1.5 times greater than the cyclic strength of fully saturated sand, all other factors being held equal. As a frame of reference, Ishihara (2001) also reported that a P-wave velocity of 500 m/s in these sands correlated with a saturation level of approximately 96%. Therefore, it may be concluded that saturation level can be a key parameter affecting soil liquefaction resistance and should be verified with P-wave velocity measurements during any in-situ liquefaction study.

2.3.2 Cyclic Strain Approach

The cyclic strain approach was originally proposed by Dobry et al. (1982) and provides a sound theoretical basis for analyzing the driving mechanism (i.e. the buildup of excess pore water pressure) behind earthquake-induced soil liquefaction. The cyclic strain approach evaluates the susceptibility of a soil to liquefaction by comparing the cyclic strain required to develop a given excess pore water pressure ratio in the soil with the cyclic strain induced in the soil by an

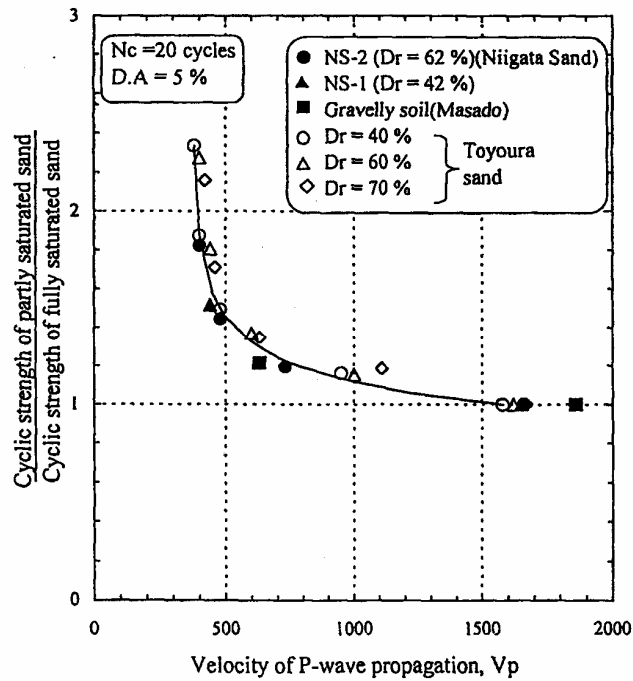


Figure 2-5 Ratio of cyclic strength between partially and fully saturated sand as a function of measured P-wave velocity (from Ishihara, 2001).

earthquake. The primary advantage of the cyclic strain approach is the direct relationship between excess pore pressure generation and cyclic shear strain amplitude. As a practical matter, this relationship is typically expressed in the form of a pore pressure generation curve such as the one shown in Figure 2-6. Pore pressure generation curves detail the increase in pore pressure ratio as a function of induced cyclic shear strain and may be developed for any practical number of uniform loading cycles (n). Pore pressure ratio (r_u) is a useful parameter because it helps one visualize how close the developed excess pore pressure has come to equaling the initial effective confining pressure (see Section 2.2.2).

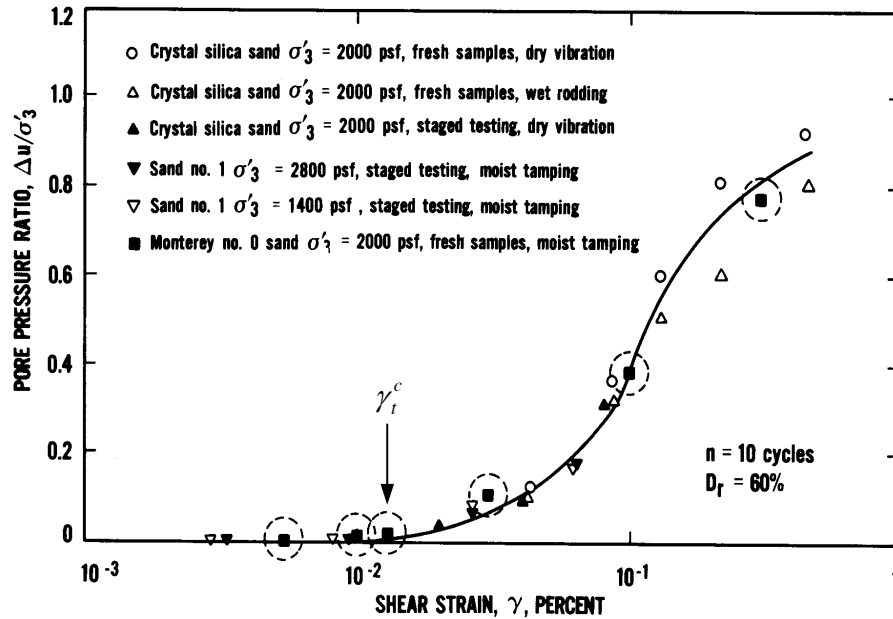


Figure 2-6 Pore pressure generation curve developed from strain-controlled cyclic triaxial tests on various sands with different specimen preparation techniques and confining pressures (modified from Dobry et al., 1982).

One of the desirable aspects of the cyclic strain approach is the existence of a cyclic threshold shear strain (γ_i^c). Shear strains below the cyclic threshold strain have no tendency to densify the soil and hence no tendency to produce excess pore water pressure (see Figure 2-6). As stated above, the fundamental triggering mechanism responsible for soil liquefaction is the generation of excess pore water pressure. Therefore, the existence of some threshold strain below which no excess pore water pressure will develop is a very important concept. It also follows that there exists some shear strain that will result in the development of excess pore water pressures that will fully liquefy the soil (i.e. $r_u = 1.0$). This

shear strain may be termed the initial liquefaction shear strain (γ_{liq}). Earthquake-induced shear strains that are greater than the threshold strain but less than the initial liquefaction shear strain may cause various degrees of movement depending on the pre-existing conditions at the site (see Section 2.2.3).

Pore pressure generation curves, such as the one shown in Figure 2-6, are developed from strain-controlled cyclic laboratory (typically cyclic triaxial and cyclic direct simple shear) tests. The tests are performed on either high-quality or reconstituted soil samples. As noted when discussing the cyclic stress approach (see Section 2.3.1), laboratory testing related to the accurate determination of soil strength for liquefaction studies has been called into question. However, experimental evidence indicates that factors that increase the cyclic shear stress (τ) required to initiate liquefaction (i.e. density, soil fabric, prior seismic straining, stress history, and aging) also increase the shear modulus (G) of the soil. Assuming that these factors influence both τ and G similarly, their influence on shear strain (γ), which is the ratio of τ/G , is much less (Dobry et al., 1982; Vucetic and Dobry, 1986; Kramer, 1996). While it is true that these issues seem to be less of a factor when strain-controlled tests are performed rather than stress-controlled tests, one must still acknowledge that the soil being tested in the laboratory has been substantially altered from its in-situ condition.

To evaluate the potential for liquefaction, one must estimate the seismic shear strain and number of loading cycles induced by the expected earthquake. This information allows direct evaluation of the expected pore pressure generation at the site based on a pore pressure generation curve. Dobry et al. (1982)

suggested three possible ways to obtain an estimate of the earthquake-induced cyclic shear strain (γ_c) from a given seismic excitation. The first, and simplest way, is based on the principle that shear strain (γ) is equal to shear stress (τ) divided by shear modulus (G). An estimate for the value of τ induced by an earthquake can be obtained from an expression similar to Equation (2-1). It then directly follows that γ_c is calculated by:

$$\gamma_c = \frac{\tau_{av}}{G(\gamma_c)} = 0.65 \frac{a_{\max}}{g} \frac{\sigma_{vo}}{G(\gamma_c)} r_d \dots\dots\dots(2-2)$$

where $G(\gamma_c)$ is the shear-strain-dependant shear modulus of the soil, and the other parameters are the same as defined in Equation (2-1). This equation must be solved iteratively until convergence is reached due to the fact that it is a function of γ_c on both sides of the equation. The $G(\gamma_c)$ function must also explicitly describe the nonlinearity of the soil as well as subsequent degradation due to pore pressure generation once the threshold strain has been surpassed.

The second way Dobry et al. (1982) suggested calculating γ_c is from site response analyses where a model of the soil is subjected to earthquake input motions. Once again, as noted above, it is imperative that the $G(\gamma_c)$ function used in the analysis account for both nonlinearity and subsequent degradation due to pore pressure generation.

The third way Dobry et al. (1982) suggested calculating γ_c originates from wave propagation theory, which states that shear strain (γ) is equal to the ground particle velocity divided by the shear wave propagation velocity. As both the

ground particle velocity and the shear wave propagation velocity are need for this method, it is really only practical for calculating shear strains at sites where instrumentation has recorded earthquake motions at various depths in the soil deposit.

The cyclic strain approach is theoretically robust in that it directly evaluates the potential of a soil to strain and hence buildup excess pore water pressure. Its major setback arises from the problem of accurately predicting the cyclic shear strain induced by an earthquake, because the shear modulus relationship needed to do so is a function of both the shear strain level and the effective stress (i.e. degradation due to pore pressure generation). Confidence in evaluating this complex interaction is limited, consequently; the cyclic strain approach is used less often in engineering practice (Chang, 2001).

2.3.3 Liquefaction Modeling

Stress-strain modeling of soil behavior has been an intense area of research over the past several decades. However, the task of replicating the complex behavior of potentially liquefiable soil has proven challenging. The nonlinear stress-strain behavior of liquefiable soil can be evaluated by nonlinear stress-strain models or by advanced constitutive models (Kramer, 1996). No attempt is made herein to compare and contrast the wide variety of models that have been proposed by various researchers. However, an interesting comparison of two separate models and their attempts to predict the measured response at an instrumented liquefaction site may be observed by referring to Dobry et al. (1989) and Keane and Prevost (1989). These two articles detail separate attempts at

accurately modeling the ground response and pore pressure generation measured at the Wildlife Liquefaction Array (WLA) during the 1987 Superstition Hills earthquake (discussed in Section 2.4).

Dobry et al. (1989) used a one-dimensional nonlinear site response model called DESRAMOD (Vucetic and Dobry, 1986), which is a modified version of the program DESRA-2 (Finn et al., 1977; Lee and Finn, 1978), to model the observed Wildlife data. The primary modification to the original program was a new pore pressure generation model referred to as “Dobry’s Pore Pressure Model”. Vucetic and Dobry (1986) stated that DESRAMOD “conducts a one-dimensional nonlinear site response analysis using: lumped masses to represent the soil profile; a hyperbolic stress-strain backbone curve for the soil in shear characterized by initial parameters $G_{\max o}$ and $\tau_{\max o}$; and an extended Masing law for cyclic loading. The program provides for stress-strain degradation due to pore pressure buildup by decreasing both $G_{\max o}$ and $\tau_{\max o}$... Migration and dissipation of pore pressures accompanied by reconsolidation, both during and after shaking, are included in the program.” The DESRAMOD analysis did a good job of predicting the magnitude of the pore pressure generated near the bottom of the liquefiable layer. However it under predicted the magnitude of the pore pressure generation near the top of the liquefiable layer. While not as important as the magnitude of pore pressure generation, the program was not able to match the slower than expected time rate of pore pressure generation at the Wildlife Liquefaction Array.

Kean and Prevost (1989) used a program called DYNA1D to model the observed Wildlife data. DYNA1D uses an effective-stress elastic-plastic constitutive model with multiple conical yield surfaces (Prevost, 1985). Implementation of earthquake loading (Prevost, 1988) is provided for using time steps with modified Newton-Raphson iterations to insure proper convergence. The finite element mesh used to represent the semi-infinite soil deposit consisted of 29 one-dimensional elements (30 nodes). Both three-dimensional kinematics (i.e. all three orthogonal components of recorded excitation were used to excite the model) and two-dimensional kinematics were used in the analysis. The three-dimensional kinematics DYNA1D analysis did a very good job at matching the magnitude of the pore pressure generation near the bottom and middle of the liquefiable layer. However, it also under predicted the magnitude of pore pressure generation near the top of the liquefiable layer. Similar to the DESRAMOD analysis, the DYNA1D analysis also failed to accurately match the slower than expected time rate of pore pressure generation. It should be noted that the DYNA1D analysis was only carried out over the first 40 seconds of the recorded motions. While most of the pore pressure generation at the site had taken place within this time frame, pore pressures continued to gradually increase through about 80 seconds of the record length.

The studies noted above illustrate two different approaches to modeling earthquake-induced soil liquefaction. While not totally accurate in their evaluations of the Wildlife Liquefaction Array data, these methods clearly show promise. Unfortunately, the complexities involved with obtaining model input

parameters and limited verification of their accuracy has restricted their use in liquefaction studies. Continued research in this area is needed. The potential for accurate liquefaction modeling is great, and its implementation will help advance the profession to deformation-based analyses. The ability to make in-situ measurements to determine model input parameters should enhance the acceptance and use of stress-strain modeling for liquefaction studies. Additionally, more in-situ measurements of the soil liquefaction phenomenon are needed to refine and verify existing models (Youd et al., 2004a).

2.4 IN-SITU SOIL LIQUEFACTION MEASUREMENTS

Several different methods have been proposed to obtain in-situ measurements of dynamic ground response and pore pressure generation during soil liquefaction. One approach, a passive approach, is to permanently instrument sites that have liquefied in previous earthquakes and wait for another large earthquake to load the soil deposit. A second approach, an active approach, is to temporarily instrument a liquefiable deposit and artificially induce dynamic energy to strain the soil and generate excess pore water pressure. Explosives have historically been used as an active source that imparts dynamic energy for the second approach. A summary of select published results from in-situ measurements of dynamic soil response and pore pressure generation is presented in Table 2-1 (Chang, 2002). Data collected from these types of in-situ measurements are of interest for two main reasons: (1) to verify the ability of models to accurately predict the measured ground response and pore pressure

Table 2-1 Select summary of some previous in situ liquefaction measurements (from Chang, 2002)

| Site | Soil Type | Collected Data | Source | Reference |
|--------------------------|-----------------|--|--|------------------------|
| Owi Island (Japan) | Silty fine sand | SPT, CPT, pore pressure, surface acceleration | Mid-Chiba earthquake $a_{max}=0.1$ g | Ishihara et al. (1981) |
| Sunamachi (Japan) | Fine sand | SPT, Vs, pore pressure, downhole acceleration | Chiba-Toho-Oki earthquake, $a_{max}=0.12$ g | Ishihara et al. (1989) |
| Lotung site (Taiwan) | Sand | Vs, CPT, pore pressure, Downhole acceleration | 18 earthquakes during 1985-1986 | Shen et al. (1989) |
| Wildlife site (USA) | Silty sand | SPT, CPT, Vs, pore pressure, downhole acceleration | Superstition Hills earthquake, $a_{max}=0.21$ g | Youd and Holzer (1994) |
| South Platte River (USA) | Coarse sand | SPT, CPT, Vs, pore pressure, particle velocity, settlement | Downhole explosions | Charlie et al. (1992) |
| Boundary Bay (Canada) | Sandy silt | CPT, Vs, pore pressure, surface acceleration, settlement | Downhole explosions | Gohl et al. (2001) |

generation during liquefaction (see Section 2.3.3), and (2) to obtain in-situ measurements of soil nonlinearity and damping characteristics prior to excess pore pressure generation (Zeghal and Elgamal, 1994; Zeghal et al., 1995).

Blasting has proven to be an effective tool for liquefying soils and subsequently monitoring the ability of foundations and structures to handle the loss of strength and the change in load that is placed on them. However, due to the extreme differences in earthquake loading and blast loading, some researchers have questioned the use of explosives when trying to systematically analyze the potential a soil has to strain, buildup pore pressure, and liquefy during an

earthquake. In particular, issues regarding the high frequency content of blast motions, the estimation of induced shear strain level, and difficulties in monitoring pore pressures due to the high-amplitude, blast-shock front require more research (Chang, 2002).

In-situ measurements of dynamic soil response and excess pore pressure generation induced by earthquakes have been made at several instrumented sites around the world (see Table 2-1). In these studies, instrumentation systems were installed and researchers waited for an earthquake to load the site. Surface and downhole accelerometers were used to monitor the ground response and pore pressure transducers were utilized to measure excess pore water pressure generation. Despite efforts to make these types of in-situ measurements for more than 25 years, only the Wildlife site (Wildlife Liquefaction Array) has recorded data indicating complete liquefaction during an earthquake (Youd and Holzer, 1994). The Lotung site (Shen et al., 1989; Zeghal et al., 1995) has recorded several events that induced lesser degrees of excess pore pressure generation, the maximum of which produced a pore pressure ratio equal to 25% of the effective confining stress in the liquefiable layer (i.e. $r_u = 0.25$). The Owi Island site (Ishihara et al., 1981) has recorded a maximum pore pressure ratio of 20%. These data sets are invaluable to the earthquake engineering profession, as they have provided case histories for verifying liquefaction modeling as well as in-situ measurements of how soil stiffness changes throughout the process of earthquake loading. It is beyond the scope of this research to discuss these individual sets of data in detail. However, the Wildlife Liquefaction Array will be discussed later in

this dissertation (see Chapter 7), as it is the site where field verification of the proposed dynamic in-situ liquefaction test was conducted.

2.5 NEED FOR A DYNAMIC IN-SITU LIQUEFACTION TEST

In-situ measurements of dynamic soil response and excess pore pressure generation have been made during several earthquakes (as noted in Section 2.4). These data sets have proven to be invaluable to the earthquake engineering community. However, despite efforts to make these types of measurements for more than 25 years, only limited amounts of data have been collected at a few select sites around the world. The major limitations of these studies include: (1) the unknown recurrence of earthquakes (hence, potentially decades of waiting), (2) durability of the sensors after long waiting periods, and (3) the inability to perform parametric studies. At this time, no systematic field test methods are available to the earthquake engineering profession that can be used to determine directly the liquefaction resistance (i.e. excess pore pressure generation as a function of induced cyclic shear strain) of soil deposits in situ. Hence, the need to develop a direct, active, field test method to evaluate liquefaction resistance.

This dissertation details work conducted by researchers from the University of Texas at Austin (UT) aimed toward the development and implementation of a new in-situ liquefaction testing technique. This technique may be used to directly evaluate the liquefaction resistance of granular soils in place. The test is based on the premise of dynamically loading a native soil deposit in a manner similar to an earthquake while simultaneously measuring its response with embedded instrumentation. Dynamic loading is performed via a

large, truck-mounted hydraulic shaker (vibroiseis) that is used to excite the ground surface and generate stress waves (primarily vertically propagating shear waves) of varying amplitudes within the soil mass. The embedded sensors consist of instrumentation to measure the coupled response of soil particle motion and pore water pressure generation. Specifically, this new test method measures: (1) excess pore water pressure generation, and (2) nonlinear shear modulus behavior in native soil deposits as a function of induced cyclic shear strain. The ability to perform these measurements in-situ provides geotechnical engineers with a powerful new tool for directly evaluating the susceptibility of a soil deposit to liquefaction. This direct test method should prove useful for refining and validating existing numerical models used for analyzing soil liquefaction, as well as for validating the effectiveness of liquefaction remediation techniques in situ.

2.6 SUMMARY

Soil liquefaction is a complicated phenomenon that may cause untold amounts of damage during earthquakes. The state-of-the-practice for evaluating a soils susceptibility to liquefaction is centered around simplified procedures based either on direct measurements of pore pressure generation in cyclic laboratory tests (Dobry et al., 1982) or indirect empirical correlations derived from various in-situ tests (Youd et al., 2001). Unfortunately, these procedures have disadvantages related to their indirect nature when empiricism is used, and sample disturbance when laboratory testing is involved. Stress-strain modeling of liquefaction soil behavior shows promise for the future. However, the task of replicating the complex behavior of potentially liquefiable soils has proven

challenging. Subsequently, the complexities involved with obtaining model input parameters and limited verification of their accuracy has restricted their use in liquefaction studies. In-situ measurements of dynamic soil response and excess pore pressure generation have been made during several earthquakes (Ishihara et al., 1981; Ishihara et al., 1989; Shen et al., 1991; Holzer et al., 1989). These data sets have proven to be invaluable to the earthquake engineering community. However, despite efforts to make these types of measurements for more than 25 years, only limited amounts of data have been collected at a few select sites around the world. At this time, no systematic field test methods are available to the earthquake engineering profession that can be used actively to determine directly the liquefaction resistance (i.e. excess pore pressure generation as a function of induced cyclic shear strain) of soil deposits in situ. This dissertation details work conducted by researchers from the University of Texas at Austin (UT) aimed toward the development and implementation of a new in-situ liquefaction testing technique. Specifically, this new test method measures: (1) excess pore water pressure generation, and (2) nonlinear shear modulus behavior in native soil deposits as a function of induced cyclic shear strain. The ability to make these measurements at the desired time and place provides geotechnical engineers with a powerful new tool for directly evaluating the susceptibility of a soil deposit to earthquake-induced liquefaction.

Chapter 3

In-Situ Dynamic Liquefaction Test

3.1 INTRODUCTION

A new liquefaction field testing technique has been developed at the University of Texas (UT) based on the premise of dynamically loading a soil deposit in a manner similar to an earthquake while simultaneously measuring its response with embedded instrumentation. The test uses a truck-mounted hydraulic shaker (vibroiseis) to actively excite the ground surface and generate predominantly vertically propagating shear waves that dynamically load the instrumented portion of the soil deposit. The soil response is monitored in terms of induced cyclic shear strain, excess pore water pressure generation, and nonlinear shear modulus behavior.

Work on this new in-situ liquefaction test is currently in its second stage of development. In the first stage, liquefaction of a large-scale, reconstituted, test specimen was successfully accomplished in the field (Chang, 2002; Rathje et al., 2005). Building on the success of the first-generation testing, it was desired to advance the technique to a second-generation level by enabling testing of native soil deposits at greater depths using vertically propagating shear waves to strain the soil. The development of the second-generation testing technique and equipment, along with results obtained from its implementation, comprise the bulk of this dissertation. The first- and second-generation in-situ liquefaction

tests are generally compared and contrasted below. In later chapters, the specific second-generation testing procedure, equipment, and in-situ test results are presented.

3.2 FIRST-GENERATION IN-SITU LIQUEFACTION TEST

Comprehensive discussions regarding the development of the first-generation in-situ liquefaction test are found in Chang (2002), Stokoe et al. (2004) and Rathje et al. (2005). The generalized first-generation testing procedure and sample results from its implementation are presented herein.

First-generation in-situ liquefaction tests used the vibroseis truck shown in Figure 3-1 as a dynamic source. A vibroseis is a truck-mounted hydraulic shaker capable of generating dynamic loads over fairly large ranges in amplitude and frequency. In first-generation tests, this machine was used to apply a dynamic vertical load to a shallow circular footing that was placed about 3.3 m away from a reconstituted sand test pit. A schematic of the test set up is shown in Figure 3-2. The test pit was 1.2 m by 1.2 m by 1.2 m, and was lined with an impermeable geosynthetic liner. The specimen was prepared in the test pit by allowing a mixture of sand and water to sediment through a shallow depth of water. This sample preparation procedure was successful in producing specimens at about 40% relative density (very loose). During sample construction, first-generation liquefaction sensors were embedded in the test pit. Each of these sensors contained a miniature pore water pressure transducer and two 28-Hz geophones (one oriented vertically and one oriented horizontally) inside a small acrylic case. A schematic of a first-generation liquefaction sensor is shown in Figure 3-3.



Figure 3-1 Picture of the vibroseis truck used as a dynamic source in the first-generation in-situ liquefaction tests (from Stokoe et al., 2004).

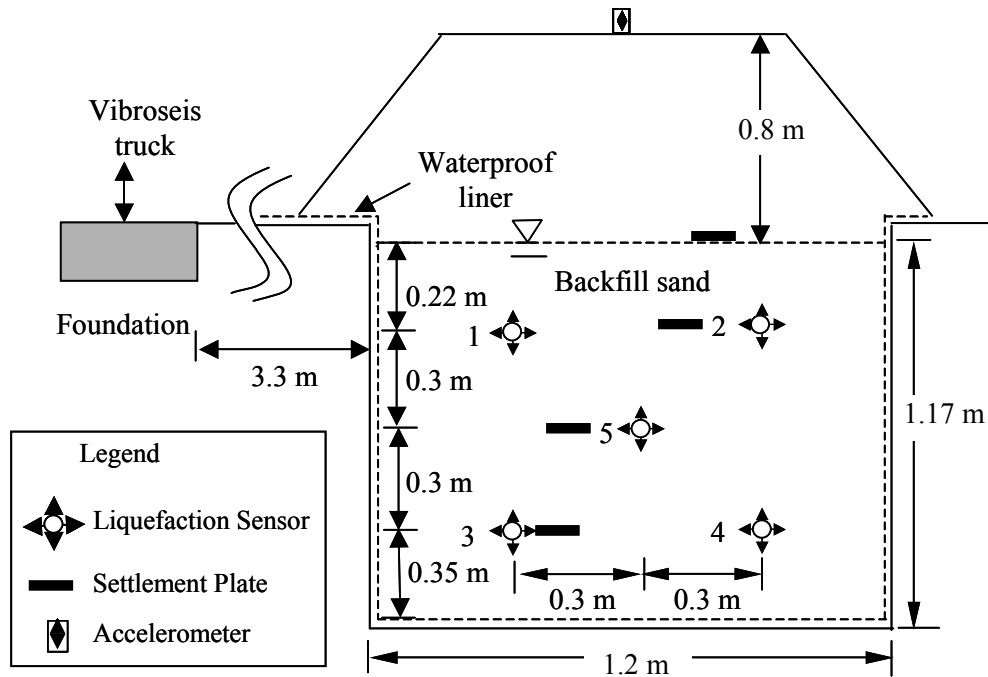


Figure 3-2 Schematic layout of vibroseis truck location, reconstituted soil test pit, and associated instrumentation used in the first-generation in-situ liquefaction test (from Chang, 2002).

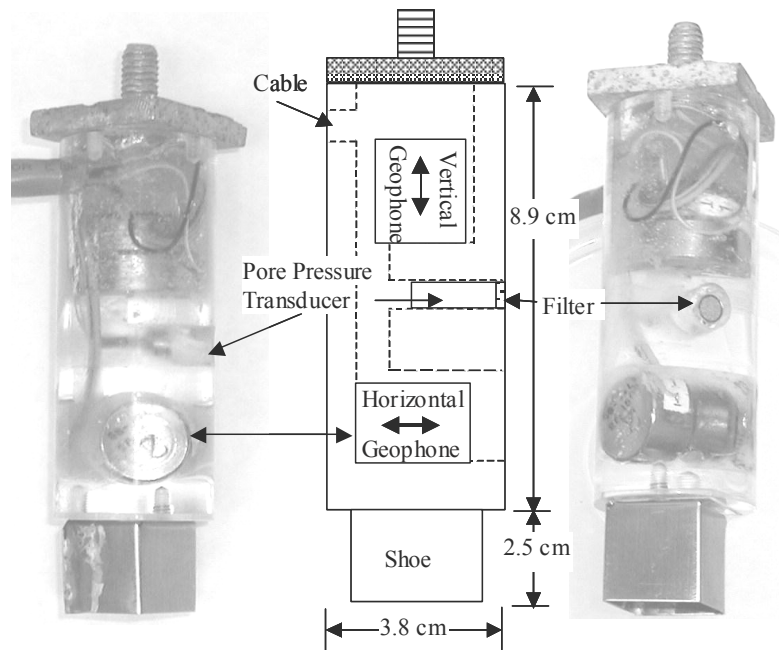


Figure 3-3 Liquefaction sensor used in the first-generation in-situ liquefaction test (from Chang, 2002).

In the first-generation tests, the vibroseis truck was used to generate surface waves that induced shear strains and significant excess pore water pressure in the sand. This information was sensed by the embedded liquefaction sensors and later processed to obtain the desired information. Staged loading was performed, beginning at small strains where no excess pore pressure was generated and continuing until significant excess pore pressure was achieved. Computed shear strain and measured excess pore water pressure-time histories from one of the stages are shown in Figure 3-4. The dynamic load in these tests was applied in the form of a 20-Hz fixed sine wave with typical durations of 20 to 60 cycles. The results, expressed in terms of pore pressure generation curves,

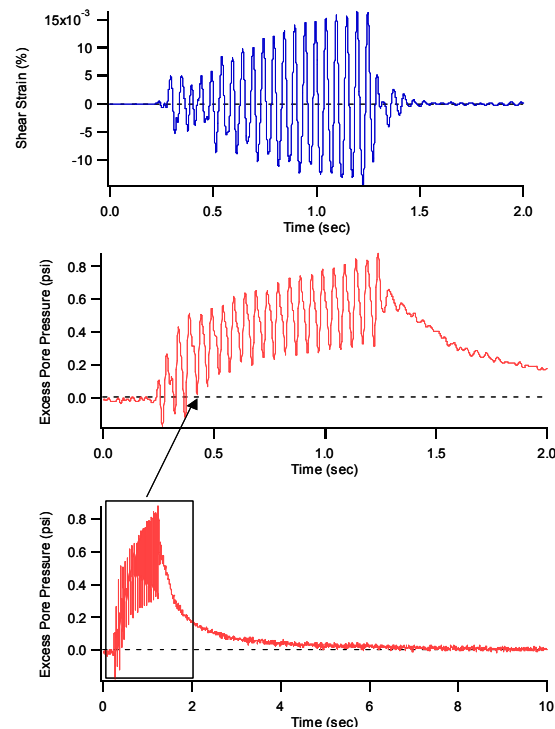


Figure 3-4 Shearing strain and excess pore water pressure time histories obtained from a first-generation in-situ liquefaction test (from Chang, 2002).

from one series of staged tests are shown in Figure 3-5. Clearly, cyclic loading at low strain levels caused no excess pore pressure to develop. As the strain level increased above the cyclic threshold strain (γ_t^c) the generation of pore pressure was readily measured. The threshold shear strains obtained from first-generation testing ($\gamma_t^c \sim 0.05\%$) were somewhat smaller than the conventional threshold shear strain ($\gamma_t^c \sim 0.2\%$) obtained from laboratory testing (Dobry, 1982; Vucetic and Dobry, 1986). This was likely due to the very loose soil conditions and extremely low confining pressures in the reconstituted sand test pit (Chang, 2002).

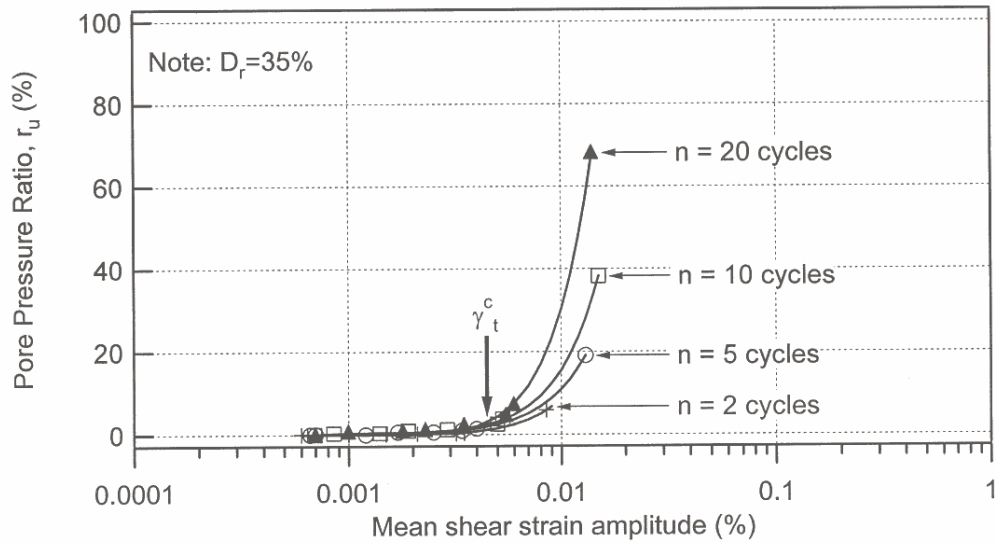


Figure 3-5 Pore pressure generation curves for different numbers of loading cycles evaluated from a first-generation in-situ liquefaction test series (from Chang, 2002).

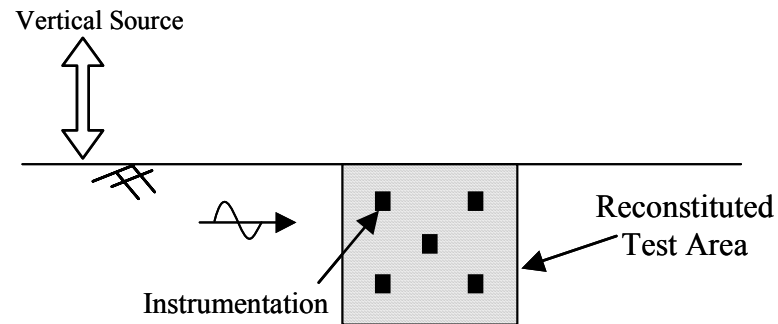
3.3 SECOND-GENERATION IN-SITU LIQUEFACTION TEST

The first-generation in-situ liquefaction test was successful in directly evaluating the cyclic threshold strain of shallow (depths less than 1.5 m), reconstituted soil deposits, using surface stress waves of the Rayleigh type for dynamic loading. However, the first-generation testing technique did not allow for determination of the nonlinear shear modulus behavior of the soil, primarily due to the complicated wave field associated with the test set up. Goals for the second-generation in-situ liquefaction test included extending the measurements to greater depths within native soil deposits, implementing the use of vertically propagating shear waves for dynamic loading, evaluating the nonlinear shear modulus behavior of the soil prior to excess pore pressure generation, and

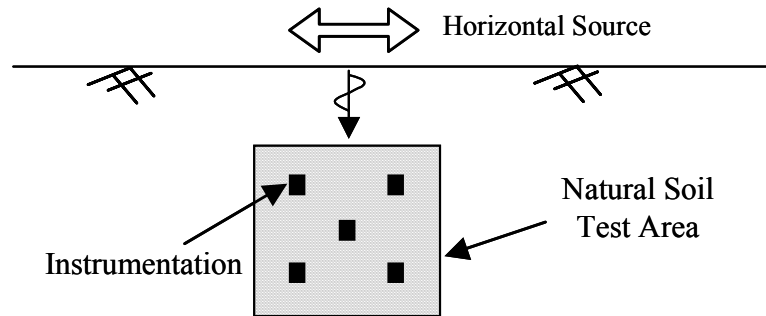
quantifying the degradation of the nonlinear shear modulus due to the generation of excess pore pressure.

A simplified schematic that illustrates the differences between the first- and second-generation testing configurations is shown in Figure 3-6. The first-generation liquefaction sensors, schematically depicted in Figure 3-6a, were placed in the reconstituted test specimen as it was being built. However, second-generation tests necessitate the development of a new type of liquefaction sensor that can be pushed to the required depth within a native soil deposit, as depicted in Figure 3-6b. The challenge arises in harmonizing a sensor that is tough enough to be inserted into the ground through various soil conditions, with a sensor that is still compact enough, and sensitive enough, to measure small dynamic strains and pore pressures. Specific details regarding the development of the new liquefaction sensor are provided later in this dissertation (see Section 4.2).

Vertically propagating shear waves are the primary component of earthquake ground motions responsible for initiating soil liquefaction. However, the first-generation in-situ liquefaction test was only able to use Rayleigh waves for dynamic loading (as shown in Figure 3-6a). This was not ideal, but was necessitated by the limitations of the first-generation source, which could only load the soil vertically (see Figure 3-1). The University of Texas has since obtained a new triaxial vibroseis truck as part of its Network for Earthquake Engineering Simulation (NEES) experimental field equipment. This new truck, affectionately named “T-Rex”, is shown in Figure 3-7. In addition to operating vertically, T-Rex can also operate horizontally, thereby allowing the generation of



a) First-generation testing configuration



b) Second-generation testing configuration

Figure 3-6 Simplified schematic of first- and second-generation in-situ liquefaction testing configurations (from Stokoe et al., 2004).

vertically propagating (downward), horizontally polarized shear waves. This represents a substantial advancement in the second-generation test capabilities.

The remainder of this dissertation focuses on the development of the second-generation testing technique (i.e. instrumentation, test configuration, and testing procedure) and the results obtained from its implementation. As the first-generation in-situ liquefaction testing technique is no longer employed (although,

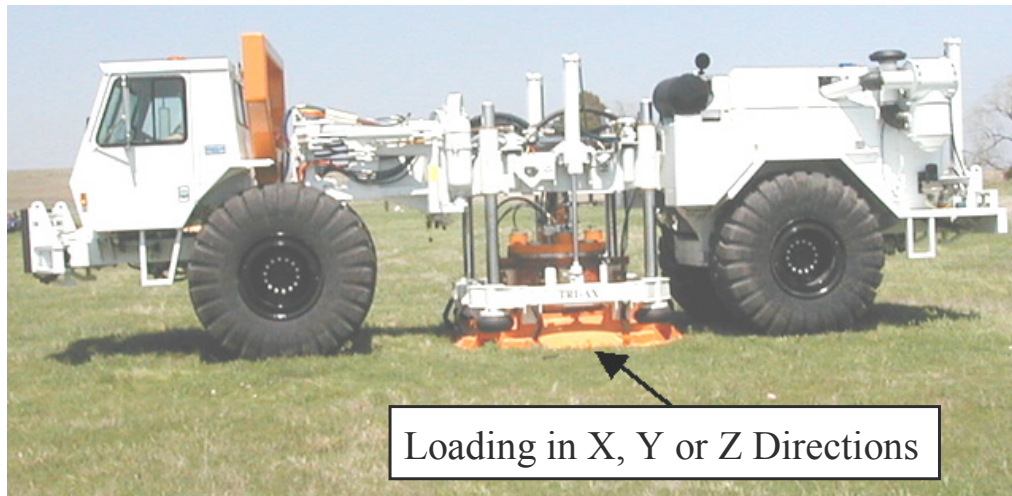


Figure 3.7 Picture of T-Rex, the new triaxial vibroseis truck used as a dynamic source for second-generation liquefaction tests (from Stokoe et al., 2004).

stand-off loading could still be used to test native soil deposits in certain circumstances), the second-generation testing technique is hereafter designated, solely for ease in discussion, as the in-situ liquefaction test.

3.4 SUMMARY

A new liquefaction field testing technique has been developed at the University of Texas. The test employs a vibroseis truck to excite the ground surface horizontally and generate shear waves that dynamically load the soil deposit. The soil response is monitored in terms of induced cyclic shear strain, excess pore water pressure generation, and nonlinear shear modulus behavior. Work on this new in-situ liquefaction test is currently in its second stage of development. In the first stage, liquefaction of a large-scale, reconstituted, test specimen was successfully accomplished in the field using Rayleigh waves for

dynamic loading. Second-generation in-situ liquefaction test goals included extending these measurements to greater depths within native soil deposits, implementing the use of vertically propagating shear waves for dynamic loading, evaluating the nonlinear shear modulus behavior of the soil prior to excess pore water pressure generation, and quantifying the degradation of the nonlinear shear modulus due to the generation of excess pore pressure. As the first-generation in-situ liquefaction testing technique is no longer employed, the second-generation testing technique is hereafter designated, solely for ease in discussion, as the in-situ liquefaction test. The remainder of this dissertation focuses on the development of the second-generation testing technique (i.e. instrumentation, test configuration, and testing procedure) and the results obtained from its implementation.

Chapter 4

In-Situ Liquefaction Test Instrumentation

4.1 INTRODUCTION

The major components of the in-situ liquefaction test instrumentation system are: (1) the liquefaction sensors, and (2) the data acquisition system used to power and record their output signals. The liquefaction sensors are composed of a sealed, miniature pore water pressure transducer and a three-component (3D) Micro-Electrical Mechanical Systems (MEMS) accelerometer. Their output signals are captured using a 72-channel dynamic signal analyzer that has VXI hardware and Data Physics software. Each of the major components of the in-situ liquefaction instrumentation system are discussed in detail below.

4.2 LIQUEFACTION SENSOR

Soil liquefaction is a complex phenomenon involving the coupled response of the soil skeleton and pore water. Therefore, a sensor used to track the soil liquefaction process must also couple the ability to simultaneously record soil particle motion and pore water pressure generation. There are several issues that must be considered in the design (Stokoe et al., 2004). First, the sensor must be small enough to avoid significant interference with the surrounding soil. Second, the unit weight of the sensor package must be similar to the total unit weight of the surrounding soil to avoid floating or sinking of the sensor after significant excess pore water pressure generation. Third, the stiffness of the sensor must be

large enough to withstand the stresses of installation and dynamic loading. Fourth, the noise level of the instrumentation needs to be small for accurate monitoring and robust data reduction. Fifth, the sensor must be able to be installed from the ground surface. Sixth, the sensor and cable must be waterproof. Finally, the sensor must be able to be retrieved upon completion of testing.

A picture of the in-situ liquefaction sensor that was designed and constructed for this research is shown in Figure 4-1. The main body of the sensor, where the instrumentation is housed, is a cylindrical, acrylic case with a 60-degree conical tip. It has an aluminum top piece that protects the acrylic main body from the heavy, steel push rods and keeps the sensor oriented during installation. The electrical cable (nominally 0.4 in. or 1.0 cm in diameter) contains six-pairs of individually twisted and shielded conductors (26 gauge) that power the instrumentation and carry their signals back to the ground surface. The polyurethane cable jacket (nominally 0.06 in. or 0.15 cm thick) is extremely tough, flexible, and waterproof. Because the sensor must be detached from the push rods prior to dynamic loading, it is also equipped with a flexible, small diameter ($3/32$ in. or 0.24 cm), stainless steel wire rope that allows it to be pulled out of the ground upon completion of testing.

An up-close view of the liquefaction sensor is shown in Figure 4-2. As can be seen, the sensor is compact, measuring 5.0 in. (12.7 cm) from tip-to-top and 1.5 in. (3.8 cm) in diameter. Its total unit weight is approximately 90 pcf (14.1 kN/m^3). The sensor houses a miniature pore water pressure transducer (PPT) and a porous bronze filter. Its vibration-sensing device is a 3-component

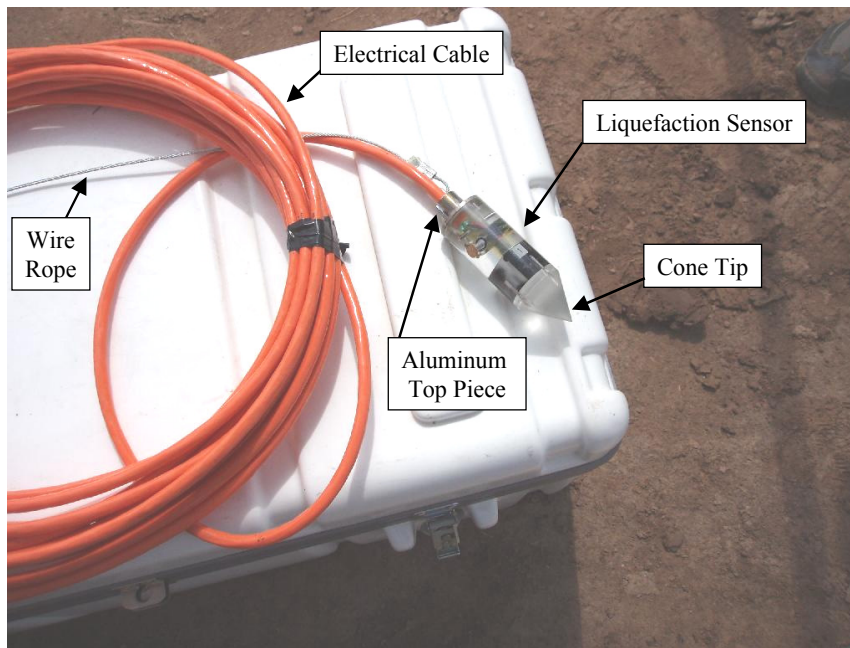


Figure 4-1 Picture of an in-situ liquefaction sensor and its associated cables.

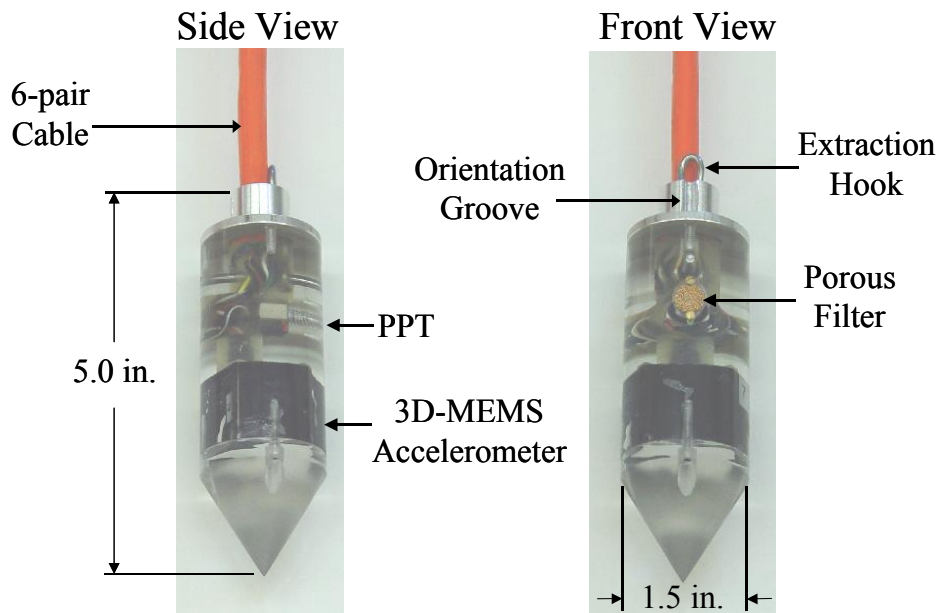


Figure 4-2 Schematic detailing the dimensions and components of the in-situ liquefaction sensor.

(3D), Micro-Electrical Mechanical Systems (MEMS) accelerometer. The aluminum top piece has cylindrical grooves that keep the sensor properly oriented on the push rods during installation. The sensor is also equipped with an extraction hook so that the wire rope used to pull the sensor out of the ground can easily be removed or replaced if broken. The PPT and MEMS accelerometer components of the liquefaction sensor are discussed in detail below.

A total of 20 in-situ liquefaction sensors were built for this research, of which, ten are still functioning. The first ten sensors that were built have all been damaged in one form or another. A few of the original sensors were destroyed during field trial tests at a local aggregate quarry (Capitol Aggregate) in Austin, Texas. Problems included fracturing of the sensor during installation and breaking of the wire retrieval rope during sensor extraction. Lessons learned from these field trials were applied to the final sensor design, and the installation and extraction procedures discussed later in the dissertation. The other original liquefaction sensors experienced varying degrees of electrical failure in the delicate MEMS accelerometer that was installed in the original ten sensors. Lessons learned from the MEMS accelerometer failures are discussed below.

4.2.1 Micro-Electrical Mechanical Systems (MEMS) Accelerometers

MEMS accelerometers are capacitance-based transducers that, unlike traditional accelerometers, have the ability to sense and respond to both static (gravity) and dynamic accelerations. MEMS accelerometers were chosen for the vibration-sensing component of the liquefaction sensor because of: (1) their compact size, (2) their high output at low frequencies of vibration, (3) their ability

to track tilt of the sensor as it is pushed into place, and (4) their ability to monitor any tilt of the sensor that might occur during liquefaction testing.

The MEMS accelerometer that was ultimately selected for use in the in-situ liquefaction sensors is a Silicon Designs model 2430-002. It is shown in Figure 4-3. This accelerometer is cube-shaped with approximate dimensions of 1.0 x 1.0 x 1.0 in. (2.5 x 2.5 x 2.5 cm). It is a triaxial sensing (3D) model with an output of 2.5 volts per g (g = acceleration of gravity). Its nominal three-decibel frequency range is 0 to 300 Hz, and it has a full-scale amplitude range of + and – 2g. The 2430 MEMS accelerometers can be powered by any direct current (DC) voltage between 11 and 16 volts. However, their output is only constant when they are supplied with a voltage between 12 and 16 volts DC. It is very important to apply the proper voltage polarity to these sensors. One of the input conductors supplies a positive (+) voltage, while the other input conductor supplies a negative (-) voltage. They, therefore, require two separate voltage power supplies. The MEMS accelerometers used in this study were always supplied with + and –12 volts DC. The 2430 accelerometers have a quasi- differential output, meaning that all three acceleration components (x, y and z) are referenced to a common output reference potential (typically ground). It should be noted here that MEMS accelerometers are fairly susceptible to damage caused by electrostatic discharge (ESD) and general over-voltage supply. However, the 2430 accelerometers are substantially less susceptible to these problems than some other models because they include on-board voltage regulation and an internal voltage reference.

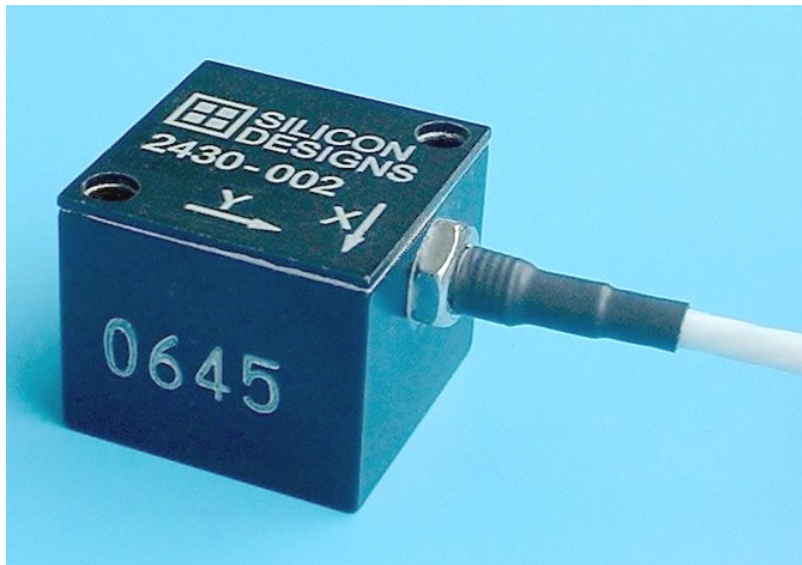


Figure 4-3 Picture of a triaxial (3D) MEMS accelerometer used as the vibration-sensing component of the in-situ liquefaction sensors (from www.silicondesigns.com).

Silicon Designs model 2422 MEMS accelerometers were selected as the vibration-sensing component for the ten original (out of commission) liquefaction sensors mentioned above. The 2422 model was chosen primarily because it had a true differential output (as opposed to the quasi-differential output of the 2430 model). However, the manufacturer (Silicon Designs) did not make it clear that model 2422 MEMS accelerometers were not equipped with the circuitry to help minimize susceptibility to ESD and over-voltage supply. This circuitry has been removed from the 2422 accelerometers to allow them to be used at very high operating temperatures. The extreme sensitivity of the model 2422 MEMS accelerometers was horribly suited for field applications because the electrical leads were constantly being handled, connected, and disconnected from the power

supply and signal recording equipments. As a result, many of the 2422 accelerometers were rapidly “fried”, thus rendering the sensors useless for vibration sensing. The model 2430 MEMS accelerometers, installed in the ten current liquefaction sensors, have performed much better. However, they are not completely immune to ESD and over-voltage supply, so the potential for damage still exists. The benefits and costs of using MEMS accelerometers should be considered when constructing more liquefaction sensors in the future.

The model 2430 3D-MEMS accelerometers were calibrated both statically (for tilt) and dynamically. Prior to calibration, each MEMS component of each liquefaction sensor was assigned a separate recording channel on the VXI dynamic signal analyzer (see Section 4.3). This allowed each accelerometer component to be calibrated on the same channel that it would be recorded with while conducting liquefaction tests in the field. The recording channels that were assigned to each component of each liquefaction sensor are listed in Table 4-1.

4.2.1.1 Tilt Calibration

MEMS accelerometer tilt calibrations were performed using the compound sine plate shown in Figure 4-4. The sine plate (borrowed from the Aerospace Engineering machine shop at UT) was used to incrementally rotate the accelerometers about a single axis while the change in output of each 3D-MEMS component (x, y and z) was monitored by the VXI dynamic signal analyzer. A 3D-MEMS accelerometer can sense simultaneous rotations about its x- and y-axes. However, it cannot sense rotations about its z-axis because the gravitational reference frame for each individual component remains constant. During

Table 4-1 VXI dynamic signal analyzer recording channels assigned to the instrumentation components of each in-situ liquefaction sensor

| Liquefaction Sensor | MEMS I.D. # | PPT I.D. # | VXI Recording Channel | | | |
|------------------------|----------------|---------------|-----------------------|--------|--------|--------|
| | | | PPT | MEMS X | MEMS Y | MEMS Z |
| 1 | 0646 | 28 | 1 | 11 | 12 | 13 |
| 2 | 0647 | 31 | 2 | 14 | 15 | 16 |
| 3 | 0648 | 32 | 3 | 17 | 18 | 19 |
| 4 | 0661 | 33 | 4 | 20 | 21 | 22 |
| 5 | 0662 | 34 | 5 | 23 | 24 | 25 |
| 6 | 0663 | 35 | 6 | 26 | 27 | 28 |
| 7 | 0664 | 37 | 7 | 29 | 30 | 31 |
| 8 | 0665 | 38 | 8 | 32 | 33 | 34 |
| 9 | 0666 | 39 | 9 | 35 | 36 | 37 |
| 10 | 0667 | 40 | 10 | 38 | 39 | 40 |

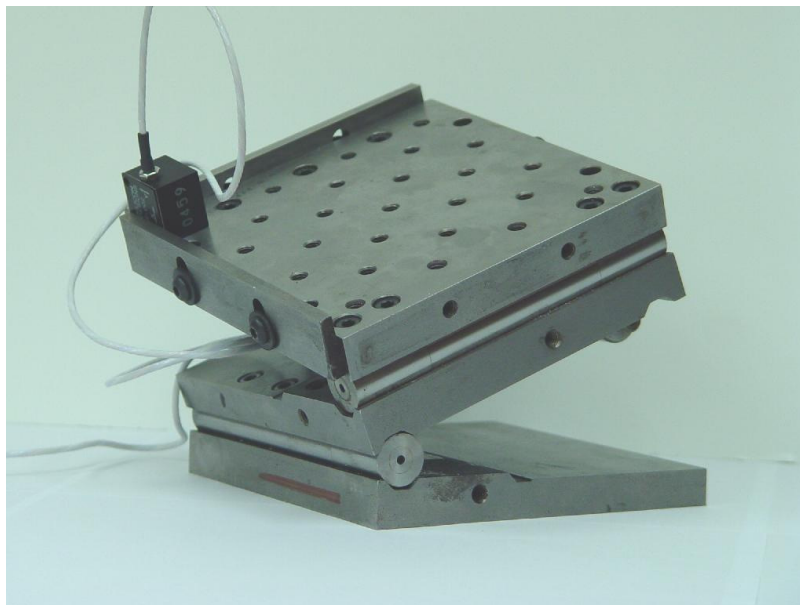


Figure 4-4 Picture of the compound sine plate used to calibrate the 3D-MEMS accelerometers for tilt.

calibration, it was found that for angles less than approximately 30 degrees, tilt about the x-axis of the transducer is a linear function of the change in output of the y-component of the transducer and tilt about the y-axis is a linear function of the change in output of the x-component. These simple linear relationships allowed sensor tilt angles to be solved for without needing to use the more complex 3D rotation matrix equations.

Figure 4-5 shows the calibration results for one of the 3D-MEMS accelerometers (I.D. #0646) rotated about its x-axis. As can be seen, the output of the x- component remains nearly constant, while the output of the y-component changes in a linear relationship with the tilt angle about the x-axis. It should be noted here that the tilt angles about each axis were defined as positive or negative by the right-hand rule. Figure 4-6 shows the calibration results for the same MEMS accelerometer rotated about its y-axis. In this case, the output of the y-component remains nearly constant, while the output of the x-component changes in a linear relationship with the tilt angle about the y-axis. Once single axis tilt calibrations had been performed for the x- and y-axes, the compound sine plate was used to simultaneously rotate each 3D-MEMS accelerometer through combinations of angles about both the x- and y-axes. This was done to ensure that simultaneous tilting about both axes did not influence the calibration results obtained from tilting about a single axis. In all instances, the calibrations were consistent.

A summary of the tilt calibration results for each liquefaction sensor is provided in Table 4-2. The tilt angle of a sensor about its x-axis may be

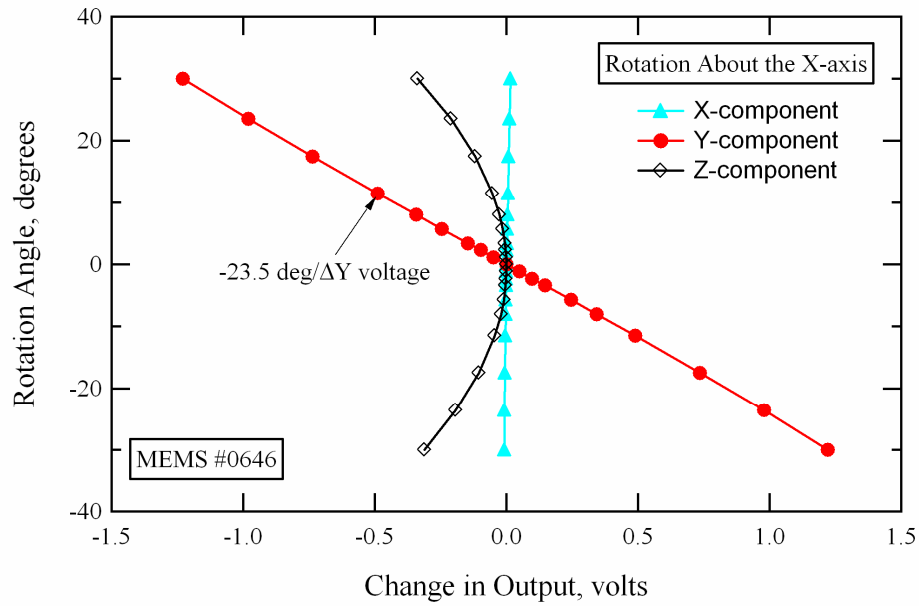


Figure 4-5 Tilt calibration results for a 3D-MEMS accelerometer rotated about its x-axis.

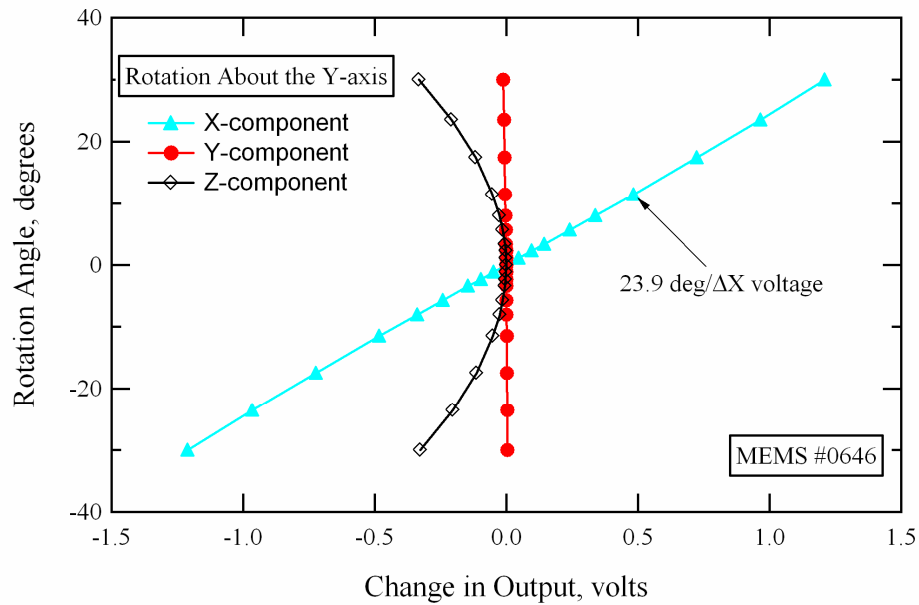


Figure 4-6 Tilt calibration results for a 3D-MEMS accelerometer rotated about its y-axis.

Table 4-2 Tilt calibration results for the 3D-MEMS accelerometer installed in each in-situ liquefaction sensor

| Liquefaction Sensor | MEMS I.D. # | X-angle slope (deg/ Δ Y volt) | Y-angle slope (deg/ Δ X volt) | Vertically-Oriented Reference Voltages | | |
|------------------------|----------------|---|---|--|---------|---------|
| | | | | X-comp. | Y-comp. | Z-comp. |
| 1 | 0646 | -23.5 | 23.9 | 0.002 | 0.150 | 2.364 |
| 2 | 0647 | -23.5 | 23.6 | 0.046 | 0.217 | 2.435 |
| 3 | 0648 | -23.5 | 23.9 | 0.095 | 0.198 | 2.393 |
| 4 | 0661 | -23.4 | 23.6 | 0.052 | 0.163 | 2.434 |
| 5 | 0662 | -23.5 | 23.4 | -0.027 | 0.092 | 2.510 |
| 6 | 0663 | -23.4 | 23.4 | -0.111 | 0.039 | 2.669 |
| 7 | 0664 | -23.3 | 23.4 | -0.003 | 0.029 | 2.514 |
| 8 | 0665 | -23.4 | 23.5 | -0.071 | 0.121 | 2.406 |
| 9 | 0666 | -23.4 | 23.3 | 0.008 | 0.090 | 2.508 |
| 10 | 0667 | -23.3 | 23.3 | 0.073 | 0.176 | 2.509 |

determined by multiplying the x-angle slope, given in Table 4-2, by the measured change in voltage of the y-component of the MEMS accelerometer. The tilt angle of the sensor about the y-axis may be determined by multiplying the y-angle slope by the measured change in voltage of the x-component. Depending on the purpose, the initial reference voltages for each MEMS accelerometer component may be determined while the sensor is vertically oriented in the lab, just prior to sensor installation, or once the sensor is at its designated location in the ground. The reference output voltages for each 3D-MEMS accelerometer component, with the sensor vertically oriented in the lab, are provided in Table 4-2.

To accurately track the position of the liquefaction sensor as it is pushed into the ground, regular readings of the output voltages of the 3D-MEMS

accelerometer components need to be taken. This procedure allows incremental tilt angles to be calculated for each reading. Then, knowing the distance the sensor has traveled over each increment, its incremental position can be estimated. This procedure was not followed during field testing because the sensor was quickly placed in a pilot hole below the ground water level to keep it saturated (see Section 5.2). Additionally, the push rods used to install the sensor are constantly being slipped on and off the sensor cable. This makes it very time consuming to take incremental readings during sensor installation because the cable needs to be disconnected from the data acquisition system so often. However, during field testing the tilt of each sensor was checked once it reached its final location. With reference to the vertical sensor orientations in the lab, the tilt values for all components in all tests were generally less than two degrees. These small values of tilt, coupled with the relatively shallow depths of insertion (less than 13 ft or 4 m) and the stiffness of the push rods, confirmed that the sensors were installed with minor deviation. The tilt angles were also checked frequently throughout testing to ensure that the sensor did not move when substantial excess pore water pressures were generated. None of the sensors tilted more than a few tenths of a degree throughout the entire in-situ liquefaction testing procedure.

4.2.1.2 Dynamic Calibration

The 3D-MEMS accelerometer dynamic calibrations were performed using the modal shaker shown in Figure 4-7. All MEMS accelerometers were calibrated for both amplitude and phase. Two different, previously calibrated,

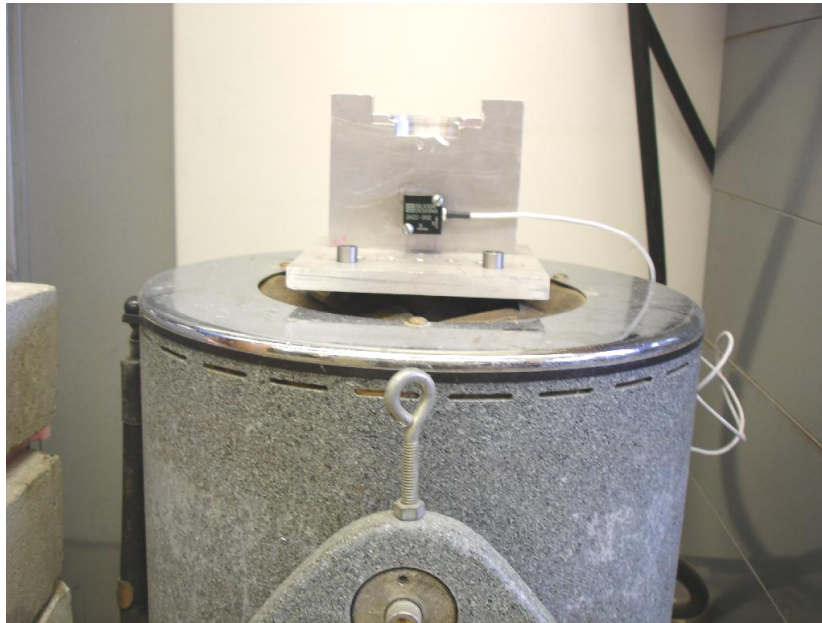


Figure 4-7 Picture of the modal shaker used to dynamically calibrate the 3D-MEMS accelerometers installed in each in-situ liquefaction sensor.

reference transducers were used as the calibration standards. A reference proximeter (displacement transducer) was used for the lower-frequency calibration (0.5 to 100 Hz), while a reference accelerometer was used for the higher-frequency calibration (15 to 500 Hz). A VXI dynamic signal analyzer (discussed in Section 4.3) was used to drive the modal shaker and simultaneously record the responses of the attached calibration instrumentation. Each component of the 3D-MEMS accelerometers had to be calibrated separately because the modal shaker can only vibrate in one direction (vertical) at a time. This was readily accomplished by rotating the cubic MEMS package so that the desired x-, y- or z-component was oriented in the vertical direction.

Dynamic calibrations were performed in a stepped-sine mode. The stepped-sine mode sweeps through a range of user-defined frequencies, creating a constant-amplitude fixed sine wave at each incremental frequency. The fixed sine waves can be applied for any given number of averaging cycles. The amplitude and phase of the transducer being calibrated is calculated at each increment by comparing its output to that of the reference transducer.

The dynamic amplitude calibration results for a single component of one of the 3D-MEMS accelerometers (x-component of MEMS #0646) are shown in Figure 4-8. Figure 4-8a presents the calibration data on a linear-frequency scale, while Figure 4-8b presents the same data on a log-frequency scale. The reference proximeter was used to calibrate the MEMS accelerometers over the frequency range of 0.5 to 100 Hz, while the reference accelerometer was used to calibrate the MEMS over the frequency range of 15 to 500 Hz. In general, very good agreement was found between the calibrations obtained from both reference transducers in the over-lapping frequency range of 15 to 100 Hz. Some small “bumps” occur in the calibration records at approximately 50 and 100 Hz with the reference proximeter, and at approximately 120 Hz with the reference accelerometer. These “bumps” have frequently been observed at the same frequencies in previous geophone calibrations and are therefore assumed to be spurious data caused by certain resonances in the calibration setup. Hence, they are “ignored” in the linear fit to the data.

The curves displayed in Figure 4-8 show a very linear amplitude response over the frequency range of 0.5 to 500 Hz. However, some of the components of

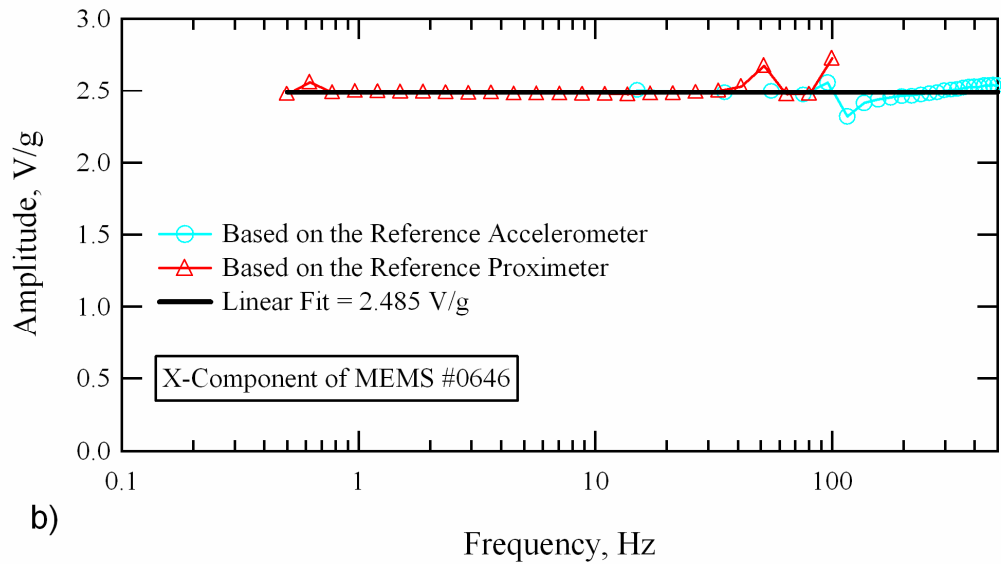
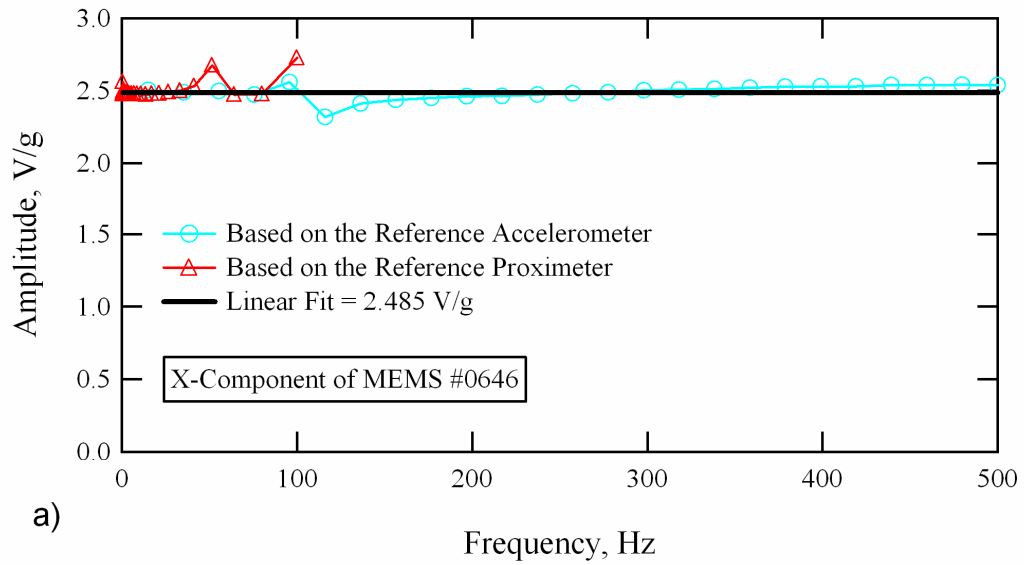


Figure 4-8 Dynamic amplitude calibration results for a single component of a 3D-MEMS accelerometer displayed on: a) a linear-frequency scale, and b) a log-frequency scale.

the MEMS accelerometers were only linear over the frequency range of approximately 2 to 100 Hz. As the in-situ liquefaction tests were planned to operate at fixed frequencies between 10 to 20 Hz, it was still feasible to use a constant calibration factor. Therefore, the constant amplitude calibration factors for each sensor were determined by linearly fitting the recorded data over the frequency range of 2 to 100 Hz. The calibration factor for the data shown in Figure 4-8 (x-component of MEMS #0646) is 2.485 V/g. This value is very close to the approximate amplitude calibration factor of 2.5 V/g suggested by the manufacturer. The amplitude calibration factors for the x-, y- and z-components of the 3D-MEMS accelerometer used in each liquefaction sensor are provided in Table 4-3.

Amplitude calibration is necessary to convert the voltage output by a transducer into units of engineering significance (i.e. acceleration, velocity or displacement). Phase calibration can also be very important. In this research, the measured phase difference between a pair of liquefaction sensors in the field is used to calculate the strain-dependant shear wave velocity of the liquefiable soil deposit during testing (as discussed in Section 6.5). In particular, the y-components of the 3D-MEMS accelerometers are used to sense the passage of vertically propagating (downward) horizontally polarized shear waves. It is therefore important to ensure that the inherent phase difference between a pair of receivers is minimal over the frequency range of interest. Figure 4-9 shows the phase difference that was measured between the y-components of MEMS accelerometers #0646 and #0666 during calibration (one of the sensor pairs used

Table 4-3 Dynamic amplitude calibration factors for the 3D-MEMS accelerometer installed in each in-situ liquefaction sensor

| Liquefaction Sensor | MEMS I.D. # | Amplitude Calibration Factors (V/g) | | |
|------------------------|----------------|-------------------------------------|---------|---------|
| | | X-comp. | Y-comp. | Z-comp. |
| 1 | 0646 | 2.485 | 2.495 | 2.480 |
| 2 | 0647 | 2.485 | 2.500 | 2.485 |
| 3 | 0648 | 2.490 | 2.520 | 2.510 |
| 4 | 0661 | 2.520 | 2.520 | 2.510 |
| 5 | 0662 | 2.510 | 2.510 | 2.510 |
| 6 | 0663 | 2.525 | 2.500 | 2.505 |
| 7 | 0664 | 2.535 | 2.505 | 2.500 |
| 8 | 0665 | 2.510 | 2.510 | 2.510 |
| 9 | 0666 | 2.525 | 2.510 | 2.500 |
| 10 | 0667 | 2.510 | 2.520 | 2.480 |

during field testing; see Chapter 8). Figure 4-9a presents the phase calibration data on a linear-frequency scale, while Figure 4-9b presents the same data on a log- frequency scale. In general terms, the phase difference between these two components tends to increase with increasing frequency. However, in the 10- to 20-Hz frequency range utilized during in-situ liquefaction testing, the phase difference is nearly constant and is less than 0.8 degrees.

Given a vertical distance between receivers of 2 ft (0.6 m) (see Section 6.5), and assuming a shear wave velocity of 400 fps (122 m/s) for the liquefiable soil, the phase differences measured between a pair of receivers for a 10-Hz loading wave and for a 20-Hz loading wave would be 18 degrees and 36 degrees, respectively. Therefore, when using phase differences measured between

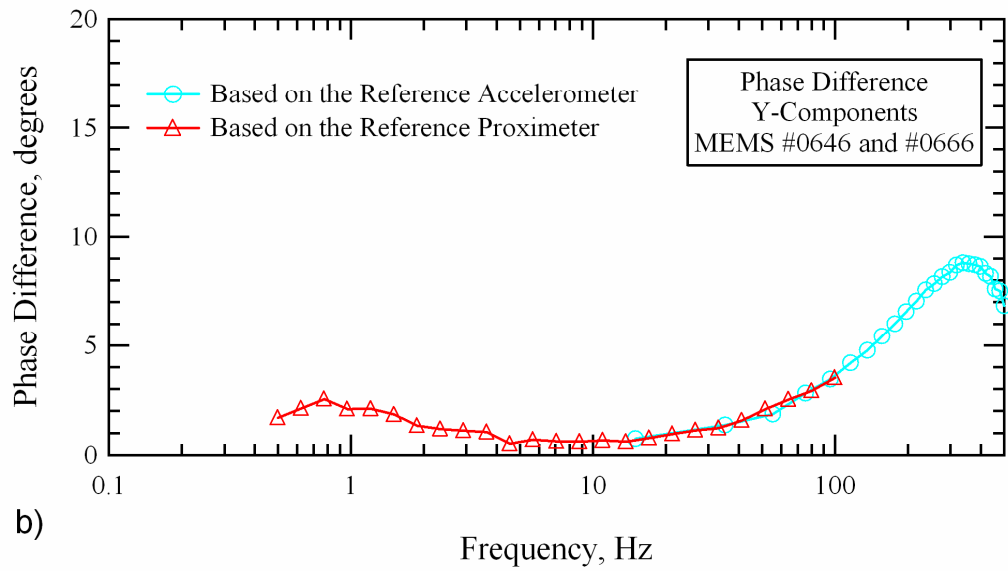
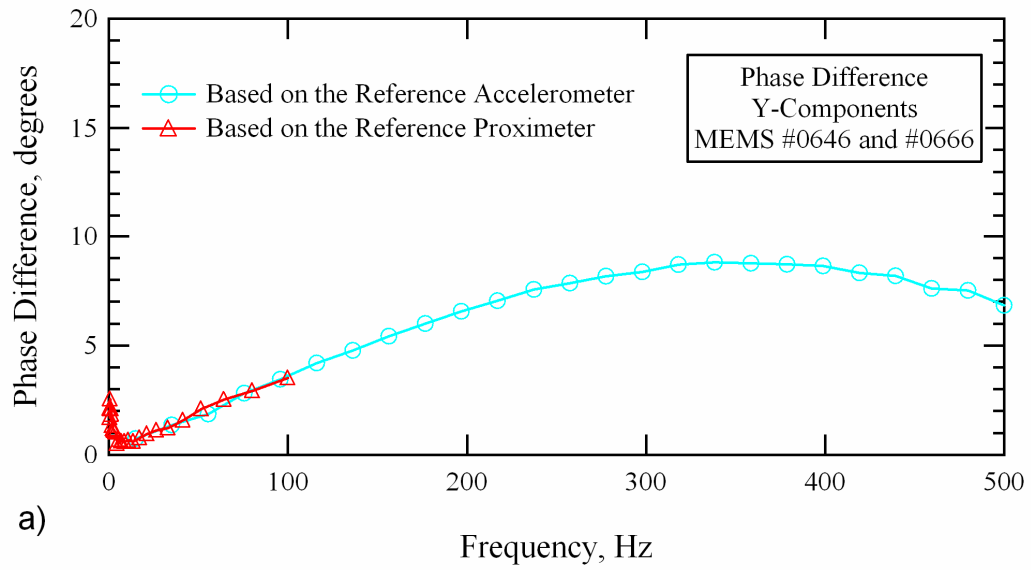


Figure 4-9 Dynamic phase calibration results between two y-components of two 3D-MEMS accelerometers displayed on: a) a linear-frequency scale, and b) a log-frequency scale.

receivers to estimate shear wave velocity, an inherent phase difference between receivers of 0.8 degrees would result in errors of just over 4% and just over 2% for 10-Hz and 20-Hz waves, respectively. The other pair of sensors used to calculate the strain-dependant shear wave velocity of the liquefiable soil deposit during field testing (y-components of MEMS #0662 and #0663) were found to have inherent phase differences of less than 0.3 degrees within the 10- to 20-Hz frequency range. When estimating shear wave velocities, these phase differences would result in errors of just less than 2% and just less than 1% for 10-Hz and 20-Hz waves, respectively. These errors are considered minor and are within the realistic limits of accurately determining the shear wave velocity of a material in situ. Therefore, the inherent phase difference between receivers is not taken into account when estimating the strain-dependant shear wave velocity of the liquefiable soil.

4.2.2 Pore Water Pressure Transducers (PPT)

Pore water pressure transducers (PPT) are needed to measure both the static and dynamic response of the pore water during in-situ liquefaction testing. The two key components of a PPT are: (1) a pressure-sensing diaphragm that converts pressure to an electrical signal via a bonded strain gage, and (2) a porous filter that separates the delicate pressure-sensing diaphragm from the surrounding soil. Additionally, a cavity between the diaphragm and the porous filter is needed to prevent any soil pressure exerted on the filter from being transferred to the pressure-sensing diaphragm.

When attempting to make dynamic pore pressure measurements, time lags and amplitude decay of the PPT signal may be caused by a relatively low permeability filter, a partially saturated filter, or air trapped in the cavity between the pressure-sensing diaphragm and the filter (Chang, 2002; Dunicliff, 1988). Careful saturation procedures can help minimize the chance of air being trapped in the filter or cavity. The permeability of the filter should be fine enough to help keep the PPT cavity saturated during installation, yet coarse enough to minimize any time lag or amplitude decay of the dynamic pressure signal. The PPT saturation procedure and filter material used in this research are discussed in detail in Section 4.2.2.3.

Static pressure measurements are also very important during in-situ liquefaction tests. Static water pressure readings are needed to estimate initial effective confining stresses and to ensure that any excess pore water pressure generated during testing has fully dissipated prior to continuation of staged loading (see Section 5.3). Static pressure readings can be affected by temperature variations, and even the amount of time the sensor has been powered-up for prior to testing. Additionally, a PPT may experience static drift even when held at a constant temperature. Some PPT's are more susceptible to these problems than others. Two different types of PPT's are employed in this research. One of them is a miniature model that is integrated in the liquefaction sensors, while the other is a larger, more stable model contained in its own acrylic case. Each PPT is discussed below.

4.2.2.1 Miniature PPT

The PPT used in all of the in-situ liquefaction sensors is an Entran model EPX-V02-25P. It is shown in Figure 4-10. This model is a miniature, strain gage based, sealed reference, pressure transducer with a nominal output of 2 mV per psi (0.3 mv/kPa) and a 25 psi (172 kPa) range. The EPX model requires 10 volts DC power and has a true differential output. This PPT's primary advantage is its compact size (just over 1.0 in. or 2.5 cm in length), which allowed it to be integrated into the liquefaction sensors.

It was necessary to use the sealed reference version of the EPX because proper venting to the atmosphere could not be guaranteed through the electrical cable of the liquefaction sensor. Because the unit is sealed, its output changes due to fluctuations of barometric pressure. This factor slightly complicates the accurate measurement of static water pressures. Miniature-type PPT's also have a tendency to drift. This phenomenon is most pronounced immediately after the PPT's are powered-up. After they have been powered for several hours, their output becomes more stable. However, their zero offset value (i.e. voltage output at atmospheric pressure) may change substantially (more than the equivalent change in barometric pressure) every time they are re-powered. The calibration effort in this study has shown that the drift phenomenon, coupled with the shifting zero offset associated with re-powering the sensor, render static water pressure measurements with the EPX-V02 unreliable. It should be noted here that Druck

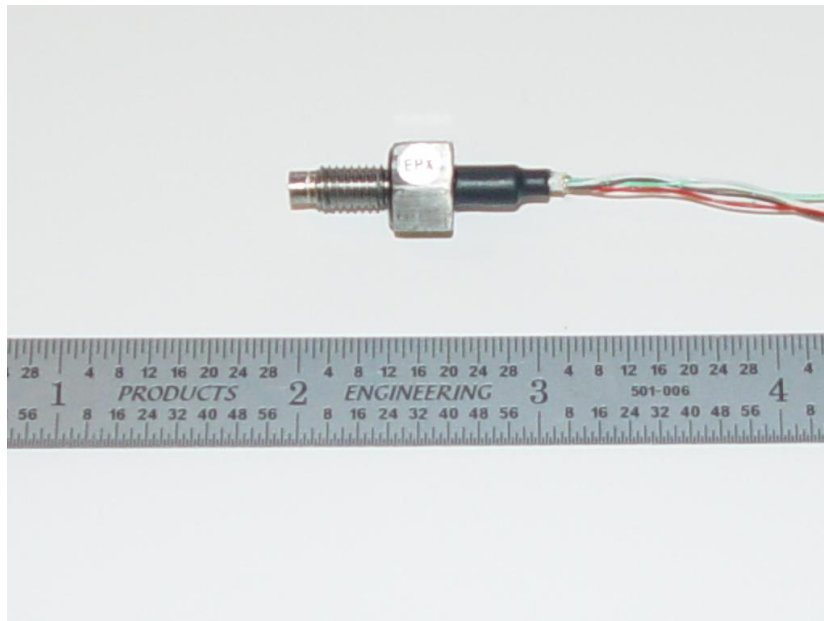


Figure 4-10 Picture of an Entran model EPX-V02-25P miniature pore water pressure transducer (PPT) used in each in-situ liquefaction sensor.

model PDCR-81 miniature PPT's were also experimented with in this research and found to have the same problems as those noted above. These issues seem to be a problem experience by miniature pressure transducers in general.

The drift phenomenon and shifting zero offset do not affect the dynamic sensitivity (i.e. relative change in voltage as a function of the change in pressure) of the miniature PPT's. To ensure this, they were calibrated many times in the laboratory and in the field. A picture of the PPT's being calibrated in the field is shown in Figure 4-11. During the calibration process, water was drained from a standpipe and voltage outputs were recorded at discrete intervals. The dynamic signal analyzer channels assigned to each PPT are listed in Table 4-1. Even though the PPT signals were small, the dynamic range of the analyzer enabled

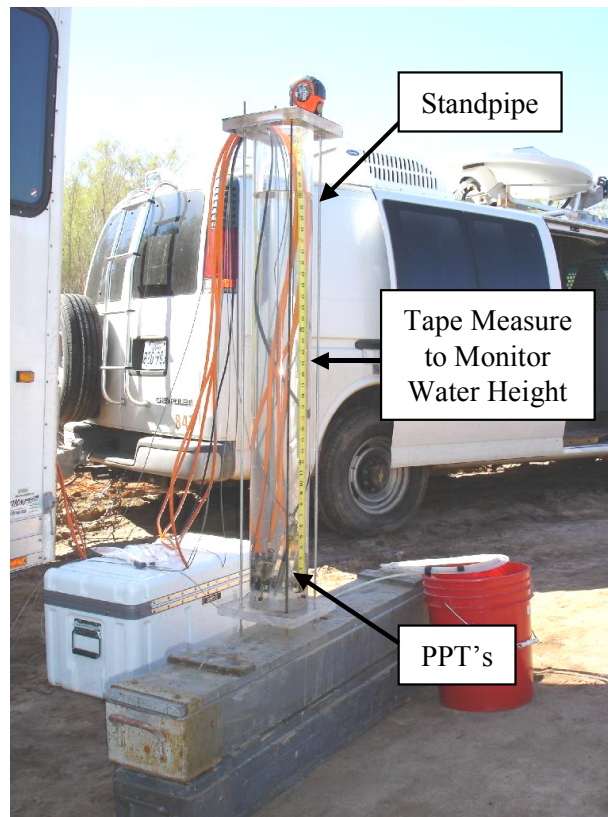


Figure 4-11 Picture of the standpipe used for calibration of the pore pressure transducer (PPT) in each liquefaction sensor during field testing.

direct recordings to be made without the use of output amplifiers. The relationship between change in water pressure and change in output voltage for the PPT's is linear over their stated pressure range.

An example of a calibration curve for one of the PPT's is shown in Figure 4-12. As can be seen, the voltage output for these transducers is a very linear function of the change in pressure. Each time the sensors are calibrated the slope

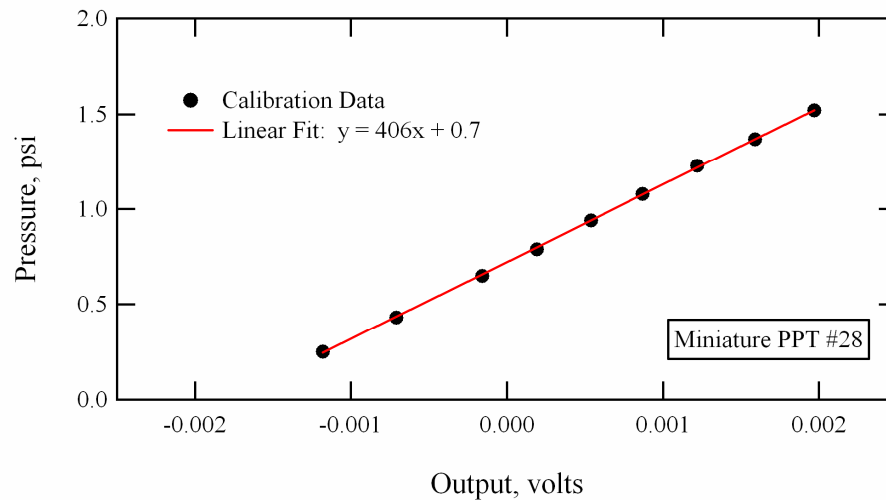


Figure 4-12 Linear calibration results for a typical pore pressure transducer (PPT) used during dynamic in-situ liquefaction tests.

of this function remains relatively constant. However, the zero offset of the sensor (i.e. y-axis intercept) changes for each calibration. The slopes and zero offsets determined for PPT #34 (liquefaction sensor #5) during multiple calibrations in the laboratory and field are listed in Table 4-4. It can be seen that the zero offset changes substantially during different calibrations. The maximum difference in recorded zero offset is 1.3 psi (9.0 kPa or 36.0 inches of water). The barometric pressure was simultaneously monitored during most calibrations and its fluctuation was only a small fraction of the change in recorded zero offset. A shifting zero offset value makes it impossible to accurately estimate static water pressures.

Despite the large fluctuations in zero offset, the slopes of the pressure calibration results shown in Table 4-4 remain quite steady. This behavior was typical for all of the miniature PPT's tested. The mean slope values and

Table 4-4 Calibration results for EPX-VO2-25P miniature PPT #34

| Liquefaction Sensor | PPT I.D. # | Calibration Date | Calibration Time | Slope (psi/V) | Zero Offset (psi) | Atm. Pres. (psi) |
|------------------------|---------------|---------------------|---------------------|------------------|----------------------|---------------------|
| 5 | 34 | 4/12/2005 | 12:30 PM | 403 | 1.1 | 14.73 |
| | | 4/13/2005 | 8:30 AM | 405 | 1.1 | 14.76 |
| | | 4/13/2005 | 4:00 PM | 404 | 1.1 | 14.73 |
| | | 4/14/2005 | 4:00 PM | 401 | 1.0 | 14.77 |
| | | 5/5/2005 | 3:30 PM | 396 | 0.7 | 14.80 |
| | | 5/6/2005 | 9:00 AM | 405 | 0.7 | 14.81 |
| | | 5/6/2005 | 3:30 PM | 397 | 0.8 | 14.74 |
| | | 5/7/2005 | 9:00 AM | 401 | 0.8 | 14.74 |
| | | 6/26/2005 | 12:00 PM | 402 | 1.5 | 14.73 |
| | | 6/26/2005 | 8:00 PM | 418 | 1.5 | 14.71 |
| | | 6/27/2005 | 8:30 AM | 409 | 1.4 | 14.77 |
| | | 6/27/2005 | 5:30 PM | 401 | 1.5 | 14.72 |
| | | 8/12/2005 | 8:30 AM | 395 | 0.6 | * |
| | | 8/16/2005 | 8:30 AM | 396 | 0.2 | * |
| | | 8/29/2005 | 9:30 AM | 407 | 0.5 | * |

Note: * Calibrations performed during or after field testing; atmospheric pressures not recorded

associated standard deviations for each PPT calibrated in this study are listed in Table 4-5. Each PPT was calibrated a minimum of eight times, while some were calibrated as many as 15 times. In general the standard deviations are less than 2% of the mean slope values. This evidence shows that the miniature PPT's can be used to make accurate dynamic (excess) pressure measurements despite their inability to accurately resolve the absolute (static) water pressure.

Table 4-5 Mean slope values and associated standard deviations for the miniature pore pressure transducer (PPT) installed in each liquefaction sensor

| Liquefaction Sensor | PPT I.D. # | Mean Slope (psi/V) | Std Dev (psi/V) |
|--------------------------------|-----------------------|-------------------------------|----------------------------|
| 1 | 28 | 403 | 6 |
| 2 | 31 | 362 | 11 |
| 3 | 32 | 398 | 7 |
| 4 | 33 | 411 | 6 |
| 5 | 34 | 404 | 6 |
| 6 | 35 | 393 | 3 |
| 7 | 37 | 386 | 6 |
| 8 | 38 | 389 | 5 |
| 9 | 39 | 355 | 4 |
| 10 | 40 | 406 | 8 |

4.2.2.2 Stable PPT

The miniature PPT's referenced above were installed in each of the liquefaction sensors with one, 3D-MEMS accelerometer (as shown in Figure 4-2). These compact sensors allowed both dynamic ground response and dynamic pore pressure generation to be measured at the same location during in-situ liquefaction testing. However, a larger, more stable pressure transducer was desired as a reference standard for both static and dynamic pressure readings. A Druck model PDCR 35/D was chosen for this application. The PDCR 35/D comes with its own rugged, integrated cable, complete with venting tube. It is approximately 4 in. (10.2 cm) in length and 0.4 in. (1.0 cm) in diameter. The

version with a 10-psi (69 kPa) range was selected for this study. It requires 10 volts DC power, has a nominal output of 10 mV per psi (1.4 mV per kPa) and is very stable both statically and dynamically.

The PDCR was calibrated five separate times between the laboratory and the field. It was found to have nearly identical results for slope and zero offset each time. The individual calibration results for the PDCR 35/D are listed in Table 4-6. Because of its stable and reliable nature both statically and dynamically, the PDCR 35/D was the primary PPT used in all of the in-situ liquefaction test data processing. The dynamic pressure data obtained from the miniature PPT's, while believed to be quite accurate, were only used in a qualitative sense.

A picture of the PDCR 35/D, epoxied in its acrylic case, is shown in Figure 4-13. The larger-size of this PPT, and its integrated cable, required it to be oriented vertically inside its case. Therefore, the total length of the PDCR push-in sensor is 8 in. (20.3 cm), as opposed to 5 in. (12.7 cm) for the liquefaction sensors.

4.2.2.3 Porous Filter Material and Sensor Saturation

Each sensor is outfitted with a porous filter to buffer the delicate pressure-sensing diaphragm of the PPT from the surrounding soil. To make accurate pressure measurements, proper care needs to be taken to saturate both the filter material and the cavity between the filter and the pressure-sensing diaphragm. The filter material used in this study is sintered bronze with nominal pore sizes of

Table 4-6 Calibration results for the Druck PDCR 35/D pressure transducer

| Calibration Date | Calibration Time | Slope (psi/V) | Zero Offset (psi) |
|------------------|------------------|---------------|-------------------|
| 6/29/2005 | 1:00 PM | 100.7 | 0.0 |
| 7/6/2005 | 1:00 PM | 101.2 | 0.0 |
| 8/12/2005 | 8:30 AM | 100.1 | 0.0 |
| 8/16/2005 | 8:30 AM | 99.8 | 0.0 |
| 8/29/2005 | 9:30 AM | 100.8 | -0.1 |

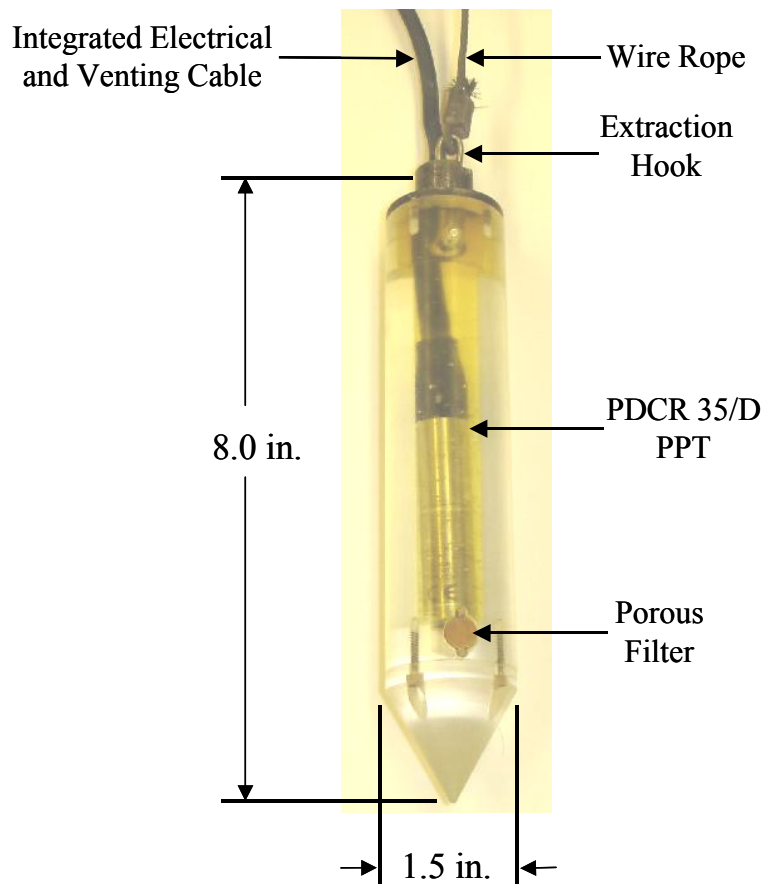


Figure 4-13 Picture of the Druck PDCR 35/D pressure transducer in its acrylic case.

20 microns. Pre-cut, disk-shaped filters with the appropriate dimensions were ordered directly from the manufacturer (Capstan California). The disks are nominally 1/16 in. (0.16 cm) thick and 3/8 in. (0.95 cm) in diameter, and are attached to the sensor cases via small set-screws. The set-screws allow the porous filters to be attached or detached from the sensor case at will. When the filter is removed, the cavity and sensing-diaphragm of the PPT are exposed. This arrangement allows for easy saturation of both the filter and the cavity.

Prior to field testing, the porous filters are saturated by boiling them in water for at least four hours. The filters are then sealed in air-tight containers until they are installed in the field. A picture of a liquefaction sensor just prior to undergoing the field saturation procedure is shown in Figure 4-14. During field testing, the sensor is placed in a bucket of water along with a container of saturated filters. The container is opened under water so that the filters are not exposed to air. Before placing a filter on the sensor, the PPT cavity is visually inspected to make sure that no air bubbles are trapped inside. After the filter is secured to the sensor with set-screws, a tightly-fitting rubber membrane is placed around the sensor while still under water. Once the membrane is on, the sensor can be removed from the bucket and oriented on the push rod. A picture of a saturated liquefaction sensor with its protective rubber membrane is shown in Figure 4-15. The procedure described above ensures that the porous filter and cavity of the sensor are completely saturated prior to field installation. The sensor installation procedure is discussed in Section 5.2.

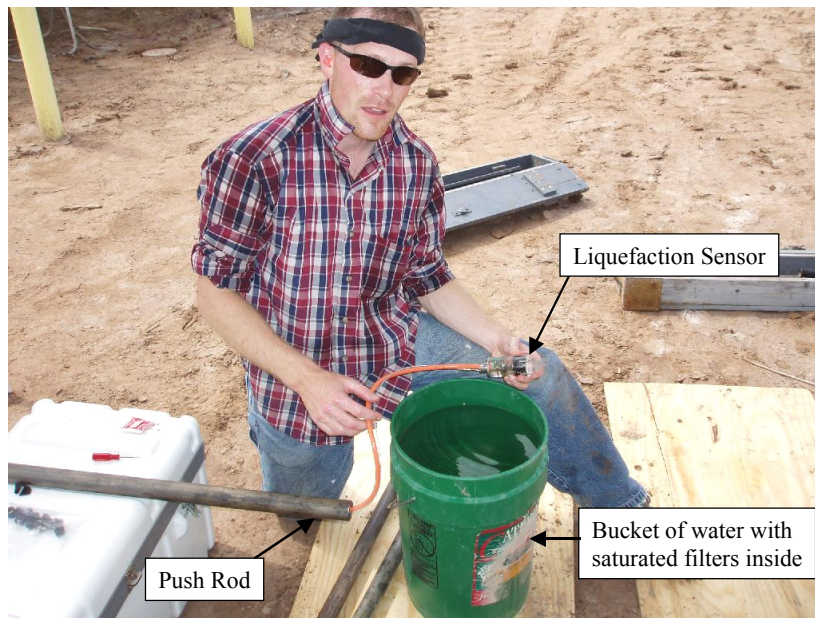


Figure 4-14 Picture of a liquefaction sensor prior to pore pressure transducer cavity saturation and filter installation.

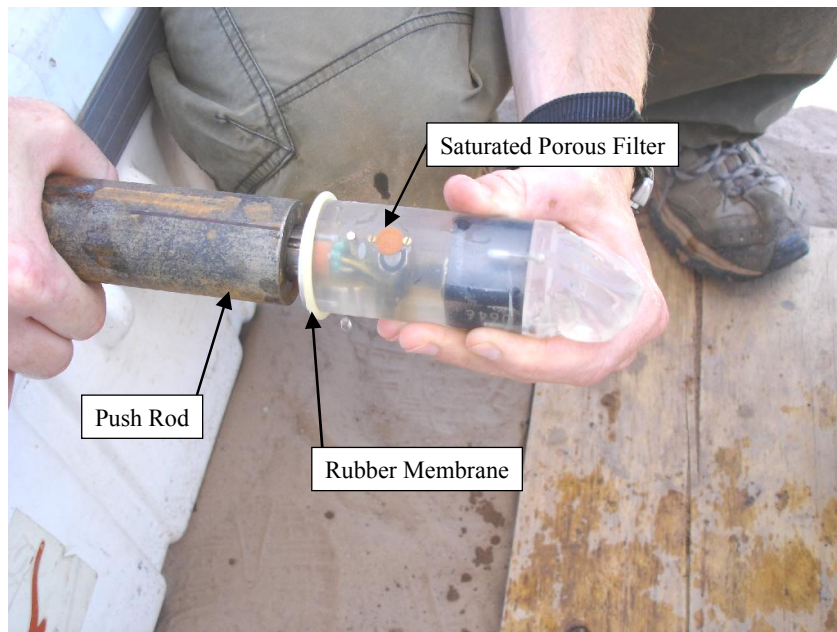


Figure 4-15 Picture of a saturated liquefaction sensor with its protective rubber membrane.

4.3 DATA ACQUISITION

Once installed in the ground, the liquefaction sensors can be used to sense dynamic soil response and pore pressure generation during in-situ liquefaction tests. For this sensing to happen, power must be supplied to the transducer inputs and an appropriate recording system must be connected to the transducer outputs. To facilitate this process, a special connector box was constructed to simultaneously link the liquefaction sensors, the DC power supplies, and the data recording system together. The connector box, power supply system, and data recording system are discussed in detail below.

4.3.1 Connector Box

As discussed in Section 4.2, the electrical cable (nominally 0.4 in. or 1.0 cm in diameter) of the liquefaction sensor contains six-pairs of individually twisted and shielded conductors that power the instrumentation and carry their signals back to the ground surface. This electrical cable must pass through the hollow interior section of the push rods. During liquefaction sensor installation (see Section 5.2), the push rods are constantly being slipped on and off of the electrical cable. Due to the relatively small inside diameter of the push rods (nominally 0.5 in. or 1.3 cm), it was very difficult to install an electrical connection on the end of the sensor cable that could readily slip through the hollow push rods. Therefore, a connector box with quick-release speaker terminals was built to easily rout the individual conductors from the liquefaction sensor cables to their appropriate inputs and outputs. A picture of the connector box is shown in Figure 4-16. The quick-release speaker terminals are color coded

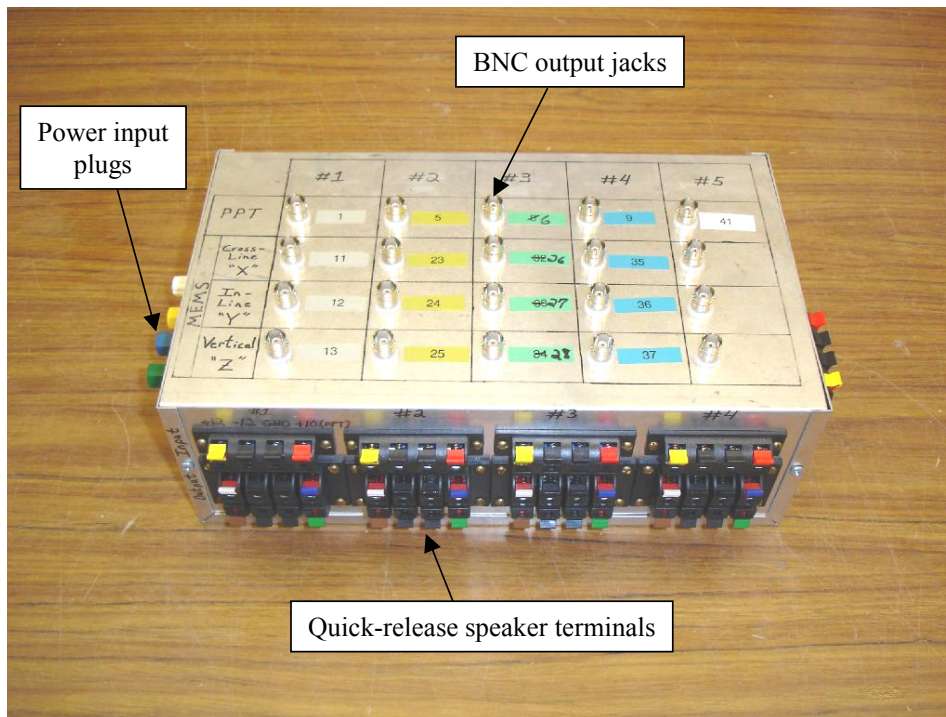


Figure 4-16 Picture of the connector box used to rout individual conductors from the liquefaction sensor cables to their appropriate inputs and outputs.

to match the individual pairs of conductors in the liquefaction cable. A total of five liquefaction sensors can simultaneously be routed through the connector box. Table 4-7 details the input or output associated with each colored conductor pair of the liquefaction sensor cable. Power is delivered to the sensors by connecting the banana plugs on the left side of the connector box to the regulated DC power supplies. This power is then carried through the connector box, to the speaker terminals, into the liquefaction sensor cable, and down to the sensor. The sensor outputs are routed up the cable, through the speaker terminals, to the male BNC jacks on top of the connector box where they are sent to the data recording system.

Table 4-7 Input or output associated with each colored conductor pair of the liquefaction sensor cable

| Color of Liquefaction Sensor Conductor Pair | Associated Input or Output |
|--|-------------------------------------|
| Yellow | Input MEMS: +12V yellow, -12V black |
| Red | Input PPT: +10V red, ground black |
| White | Output MEMS: Z-comp. - differential |
| Blue | Output MEMS: Y-comp. - differential |
| Brown | Output MEMS: X-comp. - differential |
| Green | Output PPT: differential |

4.3.2 Power Supply

As discussed in Section 4.2, the MEMS accelerometers require + and –12 volts DC power, while the PPT’s require +10 volts DC power. An Agilent E3620A dual output DC power supply is used to supply the necessary power to each transducer by setting each of the two separate outputs on the power supply to 12 volts. The – polarity component of output #1 and the + polarity component of output #2 are connected to ground. In this manner, output #1 supplies +12 volts DC and output #2 supplies –12 volts DC. These powers are readily routed to the MEMS accelerometers in each liquefaction sensor through the connector box discussed in Section 4.3.1. The +10 volts required to power the PPT’s is obtained with the aid of a 12-volt to 10-volt DC-to-DC converter. This converter accepts the +12 volts from output #1 of the power supply and converts it to +10 volts, which is then routed to the PPT’s via the connector box. An external over voltage protector (OVP) is placed in-line with each of the power supply outputs to ensure that voltage spikes will not pass through the power supply and into the sensitive

instrumentation. A picture of the power supply system is shown in Figure 4-17. It should be noted here that the DC-to-DC converter can be removed from the regulated power supply and attached to a 12-volt battery. This allows the PPT's to be powered overnight during field testing to help ensure that their outputs remain as steady as possible.

4.3.3 Dynamic Signal Analyzer

The output signals from the liquefaction sensors were recorded using a 72-channel dynamic signal analyzer that has VXI hardware and Data Physics software. As mentioned in Section 4.2, prior to field testing, each liquefaction sensor component was calibrated on the same analyzer channel that it would be recorded on in the field (see Table 4-1). During field testing, fixed frequencies of 10 and 20 Hz were used to dynamically load the soil by driving the vibroseis truck (T-Rex) with an external function generator. The sensor outputs from these tests were recorded at a constant sampling rate of 8192 samples per second. This sampling rate was chosen so that enough data points would be digitized in the time domain to allow accurate determination of the phase difference between liquefaction sensors. The phase difference between sensors is used for evaluating nonlinear soil modulus behavior (see Section 6.5). Given a vertical distance between receivers of 2 ft (0.6 m) and a sampling rate of 8192 samples per second, and assuming a shear wave velocity of 400 fps (122 m/s) for the liquefiable soil, approximately 40 points are digitized in the time that it takes the shear wave to travel from the first receiver to the second receiver. As discussed in Section 4.2.1.2, phase differences measured between sensors during dynamic testing are

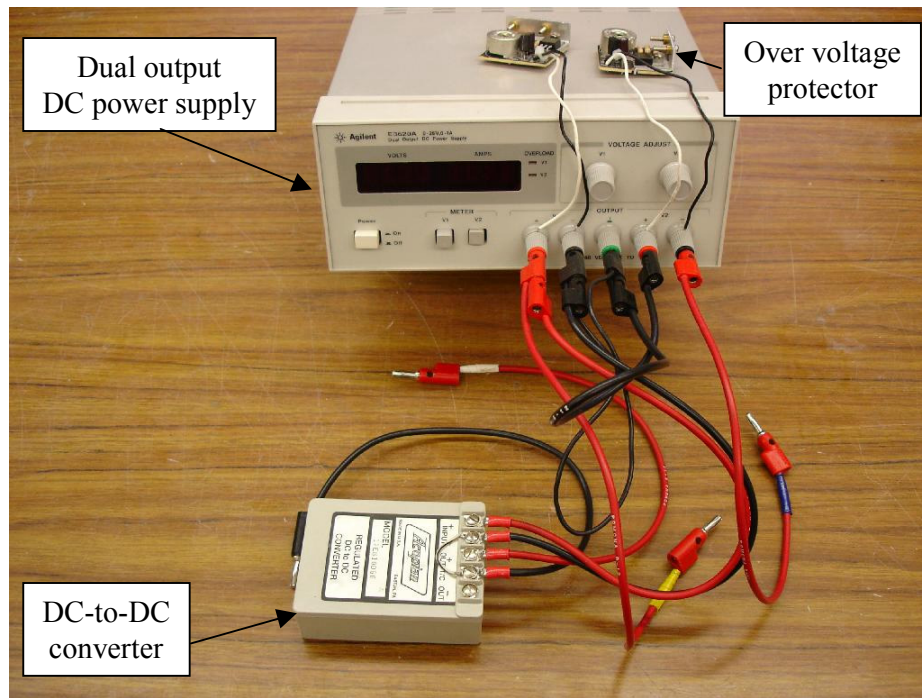


Figure 4-17 Picture of the system used to provide power to the in-situ liquefaction sensors.

generally in the range of 20 to 40 degrees. Therefore, a sampling rate of 8192 samples per second should resolve the phase difference between receivers to the nearest 0.5 to 1.0 degrees.

As discussed above, fixed frequencies of 10 and 20 Hz were used to dynamically load the soil by driving the vibroseis truck (T-Rex) with an external function generator. Typically, 100 cycles of dynamic loading were applied to the soil deposit. Therefore, when a 10-Hz driving signal was used, the maximum duration of dynamic loading was approximately ten seconds. Despite the fact that dynamic loading typically lasted for ten seconds or less, it was desired to record continuous blocks of data up to 120 seconds long in order to capture the complete

trend of pore water pressure generation and dissipation. The throughput-to-disk option of the Data Physics software allowed the liquefaction data to be streamed from the analyzer directly to the hard drive of the laptop for extended periods of time. The only disadvantage associated with the throughput-to-disk option is the inability to trigger the recording system off of an input signal. Therefore, the recording system was started manually before sending the drive signal to T-Rex.

Using the throughput-to-disk option, 19 channels of data were simultaneously recorded at 8192 samples per second for up to 120 seconds. The data recorded included: (1) the vibroseis drive signal from the function generator, (2) the ground force signal from the vibroseis truck, (3) the PDCR 35/D pressure transducer output signal, and (4) a total of 16 output signals from four separate liquefaction sensors (one miniature PPT signal and three components of vibration from the MEMS accelerometer in each liquefaction sensor). The sensor arrangement for in-situ liquefaction tests is discussed in Section 5.2.

The outputs of the PPT's and MEMS accelerometers were primarily recorded using DC coupling. DC coupling is needed to preserve the static information in the transducer signals. The PPT's output a constant voltage relative to the static water pressure around them, while each component of the MEMS accelerometers outputs a constant voltage relative to their tilt. The x- and y-components of the MEMS accelerometers output small static voltages, provided the sensor is installed fairly vertically, because they are oriented perpendicular to gravitational pull (see Table 4.2). However, the z-component has a static output of approximately 2.5 volts because it is oriented in the direction of gravitational

pull. If the z-component is recorded with DC coupling during small amplitude dynamic loading, the resolution of the dynamic signal suffers. Therefore, during dynamic loading, the z-component of the MEMS accelerometer is recorded with AC coupling, while all other signals are recorded with DC coupling. Separate static readings, where all outputs are recorded with DC coupling, are taken before and after most dynamic loads to check the static water pressure and tilt of the sensor.

A picture of the entire data acquisition system is shown in Figure 4-18. This picture was taken during field testing and provides a general view of how all of the components of the data acquisition system link together.

4.4 SUMMARY

The major components of the in-situ liquefaction instrumentation system are: (1) the liquefaction sensors, and (2) the data acquisition system used to power and record their output signals. The liquefaction sensors designed for this research are composed of a sealed, miniature pore water pressure transducer (PPT) and a three-component (3D) Micro-Electrical Mechanical Systems (MEMS) accelerometer. All PPT's and MEMS accelerometers were carefully calibrated prior to field testing. The miniature PPT's are used to monitor the dynamic response of the pore water at the same location where dynamic soil particle motions are recorded with the MEMS accelerometers. However, accurate static water pressure readings can not be made with the miniature PPT's due to problems associated with static drift and shifting zero offset values when the transducers are re-powered. Therefore, a larger, more stable pore pressure

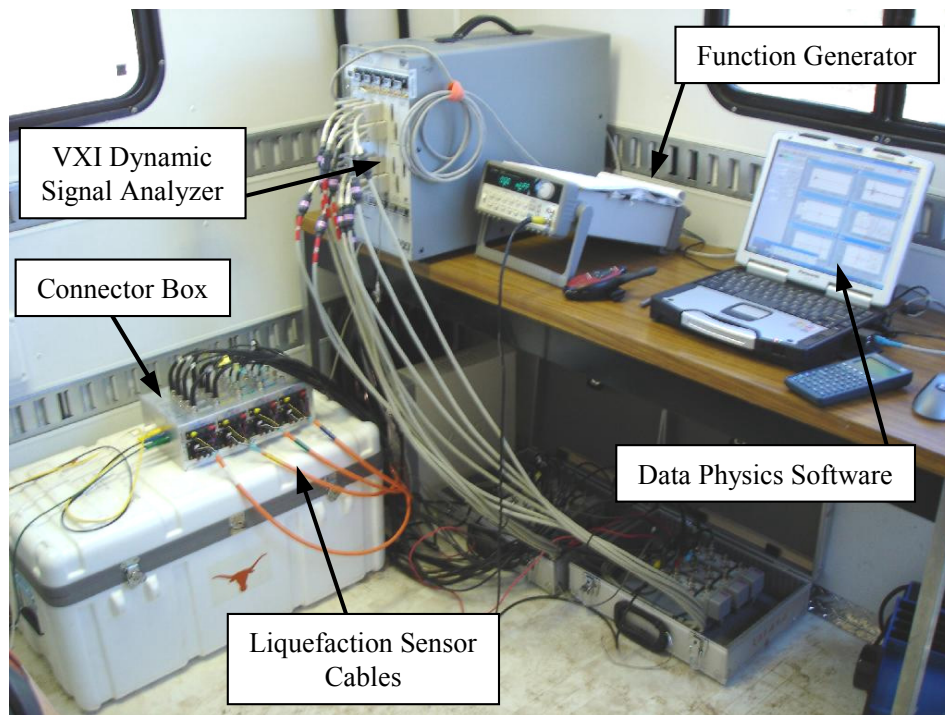


Figure 4-18 Picture of the data acquisition system used for dynamic in-situ liquefaction tests.

transducer is used as a reference standard for both static and dynamic pressure readings. Special design considerations have been taken to ensure that the PPT's can easily be saturated prior to field installation. The MEMS accelerometer outputs are used to track the dynamic response of the soil as well as static tilt of the liquefaction sensor. All transducer outputs are recorded using a 72-channel dynamic signal analyzer that has VXI hardware and Data Physics software.

Chapter 5

Generalized In-Situ Liquefaction Test Procedure

5.1 INTRODUCTION

The generalized in-situ liquefaction test procedure may be subdivided into three basic categories. They are: (1) sensor installation, (2) staged dynamic loading, and (3) sensor extraction. Each of these procedural categories is discussed below.

5.2 SENSOR INSTALLATION

The design and construction of the liquefaction sensors were a large part of this research. In this section, the sensors are referenced only in a general sense. Their exact components, design and construction are discussed in detail in Chapter 4. For review purposes, a picture of the in-situ liquefaction sensor is shown in Figure 5-1. The main body of the sensor, where the instrumentation is housed, is a cylindrical, acrylic case with a 60-degree conical tip. It has an aluminum top piece that protects the acrylic main body from the heavy, steel push rods and keeps the sensor oriented during installation. The electrical cable contains six-pairs of individually twisted and shielded conductors that power the instrumentation and carry their signals back to the ground surface. Because the sensor must be detached from the push rods prior to dynamic loading, it is also equipped with a flexible, small diameter, stainless steel wire rope that allows it to be pulled out of the ground upon completion of testing.

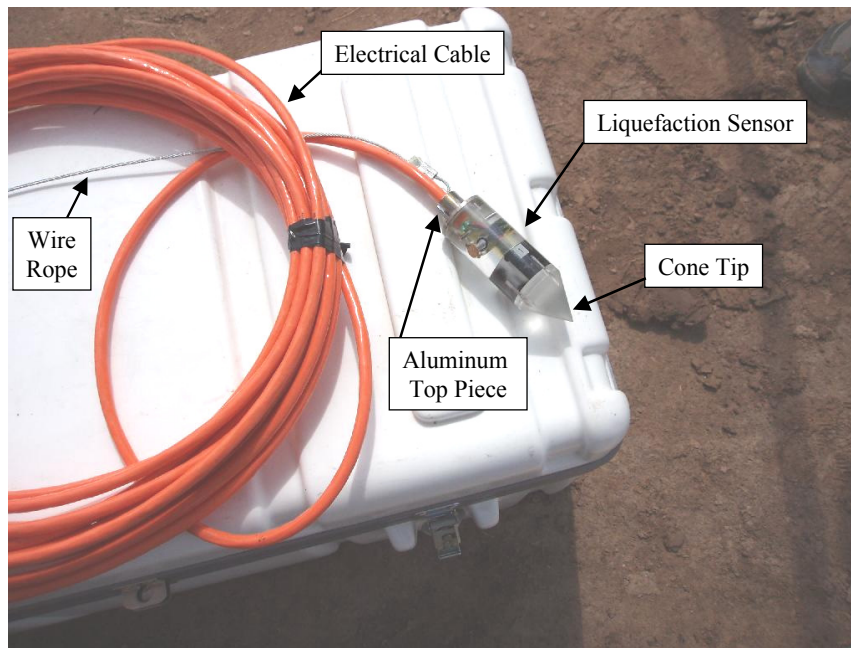


Figure 5-1 Picture of an in-situ liquefaction sensor and its associated cables.

The liquefaction sensors are installed with the aid of heavy-walled, hollow, steel push rods and a hydraulic cylinder located on the back bumper of T-Rex. A picture of the hydraulic ram inserting a push rod into the ground is shown in Figure 5-2. The hydraulic ram can operate at variable speeds and is capable of pushing with a maximum force of approximately 20,000 lb (89 kN). The push rods are Dutch Cone Penetrometer rods that are 4 ft (1.2 m) long, with an outside diameter of 1.5 in. (3.8 cm) and an inside diameter of 0.5 in. (1.3 cm). Some of the full-length push rods were cut to make 1-ft (0.3 m) and 2-ft (0.6 m) long sections to aid in sensor installation. Special pushing and pulling connections were also designed to couple the push rods to the hydraulic cylinder on the back of T-Rex.

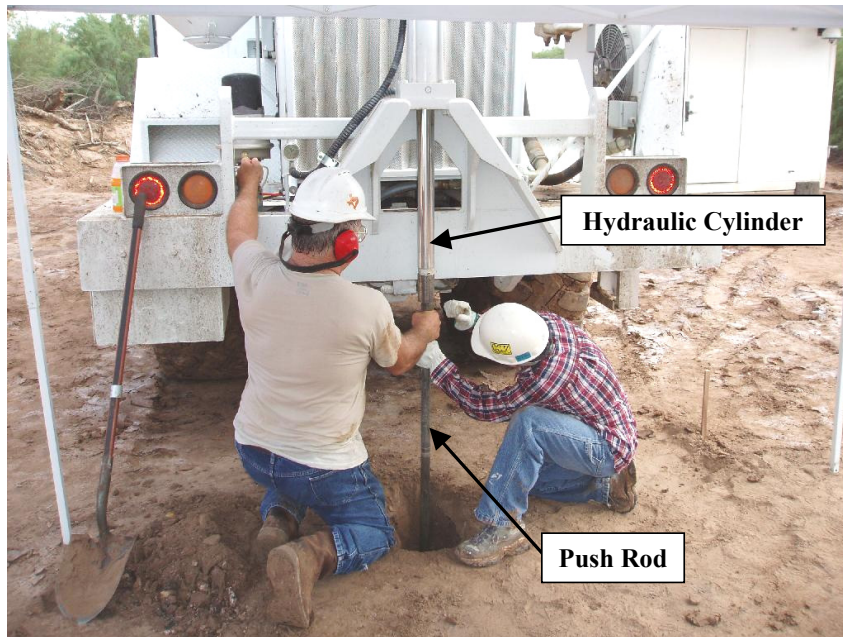


Figure 5-2 Picture of the hydraulic cylinder on the rear bumper of T-Rex used with push rods to install the liquefaction sensors in the field.

The pushing and pulling connections are shown in Figure 5-3. Both connections are easily threaded on and off the hydraulic cylinder. The coupling between the pushing connection and the rods is a simple compression fit. The pushing connection has a hollow section several inches deep, into which the butt-ends of the push rods are seated. This hollow section is just large enough to allow the push rods to slide in and out freely. A slot in the side of the connection allows the sensor cables to exit the apparatus without being smashed when pushing the rods into the ground. The pulling connection is composed of a top piece and a bottom piece. The bottom piece is a short, slotted section of a push rod with male threads. It can move up and down within the top piece over a range of several inches. It is also free to rotate inside the top piece, thereby allowing the male-

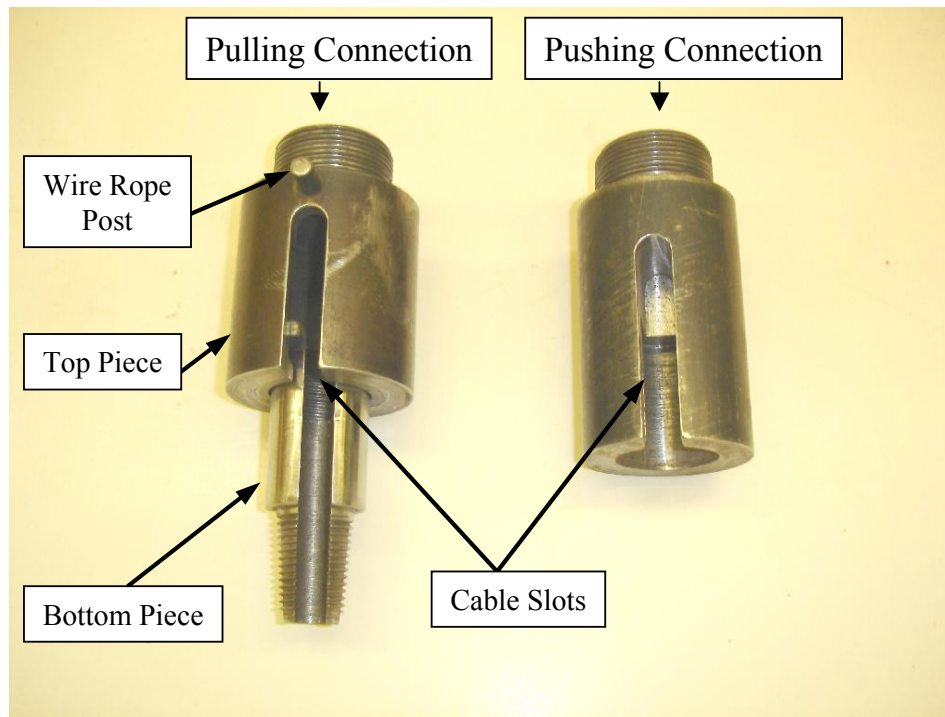


Figure 5-3 Picture of the pushing and pulling connections that couple the hydraulic cylinder on the rear bumper of T-Rex to the push rods.

threaded bottom piece to be connected to the female-threaded end of a push rod. When loaded in tension, the top piece and the bottom piece come firmly into contact, thus allowing the rods to be pulled out of the ground. A continuous slot between the top piece and bottom piece allows the sensor cables to exit the connection. The pulling connection is also equipped with a post to wrap the wire rope around during sensor extraction (see Section 5.4).

Prior to sensor installation, a slightly oversized, steel pilot cone is typically pushed to a depth just below the ground water level (GWL) and then removed. The oversized pilot cone is nominally 1.75 in. (4.4 cm) in diameter, while the push rods and liquefaction sensors are nominally 1.5 in. (3.8 cm) in

diameter. The oversized pilot cone is used to create a pilot hole, which serves two purposes: (1) it prevents the sensor from being damaged while penetrating the stiff, desiccated, near-surface soil crust, and (2) it allows the sensor to be placed by hand below the GWL with the protective membrane, that keeps the pressure transducer saturated while out of water (see Section 4.2), still in place. A picture of the oversized pilot cone is shown in Figure 5-4. For reference purposes, a steel pilot cone with the same diameter as the push rod is also shown. The smaller diameter pilot cone may be used to pilot a hole below the GWL if the soil is still quite stiff before reaching the soft liquefiable layer. The oversized pilot cone should not be pushed to close to the liquefiable layer, as this will create a void around the push rods that water can readily escape through during dynamic loading and subsequent pore pressure generation. If the GWL begins in the liquefiable layer, other means will need to be taken to either: (1) ensure the pressure transducer remains saturated during installation without using an oversized pilot cone, or (2) seal the void around the push rods so that water from the liquefiable layer cannot readily escape during dynamic loading.

As discussed above, an electrical cable and a wire rope are attached to each liquefaction sensor. The electrical cable is nominally 0.4 in. (1.0 cm) in diameter, while the wire rope is nominally 3/32 in. (0.24 cm) in diameter. These members pass through the hollow section of the push rods (nominally 0.5 in. or 1.3 cm in diameter) until they reach the ground surface. The electrical cable and wire rope fill most of the space inside the hollow rods. However, to ensure that ground water will not escape through the hollow section of the push rods during

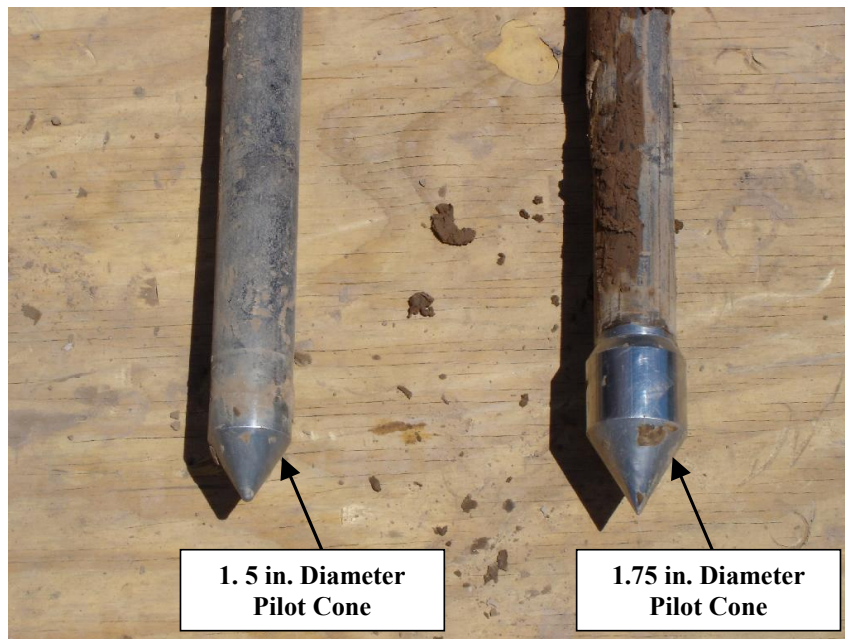


Figure 5-4 Picture of the two pilot cones used to help install the liquefaction sensors in the field.

dynamic loading, a tapered rubber gasket is placed around the cables just above the sensor connection. When the gasket is pushed into the hollow section of the rod, it compresses around the cables, thereby creating a seal that retards the escape of excess pore water pressures. A picture of the rubber gasket being installed during field testing is shown in Figure 5-5. Vacuum grease is placed around the cables in the vicinity of the gasket to help seal the plug and provide sliding lubrication when the sensor is decoupled from the push rods.

As discussed in Section 4.2, the pressure transducer saturation process occurs under water, in a bucket, prior to sensor installation. As part of this process, a tightly-fitting rubber membrane is placed around the sensor while it is still under water. Once the membrane is on, the sensor can be removed from the

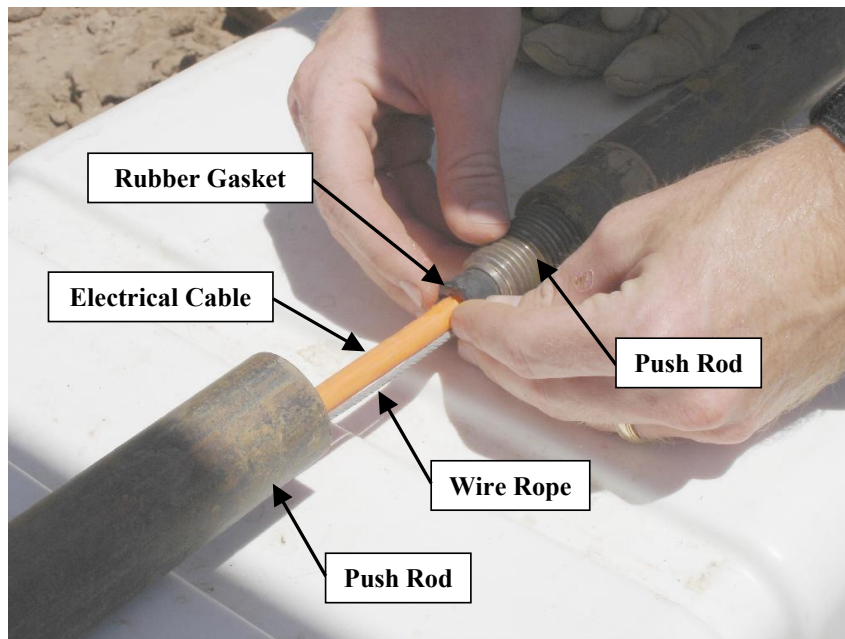


Figure 5-5 Picture of the rubber gasket used to seal the hollow section of the steel push rods.

bucket and oriented on its push rod (as shown in Figure 4-15). The sensor and push rod are coupled together via a simple compression fit. Small cylindrical grooves in the aluminum top piece of the sensor mate with pins inside the hollow push rod to keep the sensor oriented during installation (see Figure 4-2). Once the sensor is oriented on the push rod, it is lowered by hand down the oversized pilot hole to a temporary resting place just below the GWL. A picture of a sensor about to be placed in its pilot hole is shown in Figure 5-6. Note that the pilot hole begins in a shallow trench just below the ground surface. A trench is needed because the liquefaction sensor cables and the tops of the push rods must be below the ground surface during dynamic loading so that the base plate of T-Rex does not come into contact with them.

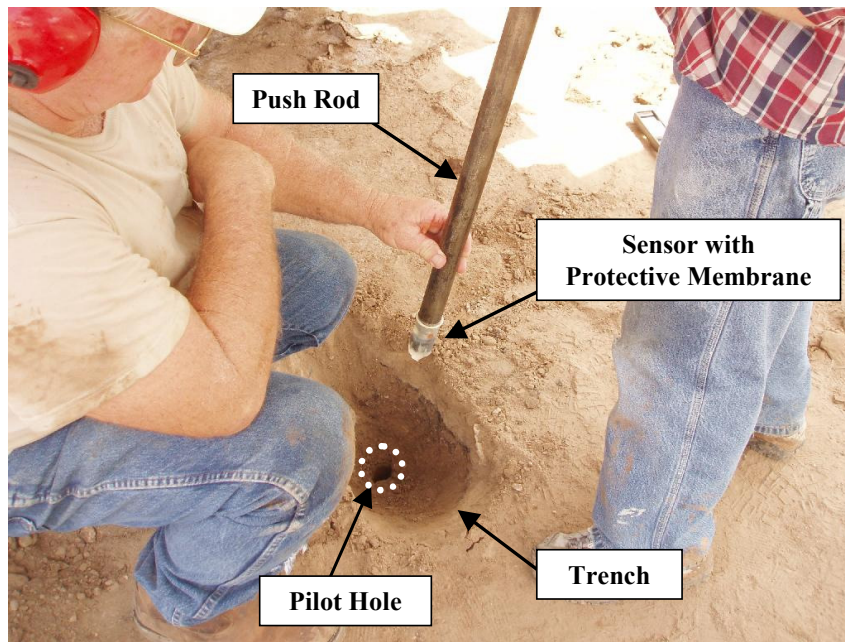


Figure 5-6 Picture of a liquefaction sensor and the pilot that enables it to be lowered to the ground water level.

After the sensor has been placed below the GWL, it is pushed the remaining distance through virgin soil to its pre-selected location. The thin rubber membrane is torn from the sensor as it is pushed into place. After the sensor is in place, the push rod is decoupled from the sensor by withdrawing the push rod a short distance (typically 3.0 in. or 7.6 cm). During this process, the relative movement between the push rods and the sensor cable is monitored to make sure that the sensor stays in place. This withdrawal helps to ensure that the dynamic movement of the sensor will not be influenced by the presence of the heavy push rods (or at least the influence of the push rods is minimized). However, the push rods remain in the hole to prevent water from escaping during dynamic loading. A square metal bracket is threaded onto the top of the push rods

to keep them from slipping back down the hole and coming into contact with the sensor. The bracket should be in firm contact with the base of the trench so that the rods cannot settle back on top of the sensor during dynamic loading. This requires careful consideration of the depth the trench should be dug to and the distance the push rods should be withdrawn.

The sensors are installed one at a time, forming a linear, two-dimensional (2D) array beneath the ground surface. A picture of the completed sensor array, as seen from the ground surface, is shown in Figure 5-7. The numbers next to each liquefaction sensor do not represent the order in which they are installed, but rather the positions of the sensors in a trapezoidal array. It should be noted that the cable exiting the center of the array (Position No. 5) is different from the cables exiting the ends of the array (Position Nos. 1-4) because Position No. 5 is occupied by a sensor containing the stable PDCR 35/D pressure transducer, while position Nos. 1-4 are occupied by in-situ liquefaction sensors containing a 3D-MEMS accelerometer and a miniature pore pressure transducer (see Section 4.2). While slightly difficult to see because of lighting, the square metal brackets that keep the push rods from sliding back down the hole can also be seen in Figure 5-7. Paper towels are stuffed into the small void between the metal bracket and the sensor cables to prevent backfill soil from falling into the hollow rods.

A cross-sectional schematic of the sensor array, as viewed from below the ground surface, is shown in Figure 5-8. The array is in the form of a trapezoid, with an in-situ liquefaction sensor occupying each of its four corners. Typical array dimensions are provided in Figure 5-8. The corner sensor positions may be

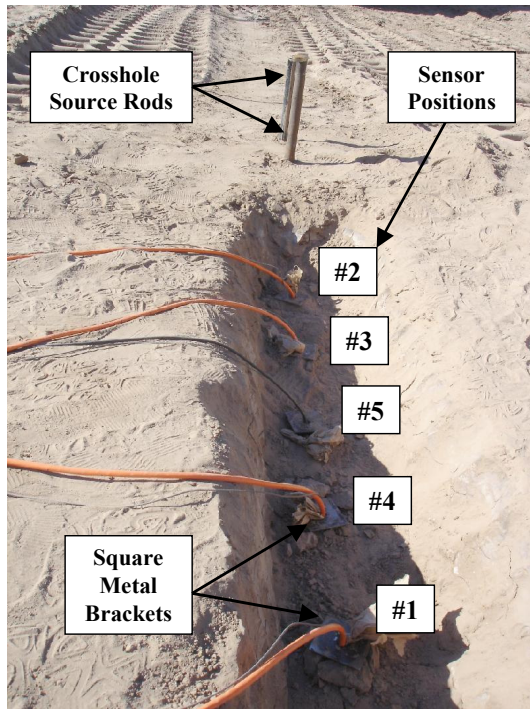


Figure 5-7 Picture of the installed liquefaction sensor array and crosshole source rods.

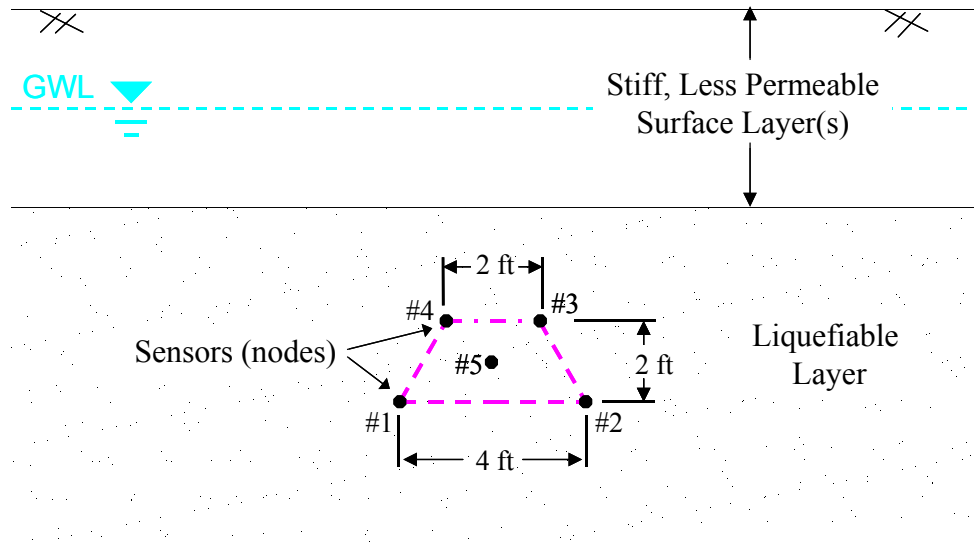


Figure 5-8 Cross-sectional schematic of the trapezoidal sensor array used for in-situ liquefaction tests.

considered as nodes of a single quadrilateral finite element. This configuration allows the shear strains anywhere within the element to be calculated as a function of the displacements sensed at each of the nodes (discussed in Section 6.3). As strains are most often calculated at the center of the element, the stable PDCR 35/D sensor is placed at the center so that the calculated shear strains can be coupled with precise measurements of pore water pressure generation.

After all sensors have been installed, two crosshole source rods are inserted in line with the array (see Figure 5-7). They are placed just far enough away from the sensor array so that they will be out from under the base plate of T-Rex during dynamic loading. One of the crosshole rods is inserted so that its tip is located at approximately the same elevation as sensor No. 1 and No. 2, while the other is inserted so that its tip is located at approximately the same elevation as sensor No. 3 and No. 4. This configuration allows crosshole seismic tests to be performed between each pair of sensors prior to, and after, dynamic loading. The horizontal, in-line component of the 3D-MEMS accelerometer in each sensor is used to sense compression wave (P-wave) arrivals, while the vertical component is used to sense horizontally propagating, vertically polarized shear wave (S_{hv} -wave) arrivals. Interval travel times between sensors are then used to calculate wave velocities. The most important reason for making P-wave velocity measurements is to verify the saturation of the liquefiable material (see Section 2.3.1). The S_{hv} -wave velocities are used to determine how the shear stiffness of the material is affected by dynamic loading.

Once the sensors and crosshole source rods have been installed, the liquefaction sensor cables are routed through the trench to a location several feet beyond the extent where the vibroseis base plate will be placed. The trench is then backfilled with loose soil. The backfill soil holds the sensor cables in the trench and prevents them from coming into direct contact with the base plate of the vibroseis during dynamic loading. A picture of the backfilled sensor trench, including a square outline that marks the approximate extent of the vibroseis base plate, is shown in Figure 5-9.

After the sensor cables have been routed beyond the extent of the base plate, and the trench has been backfilled with soil, T-Rex is brought into position with its base plate directly over the center of the instrumentation array. A picture of the base plate in position over the top of the liquefaction sensor array is shown in Figure 5-10. The base plate of T-Rex is 7.5 ft x 7.5 ft (2.3 m x 2.3 m), while the linear extent of the liquefaction array is only 4 ft (1.2 m; see Figure 5-8). Therefore, the base plate completely covers the vertical projection of the sensor array. The crosshole source rods are approximately 0.5 and 1.5 ft (0.15 and 0.46 m) from the edge of the base plate.

A static hold-down force must be applied to the base plate to keep it coupled to the ground during dynamic loading. The pressure applied by the base plate hold-down force changes the state of stress in the instrumented soil deposit. It is important to know how the state of stress has been altered so that it can be taken into account in the data reduction process. Prior to the field testing, the base plate hold-down force was calibrated as a function of the pressure applied to

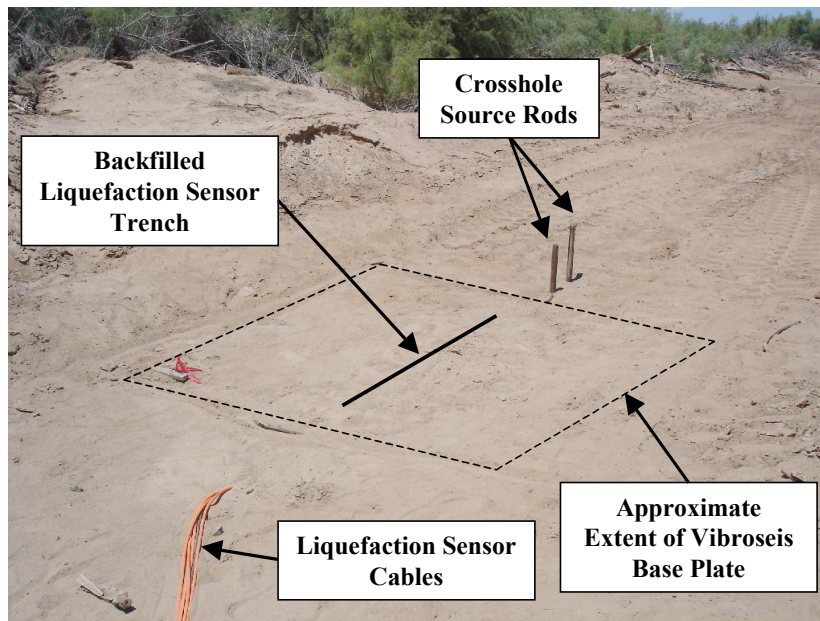


Figure 5-9 Picture of the backfilled liquefaction sensor trench.

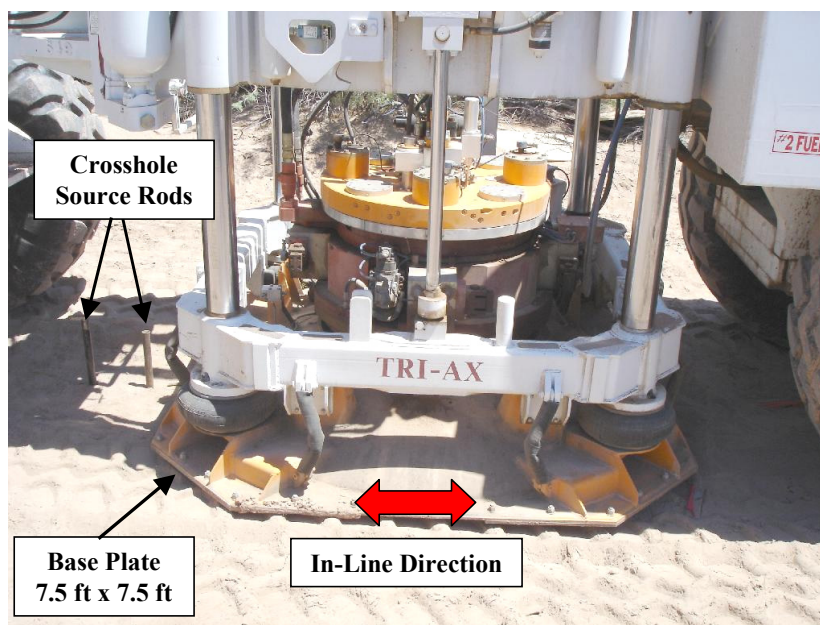


Figure 5-10 Picture of the base plate of T-Rex centered over the top of the liquefaction sensor array.

the hydraulic rams that load the plate. The results from two separate calibration trials are shown in Figure 5-11. These results indicate, that in its current configuration, the hold-down force is approximately 45,000 lb (200 kN) at the maximum hold-down cylinder pressure of approximately 1,800 psi (12,410 kPa). All field tests were run with the maximum pressure supplied to the base plate hydraulic cylinders. Therefore, it is expected that the uniform surface pressure (assuming the base plate to be rigid) applied by the base plate during testing is approximately 800 psf (38 kPa). The change in vertical stress at depth due to the uniform surface pressure applied by the vibroseis base plate was calculated using both Boussinesq's and Westergaard's elastic stress distribution solutions (Coduto, 1994). Both solutions gave very similar results at the depths of the sensor arrays. The individual results of the stress distribution calculations for each test location are discussed in Chapters 8, 9, and 10.

5.3 STAGED DYNAMIC LOADING

During dynamic loading, T-Rex is used to excite the instrumented soil mass in shear by driving the base plate horizontally in line with the direction of the sensor array. Operating T-Rex in the horizontal, in-line mode excites the soil directly beneath the base plate and creates strong shear waves, which propagate vertically past the sensor array. This process is depicted in Figure 5-12. To evaluate in-situ pore pressure generation curves and nonlinear shear modulus behavior, a wide range of cyclic shear strains need to be induced in the soil within the instrumented array. A staged dynamic loading sequence is used to generate the wide strain range.

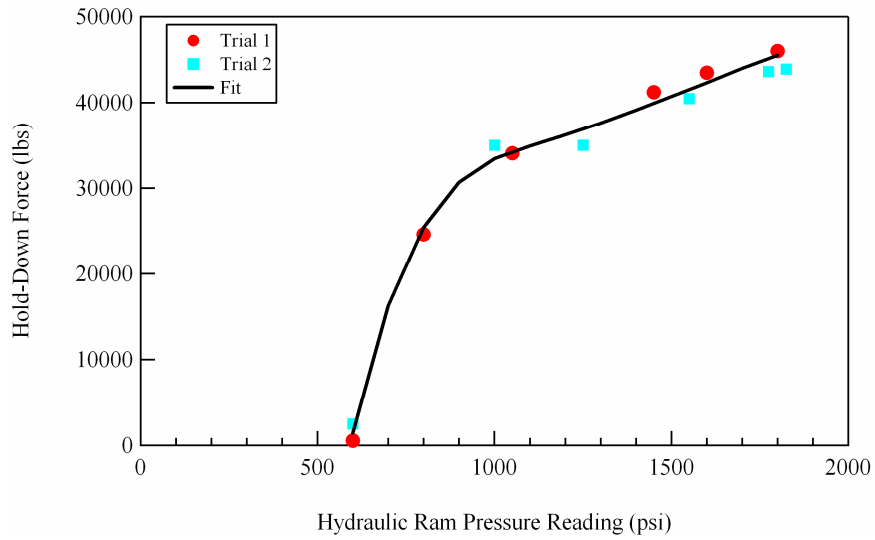


Figure 5-11 Calibration results for the base plate hold-down force of T-Rex.

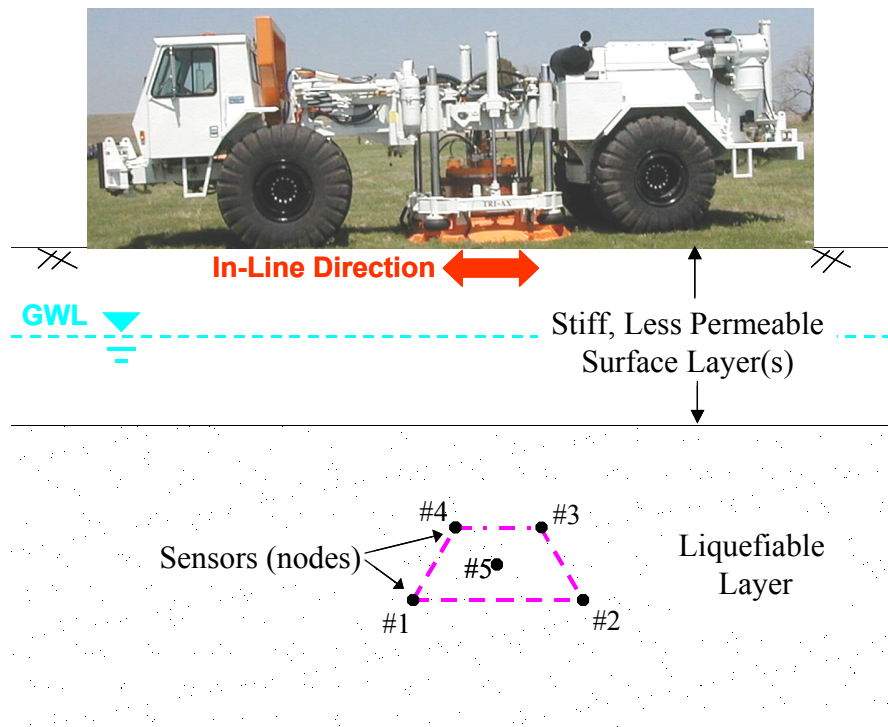


Figure 5-12 Schematic showing the location and mode of operation of T-Rex during staged dynamic loading of the instrumented liquefiable layer.

At the beginning of the dynamic test sequence, the vibroseis is driven at its lowest possible output. A typical dynamic load used during field testing is 100 cycles of a 10- or 20-Hz fixed sine wave. After this excitation is applied, the recorded data is monitored to ensure no excess pore pressure is generated. Then, the dynamic load is applied again at a slightly higher amplitude. In this manner, shear strain within the soil mass is sequentially elevated until a small amount of excess pore pressure is measured (typically $r_u < 5\%$). This indicates that the shear strain induced in the instrumented portion of the soil deposit has just surpassed the cyclic threshold strain (γ_r^c ; as discussed in Section 2.3.2). At this point, the test is paused while the excess pressure is allowed to dissipate. When the pressure comes to equilibrium at its hydrostatic value, staged testing is resumed. However, at this point the vibroseis is generally driven at its maximum output to avoid repetitive loading beyond the cyclic threshold strain.

Two staged dynamic loading series were conducted at each test location at the Wildlife Liquefaction Array. The first staged loading series was run to completion in the manner noted above. The soil deposit was then allowed to rest for approximately one day before the second series of staged dynamic loading was applied.

5.4 SENSOR EXTRACTION

After staged dynamic loading is over, the liquefaction sensors must be extracted. Because the push rods are decoupled from the sensors during installation, a pre-attached wire rope is used to pull them out of the ground. This process is made a little easier by withdrawing the push rods from the hole

simultaneously with extraction of the sensor. A picture of the sensor extraction process is shown in Figure 5-13. The push rods and wire rope are pulled on simultaneously by attaching them both to the hydraulic ram pulling connection (see Figure 5-3). The rods are threaded onto the connection, while the wire rope is wrapped several times around a post on the connection and held in place manually. Even though the sensor and the rods are not physically connected together (they are actually separated by approximately 3 in. or 7.6 cm), the rods help to keep the hole from collapsing too far ahead of the sensor. This relieves a lot of the stress placed on the sensor and minimizes the chance of breaking the wire rope.

As discussed in Section 4.2, several wire ropes were broken during trial field tests at a local aggregate quarry (Capitol Aggregate) in Austin, Texas. At the time, a 1/16 in. (0.16 cm) diameter wire rope was being used to extract the sensors. As a result of these breaks, a 3/32 in. (0.24 cm) diameter wire rope was installed on the liquefaction sensors. None of the wire ropes broke during field tests conducted at the Wildlife Liquefaction Array.

5.5 SUMMARY

The generalized in-situ liquefaction test procedure consists of: (1) sensor installation, (2) staged dynamic loading, and (3) sensor extraction. During the installation stage, the sensors are placed in a two-dimensional array within the liquefiable soil deposit. The array configuration helps facilitate data collection and reduction. To evaluate in-situ pore pressure generation curves and nonlinear shear modulus behavior, a wide range of cyclic shear strains need to be induced in

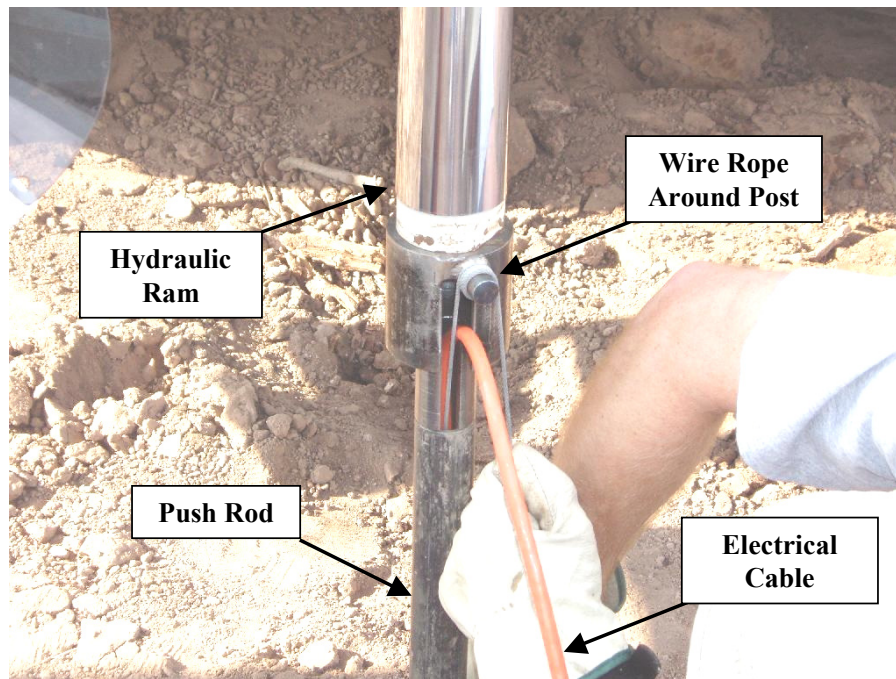


Figure 5-13 Picture detailing the simultaneous withdrawal of the push rods and wire rope during liquefaction sensor extraction.

the soil within the instrumented array. A staged dynamic loading sequence is used to generate the wide strain range. Upon completion of the test, the liquefaction sensors are removed from the ground.

Chapter 6

In-Situ Liquefaction Test Data Analysis

6.1 INTRODUCTION

The raw data recorded during an in-situ dynamic liquefaction test consists of acceleration and pore water pressure time histories generated at each sensor location. The processed data desired from an in-situ dynamic liquefaction test are: (1) induced cyclic shear strain, (2) excess pore water pressure ratio as a function of induced cyclic shear strain and number of loading cycles, and (3) nonlinear soil shear modulus as a function of induced cyclic shear strain and change in pore water pressure. The analysis techniques used to take the data from its raw state to its desired processed form are discussed below. Chapter 4 should be consulted for specific details regarding the calibration factors for each transducer and information about the data recording system.

6.2 RECORDED RAW DATA

The raw data recorded during an in-situ dynamic liquefaction test consists of acceleration and pore water pressure time histories generated at each sensor location. The acceleration time histories are recorded from the output of the 3D-MEMS accelerometer in each liquefaction sensor, while the pore water pressure time histories are recorded from the output of the PPT's. Calibration factors are applied to each raw output to convert the voltages recorded by the analyzer into units of engineering significance.

6.2.1 Raw Pore Pressure Transducer Data

Raw pore pressure time histories are typically recorded from five separate PPT's during dynamic in-situ liquefaction testing. Four of the signals come from the miniature PPT's contained in the liquefaction sensors that are located at the four corners of the trapezoidal array. The fifth PPT signal is generated by the PDCR 35/D pressure transducer that is located at the center of the array (discussed in Section 5.2). The calibration factors for the PPT's are not a function of frequency, and may therefore be applied directly to the time-domain signals by multiplying every digitized data point by the constant calibration factor for the transducer (see Section 4.2.2). This process converts the raw voltages output by the PPT's into units of pressure. The pore water pressure time histories can then be analyzed directly to obtain excess pore water pressure ratios (discussed in Section 6.4).

6.2.2 Raw MEMS Accelerometer Data

Raw acceleration time histories are typically recorded from four separate 3D-MEMS accelerometers during dynamic in-situ liquefaction testing. These accelerometers are contained in the liquefaction sensors that are located at the four corners of the trapezoidal array. Each 3D-MEMS accelerometer outputs a separate acceleration time history from the x-, y-, and z-components. An example of the raw acceleration time histories output by a 3D-MEMS accelerometer is shown in Figure 6-1. In this case, the dynamic load from the vibroseis truck was 100 cycles of a 10-Hz fixed sine wave. The y-component (horizontal, in-line component) of vibration has the largest amplitude because the vibroseis is

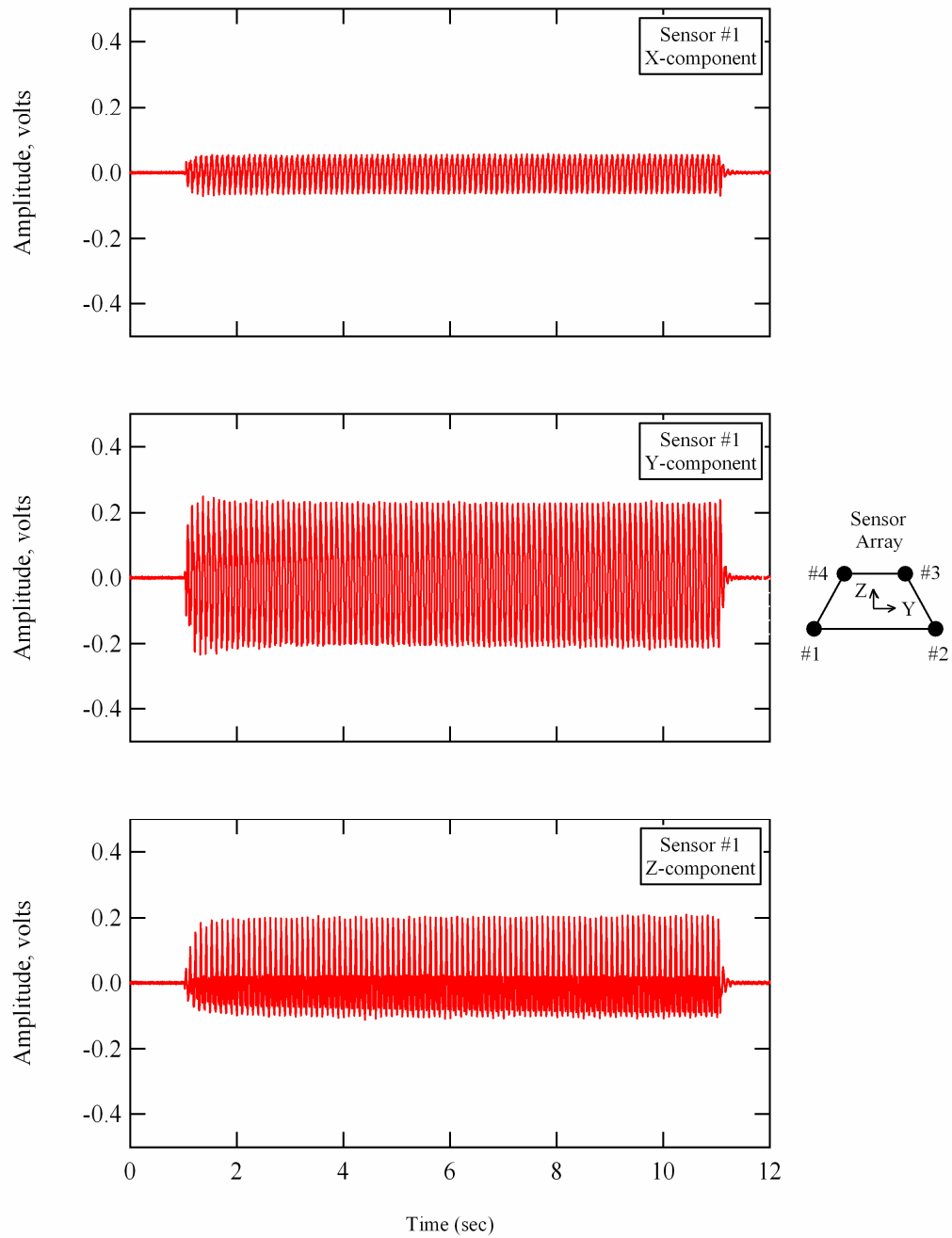


Figure 6-1 Raw output signals from the x-, y-, and z-components of a 3D-MEMS accelerometer during dynamic in-situ liquefaction testing.

operated in the shear mode, horizontally in line with the array. The z-component (vertical component) has the next largest amplitude of vibration. The vertical motions are likely caused by rocking of the base plate. The x-component (horizontal, cross-line component) has the smallest amplitude of vibration. The individual accelerometer components were oriented in these directions during all in-situ liquefaction tests. The dynamic amplitude calibration factors need to be applied to each accelerometer signal to convert the measured voltage to units of acceleration (see Section 4.2.1.2).

The dynamic calibration factors for the MEMS accelerometers are a function of frequency, and must therefore be applied in the frequency domain. The output of the MEMS accelerometers used in this study are typically very linear in the frequency range of 2 to 100 Hz. As in-situ liquefaction tests were carried out at fixed frequencies of 10 and 20 Hz, it was not necessary to account for nonlinearity in the amplitude calibration curve outside the 2 to 100 Hz frequency range. Therefore, a constant amplitude calibration factor was applied to the recorded data. Because the MEMS accelerometers have a constant calibration factor over a frequency range much wider than the frequencies used during field testing, the calibration factors could have been applied directly in the time domain. However, the raw accelerometer signals were all transferred to the frequency domain to inspect their frequency content and ensure that significant energy was not being recorded outside the frequency range of 2 to 100 Hz. Figure 6-2 shows the y-component raw data from Figure 6-1 in both the time domain (Figure 6-2a) and the frequency domain (Figure 6-2b). It is obvious that the

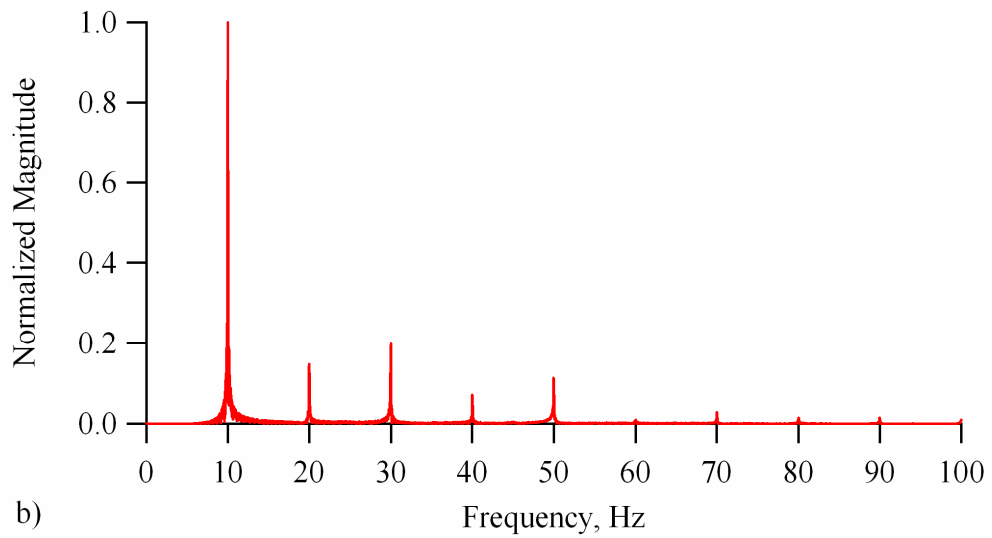
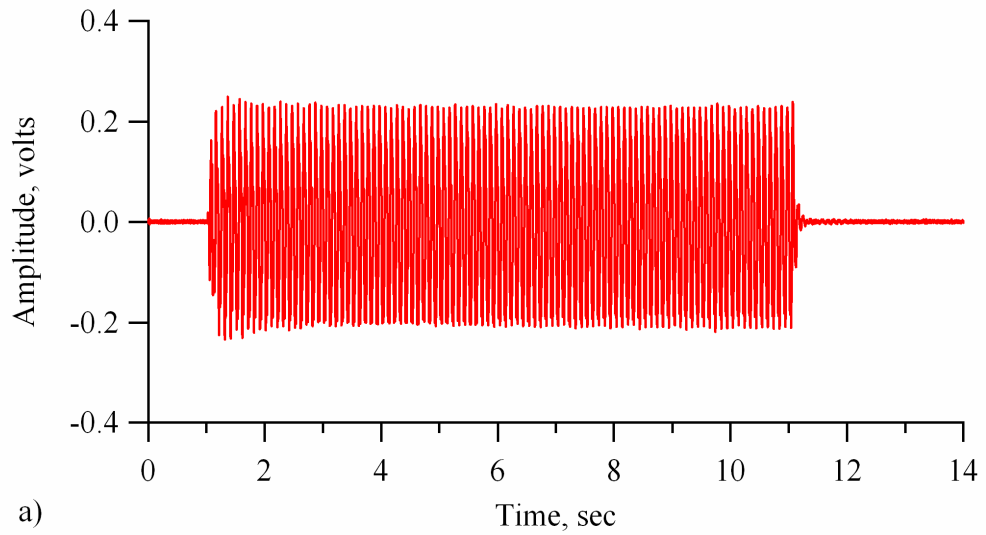


Figure 6-2 Raw output signal from a single component of a 3D-MEMS accelerometer during dynamic in-situ liquefaction testing; displayed in the: a) time domain, and b) frequency domain.

predominant portion of the raw accelerometer output signal occurs at 10 Hz (the vibroseis driving frequency), while smaller portions of the signal occur at the 20-, 30-, 40-, and 50-Hz harmonics. There is no energy in the raw signal at frequencies outside the 2 to 100 Hz constant amplitude calibration factor range.

Once the raw output voltages from the accelerometers have been converted into units of acceleration, the acceleration time histories are numerically integrated once to obtain velocity time histories, and twice to obtain displacement time histories. Numerical integration was performed in the time domain using the trapezoidal rule. The trapezoidal rule provides for integration of an acceleration time history to obtain a velocity time history according to the following equation:

$$\dot{u}_j = \dot{u}_{j-1} + \frac{1}{2}(\ddot{u}_j + \ddot{u}_{j-1}) \cdot \Delta t \dots\dots\dots(6-1)$$

where j is a discrete data point in the time histories; \dot{u}_j = the velocity at time $t = j \cdot \Delta t$; \ddot{u}_j = the acceleration at time $t = j \cdot \Delta t$; and Δt = the time step in the original acceleration time history. The initial velocity is set to zero ($\dot{u}_0 = 0$) and the successive velocities are calculated through the end of the acceleration record. The displacement time histories may be obtained from integrating the velocity time histories in a similar manner.

Baseline correction to remove drift in the integrated signals was performed in the frequency domain by high-pass filtering. A cut-off frequency of 2 Hz was used, as there was no evident energy in the original raw accelerometer data at

frequencies below this value (see Figure 6-2b). Figure 6-3 shows the velocity data obtained from integrating the accelerometer time history, shown in Figure 6-2, after the appropriate calibration factor had been applied. Figure 6-3a displays the velocity data in the time domain, while Figure 6-3b displays the same data in the frequency domain. Figure 6-4 shows the displacement data obtained from integrating the velocity data shown in Figure 6-3. Figure 6-4a displays the displacement data in the time domain, while Figure 6-4b displays the same data in the frequency domain. It is evident that the harmonic signals present in the acceleration record are much less influential in the velocity and displacement records, respectively. The displacement time histories are of primary interest in the subsequent shear strain evaluation procedures.

6.3 SHEAR STRAIN EVALUATION

The data collected during in-situ liquefaction tests allow shear strains induced in the instrumented portion of the soil to be calculated in several different ways. The two primary shear strain evaluation methods can be categorized as: (1) displacement-based (DB), and (2) wave propagation-based (WB). DB shear strain evaluation methods use the displacement time histories at each liquefaction sensor and the relative distances between sensors to evaluate shear strain time histories. WB shear strain evaluation methods use the ratio of the particle velocity time histories at each sensor and the strain-dependant shear wave velocity measured between sensors to evaluate shear strain time histories. Both of these methods are discussed below and comparisons of the shear strains calculated from each method are presented.

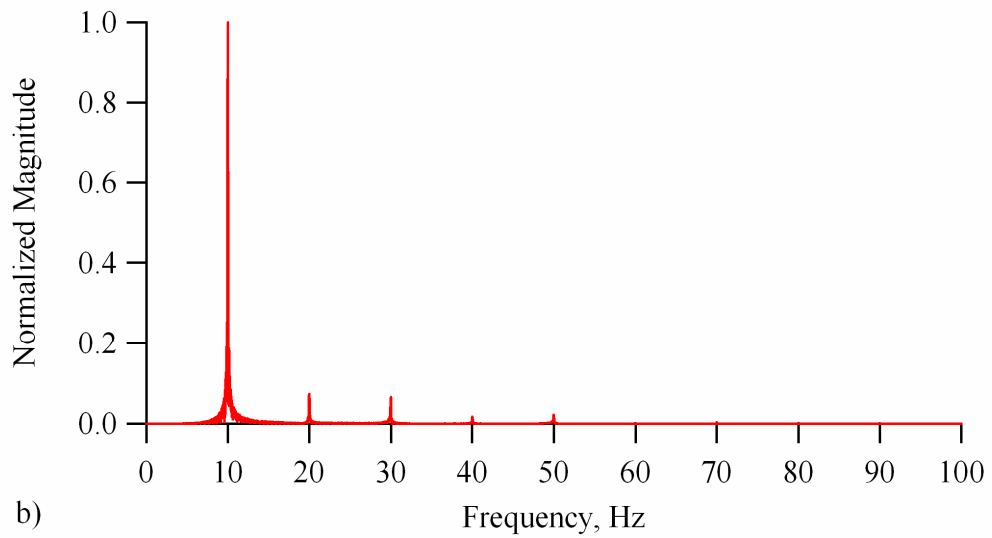
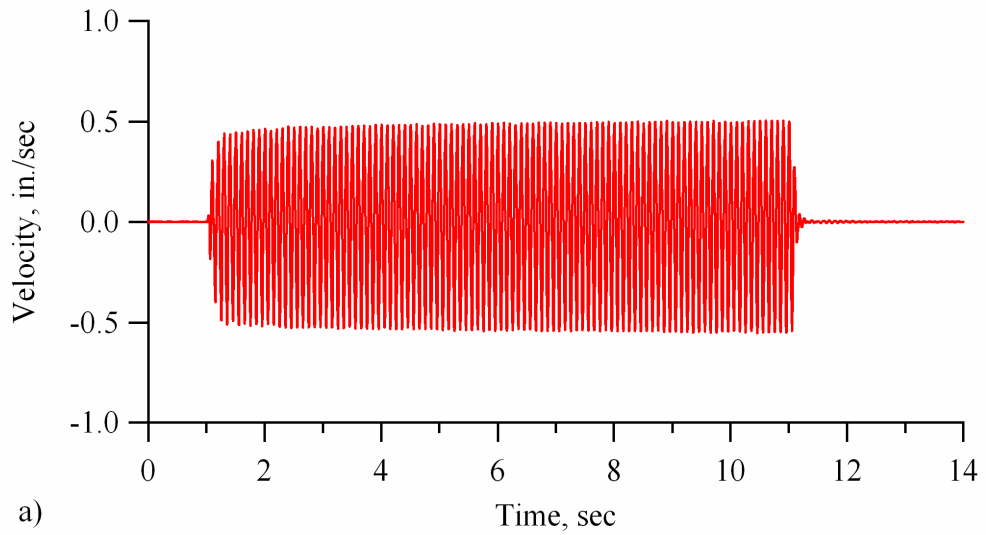


Figure 6-3 Velocity signal obtained from integrating a single component of a 3D-MEMS accelerometer recorded during dynamic in-situ liquefaction testing; displayed in the: a) time domain, and b) frequency domain.

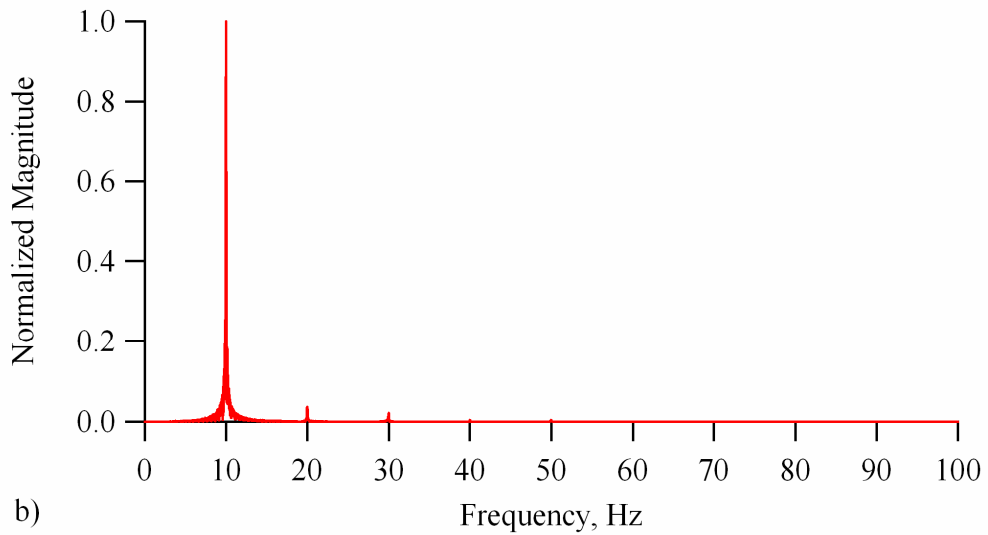
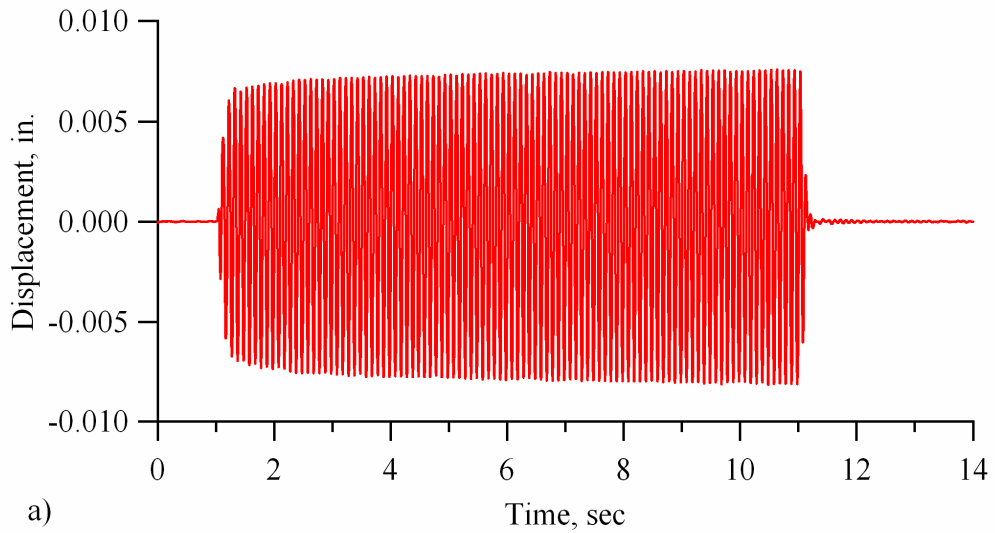


Figure 6-4 Displacement signal obtained from double integration of a single component of a 3D-MEMS accelerometer recorded during dynamic in-situ liquefaction testing; displayed in the: a) time domain, and b) frequency domain.

6.3.1 Displacement-Based (DB) Shear Strain Methods

DB shear strain evaluation methods use the displacement time histories at each liquefaction sensor and the relative distances between sensors to evaluate shear strain time histories. As discussed in Section 5.2, the in-situ liquefaction sensors are installed in a linear, two-dimensional array within the liquefiable soil layer (see Figure 5-8). The array is in the form of a trapezoid, with a liquefaction sensor occupying each of its four corners. The corner sensor positions may be considered as nodes of a single, quadrilateral finite element. This configuration allows the strains anywhere within the element to be calculated from the displacements at the sensors (nodes) using a 4-node, isoparametric finite element formulation (Chang 2002; Rathje et al., 2004). This formulation may be found in many general finite element textbooks (e.g. Bathe, 1995; Cook et al., 1989).

6.3.1.1 4-Node, Isoparametric Finite Element Formulation (Chang, 2002)

Chang (2002) used a 4-node, isoparametric finite element formulation to solve for the shear strains induced at the center of the liquefaction sensor array during first-generation, in-situ dynamic liquefaction tests. The following detailed description of the 4-node, isoparametric finite element formulation is taken directly from Chang (2002):

“The analytical framework used for the strain calculation is the isoparametric finite element formulation, which describes the element geometry and the variation of displacements across an element with the same interpolation functions. These interpolation functions, or shape functions, describe the variation of parameters (i.e., locations, displacements) in terms of a simplified natural

coordinate system. Consider a 4-node element in a global coordinate system (Figure 6-5a) and its simple, square representation in the natural coordinate system (Figure 6-5b). Points within the element in the natural coordinate system (r,s) can be related to points within the element in the global coordinate system (x, y) using:

$$x = \sum_{i=1}^4 N_i(r,s)x_i \dots\dots\dots(6-2a)$$

$$y = \sum_{i=1}^4 N_i(r,s)y_i \dots\dots\dots(6-2b)$$

where x, y are the global coordinates for a point inside the element; x_i, y_i are the coordinates of each node in the global coordinate system; $N_i(r,s)$ is the shape function for node i , expressed in the natural coordinate system of the element.

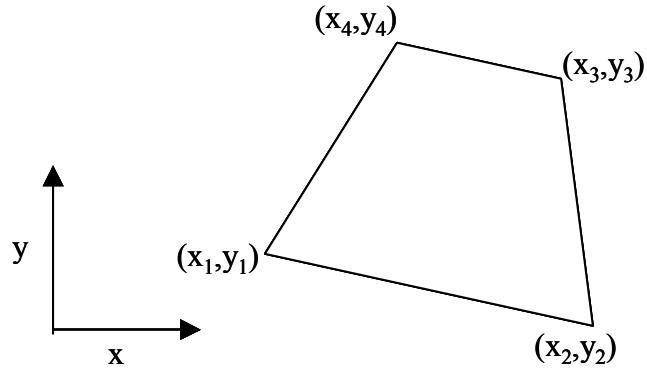
The fundamental property of the shape functions (N_i) is that it is equal to unity at node i and equal to zero at all other nodes in the natural coordinate system. Using the Lagrange polynomials in two dimensions yields the following shape functions for the element shown in Figure 6-5b:

$$N_1 = \frac{1}{4}(1-r)(1-s) \dots\dots\dots(6-3a)$$

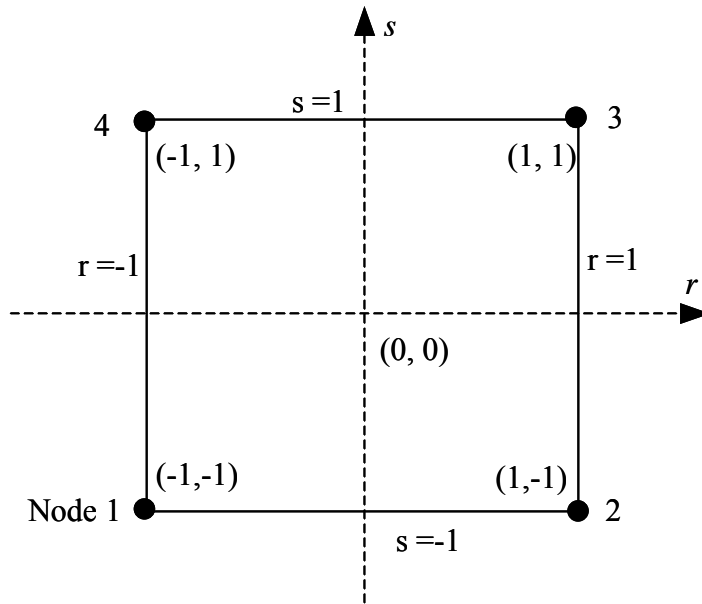
$$N_2 = \frac{1}{4}(1+r)(1-s) \dots\dots\dots(6-3b)$$

$$N_3 = \frac{1}{4}(1+r)(1+s) \dots\dots\dots(6-3c)$$

$$N_4 = \frac{1}{4}(1-r)(1+s) \dots\dots\dots(6-3d)$$



(a) Representation of 4-node element in the global coordinate system



(b) Representation of 4-node element in the natural coordinate system

Figure 6-5 Representation of 4-node element in (a) the global coordinate system and (b) the natural coordinate system (from Chang, 2002).

The displacements inside an element are interpolated from the nodal displacements using the same shape functions, which yields:

$$u = \sum_{i=1}^4 N_i(r,s)u_i \dots\dots\dots(6-4a)$$

$$v = \sum_{i=1}^4 N_i(r,s)v_i \dots\dots\dots(6-4b)$$

where u, v are the displacements in the x and y directions, respectively, at location (r,s) in the natural coordinate system and the corresponding location (x,y) in the global coordinate system; and u_i, v_i are the nodal displacements at node i in the x and y directions, respectively. Using Equation (6-4), the displacement at any point (x,y) within the element can be computed from the nodal displacements and the corresponding natural coordinates of the point of interest.

The element strain vector, $\underline{\varepsilon}^T = [\varepsilon_x \quad \varepsilon_y \quad \gamma_{xy}]$, in the global coordinate system can be obtained from the derivatives of the element displacements with respect to the global coordinates:

$$\varepsilon_x = \frac{\partial u}{\partial x} \dots\dots\dots(6-5a)$$

$$\varepsilon_y = \frac{\partial v}{\partial y} \dots\dots\dots(6-5b)$$

$$\gamma_{xy} = \frac{\partial u}{\partial y} + \frac{\partial v}{\partial x} \dots\dots\dots(6-5c)$$

Using Equations (6-4) and (6-5), the element strain vector can be expressed in matrix form as:

$$\underline{\varepsilon} = \underline{\underline{B}} \cdot \underline{u} \dots\dots\dots(6-6)$$

where $\underline{u}^T = [u_1 \quad v_1 \quad u_2 \quad v_2 \quad u_3 \quad v_3 \quad u_4 \quad v_4]$

u_i = horizontal displacement at node i , $i=1$ to 4,

v_i = vertical displacement at node i , $i=1$ to 4, and

$\underline{\underline{B}}$ = strain-displacement transformation matrix.

The explicit form of $\underline{\underline{B}}$ is:

$$\underline{\underline{B}} = \begin{bmatrix} \frac{\partial N_1}{\partial x} & 0 & \frac{\partial N_2}{\partial x} & 0 & \frac{\partial N_3}{\partial x} & 0 & \frac{\partial N_4}{\partial x} & 0 \\ 0 & \frac{\partial N_1}{\partial y} & 0 & \frac{\partial N_2}{\partial y} & 0 & \frac{\partial N_3}{\partial y} & 0 & \frac{\partial N_4}{\partial y} \\ \frac{\partial N_1}{\partial y} & \frac{\partial N_1}{\partial x} & \frac{\partial N_2}{\partial y} & \frac{\partial N_2}{\partial x} & \frac{\partial N_3}{\partial y} & \frac{\partial N_3}{\partial x} & \frac{\partial N_4}{\partial y} & \frac{\partial N_4}{\partial x} \end{bmatrix} \dots\dots\dots(6-7)$$

Because the shape functions, $N_i(r,s)$, are defined in terms of r and s , a relationship between the natural coordinate derivatives and the global coordinate derivatives is needed. This relationship is the Jacobian operator. In 2-dimensional formulations, the Jacobian operator is a 2-by-2 matrix and is defined as:

$$\begin{Bmatrix} dx \\ dy \end{Bmatrix} = \mathbf{J}^T \begin{Bmatrix} dr \\ ds \end{Bmatrix} \dots\dots\dots(6-8)$$

where $\mathbf{J} = \begin{bmatrix} \frac{\partial x}{\partial r} & \frac{\partial y}{\partial r} \\ \frac{\partial x}{\partial s} & \frac{\partial y}{\partial s} \end{bmatrix}$ (Jacobian matrix)

The derivatives of the shape functions with respect to the global coordinate system (i.e., entries in Equation (6-7)) can be calculated by:

$$\begin{bmatrix} \frac{\partial N_i(r,s)}{\partial x} \\ \frac{\partial N_i(r,s)}{\partial y} \end{bmatrix} = \mathbf{J}^{-1} \begin{bmatrix} \frac{\partial N_i(r,s)}{\partial r} \\ \frac{\partial N_i(r,s)}{\partial s} \end{bmatrix} \dots\dots\dots(6-9)$$

Using Equations (6-6) and (6-7), and the corrected displacement-time histories at the nodal points, the strain-time history at any point inside the field array can be computed.”

6.3.1.2 Displacement-Based (DB) 4-Node Shear Strain Calculations

Shear strain time histories are calculated at the center of the in-situ liquefaction test trapezoidal array using a 4-node, finite element formulation similar to that presented by Chang (2002). It should be noted that Chang (2002) used x and y to represent the global horizontal and vertical directions, respectively, while the current study uses y and z to represent the global horizontal and vertical directions, respectively. It therefore follows that the in-plane shear strain (γ) calculated in this study should be referenced as γ_{yz} . A schematic detailing the in-situ liquefaction test trapezoidal array, the direction of

dynamic excitation, the primary components of particle displacement, and the governing equation used to calculate the strain vector (ϵ) for the element is presented in Figure 6-6. The shear strain (γ_{yz}) is the third component of the strain vector and is of primary interest in this problem.

An example of a shear strain time history calculated at the center of the trapezoidal array is shown in Figure 6-7. This shear strain time history was generated by 100 cycles of dynamic loading in the form of a 10-Hz fixed sine wave and has amplitudes very close to the theoretical cyclic threshold strain ($\gamma_t \sim 0.02\%$; see Section 2.3.2). Dynamic in-situ liquefaction tests are not strictly stress-controlled, or strain-controlled tests. Despite this, the strain time histories calculated at the center of the array generally have very consistent amplitudes over all 100 cycles of excitation throughout much of the staged loading program. However, once significant excess pore water pressures are generated within the array, the strain behavior can become quite irregular. These cases are discussed on an individual basis when specific test results are presented in Chapters 8, 9, and 10.

The most critical assumption incorporated in the 4-node, isoparametric finite element strain formulation is the linear variation of displacement between nodes (Rathje et al., 2004). For this assumption to be valid, the size of the array in the direction of wave propagation should be less than about one-quarter of the wavelength of the highest significant frequency (i.e., the shortest wavelength) used during testing (Chang, 2002). The highest significant frequency used during in-situ dynamic liquefaction tests was 20 Hz. The liquefiable soil tested in these

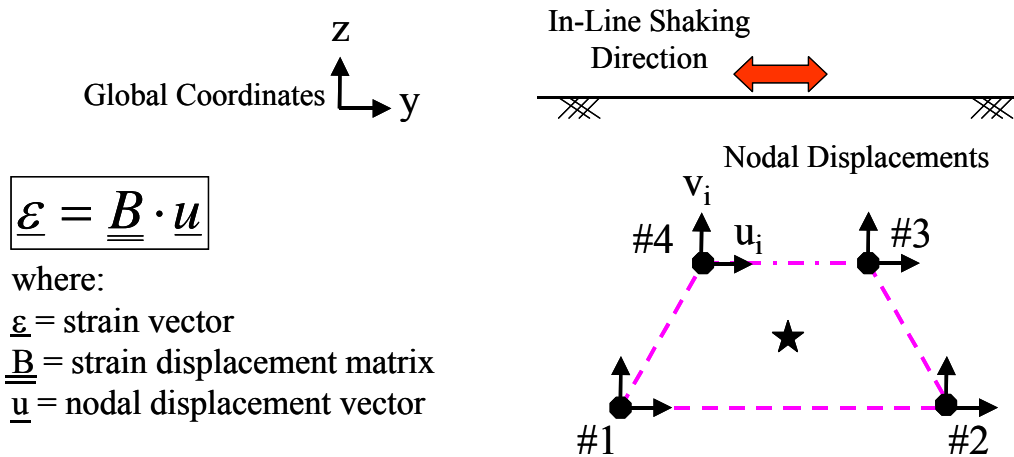


Figure 6-6 Schematic detailing the liquefaction sensor array, the direction of dynamic excitation, the primary components of particle displacement, and the equation used to calculate the strain vector at the center of the element using a 4-node, finite element formulation.

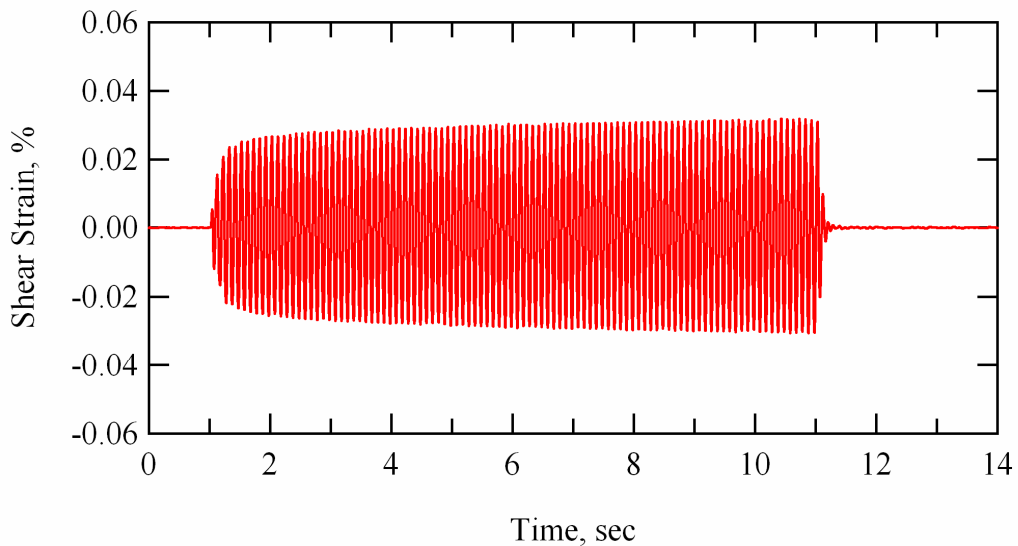


Figure 6-7 Example of a shear strain time history calculated at the center of the in-situ liquefaction sensor array using a 4-node, finite element strain formulation.

studies has a shear wave velocity (V_s) of approximately 400 fps (122 m/s). Therefore, a 20-Hz wave propagating through this material would have a wavelength of about 20 ft (6 m), which is ten times greater than the vertical dimension of the liquefaction sensor array (shown in Figure 5-8). It is therefore believed that a linear variation of displacement between nodes is a valid assumption for this test setup. The 4-node, isoparametric finite element formulation provides strain values within the element that are first-order accurate.

The 4-node, isoparametric finite element strain computation method was the only method used to calculate shear strains for the dynamic in-situ liquefaction test results provided later in this dissertation. However, other shear strain computation methods were investigated in hopes of determining an accurate method for calculating shear strains that would require less instrumentation.

6.3.1.3 Displacement-Based (DB) 2-Node Strain Calculations

In-plane shear strain time histories can also be estimated using the horizontal, in-line displacements from only 2-nodes in the liquefaction sensor array using the following equation:

$$\gamma_{yz} = \frac{u_3 - u_2}{\Delta z} \dots\dots\dots(6-10)$$

where γ_{yz} = the in-plane shear strain; u_3 = the horizontal, in-line displacement at node No. 3; u_2 = the horizontal, in-line displacement at node No. 2; and Δz = the vertical distance between nodes No. 3 and No. 2. Equation (6-10) provides estimates of γ_{yz} midway between nodes No. 3 and No. 2. This equation is meant

to be used with nodes that have little horizontal separation (Δy) relative to the vertical distance (Δz) between them. Figure 5-8 shows that Δy between nodes No. 3 and No. 2 is typically 1 ft (0.3 m), while Δz between them is typically 2 ft (0.6 m). This is not believed to be a problem because the horizontal, in-line motions at a given depth are nearly constant at all locations beneath the rigid base plate. Therefore, γ_{yz} calculated using Equation (6-10) should be nearly equal to γ_{yz} calculated by replacing nodes No. 3 and No. 2 in Equation (6-10) with nodes No. 4 and No. 1, respectively.

A comparison of the in-plane shear strains calculated using the 2-node DB method with two separate nodal pairs (i.e. nodes No. 3 & No. 2, and nodes No. 4 & No. 1) is shown in Figure 6-8. These shear strain values were calculated from two separate staged loading series at the Wildlife Liquefaction Array, Test Location C (discussed in Chapter 8), and are the mean values over 100 cycles of loading. As a point of reference, the 2-node DB shear strain values (plotted on the y-axis) are compared with the 4-node DB shear strain values (plotted on the x-axis). The 2-node shear strain values calculated using two separate nodal pairs are virtually identical. However, the 2-node DB shear strains are significantly lower than the 4-node DB shear strains. This same data, presented in the form of percentage of the shear strain predicted by the 4-node DB method, is shown in Figure 6-9. Clearly, the 2-node and 4-node DB methods tend to agree more closely in the small strain range. The 2-node DB shear strains are approximately 80% of the 4-node values at a shear strains near 0.001%, while they are only about 60% of the 4-node values at a shear strains near 0.05%

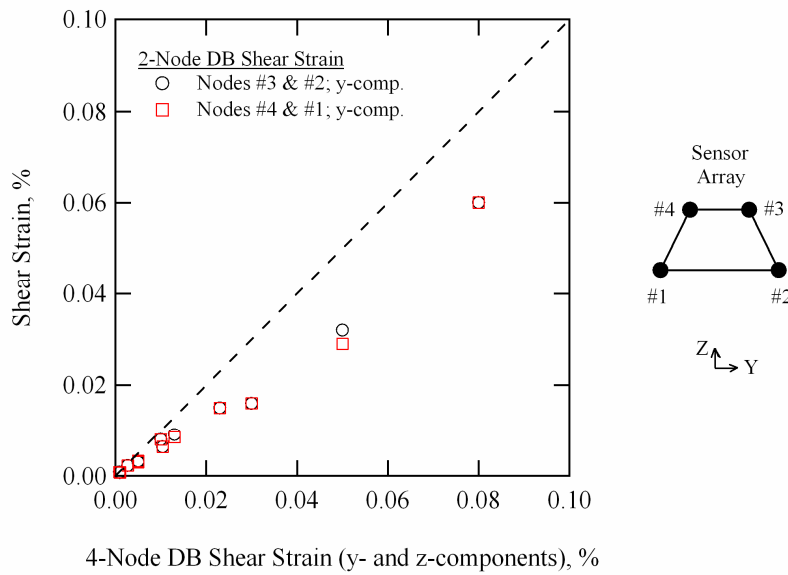


Figure 6-8 Comparisons between in-plane shear strains (γ_{yz}) calculated using the 4-node displacement-based (DB) method and the 2-node DB method.

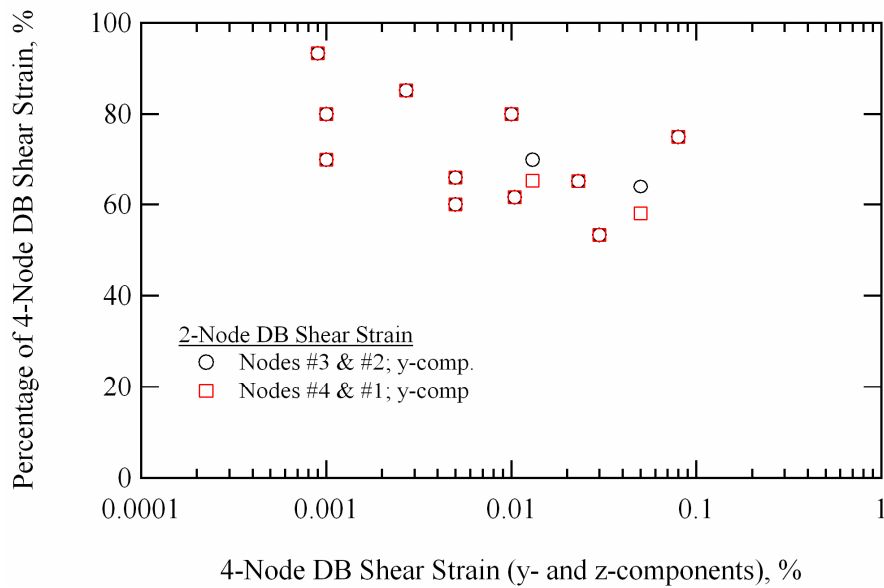


Figure 6-9 In-plane shear strains (γ_{yz}) predicted by the 2-node DB method, as percentages of the shear strains calculated using the 4-node DB method.

It seems that the reason why the 2-node DB method and the 4-node DB method tend to agree more closely in the small strain range (see Figure 6-9) is that at small driving amplitudes the base plate moves very little, so there is minimal rocking. However, as the driving amplitude increases, the magnitude of rocking increases. Thus, at higher driving amplitudes the vertical particle motions induced by rocking contributing more to the shear strain induced in the soil.

It is believed that the 2-node DB method and the 4-node DB method would yield identical shear strain estimates if the vertical particle motions at a given depth were identical at all in-line locations beneath the base plate. However, the rocking of the base plate causes vertical particle motions to be out of phase in the in-line direction across the array, and thus contribute to the shear strain induced in the soil. To prove this, the vertical particle displacements at each node were set equal to zero and the 4-node DB method was used to estimate the shear strains induced at the center of the array. A comparison of the in-line shear strains calculated using the 4-node DB method with and without vertical particle motions is shown in Figure 6-10. As reference points, the 2-node shear strain values are also presented. The 4-node DB shear strains calculated at the center of the array, without vertical particle motions, are nearly identical to the 2-node DB shear strains calculated at either side of the array. This finding supports the fact that horizontal, in-line displacements at a given depth are indeed uniform at all locations beneath the rigid base plate. However, it is also apparent that the vertical particle motions cannot be neglected when calculating shear strains induced in the soil while operating with the current test setup.

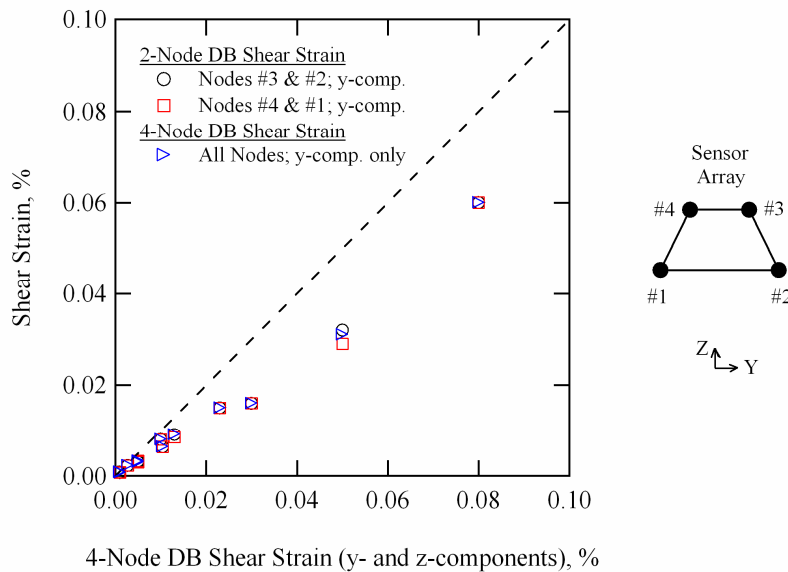


Figure 6-10 Comparisons between in-plane shear strains (γ_{yz}) calculated using the 4-node displacement-based (DB) method, the 4-node DB method with only y-component particle displacements, and the 2-node DB method.

Tabulated values of the in-plane shear strains predicted using the 4-node DB method, the 4-node DB method without vertical (z) particle motions, and the 2-node DB method are provided in Table 6-1. The values are arranged in order of increasing strain as calculated by the traditional 4-node DB method.

The 2-node DB method was also used to estimate the out-of-plane shear strain (γ_{xz}) induced in the liquefaction sensor array by using the x-component displacements at the nodes instead of the y-component displacements. These shear strains likely have some effect on the buildup of pore water pressure, yet they cannot be calculated using the 4-node DB method with the current receiver configuration. A comparison between the 2-node out-of-plane shear strains (γ_{xz} ;

Table 6-1 Tabulated values of in-plane shear strains predicted using the 4-node displacement-based (DB) method, the 4-node DB method without vertical particle motions, the 2-node DB method, and the wave-based (WB) method; Wildlife Liquefaction Array (WLA) Test Location C

| WLA Test C I.D. # | In-Plane Shear Strain (γ_{yz}), % | | | | |
|-------------------------|--|----------------|-------------------|-------------------|-------------------------------------|
| | Displacement-Based | | | | Wave-Based |
| | 4-Node | | 2-Node | | Cycle-by-Cycle 4-Node Average |
| | y- & z- comp | y-comp only | #3 & #2 y-comp | #4 & #1 y-comp | |
| 12 | 0.0009 | 0.0009 | 0.0008 | 0.0008 | 0.0008 |
| 1 | 0.0010 | 0.0007 | 0.0007 | 0.0007 | 0.0007 |
| 4 | 0.0010 | 0.0008 | 0.0008 | 0.0008 | 0.0008 |
| 9 | 0.0012 | 0.0007 | 0.0007 | 0.0007 | 0.0009 |
| 5 | 0.0026 | 0.0023 | 0.0023 | 0.0023 | 0.0020 |
| 13 | 0.0026 | 0.0023 | 0.0023 | 0.0023 | 0.0020 |
| 2 | 0.0049 | 0.0033 | 0.0033 | 0.0033 | 0.0028 |
| 10 | 0.0050 | 0.0030 | 0.0030 | 0.0030 | 0.0030 |
| 14 | 0.0092 | 0.0080 | 0.0080 | 0.0080 | 0.0062 |
| 6 | 0.0102 | 0.0064 | 0.0064 | 0.0064 | 0.0064 |
| 3 | 0.0110 | 0.0080 | 0.0080 | 0.0080 | 0.0074 |
| 11 | 0.0128 | 0.0091 | 0.0091 | 0.0085 | 0.0078 |
| 7 | 0.0234 | 0.0150 | 0.0150 | 0.0150 | 0.0111 |
| 15 | 0.0287 | 0.0160 | 0.0160 | 0.0160 | 0.0144 |
| 8 | 0.0451 | 0.0310 | 0.0320 | 0.0290 | 0.0220 |
| 16 | 0.0754 | 0.0600 | 0.0600 | 0.0600 | 0.0290 |

plotted on the y-axis) and the 4-node in-plane shear strains (γ_{yz} ; plotted on the x-axis) is shown in Figure 6-11. The magnitudes of the 2-node DB method out-of-plane shear strains were found to be small compared to the magnitudes of the 4-node in-plane shear strains. This same data, presented in the form of percentage of the shear strain predicted by the traditional 4-node DB method, is shown in Figure 6-12. The 2-node out-of-plane DB shear strains are approximately 20% of the 4-node in-plane values at a shear strains near 0.001%, while they are about 10% of the 4-node values at a shear strains near 0.05%. Even though the magnitudes of the out-of-plane shear strains induced in the soil appear to be somewhere between 10 to 20% of the magnitudes of the in-plane shear strains, it is unlikely that these two separate strain components act in phase. Additionally, there is no known way to include the out-of-plane shear strains in the current data analysis techniques. Therefore, the influence of the out-of-plane shear strain (believed to be minor) is neglected at this time.

6.3.2 Wave Propagation-Based (WB) Shear Strain Calculation

Wave propagation-based (WB) strain calculation methods use the ratio of particle velocity to wave propagation velocity to compute various strain components (Richart et al., 1970; Rathje et al., 2004). These strain computation methods assume one-dimensional (1D) stress wave propagation. The in-plane shear strain (γ_{yz}) induced in the instrumented in-situ liquefaction array can be estimated from the following equation:

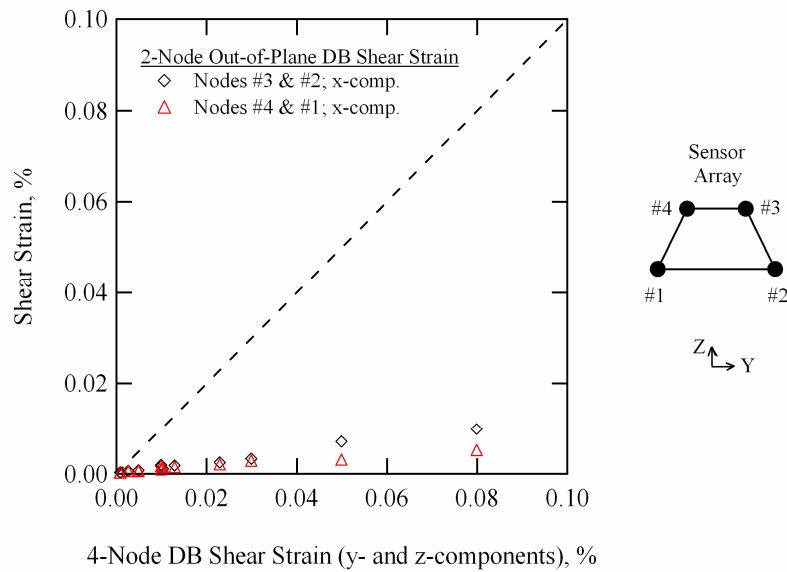


Figure 6-11 Comparisons between in-plane shear strains (γ_{yz}) calculated using the 4-node displacement-based (DB) method and the out-of-plane shear strains (γ_{xz}) calculated using the 2-node DB method.

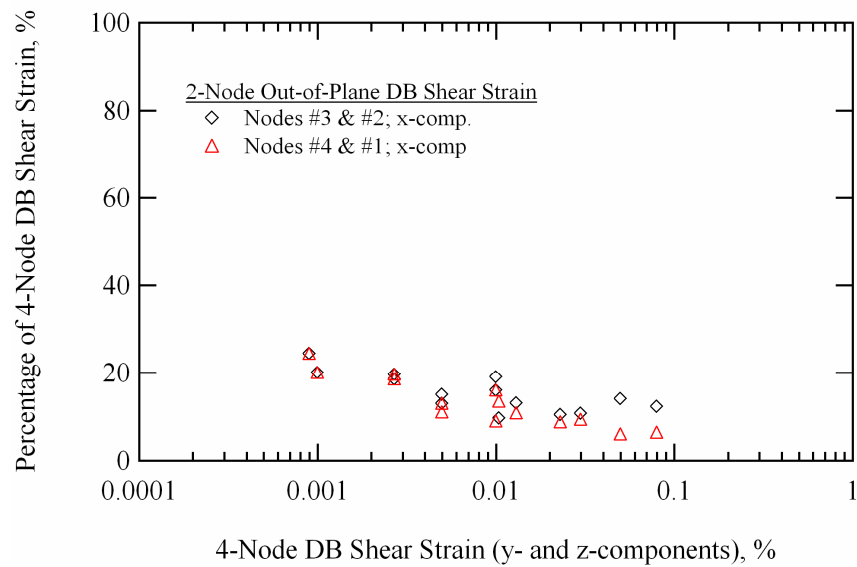


Figure 6-12 Out-of-plane shear strains (γ_{xz}) predicted by the 2-node DB method, as percentages of the shear strains calculated using the 4-node DB method.

$$\gamma_{yz} = \frac{-\dot{u}}{V_{S,vh}} \dots\dots\dots(6-11)$$

where γ_{yz} = the in-plane shear strain; \dot{u} = the horizontal, in-line particle velocity; and $V_{S,vh}$ = the shear wave velocity of a vertically propagating, horizontally polarized shear wave. The minus sign in Equation (6-11) indicates that strain is 180 degrees out of phase with particle velocity. Horizontal, in-line particle velocity time histories are available at each of the four liquefaction sensors in the array. The vertically propagating shear wave velocity can be obtained from the phase difference between two vertically spaced sensors. Because $V_{S,vh}$ is strain dependant, its value must constantly be evaluated throughout the course of dynamic loading. A detailed description of the cycle-by-cycle evaluation of $V_{S,vh}$ is presented in Section 6.5.

In-plane shear strain time histories were calculated at each liquefaction sensor using the horizontal, in line component (y-component) of particle velocity and the average cycle-by-cycle $V_{S,vh}$ obtained from the phase difference between each distinct pair of vertically separated receivers (i.e. sensors No. 3 & No. 2, and sensors No. 4 & No. 1). These four separate shear strain time histories were then averaged to come up with an estimate for the mean shear strain induced in the array. Tabulated values of the in-plane shear strains predicted using the WB method are provided in Table 6-1. As previously discussed, these shear strain values represent the average strain over 100 cycles of loading.

A comparison between the in-plane shear strain values obtained from the WB method and the 4-node DB method is shown in Figure 6-13. The WB shear strain values are significantly smaller than the 4-node DB shear strain values. Once again it is believed that the primary reason for this disagreement is the vertical components of particle motion that are contributing to the shear strain in the element. The WB method does not take these motions into account because it is based on the assumption of 1D wave propagation. For comparison purposes, the 4-node DB shear strain values calculated without vertical particle motions are also shown in Figure 6-13. The 4-node DB shear strain values calculated without vertical particle motions are fairly close to the WB shear strain values in the smaller-strain range. However, the WB shear strains do not match well with the 4-node DB shear strains calculated without vertical particle motions in the higher-strain range. The reason for this is unknown. This same data, presented in the form of percentage of the shear strain predicted by the traditional 4-node DB method, is shown in Figure 6-14. The shear strain values predicted by the WB method are less than 50% of the values predicted by the traditional 4-node DB method at shear strains greater than approximately 0.02 %.

The evidence presented above clearly shows that the 4-node DB shear strain evaluation method is the most accurate method for calculating shears strains induced in the liquefaction sensor array. The 2-node DB shear strain method and the WB shear strain method are not able to take into account the vertical motions induced in the array by base plate rocking, and hence tend to under-predict the level of induced shear strain.

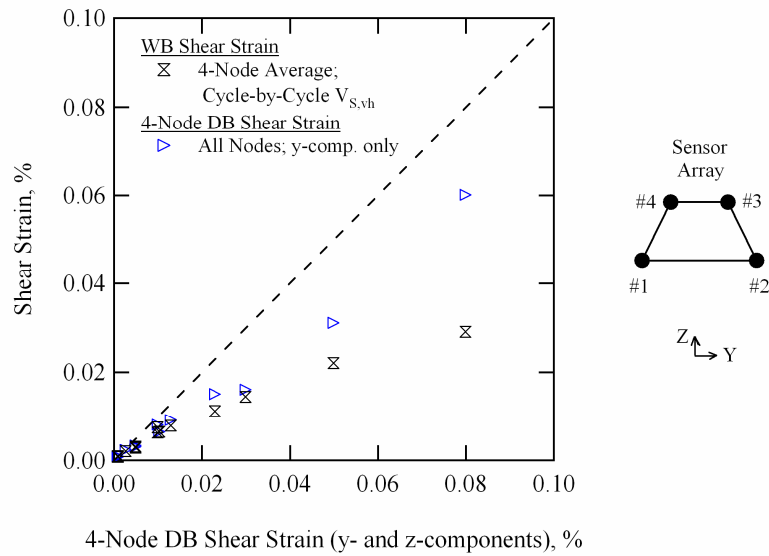


Figure 6-13 Comparisons between in-plane shear strains (γ_{yz}) calculated using the 4-node displacement-based (DB) method, the 4-node DB method with only y-component particle displacements, and the wave based (WB) method.

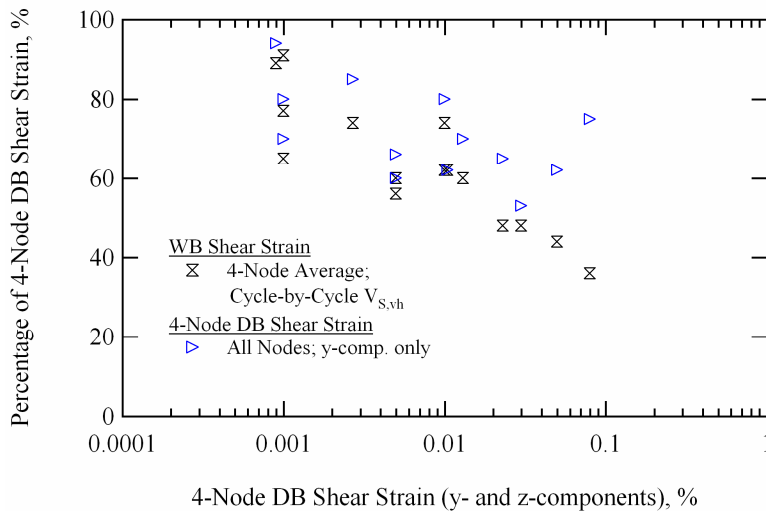


Figure 6-14 In-plane shear strains (γ_{yz}) predicted by the wave-based (WB) method, and the 4-node displacement-based (DB) method with only y-component particle displacements, as percentages of the shear strains calculated using the traditional 4-node DB method.

6.4 PORE PRESSURE RATIO EVALUATION

Examples of a pore water pressure time histories obtained from the PDCR 35/D sensor (installed at the center of the sensor array) during in-situ liquefaction testing are shown in Figure 6-15. Figure 6-15a shows a pore pressure time history obtained from a test in which shear strains induced in the instrumented soil deposit ($\gamma_{yz} \sim 0.012\%$) were not large enough to generate excess pore water pressure. Figure 6-15b shows a pore pressure time history obtained from a test in which shear strains induced in the instrumented soil deposit ($\gamma_{yz} \sim 0.027\%$) were sufficiently large to generate excess pore water pressure. The static water pressure prior to shaking is approximately 3 psi (20.7 kPa or 6.9 ft of water) in both records. Once vibroseis loading begins, the 10-Hz dynamic signal can be clearly be seen in Figure 6-15b. The 10-Hz dynamic signal is also present in Figure 6-15a, although it is much less pronounced. This dynamic portion of the signal is referred to as the hydrodynamic pressure (Chang, 2002). In Figure 6-15b, the hydrodynamic pressure is superimposed on a portion of the pressure transducer record that is constantly trending upward throughout the duration of dynamic loading. This upward-trending portion of the signal is referred to as the residual pressure. When dynamic loading stops, the pore water pressure has built to a value of approximately 4.2 psi (29.0 kPa or 9.7 ft of water). The excess pore pressure generated during dynamic loading is the difference between the static and final pore water pressures (i.e. approximately 1.2 psi, 8.3 kPa or 2.8 ft of water). There is no residual pore pressure buildup in the record shown in Figure 6-15a despite the fact that the shear strain induced in the soil deposit during

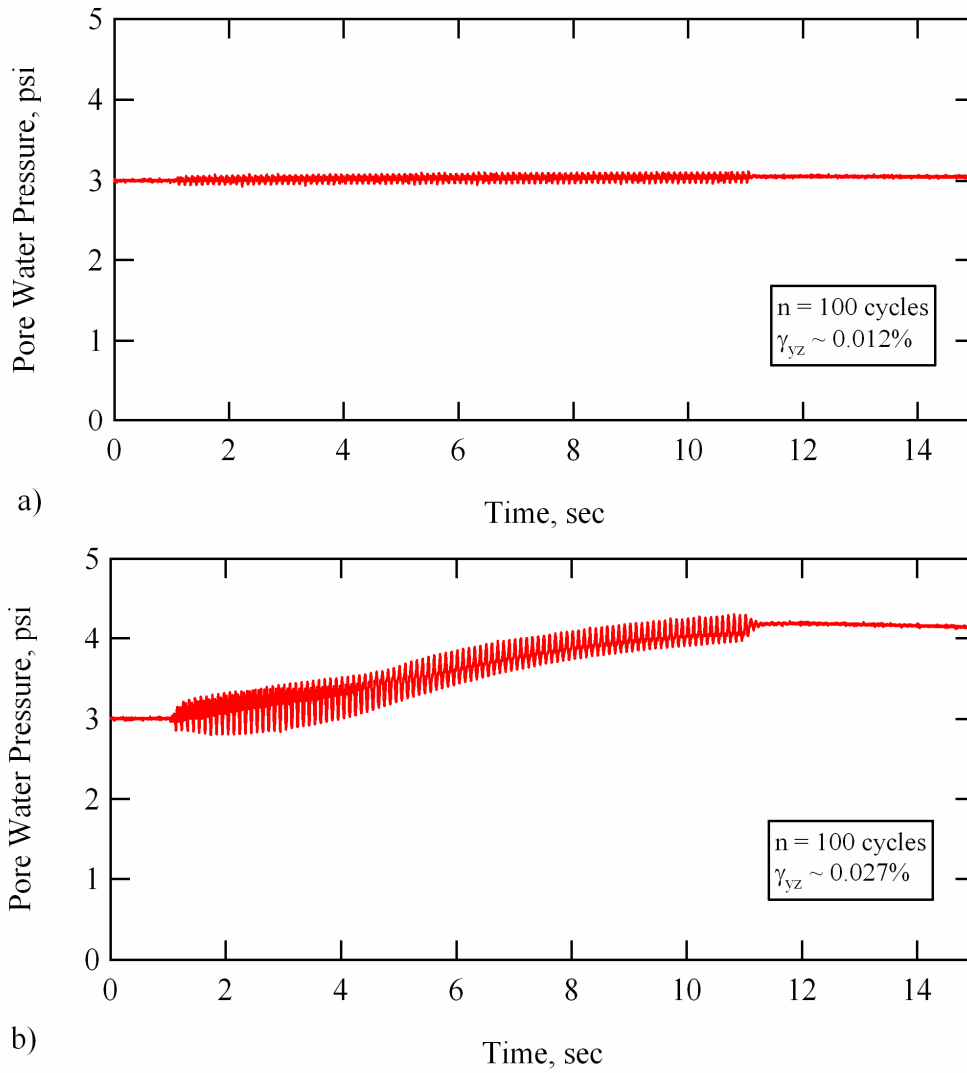


Figure 6-15 Examples of pore pressure time histories obtained during in-situ liquefaction testing in which: a) induced shear strains were not large enough to generate excess pore water pressure, and b) induced shear strains were large enough to generate excess pore water pressure.

dynamic loading ($\gamma_{yz} \sim 0.012\%$) is just slightly smaller than the shear strain that generated the excess pore water pressure ($\gamma_{yz} \sim 0.027\%$) shown in the record of Figure 6-15b. It is evident that the cyclic threshold shear strain (γ_t^c) of the soil deposit has a value between 0.012% and 0.027%.

When processing pore pressure data from dynamic in-situ liquefaction tests, it is common to subtract the initial static water pressure from the record data so that only the excess pore pressure generated during dynamic loading is seen. Figure 6-16a shows the pore pressure data from Figure 6-15b after the static water pressure has been subtracted from the signal. The residual buildup of pore water pressure is of primary interest in liquefaction testing because it tends to decrease the effective stress within the soil mass. The hydrodynamic pressure only affects the instantaneous state of effective stress and hence does not have a lasting impact on the soil stiffness or strength.

It is simple to evaluate the residual pressure at the end of dynamic loading because the hydrodynamic portion of the signal has ceased. However, to effectively evaluate the increase in residual pressure at various times during shaking, the hydrodynamic portion of the signal must be separated from the residual portion of the signal. This separation is most readily accomplished using frequency-domain filtering. The residual pressure components of all PPT signals acquired during in-situ liquefaction testing were obtained by applying a 3-Hz low-pass filter to the excess pore pressure records. The hydrodynamic pressure components (if desired) may be obtained by subtracting the residual pressure component from the original excess pore pressure record. Figure 6-16b shows the

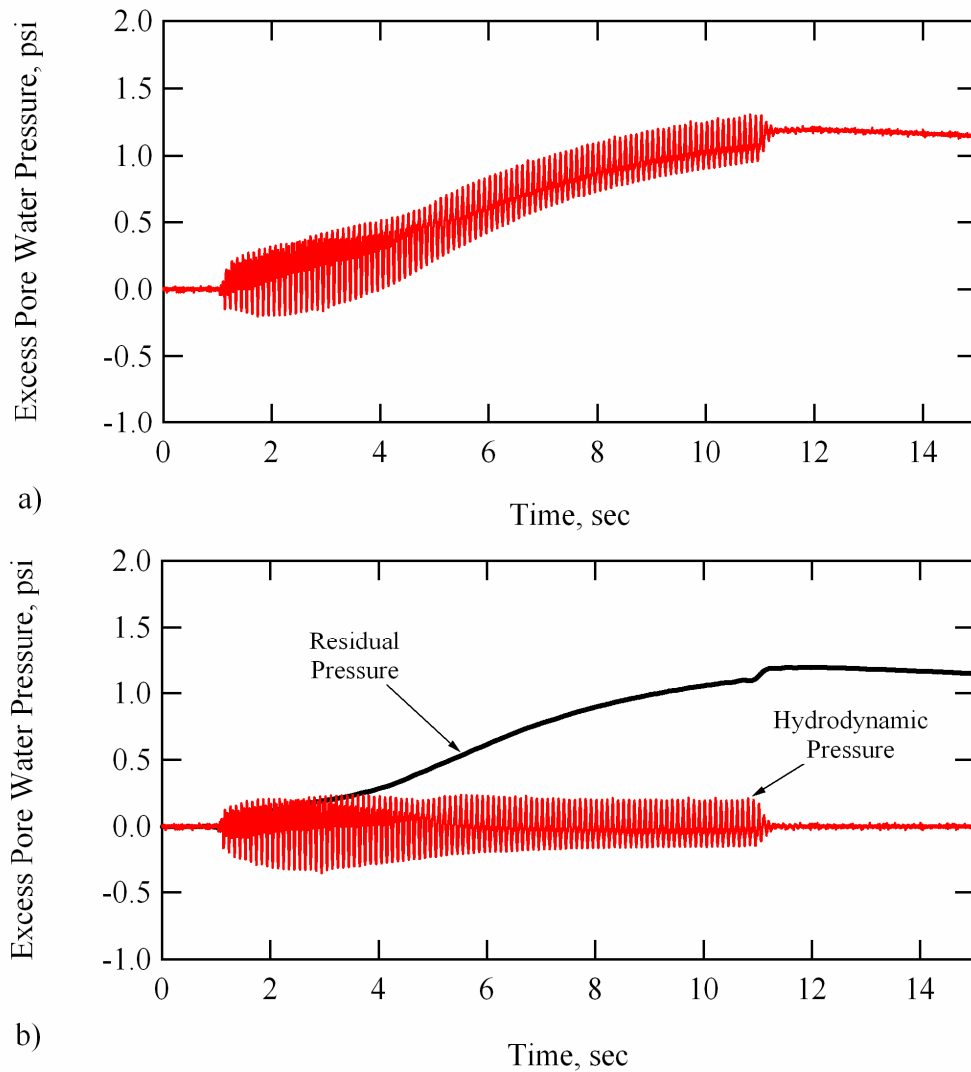


Figure 6-16 Example of an excess pore water pressure time history obtained during in-situ liquefaction testing: a) prior to frequency-domain filtering, and b) after frequency domain filtering to separate the hydrodynamic and residual portions of the signal.

separate residual and hydrodynamic portions of the excess pore pressure record that is displayed in Figure 6-16a.

In regards to evaluating soil liquefaction, pore water pressure data are typically quantified in terms of a pore pressure ratio (r_u) (De Alba et al., 1975; Seed et al., 1975; Kramer, 1996). Pore pressure ratio values are obtained by normalizing the excess pore water pressure generated during dynamic loading by the initial effective confining pressure acting on the soil. In field studies, the normalizing stress is the initial vertical effective stress (i.e. $r_u = \Delta u / \sigma_v'$, where Δu is excess pore water pressure and σ_v' is initial vertical effective stress). The r_u value helps one visualize how close the buildup in residual pressure has come to completely liquefying the soil. A r_u value equal to 1.0 (or 100%) means that the excess pore pressure has built to the point where it is equal to the initial vertical effective stress, and the soil is said to have fully liquefied. As stated in Chapter 2, surface evidence of soil liquefaction may not occur at all sites that experience a complete reduction of effective stress within some soil layer at depth. This is especially true for level ground sites with no man-made structures on them. Conversely, surface expressions of liquefaction may occur at sites that experience pore pressure ratios of less than 1.0. This is especially true for sites with substantial, preexisting shear stresses in the soil due to sloping ground or man-made structures (see Section 2.2.3).

The normalizing vertical effective stress, used to obtain r_u values, was calculated by superimposing the change in vertical stress due to the applied surface load of the vibroseis base plate onto the preexisting effective vertical

overburden stresses at each sensor location (see Section 5.2). The change in vertical stress due the load applied by the vibroseis base plate was calculated using both Boussinesq's and Westergaard's elastic stress distribution solutions (Coduto, 1994). Both solutions gave very similar results at the depths of the sensor array. The individual results of the stress distribution calculations and the normalizing vertical effective stresses used to obtain r_u values for each test location are discussed in Chapters 8, 9, and 10.

Residual pore water pressure values obtained from all five pressure transducers (4 miniature PPT's located in the liquefaction sensors placed at each node and the larger PDCR 35/D pressure transducer located at the center of the array) were used to calculate r_u values for each stage of the in-situ liquefaction tests. However, the r_u values used to construct the pore pressure generation curves for each site were obtained solely from the PDCR 35/D transducer located at the center of the array. The r_u values obtained from the miniature PPT's were only used in a qualitative sense to observe how the pore pressure generation varied within the instrumented soil mass.

6.5 NONLINEAR SHEAR MODULUS EVALUATION

The stress-strain behavior of soil is nonlinear under high-amplitude dynamic excitation (Seed and Idriss, 1970; Hardin, 1978). It is often important to quantify the nonlinear behavior of soils to accurately assess the earthquake hazard at a site. Nonlinear soil behavior is most often characterized in terms of the variation of shear modulus (G) with induced shear strain (γ). Nonlinear soil shear modulus behavior is commonly measured in the laboratory using cyclic triaxial,

cyclic simple shear, cyclic torsional shear, and resonant column tests. Other researchers have obtained in situ estimates of nonlinear soil shear modulus behavior by back-calculations performed on earthquake strong-motion records (Zeghal and Elgamal, 1994; Zeghal et al., 1995).

The shear moduli of soils are generally independent of shear strain amplitude in the small-strain range (i.e. shear strains less than approximately 0.001%, depending on soil type and confining pressure). The small-strain shear modulus is referred to as G_{\max} . Shear modulus behavior switches from linear, strain amplitude independent to nonlinear, strain amplitude dependant in the larger-strain range. It is common to normalize shear moduli values obtained in the larger-strain range by the small-strain shear modulus G_{\max} . An example of a generic modulus reduction curve (G/G_{\max}) for clean sand is shown in Figure 6-17 (Seed et al., 1986). The shear strain value where the soil switches from linear, strain amplitude independent to nonlinear strain amplitude dependant is termed the elastic threshold strain (γ_t^e). As a general approximation, the elastic threshold strain is often considered to have a value of approximately 0.001%. The soil shear modulus decays in a nonlinear fashion at strains greater than the elastic threshold strain, however the nonlinear behavior is independent of the number of loading cycles applied to the soil until the cyclic threshold strain (γ_t^c) is surpassed. As a general approximation, the cyclic threshold strain is often considered to have a value of approximately 0.01%. The cyclic threshold strain is marked by the tendency of the soil shear modulus to begin degrading with increasing number of loading cycles applied at a constant shear strain. In

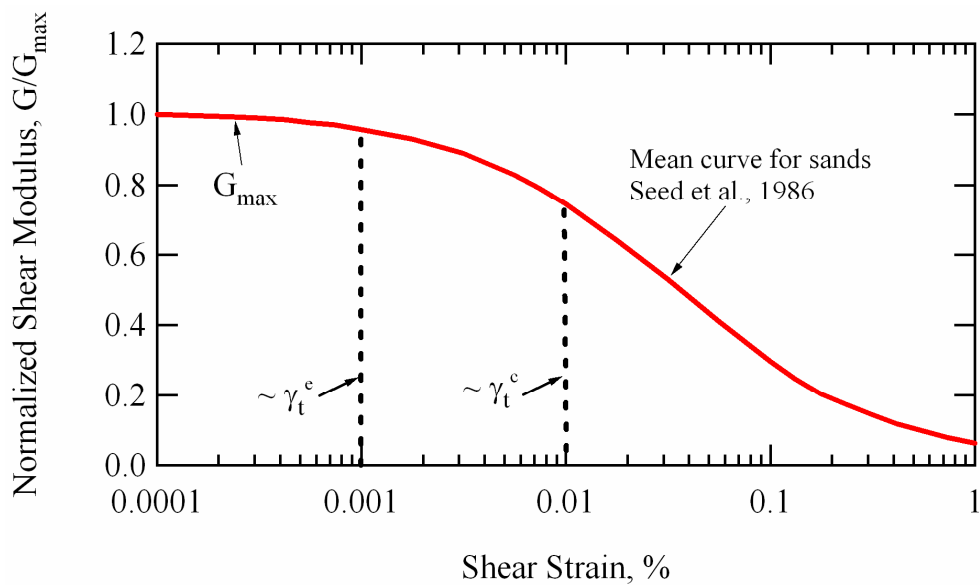


Figure 6-17 Mean modulus reduction curve for sands proposed by Seed et al., (1986).

saturated soils, the cyclic threshold strain is also revealed as the point where excess pore water pressure generation begins (see Section 2.3.2).

The shear modulus of a soil deposit can be obtained from its shear wave velocity according to the following equation:

$$G = \rho \cdot V_s^2 \dots\dots\dots(6-12)$$

where G = the shear modulus of the soil; ρ = the mass density of the soil; and V_s = the shear wave velocity of the soil. The procedure used to make this calculation in the context of the in-situ dynamic liquefaction test is illustrated in Figure 6-18. The horizontal excitation generated by the vibroseis truck at the ground surface produces vertically propagating (downward), horizontally polarized shear waves

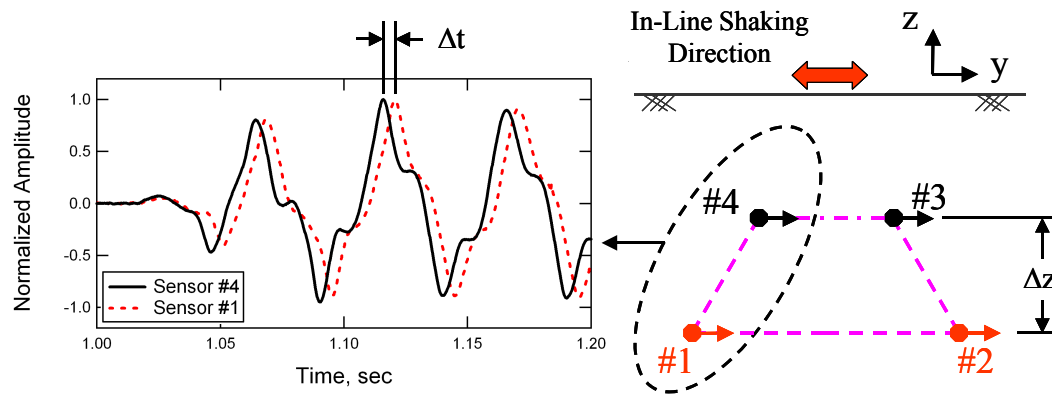


Figure 6-18 Schematic detailing the liquefaction sensor array and the components of particle motion used to calculate the strain dependent shear wave velocity of the instrumented soil mass.

(S_{vh} waves). These shear waves are sensed by the horizontal, in-line components (y -components) of the embedded instrumentation as they propagate downward from the ground surface. Sensors (nodes) No. 3 and No. 4 first detect the shear waves, followed by sensors No. 1 and No. 2. The strain dependent shear wave velocity of the instrumented soil mass may be obtained by dividing the vertical distance (Δz) between sensors by the time lag (Δt) between the top and bottom sensors. A different Δt may be obtained for each cycle of loading so that degradation, as well as nonlinearity, may be evaluated. This process enables one to track the changes in shear modulus throughout the entire process of in-situ liquefaction testing.

The raw outputs of the in-line components (y -components) of the MEMS accelerometers were used to calculate the time lag between each sensor pair (i.e. sensors No. 3 & No. 2, and sensors No. 4 & No. 1). Cycle-by-cycle time lags

were measured between both the peaks and the troughs of the records. The peak and trough time lags for each sensor pair were then averaged together on a cycle-by-cycle basis to obtain average vertically propagating (downward), horizontally polarized shear wave velocities ($V_{S,vh}$) within the instrumented soil mass. An example of the average cycle-by-cycle shear wave velocities obtained from records collected during an in-situ liquefaction test is shown in Figure 6-19. The average shear strain (averaged over 100 cycles of loading) induced at the center of the array during this test was approximately 0.009%, which is below the cyclic threshold strain for the liquefiable soil deposit. This point is substantiated by the fact that there was no excess pore pressure generated in the array. Therefore, it is not surprising to see that the cycle-by-cycle shear wave velocities remain essentially constant throughout loading. An example of the average cycle-by-cycle shear wave velocities obtained from records collected during a higher-strain in-situ liquefaction test is shown in Figure 6-20. In this case, the average strain induced at the center of the array was approximately 0.045%, which is beyond the cyclic threshold strain for the liquefiable soil deposit. This point is substantiated by the fact that a pore pressure ratio of approximately 12% was induced at the center of the array after 100 cycles of loading. The cycle-by-cycle shear wave velocities are clearly decaying throughout the duration of loading. The combined effects of softening due to pore water pressure generation and cyclically loading the soil beyond its cyclic threshold strain cause this degradation.

The procedure described above assumes that the shear waves propagating through the instrumentation array are plane waves. This assumption is believed to

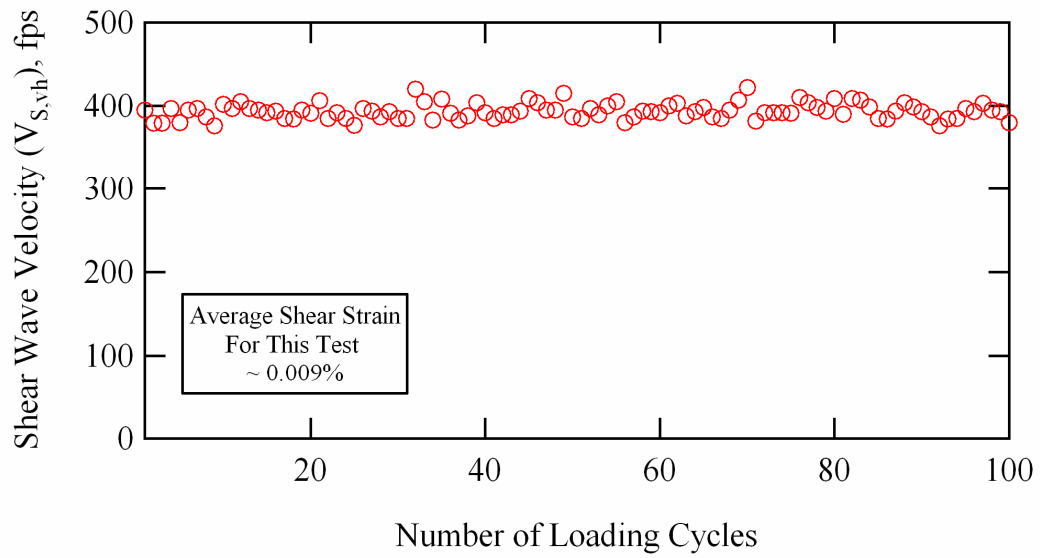


Figure 6-19 Cycle-by-cycle shear wave velocities from an in-situ liquefaction test with relatively moderate induced shear strains ($\gamma \sim 0.009\%$).

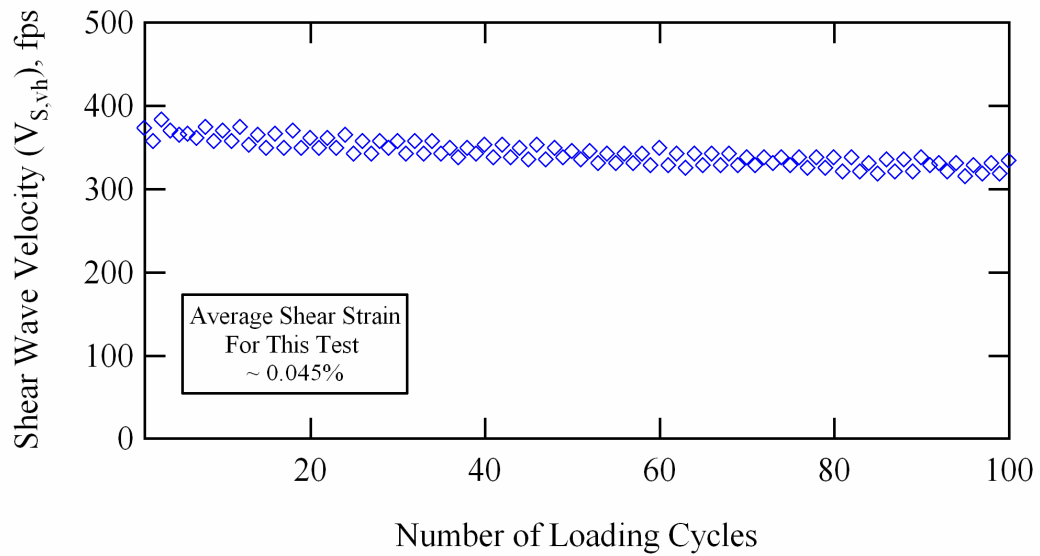


Figure 6-20 Cycle-by-cycle shear wave velocities from an in-situ liquefaction test with relatively large induced shear strains ($\gamma \sim 0.045\%$).

be reasonable, at least as a first order approximation, because the array is located directly below the center of the rigid base plate. The plane wave assumption may also be verified by comparing the amplitude and phase of the waves detected by the horizontal, in-line components of each sensor located at the same depth. A comparison in this manner is made between sensors No. 3 and No. 4 in Figure 6-21. The amplitude and phase of the in-line components are practically identical despite the fact that the sensors are located on opposite sides of the centerline of the base plate. This evidence lends credence to the above mentioned plane wave assumption.

Cross correlations between records in the time-domain and the cross power spectrum of records in the frequency-domain were also used to obtain shear wave velocity measurements. However, in order to obtain cycle-by-cycle velocities using these two procedures, the records must be windowed over every loading cycle in either the time-domain or the frequency domain. These procedures are substantially more labor intensive and tended to produce results that were less consistent than the simple time domain analysis described above.

As mentioned in Section 4.3.3, all records were recorded at a constant rate of 8192 samples per second. While considered as over-sampling for recording frequencies of 10 and 20 Hz, this sampling rate was chosen to obtain adequate resolution for phase determination between sensors in the time domain. Harmonic distortion and noise in some of the raw accelerometer records made it extremely difficult to obtain precise values for the time lags between sensors. For example, assuming a shear wave velocity for the soil of 400 fps (122 m/s) and a

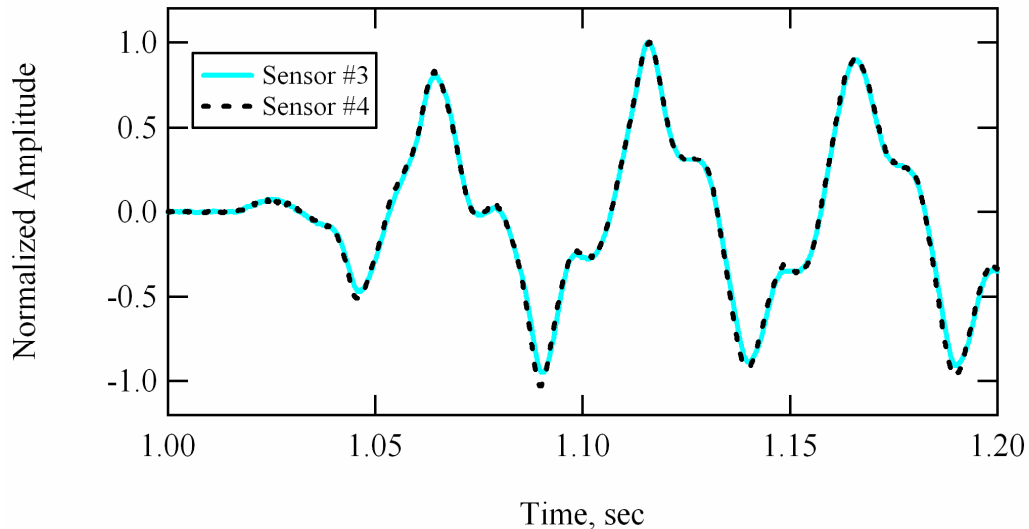


Figure 6-21 Comparison between the amplitudes and phase of two separate receivers located at the same depth on either side of the base plate centerline during an in-situ dynamic liquefaction test.

vertical distance between sensors of 2 ft (0.6 m), a sampling rate of 8192 samples per second yields approximately 40 digitized points between wave arrival times. If one were to be off by 4 data points (0.0005 seconds) in determining the time lag between sensors, the estimated shear wave velocity would be off by approximately 10%. This would alter the estimated shear modulus by approximately 20%. Frequency-domain filtering and time-domain integration were experimented with in an attempt to reduce the influence of harmonic distortion and noise in the raw accelerometer records and isolate the driving frequency. While these efforts made the records look much cleaner, the time lags between sensors were adversely altered. Therefore, the raw accelerometer signals were solely used to obtain estimates of the nonlinear shear modulus behavior during all in-situ liquefaction tests. If the raw accelerometer records were not

clean enough to make accurate estimates, the shear modulus values were not reported.

6.6 SUMMARY

The raw data recorded during an in-situ dynamic liquefaction test consists of acceleration and pore water pressure time histories generated at each sensor location. The processed data desired from an in-situ dynamic liquefaction test are: (1) induced cyclic shear strain, (2) excess pore water pressure ratio as a function of induced cyclic shear strain and number of loading cycles, and (3) nonlinear soil shear modulus as a function of induced cyclic shear strain and change in pore water pressure. Various displacement-based (DB) and wave propagation-based (WB) strain evaluation methods were experimented with to calculate shear strains induced in the instrumented soil mass. It was determined that shear strain evaluation methods that did not include contributions from vertical particle motions (caused by base plate rocking) tended to under predict the induced shear strains. Therefore, a 4-node, isoparametric finite element procedure was used to evaluate all shear strains during the data reduction process. Excess pore water pressure ratios were calculated during each stage of loading by dividing the residual pore water pressure generated at the center of the array by the initial, vertical effective stress at the depth of each transducer. Nonlinear shear moduli within the array were evaluated by tracking the cycle-by-cycle change in velocity of vertically propagating (downward), horizontally polarized shear waves during each stage of loading.

Chapter 7

The Wildlife Liquefaction Array; Imperial Valley, California

7.1 INTRODUCTION

The validity of the proposed in-situ dynamic liquefaction test has been demonstrated by conducting field experiments at the Wildlife Liquefaction Array (WLA) in Imperial Valley, California. The WLA site has been intensely studied over the past 25 years (Bennett et al., 1984; Bierschwale and Stokoe, 1984; Hagg and Stokoe, 1985; Vucetic and Dobry, 1986; Youd and Bartlett, 1988; Holzer et al., 1989; Dobry et al., 1992; Youd and Holzer, 1994; Zeghal and Elgamal, 1994). It has also recently been designated as a Network for Earthquake Engineering Simulation (NEES) site for the study of soil liquefaction (<http://nees.ucsb.edu>). The extensive site characterization, its documented occurrence of earthquake-induced soil liquefaction twice in the 1980's (1981, $M_w = 5.9$ Westmorland earthquake; and 1987, $M_w = 6.6$ Superstition Hills earthquake), and its likelihood for re-liquefaction during subsequent earthquakes make the WLA an ideal location for verifying the proposed in-situ dynamic liquefaction test method. Three separate in-situ liquefaction tests at three different locations were conducted at this site. The individual test results are discussed in Chapters 8, 9, and 10. Background information and characteristics of the WLA site are presented in this chapter.

7.2 IMPERIAL VALLEY, CALIFORNIA

The Imperial Valley is a lightly populated, agricultural valley located in Southern California near the border with Mexico. It lies in the southern part of the Salton Basin, which was formed by the crustal rifting that opened the Gulf of California (Youd and Wieczorek, 1984). Many of these tectonic processes are still very active and generate earthquakes at frequent intervals (Sharp, 1982). Mapped seismogenic faults in the area include the Imperial and Brawley faults in the valley, the San Andreas fault complex to the northwest, the Mexicali fault to the south, the Elsinor fault along the southwest edge of the Salton Basin, and the Superstition Hills and Superstition Mountain faults to the west (Moss et al., 2005). Four substantial earthquakes have shaken the region in the past 30 years (1979, $M_w = 6.5$ Imperial Valley earthquake; 1981, $M_w = 5.9$ Westmorland earthquake; 1987, $M_w = 6.2$ Elmore Ranch earthquake; and 1987, $M_w = 6.6$ Superstition Hills earthquake). Because of the widespread distribution of susceptible sediment in the valley, soil liquefaction has been induced at many locations by each of these events (Youd and Holzer, 1994). A site named the Wildlife Liquefaction Array (WLA) was fully liquefied by two of these earthquakes (1981, $M_w = 5.9$ Westmorland earthquake; and 1987, $M_w = 6.6$ Superstition Hills earthquake). This site was chosen as the appropriate location to verify the proposed in-situ dynamic liquefaction test.

7.3 WILDLIFE LIQUEFACTION ARRAY (WLA)

Following the 1981 Westmorland earthquake, a special field test site, where pronounced soil liquefaction had been observed (in terms of sand boils and

lateral spreading), was identified by personnel from the United States Geological Survey (USGS). USGS personnel later instrumented this site with the goal of making in-situ measurements of dynamic ground response and excess pore pressure generation in future earthquakes (Bennett et al., 1984). This instrumented test site has since become known as the Wildlife Liquefaction Array (WLA), or simply, the Wildlife Site. A map that shows the location of the WLA is presented in Figure 7-1. This map also shows the relative locations of the epicenters for the three most recent significant-magnitude earthquakes that have shaken the site. These three earthquakes are: (1) the 1981 Westmorland earthquake ($M_w = 5.9$), (2) the 1987 Elmore Ranch earthquake ($M_w = 6.2$), and (3) the 1987 Superstition Hills earthquake ($M_w = 6.6$). The 1987 Elmore Ranch earthquake preceded the Superstition Hills earthquake by just over 11 hours.

Shallow soil deposits at WLA consist of floodplain sediments that fill an old incised channel of the Alamo River. A simplified soil profile for the site is shown in Figure 7-2b. The uppermost unit is a 8.2-ft (2.5-m) thick silt to clayey silt bed that overlies the unit that liquefied, a 14.1-ft (4.3-m) thick silty-sand layer. Beneath these floodplain deposits is a stiff 17.1-ft (5.2-m) thick clay to silty-clay layer (Bennett et al., 1984). The ground water table at the site is controlled by the Alamo River and is typically found at a depth of about 4.0 ft (1.2 m) (Holzer et al., 1989). Figure 7-2 also shows the instrumentation (accelerometers and piezometers) that was installed at the site by USGS personnel following the 1981 Westmorland earthquake.

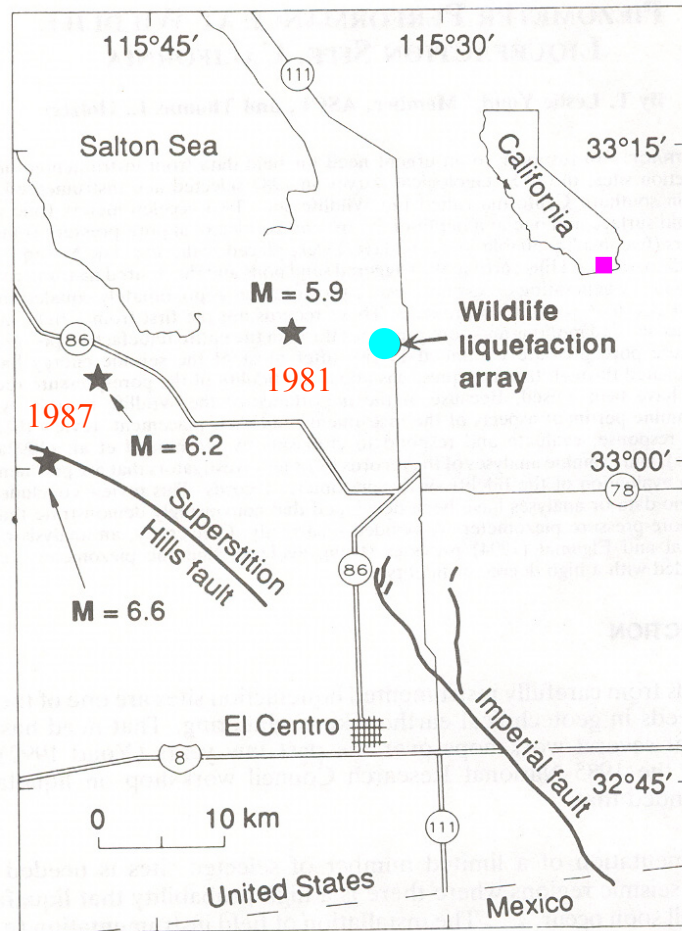


Figure 7-1 Map showing the location of the Wildlife Liquefaction Array (WLA) and the epicenters for the 1981 Westmorland earthquake ($M_w = 5.9$), the 1987 Elmore Ranch earthquake ($M_w = 6.2$), and the 1987 Superstition Hills ($M_w = 6.6$) earthquake (after Holzer et al., 1989).

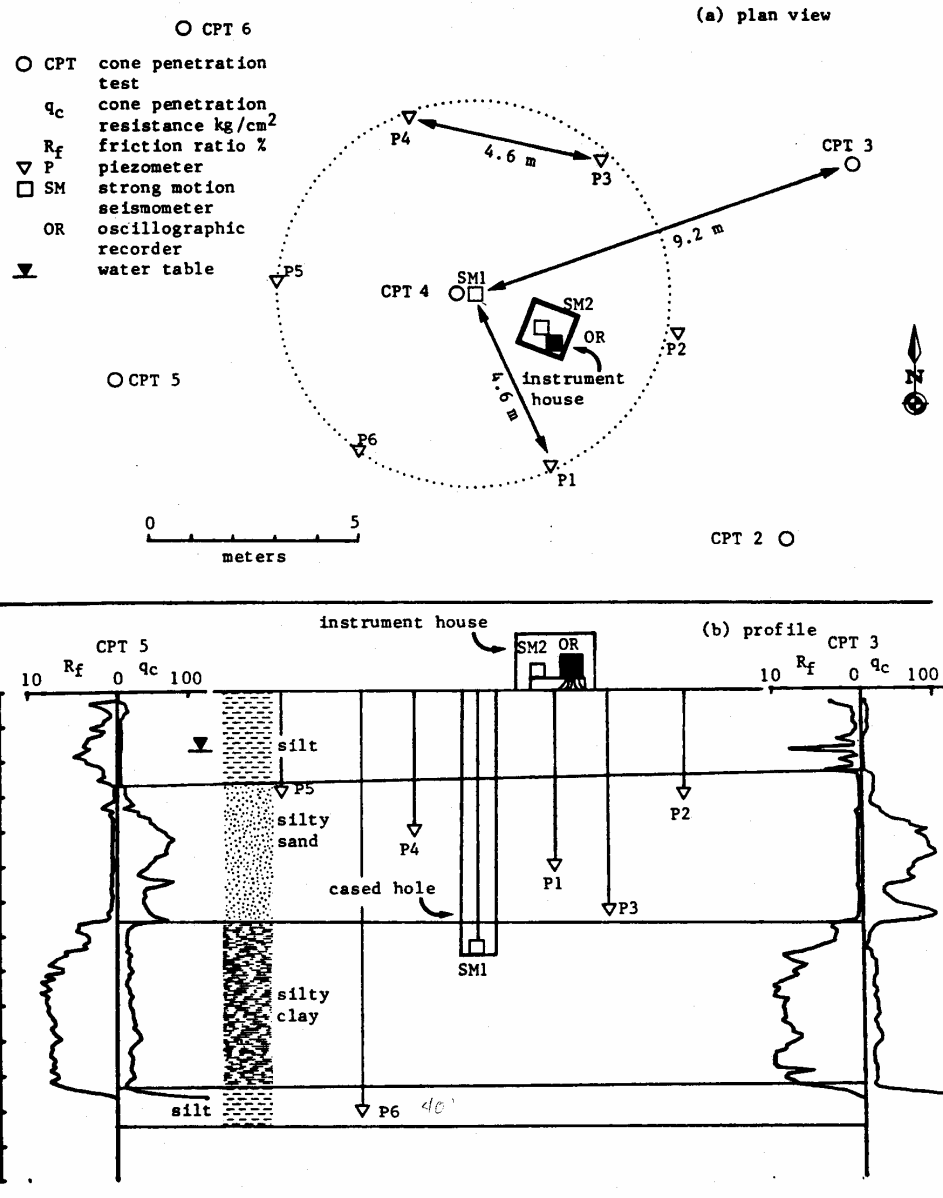


Figure 7-2 Plan view and cross section of the Wildlife Liquefaction Array (WLA) showing sediment stratigraphy and locations of accelerometers and piezometers installed by USGS personnel (from Bennett et al., 1984): a) plan view, and b) cross section.

7.3.1 Wildlife Site Field and Laboratory Studies

Between 1981 and 1985, several investigators conducted field and laboratory studies to measure soil properties at the Wildlife Site. Field investigations included CPT, SPT, seismic velocity, piezocone, dilatometer, and other tests (Bennett et al., 1984; Bierschwale and Stokoe, 1984; Stokoe and Nazarian, 1985). Laboratory investigations included standard classification tests, resonant column tests, cyclic triaxial tests, and cyclic simple shear tests (Hagg and Stokoe, 1985; Vucetic and Dobry, 1986). The WLA is one of the most studied liquefaction sites in the world (Youd and Bartlett, 1988; Dobry et al., 1992). Some of the more relevant findings from these studies are presented below.

7.3.1.1 Original Wildlife Site Characterization and Instrumentation

In May 1982, just over one year after the 26 April 1981 Westmorland earthquake liquefied the Wildlife Site, personnel from the USGS visited the area to investigate sediment properties and soil profiles. Both cone penetration tests (CPT) and standard penetration tests (SPT) were used to define stratigraphic units and measure penetration resistance. Soil samples were obtained by SPT and auger sampling (Bennett et al., 1984). Table 7-1 details the numbers and types of tests conducted at the Wildlife Site along with their associated nomenclatures. A total of 16 CPT tests, six SPT tests, and five auger sample tests were conducted at the site. Figure 7-3 shows the locations of these tests relative to the instrumentation that was later installed. The information garnered from these tests was used to develop the soil profile discussed in this section (Section 7.3) and shown in Figure 7-2b.

Table 7-1 Summary of the field tests performed at the Wildlife Site by Bennett et al. (1984)

| Number of Tests | Test Designation | | |
|--------------------|------------------|-------|-------|
| | CPT | SPT | Auger |
| 1 | 1Cg | 1Ns | 1Ap |
| 2 | 1Cp | 2Ng1* | 3Ap |
| 3 | 2Cg | 2Ng2 | 3Ag* |
| 4 | 3Cg | 2Ng3 | 7Ap |
| 5 | 3Cp | 3Ns | 9Ap |
| 6 | 4Cg | 5Ng | |
| 7 | 5Cg | | |
| 8 | 5Cp | | |
| 9 | 6Cg | | |
| 10 | 6Ct | | |
| 11 | 7Cg | | |
| 12 | 7Cp | | |
| 13 | 8Cg | | |
| 14 | 9Cg | | |
| 15 | 9Cp | | |
| 16 | 10Cg | | |

Note: * Samples tested by Bennett et al. (1984) to determine average grain size characteristics and water content and plasticity properties

Average sediment properties from the tests conducted at the Wildlife Site are shown in Figure 7-4. While not shown in Figure 7-2b, Bennett et al. (1984) subdivided the liquefiable layer into an upper unit (B1) and a lower unit (B2). The upper unit extends from a depth of approximately 8.2 ft (2.5 m) down to a depth of about 11.5 ft (3.5 m), while the lower unit extends from this point down

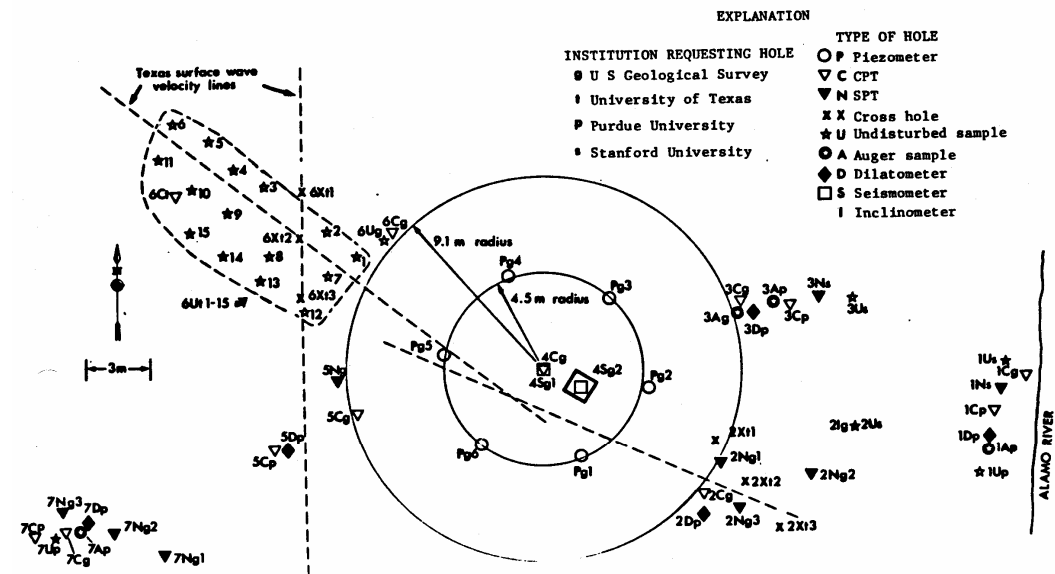


Figure 7-3 Plan view of the Wildlife Liquefaction Array (WLA) showing the locations of instrumentation and tests performed by various researchers (from Bennett et al., 1984).

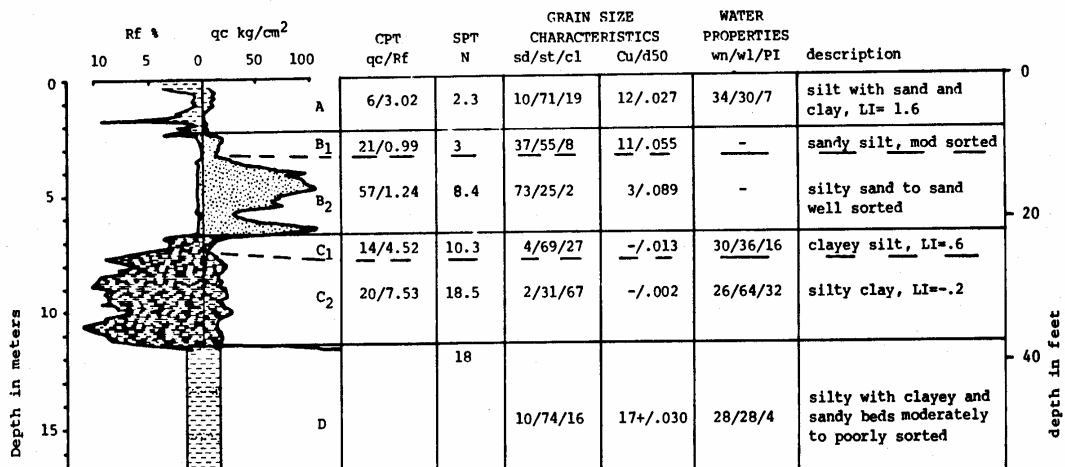


Figure 7-4 Average sediment properties and test parameters for the soil layers at the Wildlife Liquefaction Array (WLA) (after Bennett et al., 1984).

to a depth of approximately 22.3 ft (6.8 m). Average CPT values, SPT values, grain size characteristics, water content and plasticity properties, and soil descriptions for the upper and lower liquefiable units are provided in Figure 7-4. It should be noted that the average grain size characteristics and water content and plasticity properties reported in Figure 7-4 were obtained using samples from only one SPT borehole (2Ng1) and one auger sample borehole (3Ag) (refer to Table 7-1). All of the samples within the liquefiable layer that were obtained from 2Ng1 and 3Ag are listed in Table 7-2. The samples have been designated as upper-unit or lower-unit based on the depth ranges noted above. The individual sample percentages of sand, silt, and clay, as determined by Bennett et al. (1984), are also shown.

It is interesting to note that the writer obtained average percentages of sand, silt and clay in the upper liquefiable unit of 55, 40 and 5, respectively, while Bennett et al. (1984) indicate average percentages of 37, 55 and 8, respectively (refer to Figure 7-4, unit B1). However, the writer obtained essentially the same average percentages of sand, silt, and clay as Bennett et al. (1984) in the lower liquefiable unit. Upon closer inspection, it appears that Bennett et al. (1984) only used the grain size data from samples within the depth range of 7.9 to 9.5 ft (2.4 to 2.9 m) to determine their upper-unit sand, silt and clay averages. The three shallower samples from the upper-unit do indeed seem to be more alike, while the three deeper samples from the upper-unit seem to have grain size characteristics more similar to the lower-unit. However, results from Haag and Stokoe (1985) presented later in this chapter (Section 7.3.1.2) indicate high percentages of silt-

Table 7-2 Summary of the grain size characteristics for all of the samples obtained from the upper (B1) and lower (B2) units of the liquefiable layer at the Wildlife Site as reported by Bennett et al. (1984)

| Test Designation | Depth (ft) | Upper- or Lower-Unit ¹ | Sand (%) | Silt (%) | Clay (%) | FC ² (%) | Average ³ FC (%) | Std. Dev. ³ FC (%) |
|------------------|-------------|-----------------------------------|----------|----------|----------|---------------------|-----------------------------|-------------------------------|
| SPT - 2Ng1 | 7.9 - 8.5 | upper | 30 | 66 | 4 | 70 | 45 | 21 |
| Auger - 3Ag | 9.0 | upper | 37 | 53 | 10 | 63 | | |
| Auger - 3Ag | 9.5 | upper | 44 | 46 | 10 | 56 | | |
| SPT - 2Ng1 | 10.0 - 10.9 | upper | 66 | 34 | 0 | 34 | | |
| SPT - 2Ng1 | 10.9 - 11.5 | upper | 83 | 17 | 0 | 17 | | |
| Auger - 3Ag | 11.4 | upper | 69 | 26 | 5 | 31 | | |
| SPT - 2Ng1 | 13.0 - 13.9 | lower | 73 | 26 | 1 | 27 | 27 | 10 |
| Auger - 3Ag | 13.5 | lower | 78 | 19 | 3 | 22 | | |
| SPT - 2Ng1 | 13.9 - 14.5 | lower | 80 | 20 | 0 | 20 | | |
| Auger - 3Ag | 15.0 | lower | 74 | 23 | 3 | 26 | | |
| Auger - 3Ag | 18.0 | lower | 69 | 26 | 5 | 31 | | |
| SPT - 2Ng1 | 18.0 - 18.5 | lower | 67 | 29 | 4 | 33 | | |
| Auger - 3Ag | 19.5 | lower | 51 | 43 | 6 | 49 | | |
| Auger - 3Ag | 21.0 | lower | 79 | 18 | 3 | 21 | | |
| SPT - 2Ng1 | 22.0 - 23.5 | lower | 82 | 17 | 1 | 18 | | |

Notes: 1. From layering proposed by Bennett et al. (1984)

2. Fines content (FC) = percent silt + percent clay; calculated by Cox herein

3. FC average and standard deviation calculated for each unit by Cox herein

and caly-size particles in specimens obtained from depths between 10 to 11 ft (3.0 to 3.3 m). The upper-unit simply appears to have grain size characteristics that are more variable than the lower-unit. Note that the fines content (FC) of the soil is equal to the percentage of silt-size soil particles plus the percentage of clay-size particles. The specimens from the upper-unit have an average FC of 45% with a

21% standard deviation. The specimens from the lower-unit have an average FC of 27% with a standard deviation of 10%. All of the liquefiable soil samples tested by Bennett et al. (1984) were found to be non-plastic.

USGS personnel instrumented the Wildlife Site with two strong-motion accelerometers and six piezometers. One of the accelerometers was placed at the ground surface and the other at a depth of 24.6 ft (7.5 m). Five of the piezometers were placed in the liquefiable soil layer, while one was placed at a depth of 40.0 ft (12.2 m). The locations of the accelerometers and piezometers are shown in Figure 7-2. To avoid disturbance around the instrumentation, no field testing, other than that associated with the placement of instrumentation, was conducted within a 29.9 ft (9.1 m) radius of the accelerometer placed at depth (refer to Figures 7-2 and 7-3).

7.3.1.2 Field and Laboratory Tests Performed by The University of Texas

In January 1983, soil sampling and field seismic tests were performed at the Wildlife Site by personnel from the University of Texas (Haag and Stokoe, 1985). The field seismic tests included both crosshole and Spectral-Analysis-of-Surface-Waves (SASW) measurements. The locations of the crosshole boreholes and the SASW array lines are shown in Figure 7-3. The SASW and crosshole shear wave velocity (V_s) profiles determined for the site are shown in Figure 7-5. From these profiles, Bierschwale and Stokoe (1984) reported high, average and low V_s values in the liquefiable layer of 425 fps (130 m/s), 380 fps (116 m/s) and 340 fps (104 m/s), respectively.

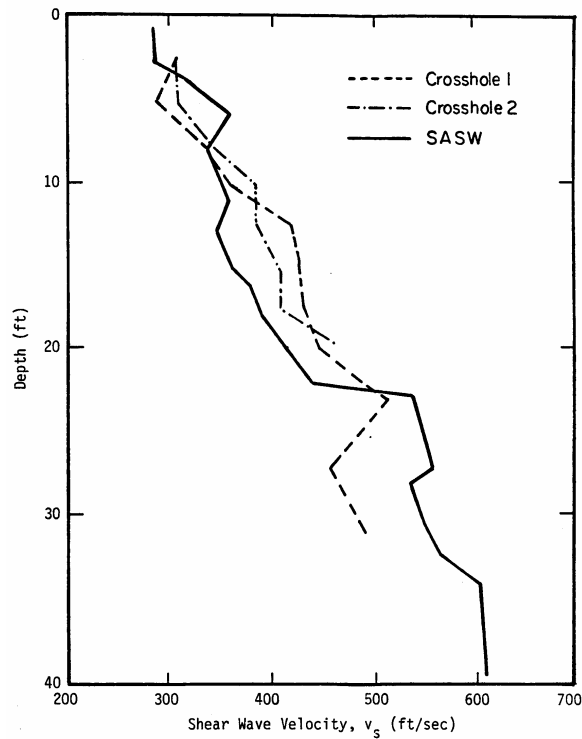


Figure 7-5 Shear wave velocity profiles obtained from SASW and crosshole tests performed at the Wildlife Liquefaction Array (from Bierschwale and Stokoe, 1984).

University of Texas personnel used fixed-piston sampling to recover approximately 27 tubes of soil from the Wildlife Site. The samples were taken from the area indicated by a dashed, rectangular-shaped box in the upper left-hand corner of Figure 7-3. Of these 27 tubes, seven were transported to the University of Texas (UT), eight were transported to Woodward-Clyde (WC) Laboratory in New Jersey, and 12 were transported to Renssalaer Polytechnic Institute (RPI) in Troy, New York. The laboratory tests performed on the samples that were transported to the University of Texas are discussed below. The laboratory tests

performed on the samples that were transported to WC and RPI are discussed in Section 7.3.1.3.

Haag and Stokoe (1985) performed six resonant column tests and four consolidated-undrained (CU) triaxial tests on intact specimens retrieved from the liquefiable layer at the Wildlife Site. Each of these specimens was classified according to the Unified Soil Classification System (USCS) using results from grain size analyses and Atterberg limit tests. Haag and Stokoe (1985) tested soils from two separate depth ranges in the liquefiable layer. They referred to the upper-level of the liquefiable layer as level A and the lower-level as level B. Levels A and B basically correspond to the upper-unit (B1) and lower-unit (B2), respectively, designated by Bennett et al. (1984). All of the level A specimens tested by Haag and Stokoe (1985) came from depths between 8.8 ft (2.7 m) and 10.7 ft (3.3 m). All of the level B specimens came from depths between 14.6 ft (4.5 m) and 16.1 ft (4.9 m). Haag and Stokoe (1985) reported that specimens from the upper-level generally classified as low plasticity silt (ML), while specimens from the lower-layer generally classified as poorly graded silty-sand (SM).

Table 7-3 details the specimen properties of the liquefiable soil samples tested by Haag and Stokoe (1985) using CU triaxial tests. Two of the CU tests were performed on specimens from the upper-layer (A included in the specimen designation), while two of the tests were performed on specimens from the lower-layer (B included in the specimen designation). The lower-layer specimens switched from contractive to dilative behavior at axial strains on the order of 0.2

Table 7-3 Summary of the soil properties of specimens from upper (A) and lower (B) portions of the liquefiable layer at the Wildlife Site that were tested in consolidated-drained (CU) triaxial tests by Haag and Stokoe (1985)

| Specimen | Depth (ft) | Fines Content (% < 75 μm) | Clay Content (% < 5 μm) | Liquid Limit (%) | Plastic Limit (%) | Soil Type (USCS) | Void Ratio e | Effective Friction Angle ϕ' (deg) |
|----------|------------|---------------------------------------|-------------------------------------|------------------|-------------------|------------------|--------------|--|
| W11A3 | 10.0 | 62 | 18 | 25.1 | NP | ML | 0.88 | 34.7 |
| W11A4 | 10.6 | 87 | 18 | 25.1 | NP | ML | 0.79 | 36.6 |
| W11B3 | 15.5 | 25 | 10 | 23.4 | NP | SM | 0.74 | 44.6 |
| W11B4 | 16.1 | 30 | 10 | 23.9 | NP | SM | 0.54 | 38.1 |

to 0.5%. The upper-layer specimens switched from contractive to dilative at axial strains on the order of 2.0 to 2.5%. The fines contents (FC) of the two upper-layer specimens (62% and 87% for the specimens from depths of 10.0 and 10.6 ft, respectively) are more characteristic of the FC obtained from specimens in the depth range of 7.9 to 9.5 ft (2.4 to 2.9 m) by Bennett et al. (1984) (see Table 7-2). The FC of the specimen from 10.0-ft (3.0-m) is within one standard deviation (21%) of the average upper-unit FC (45%) of the samples obtained by Bennett et al. (1984). However, the FC of the specimen from 10.6-ft (3.2-m) is two standard deviations above this same average upper-unit FC. These results clearly validate the variability of the FC in the upper-unit. The FC for the two lower-layer specimens (25% and 30% for the specimens from depths of 15.5 and 16.1 ft, respectively) are very similar to the average lower-unit FC (27%) of the samples obtained by Bennett et al. (1984). Despite having clay-sized particle contents between 10 – 18%, all four specimens were found to be non-plastic (NP).

Table 7-4 details the specimen properties of the liquefiable soil samples tested by Haag and Stokoe (1985) in the resonant column device. Resonant column tests were performed on three specimens from the upper liquefiable layer and three specimens from the lower liquefiable layer. All RC tests were performed on unsaturated, intact samples. Haag and Stokoe (1985) determined that specimen W12A1 was atypical of the upper-layer (both in its dynamic response and its soil properties) and did not include it in any of their averaged upper-layer results. The FC of the remaining two upper-layer specimens (57% and 50%) are well within one standard deviation (21%) of the average upper-unit FC (45%) of the samples obtained by Bennett et al. (1984). The FC for the three lower-layer specimens (38%, 12% and 23%) average out to be (24%) approximately equal to the average lower-unit FC (27%) of the samples obtained by Bennett et al. (1984). The lower-layer specimens are all NP. One of the upper-layer specimens is NP and the other has a plasticity index (PI) of 2.4 (very low).

The range of modulus reduction curves determined by Haag and Stokoe (1985) from performing resonant column tests on two upper-layer specimens at confining pressures of 8, 16 and 32 psi (55, 110 and 220 kPa) is shown in Figure 7-6. The range of modulus reduction curves determined from performing resonant column tests on three lower-layer specimens at confining pressures of 8, 16 and 32 psi (55, 110 and 220 kPa) is shown in Figure 7-7. The nonlinear behavior of the upper liquefiable layer specimens has a broader range than the

Table 7-4 Summary of the soil properties of specimens from upper (A) and lower (B) portions of the liquefiable layer at the Wildlife Site that were tested in the resonant column device by Haag and Stokoe (1985)

| Specimen | Depth (ft) | Fines Content (% < 75 μm) | Clay Content (% < 5 μm) | Liquid Limit (%) | Plastic Limit (%) | Soil Type (USCS) | Void Ratio e | Degree of Saturation (%) | G_{max}^1 (psf) | V_{max}^2 (fps) |
|----------|------------|---------------------------------------|-------------------------------------|------------------|-------------------|------------------|--------------|--------------------------|--------------------------|--------------------------|
| W12A1* | 8.8 | 95 | 22 | 32.6 | 25.7 | ML | 0.92 | 99 | 297000 | 282 |
| W3A4 | 10.7 | 57 | 15 | 23.3 | 20.9 | ML | 0.80 | 97 | 558000 | 387 |
| W11A1 | 8.8 | 50 | 11 | 23.3 | NP | SM | 0.81 | 78 | 643000 | 415 |
| W3B3 | 15.8 | 38 | 18 | 24.7 | NP | SM | 0.84 | 90 | 570000 | 391 |
| W3B1 | 14.6 | 12 | 2 | 21.5 | NP | SP-SM | 0.74 | 44 | 860000 | 480 |
| W12B2 | 14.9 | 23 | 10 | 22.7 | NP | SM | 0.75 | 77 | 655000 | 419 |

Notes: * Identified as atypical; not included in any averaged layer properties (Haag and Stokoe 1985)

1. G_{max} at estimated in-situ confining pressure (Haag and Stokoe 1985)

2. V_{max} calculated using Equation (6-12) with $\rho = \gamma/g = (120 \text{ pcf})/(32.2 \text{ ft/sec}^2)$

nonlinear behavior of the lower liquefiable layer specimens. In fact, Figure 7-8 shows that the range of modulus reduction curves for the lower-layer specimens falls within the range of modulus reduction curves for the upper-layer specimens. Therefore, the upper-layer modulus reduction curve range appears to be a good bracket for the nonlinear behavior of the Wildlife liquefiable soil layer in general.

Figure 7-9 compares the modulus reduction curve range for the liquefiable soil layer at the Wildlife Site to the modulus reduction curve range for clean sands proposed by Seed et al. (1986). The Wildlife Site modulus reduction curves are substantially more linear than the general modulus reduction curves for sands. This is likely due to the high concentration of fine-grained soil particles (both silt- and clay-size) in the Wildlife Site liquefiable soil layer.

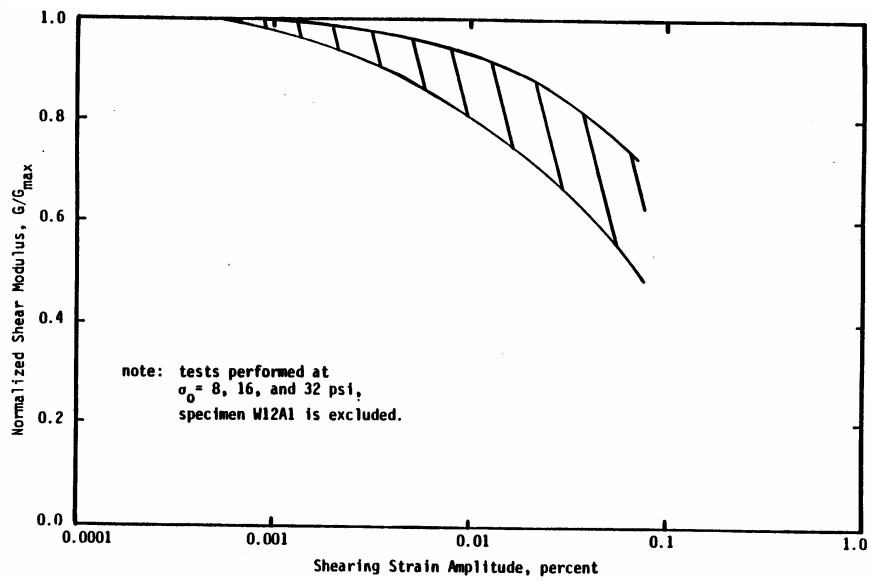


Figure 7-6 Range in modulus reduction curves for upper liquefiable layer (A) Wildlife Site specimens tested in the resonant column device (from Haag and Stokoe, 1985).

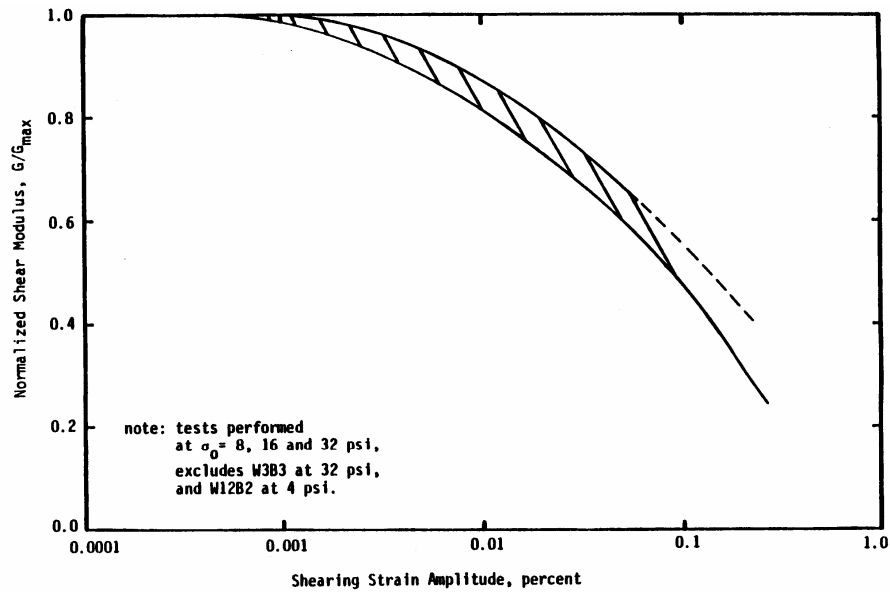


Figure 7-7 Range in modulus reduction curves for lower liquefiable layer (B) Wildlife Site specimens tested in the resonant column device (from Haag and Stokoe, 1985).

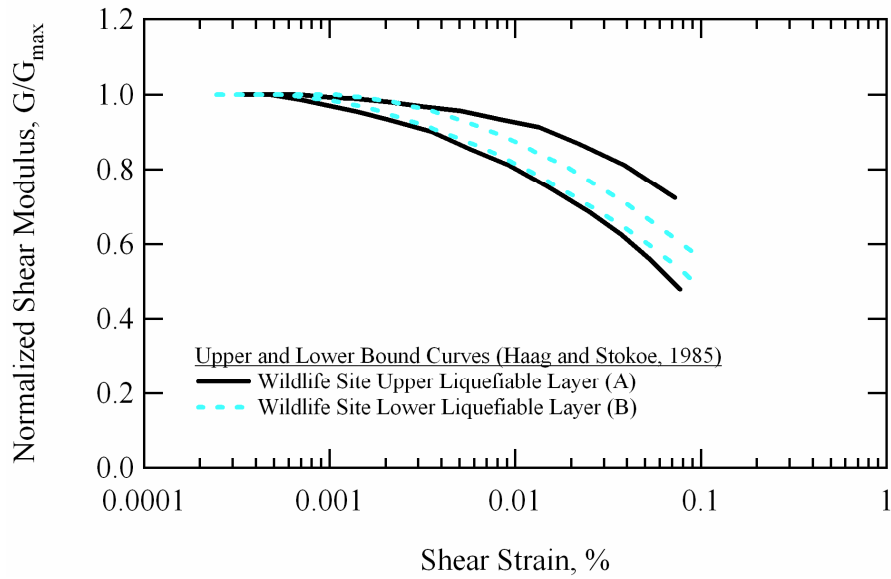


Figure 7-8 Comparison between the range in modulus reduction curves for upper (A) and lower (B) liquefiable layer Wildlife Site specimens tested in the resonant column device by Haag and Stokoe (1985).

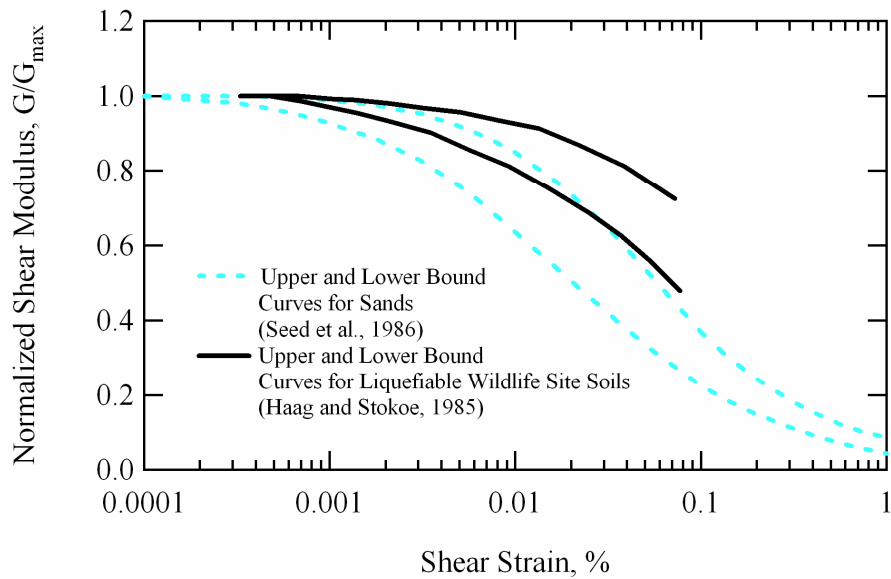


Figure 7-9 Comparison between the range in modulus reduction curves for liquefiable Wildlife Site soils and clean sands.

7.3.1.3 Laboratory Tests Performed at Renssalaer Polytechnic Institute

University of Texas personnel used fixed-piston sampling to recover approximately 27 tubes of soil from the Wildlife Site in January 1983. Of these 27 tubes, seven were transported to the University of Texas (UT), eight were transported to Woodward-Clyde (WC) Laboratory in New Jersey, and 12 were transported to Renssalaer Polytechnic Institute (RPI) in Troy, New York. The laboratory tests performed on these specimens by RPI and WC are addressed below.

All of the results from laboratory tests conducted at RPI are contained in Vucetic and Dobry (1986). Vucetic and Dobry (1986) also summarize the results from unpublished tests conducted by R.S. Ladd at WC. Similar to Haag and Stokoe (1985), Vucetic and Dobry (1986) and R.S. Ladd tested specimens obtained from two separate depth ranges in the Wildlife Site liquefiable soil layer. They also referred to the upper-level of the liquefiable layer as level A and the lower-level as level B. Both intact and reconstituted specimens were tested. All of the intact level A specimens came from the narrow depth range of 8.9 ft (2.7 m) to 9.3 ft (2.8 m). All of the intact level B specimens came from depths between 13.5 ft (4.1 m) and 14.8 ft (4.5 m).

Table 7-5 summarizes the numbers and types of laboratory tests performed on soils from the Wildlife liquefiable soil layer by Vucetic and Dobry (1986) at RPI and R.S. Ladd at WC. The strain-controlled cyclic triaxial (CyT) and cyclic direct simple shear (CyDSS) tests were performed with the explicit goal of developing Dobry's pore pressure model (refer to Section 2.3.3) for liquefiable

Table 7-5 Summary of the numbers and types of laboratory tests conducted on specimens from the Wildlife Site liquefiable soil layer at Renssalaer Polytechnic Institute (RPI) and Woodward-Clyde (WC) Laboratory (after Vucetic and Dobry, 1986)

| | | Numbers and Types of Laboratory Tests Run | | | |
|--|--|---|--|-----------------------------|-------------------------|
| | | Strain-Controlled | | Stress-Controlled | Monotonic |
| Wildlife Site Liquefiable Soil Layer | Depth Range of Intact Specimens (ft) | Cyclic Triaxial Tests | Cyclic Direct Simple Shear Tests | Cyclic Triaxial Tests | CU Triaxial Tests |
| Upper (A) | 8.9 - 9.3 | 6 | 4 | 1 (4)* | 2 |
| Lower (B) | 13.5 - 14.8 | 7 (1)* | 4 | 3 (2)* | 2 |

Notes: * Tests performed by R.S. Ladd at Woodward-Clyde Laboratory, New Jersey

Wildlife soils. The effect of testing procedure was evaluated by comparing the pore pressure models obtained from the CyT and CyDSS tests. Additionally, the CyT and CyDSS tests were conducted on intact and reconstituted specimens to examine the effect of soil fabric/sample disturbance on Dobry's model. The CU triaxial tests were performed at two separate constant rates of strain to compare the behavior of the soil under slow and fast monotonic loading. The stress-controlled CyT tests were performed to evaluate the consistency and usefulness of stress controlled tests in dynamic studies (Vucetic and Dobry, 1986).

As stated above, the strain-controlled cyclic triaxial (CyT) and cyclic direct simple shear (CyDSS) tests were performed with the explicit goal of developing Dobry's pore pressure model for liquefiable Wildlife soils. To accomplish this goal, CyDSS tests were performed at shear strains of 0.1% and 1.0%, while CyT tests were conducted in such a way as to achieve approximate shear strains of 0.03%, 0.1% and 0.3%. Vucetic and Dobry (1986) found that

when performed carefully, the pore pressure generation results from strain-controlled CyT and CyDSS tests were quite consistent at shear strains less than 0.3%. They also determined that, while the upper and lower portions of the Wildlife liquefiable soil layer are somewhat different in terms of fines content and density, their pore pressure generation characteristics under strain-controlled cyclic loading are very similar. This similarity allowed Vucetic and Dobry (1986) to fit the same pore pressure generation model to the test results from both the upper and lower liquefiable layer specimens. The equation for Dobry's pore pressure model determined for the Wildlife Site liquefiable soil layer is as follows:

$$r_u = \frac{1.04 \cdot n_c \cdot 2.6 \cdot (\gamma_{cy} - 0.02)^{1.7}}{1.0 + n_c \cdot 2.6 \cdot (\gamma_{cy} - 0.02)^{1.7}} \dots\dots\dots(7-1)$$

where r_u = the excess pore pressure ratio, which is equal to the change in pore water pressure (Δu) divided by the effective confining pressure (σ'); γ_{cy} = the applied cyclic shear strain expressed as a percentage; and n_c = the number of uniform loading cycles. This equation was developed from cyclic test results with up to 30 cycles of loading. The number 0.02 contained in parentheses represents the cyclic threshold shear strain (γ_t^c) for the Wildlife liquefiable soils (i.e. 0.02%). Vucetic and Dobry (1986) assumed this strain value based on previous experience, as the tests that they conducted on Wildlife soils were not carried out at strains less than 0.03%. Figure 7-10 shows the pore pressure generation curves predicted for the Wildlife liquefiable soils using Dobry's pore pressure model

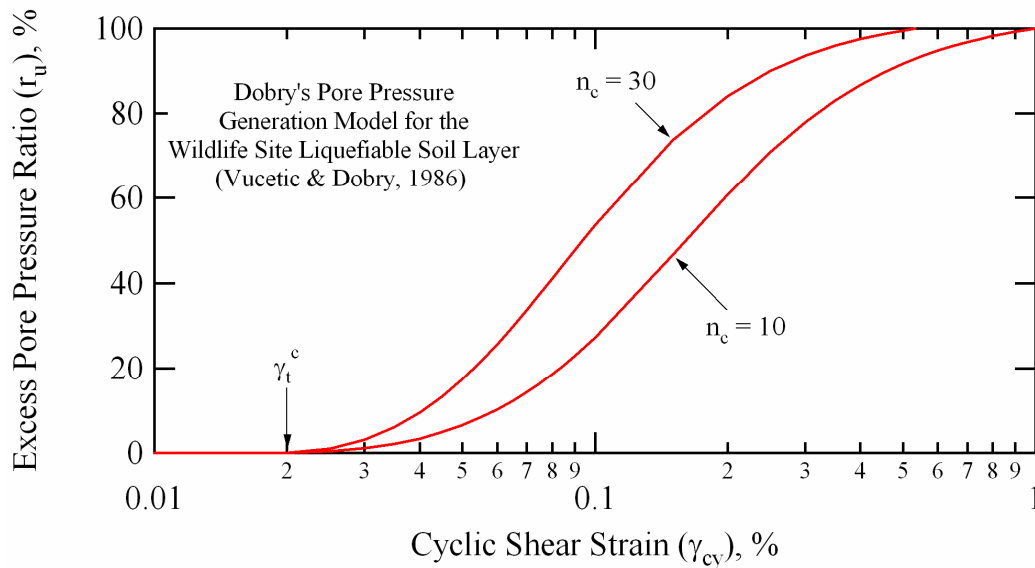


Figure 7-10 Dobry's pore pressure generation model (Vucetic and Dobry, 1986) for the Wildlife Site liquefiable soil layer.

(Equation 7-1) with 10 and 30 cycles of loading. By definition, no excess pore pressure is generated by cycling at strains below the cyclic threshold, while cycling at shear strains above the threshold value produces excess pore water pressures, with increasing numbers of loading cycles inducing higher pore pressure ratios for a given shear strain amplitude.

Even though Vucetic and Dobry (1986) found that the results from strain-controlled cyclic tests on intact and reconstituted Wildlife soil specimens yielded very similar pore pressure generation characteristics, they found that the stress-controlled CyT test results showed substantial scatter between intact and reconstituted specimens. This evidence further substantiates the superiority of strain-controlled dynamic laboratory testing over stress-controlled testing (refer to Section 2.3). Vucetic and Dobry (1986) reported that the monotonic CU triaxial

test performed on upper and lower liquefiable soil specimens yielded effective stress friction angles (ϕ') for both soils of approximately 37 degrees, and concluded that monotonic strain rate had little effect on the test results for these soils. They also reported that lower-layer specimens switched from contractive to dilative behavior at axial strains between 0.17 and 0.24%, while upper-layer specimens switched from contractive to dilative at axial strains between 0.29 to 0.36%. These upper-layer axial strain values, at which dilative behavior began, are considerably smaller than those (2.0 to 2.5 %) reported by Haag and Stokoe (1985).

Vucetic and Dobry (1986) performed a single grain size sieve analysis on separate “mixtures” of both the upper and lower liquefiable soil layers. They reported a FC of 37% for the upper-layer and 24% for the lower-layer. They did not report grain size analyses, Atterberg limit test results, or soil classifications for any of their individual test specimens. R.S. Ladd performed a single permeability test on the lower-layer soil and determined that the permeability ranged from 8.7×10^{-4} to 1.0×10^{-3} in./sec (2.2×10^{-3} to 2.6×10^{-3} cm/sec) for isotropic confining pressures varying between 3.5 and 13.9 psi (23.9 and 95.8 kPa).

7.4 THE 1987 ELMORE RANCH AND SUPERSTITION HILLS EARTHQUAKES

In 1987, two significant earthquakes shook the Imperial Valley and triggered instrumental responses at the Wildlife Liquefaction Array (WLA). The first event, the 23 November 1987 Elmore Ranch earthquake ($M_w=6.2$), triggered the instrumentation but no excess pore pressure was generated. The second event, the 24 November 1987 Superstition Hills earthquake ($M_w=6.6$), triggered the

instrumentation and generated excess pore water pressures in the liquefiable soil layer that rose to nearly 100% of the overburden pressure, creating a liquefied condition (Youd and Holzer, 1994). Soil liquefaction at the site was confirmed by the eruption of multiple sand boils and the opening of several ground fissures (Holzer et al., 1989). The WLA instrumentation records are the first from a field site that trace ground motions and pore pressure response through the entire liquefaction process. If correctly recorded, these records provide a landmark addition to the geotechnical engineering literature (Youd and Holzer, 1994).

The processed acceleration and excess pore pressure time histories recorded at the WLA during the 1987 Superstition Hills earthquake are shown in Figure 7-11. The locations of the instrumentation at the WLA are shown in Figure 7-2. Numerous researchers have examined and analyzed these records (Youd and Bartlett, 1988; Holzer et al., 1989; Dobry et al., 1989; Keane and Prevost, 1989; Hushmand et al., 1992; Youd and Holzer, 1994; Zeghal and Elgamal, 1994). It is beyond the scope of this research to discuss all of their conclusions. Suffice it to say that the recorded pore pressure generation behavior was different than expected. Specifically, pore pressures continued to rise in the liquefiable soil layer after the passage of the most significant acceleration pulses. Many researchers accepted this behavior and tried to figure out what caused it, while others argued that the pore pressure transducer data was flawed. Youd and Holzer (1994) provide a very good summary on much of this research.

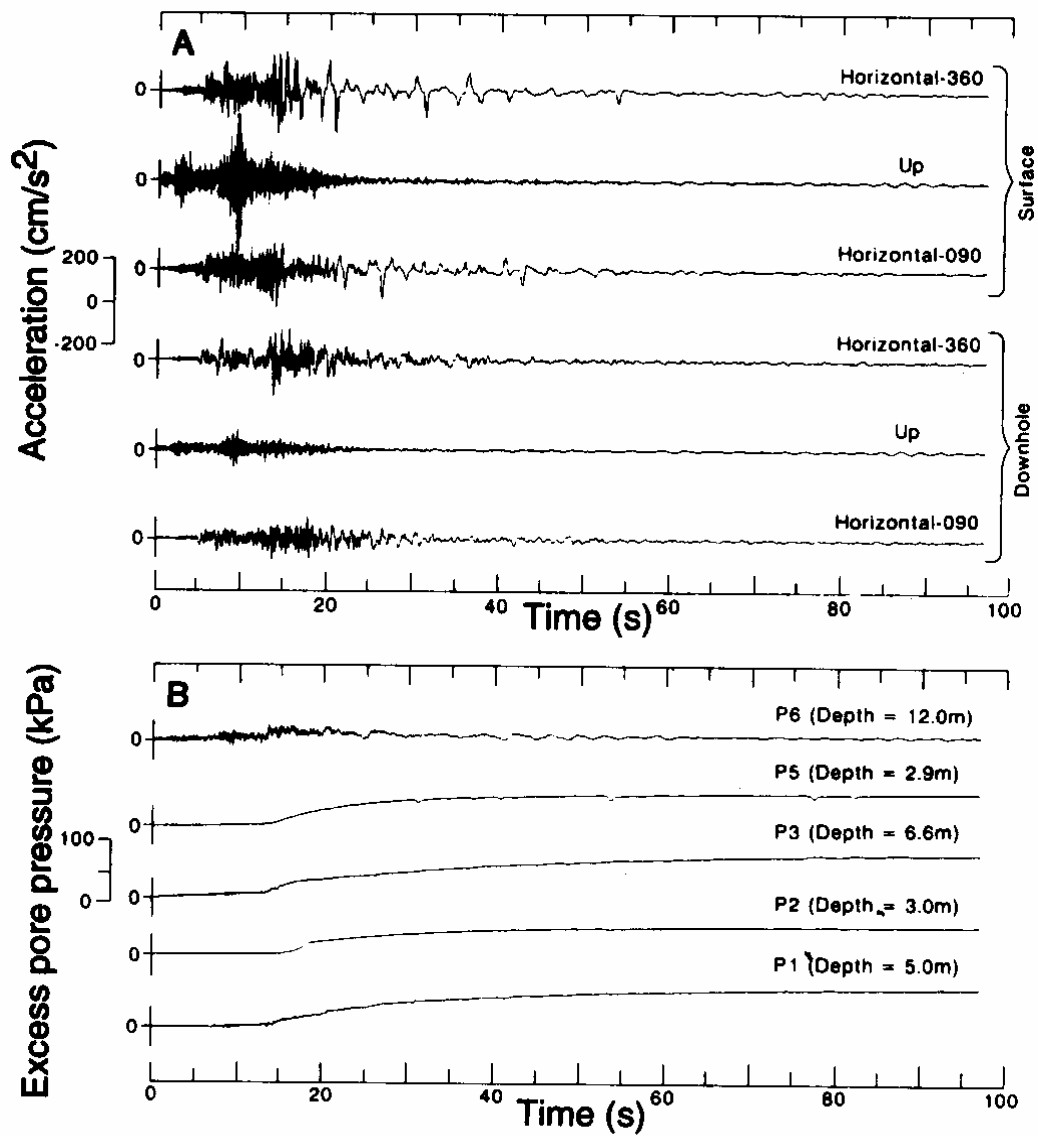


Figure 7-11 Acceleration (a) and pore pressure time histories (b) recorded at the Wildlife Liquefaction Array during the 1987 Superstition Hills earthquake ($M_w = 6.6$) (from Holzer et al., 1989).

Dobry et al (1989) and Keane and Prevost (1989) made attempts at trying to match the measured pore pressure response at the Wildlife Site using two different soil liquefaction modeling approaches. The soil parameters for their models primarily came from data collected during the intense site characterization efforts summarized in Section 7.3. While not totally accurate in their evaluations of the WLA records, these methods clearly show promise. The ability to make in-situ measurements to determine and verify model input parameters should enhance the acceptance and use of stress-strain modeling for liquefaction studies. The proposed in-situ dynamic liquefaction test will not only aid in evaluating model input parameters, but will also provide additional dynamic ground response and pore pressure generation data to refine and verify existing models. A more detailed description of the modeling efforts made by Dobry et al. (1989) and Keane and Prevost (1989) may be found in Section 2.3.3.

Zeghal and Elgamal (1994) conducted an extensive analysis of the instrumentation records obtained at WLA during both the 1987 Elmore Ranch (ER) and 1987 Superstition Hills (SH) earthquakes. In particular, they used the surface and downhole acceleration records to estimate shear strain (γ) and shear stress (τ) time histories induced in the soil by these earthquakes. Equivalent linear (secant) shear moduli were then evaluated as a function of strain amplitude from shear stress-strain loops of the ER and SH earthquakes. The nonlinear shear moduli calculated by Zeghal and Elgamal (1994) are shown in Figure 7-12. These back-calculated data points are compared with moduli that they estimated from resonant column test results obtained by Haag and Stokoe (1985). The peak

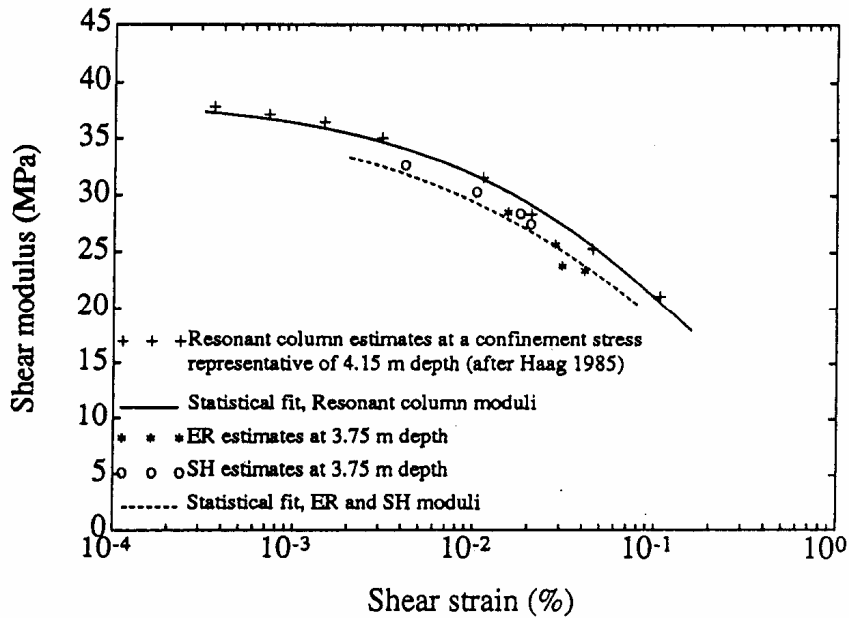


Figure 7-12 Wildlife Site shear moduli values estimated from the 1987 Elmore Ranch (ER) and Superstition Hills (SH) earthquakes using shear stress-strain loops obtained from surface and downhole accelerometer records (from Zeghal and Elgamal, 1994).

shear strain induced in the liquefiable soil by the ER event was calculated as 0.04%. Shear modulus estimates from the ER records were made at four shear strain levels between approximately 0.015% and 0.04%. Zeghal and Elgamal (1994) reported that the ER earthquake records showed strain-dependant response but no appreciable stiffness degradation. This conclusion fits with the observation that no substantial excess pore pressure was generated during the event. Zeghal and Elgamal (1994) were only able to track the nonlinear soil behavior at the Wildlife Site through approximately the first 14 seconds of the SH earthquake records. After this point, the stress-strain loops became very irregular due to substantial excess pore pressure generation and subsequent shear stiffness

softening. Shear modulus estimates from the SH records were made at four shear strain levels between approximately 0.004% and 0.02%.

Zeghal and Elgamal (1994) were not able to obtain shear modulus estimates at low enough shear strains to obtain the strain-independent shear modulus, G_{\max} . However, the in-situ shear wave velocity measurements reported by Bierschwale and Stokoe (1984) (refer to Figure 7-5) allow for an estimate of G_{\max} at the depth (12.3 ft or 3.75 m) where Zeghal and Elgamal (1994) determined their in-situ nonlinear soil shear moduli. The average in-situ shear wave velocity at this depth is approximately 380 fps (116 m/s), which equates to a G_{\max} value of approximately 538 ksf (25.8 MPa) (refer to Equation 6-12). This value is lower than most of the strain-dependant moduli shown in Figure 7-12. The reason for this anomaly is unknown, but may have something to do with the fact that the nonlinear moduli estimates made by Zeghal and Elgamal (1994) include changes that are occurring over the entire top 23 ft (7 m) of the soil profile (i.e. the distance between the surface and downhole accelerometers), rather than just within the liquefiable soil layer. An extrapolated value for G_{\max} can be made by extending the nonlinear trend observed by Zeghal and Elgamal (1994) back to very small shear strains. This extrapolation yields a G_{\max} value of approximately 731 ksf (35 MPa), which equates to a shear wave velocity of approximately 443 fps (135 m/s).

Figure 7-13 shows the modulus reduction curve obtained from normalizing the strain-dependant shear moduli estimated by Zeghal and Elgamal (1994) by an extrapolated value of G_{\max} equal to 731 ksf (35 MPa). For

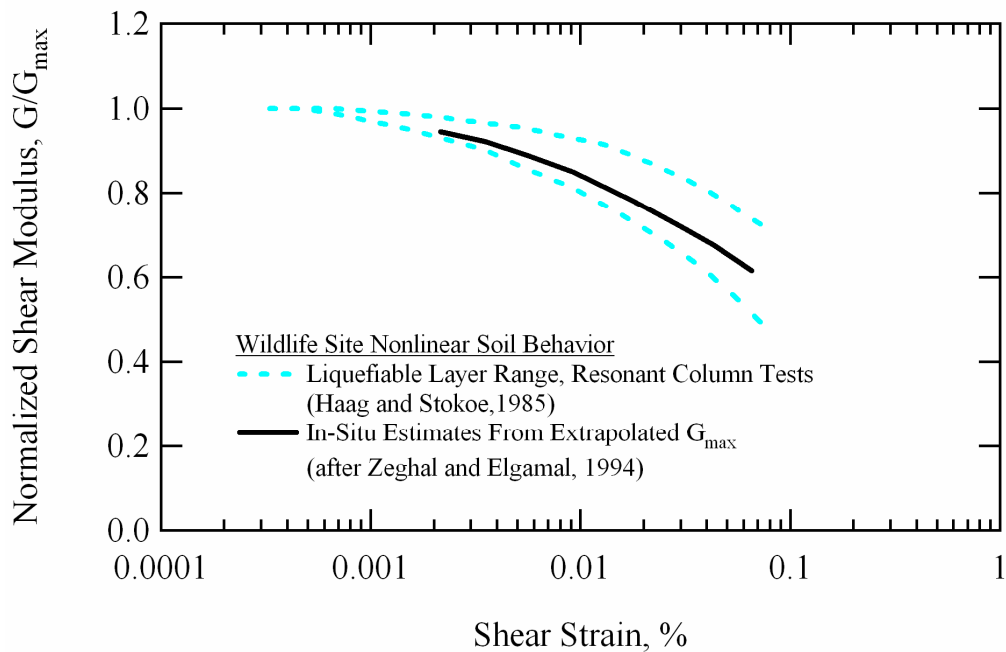


Figure 7-13 Comparison between the range in modulus reduction curves obtained from resonant column tests performed on liquefiable soils from the Wildlife Site with in-situ estimates obtained from the 1987 Elmore Ranch and Superstition Hills earthquakes.

comparison purposes, the range in modulus reduction curves for the Wildlife Site liquefiable soil layer determined by Haag and Stokoe (1985) is also shown. When normalized, the in-situ nonlinear shear moduli estimated by Zeghal and Elgamal (1994) fall within the range determined by Haag and Stokoe (1985) for the Wildlife Site liquefiable soil layer. Normalized nonlinear soil shear moduli determined from dynamic in-situ liquefaction tests at WLA are compared with these modulus reduction curves in Chapter 8 (see Section 8.5).

7.5 WLA RE-INSTRUMENTED AS A NEES SITE

The pore pressure transducers at WLA ceased functioning sometime after the 1987 records were obtained. Many researchers desired to see WLA re-instrumented because of its importance as a soil liquefaction study site. An opportunity to move and upgrade the site arose through funding provided by the Network for Earthquake Engineering Simulation (NEES). A new location to install instrumentation was chosen approximately 200 ft (60 m) north of the old site near a steep bank of the Alamo River. The location of the new WLA instrumentation site (2004 Site), relative to the old WLA instrumentation site (1982 Site), is shown in Figure 7-14. The new site is maintained and operated through NEES by the University of California at Santa Barbara. It has been instrumented with extensive arrays of downhole and surface accelerometers, pore pressure transducers, and ground-deformation measuring devices (Youd et al., 2004a). Detailed information regarding the instrumentation and extensive site characterization efforts at the new WLA site can be found at <http://nees.ucsb.edu>. It is beyond the scope of this research to discuss in detail the instrumentation installed at the new WLA site. However, some of the important information that was gathered during the process of site investigation and instrumentation installation, particularly in regards to the liquefiable soil layer, is presented below.

As part of the re-instrumentation program for the new NEES WLA site, 24 CPT soundings were performed to define sediment stratigraphy and better characterize the soil. The CPT sounding locations for both the new (24 total CPT soundings) and old (16 total CPT soundings, refer to Table 7-1 and Figure 7-3)

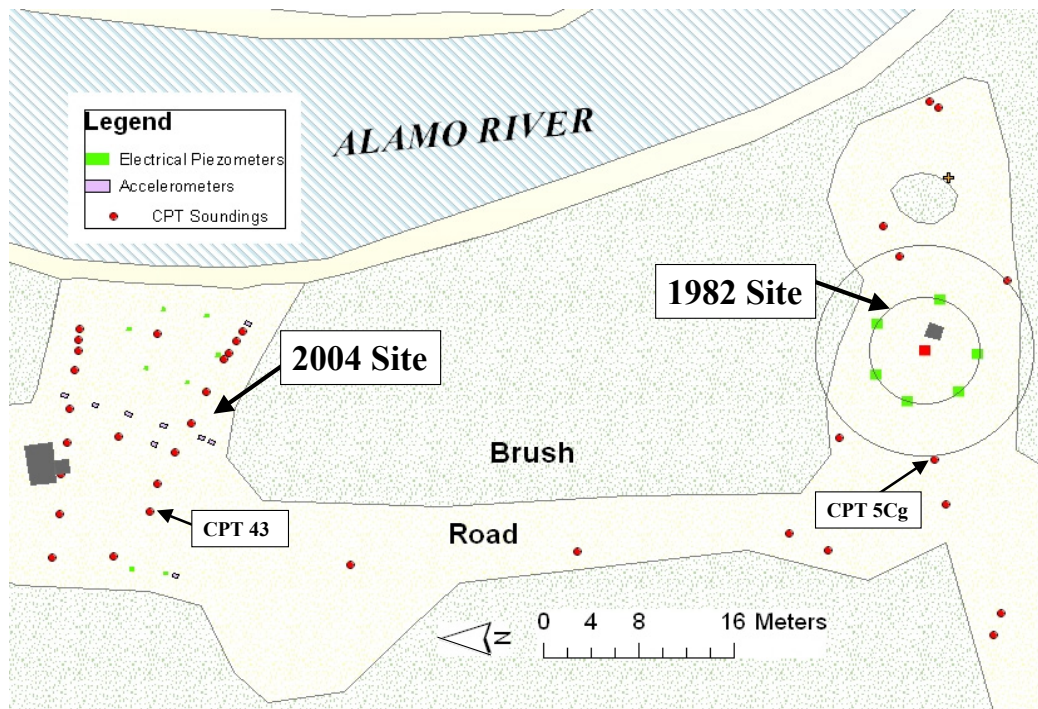


Figure 7-14 Relative locations of the 1982 (old) and 2004 (new) Wildlife Liquefaction Array (WLA) instrumentation sites (after <http://nees.ucsb.edu>).

are shown as solid circles in Figure 7-14. One CPT sounding from the old site (CPT 5Cg) and one CPT sounding from the new site (CPT 43) are highlighted in this figure. The tip resistance and friction ratio values for these two CPT soundings are plotted as a function of depth in Figure 7-15. Figure 7-15a shows the information for CPT 5Cg (old WLA site), while Figure 7-15b shows the information for CPT 43 (new WLA site). CPT 5Cg is one of the soundings that was used by Bennett et al. (1984) to define the generalized soil stratigraphy at the old WLA instrumentation site (refer to Figure 7-2). As detailed in Section 7.3.1, Bennett et al. (1984) determined that the liquefiable soil layer at the old site was

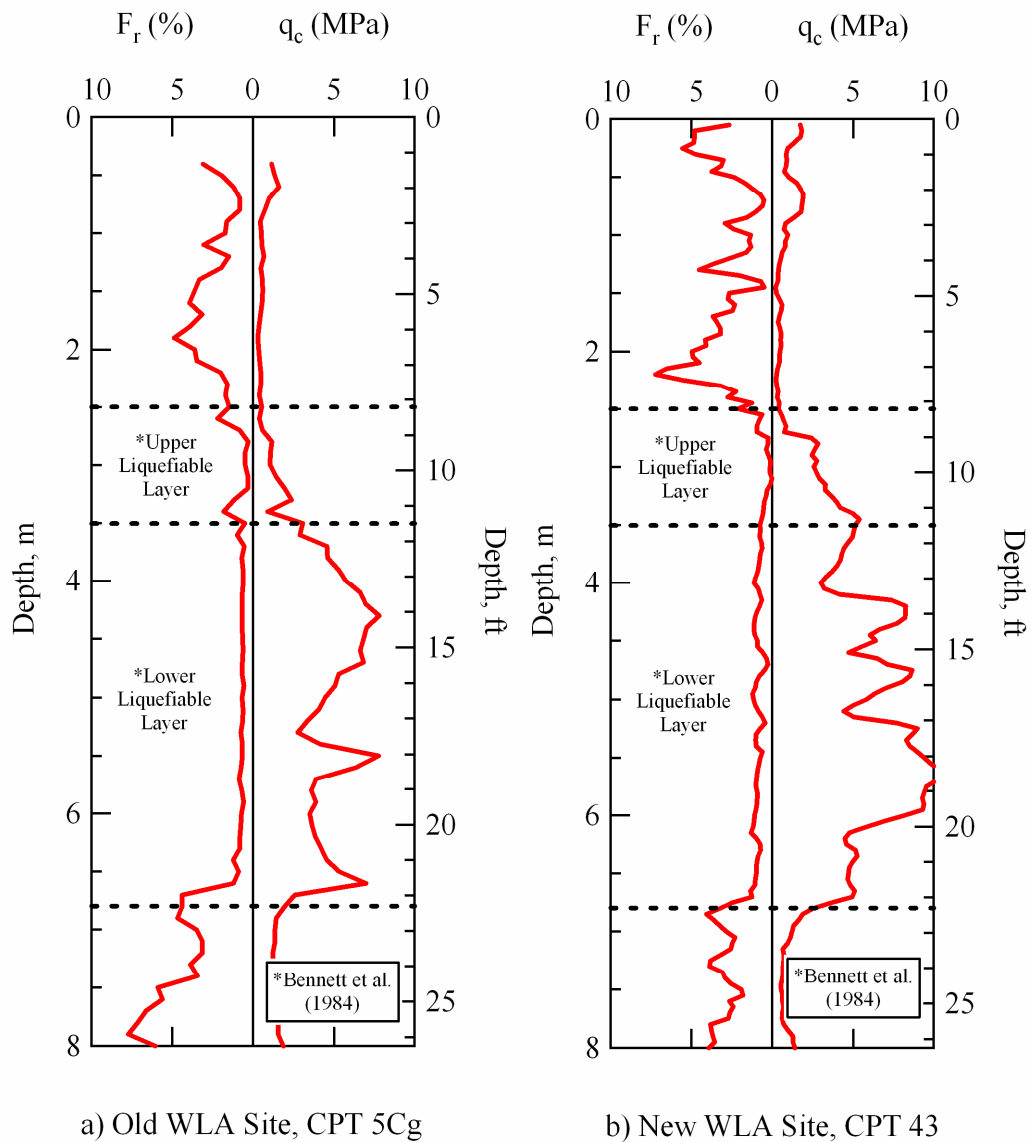


Figure 7-15 CPT soundings from the: a) old Wildlife Liquefaction Array (WLA) site, and b) new WLA site including the approximate locations of the upper and lower liquefiable soil layers proposed by Bennett et al. (1984) (raw CPT data from <http://nees.ucsb.edu>).

found roughly between the depths of 8.2 ft (2.5 m) and 22.3 ft (6.8 m). They further divided this 14.1-ft (4.3-m) thick liquefiable soil layer into an upper unit and a lower unit. The 3.3-ft (1.0-m) thick upper-unit extended from a depth of approximately 8.2 ft (2.5 m) down to a depth of about 11.5 ft (3.5 m), while the 10.8-ft (3.3-m) thick lower-unit extended from a depth of approximately 11.5 ft (3.5 m) down to a depth of about 22.3 ft (6.8 m). The boundaries of the upper and lower liquefiable soil layers are shown in Figure 7-15. In general, the liquefiable soil layer is marked by relatively large values of CPT tip resistance (q_c) and relatively small values of CPT friction ratio (F_r) in comparison with the soil layer above it. Figure 7-15 shows that the liquefiable soil layer determined by Bennett et al (1984) at the old WLA instrumentation site is a very good approximation for the liquefiable soil layer at the new WLA instrumentation site. Additionally, Proctor (2004) performed liquefaction analyses using the data collected from all 24 CPT soundings at the new site and found that in general, the soil at depths between 8.2 ft (2.5 m) and 23.0 ft (7.0 m) is predicted as susceptible to liquefaction.

An expanded view of the 2004 WLA instrumentation site is shown in Figure 7-16. This figure details the locations of instrumentation installed, and in-situ soil characterization tests performed, at the new site. In addition to the CPT soundings already discussed, SPT tests were also performed in many of the boreholes that were drilled to install instrumentation. SPT tests were primarily conducted in the liquefiable layer. Atterberg limit tests and grain size analyses were performed on the disturbed split-spoon soil samples that were retrieved

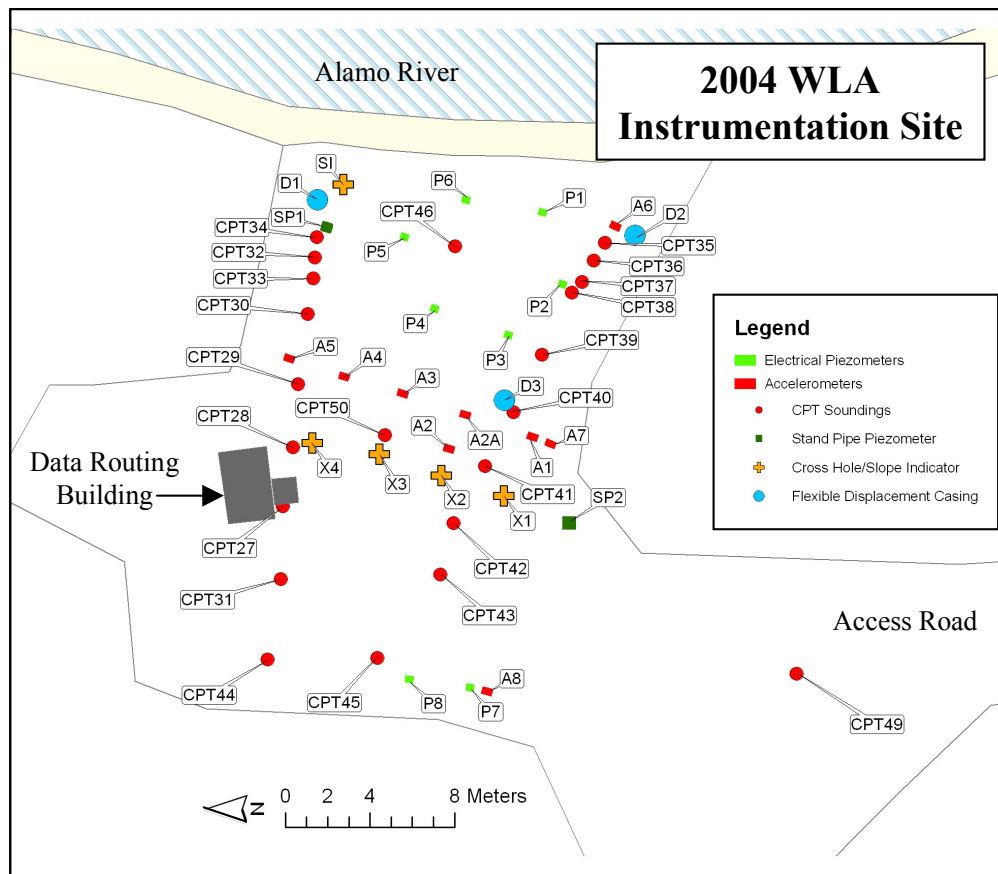


Figure 7-16 Locations of the in-situ soil characterization tests performed, and instrumentation installed, at the 2004 (new) Wildlife Liquefaction Array (WLA) instrumentation site (after <http://nees.ucsb.edu>).

during SPT testing (Bartholomew, 2004). Table 7-6 summarizes the grain size characteristics, Unified Soil Classification System (USCS) designations, and raw blow counts obtain from the SPT tests performed within the depth range of the upper liquefiable soil layer (i.e. approximately 8.2 ft to 11.5 ft, or 2.5 m to 3.5 m) at the new WLA site. The data is sorted by depth, and the locations of the boreholes where the information was obtained from can be found in Figure 7-16. All of these soil samples were reported as non-plastic by Bartholomew (2004),

Table 7-6 Summary of the soil properties determined from SPT split-spoon samples obtained from the upper liquefiable layer at the 2004 (new) Wildlife Liquefaction Array (WLA) (data from <http://nees.ucsb.edu>)

| Borehole | Depth (ft) | Fines Content (% < 75 μm) | Clay Content (% < 5 μm) | Soil Type (USCS) | Raw SPT Blow Count (N) |
|---------------------------------------|-----------------------|---|---|---------------------------------|---------------------------------------|
| P3 | 8.0 - 9.5 | 87 | 24 | ML | 9 |
| SI1 | 8.0 - 9.5 | 49 | 8 | SM | 10 |
| P1 | 8.75 - 9.5 | 35 | 19 | SM | 7 |
| D2 | 9.0 - 10.5 | 40 | 15 | SM | 20 |
| X2 | 9.0 - 9.9 | 57 | 7 | ML | 18 |
| P2 | 9.3 - 9.5 | 70 | 13 | ML | 11 |
| P7 | 9.5 - 11.0 | 61 | 18 | ML | 5 |
| X2 | 9.9 - 10.5 | 38 | 2 | SM | - |
| P3 | 10.0 - 11.5 | 35 | 13 | SM | 19 |
| P5 | 10.0 - 11.5 | 45 | 16 | SM | 18 |
| P6 | 10.0 - 11.5 | 39 | 18 | SM | 23 |
| X1 | 10.0 - 11.5 | 40 | 10 | SM | 5 |
| P2 | 11.0 - 12.5 | 24 | 8 | SM | 17 |
| SI1 | 11.0 - 12.5 | 37 | 7 | SM | 10 |
| Upper Layer Avg. (Std. Dev.) = | | 47 (17) | 13 (6) | - | 13 (6) |

and generally classify as sandy silt to silty-sand (ML to SM). The average fines content of the samples taken from the upper liquefiable layer is 47% with a standard deviation of 17%, while the average clay content (5 μm) is 13% with a standard deviation of 6%. This average FC and standard deviation are practically identical to the average upper-unit FC (45%) and standard deviation (21%) of the

samples obtained by Bennett et al. (1984) at the 1982 WLA site. Table 7-7 summarizes the grain size characteristics, Unified Soil Classification System (USCS) designations, and raw blow counts obtain from the SPT tests performed within the depth range of the lower liquefiable soil layer (i.e. approximately 11.5 ft to 22.3 ft, or 3.5 m to 6.8 m) at the new WLA site. The data is sorted by depth. All of these soil samples were reported as non-plastic by Bartholomew (2004), and generally classify as silty-sand (SM). The average fines content of the samples taken from the lower liquefiable layer is 27% with a standard deviation of 10%, while the average clay content ($5 \mu\text{m}$) is 11% with a standard deviation of 7%. This average FC and standard deviation are identical to the average lower-unit FC (27%) and standard deviation (10%) of the samples obtained by Bennett et al. (1984) at the 1982 WLA site.

The information summarized above is just a small portion of the data that were collected by researchers during re-instrumentation of the Wildlife Site. Other information includes consolidation, shear strength, and clay mineral data for the cohesive materials above and below the liquefiable soil layer, in-situ permeability data for the liquefiable soil layer, SPT borehole logs, photographs of SPT split-spoon samples, and CPT sounding logs (Youd et al., 2004b). All of this data can be found at <http://nees.ucsb.edu>.

7.6 GENERALIZED WLA LIQUEFIABLE SOIL LAYER PROPERTIES

Sections 7.3 through 7.5 summarize a wealth of information about the Wildlife Site that has been gathered by various researchers over the past 25 years. Some of this information has been gathered in regards to the 1982 (old) WLA

Table 7-7 Summary of the soil properties determined from SPT split-spoon samples obtained from the lower liquefiable layer at the 2004 (new) Wildlife Liquefaction Array (WLA) (data from <http://nees.ucsb.edu>)

| Borehole | Depth (ft) | Fines Content (% < 75 μm) | Clay Content (% < 5 μm) | Soil Type (USCS) | Raw SPT Blow Counts |
|---------------------------------------|-----------------------|---|---|---------------------------------|------------------------------------|
| D2 | 12.0 - 13.5 | 40 | 18 | SM | 12 |
| X2 | 12.0 - 13.5 | 24 | 6 | SM | 15 |
| P5 | 13.0 - 14.5 | 31 | 17 | SM | 13 |
| P6 | 13.0 - 14.5 | 35 | 18 | SM | 16 |
| P8 | 13.0 - 14.5 | 48 | 21 | SM | 10 |
| X1 | 13.0 - 14.5 | 15 | 2 | SM | 20 |
| P2 | 14.0 - 15.5 | 38 | 12 | SM | 14 |
| S11 | 14.0 - 15.5 | 39 | 9 | SM | 22 |
| D2 | 15.0 - 16.5 | 35 | 16 | SM | 19 |
| X2 | 15.0 - 16.5 | 20 | 3 | SM | 18 |
| P5 | 16.0 - 17.5 | 35 | 18 | SM | 19 |
| P2 | 17.0 - 18.5 | 34 | 16 | SM | 11 |
| S11 | 17.0 - 18.5 | 27 | 9 | SM | 24 |
| X1 | 17.0 - 18.5 | 25 | 4 | SM | 15 |
| D2 | 18.0 - 19.5 | 26 | 18 | SM | 19 |
| X2 | 18.0 - 19.5 | 11 | 4 | SP-SM | 21 |
| P5 | 19.0 - 20.5 | 25 | 17 | SM | 22 |
| P2 | 20.0 - 21.5 | 16 | 9 | SM | 26 |
| S11 | 20.0 - 21.5 | 25 | 9 | SM | 20 |
| X1 | 20.0 - 21.5 | 15 | 2 | SM | 26 |
| X2 | 21.0 - 22.5 | 10 | 2 | SP-SM | - |
| Lower Layer Avg. (Std. Dev.) = | | 27 (10) | 11 (7) | - | 18 (5) |

instrumentation site, while other information has been collected for the 2004 (new) NEES WLA instrumentation site. In general, this research has shown that the liquefiable layer at the site is found between the depths of 8.2 ft (2.5 m) and 22.3 ft (6.8 m). The soil in this layer generally classifies as sandy silt to silty-sand (ML to SM) and is considered non-plastic. The soil nearer to the bottom of the layer is typically denser and coarser grained, while the soil nearer to the top of the layer is looser and finer grained. Various researchers have divided the liquefiable soil layer into an upper and lower layer. The upper-unit (layer) has been defined as the top 3.3 ft (1 m) of the liquefiable layer, while the lower-unit (layer) has been defined as the bottom 10.8 ft (3.3 m).

Table 7-8 details grain size data that has been collected from multiple researchers and grouped according to depth as upper liquefiable layer specimens. The number of samples tested by the researchers, as well as the average and standard deviation values for the fines (75 μm) contents and clay-size particle (5 μm) contents that they obtained, are provided. There is no noticeable difference between the values obtained from the old site and the values obtained from the new site. The total number of upper layer samples tested by various researchers is 25. The average FC for the soil samples tested by all researchers is 49% with a standard deviation of 18%. The average clay-size particle content for the soil samples tested by all researchers is 11% with a standard deviation of 6%.

Table 7-9 details the grain size data that has been collected from multiple researchers and grouped according to depth as lower liquefiable layer specimens. The number of samples tested by the researchers, as well as the average and

Table 7-8 Summary of the grain size characteristics obtained by various researchers for soil samples obtained from the upper liquefiable layer at the 1982 (old) and 2004 (new) WLA instrumentation sites

| Research | Number of Samples Tested | Upper Layer (8.2 - 11.5 ft) | | | |
|--|--------------------------|---------------------------------------|-----------|--|-----------|
| | | Fines Content (% < 75 μm) | | Clay-Size Content (% < 5 μm) | |
| | | Average | Std. Dev. | Average | Std. Dev. |
| Bennett et al. (1984) ¹ | 6 | 45 | 21 | 5 | 4 |
| Haag & Stokoe (1985) ¹ | 4 | 64 | 16 | 16 | 3 |
| Vucetic & Dobry (1986) ¹ | 1 | 37 | - | - | - |
| Bartholomew (2004) ² http://nees.ucsb.edu | 14 | 47 | 17 | 13 | 6 |
| All Researchers Combined ³ | 25 | 49 | 18 | 11 | 6 |

- Notes: 1. Soil samples obtained from the 1982 (old) WLA instrumentation site
2. Soil samples obtained from the 2004 (new) WLA instrumentation site
3. Individual samples from each researcher averaged

standard deviation values for the fines (75 μm) contents and clay-size particle (5 μm) contents that they obtained, are provided. There is no noticeable difference between the values obtained from the old site and the values obtained from the new site. The total number of upper layer samples tested by various researchers is 36. The average FC for the soil samples tested by all researchers is 279% with a standard deviation of 10%. The average clay-size particle content for the soil samples tested by all researchers is 9% with a standard deviation of 7%.

Table 7-9 Summary of the grain size characteristics obtained by various researchers for soil samples obtained from the lower liquefiable layer at the 1982 (old) and 2004 (new) WLA instrumentation sites

| Research | Number of Samples Tested | Lower Layer (11.5 - 22.3 ft) | | | |
|--|--------------------------|---------------------------------------|-----------|--|-----------|
| | | Fines Content (% < 75 μm) | | Clay-Size Content (% < 5 μm) | |
| | | Average | Std. Dev. | Average | Std. Dev. |
| Bennett et al. (1984) ¹ | 9 | 27 | 10 | 3 | 2 |
| Haag & Stokoe (1985) ¹ | 5 | 26 | 10 | 10 | 6 |
| Vucetic & Dobry (1986) ¹ | 1 | 24 | - | - | - |
| Bartholomew (2004) ² http://nees.ucsb.edu | 21 | 27 | 10 | 11 | 7 |
| All Researchers Combined ³ | 36 | 27 | 10 | 9 | 7 |

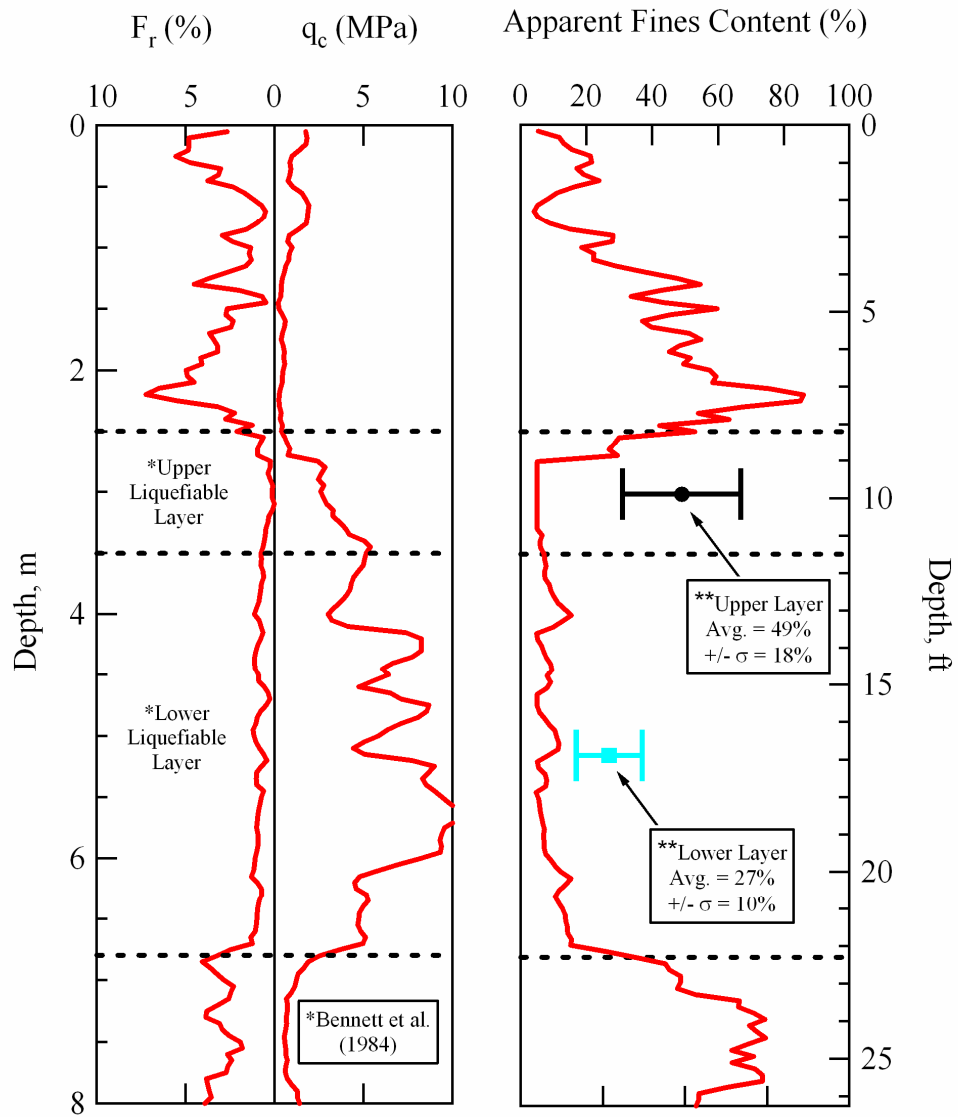
Notes: 1. Soil samples obtained from the 1982 (old) WLA instrumentation site
 2. Soil samples obtained from the 2004 (new) WLA instrumentation site
 3. Individual samples from each researcher averaged

It is also possible to obtain estimates of the fines content in the liquefiable soil layer using the wealth of CPT data collected at the Wildlife Site. Estimates of fines content obtained from CPT data are typically referred to as apparent fines contents (Youd et al. 2001). Proctor (2004) made apparent fines content calculations for all of the CPT soundings conducted at the old and new WLA instrumentation sites as part of a liquefaction susceptibility study for the site (<http://nees.ucsb.edu>). The tip resistance (q_c), friction ratio (F_r), and apparent fines content values obtained from CPT 43 (previously detailed in Figures 7-14 and 7-15) are shown in Figure 7-17. The boundaries of the upper and lower

liquefiable soil layers proposed by Bennett et al. (1984) are also shown. Apparent fines content values of 49% and 27% for the upper and lower layers, respectively, are demarcated in the figure. The plus and minus one standard deviation values for the fines contents in each layer are also shown (18% and 10% for the upper and lower layers, respectively) (see Tables 7-8 and 7-9). It is obvious that the CPT apparent fines calculation grossly under-predicts the fines contents in the liquefiable soil layer. In general, the apparent fines content estimates from the CPT soundings at the site yield fines contents in the liquefiable layer between 10 and 15%. Clearly these estimates are unreliable and should not be used.

The distinction between the upper and lower liquefiable soil layers is really quite vague. In general, it seems that the fines content of the liquefiable layer as a whole tends to gradually increase from bottom to top. The stiffness of the liquefiable layer follows a similar trend, in that it is generally least stiff at the top of the layer and gradually increases in stiffness with depth. This trend is reflected in the shear wave velocity profiles shown in Figure 7-5 and the cone tip resistance profiles provided in Figure 7-15.

As far as their dynamic response is concerned, it appears that the upper and lower portions of the liquefiable soil layer behave quite similarly. Vucetic and Dobry (1986) found that the pore pressure generation characteristics of the



**Note: Average and standard deviation fines content values obtained from 25 samples of upper liquefiable layer soil and 36 samples of lower liquefiable layer soil

Figure 7-17 Tip resistance (q_c), friction ratio, and apparent fines content values obtained from CPT 43 (<http://nees.ucsb.edu>) at the Wildlife Site.

upper and lower portions of the liquefiable soil layer could be fit with a single model (refer to Equation 7-1). The resonant column tests performed by Haag and Stokoe (1984) show that range of nonlinear soil behavior of the upper portion of the liquefiable soil layer brackets the range of nonlinear soil behavior determined for the lower layer (refer to Figure 7-8). Therefore, the upper layer range may be considered as typical for the entire layer. The in-situ nonlinear soil shear modulus estimates made by Zeghal and Elgamal (1994) also fall within this range (refer to Figure 7-13).

Another important piece of information related to the general Wildlife Site characterization is the existence of two deep shear wave velocity (V_s) profiles for the site. The first one was obtained using a suspension logger (P-S logger) in the deep downhole array borehole that was drilled at the new WLA site (<http://nees.ucsb.edu>). The second one was obtained from Spectral-Analysis-of-Surface-Waves (SASW) testing performed by the writer as part of the overall in-situ liquefaction testing project. The SASW testing was performed along the access road between the old and new WLA sites (refer to Figure 7-14) using T-Rex as an active surface wave source. Both of these V_s profiles are shown in Figure 7-18. In general, both profiles agree very well at depths greater than 25 ft (7.6 m). The V_s values obtained from the P-S logger tend to jump around a lot at shallower depths. This behavior is somewhat typical, as the P-S logger can have difficulty measuring accurate velocities near the ground surface (Stokoe et al., 2003).

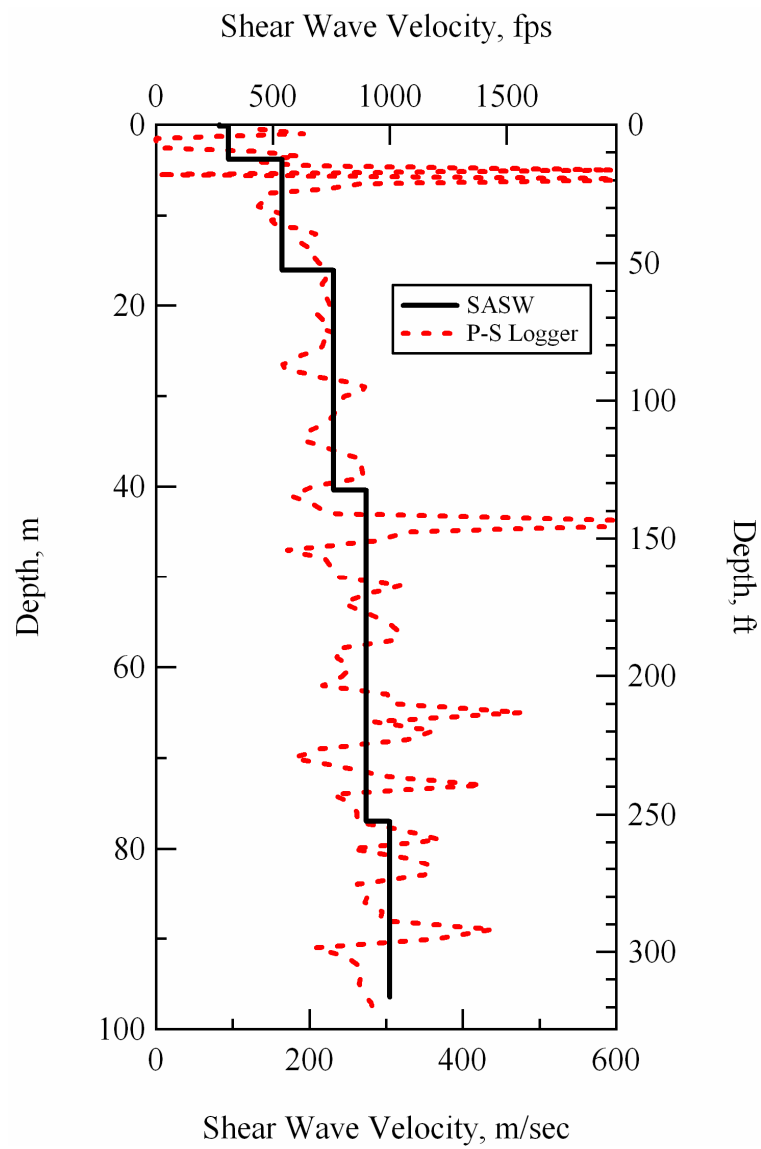


Figure 7-18 Deep shear wave velocity profiles obtained from SASW testing and P-S logger measurements (<http://nees.ucsb.edu>) at the Wildlife Site.

7.7 IN-SITU LIQUEFACTION TESTS AT THE WILDLIFE SITE

The extensive site characterization, its documented occurrence of complete soil liquefaction twice in the past 25 years, and its likelihood for re-liquefaction during subsequent earthquakes make the Wildlife Site an ideal location for verifying the proposed in-situ dynamic liquefaction test method. In-situ liquefaction tests were conducted at the Wildlife Site between August 8 and August 19, 2005. Three separate tests were conducted at the site. The approximate test locations (denoted as locations A, B and C) are shown in Figure 7-19. Test A was conducted at the 2004 site, while Test B was conducted at the 1982 site. Test C was conducted on the access road between the old and new sites. The in-situ liquefaction test results obtained from each of these locations are discussed in Chapters 8, 9 and 10 for Test Locations C, B and A, respectively.

7.8 SUMMARY

The Imperial Valley, California is an area of high seismicity. Widespread soil liquefaction has been documented in the valley following significant earthquakes in the recent past. A site named the Wildlife Liquefaction Array (WLA) has shown surface manifestations of full liquefaction during at least two of these earthquakes (1981, $M_w = 5.9$ Westmorland earthquake; and 1987, $M_w = 6.6$ Superstition Hills earthquake). The WLA site has been intensely studied over the past 25 years (Bennett et al., 1984; Bierschwale and Stokoe, 1984; Hagg and Stokoe, 1985; Vucetic and Dobry, 1986; Youd and Bartlett, 1988; Holzer et al., 1989; Dobry et al., 1992; Youd and Holzer, 1994; Zeghal and Elgamal, 1994). It has also recently been designated as a Network for Earthquake Engineering

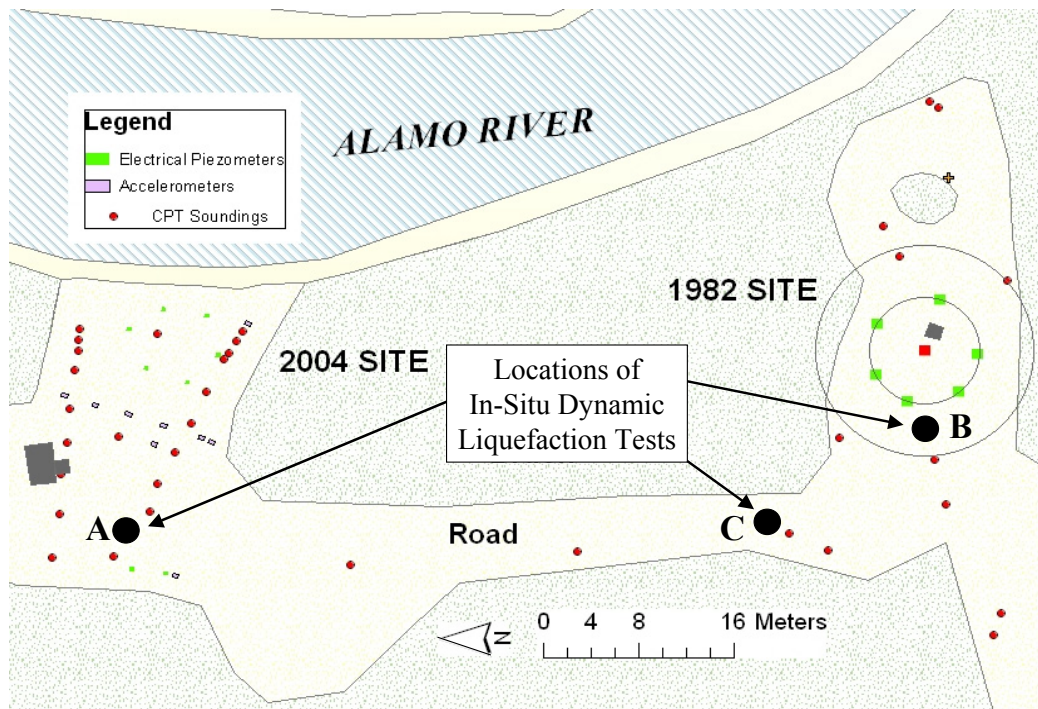


Figure 7-19 Approximate locations of the three in-situ dynamic liquefaction tests that were carried out at the Wildlife Liquefaction Array (WLA) (after <http://nees.ucsb.edu>).

Simulation (NEES) site for the study of soil liquefaction (<http://nees.ucsb.edu>). The extensive site characterization, its documented occurrence of earthquake-induced soil liquefaction twice in the 1980's, and its likelihood for re-liquefaction during subsequent earthquakes make the WLA an ideal location for verifying the proposed in-situ dynamic liquefaction test method. Three separate in-situ liquefaction tests were conducted at this site. The individual test results are discussed in Chapters 8, 9, and 10.

Chapter 8

In-Situ Liquefaction Test Results: Test Location C, WLA

8.1 INTRODUCTION

Three separate in-situ dynamic liquefaction tests were conducted at the Wildlife Liquefaction Array (WLA) between August 8 and August 19, 2005. The general locations of these tests are shown in Figure 7-19. In this chapter, the pore pressure generation curves and nonlinear soil shear modulus behavior measured in the liquefiable soil layer at Test Location C are presented and discussed. Test Location C was sequentially the third location where tests were performed at the WLA. However, the results obtained at Test Location C are discussed first because the most complete set of data was obtained at this location. The results obtained at Test Locations B and A are presented in Chapters 9 and 10, respectively.

8.2 TEST C: ARRAY LOCATION AND PRE-DYNAMIC LOADING INFORMATION

The in-situ liquefaction sensor array at Test Location C was installed on August 16, 2005. The approximate location of the array is shown in Figure 8-1. The sensor array was installed under the dirt access road between the 1982 (old) WLA Site and the 2004 (new) WLA Site. Its center point was positioned at radial distances of approximately 4.6 ft (1.4 m) and 29.6 ft (9.0 m) from CPT 47 and CPT 6Cg, respectively. These CPT locations are marked in the field, and were also surveyed by Proctor (2004) relative to several benchmarks at the site. The

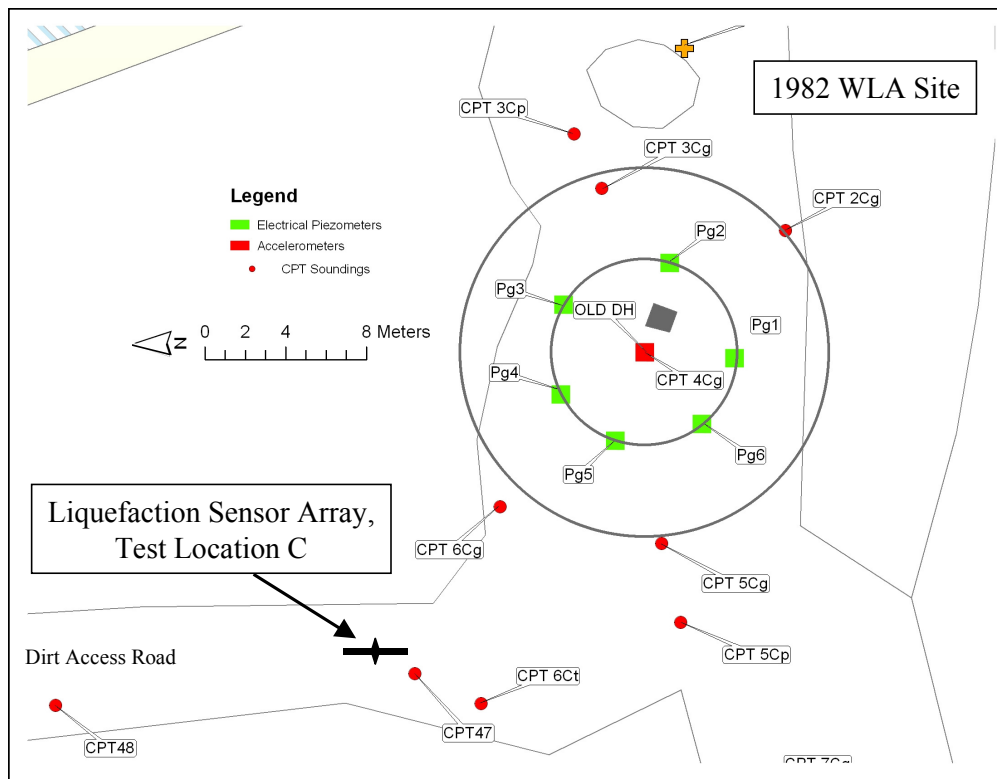


Figure 8-1 Approximate location of the in-situ liquefaction sensor array installed at Test Location C, Wildlife Liquefaction Array (WLA) (after <http://nees.ucsb.edu>).

results from this survey can be found at <http://nees.ucsb.edu>. This information should be sufficient to relocate the position of the array if necessary.

The linear array at Test Location C extended along the access road in the north-south direction. The sensors were installed according to the procedure detailed in Section 5.2. A picture of an installed liquefaction sensor array, as viewed from the ground surface, is shown in Figure 8-2. As discussed in Section 5.2, the numbers next to each liquefaction sensor do not represent the order in which they were installed, but rather the positions of the sensors in the embedded

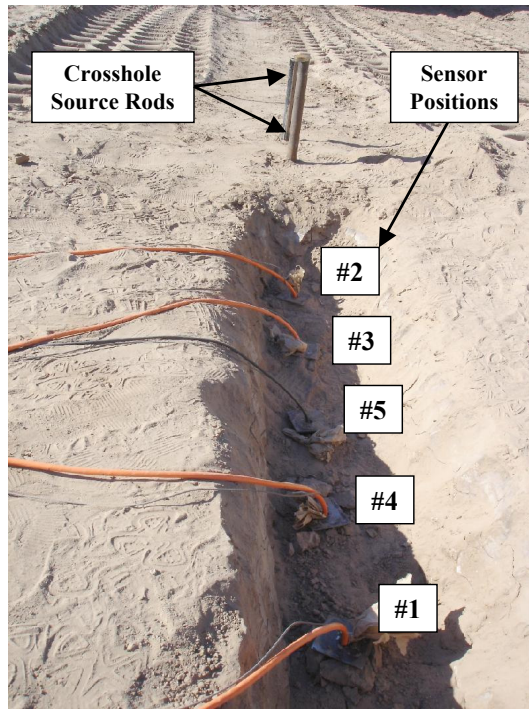


Figure 8-2 Picture of an installed liquefaction sensor array as seen from the ground surface.

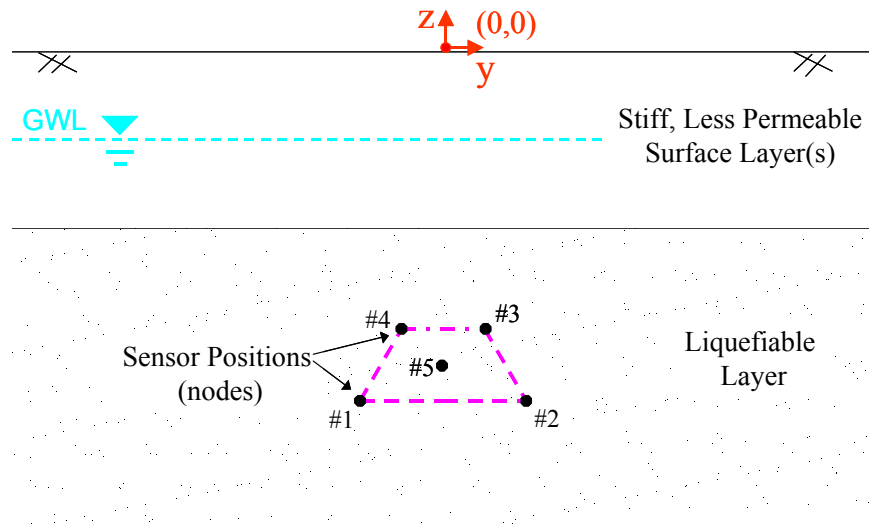


Figure 8-3 Cross-sectional schematic of an embedded liquefaction sensor array.

trapezoidal array. A cross-sectional schematic of the sensor array, as viewed from below the ground surface, is shown in Figure 8-3. The sensor positions may be considered as nodes of a single quadrilateral finite element. The specific sensors that were installed in each of the nodal positions at Test Location C are listed in Table 8-1. Sensor positions No. 1 through No. 4 were occupied by liquefaction sensors containing a 3D-MEMS accelerometer and a miniature pore water pressure transducer (PPT), while sensor position No. 5 was occupied by the Druck PDCR 35/D pressure transducer. The individual calibration factors for the sensors occupying each nodal position are provided in Section 4.2.

Table 8-1 also details the relative positions of each sensor in the form of y- and z-coordinates. These coordinates are referenced from a point on the ground surface directly above sensor position No. 5 (refer to Figure 8-3). The y-coordinate represents the horizontal, in-line distance from the center of the array, while the z-coordinate represents the vertical distance below the ground surface (depth). There is no need to provide an x-coordinate for the sensor locations because they were all installed within the same in-line plane (i.e. $x = 0$). As can be seen, the liquefaction sensors occupying positions No. 1 and No. 2 were installed roughly 2.0-ft (0.6-m) on either side of the array centerline at a depth just less than 13.0-ft (4.0-m) below the ground surface, while the liquefaction sensors occupying positions No. 3 and No. 4 were installed roughly 1.0-ft (0.3-m) on either side of the array centerline at a depth just less than 11.0-ft (3.4-m) below the ground surface. The PDCR 35/D sensor was placed at the center of the array (position No. 5) at a depth just less than 12.0-ft (3.7-m) below the ground surface.

Table 8-1 Coordinates and tilt angles for the sensors installed in the liquefaction sensor array at Test Location C, Wildlife Liquefaction Array (WLA)

| Sensor Position (Node #) | Sensor Designation | y-coordinate (ft) | z-coordinate (ft) | Tilt Angle (degrees) | |
|-----------------------------|-----------------------|----------------------|----------------------|----------------------|--------|
| | | | | x-axis | y-axis |
| #1 | Liquefaction Sensor 1 | -2.02 | -12.86 | 0.3 | -0.3 |
| #2 | Liquefaction Sensor 5 | 1.96 | -12.80 | -0.8 | 0.1 |
| #3 | Liquefaction Sensor 6 | 1.00 | -10.84 | 0.6 | 0.8 |
| #4 | Liquefaction Sensor 9 | -1.02 | -10.90 | 0.2 | -1.3 |
| #5 | Druck PDCR 35/D PPT | 0.00 | -11.91 | NA | NA |

The sensor coordinates presented in Table 8-1 are based on measurements made from the ground surface. The accuracy of these measurements is contingent on the ability to install the sensors from the ground surface with minimal deviation (tilt). The tilt of the liquefaction sensors can be monitored via the 3D-MEMS accelerometer installed in each of them (see Section 4.2.1). Tilt about both the x- and y-axes can be sensed. The tilt angles obtained from the MEMS accelerometer in each liquefaction sensor are provided in Table 8-1. These angles were obtained from measurements taken after the sensors had reached their final locations. The tilt angles about the x- and y-axes are generally less than one degree off vertical, indicating that the sensors were installed with minimal deviation. If a tilt angle of one degree is projected 13-ft (4.0-m) below the ground surface (the approximate depth of the bottom pair of sensors) the horizontal deviation is less than 3 in. (7.6 cm). This is a worst-case scenario. It is likely that the sensors incrementally tilted as they were pushed deeper into the ground. However, incremental tilt readings could not be taken for the reasons discussed in

Section 4.2.1.1. Therefore, the angles listed in Table 8-1 only represent the final resting position of the sensors. The path resulting in those angles is unknown. Decoupling the sensors from the push rods may have even induced a small amount of tilt, which would not have influenced the deviations of the sensors as they were pushed into place. Crosshole P-wave velocity measurements (see Section 8.2.1) of approximately 5000 fps (1500 m/s) also indicate that the assumed spacing between receivers is correct. The PDCR 35/D sensor does not contain a MEMS accelerometer and hence does not have the ability of monitoring tilt. However, it is assumed that its deviation would be similar to the deviations experienced by the liquefaction sensors, as they are all installed in the same manner.

The position of the liquefaction sensor array, relative to the generalized soil profile at the site, is shown in Figure 8-4. The uppermost soil layer is an 8.2-ft (2.5-m) thick silt to clayey-silt bed that overlies a 14.1-ft (4.3-m) thick silty-sand layer. Beneath these floodplain deposits is a stiff 17.1-ft (5.2-m) thick clay to silty-clay layer (Bennett et al., 1984). The top of the array is approximately 3 ft (0.9 m) below the top of the liquefiable silty-sand layer. Bennett et al. (1984) originally partitioned the liquefiable silty-sand layer into an upper and lower unit, with the division between the units occurring at a depth of approximately 11.5 ft (3.5 m). Several researchers who conducted resonant column tests, cyclic triaxial tests, and cyclic simple shear tests on soil from the Wildlife Site in the 1980's also followed this notation (Haag and Stokoe, 1984; Vucetic and Dobry, 1986). The liquefaction sensor array is located partially in the upper liquefiable layer and

partially in the lower liquefiable soil layer. As mentioned in Section 7.6, the upper-layer has an average fines content of 49% and an average clay-size particle content of 12%, while the lower-layer has an average fines content of 27% and an average clay-size particle content of 9%. However, the transition from the lower-layer to the upper-layer is very subtle, with fines contents generally increasing from the bottom to the top of the liquefiable soil layer. If the grain size characteristics from various researchers (see Chapter 7) obtained only from soil samples within the depth range of the liquefaction sensor array are averaged, the fines and clay-size (5 μm) particle contents are equal to 33% and 10%, respectively.

More recently, researchers have primarily referred to the liquefiable soil layer as a single unit (Youd and Holzer, 1994; Zeghal and Elgamal, 1994). Additionally, resonant column tests performed by Haag and Stokoe (1985) indicate that the nonlinear soil behavior of specimens from the lower liquefiable layer fall within the range of the nonlinear soil behavior of specimens from the upper liquefiable soil layer (see Figure 7-8). Similarly, Vucetic and Dobry (1986) found that the pore pressure generation data obtained from strain controlled cyclic laboratory tests on specimens from the upper and lower liquefiable soil layers could be fit with a single model (see Section 7.3.1.3). Therefore, it seems that in terms of dynamic response, the upper and lower liquefiable layers are very similar.

The approximate depth of the ground water level (GWL) at the time of testing is also shown in Figure 8-4. The GWL was evaluated from measurements

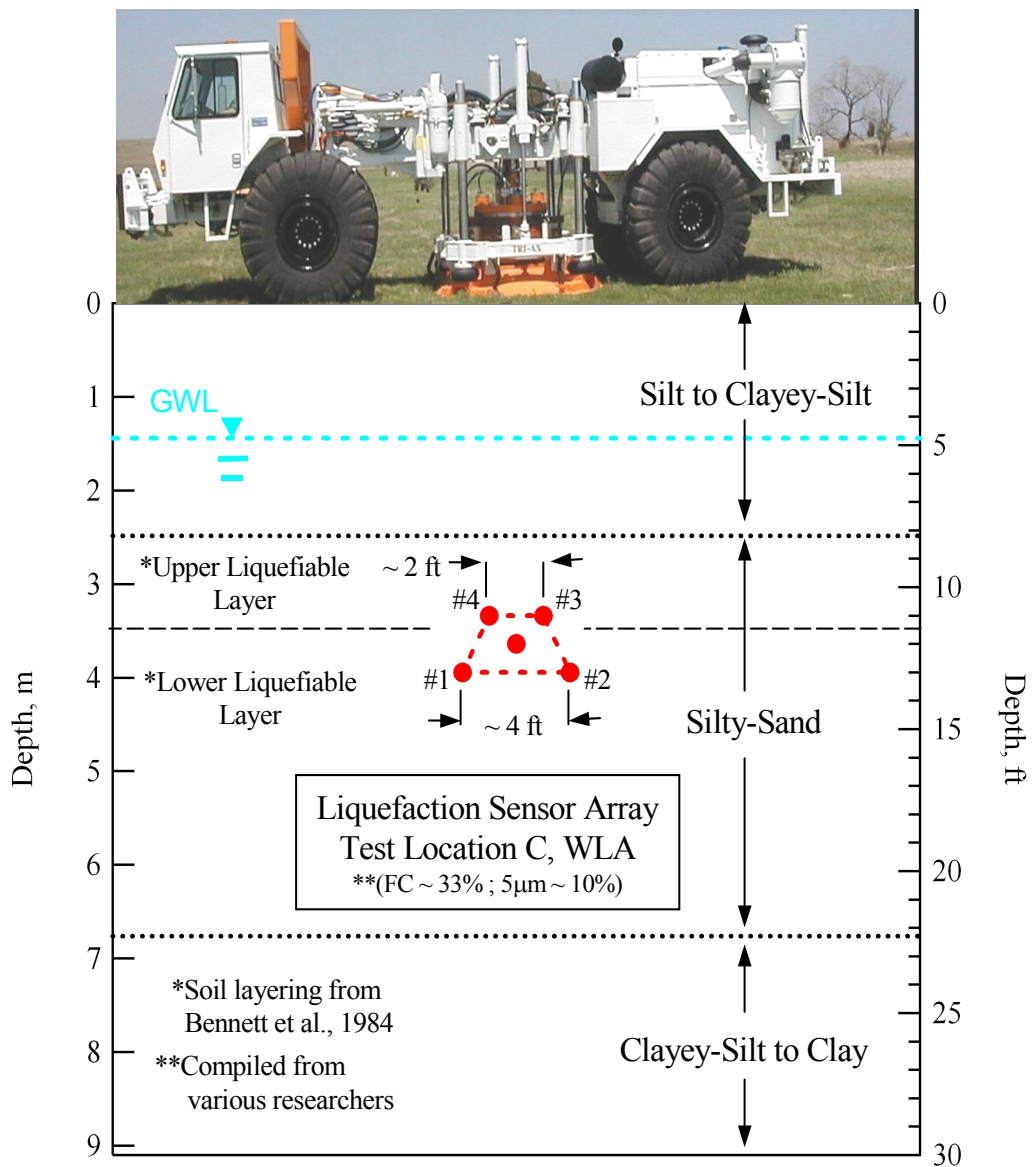


Figure 8-4 Position of the liquefaction sensor array at Test Location C, shown with respect to the general soil layering at the Wildlife Site as proposed by Bennett et al. (1984).

taken in a standpipe and from readings obtained with the PDCR 35/D pressure transducer, located at the center of the array. The standpipe was located near the 1982 Site (approximately 65 ft or 20 m south of the array), and three separate readings taken between August 17 and August 18 placed the GWL between 4.5 and 4.6 ft (1.37 and 1.40 m) below the ground surface. More than 30 measurements made with the PDCR 35/D transducer over the same time period consistently placed the static GWL between 4.7 and 4.8 ft (1.43 and 1.46 m) below the ground surface. Considering the distance between measurement points, these differences are minor and show the stability and accuracy of the PDCR 35/D pressure transducer.

The liquefaction sensor array at Test Location C was installed very near to CPT 47. The soil layering in the immediate vicinity of the liquefaction sensor array can be verified by examining the tip resistance (q_c) and friction ratio (F_r) values obtained from CPT 47. The liquefiable soil layer boundaries proposed by Bennett et al. (1984), and the depth range (approximately 11- to 13-ft or 3.4- to 4.0-m) of the in-situ liquefaction sensor array, are plotted with the tip resistance and friction ratio values from CPT 47 in Figure 8-5. In general, the liquefiable soil layer is marked by relatively large values of CPT tip resistance and relatively small values of CPT friction ratio as compared to the layer above it. The liquefiable soil layer determined by Bennett et al. (1984) at the 1982 (old) WLA instrumentation site is a very good approximation for the liquefiable soil layer at Test Location C.

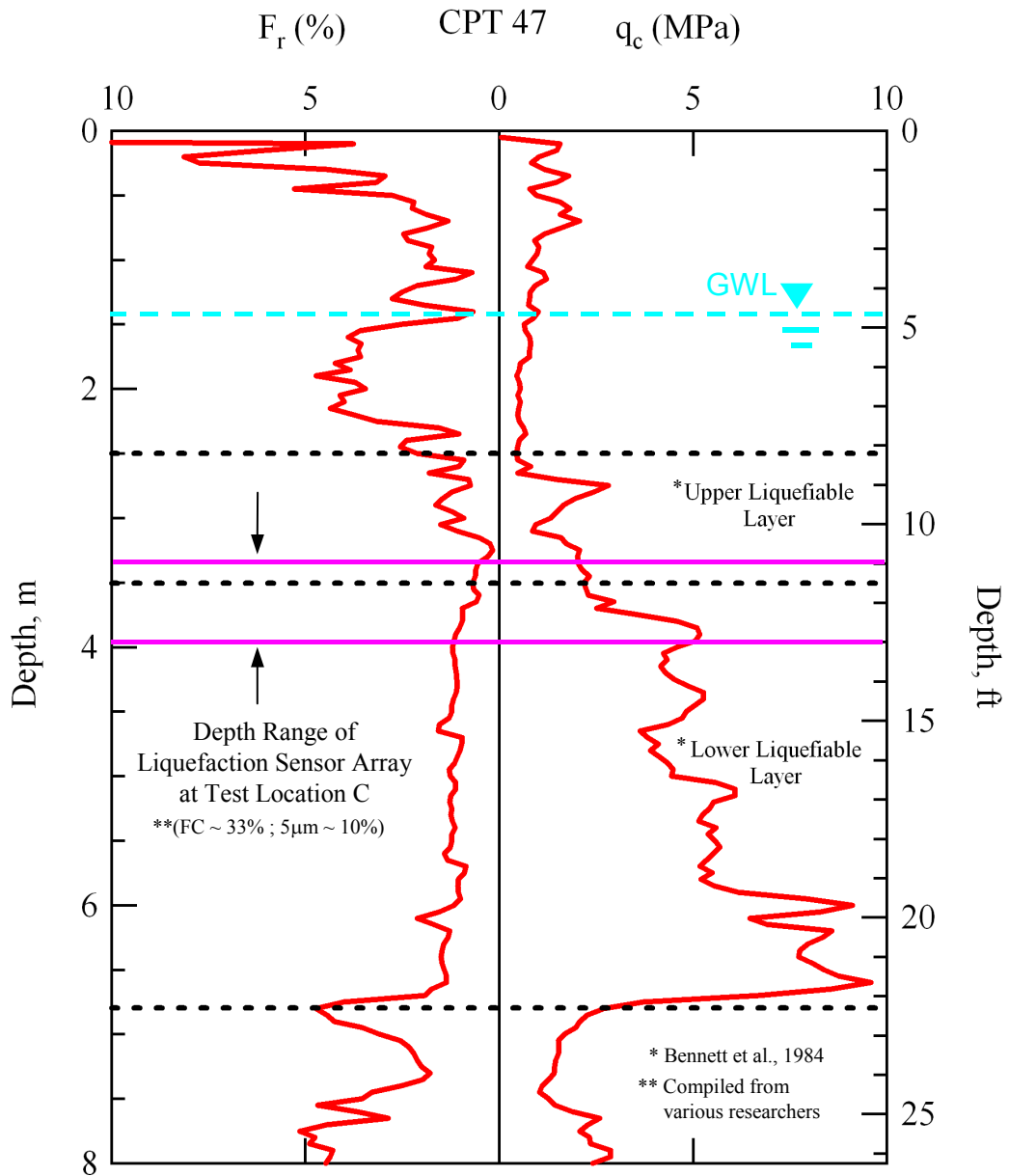


Figure 8-5 Depth range of the liquefaction sensor array at Test Location C, shown with respect to the tip resistance (q_c) and friction ratio (F_r) values obtained from CPT 47 and the upper and lower liquefiable soil layers proposed by Bennett et al. (1984) (raw CPT data from <http://nees.ucsb.edu>).

It is important to know the initial vertical effective stress at the sensor locations so that excess pore pressure ratios (r_u) induced in the instrumented soil mass during dynamic loading can be calculated from the recorded excess pore water pressure data (i.e. $r_u = \Delta u / \sigma_v'$, where Δu is excess pore water pressure and σ_v' is initial vertical effective stress). The effective overburden pressures can readily be calculated knowing the depth of each sensor, the location of the GWL, and the unit weight of the soil ($\gamma \sim 120$ pcf or ~ 19.0 kN/m³). The effective overburden pressures calculated at the approximate depth of each sensor are listed in Table 8-2. These values were calculated with the static GWL located approximately 4.75-ft (1.4-m) below the ground surface.

As discussed in Section 5.2, when estimating the vertical effective stress at each sensor location, the increase in stress caused by the static hold-down force of the vibroseis base plate must also be accounted for. The uniform surface pressure (assuming the base plate to be rigid) applied by the base plate during testing was approximately 800 psf (38 kPa). The change in vertical stress beneath the center of the base plate at the depth of each sensor was calculated using both Boussinesq's and Westergaard's elastic stress distribution solutions (Coduto, 1994). Estimates for the changes in vertical stress obtained from calculating Boussinesq's and Westergaard's solutions at the depth of each sensor are given in Table 8-2. As can be seen, both of these solutions give very similar results. The total initial vertical effective stress at each sensor depth was calculated by superimposing the change in vertical stress caused by the applied surface load of the vibroseis base plate onto the preexisting effective overburden pressure. Table

Table 8-2 Estimates for the effective overburden stress, increase in vertical stress due to the vibroseis base plate load, and total vertical effective stress at the approximate depth of each sensor in the liquefaction sensor array at Test Location C, Wildlife Liquefaction Array (WLA)

| Sensor Position (Node #) | Approximate Depth (ft) | Effective Overburden Stress (psf) ¹ | Increase in Stress Due to Vibroseis Base Plate Load (psf) ² | | Total Effective Vertical Stress (psf) |
|--------------------------|------------------------|--|--|--------------------------|---------------------------------------|
| | | | Boussinesq | Westergaard ³ | |
| #1 | 13 | 1045 | 112 | 116 | 1160 |
| #2 | 13 | 1045 | 112 | 116 | 1160 |
| #3 | 11 | 930 | 149 | 149 | 1080 |
| #4 | 11 | 930 | 149 | 149 | 1080 |
| #5 | 12 | 990 | 128 | 131 | 1120 |

Notes: 1. Calculated using $\gamma = 120$ pcf and GWL at 4.75 ft below ground surface
 2. Calculated beneath center of base plate with a uniform surface pressure = 800 psf
 3. Calculated with Poisson's Ratio = 0.3

8-2 details the estimates obtained for the total vertical effective stress at each sensor depth. These values were used to normalize the excess pore water pressures recorded during dynamic loading to obtain excess pore pressure ratios.

As discussed in Section 6.4, readings obtained from all five pressure transducers (4 miniature PPT's located in the liquefaction sensors placed at each corner node and the larger PDCR 35/D pressure transducer located at the center of the array) were used to calculate r_u values for each stage of the in-situ liquefaction tests. However, the r_u values used to construct the pore pressure generation curves for each site were obtained solely from the PDCR 35/D transducer located at the center of the array.

8.2.1 Crosshole Test Results

As discussed in Section 5.2, crosshole seismic tests are conducted between sensors at the same depth, both before and after dynamic loading, to verify saturation and determine how the small-strain shear stiffness of the liquefiable soil was affected by liquefaction testing. A cross-sectional schematic showing the liquefaction sensor array, the crosshole source rods, and the base plate of T-Rex is shown in Figure 8-6. At Test Location C, source rods A and B were placed in-line with the sensor array at distances of approximately 0.75 ft (0.23 m) and 1.75 ft (0.53 m) from the edge of the base plate of T-Rex, respectively. Crosshole source rod B was inserted so that its tip was located at the same elevation as sensors No. 1 and No. 2 (approximately 13-ft or 4.0-m deep), while crosshole source rod A was inserted so that its tip was located at the same elevation as sensors No. 3 and No. 4 (approximately 11-ft or 3.4-m deep). Crosshole tests were performed by vertically impacting the top of one of the source rods while simultaneously recording the vibration-sensing outputs of the two sensors located at the same depth as the tip of the rod. The horizontal, in-line component (y-component) of the 3D-MEMS accelerometer in each sensor was used to sense horizontally propagating compression wave (P_h -wave) arrivals, while the vertical component (z-component) was used to sense horizontally propagating, vertically polarized shear wave (S_{hv} -wave) arrivals.

Interval wave travel times between the near and far sensors were used to calculate wave velocities. Figure 8-7 shows an example of typical records that were collected from performing crosshole tests at Location C. These particular

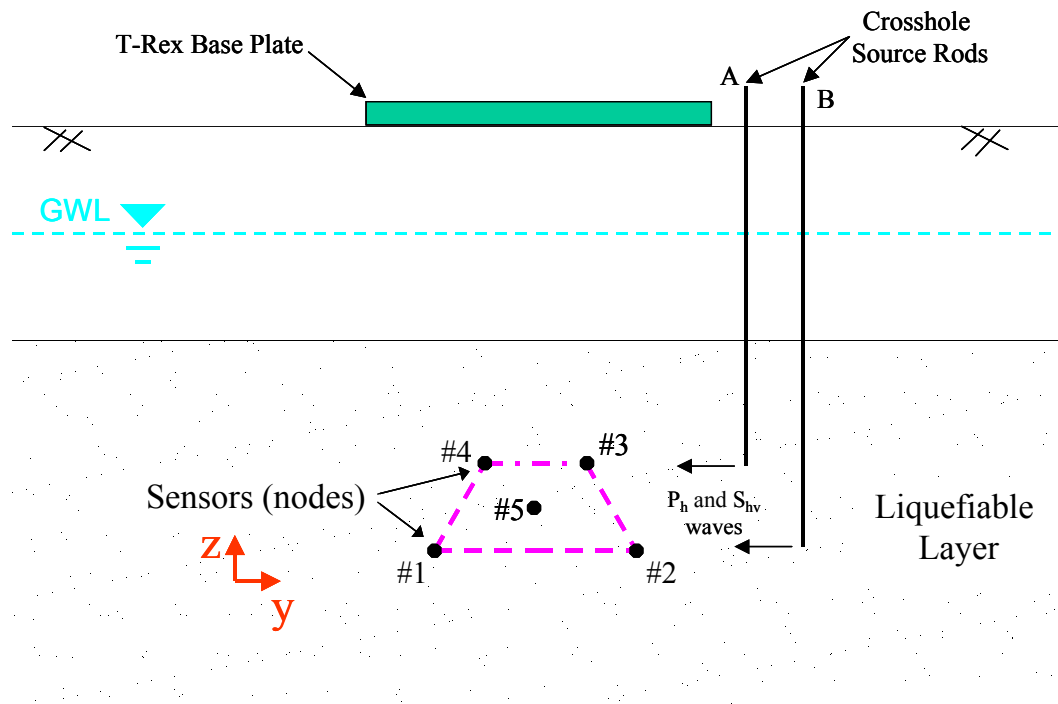
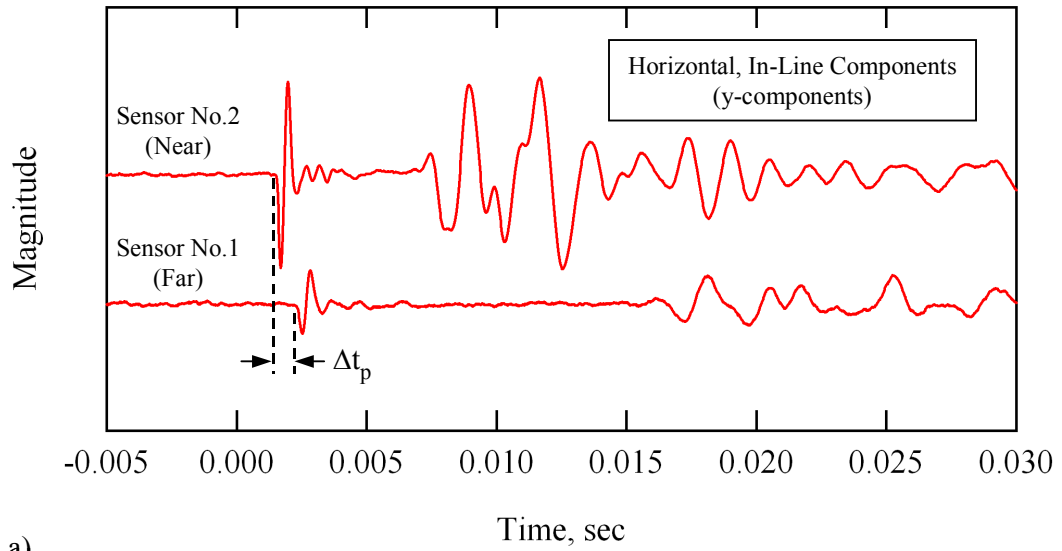
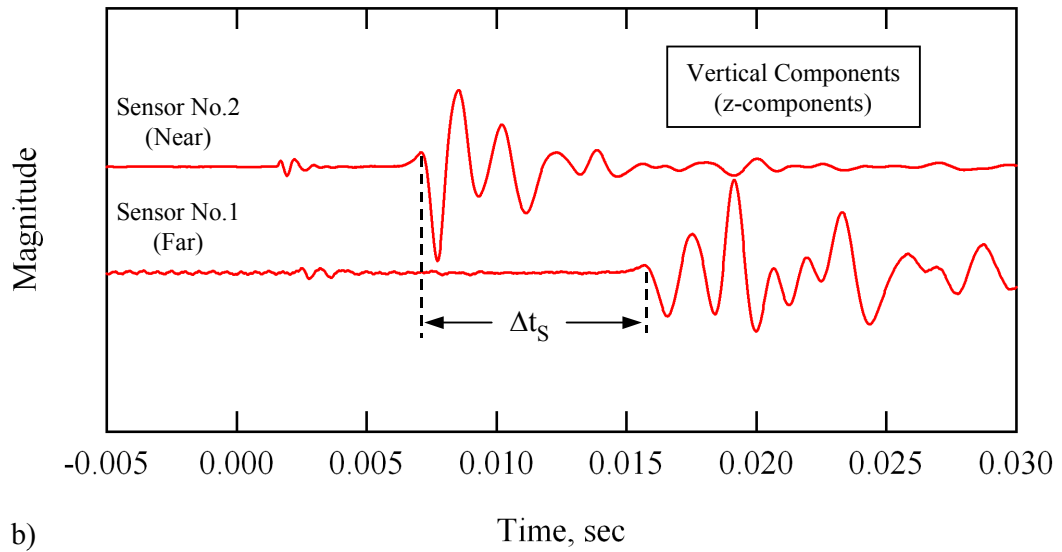


Figure 8-6 Cross-sectional schematic of the liquefaction sensor array, the crosshole source rods, and the base plate of T-Rex.

waveforms were recorded by sensors No. 1 and No. 2. Figure 8-7a shows the waveforms that were sensed by the horizontal, in-line components (y -components) of these sensors. The P_h -wave arrivals are identified as the first seismic energy to reach each sensor. The P_h -wave velocity (V_p) of the material between the sensors is equal to the horizontal distance between them (3.98 ft or 1.21 m; see Table 8-1) divided by the P_h -wave interval travel time (Δt_p). Figure 8-7b shows the waveforms that were sensed by the vertical components (z -components) of sensors No. 1 and No. 2. Given a downward impact at the source rod, and knowing the polarity of the sensors, the S_{hv} -wave arrivals are identified as the first major downward departure in the records. The S_{hv} -wave velocity



a)



b)

Figure 8-7 Crosshole waveforms recorded by the: a) horizontal, in-line components (P_h -waves identified on), and b) vertical components (S_{hv} -waves identified on) of sensors No. 2 (near) and No. 1 (far) at Test Location C.

($V_{S,hv}$) of the material between the sensors is equal to the horizontal distance between them divided by the S_{hv} -wave interval travel time (Δt_s). As a side note, the S_{hv} -wave arrivals can be seen on the y-component records and the P-wave arrivals can be seen on the z-component records. However, the wave arrival times are most accurately determined by using the proper sensing components as noted above.

The P_h -wave and S_{hv} -wave velocities obtained from performing crosshole tests at Location C are provided in Table 8-3. Crosshole tests were performed three separate times throughout the course of in-situ liquefaction testing at Location C. The first set of crosshole tests was performed prior to bringing T-Rex into position over the top of the liquefaction sensor array. This set of tests was conducted to provide baseline velocities for the soil prior to application of the base plate hold-down force and subsequent staged dynamic loading. The second set of crosshole tests was performed after the full, static base plate hold-down force of T-Rex had been applied to the soil, but prior to any dynamic loading. After the first two sets of crosshole measurements had been performed, the first series of staged dynamic loading was conducted at Location C (discussed in Section 8.3). Then, the soil was allowed to recover for approximately 18 hours and a second series of dynamic loading was conducted (discussed in Section 8.4). The third set of crosshole measurements was performed immediately before the second series of staged dynamic loading.

The baseline crosshole test results listed in Table 8-3 show that the V_p values between the top (sensors No. 3 and No. 4) and bottom (sensors No. 2 and

Table 8-3 Results from three separate sets of crosshole tests performed between the top (sensors No. 3 and No. 4) and bottom (sensors No. 2 and No. 1) sensor pairs in the liquefaction sensor array at Test Location C, Wildlife Liquefaction Array (WLA)

| Date | Time | Condition | No. 3 to No. 4 ~ 11-ft Deep | | No. 2 to No. 1 ~ 13-ft Deep | |
|-----------|----------|--|--------------------------------|-------------|--------------------------------|-------------|
| | | | $V_{S,hv}$ (fps) | V_p (fps) | $V_{S,hv}$ (fps) | V_p (fps) |
| 8/17/2005 | 12:42 PM | Initial Baseline Readings: Prior to Static Hold-Down Force | 400 | 5170 | 460 | 5095 |
| 8/17/2005 | 1:07 PM | After Static Hold-Down Force, Prior to Series 1 Dynamic Loading | 400 | 5170 | 460 | 5095 |
| 8/18/2005 | 8:09 AM | Prior to Series 2 Dynamic Loading | 405 | 5170 | 450 | 5095 |

No. 1) sensor pairs in the array are slightly greater than 5000 fps (1500 m/s). As discussed in Section 2.3.1, fully saturated soils have P-wave velocities of approximately 5000 fps (i.e. the velocity of a compression wave traveling through water). Therefore, it may be concluded that the soil within the depth range of the liquefaction sensor array at Test Location C (approximately 11 to 13 ft or 3.4 to 4.0 m) was saturated prior to dynamic loading. The baseline crosshole test results listed in Table 8-3 show that the $V_{S,hv}$ between the top sensors in the array is approximately 400 fps (122 m/s) and the $V_{S,hv}$ between the bottom sensors in the array is approximately 460 fps (140 m/s).

The crosshole results listed in Table 8-3 also indicate that the $V_{S,hv}$ between the top and bottom sensor pairs were not noticeably affected by the application of the base plate hold-down force. This lack of sensitivity is not

surprising as the increase in vertical stress at the sensor locations due to the base plate hold-down force was estimated to be between 10 to 15% of the initial effective overburden stress (see Table 8-2). Since the shear wave velocity of soil theoretically changes according to about the quarter-power of the change in mean effective stress, it is expected that the velocities would have only increased between 2 to 4%. Results from the third set of crosshole tests indicate that the small-strain shear stiffness of the instrumented portion of the soil mass (reflected in the $V_{s,hv}$ values) was affected very little by the first series of staged dynamic loading.

8.3 TEST C: STAGED DYNAMIC LOADING SERIES 1

The in-situ liquefaction sensor array at Test Location C was installed on August 16, 2005. The sensor installation process required a full day to complete. The pore water pressure transducer (PPT) in each sensor was powered overnight using a 12-volt battery and a DC-to-DC converter to help ensure that the static PPT outputs remained as steady as possible during testing the following day (as discussed in Section 4.3.2). The first series (Series 1) of staged dynamic loading began in the afternoon of August 17.

8.3.1 Loading Stages in Series 1

In Series 1, eight separate dynamic loading stages were applied to the instrumented soil mass. The dynamic shear loads were applied by driving T-Rex in the horizontal, in-line direction. An external function generator was used to control the frequency, number of cycles, and drive voltage amplitude supplied to

T-Rex. Details of the Series 1 staged dynamic loading sequence are provided in Table 8-4. The first three dynamic loads were applied at a frequency of 20 Hz. The last five dynamic loads were applied at a frequency of 10 Hz. All of the staged loads had a duration of 100 cycles, except loading stage No. 8, which had a duration of 200 cycles. Previous tests conducted at Test Location A (discussed in Chapter 10) had shown that higher peak shear strains could be induced in the soil deposit at a frequency of 10 Hz than at a frequency of 20 Hz. However, T-Rex has more harmonic distortion when operating at 10 Hz than at 20 Hz. As discussed in Section 6.5, harmonic distortion in the ground motion signals recorded during testing complicates the evaluation of the nonlinear shear modulus of the soil. Therefore, tests were conducted at 20 Hz with the goal of being able to more accurately resolve the nonlinear shear modulus behavior, and at 10 Hz to generate shear strains as large as possible within the instrumented soil mass. However, to avoid loading the soil beyond its cyclic threshold strain (γ_t^e), the 20-Hz loads were only carried to the point where a minute amount of excess pore water pressure was generated at the center of the liquefaction sensor array (i.e. $r_u < 1\%$). At this point, the loading frequency was decreased to 10 Hz, the drive amplitude was dropped back down to a low level, and staged dynamic loading was begun again.

Shear strains (γ) induced in the instrumented soil mass were calculated at the center of the liquefaction sensor array for every stage of dynamic loading using the 4-node, isoparametric finite element formulation presented in Section 6.3. Dynamic in-situ liquefaction tests are not strictly stress-controlled, or strain-

Table 8-4 Details of the Series 1 staged dynamic loading sequence conducted at Test Location C, Wildlife Liquefaction Array (WLA)

| Time on 8/17/2005 | Staged Load Number | Function Generator Drive Signal | | | Approximate Ground Force (lb) |
|----------------------|-----------------------|---------------------------------|---------------------|----------------------|-------------------------------------|
| | | Frequency (Hz) | Number of Cycles | Amplitude (volts) | |
| 1:20 PM | 1 | 20 | 100 | 0.4 | 2000 |
| 1:24 PM | 2 | 20 | 100 | 0.8 | 5000 |
| 1:28 PM | 3 | 20 | 100 | 1.5 | 7500 |
| 1:39 PM | 4 | 10 | 100 | 0.4 | 2000 |
| 1:43 PM | 5 | 10 | 100 | 0.8 | 5000 |
| 1:47 PM | 6 | 10 | 100 | 1.5 | 15000 |
| 1:52 PM | 7 | 10 | 100 | 2.5 | 20000 |
| 2:03 PM | 8 | 10 | 200 | 5 | 30000 |

controlled tests. Despite this, the shear strain time histories calculated at the center of the array generally have very consistent amplitudes throughout the duration of loading (as presented in Section 8.3.2). However, once significant excess pore water pressures are generated within the array, the strain behavior can become more irregular. Because the shear strain time histories do not always have a constant amplitude, it is necessary to average the shear strain amplitudes over various numbers of loading cycles. Figure 8-8 illustrates how the average shear strains over 50 and 200 cycles of loading were obtained for the shear strain time history generated during loading stage No. 8 of staged loading Series 1 at Test Location C (discussed in Section 8.3.2.8). This shear strain time history was the most irregular of the shear strain time histories from staged loading Series 1. Loading stage No. 8 was also the only loading stage in Series 1 to have a duration

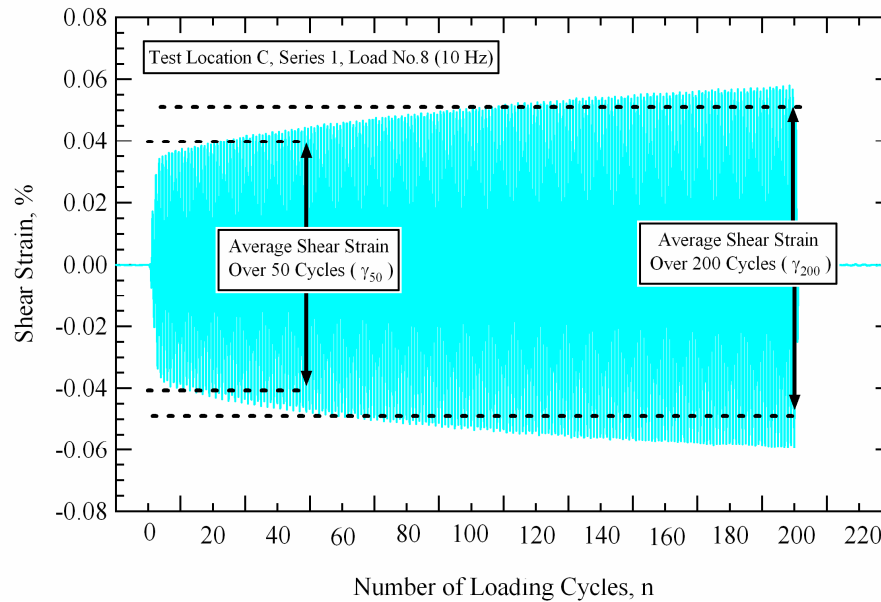


Figure 8-8 Illustration of how cyclic shear strains are averaged over various numbers of loading cycles.

of 200 cycles. As detailed in Figure 8-8, the 50-cycle shear strain (γ_{50}) and the 200-cycle shear strain (γ_{200}) are determined by averaging all of the cyclic shear strains from zero to 50 and 200 cycles, respectively. Using this procedure, average shear strain amplitudes can be determined for any desired number of loading cycles.

The pore pressure ratios (r_u) at each sensor location were obtained by dividing the measured residual pore water pressure, obtained from processing the raw pore pressure transducer (PPT) records according to the procedure outlined in Section 6.4, by the total vertical effective stress at each sensor location (see Table 8-2). The r_u values used to construct the pore pressure generation curves for each site were obtained solely from the PDCR 35/D transducer located at the center of

the array (Sensor No. 5). The r_u values obtained from the miniature PPT's (Sensors No. 1 – No. 4) were only used in a qualitative sense to observe how the pore pressure generation varied within the instrumented soil mass.

The nonlinear soil shear modulus of the soil within the liquefaction sensor array was obtained for each staged load using the average cycle-by-cycle, vertically propagating (downward), horizontally polarized, shear wave velocities ($V_{s,vh}$) determined according to the procedure detailed in Section 6.5.

8.3.2 Response of the Deposit During Loading Series 1

8.3.2.1 Loading Stage No. 1

The force applied at the ground surface by T-Rex, the shear strain induced at the center of the liquefaction sensor array, and the pore pressure ratios generated at each PPT location during loading stage No. 1 of staged loading Series 1 are shown in Figure 8-9. The ground force during loading stage No. 1 was less than 2000 lb (8.9 kN) throughout the 100 cycles of 20-Hz loading. This load induced fairly uniform cyclic shear strains at the center of the liquefaction sensor array of approximately 0.001%. These shear strains did not trigger the generation of any excess pore water pressure in the instrumented soil mass, as indicated by the fact that the pore pressure ratios at each sensor location remained equal to zero.

Tabulated values for the pore pressure ratios and average shear strains (averaged over the given number of loading cycles) induced in the soil during loading stage No. 1 of staged loading Series 1 are provided in Table 8-5. These

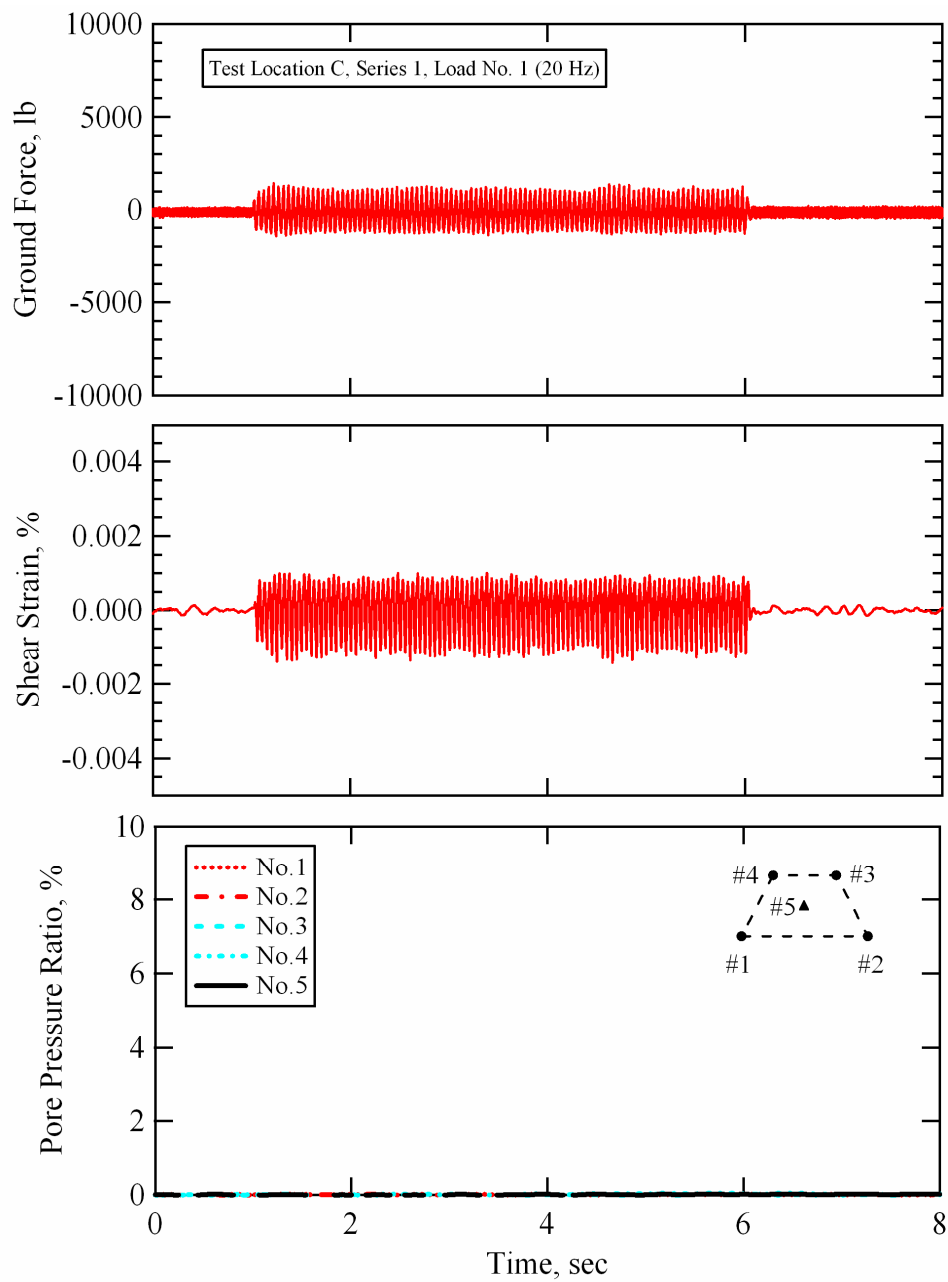


Figure 8-9 Force applied at the ground surface by T-Rex, shear strain induced at the center of the instrumented soil mass, and pore pressure ratios generated at each sensor location during Series 1, loading stage No. 1; Test Location C, Wildlife Liquefaction Array.

Table 8-5 Pore pressure ratios and average shear strains at the center of the liquefaction sensor array for different numbers of loading cycles; Series 1, Test Location C, Wildlife Liquefaction Array (WLA)

| Number of Cycles | γ or r_u | Pore Pressure Ratio ¹ (r_u) and Average Shear Strain ² (γ) Values, % | | | | | | | |
|------------------|-------------------|---|--------|--------|--------|--------|--------|--------|--------|
| | | Series 1: Staged Load Number | | | | | | | |
| | | No. 1 | No. 2 | No. 3 | No. 4 | No. 5 | No. 6 | No. 7 | No. 8 |
| 10 | γ | 0.0010 | 0.0047 | 0.0106 | 0.0010 | 0.0026 | 0.0092 | 0.0200 | 0.0357 |
| | r_u | 0 | 0 | 0 | 0 | 0 | 0 | 0 | 1 |
| 20 | γ | 0.0010 | 0.0048 | 0.0107 | 0.0010 | 0.0026 | 0.0096 | 0.0211 | 0.0376 |
| | r_u | 0 | 0 | 0 | 0 | 0 | 0 | 1 | 4 |
| 30 | γ | 0.0010 | 0.0048 | 0.0108 | 0.0010 | 0.0026 | 0.0098 | 0.0217 | 0.0390 |
| | r_u | 0 | 0 | 0 | 0 | 0 | 0 | 1 | 5 |
| 40 | γ | 0.0010 | 0.0048 | 0.0108 | 0.0010 | 0.0026 | 0.0098 | 0.0221 | 0.0402 |
| | r_u | 0 | 0 | 0 | 0 | 0 | 0 | 2 | 7 |
| 50 | γ | 0.0010 | 0.0048 | 0.0109 | 0.0010 | 0.0026 | 0.0099 | 0.0224 | 0.0412 |
| | r_u | 0 | 0 | 0 | 0 | 0 | 0 | 2 | 8 |
| 60 | γ | 0.0010 | 0.0048 | 0.0109 | 0.0010 | 0.0026 | 0.0100 | 0.0227 | 0.0421 |
| | r_u | 0 | 0 | 0 | 0 | 0 | 0 | 2 | 9 |
| 70 | γ | 0.0010 | 0.0049 | 0.0110 | 0.0010 | 0.0026 | 0.0101 | 0.0229 | 0.0429 |
| | r_u | 0 | 0 | 0 | 0 | 0 | 0 | 2 | 10 |
| 80 | γ | 0.0010 | 0.0049 | 0.0110 | 0.0010 | 0.0026 | 0.0101 | 0.0231 | 0.0437 |
| | r_u | 0 | 0 | 0 | 0 | 0 | 0 | 2 | 11 |
| 90 | γ | 0.0010 | 0.0049 | 0.0110 | 0.0010 | 0.0026 | 0.0101 | 0.0232 | 0.0444 |
| | r_u | 0 | 0 | 0 | 0 | 0 | 0 | 3 | 12 |
| 100 | γ | 0.0010 | 0.0049 | 0.0110 | 0.0010 | 0.0026 | 0.0102 | 0.0234 | 0.0451 |
| | r_u | 0 | 0 | 0 | 0 | 0 | 0 | 3 | 12 |
| 150 | γ | - | - | - | - | - | - | - | 0.0479 |
| | r_u | - | - | - | - | - | - | - | 15 |
| 200 | γ | - | - | - | - | - | - | - | 0.0501 |
| | r_u | - | - | - | - | - | - | - | 17 |

Notes: 1. r_u from the PDCR 35/D pressure transducer at the center of the array after the given number of loading cycles
2. γ calculated at the center of the array and averaged over the given number of loading cycles

values are provided for different numbers of total loading cycles for all of the loading stages applied during staged loading Series 1.

8.3.2.2 Loading Stage No. 2

The force applied at the ground surface by T-Rex, the shear strain induced at the center of the liquefaction sensor array, and the pore pressure ratios generated at each PPT location during loading stage No. 2 of staged loading Series 1 are shown in Figure 8-10. The ground force during loading stage No. 2 was slightly less than 5000 lb (22.2 kN) throughout the 100 cycles of 20-Hz loading. This load induced fairly uniform cyclic shear strains at the center of the liquefaction sensor array of approximately 0.005% (see Table 8-5 for strain values averaged over various numbers of loading cycles). These shear strains did not trigger the generation of any excess pore water pressure in the instrumented soil mass, as indicated by the fact that the pore pressure ratios at each sensor location remained equal to zero.

8.3.2.3 Loading Stage No. 3

The force applied at the ground surface by T-Rex, the shear strain induced at the center of the liquefaction sensor array, and the pore pressure ratios generated at each PPT location during loading stage No. 3 of staged loading Series 1 are shown in Figure 8-11. The ground force during loading stage No. 3 was approximately 7500 lb (33.4 kN) throughout the 100 cycles of 20-Hz loading. This load induced fairly uniform cyclic shear strains at the center of the liquefaction sensor array of approximately 0.011% (see Table 8-5 for strain values

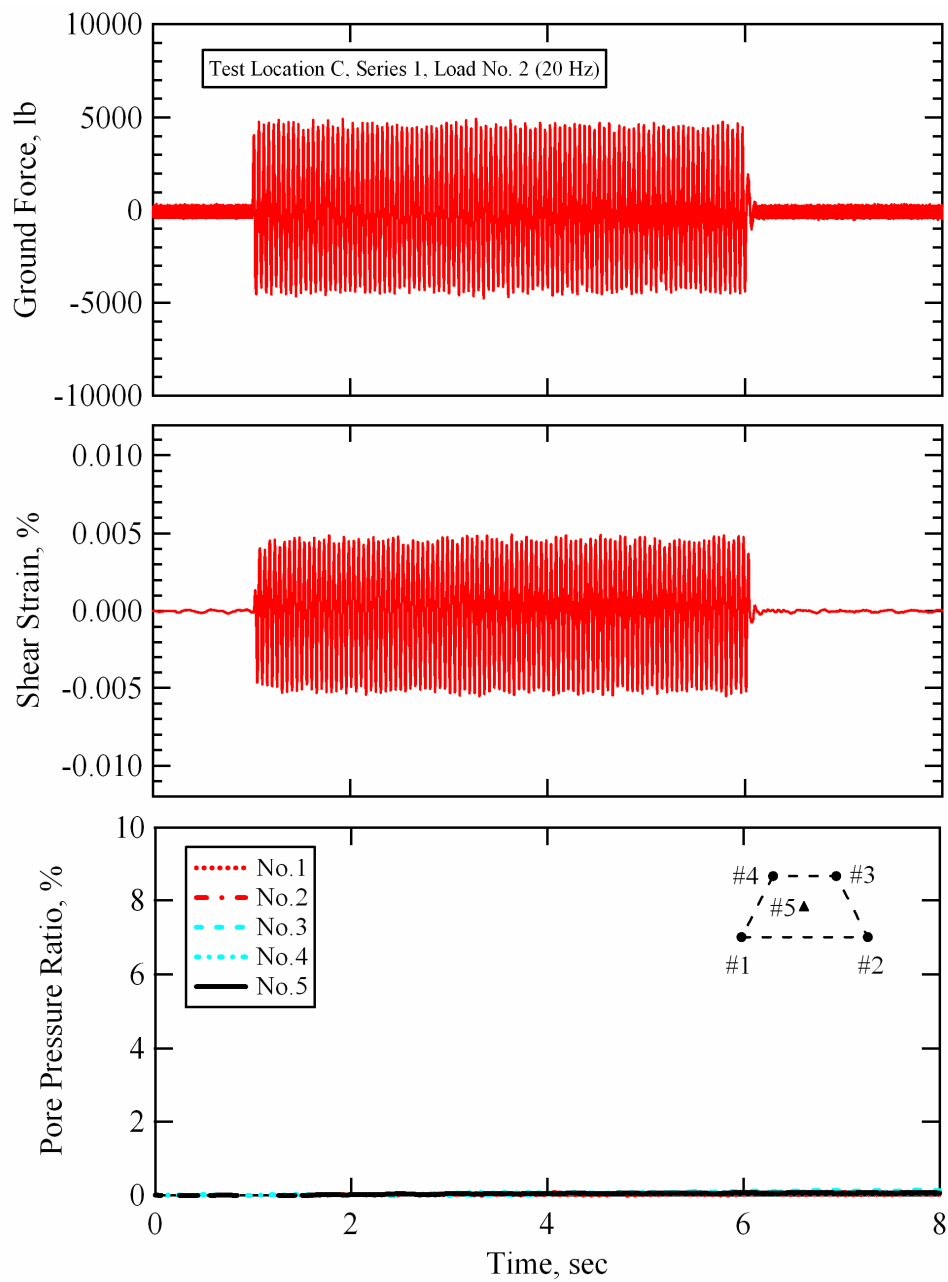


Figure 8-10 Force applied at the ground surface by T-Rex, shear strain induced at the center of the instrumented soil mass, and pore pressure ratios generated at each sensor location during Series 1, loading stage No. 2; Test Location C, Wildlife Liquefaction Array.

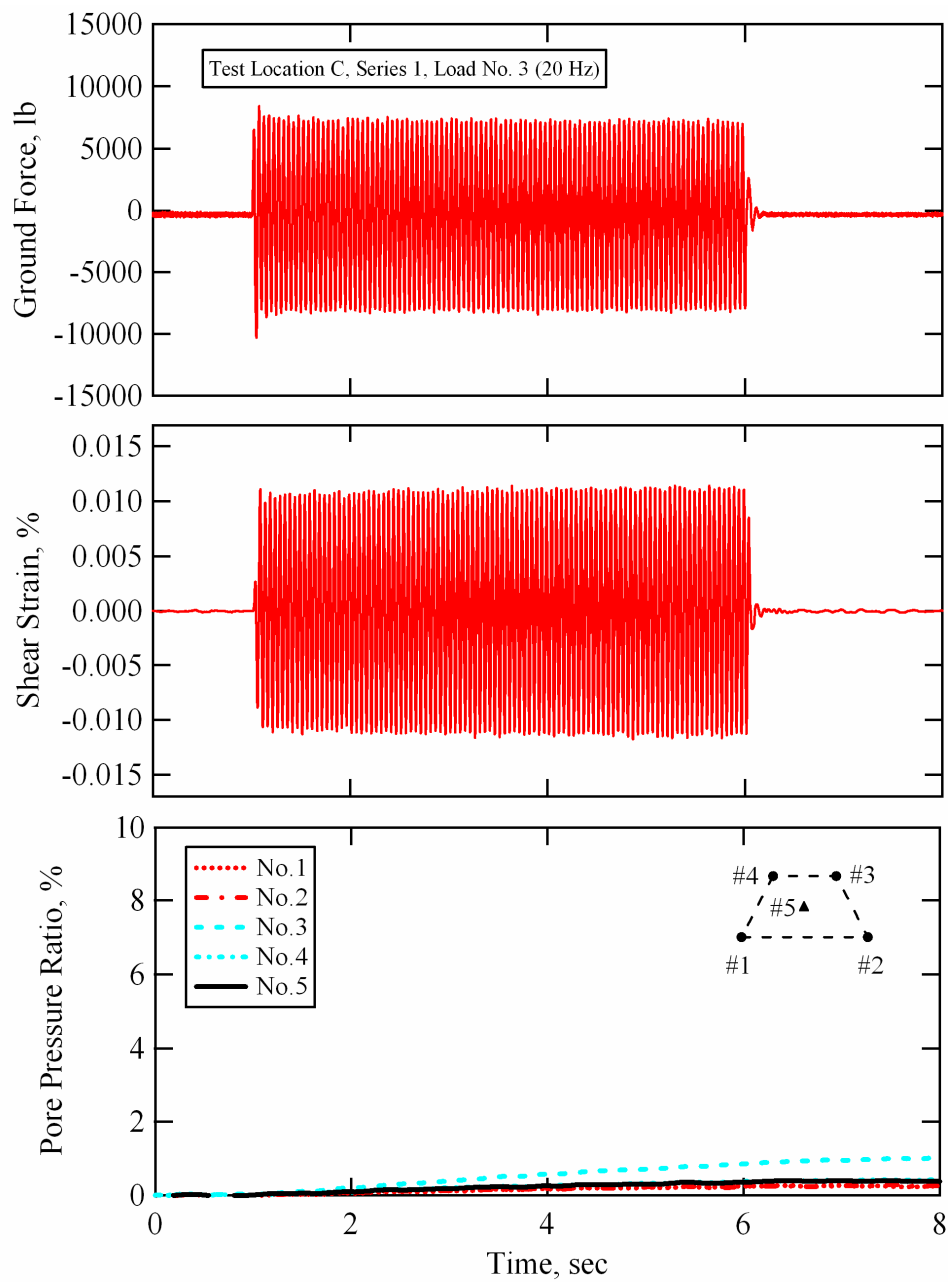


Figure 8-11 Force applied at the ground surface by T-Rex, shear strain induced at the center of the instrumented soil mass, and pore pressure ratios generated at each sensor location during Series 1, loading stage No. 3; Test Location C, Wildlife Liquefaction Array.

averaged over various numbers of loading cycles). A minute amount of excess pore water pressure was generated in the instrumented soil mass during this test. The pore pressure ratio at Sensor No. 3 reached a value of nearly 1%, while the other transducers indicated pore pressure ratios of less than 0.25%. At this point, testing was halted for approximately 10 minutes (see Table 8-4) while the pore pressures within the array were allowed to dissipate back to their static values (as monitored by the PDCR 35/D transducer). The actual time required for the pressure to return to its static condition was substantially less than the allotted time. After loading stage No. 3, the loading frequency was decreased to 10 Hz, the drive amplitude was dropped back down to a low level, and staged dynamic loading began again.

8.3.2.4 Loading Stage No. 4

The force applied at the ground surface by T-Rex, the shear strain induced at the center of the liquefaction sensor array, and the pore pressure ratios generated at each PPT location during loading stage No. 4 of staged loading Series 1 are shown in Figure 8-12. The ground force during loading stage No. 4 was slightly less than 2000 lb (8.9 kN) throughout the 100 cycles of 10-Hz loading. This load induced fairly uniform cyclic shear strains at the center of the liquefaction sensor array of approximately 0.001% (see Table 8-5 for strain values averaged over various numbers of loading cycles). These shear strains did not trigger the generation of any excess pore water pressure in the instrumented soil mass, as indicated by the fact that the pore pressure ratios at each sensor location remained equal to zero.

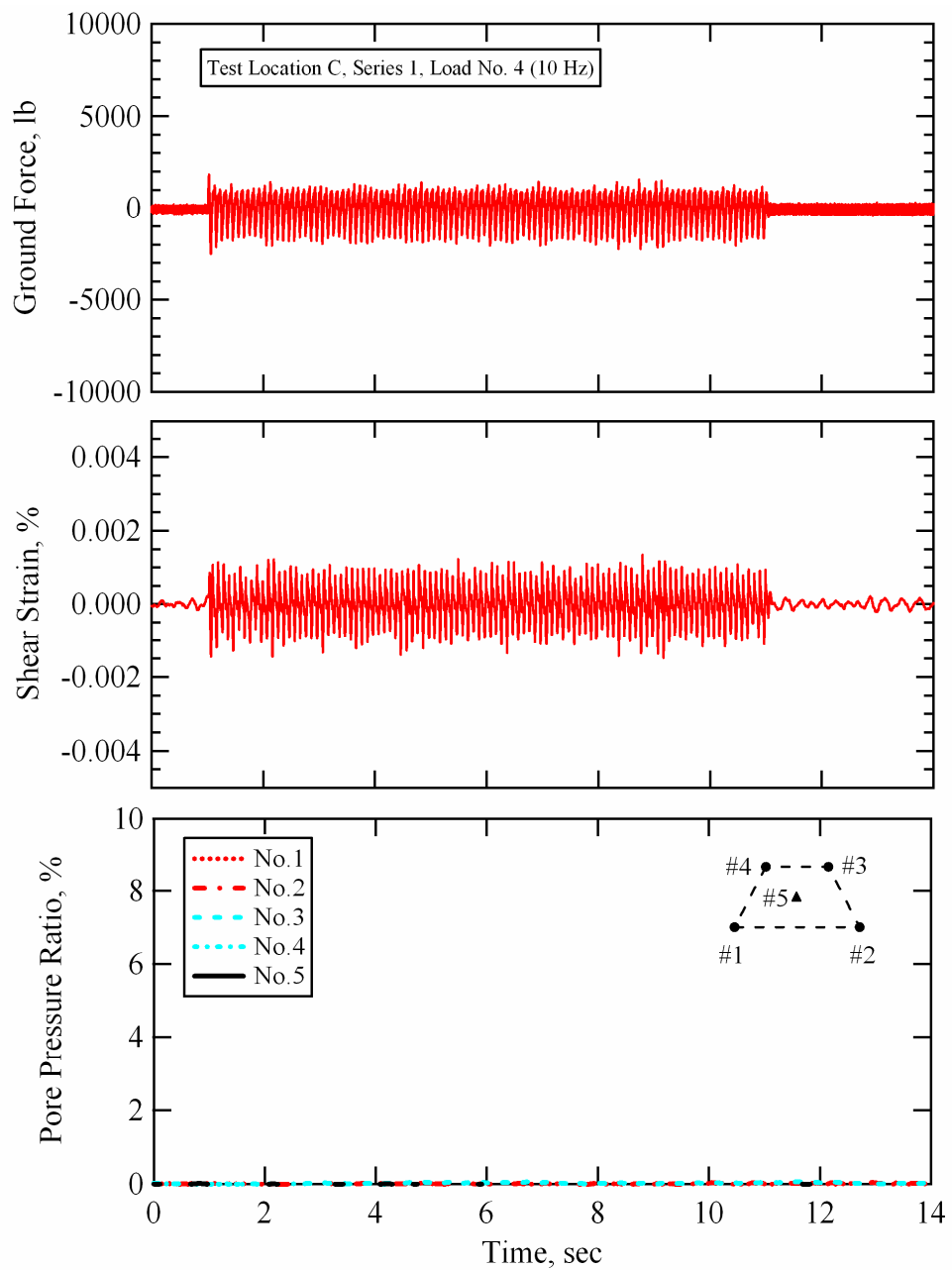


Figure 8-12 Force applied at the ground surface by T-Rex, shear strain induced at the center of the instrumented soil mass, and pore pressure ratios generated at each sensor location during Series 1, loading stage No. 4; Test Location C, Wildlife Liquefaction Array.

8.3.2.5 Loading Stage No. 5

The force applied at the ground surface by T-Rex, the shear strain induced at the center of the liquefaction sensor array, and the pore pressure ratios generated at each PPT location during loading stage No. 5 of staged loading Series 1 are shown in Figure 8-13. The ground force during loading stage No. 5 was slightly less than 5000 lb (22.2 kN) throughout the 100 cycles of 10-Hz loading. This load induced fairly uniform cyclic shear strains at the center of the liquefaction sensor array of approximately 0.0026% (see Table 8-5 for strain values averaged over various numbers of loading cycles). These shear strains did not trigger the generation of any excess pore water pressure in the instrumented soil mass, as indicated by the fact that the pore pressure ratios at each sensor location remained equal to zero.

8.3.2.6 Loading Stage No. 6

The force applied at the ground surface by T-Rex, the shear strain induced at the center of the liquefaction sensor array, and the pore pressure ratios generated at each PPT location during loading stage No. 6 of staged loading Series 1 are shown in Figure 8-14. The ground force during loading stage No. 6 was about 15000 lb (66.7 kN) throughout the 100 cycles of 10-Hz loading. This load induced uniform fairly cyclic shear strains at the center of the liquefaction sensor array of approximately 0.01% (see Table 8-5 for strain values averaged over various numbers of loading cycles). A minute amount of excess pore water pressure was generated at Sensor No. 3 during this test ($r_u < 0.5\%$). None of the other transducers sensed any appreciable excess pore water pressure generation.

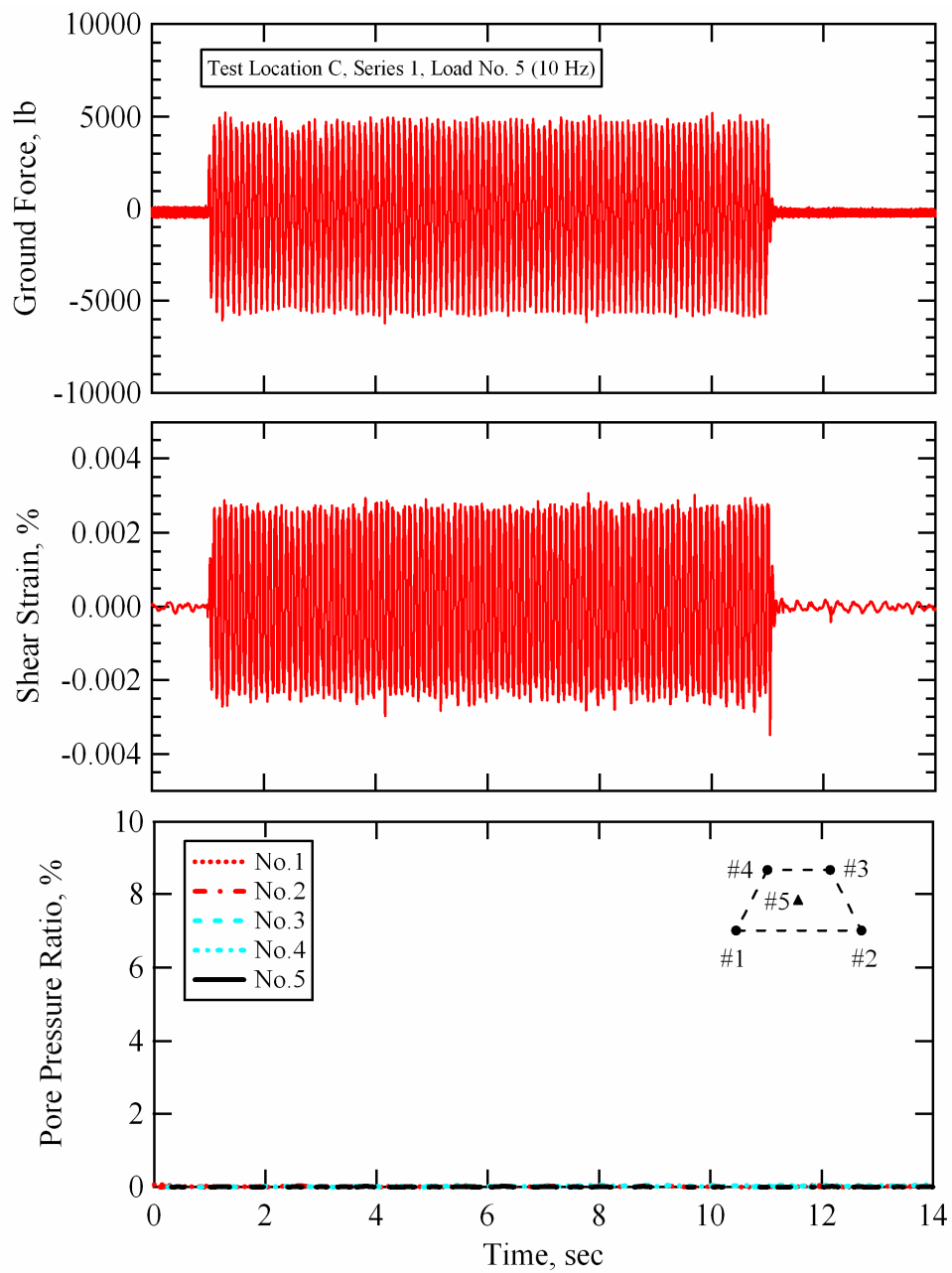


Figure 8-13 Force applied at the ground surface by T-Rex, shear strain induced at the center of the instrumented soil mass, and pore pressure ratios generated at each sensor location during Series 1, loading stage No. 5; Test Location C, Wildlife Liquefaction Array.

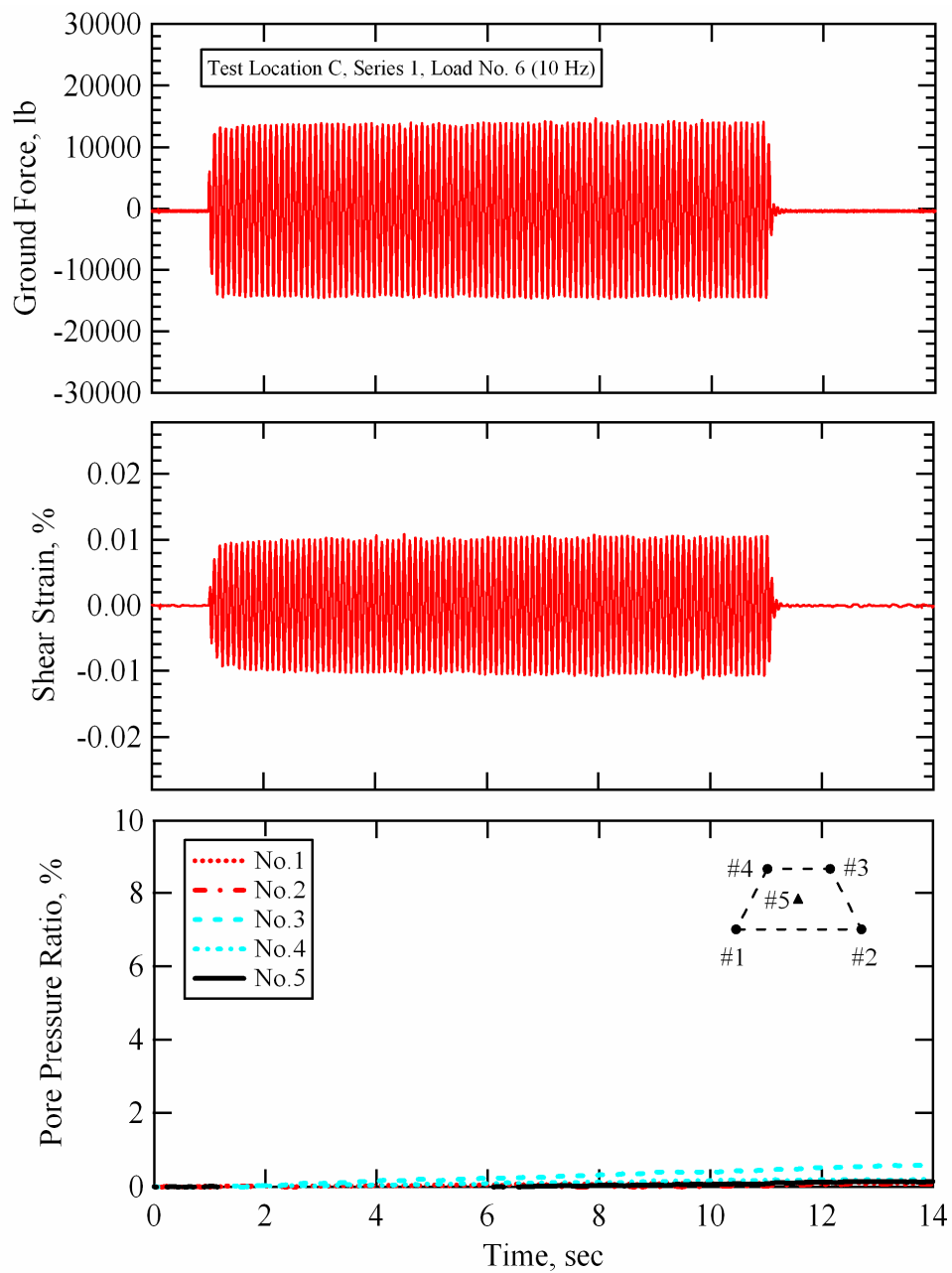


Figure 8-14 Force applied at the ground surface by T-Rex, shear strain induced at the center of the instrumented soil mass, and pore pressure ratios generated at each sensor location during Series 1, loading stage No. 6; Test Location C, Wildlife Liquefaction Array.

8.3.2.7 Loading Stage No. 7

The force applied at the ground surface by T-Rex, the shear strain induced at the center of the liquefaction sensor array, and the pore pressure ratios generated at each PPT location during loading stage No. 7 of staged loading Series 1 are shown in Figure 8-15. The ground force during loading stage No. 7 was slightly larger than 20000 lb (88.9 kN) throughout the 100 cycles of 10-Hz loading. This load induced fairly uniform cyclic shear strains at the center of the liquefaction sensor array of just over 0.02%. These cyclic shear strains induced measurable excess pore water pressures at all sensor locations in the instrumented soil mass.

The two deeper sensors (No. 1 and No. 2) in the array recorded nearly identical pressures that leveled off at the end of shaking following loading stage No. 7. Both of these sensors indicated pore pressure ratios of just less than 2% at the end of 100 cycles of loading. The PDCR 35/D transducer (Sensor No. 5) recorded pressures that steadily increased throughout dynamic loading, reached a peak at a pore pressure ratio of approximately 3% at the end of shaking, and then began to dissipate. The two shallower sensors (No. 3 and No. 4) recorded different magnitudes of pore pressure generation. Sensor No. 4 sensed excess pore pressures very similar in magnitude to those sensed by Sensor No. 5. However, the pressures did not decay as rapidly at the end of shaking on Sensor No. 4. Pore pressure data was recorded for approximately 60 seconds during loading stage No. 7. Figure 8-16 shows the pore pressure ratios measured at each sensor location with a time scale of 60 seconds. The pore pressures recorded by

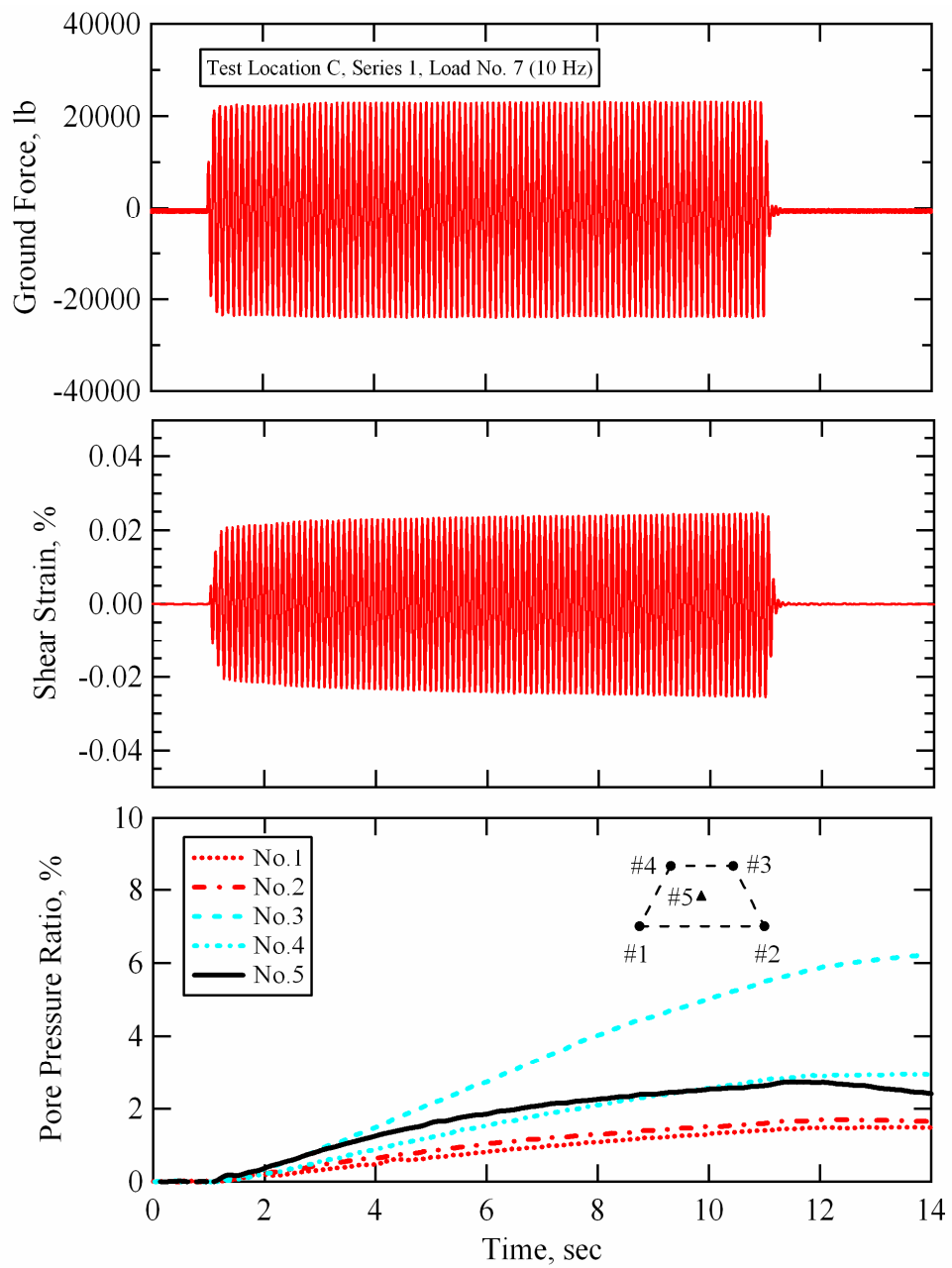


Figure 8-15 Force applied at the ground surface by T-Rex, shear strain induced at the center of the instrumented soil mass, and pore pressure ratios generated at each sensor location during Series 1, loading stage No. 7; Test Location C, Wildlife Liquefaction Array.

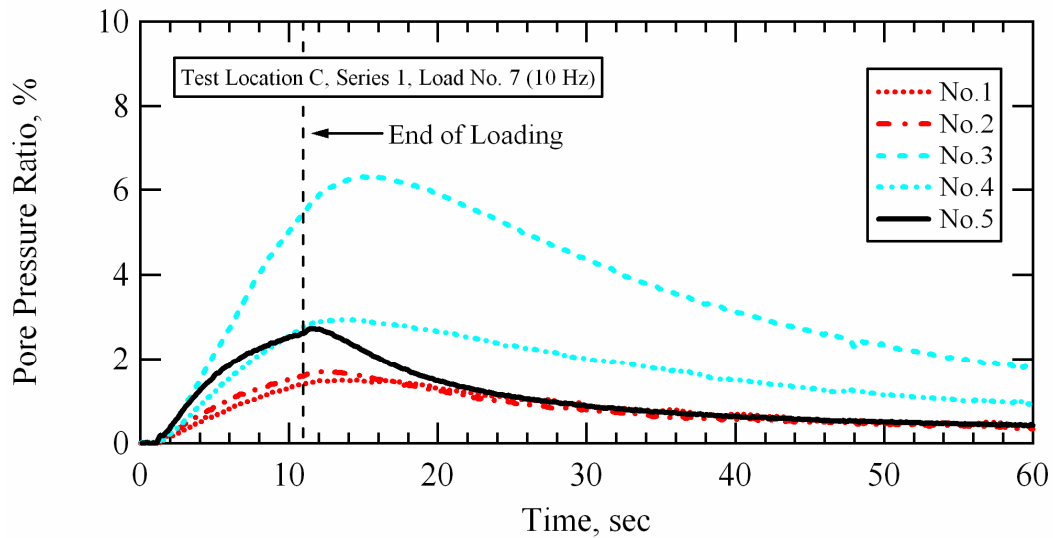


Figure 8-16 Pore pressure ratios generated at each sensor location during Series 1, loading stage No. 7; Test Location C, Wildlife Liquefaction Array.

Sensors No. 3 and No. 4 did not decay as quickly as those recorded by the other sensors. In fact, Sensor No. 3 sensed higher excess pore pressures that continued to build after the end of shaking. It is likely that higher excess pore water pressures generated in the liquefiable material above the sensor array were dissipating downward, thus causing the pressure at Sensor No. 3 to continue to increase and the pressure at Sensor No. 4 to remain elevated for a longer period of time. The soil near Sensor No. 3 may have been more permeable or less stiff, causing it to sense higher pore water pressures during and after loading. Sensor No. 3 also sensed higher pressures during loading stages No. 3 and No. 6. The pore pressure ratios at all sensor locations had dropped below 2% after 50 seconds had passed from the end of loading.

As mentioned previously, the r_u values used to construct the pore pressure generation curves for the site were obtained solely from the PDCR 35/D transducer located at the center of the array (Sensor No. 5). The averaged shear strain values and pore pressure ratios calculated at the center of the liquefaction sensor array for loading stage No. 7 are presented in Table 8-5 as a function of various numbers of loading cycles. After loading stage No. 7, testing was halted for approximately 10 minutes (see Table 8-4) while the excess pore water pressure within the array was allowed to dissipate back to static conditions (monitored by the PDCR 35/D transducer).

8.3.2.8 Loading Stage No. 8

During loading stage No. 8, T-Rex was driven at its maximum output (in shear mode) for 200 cycles of 10-Hz loading. The force applied at the ground surface, the shear strain induced at the center of the liquefaction sensor array, and the pore pressure ratios generated at each PPT location during loading stage No. 8 are shown in Figure 8-17. The ground force during loading stage No. 8 was consistently around 30000 lb (133.4 kN), with some spurious peaks every few cycles as high as 37000 lb (164.6 kN). The shear strain time history is not as uniform as the ones presented for loading stages No. 1 through No. 7. The average shear strain over the first 10 cycles of loading is 0.0357%, while the average shear strain over the first 100 cycles of loading is 0.0451% (see Table 8-5).

The trends in the pore pressure generation within the sensor array during Load No. 8 are similar to those discussed for Load No. 7. The two deeper sensors

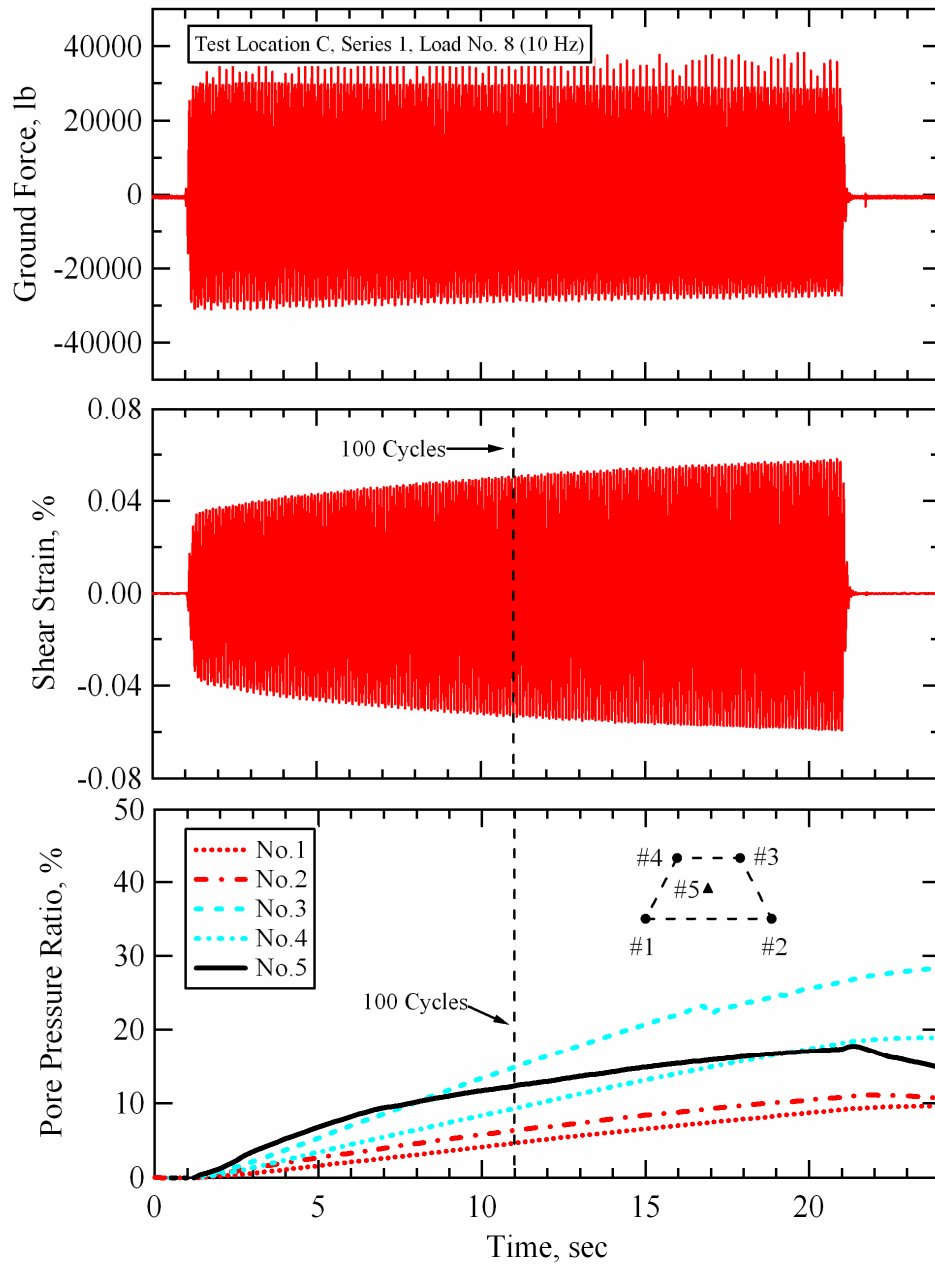


Figure 8-17 Force applied at the ground surface by T-Rex, shear strain induced at the center of the instrumented soil mass, and pore pressure ratios generated at each sensor location during Series 1, loading stage No. 8; Test Location C, Wildlife Liquefaction Array.

(No. 1 and No. 2) recorded similar pressures that leveled off at the end of shaking. The PDCR 35/D transducer (Sensor No. 5) recorded pressures steadily increased throughout dynamic loading. However, the rate of pore pressure generation was greatest during the first 50 cycles of applied load. Sensor No. 5 recorded excess pore pressures equivalent to pore pressure ratios of about 12% and 17% at the end of 100 and 200 cycles of loading, respectively (see Table 8-5). At the end of dynamic loading the pore pressures recorded by Sensor No. 5 rapidly began to dissipate. Once again, the two shallower sensors (No. 3 and No. 4) recorded different magnitudes of excess pore water pressure, with Sensor No. 3 sensing higher pressures. Pore pressure data was recorded for approximately 90 seconds during loading stage No. 8. Figure 8-18 shows the pore pressure ratios measured at each sensor location with a time scale of 90 seconds. Similar to loading stage No. 7 (see Figure 8-16), the pore pressures recorded by Sensors No. 3 and No. 4 did not decay as quickly as those recorded by the other sensors. It is likely that higher excess pore water pressures generated in the liquefiable material above the sensor array were dissipating downward, thus causing the pressure at Sensors No. 3 and No. 4 to remain elevated for a longer period of time. The soil near Sensor No. 3 may have been more permeable or less stiff, causing it to sense higher pore water pressures during and after loading. Sensor No. 3 also sensed higher pressures during loading stages No. 3, No. 6 and No.7. The pore pressure ratios at all sensor locations had dropped below approximately 5% after 70 seconds had passed from the end of loading.

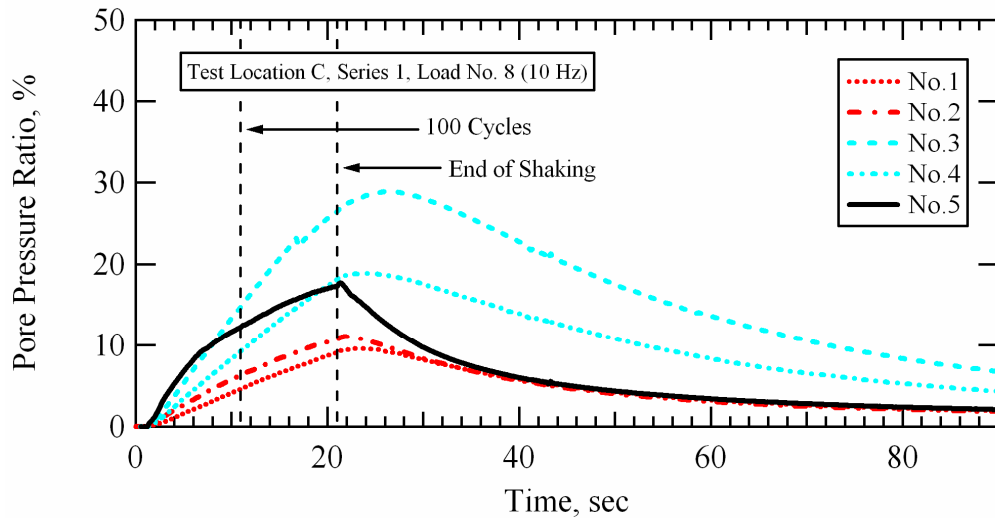


Figure 8-18 Pore pressure ratios generated at each sensor location during Series 1, loading stage No. 8; Test Location C, WLA.

8.3.3 Pore Pressure Generation Curves; Loading Series 1

Pore pressure generation curves for this series of testing can readily be constructed from the data presented in Table 8-5 using any of the given numbers of loading cycles. Figure 8-19 shows the pore pressure generation curves for 10, 20, 50, and 100 cycles of loading determined at Test Location C during staged dynamic loading Series 1. The cyclic threshold shear strain (γ_t^e) depends on the number of cyclic shear strain cycles (n) and ranges from 0.01% for $n = 100$ to 0.02% for $n = 10$. Multiple data points between 0.001% and 0.01% confirm the lack of excess pore pressure generation below γ_t^e . As expected, the data shows that for a given cyclic shear strain above γ_t^e , higher pore pressures are generated with increasing numbers of loading cycles.

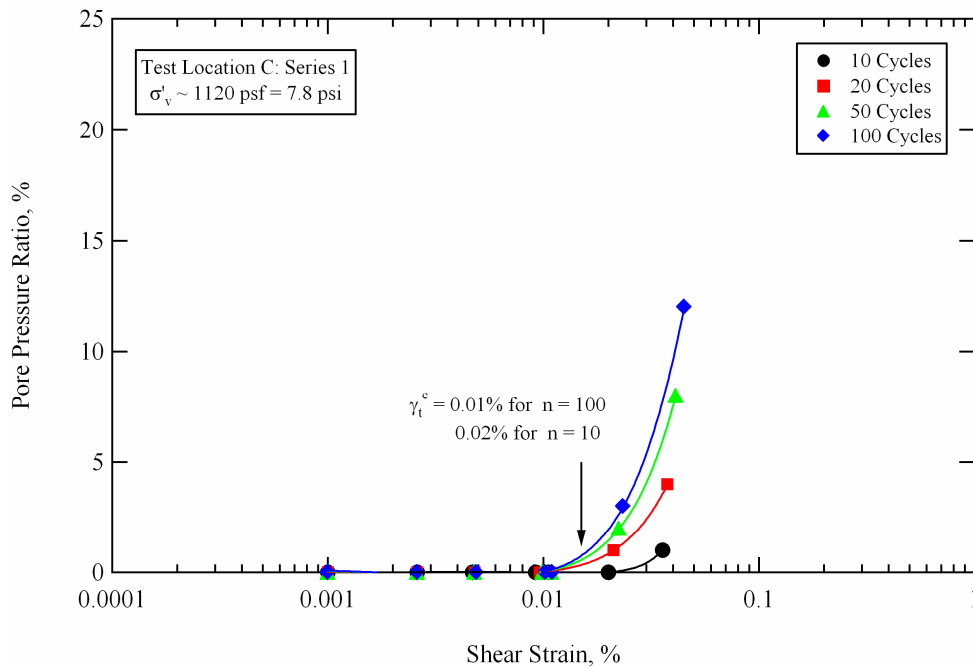


Figure 8-19 Pore pressure generation curves obtained from in-situ liquefaction tests conducted during staged dynamic loading Series 1 at Test Location C, Wildlife Liquefaction Array.

Figure 8-20 compares the in-situ pore pressure generation curves determined for Test Location C during staged dynamic loading Series 1 with Dobry's pore pressure generation model for liquefiable soils from the Wildlife Site (Vucetic and Dobry, 1986). As discussed in Section 7.3.1.3, Dobry's model for Wildlife liquefiable soils was developed from cyclic laboratory test results. A cyclic threshold shear strain of 0.02% was assumed for the model (based on experience gained from previous laboratory tests) because the laboratory tests conducted in the study were not performed at shear strains that were low enough to actually determine the cyclic threshold. This cyclic threshold shear strain was assumed to be the same for any given number of loading cycles. The cyclic tests

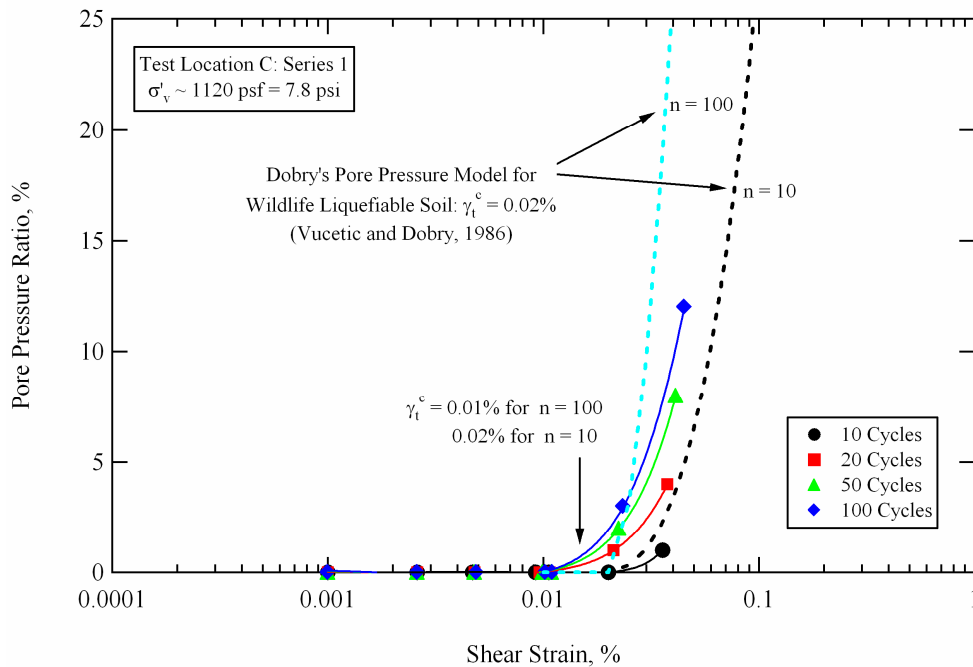


Figure 8-20 Comparison between Dobry's pore pressure generation model (Vucetic and Dobry, 1986) and pore pressure generation curves obtained from in-situ liquefaction tests conducted during staged dynamic loading Series 1 at Test Location C, Wildlife Liquefaction Array.

used to develop the model for Wildlife soils employed up to 30 cycles of strain-controlled loading. The assumed cyclic threshold value is equivalent to the $n = 10$ cyclic threshold shear strain determined from in-situ liquefaction tests conducted during staged loading Series 1. In Figure 8-20, Dobry's pore pressure generation model is shown for 10 loading cycles ($n = 10$) and for 100 loading cycles ($n = 100$), as calculated using Equation 7-1. The in-situ test results indicate a slightly lower threshold shear strain for 20, 50 and 100 cycles of loading. However, the in-situ results generally fall within the range predicted by Dobry's model. Because the pore pressure ratios induced at the center of the liquefaction sensor

array during Series 1 tests were less than 15%, the pore pressure generation curves presented in Figures 8-19 and 8-20 are shown with a maximum pore pressure ratio scale of 25%. For perspective purposes, Figure 8-21 presents the pore pressure generation curves with a maximum pore pressure ratio scale of 100%.

It should be noted here, that to an unknown extent, the pore pressures being generated over a finite loaded area during in-situ liquefaction tests are simultaneously redistributing inside of, and dissipating away from, the loaded area. Given that the material is saturated, it is unlikely that the pore water pressure can dissipate very much over the short duration of cyclic loading. Additionally, the shear stresses applied at the ground surface by T-Rex are spreading over a larger and larger area with depth. Therefore, the loaded area at depth is greater than the 7.5-ft by 7.5-ft (2.3-m by 2.3-m) base plate area. It has already been shown that the horizontal, in-line particle motions at a given depth below the ground surface are virtually identical at all locations under the base plate (see Section 6.5). It would not be surprising if this was also true for some distance past the edges of the base plate.

During laboratory tests, pore pressure generation is measured on a very small specimen where the boundary conditions are carefully controlled (i.e. no pore pressure dissipation is allowed). The only exception to this is when membrane penetration occurs on coarse-grained soils, thus allowing some volume change when pore pressures begin to generate. Conversely, an earthquake simultaneously loads an immense area with varying soil stiffnesses, permeabilities, and anomalies

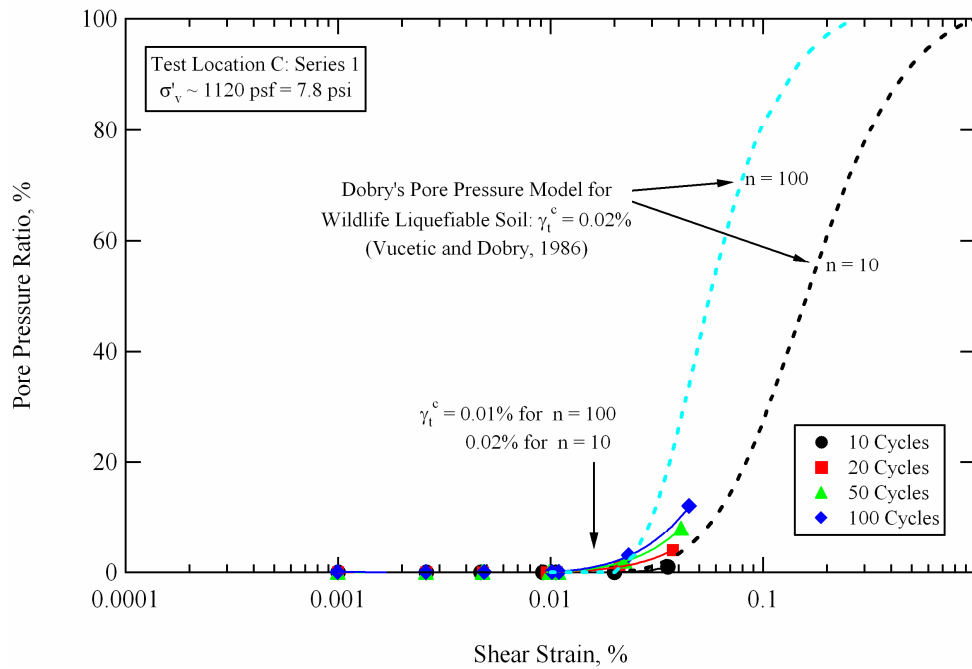


Figure 8-21 Full pore pressure ratio scale comparison between Dobry's pore pressure generation model (Vucetic and Dobry, 1986) and pore pressure generation curves obtained from in-situ liquefaction tests conducted during staged dynamic loading Series 1 at Test Location C, Wildlife Liquefaction Array.

(i.e. cracks that allow venting to the ground surface) that affect the buildup, redistribution, and dissipation of pore water pressures during and after shaking. For a given induced shear strain level, it is likely that laboratory tests yield the highest pore pressure generation, followed by actual earthquakes, followed by the in-situ liquefaction tests. However, these differences are unquantifiable at this time.

8.3.4 Evaluation of Nonlinear Shear Modulus; Loading Series 1

The nonlinear shear modulus of the soil within the liquefaction sensor array at Test Location C was obtained for each staged loading of Series 1 using the average cycle-by-cycle, vertically propagating, horizontally polarized, shear wave velocities ($V_{S,vh}$) determined according to the procedure detailed in Section 6.5. The cycle-by-cycle $V_{S,vh}$ values determined for loading stage No. 1 are shown in Figure 8-22. The average 100-cycle shear strain induced during this load was 0.001% (see Table 8-5). The individual velocity values tend to vacillate up and down. This behavior is attributed to the epistemic uncertainty associated with evaluating the phase difference between receiver pairs. Despite this fact, the mean value remains essentially constant throughout loading. This is not surprising as the strain induced during this test is below the cyclic threshold strain, where theoretically, no modulus degradation should occur. The average 100-cycle shear wave velocity during loading stage No. 1 was determined to be 425 fps (130 m/sec) with a standard deviation (σ) of 14 fps (4.3 m/sec).

In general, the mean $V_{S,vh}$ values were quite consistent for the loads in Series 1 where the induced shear strains were less than the cyclic threshold strain. Even during loading stage No. 7, for which the average 100-cycle shear strain (0.0234%; see Table 8-5) was very close to the cyclic threshold strain, a fairly consistent mean value was found. The cycle-by-cycle $V_{S,vh}$ values determined for loading stage No. 7 are shown in Figure 8-23. The average 100-cycle shear wave velocity during loading stage No. 7 was determined to be 384 fps (117 m/sec) with a standard deviation (σ) of 15 fps (4.6 m/sec). It appears that, as long as the

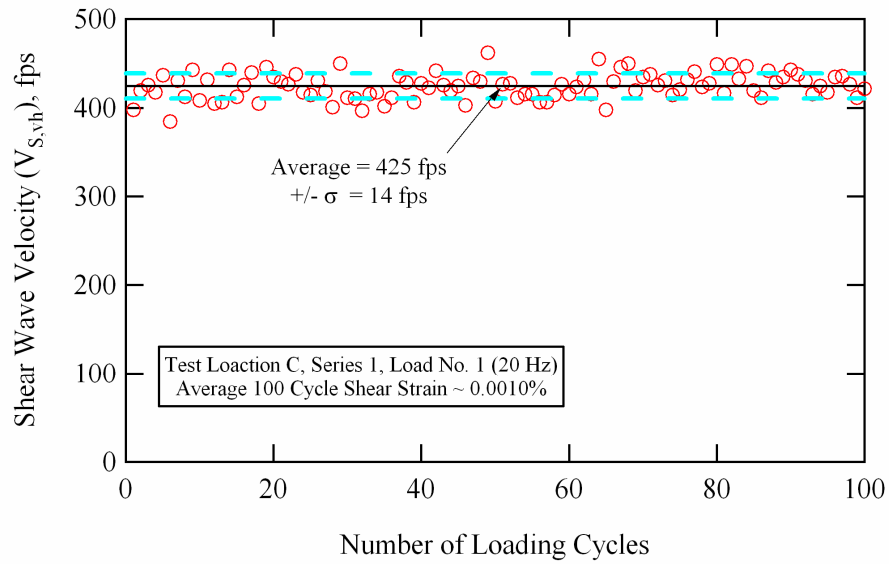


Figure 8-22 Cycle-by-cycle shear wave velocities from loading stage No. 1 ($\gamma \sim 0.0010\%$) of staged dynamic loading Series 1 at Test Location C, Wildlife Liquefaction Array.

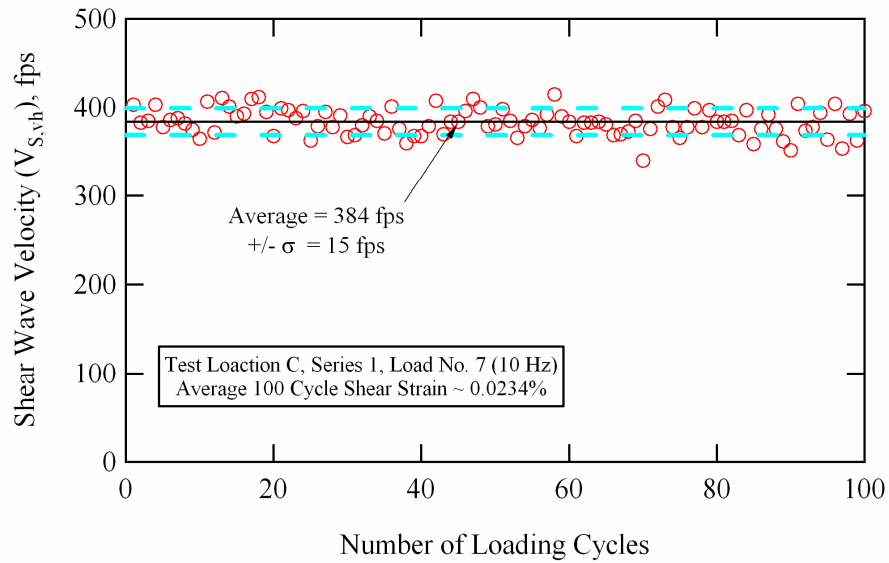


Figure 8-23 Cycle-by-cycle shear wave velocities from loading stage No. 7 ($\gamma \sim 0.0234\%$) of staged dynamic loading Series 1 at Test Location C, Wildlife Liquefaction Array.

shear strain induced in the array is less than the cyclic threshold shear strain, the greater the number of loading cycles included in the average $V_{S,vh}$ calculation the lower the epistemic uncertainty in the estimates. Therefore, for loading stages No. 1 through No. 7, the $V_{S,vh}$ values were all obtained by averaging over 100 cycles of loading. The average 100-cycle $V_{S,vh}$ values and standard deviations determined for loading stages No. 1 through No. 7 are given in Table 8-6. The shear modulus (G) values calculated from these velocities are also given.

The $V_{S,vh}$ values obtained from loading stage No. 8, which had an average 100 cycle shear strain (0.0451%) above the cyclic threshold strain, are shown in Figure 8-24. Loading stage No. 8 had a duration of 200 cycles, thus the $V_{S,vh}$ values for all 200 cycles are shown. The downward trending velocities clearly indicate that modulus degradation is occurring as excess pore pressures are generating within the array. This marked tendency appears to overshadow some of the epistemic uncertainty in the calculations because the cycle-by-cycle velocities are more tightly grouped. In fact, as the soil softens, the phase difference between receivers increases, thus allowing a more accurate determination of the velocity. It is possible to track the cyclic degradation of the shear modulus within the array by averaging these velocities over various numbers of loading cycles. The $V_{S,vh}$ values and standard deviations determined from averaging over 10, 20, 50, 100, 150 and 200 cycles of loading during loading stage No. 8 are given in Table 8-7. The shear modulus (G) values calculated from these velocities are also given.

Table 8-6 Average 100-cycle shear strains, shear wave velocities and shear moduli obtained from loading stages No. 1 through No. 7 of staged loading Series 1 at Test Location C, Wildlife Liquefaction Array

| Staged Loading Series 1, Test Location C, Wildlife Liquefaction Array | | | | |
|---|--|---|-----------|--------------------------------------|
| Loading Stage No. | 100 Loading Cycles | | | |
| | Shear Strain ¹ , γ (%) | Shear Wave Velocity ² , $V_{S,vh}$ (fps) | | Shear Modulus ³ , G (psf) |
| | Average | Average | Std. Dev. | from Avg. $V_{S,vh}$ |
| 1 | 0.0010 | 425 | 14 | 673137 |
| 2 | 0.0049 | 406 | 15 | 614296 |
| 3 | 0.0110 | 385 | 12 | 552391 |
| 4 | 0.0010 | 404 | 24 | 608258 |
| 5 | 0.0026 | 404 | 14 | 608258 |
| 6 | 0.0102 | 376 | 20 | 526867 |
| 7 | 0.0234 | 384 | 15 | 549525 |

- Notes: 1. γ calculated at the center of the array and averaged over 100 loading cycles
 2. $V_{S,vh}$ values averaged over 100 loading cycles
 3. G values obtained from $V_{S,vh}$ values using $\rho = (120 \text{ psf}) / (32.2 \text{ ft/sec}^2)$

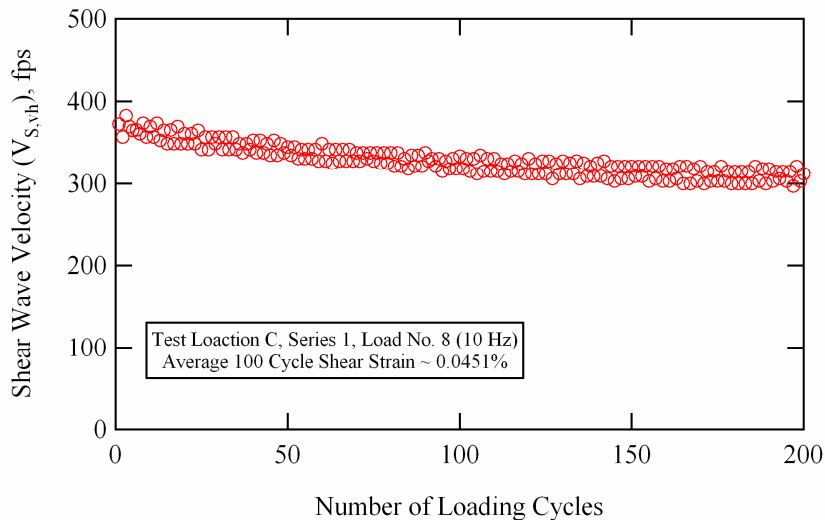


Figure 8-24 Cycle-by-cycle shear wave velocities from loading stage No. 8 ($\gamma \sim 0.0451\%$) of staged dynamic loading Series 1 at Test Location C, Wildlife Liquefaction Array.

Table 8-7 Shear strains, shear wave velocities and shear moduli obtained from averaging over various numbers of cycles during loading stage No. 8 of staged loading Series 1 at Test Location C, Wildlife Liquefaction Array

| Staged Loading Series 1, Test Location C, Wildlife Liquefaction Array | | | | |
|---|--|---|-----------|--------------------------------------|
| Number of Cycles | Loading Stage No. 8 | | | |
| | Shear Strain ¹ , γ (%) | Shear Wave Velocity ² , $V_{S,vh}$ (fps) | | Shear Modulus ³ , G (psf) |
| | Average | Average | Std. Dev. | from Avg. $V_{S,vh}$ |
| 10 | 0.0357 | 368 | 8 | 504686 |
| 20 | 0.0376 | 363 | 10 | 491065 |
| 50 | 0.0412 | 354 | 12 | 467016 |
| 100 | 0.0451 | 343 | 15 | 438443 |
| 150 | 0.0479 | 335 | 17 | 418230 |
| 200 | 0.0501 | 329 | 19 | 403383 |

- Notes: 1. γ calculated at the center of the array and averaged over the given number of loading cycles
 2. $V_{S,vh}$ values averaged over the given number of loading cycles
 3. G values obtained from $V_{S,vh}$ values using $\rho = (120 \text{ psf})/(32.2 \text{ ft/sec}^2)$

It is uncertain whether or not averaging the $V_{S,vh}$ values over a given number of loading cycles is the best method to characterize the nonlinear behavior of the soil once modulus degradation begins. However, the shear strains during loading stage No. 8 are not uniform (see Figure 8-17) and must be averaged over a given cyclic interval. Therefore, there is some uncertainty as to exactly what equivalent shear strain and number of loading cycles produced the measured degraded shear modulus. The only other option would be to pair the shear strain averaged over a given number of loading cycles with the un-averaged degraded modulus value measured at the end of the given number of loading cycles (similar to what is done when constructing pore pressure generation curves).

The 100-cycle shear modulus (G) values for loading stages No. 1 through No. 7 of dynamic loading Series 1 are plotted in Figure 8-25. The G values for loading stage No. 8 obtained over 10, 20, 50 and 100 cycles of loading are also shown. The G values for loading stage No. 8 obtained over 150 and 200 cycles of loading are not plotted because the maximum number of loading cycles in all other tests was only 100. Because the shear strains induced during loading stage No. 8 are beyond the cyclic threshold strain, the modulus values decay due to combined effects of nonlinearity (i.e. the shear strain is increasing with increasing number of loading cycles) and degradation (i.e. the pore pressure is increasing with increasing number of loading cycles). The two loads with the smallest induced shear strains were loading stage No. 1 (20 Hz) and loading stage No. 4 (10 Hz). Both of these loads induced shear strains in the instrumented soil mass very close to 0.001% (see Table 8-6). The G values obtained from loading stage No.1 are slightly larger than those obtained from loading stage No. 4. The 100-cycle modulus values from both loads were averaged together to obtain the small-strain normalizing shear modulus ($G_{\max} = 640698 \text{ psf} = 30.6 \text{ MPa}$).

For comparison purposes, the small-strain shear modulus values obtained from the crosshole tests conducted between the top and bottom sensor pairs in the liquefaction sensor array prior to staged dynamic loading (see Table 8-3) are also shown in Figure 8-22. The small-strain modulus values obtained from $V_{S,vh}$ during staged dynamic testing fall within the small-strain modulus range obtained using $V_{S,hv}$ values from crosshole tests. However, it is not expected that these two test methods would produce the exact same results due to: (1) material anisotropy,

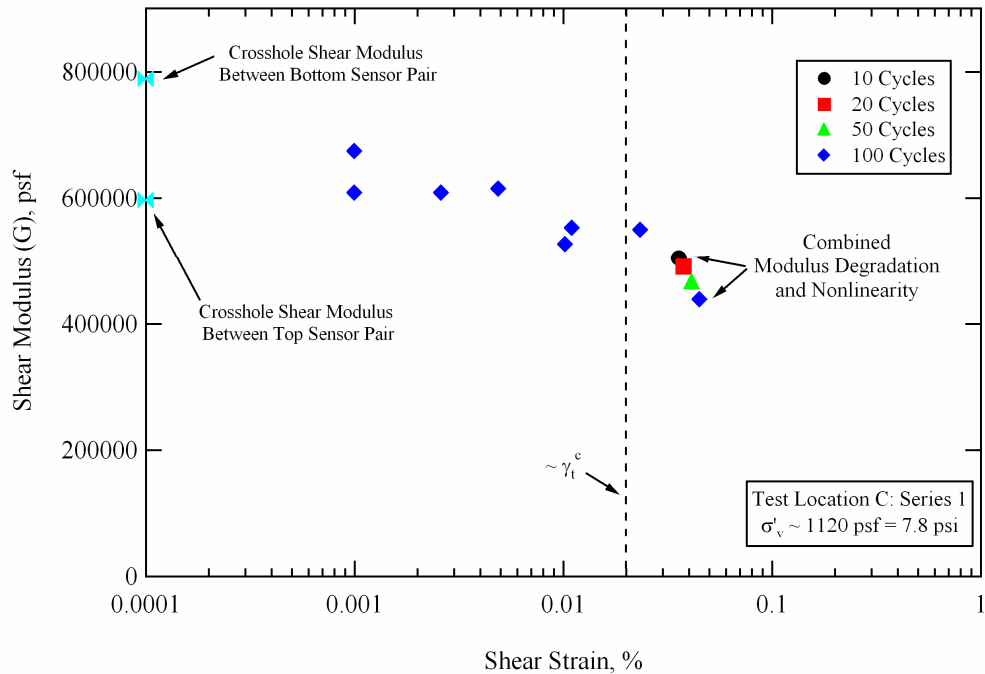


Figure 8-25 Shear modulus values (G) calculated from the data collected during staged dynamic loading Series 1 at Test Location C, Wildlife Liquefaction Array.

(2) the use of substantially different wavelengths (i.e. 20- to 40-ft wavelengths during staged dynamic testing vs. approximately 0.5 to 1.0-ft wavelengths during crosshole tests), and (3) the sampling of different volumes of material (i.e. the crosshole test samples a smaller volume of material and the waves will tend to find the stiffest (fastest) path between receivers). It is therefore believed that the small-strain modulus obtained from staged dynamic loading is the proper modulus with which to normalize the other staged loading moduli.

The normalized shear modulus (G/G_{\max}) values determined from the staged dynamic loads in Series 1 are shown in Figure 8-26. With the exception of

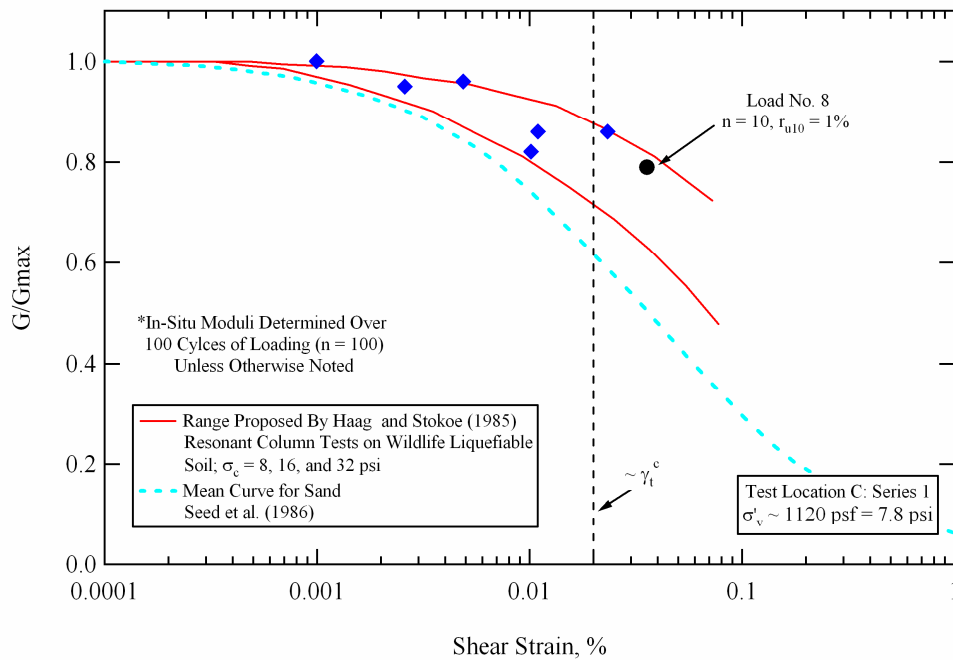


Figure 8-26 Normalized shear modulus (G/G_{max}) – $\log \gamma$ relationship calculated from the data collected during staged dynamic loading Series 1 at Test Location C, Wildlife Liquefaction Array.

the highest shear strain data point (from loading stage No. 8), all of the normalized modulus values were obtained using the moduli calculated from averaging over 100 cycles of loading. As mentioned above, the modulus values during loading stage No. 8 decay with increasing number of cycles due to combined nonlinearity and degradation. During loading stage No. 8, a pore pressure ratio of only 1% had been induced in the soil after 10 cycles of loading (see Table 8-5). Therefore, it is believed that the modulus value obtained from the first 10 cycles of loading only reflects the nonlinearity of the soil and contains no measurable degradation from pore water pressure generation. For comparison purposes, the range of modulus reduction curves determined by Haag and Stokoe

(1985) for Wildlife liquefiable soil, and the mean modulus reduction curve proposed by Seed et al. (1986) for sands, are also shown. The in-situ values agree very well with the range proposed by Haag and Stokoe (1985). It is not surprising that the Wildlife liquefiable soils behave more linearly than the mean curve for sand, as they contain significant amounts of non-plastic fines (i.e. on average between 27 and 49%; see Section 7.6) with approximately 10% clay-size particles.

Reductions in shear modulus from the combined effects of nonlinearity and degradation due to pore water pressure generation were observed in the data recorded during loading stage No.8. The G/G_{\max} values for various numbers of loading cycles during stage No. 8 are shown in Figure 8-27. During loading stage No. 8, the pore pressure ratio and average shear strain induced in the instrumented soil mass after 10 cycles of loading were 1% and 0.0357%, respectively (see Table 8-5). After 20 cycles of loading, the pore pressure ratio and average shear strain had increased to 4% and 0.0376%, respectively. After 50 cycles of loading, the pore pressure ratio and average shear strain had increased to 8% and 0.0412%, respectively. Finally, after 100 cycles of loading, the pore pressure ratio and average shear strain had increased to 12% and 0.0451%, respectively. Using the 10-cycle modulus value as a reference point, it is possible to try to predict the decrease in modulus for any of the other numbers of loading cycles by knowing the change in shear strain and the change in pore pressure ratio.

The procedure used to try to predict the 100-cycle normalized shear modulus (G/G_{\max}) obtained during loading stage No. 8 from the 10-cycle G/G_{\max}

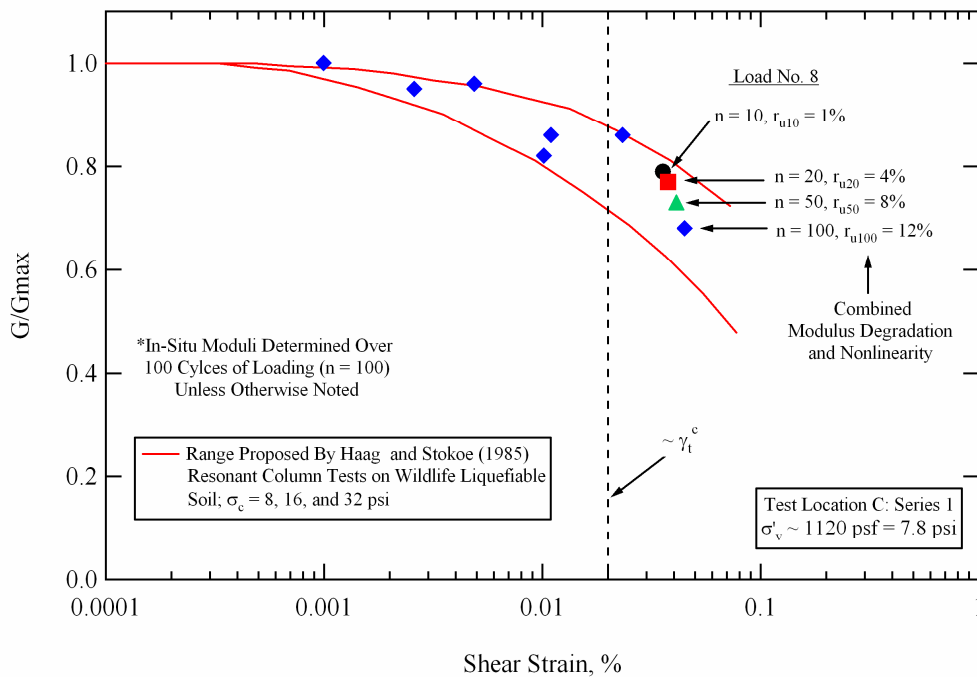


Figure 8-27 Normalized shear modulus values (G/G_{max}) resulting from the combined effects of modulus nonlinearity and modulus degradation due to excess pore water pressure generation during loading stage No. 8 of Series 1 at Test Location C, Wildlife Liquefaction Array.

value is depicted in Figure 8-28. The 10-cycle G/G_{max} value is equal to 0.79. The 100-cycle G/G_{max} value is equal to 0.68. The generation of excess pore water pressure reduces the effective stress within the soil deposit, thereby reducing the soil stiffness. The degradation in shear modulus due to pore pressure generation is typically accounted for by reducing the soil shear modulus according to a function that takes into account the change in effective stress within the soil deposit do to pore water pressure generation. The following equation is typically used:

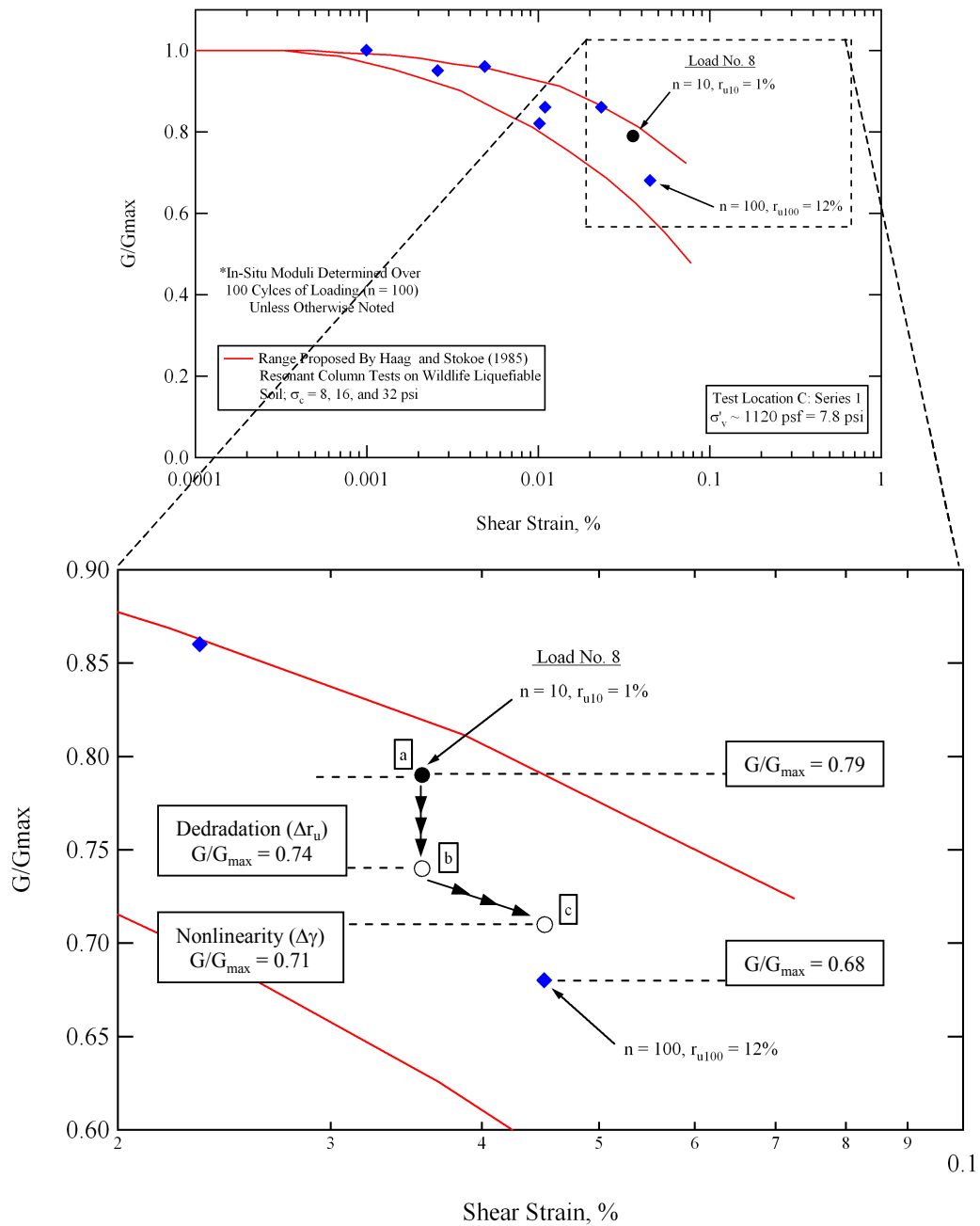


Figure 8-28 Illustration of the process used to try to predict the 100-cycle normalized shear modulus value obtained during loading stage No.8 from the 10-cycle normalized shear modulus value obtained during loading stage No. 8.

$$G_d = G_o \cdot \left[\frac{\sigma'_v}{\sigma'_{vo}} \right]^{0.5} \dots\dots\dots(8-1)$$

where G_d = the degraded shear modulus at a given shear strain level do to excess pore water pressure generation; G_o = the initial shear modulus at a given strain level; σ'_v = the vertical effective stress acting on the soil after excess pore pressure generation; and σ'_{vo} = the initial vertical effective stress acting on the soil.

In Figure 8-25, the 10-cycle G/G_{max} value (0.79) is considered as G_o , and is marked by point (a). During loading stage No. 8, a pore pressure ratio of 12% was induced in the soil after 100 cycles of loading (i.e. the effective stress was reduced by 12%). Therefore, according to Equation 8-1, G_o should be multiplied by a factor of 0.94 to obtain an estimate for G_d . In Figure 8-28, G_d is marked by point (b), which has a G/G_{max} value equal to 0.74. This reduction in shear modulus accounts for the theoretical degradation due to the pore water pressure generation after 100 loading cycles. There is also a difference in the induced shear strain between the 10-cycle G/G_{max} and 100-cycle G/G_{max} moduli. As a result, the nonlinearity in the soil shear modulus between these points must also be accounted for. The nonlinearity can be accounted for by moving between the 10-cycle shear strain value and the 100-cycle shear strain value along a route parallel to the upper-bound curve proposed by Haag and Stokoe (1985). . In Figure 8-28, this route is identified as the path between point (b) and point (c). At point (c), the G/G_{max} value is approximately 0.71. Therefore, the modulus

estimated by taking into account the combined effects of nonlinearity and degradation due to excess pore pressure generation is just slightly greater than the actual 100-cycle G/G_{\max} value of 0.68.

This same process can be repeated for other stage No. 8 loading cycles using the pore pressure ratio, shear strain, and shear modulus values provided in Tables 8-5 and 8-7. The loading stage No. 8 20-, 50-, 100-, 150- and 200-cycle measured G/G_{\max} values and predicted G/G_{\max} values (after taking into account the combined effects of degradation and nonlinearity) are given in Table 8-8. The differences between the measured and predicted values are also given. In general, the G/G_{\max} values predicted from the 10-cycle G/G_{\max} values by taking into account the combined effects of degradation and nonlinearity are slightly greater than the measured G/G_{\max} values. However, even after 200 cycles of loading, the predicted G/G_{\max} value is only 0.04 (absolute) greater than the measured G/G_{\max} value.

8.3.5 Link Between u - and G -log γ -N Relationships; Loading Series 1

The pore pressure generation characteristics and the nonlinear shear modulus behavior of a liquefiable soil deposit are inseparably linked. Therefore, it is beneficial to view these two types of data in the same figure. The pore pressure generation curves and normalized nonlinear soil shear modulus values obtained during Series 1 staged dynamic loading at Test Location C are presented together in Figure 8-29. The shear modulus of the soil exhibits nonlinearity once shear strains greater than the elastic threshold shear strain (γ_i^e) have been induced in the soil deposit. The in-situ modulus results and the upper-bound curve by

Table 8-8 Measure G/G_{\max} values and predicted G/G_{\max} values obtained from taking into account the combined effects of modulus degradation and nonlinearity after 20, 50, 100, 150 and 200 cycles of loading during stage No. 8 of staged loading Series 1 at Test Location C, Wildlife Liquefaction Array

| Staged Loading Series 1, Test Location C, Wildlife Liquefaction Array | | | | |
|---|---|--|---|---|
| Number of Cycles | Loading Stage No. 8; 10-cycle $G/G_{\max} = 0.79$ | | | |
| | Measured G/G_{\max} | Predicted G/G_{\max} After Degradation | Predicted G/G_{\max} After Nonlinearity | Final Difference in G/G_{\max} Predicted - Measured |
| 20 | 0.77 | 0.77 | 0.77 | 0.00 |
| 50 | 0.73 | 0.76 | 0.74 | 0.01 |
| 100 | 0.68 | 0.74 | 0.71 | 0.03 |
| 150 | 0.65 | 0.73 | 0.69 | 0.04 |
| 200 | 0.63 | 0.72 | 0.67 | 0.04 |

Haag and Stokoe (1985) indicate that the elastic threshold shear strain is close to 0.002%. The soil does not generate excess pore water pressure until shear strains greater than the cyclic threshold shear strain (γ_t^c) have been induced in the soil. The in-situ pore pressure generation curves indicate that the cyclic threshold shear strain (γ_t^c) depends on the number of cyclic shear strain cycles (n) and ranges from 0.01% for n = 100 to 0.02% for n = 10. For the in-situ results shown in Figure 8-29, noticeable shear modulus degradation due to pore pressure generation did not occur until pore pressure ratios of a least 4% were generated at the center of the instrumented soil mass. As discussed previously, the shear moduli from loading stage No. 7 did not show any noticeable degradation with increasing numbers of loading cycles even though the pore pressure ratio at the center of the array had reached a value of 3% by the end of 100 cycles of loading.

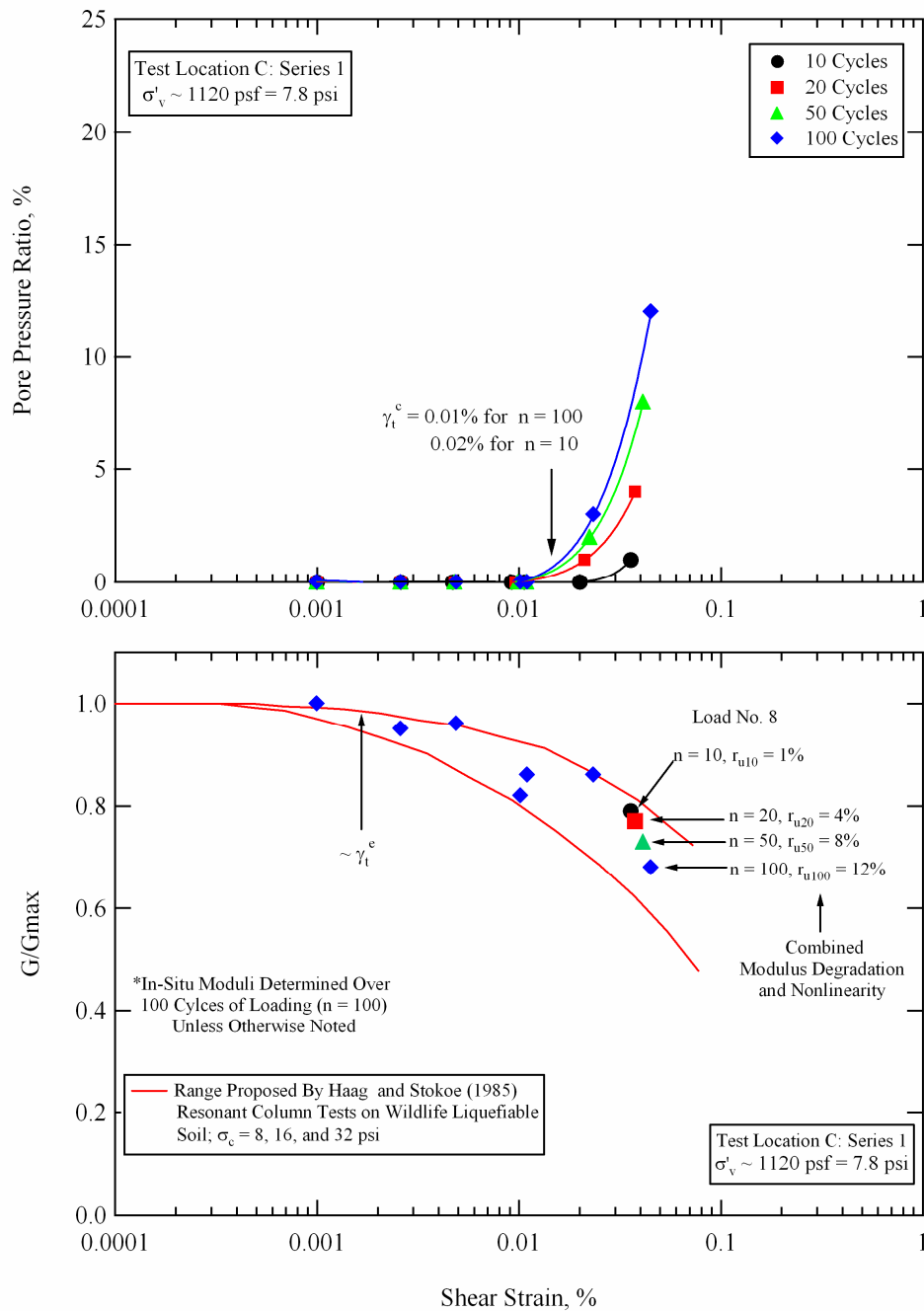


Figure 8-29 Pore pressure generation curves and nonlinear soil shear modulus values obtained during Series 1 staged dynamic loading at Test Location C, Wildlife Liquefaction Array (WLA).

8.4 TEST C: STAGED DYNAMIC LOADING SERIES 2

The in-situ liquefaction sensor array at Test Location C was installed on August 16, 2005. The first series (Series 1) of staged dynamic loading was conducted on the afternoon of August 17, and lasted approximately 45 minutes. In-situ liquefaction testing was then stopped until the next day. The pore water pressure transducer (PPT) in each sensor was powered overnight using a 12-volt battery and a DC-to-DC converter to help ensure that the static PPT outputs remained as steady as possible during testing the following day (as discussed in Section 4.3.2). The second series (Series 2) of staged dynamic loading began in the morning of August 18.

8.4.1 Loading Stages in Series 2

In Series 2, eight separate dynamic loading stages were applied to the instrumented soil mass. The dynamic shear loads were applied by driving T-Rex in the horizontal, in-line direction. An external function generator was used to control the frequency, number of cycles, and drive voltage amplitude supplied to T-Rex. Details of the Series 2 staged dynamic loading sequence are provided in Table 8-9. The first three dynamic loads were applied at a frequency of 20 Hz. The last five dynamic loads were applied at a frequency of 10 Hz. All of the loads had a duration of 100 cycles, except Load No. 16, which had a duration of 200 cycles. Previous tests at WLA had shown that higher peak shear strains could be induced in the soil deposit at a frequency of 10 Hz than at a frequency of 20 Hz. However, T-Rex has more harmonic distortion when operating at 10 Hz than at 20 Hz. As discussed in Section 6.5, harmonic distortion in the ground motion

Table 8-9 Details of the Series 2 staged dynamic loading sequence conducted at Test Location C, Wildlife Liquefaction Array (WLA)

| Time on 8/18/2005 | Dynamic Load Number | Function Generator Drive Signal | | | Approximate Ground Force (lb) |
|-------------------|---------------------|---------------------------------|------------------|-------------------|-------------------------------|
| | | Frequency (Hz) | Number of Cycles | Amplitude (volts) | |
| 8:16 AM | 9 | 20 | 100 | 0.4 | 2000 |
| 8:23 AM | 10 | 20 | 100 | 0.8 | 5000 |
| 8:28 AM | 11 | 20 | 100 | 1.5 | 10000 |
| 8:37 AM | 12 | 10 | 100 | 0.4 | 2000 |
| 8:40 AM | 13 | 10 | 100 | 0.8 | 5000 |
| 8:45 AM | 14 | 10 | 100 | 1.5 | 15000 |
| 8:52 AM | 15 | 10 | 100 | 2.5 | 25000 |
| 9:02 AM | 16 | 10 | 200 | 5 | 30000 |

signals recorded during testing complicates the evaluation of the nonlinear shear modulus of the soil. Therefore, tests were conducted at 20 Hz with the goal of being able to more accurately resolve the nonlinear shear modulus behavior, and at 10 Hz to generate shear strains as large as possible within the instrumented soil mass. However, to avoid loading the soil beyond its cyclic threshold strain (γ_t^c), the 20-Hz loads were only carried to the point where a minute amount of excess pore water pressure was generated at the center of the liquefaction sensor array (i.e. $r_u < 1\%$). At this point, the loading frequency was decreased to 10 Hz, the drive amplitude was dropped back down to a low level, and staged dynamic loading was begun again.

Shear strains (γ) induced in the instrumented soil mass were calculated at the center of the liquefaction sensor array for every stage of dynamic loading

using the 4-node, isoparametric finite element formulation presented in Section 6.3. Dynamic in-situ liquefaction tests are not strictly stress-controlled, or strain-controlled tests. Despite this, the shear strain time histories calculated at the center of the array generally have very consistent amplitudes throughout the duration of loading (as presented in Section 8.4.2). However, once significant excess pore water pressures are generated within the array, the strain behavior can become more irregular. Because the shear strain time histories do not always have a constant amplitude, it is necessary to average the shear strain amplitudes over various numbers of loading cycles. The process used to average the cyclic shear strains is detailed in Section 8.3.1 and illustrated in Figure 8-8.

The pore pressure ratios (r_u) at each sensor location were obtained by dividing the measured residual pore water pressure, obtained from processing the raw pore pressure transducer (PPT) records according to the procedure outlined in Section 6.4, by the total vertical effective stress at each sensor location (see Table 8-2). The r_u values used to construct the pore pressure generation curves for each site were obtained solely from the PDCR 35/D transducer located at the center of the array (Sensor No. 5). The r_u values obtained from the miniature PPT's (Sensors No. 1 – No. 4) were only used in a qualitative sense to observe how the pore pressure generation varied within the instrumented soil mass.

The nonlinear shear modulus of the soil within the liquefaction sensor array was obtained for each staged load using the average cycle-by-cycle, vertically propagating (downward), horizontally polarized, shear wave velocities ($V_{S,vh}$) determined according to the procedure detailed in Section 6.5.

8.4.2 Response of the Deposit During Loading Series 2

8.4.2.1 Loading Stage No. 9

The force applied at the ground surface by T-Rex, the shear strain induced at the center of the liquefaction sensor array, and the pore pressure ratios generated at each PPT location during dynamic loading stage No. 9 of staged loading Series 2 are shown in Figure 8-30. The ground force during loading stage No. 9 was less than 2000 lb (8.9 kN) throughout the 100 cycles of 20-Hz loading. This load induced fairly uniform cyclic shear strains at the center of the liquefaction sensor array of approximately 0.0012%. These shear strains did not trigger the generation of any excess pore water pressure in the instrumented soil mass, as indicated by the fact that the pore pressure ratios at each sensor location remained equal to zero.

Tabulated values for the pore pressure ratios and average shear strains (averaged over the given number of loading cycles) induced in the soil during loading stage No. 9 of staged loading Series 2 are provided in Table 8-10. These values are provided for different numbers of total loading cycles for all of the loads applied during Series 2.

8.4.2.2 Loading Stage No. 10

The force applied at the ground surface by T-Rex, the shear strain induced at the center of the liquefaction sensor array, and the pore pressure ratios generated at each PPT location during loading stage No. 10 of staged loading Series 2 are shown in Figure 8-31. The ground force during loading stage No. 10

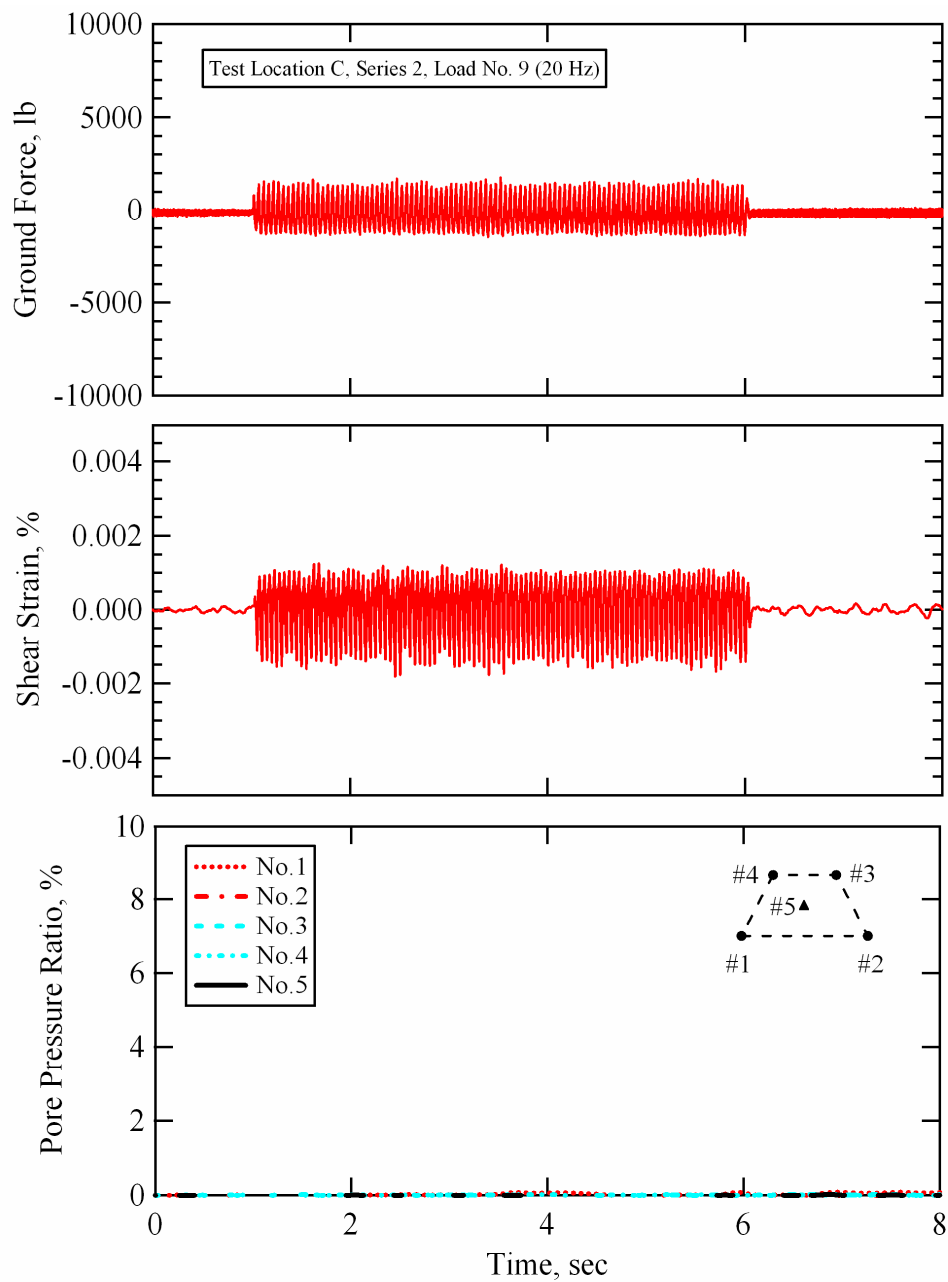


Figure 8-30 Force applied at the ground surface by T-Rex, shear strain induced at the center of the instrumented soil mass, and pore pressure ratios generated at each sensor location during Series 2, loading stage No. 9; Test Location C, Wildlife Liquefaction Array.

Table 8-10 Pore pressure ratios and average shear strains at the center of the liquefaction sensor array for different numbers of loading cycles; Series 2, Test Location C, Wildlife Liquefaction Array

| Number of Cycles | γ or r_u | Pore Pressure Ratio ¹ (r_u) and Average Shear Strain ² (γ) Values, % | | | | | | | |
|------------------|-------------------|---|--------|--------|--------|--------|--------|--------|--------|
| | | Series 2: Staged Load Number | | | | | | | |
| | | No. 9 | No. 10 | No. 11 | No. 12 | No. 13 | No. 14 | No. 15 | No. 16 |
| 10 | γ | 0.0012 | 0.0049 | 0.0123 | 0.0009 | 0.0026 | 0.0084 | 0.0229 | 0.0478 |
| | r_u | 0 | 0 | 0 | 0 | 0 | 0 | 0 | 2 |
| 20 | γ | 0.0012 | 0.0050 | 0.0125 | 0.0009 | 0.0026 | 0.0086 | 0.0249 | 0.0543 |
| | r_u | 0 | 0 | 0 | 0 | 0 | 0 | 0 | 5 |
| 30 | γ | 0.0012 | 0.0050 | 0.0126 | 0.0009 | 0.0026 | 0.0088 | 0.0259 | 0.0580 |
| | r_u | 0 | 0 | 0 | 0 | 0 | 0 | 1 | 8 |
| 40 | γ | 0.0012 | 0.0050 | 0.0126 | 0.0009 | 0.0026 | 0.0089 | 0.0265 | 0.0608 |
| | r_u | 0 | 0 | 0 | 0 | 0 | 0 | 1 | 10 |
| 50 | γ | 0.0012 | 0.0050 | 0.0127 | 0.0009 | 0.0026 | 0.0089 | 0.0271 | 0.0633 |
| | r_u | 0 | 0 | 0 | 0 | 0 | 0 | 1 | 12 |
| 60 | γ | 0.0012 | 0.0050 | 0.0127 | 0.0009 | 0.0026 | 0.0090 | 0.0275 | 0.0655 |
| | r_u | 0 | 0 | 0 | 0 | 0 | 0 | 1 | 14 |
| 70 | γ | 0.0012 | 0.0050 | 0.0127 | 0.0009 | 0.0026 | 0.0090 | 0.0278 | 0.0677 |
| | r_u | 0 | 0 | 0 | 0 | 0 | 0 | 1 | 16 |
| 80 | γ | 0.0012 | 0.0050 | 0.0128 | 0.0009 | 0.0026 | 0.0091 | 0.0281 | 0.0698 |
| | r_u | 0 | 0 | 0 | 0 | 0 | 0 | 1 | 19 |
| 90 | γ | 0.0012 | 0.0050 | 0.0128 | 0.0009 | 0.0026 | 0.0091 | 0.0284 | 0.0722 |
| | r_u | 0 | 0 | 0 | 0 | 0 | 0 | 2 | 21 |
| 100 | γ | 0.0012 | 0.0050 | 0.0128 | 0.0009 | 0.0026 | 0.0092 | 0.0287 | 0.0754 |
| | r_u | 0 | 0 | 0 | 0 | 0 | 0 | 2 | 23 |
| 150 | γ | - | - | - | - | - | - | - | * |
| | r_u | - | - | - | - | - | - | - | 32 |
| 200 | γ | - | - | - | - | - | - | - | * |
| | r_u | - | - | - | - | - | - | - | 32 |

- Notes: 1. r_u from the PDCR 35/D pressure transducer at the center of the array after the given number of loading cycles
2. γ calculated at the center of the array and averaged over the given number of loading cycles
* γ could not accurately be calculated after 100 cycles of loading

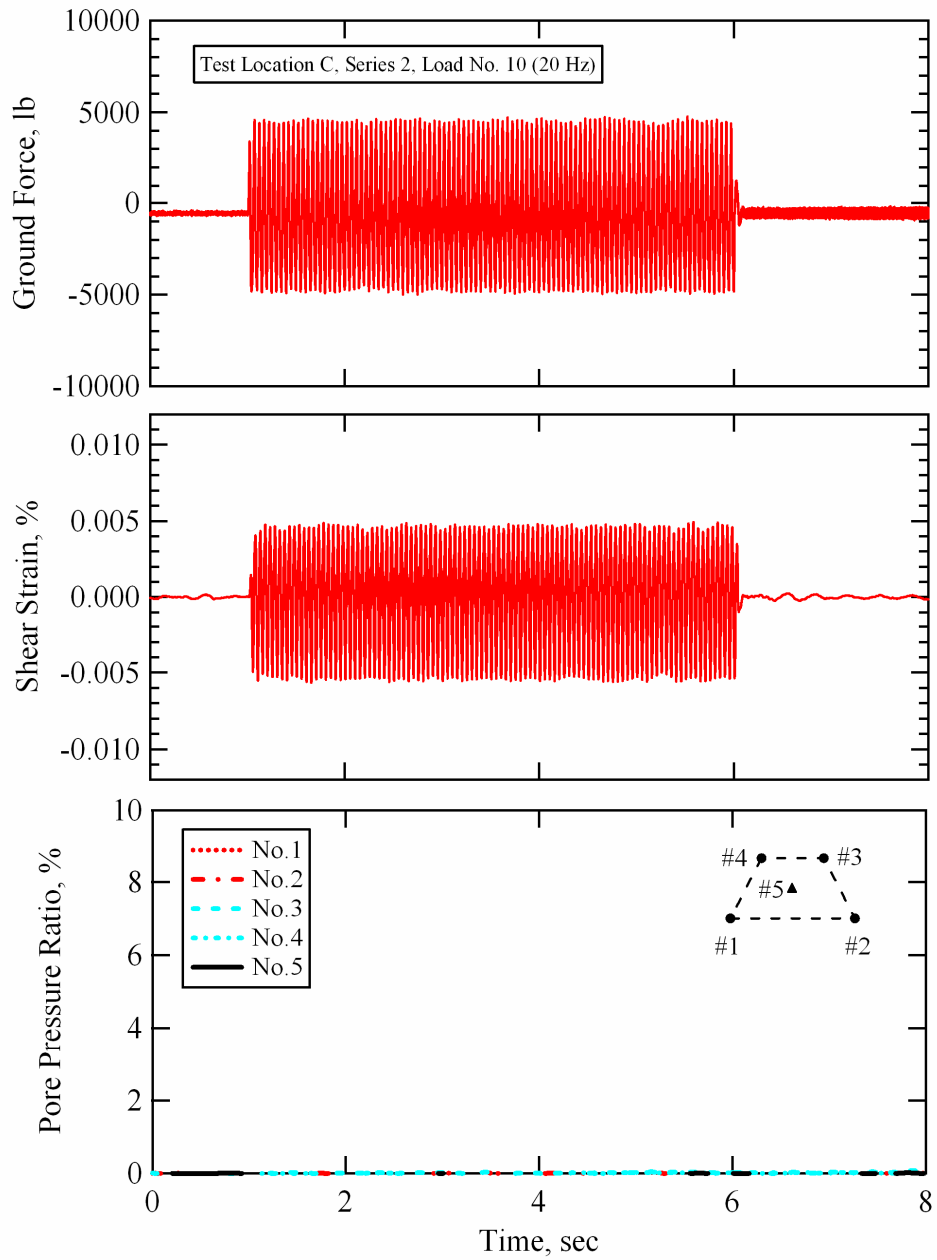


Figure 8-31 Force applied at the ground surface by T-Rex, shear strain induced at the center of the instrumented soil mass, and pore pressure ratios generated at each sensor location during Series 2, loading stage No. 10; Test Location C, Wildlife Liquefaction Array.

was slightly less than 5000 lb (22.2 kN) throughout the 100 cycles of 20-Hz loading. This load induced fairly uniform cyclic shear strains at the center of the liquefaction sensor array of approximately 0.005% (see Table 8-10 for strain values averaged over various numbers of loading cycles). These shear strains did not trigger the generation of any excess pore water pressure in the instrumented soil mass, as indicated by the fact that the pore pressure ratios at each sensor location remained equal to zero.

8.4.2.3 Loading Stage No. 11

The force applied at the ground surface by T-Rex, the shear strain induced at the center of the liquefaction sensor array, and the pore pressure ratios generated at each PPT location during loading stage No. 11 of staged loading Series 2 are shown in Figure 8-32. The ground force during loading stage No. 11 was slightly less than 10000 lb (44.5 kN) throughout the 100 cycles of 20-Hz loading. This load induced fairly uniform cyclic shear strains at the center of the liquefaction sensor array of approximately 0.0128% (see Table 8-10 for strain values averaged over various numbers of loading cycles). A minute amount of excess pore water pressure was generated in the instrumented soil mass during this test. The pore pressure ratio at Sensor No. 3 reached a peak value of less than 1%, while the other transducers indicated pore pressure ratios of less than 0.25%. At this point, testing was halted for approximately 10 minutes (see Table 8-9) while the pore pressures within the array were allowed to dissipate back to their static values (as monitored by the PDCR 35/D transducer). The actual time required for the pressure to return to its static condition was substantially less than

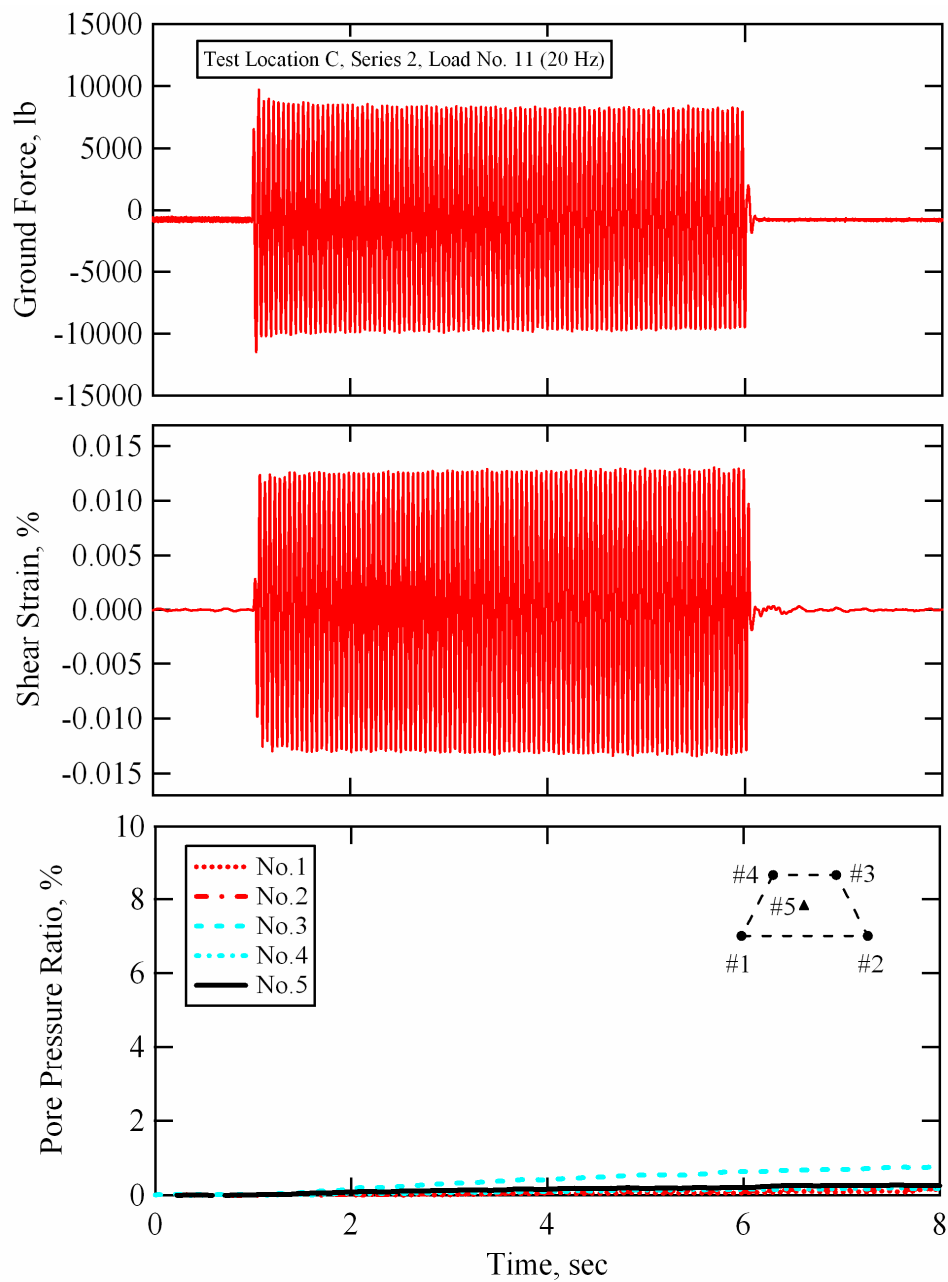


Figure 8-32 Force applied at the ground surface by T-Rex, shear strain induced at the center of the instrumented soil mass, and pore pressure ratios generated at each sensor location during Series 2, loading stage No. 11; Test Location C, Wildlife Liquefaction Array.

the allotted time. After dynamic Load No. 11, the loading frequency was decreased to 10 Hz, the drive amplitude was dropped back down to a low level, and staged dynamic loading began again.

8.4.2.4 Loading Stage No. 12

The force applied at the ground surface by T-Rex, the shear strain induced at the center of the liquefaction sensor array, and the pore pressure ratios generated at each PPT location during loading stage No. 12 of staged loading Series 2 are shown in Figure 8-33. The ground force during loading stage No. 12 was slightly less than 2000 lb (8.9 kN) throughout the 100 cycles of 10-Hz loading. This load induced fairly uniform cyclic shear strains at the center of the liquefaction sensor array of approximately 0.0009% (see Table 8-10 for strain values averaged over various numbers of loading cycles). These shear strains did not trigger the generation of any excess pore water pressure in the instrumented soil mass, as indicated by the fact that the pore pressure ratios at each sensor location remained equal to zero.

8.4.2.5 Loading Stage No. 13

The force applied at the ground surface by T-Rex, the shear strain induced at the center of the liquefaction sensor array, and the pore pressure ratios generated at each PPT location during loading stage No. 13 of staged loading Series 2 are shown in Figure 8-34. The ground force during loading stage No. 13 was approximately 5000 lb (22.2 kN) throughout the 100 cycles of 10-Hz loading. This load induced fairly uniform cyclic shear strains at the center of the

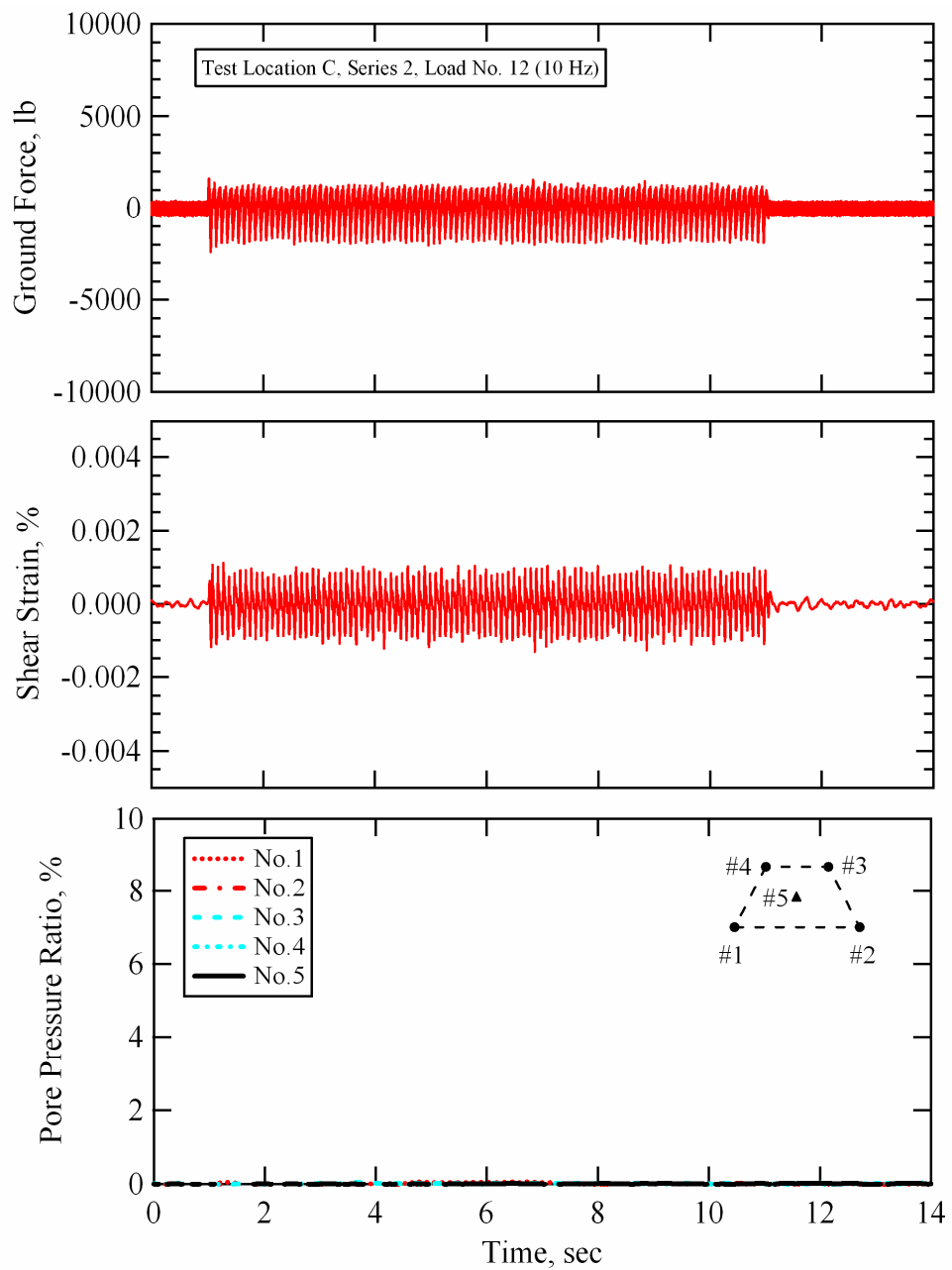


Figure 8-33 Force applied at the ground surface by T-Rex, shear strain induced at the center of the instrumented soil mass, and pore pressure ratios generated at each sensor location during Series 2, loading stage No. 12; Test Location C, Wildlife Liquefaction Array.

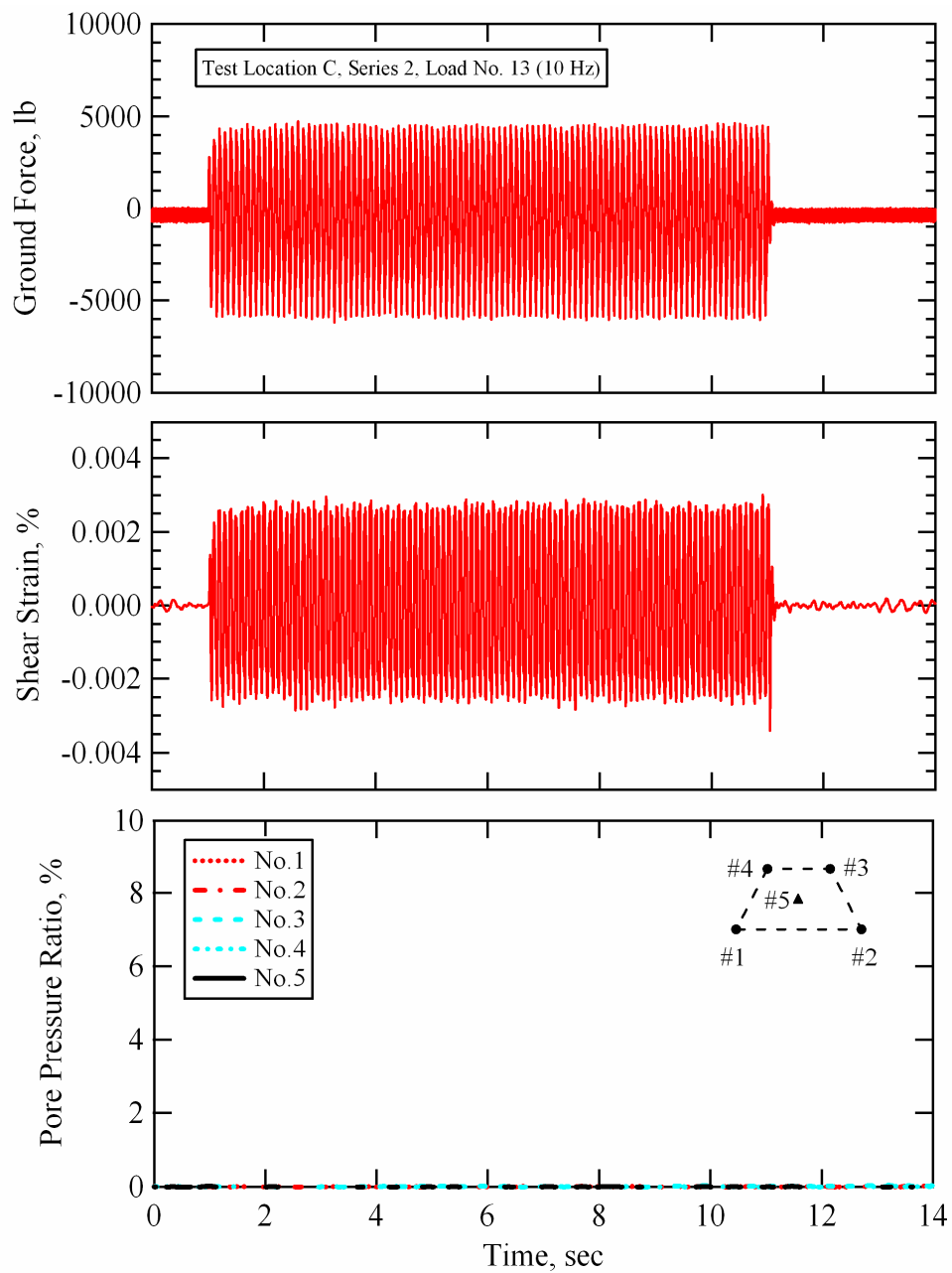


Figure 8-34 Force applied at the ground surface by T-Rex, shear strain induced at the center of the instrumented soil mass, and pore pressure ratios generated at each sensor location during Series 2, loading stage No. 13; Test Location C, Wildlife Liquefaction Array.

liquefaction sensor array of approximately 0.0026% (see Table 8-10 for strain values averaged over various numbers of loading cycles). These shear strains did not trigger the generation of any excess pore water pressure in the instrumented soil mass, as indicated by the fact that the pore pressure ratios at each sensor location remained equal to zero.

8.4.2.6 Loading Stage No. 14

The force applied at the ground surface by T-Rex, the shear strain induced at the center of the liquefaction sensor array, and the pore pressure ratios generated at each PPT location during loading stage No. 14 of staged loading Series 2 are shown in Figure 8-35. The ground force during loading stage No. 14 was about 15000 lb (66.7 kN) throughout the 100 cycles of 10-Hz loading. This load induced fairly uniform cyclic shear strains at the center of the liquefaction sensor array of approximately 0.009% (see Table 8-10 for strain values averaged over various numbers of loading cycles). These shear strains did not trigger the generation of any excess pore water pressure in the instrumented soil mass, as indicated by the fact that the pore pressure ratios at each sensor location remained equal to zero.

8.4.2.7 Loading Stage No. 15

The force applied at the ground surface by T-Rex, the shear strain induced at the center of the liquefaction sensor array, and the pore pressure ratios generated at each PPT location during loading stage No. 15 of staged loading Series 2 are shown in Figure 8-36. The ground force during loading stage No. 15

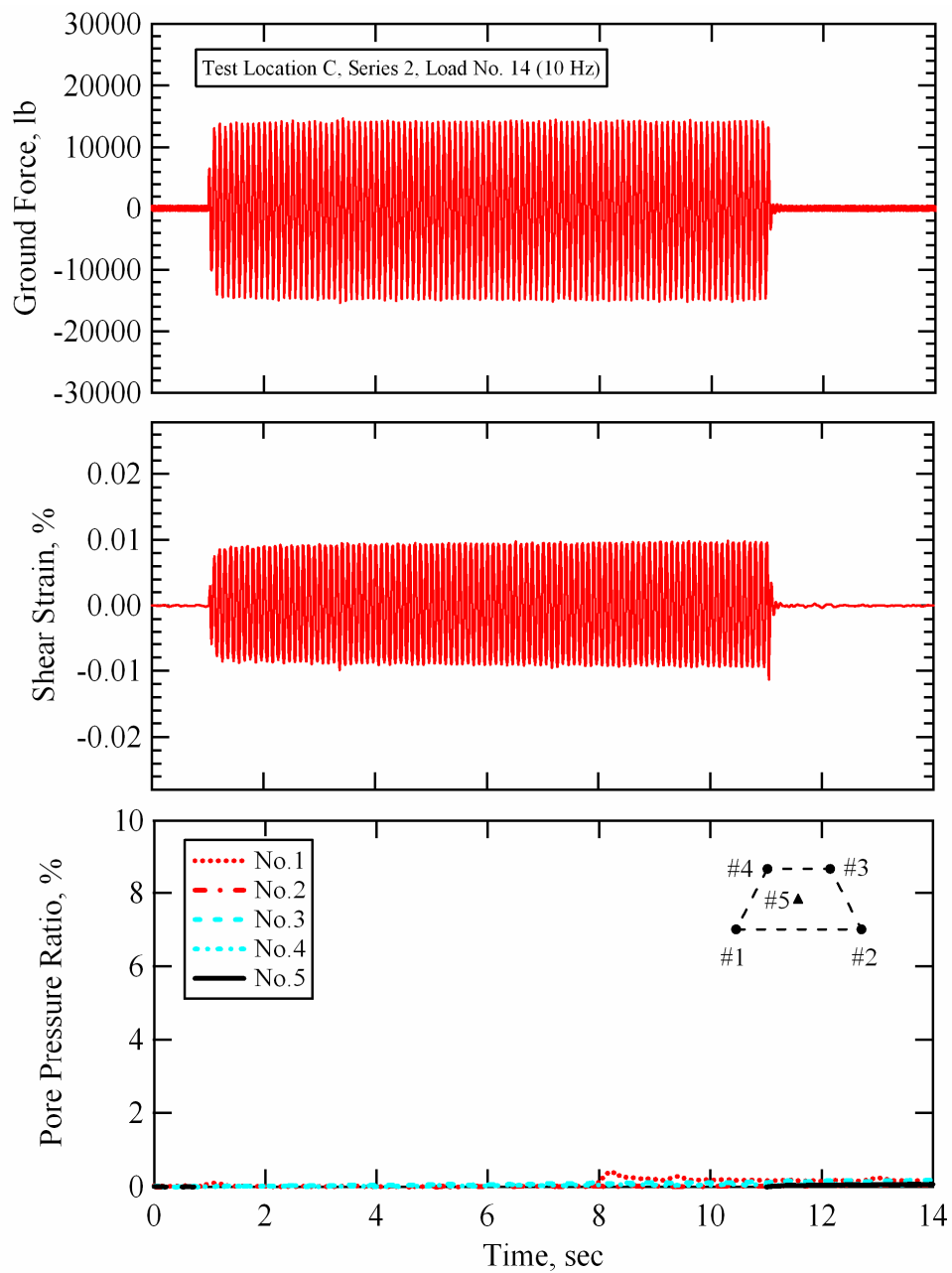


Figure 8-35 Force applied at the ground surface by T-Rex, shear strain induced at the center of the instrumented soil mass, and pore pressure ratios generated at each sensor location during Series 2, loading stage No. 14; Test Location C, Wildlife Liquefaction Array.

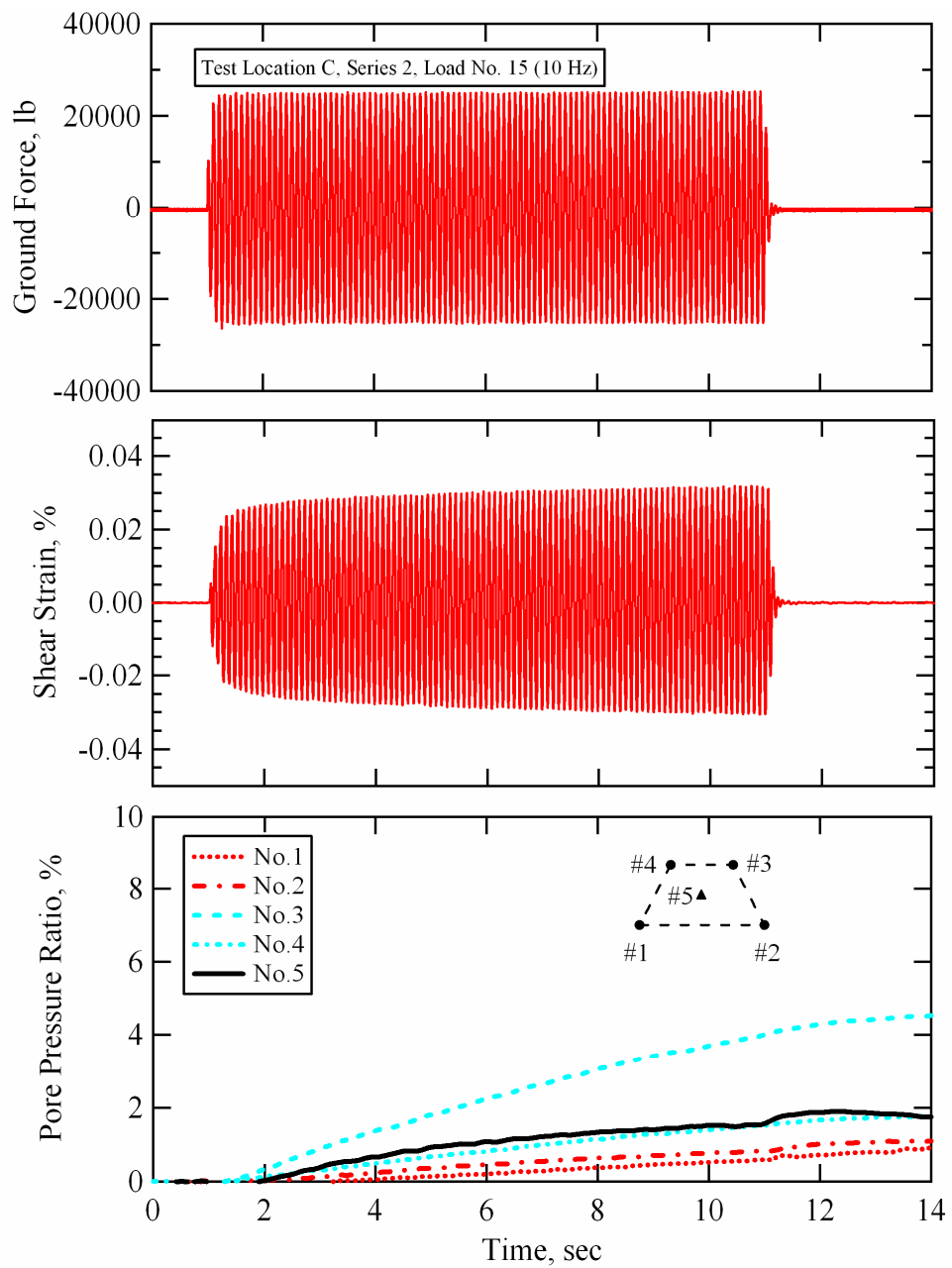


Figure 8-36 Force applied at the ground surface by T-Rex, shear strain induced at the center of the instrumented soil mass, and pore pressure ratios generated at each sensor location during Series 2, loading stage No. 15; Test Location C, Wildlife Liquefaction Array.

was approximately 25000 lb (111.2 kN) throughout the 100 cycles of 10-Hz loading. The shear strain time history is slightly less uniform than the ones presented for loading stages No. 9 through No. 14. The average shear strain over the first 10 cycles of loading is 0.0229%, while the average shear strain over the entire 100 cycles of loading is 0.0287% (see Table 8-10).

The two deeper sensors (No. 1 and No. 2) in the array recorded nearly identical pressures that rose slowly throughout the duration of shaking. Both of these sensors indicated pore pressure ratios of just less than 1% at the end of 100 cycles of loading. The PDCR 35/D transducer (Sensor No. 5) recorded pressures that steadily increased throughout dynamic loading, reached a pore pressure ratio of approximately 2% at the end of shaking, and then began to dissipate a couple of seconds after the end of shaking. The two shallower sensors (No. 3 and No. 4) recorded different magnitudes of pore pressure generation. Sensor No. 4 sensed excess pore pressures very similar in magnitude to those sensed by Sensor No. 5. Sensor No. 3 sensed higher excess pore pressures that continued to build after the end of shaking. Pore pressure data was recorded for approximately 60 seconds during loading stage No. 15. Figure 8-37 shows the pore pressure ratios measured at each sensor location with a time scale of 60 seconds. The pore pressures recorded by Sensors No. 3 and No. 4 did not decay as quickly as those recorded by the other sensors. In fact, Sensor No. 3 sensed higher excess pore pressures that continued to build after the end of shaking. It is likely that higher excess pore water pressures generated in the liquefiable material above the sensor array were dissipating downward, thus causing the pressure at Sensor No. 3 to continue to

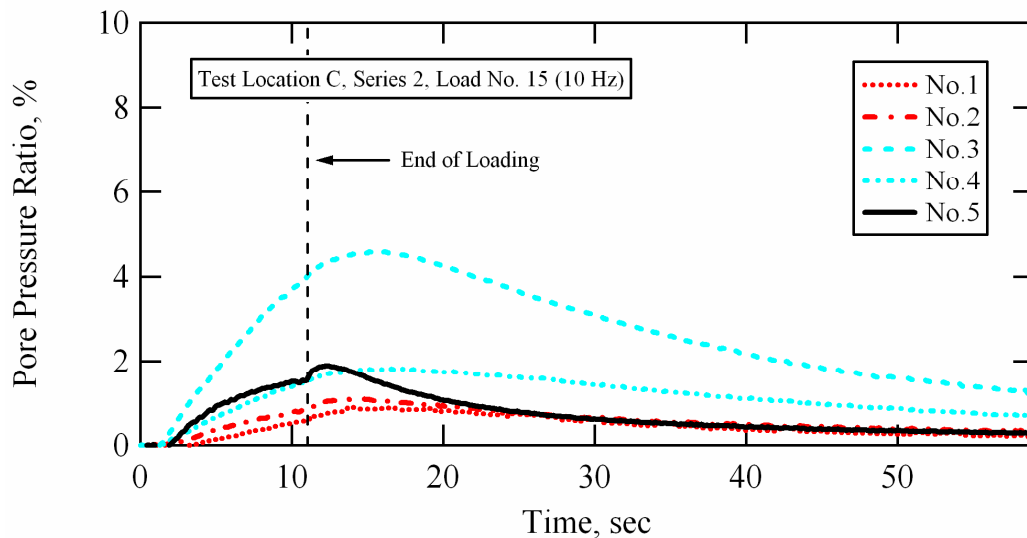


Figure 8-37 Pore pressure ratios generated at each sensor location during Series 2, loading stage No. 15; Test Location C, Wildlife Liquefaction Array.

increase and the pressure at Sensor No. 4 to remain elevated for a longer period of time. The soil near Sensor No. 3 may have been more permeable or less stiff, causing it to sense higher pore water pressures during and after loading. Sensor No. 3 also sensed higher pressures during loading stage No. 11 of Series 2 and loading stages No. 3, No. 6, No.7, and No. 8 of Series 1. The pore pressure ratios at all sensor locations had dropped below 2% after 50 seconds had passed from the end of loading.

As mentioned previously, the r_u values used to construct the pore pressure generation curves for the site were obtained solely from the PDCR 35/D transducer located at the center of the array (Sensor No. 5). The averaged shear strain values and pore pressure ratios calculated at the center of the liquefaction

sensor array for loading stage No. 15 are presented in Table 8-10 as a function of various numbers of loading cycles. After loading stage No. 15, testing was halted for approximately 10 minutes (see Table 8-9) while the excess pore water pressure within the array was allowed to dissipate back to static conditions (monitored by the PDCR 35/D transducer).

8.4.2.8 Loading Stage No. 16

During loading stage No. 16, T-Rex was driven at its maximum output (in shear mode) for 200 cycles of 10 Hz loading. The force applied at the ground surface, the shear strain induced at the center of the liquefaction sensor array, and the pore pressure ratios generated at each PPT location during loading stage No. 16 are shown in Figure 8-38. The ground force during loading stage No. 16 was not as consistent as the ground force records from previous loading stages in Series 2. The ground force started out at approximately 35000 lb (155.7 kN) and then decayed to approximately 27000 lb (120.1 kN) at the end of shaking. It is likely that the soil was softening to the point where it could not offer enough resistance to keep the ground force at a consistently elevated level.

The shear strain time history shown in Figure 8-38 is very irregular for the first time. During the first 100 cycles of loading there is a steady increase in shear strain with increasing number of loading cycles. The average shear strain over the first 10 cycles of loading is 0.0478%, while the average shear strain over the first 100 cycles of loading is 0.0754% (see Table 8-10). After approximately the first 100 cycles of loading, the shear strain nearly doubles over a short number of loading cycles.

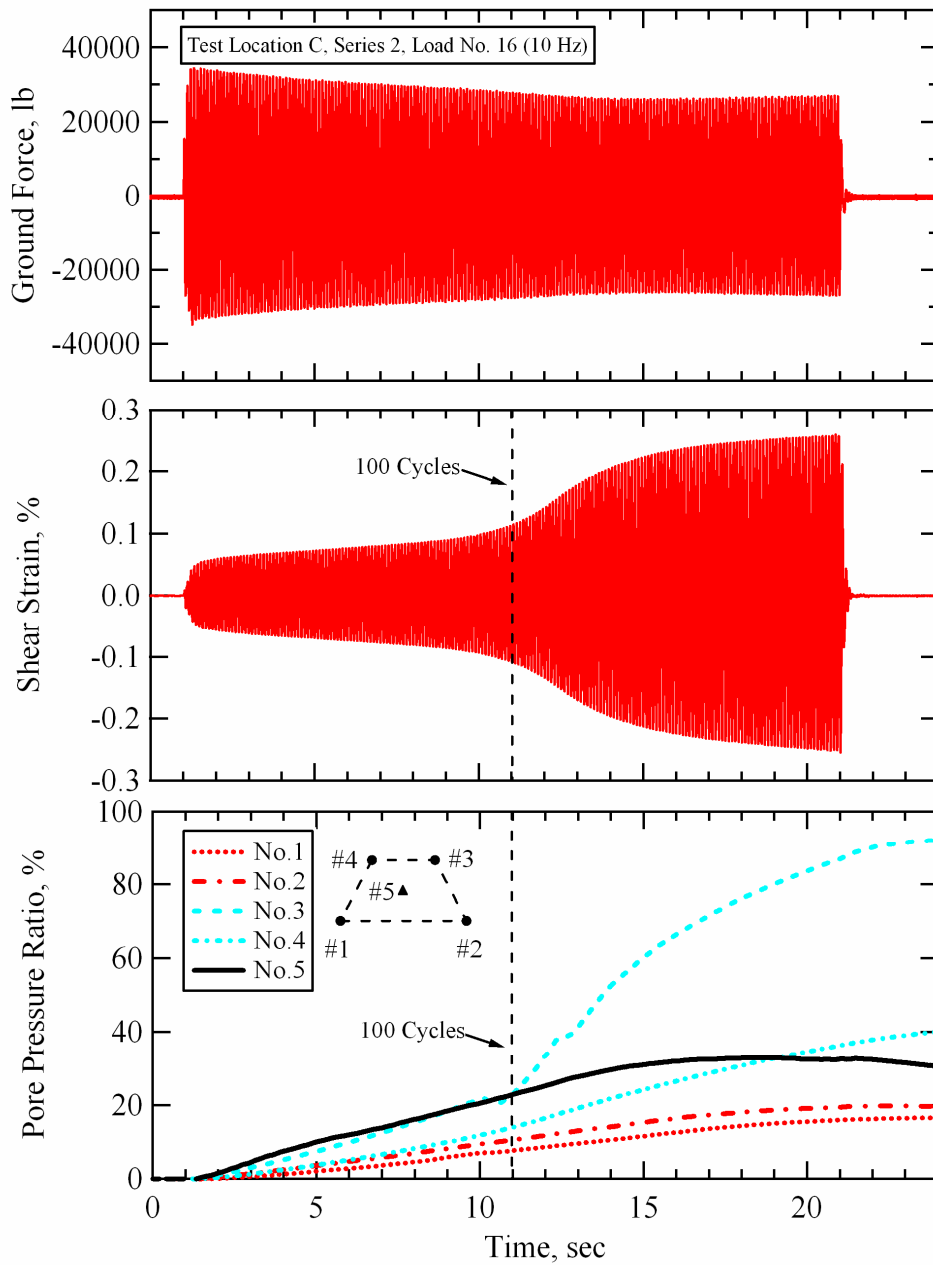


Figure 8-38 Force applied at the ground surface by T-Rex, shear strain induced at the center of the instrumented soil mass, and pore pressure ratios generated at each sensor location during Series 2, loading stage No. 16; Test Location C, Wildlife Liquefaction Array.

The large increase in shear strain during loading stage No. 16 coincides with an abrupt increase in the pore pressure recorded by Sensor No. 3. Over the last 100 cycles of loading, the excess pore pressure recorded by sensor No. 3 reached a value equal to a pore pressure ratio of just less than 95%, which for this sensor depth, indicates excess pore water pressures of approximately 1020 psf (49.1 kPa or 16.5 ft of water). However, at the same depth, just a couple of feet away, Sensor No. 4 only recorded excess pore water pressures at the end of shaking equal to a pore pressure ratio of approximately 40%. The excess pressures recorded by Sensors No. 1 and No. 2 were quite similar, and built to values equal to a pore pressure ratio of approximately 15% at the end of shaking. The excess pore water pressure recorded at the center of the array by Sensor No. 5 peaked-out during the last 100 cycles of loading at a pore pressure ratio of approximately 30%. In fact, the pore pressures recorded by Sensor No. 5 began to show slight signs of dissipation even before the end of shaking.

Pore pressure data was recorded for approximately 120 seconds during loading stage No. 16. Figure 8-39 shows the pore pressure ratios measured at each sensor location with a time scale of 120 seconds. The pore pressures recorded by Sensors No. 3 and No. 4 did not decay as quickly as those recorded by the other sensors. It is likely that higher excess pore water pressures generated in the liquefiable material above the sensor array were dissipating downward, thus causing the pressure at Sensors No. 3 and No. 4 to remain elevated for a longer period of time. The soil near Sensor No. 3 may have been more permeable or less stiff, causing it to sense higher pore water pressures during and after loading.

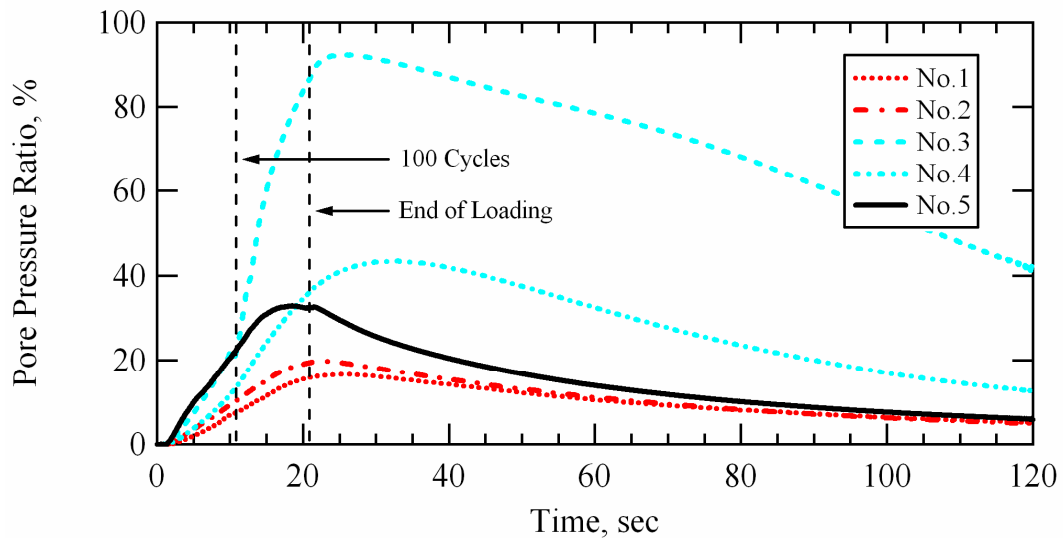


Figure 8-39 Pore pressure ratios generated at each sensor location during Series 2, loading stage No. 16; Test Location C, Wildlife Liquefaction Array.

Sensor No. 3 also recorded higher excess pore water pressures during loading stages No. 11 and No. 15 of Series 2 and loading stages No. 3, No. 6, No.7, and No. 8 of Series 1. The pore pressure ratio at Sensor No. 3 remained above 40% even after 100 seconds had passed from the end of loading. The pore pressure ratios at all other sensor locations had dropped below 10% after this same time period.

Despite the irregular pore water pressure and shear strain behavior in the instrumented soil mass during the last 100 cycles of loading stage No. 16, the first 100 cycles of loading show similar behavior to that demonstrated in prior staged loads. It appears that the irregular behavior after the first 100 cycles of loading was triggered by elevated pore water pressure generation at Sensor No. 3. An

examination of the horizontal, in-line component (y-component) particle displacement time histories recorded at each liquefaction sensor location shows that the displacements measured at Sensor No. 3 were indeed quite different than those recorded at the other sensor locations. Figure 8-40 shows the y-component particle displacement time histories recorded by Sensors No. 1, No. 2, No. 3, and No. 4 during loading stage No. 16. It is obvious that the irregular shape of the shear strain time history after 100 cycles of loading (see Figure 8-38) is driven by the large, irregular displacements recorded by the horizontal, in-line component (y-component) of Sensor No. 3. The y-component displacements of Sensor No. 4 are very similar to those of Sensor No. 3 until just after the first 100 cycles of loading. At this point, the y-component displacements recorded by Sensor No. 4 actually decrease instead of increase, while the displacements at Sensor No. 3 increase significantly. Similarly, the y-component displacements recorded by Sensors No. 2 and No. 1 also exhibit a slight tendency to decrease in amplitude after the first 100 cycles of loading.

The irregular displacement behavior after 100 cycles of loading shown in Figure 8-40 certainly violates the assumption of a linear displacement between nodes that is made during the 4-node, isoparametric finite element strain formulation (see Section 6.3.1). Therefore, the shear strain calculations are rendered unreliable after this point. This evidence further substantiates the fact that only the first 100 cycles of dynamic loading from this record should be used in the pore pressure generation curves and nonlinear soil shear modulus data reduction processes.

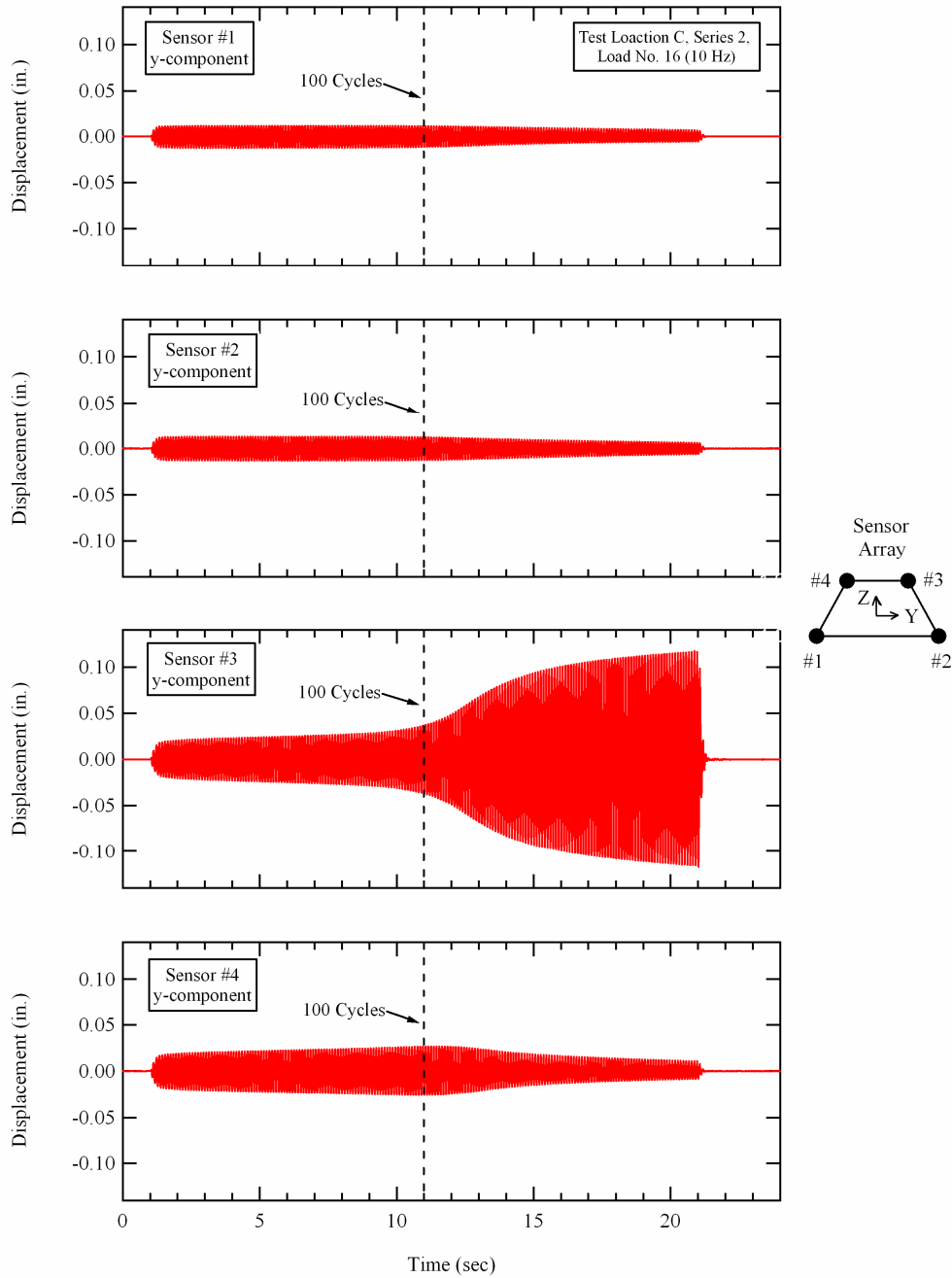


Figure 8-40 Horizontal, in-line component (y-component) particle displacements recorded at each of the liquefaction sensor location during Series 2, loading stage No. 16; Test Location C, Wildlife Liquefaction Array.

8.4.3 Pore Pressure Generation Curves; Loading Series 2

Pore pressure generation curves from this series of testing can readily be constructed from the data presented in Table 8-10 using any of the given numbers of loading cycles. Figure 8-41 shows the pore pressure generation curves for 10, 20, 50, and 100 cycles of loading determined at Test Location C during staged dynamic loading Series 2. The cyclic threshold shear strain (γ_t^e) depends on the number of cyclic shear strain cycles (n) and ranges from approximately 0.015% for n = 100 to 0.025% for n = 10. These threshold shear strains are just slightly higher than the cyclic threshold shear strains (γ_t^e) that were determined during Series 1 (0.01% for n = 100 and 0.02% for n = 10, see Figure 8-19). The Series 1 and Series 2 pore pressure generation curves are compared in Section 8.5. Multiple data points between 0.0009% and 0.015% confirm the lack of excess pore pressure generation below γ_t^e . As expected, the data show that for a given cyclic shear strain above γ_t^e , higher pore pressures are generated with increasing numbers of loading cycles.

Figure 8-42 compares the in-situ pore pressure generation curves determined for Test Location C during staged dynamic loading Series 2 with Dobry's pore pressure generation model for liquefiable soils from the Wildlife Site (Vucetic and Dobry, 1986). As discussed in Section 7.3.1.3, Dobry's model for liquefiable soils from the Wildlife Site was developed from cyclic laboratory test results. A cyclic threshold shear strain of 0.02% was assumed for the model (based on experience gained from previous laboratory tests) because the laboratory tests conducted in the study were not performed at shear strains that

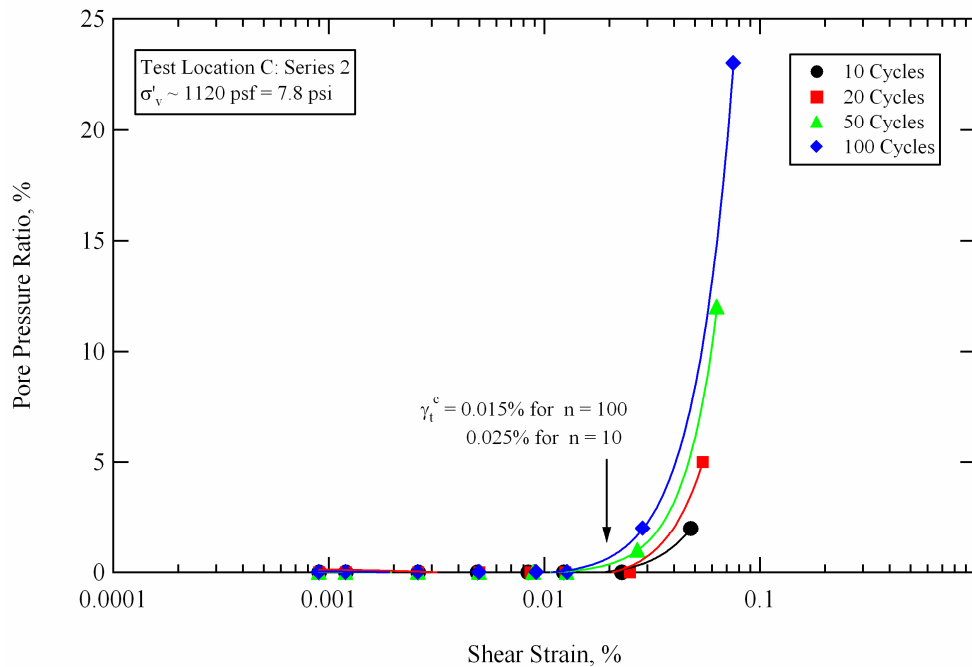


Figure 8-41 Pore pressure generation curves obtained from in-situ liquefaction tests conducted during staged dynamic loading Series 2 at Test Location C, Wildlife Liquefaction Array.

were low enough to actually determine the cyclic threshold. This cyclic threshold shear strain was assumed to be the same for any given number of loading cycles. The cyclic tests used to develop the model for Wildlife soils employed up to 30 cycles of strain-controlled loading. The assumed cyclic threshold value is within the range of the cyclic threshold shear strains for $n = 10$ and $n = 100$ determined from in-situ liquefaction tests conducted during staged loading Series 2. In Figure 8-42, Dobry's pore pressure generation model is shown for 10 loading cycles ($n = 10$) and for 100 loading cycles ($n = 100$), as calculated using Equation 7-1. The in-situ test results exhibit slightly less pore pressure generation at a given shear strain level and number of loading cycles than predicted by Dobry's model.

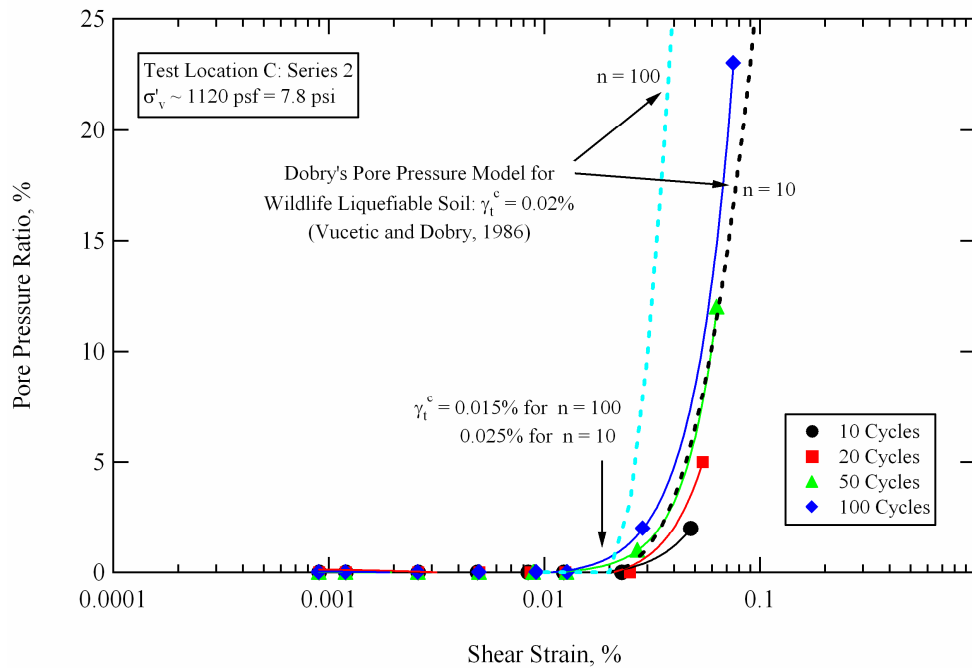


Figure 8-42 Comparison between Dobry's pore pressure generation model (Vucetic and Dobry, 1986) and pore pressure generation curves obtained from in-situ liquefaction tests conducted during staged dynamic loading Series 2 at Test Location C, Wildlife Liquefaction Array.

However, the in-situ results follow a trend in pore pressure generation very similar to Dobry's model. Because the pore pressure ratios induced at the center of the liquefaction sensor array during Series 2 tests were less than 23%, the pore pressure generation curves presented in Figures 8-41 and 8-42 are shown with a maximum pore pressure ratio scale of 25%. For perspective purposes, Figure 8-43 presents the pore pressure generation curves with a maximum pore pressure ratio scale of 100%.

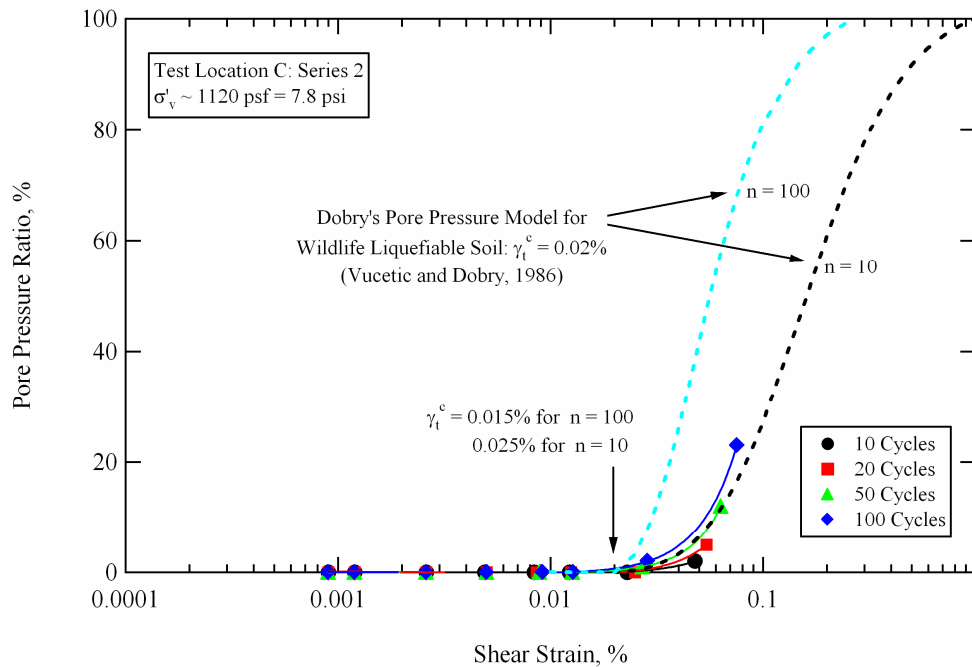


Figure 8-43 Full pore pressure ratio scale comparison between Dobry's pore pressure generation model (Vucetic and Dobry, 1986) and pore pressure generation curves obtained from in-situ liquefaction tests conducted during staged dynamic loading Series 2 at Test Location C, Wildlife Liquefaction Array.

As discussed in Section 8.3.3, to an unknown extent, the pore pressures being generated over a finite loaded area during in-situ liquefaction tests are simultaneously redistributing inside of, and dissipating away from, the loaded area. Given that the material is saturated, it is unlikely that the pore water pressure can dissipate very much over the short duration of cyclic loading (10 sec). On the other hand, during laboratory tests, pore pressure generation is measured on a very small specimen where the boundary conditions are carefully controlled (i.e. no pore pressure dissipation is allowed). Conversely, an earthquake simultaneously loads an immense area with varying soil stiffnesses,

permeabilities, and anomalies (i.e. cracks that allow venting to the ground surface) that affect the buildup, redistribution, and dissipation of pore water pressures during and after shaking. For a given induced shear strain level, it is likely that laboratory tests yield the highest pore pressure generation, followed by actual earthquakes, followed by the in-situ liquefaction tests. However, these differences are unquantifiable at this time.

8.4.4 Evaluation of Nonlinear Shear Modulus; Loading Series 2

The nonlinear shear modulus of the soil within the liquefaction sensor array at Test Location C was obtained for each staged loading of Series 2 using the average cycle-by-cycle, vertically propagating (downward), horizontally polarized, shear wave velocities ($V_{S,vh}$) determined according to the procedure detailed in Section 6.5.

The cycle-by-cycle $V_{S,vh}$ values determined for loading stage No. 9 are shown in Figure 8-44. The average 100-cycle shear strain induced during this load was 0.0012% (see Table 8-10). The individual velocity values tend to vacillate up and down. This behavior is attributed to the epistemic uncertainty associated with evaluating the phase difference between receiver pairs. Despite this fact, the mean value remains essentially constant throughout loading. This is not surprising as the strain induced during this test is below the cyclic threshold strain, where theoretically, no modulus degradation should occur. The average 100-cycle shear wave velocity during loading stage No. 9 was determined to be 408 fps (124 m/sec) with a standard deviation (σ) of 14 fps (4.3 m/sec).

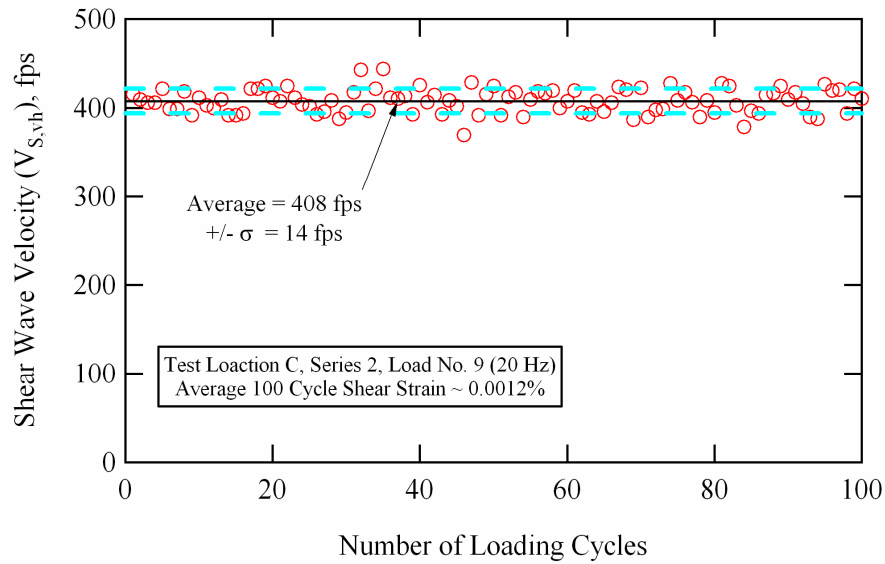


Figure 8-44 Cycle-by-cycle shear wave velocities from loading stage No. 9 ($\gamma \sim 0.0012\%$) of staged dynamic loading Series 2 at Test Location C, Wildlife Liquefaction Array.

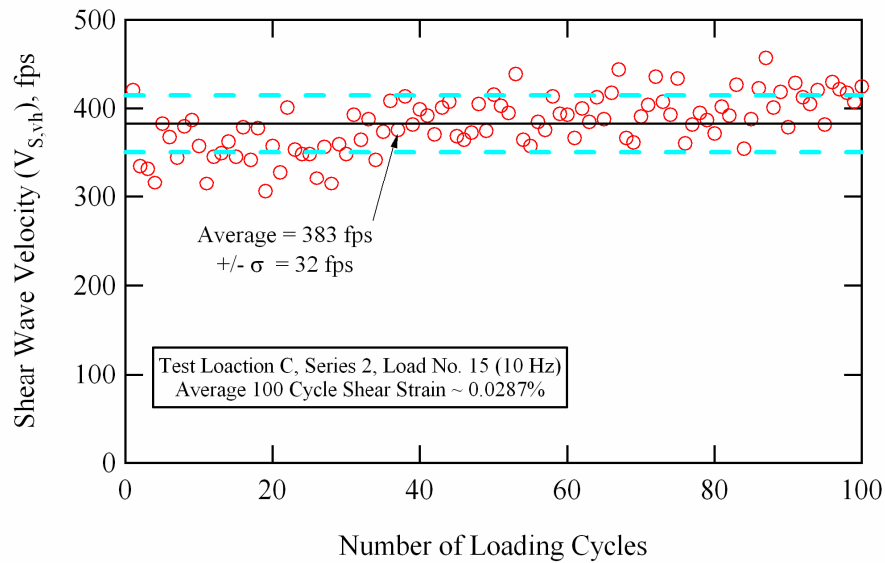


Figure 8-45 Cycle-by-cycle shear wave velocities from loading stage No. 15 ($\gamma \sim 0.0287\%$) of staged dynamic loading Series 2 at Test Location C, Wildlife Liquefaction Array.

In general, the mean $V_{S,vh}$ values were quite consistent for the loads in Series 2 where the induced shear strains were less than the cyclic threshold strain. However, the $V_{S,vh}$ values for Load No. 15, which had an average 100-cycle shear strain (0.0287%) very close to the cyclic threshold strain, showed significant scatter (see Figure 8-45). In fact, the $V_{S,vh}$ values determined from early loading cycles were noticeably smaller than the values determined from later loading cycles despite the fact that at the end of loading a pore pressure ratio of 2% had been induced at the center of the array. This trend is opposite to that which is expected and is attributed to a greater degree of difficulty in accurately resolving the phase differences between the receivers during the early cycles of Load No. 15. Therefore, the $V_{S,vh}$ values were obtained by averaging over 100 cycles of loading with the goal of reducing some of the epistemic uncertainty in the calculations. The average 100-cycle shear wave velocity during loading stage No. 15 was determined to be 383 fps (117 m/sec) with a standard deviation (σ) of 32 fps (9.7 m/sec).

The average 100-cycle $V_{S,vh}$ values and standard deviations determined for loading stages No. 9 through No. 15 are given in Table 8-11. The shear modulus (G) values calculated from these velocities are also given. The $V_{S,vh}$ values for loading stage No. 12 were not able to be resolved accurately, therefore no velocities are tabulated for this stage.

The $V_{S,vh}$ values obtained from loading stage No. 16, which had an average 100 cycle shear strain (0.07541%) above the cyclic threshold strain, are shown in Figure 8-46. Loading stage No. 16 had a duration of 200 cycles.

Table 8-11 Average 100-cycle shear strains, shear wave velocities and shear moduli obtained from loading stages No. 9 through No. 15 of staged loading Series 2 at Test Location C, Wildlife Liquefaction Array

| Staged Loading Series 2, Test Location C, Wildlife Liquefaction Array | | | | |
|---|--|---|-----------|--------------------------------------|
| Loading Stage No. | 100 Loading Cycles | | | |
| | Shear Strain ¹ , γ (%) | Shear Wave Velocity ² , $V_{S,vh}$ (fps) | | Shear Modulus ³ , G (psf) |
| | Average | Average | Std. Dev. | from Avg. $V_{S,vh}$ |
| 9 | 0.0012 | 408 | 14 | 620363 |
| 10 | 0.0050 | 401 | 13 | 599258 |
| 11 | 0.0128 | 395 | 12 | 581460 |
| 12 | 0.0009 | * | * | * |
| 13 | 0.0026 | 407 | 18 | 617325 |
| 14 | 0.0092 | 394 | 9 | 578519 |
| 15 | 0.0287 | 383 | 32 | 546667 |

- Notes: 1. γ calculated at the center of the array and averaged over 100 loading cycles
 2. $V_{S,vh}$ values averaged over 100 loading cycles
 3. G values obtained from $V_{S,vh}$ values using $\rho = (120 \text{ psf})/(32.2 \text{ ft/sec}^2)$
 * $V_{S,vh}$ values could not accurately be resolved

However, as discussed in Section 8.4.2.8, the shear strains could not accurately be determined after 100 cycles of loading. Additionally, the $V_{S,vh}$ values after 100-cycles of loading were unable to be accurately resolved. Thus, the $V_{S,vh}$ values for loading stage No. 16 are only shown for the first 100 cycles of loading. The downward trending velocities clearly indicate that modulus degradation is occurring as excess pore pressures are generating within the array. This marked tendency appears to overshadow some of the epistemic uncertainty in the calculations because the cycle-by-cycle velocities are more tightly grouped. In fact, as the soil softens, the phase difference between receivers increases, thus allowing a more accurate determination of the velocity. It is possible to track the

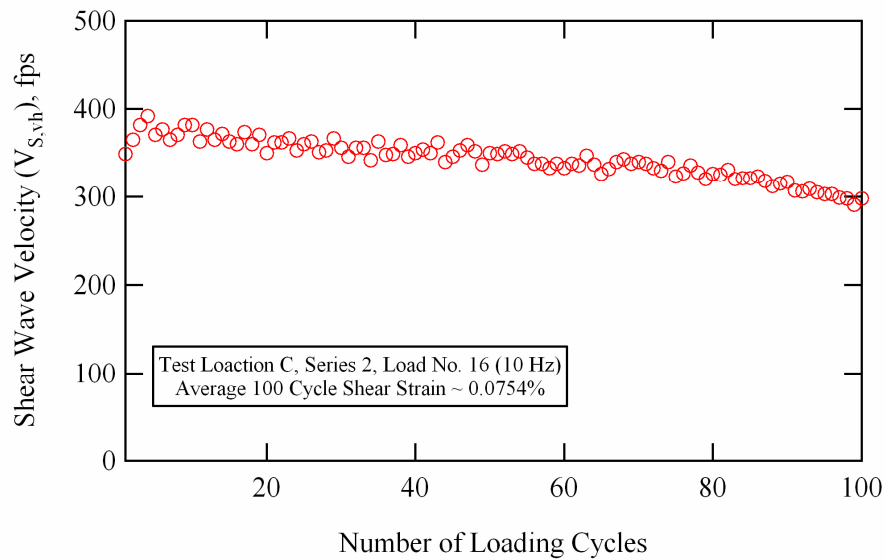


Figure 8-46 Cycle-by-cycle shear wave velocities from Load No. 16 ($\gamma \sim 0.0754\%$) of staged dynamic loading Series 2 at Test Location C, Wildlife Liquefaction Array.

cyclic degradation of the shear modulus within the array by averaging these velocities over various numbers of loading cycles. The $V_{S,vh}$ values and standard deviations determined from averaging over 10, 20, 50 and 100 cycles of loading during loading stage No. 16 are given in Table 8-12. The shear modulus (G) values calculated from these velocities are also given.

As discussed in Section 8.3.4, it is uncertain whether or not averaging the $V_{S,vh}$ values over a given number of loading cycles is the best method to characterize the nonlinear behavior of the soil once modulus degradation begins. However, the shear strains during loading stage No. 16 are not uniform (see Figure 8-38) and must be averaged over a given cyclic interval. Therefore, there is some uncertainty as to exactly what equivalent shear strain and number of

Table 8-12 Shear strains, shear wave velocities and shear moduli obtained from averaging over various numbers of cycles during loading stage No. 16 of staged loading Series 2 at Test Location C, Wildlife Liquefaction Array

| Staged Loading Series 2, Test Location C, Wildlife Liquefaction Array | | | | |
|---|--|---|-----------|--------------------------------------|
| Number of Cycles | Loading Stage No. 16 | | | |
| | Shear Strain ¹ , γ (%) | Shear Wave Velocity ² , $V_{S,vh}$ (fps) | | Shear Modulus ³ , G (psf) |
| | Average | Average | Std. Dev. | from Avg. $V_{S,vh}$ |
| 10 | 0.0478 | 374 | 8 | 521277 |
| 20 | 0.0543 | 370 | 10 | 510186 |
| 50 | 0.0633 | 360 | 12 | 482981 |
| 100 | 0.0754 | 343 | 15 | 438443 |

Notes: 1. γ calculated at the center of the array and averaged over the given number of loading cycles
 2. $V_{S,vh}$ values averaged over the given number of loading cycles
 3. G values obtained from $V_{S,vh}$ values using $\rho = (120 \text{ psf})/(32.2 \text{ ft/sec}^2)$

loading cycles produced the measured degraded shear modulus. The only other option would be to pair the shear strain averaged over a given number of loading cycles with the un-averaged degraded modulus value measured at the end of the given number of loading cycles (similar to what is done when constructing pore pressure generation curves).

The 100-cycle shear modulus (G) values for loading stages No. 9 through No. 15 of dynamic loading Series 2 are plotted in Figure 8-47. The G values for loading stage No. 16 obtained over 10, 20, 50 and 100 cycles of loading are also shown. Because the shear strains induced during loading stage No. 16 are beyond the cyclic threshold strain, the modulus values decay due to combined effects of nonlinearity (i.e. the shear strain is increasing with increasing number of loading

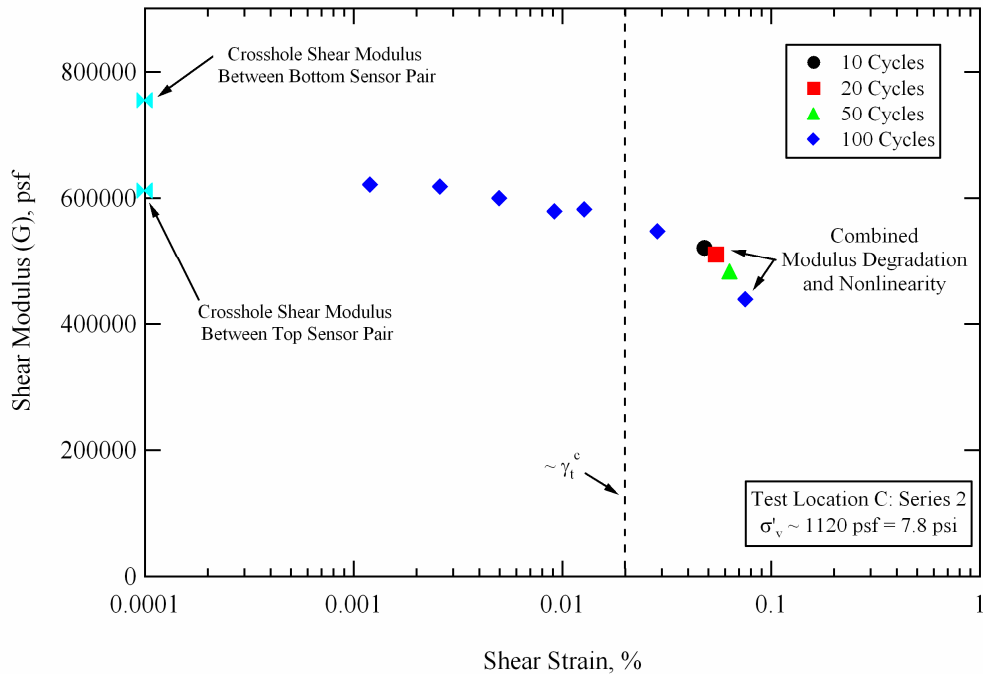


Figure 8-47 Shear modulus values (G) calculated from the data collected during staged dynamic loading Series 2 at Test Location C, Wildlife Liquefaction Array.

cycles) and degradation (i.e. the pore pressure is increasing with increasing number of loading cycles). The two loads with the smallest induced shear strains were Load No. 9 (20 Hz) and Load No. 12 (10 Hz). However, the modulus values for Load No. 12 could not accurately be resolved. Therefore, the 100-cycle modulus obtained from Load No. 9 was used for the small-strain normalizing shear modulus ($G_{\max} = 620363 \text{ psf} = 29.7 \text{ MPa}$). This value is quite close to the G_{\max} value used to normalize the results from Series 1 ($G_{\max} = 640698 \text{ psf} = 30.6 \text{ MPa}$). The G_{\max} values for Series 1 and Series 2 are equivalent to small-strain $V_{S, \text{vh}}$ values of 414 fps (126 m/s) and 408 fps (124 m/s), respectively.

For comparison purposes, the small-strain shear modulus values obtained from the crosshole tests conducted between the top and bottom sensor pairs in the liquefaction sensor array prior to Series 2 (see Table 8-3) are also shown in Figure 8-47. The small-strain modulus values obtained from $V_{S,vh}$ during staged dynamic testing fall within the small-strain modulus range obtained using $V_{S,hv}$ values from crosshole tests. However, it is not expected that these two test methods would produce the exact same results due to: (1) material anisotropy, (2) the use of substantially different wavelengths/frequencies (i.e. 20- to 40-ft wavelengths during staged dynamic testing vs. approximately 0.5 to 1.0-ft wavelengths during crosshole tests), and (3) the sampling of different volumes of material (i.e. the crosshole test samples a smaller volume of material and the waves will tend to find the stiffest (fastest) path between receivers). In regards to point number two above, G_{max} may increase by 5% going from 10 Hz to 100 Hz loading (i.e. one log cycle). It is therefore believed that the small-strain modulus obtained from staged dynamic loading is the proper modulus to normalize the other staged loading moduli values by.

The normalized shear modulus (G/G_{max}) values determined from the staged dynamic loads in Series 2 are shown in Figure 8-48. With the exception of the highest shear strain data point (from loading stage No. 16), all of the normalized modulus values were obtained using the moduli calculated from averaging over 100 cycles of loading. As mentioned above, the modulus values during loading stage No. 16 were decaying with increasing number of cycles due to combined nonlinearity and degradation. During loading stage No. 16, a pore

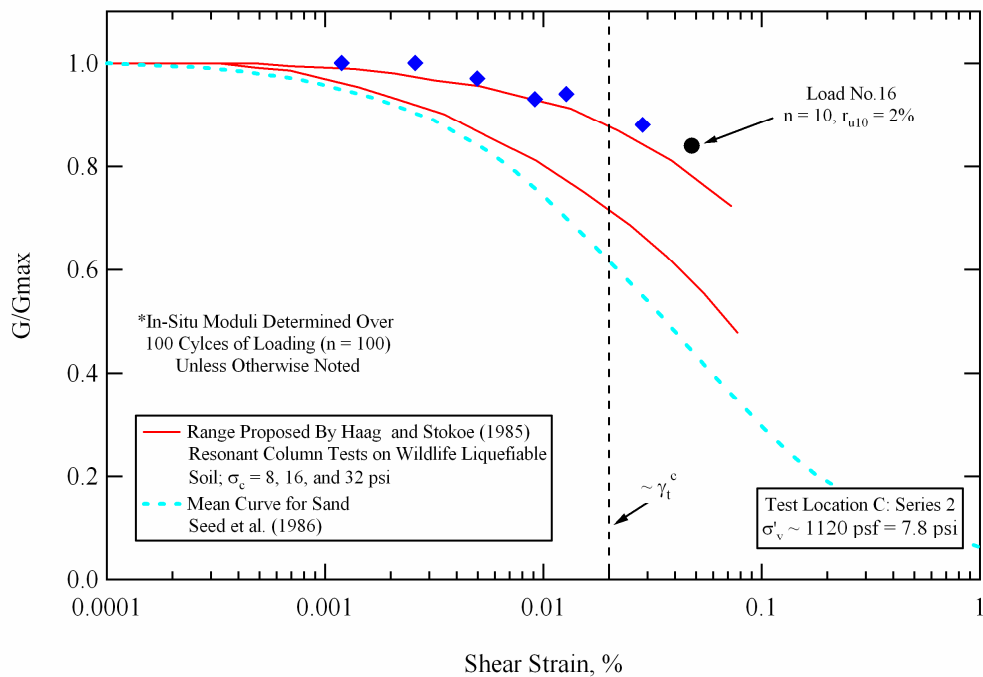


Figure 8-48 Normalized shear modulus (G/G_{max}) – $\log \gamma$ relationship calculated from the data collected during staged dynamic loading Series 1 at Test Location C, Wildlife Liquefaction Array.

pressure ratio of only 2% had been induced in the soil after 10 cycles of loading (see Table 8-10). Therefore, it is believed that the modulus value obtained from the first 10 cycles of loading only reflects the nonlinearity of the soil and contains minimal degradation from pore water pressure generation. For comparison purposes, the range of modulus reduction curves determined by Haag and Stokoe (1985) for Wildlife liquefiable soil, and the mean modulus reduction curve proposed by Seed et al. (1986) for sands, are also shown. The in-situ values are very close to the upper-bound modulus reduction curve determined by Haag and Stokoe (1985). Haag and Stokoe (1985) performed resonant column tests on

Wildlife liquefiable soils using confining pressures of 8, 16, and 32 psi (221 kPa). The upper-bound curve in their range of results likely came from tests performed at the highest confining pressure. Therefore, it appears that the in-situ soil (estimated to have a vertical effective stress of approximately 7.8 psi (54 kPa) over the depth range tested) behaves more linearly than the soil tested in the laboratory at equivalent confining pressures. It is not surprising that the Wildlife liquefiable soils behave more linearly than the mean curve for sand, as they contain significant amounts of non-plastic fines (i.e. on average between 27 and 49%; see Section 7.6) with approximately 10% clay-size particles.

Reductions in shear modulus from the combined effects of nonlinearity and degradation due to pore water pressure generation were observed in the data recorded during loading stage No. 16. The G/G_{\max} values for various numbers of loading cycles during stage No. 16 are shown in Figure 8-49. During loading stage No. 16, the pore pressure ratio and average shear strain induced in the instrumented soil mass after 10 cycles of loading were 2% and 0.0478%, respectively. After 20 cycles of loading, the pore pressure ratio and average shear strain had increased to 5% and 0.0543%, respectively. After 50 cycles of loading, the pore pressure ratio and average shear strain had increased to 12% and 0.0633%, respectively. Finally, after 100 cycles of loading, the pore pressure ratio and average shear strain had increased to 23% and 0.0754%, respectively. Using the 10-cycle modulus value as a reference point, it is possible to try to predict the decrease in modulus for any of the other numbers of loading cycles by knowing the change in shear strain and the change in pore pressure ratio.

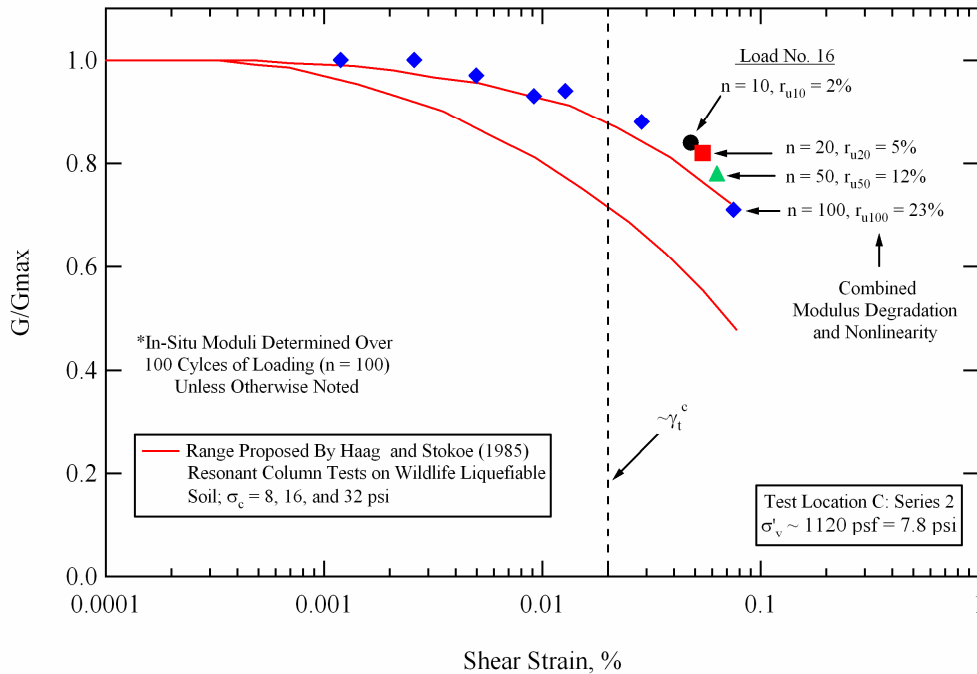


Figure 8-49 Normalized shear modulus values (G/G_{\max}) resulting from the combined effects of modulus nonlinearity and modulus degradation due to excess pore water pressure generation during loading stage No. 16 of Series 2 at Test Location C, Wildlife Liquefaction Array.

The procedure used to try to predict the 100-cycle normalized shear modulus (G/G_{\max}) obtained during loading stage No.16 from the 10-cycle G/G_{\max} value is depicted in Figure 8-50. The 10-cycle G/G_{\max} value is equal to 0.84. The 100-cycle G/G_{\max} value is equal to 0.71. The generation of excess pore water pressure reduces the effective stress within the soil deposit, thereby reducing the soil stiffness. The degradation in shear modulus due to pore pressure generation is typically accounted for by reducing the soil shear modulus according to a function that takes into account the change in effective stress within the soil deposit do to pore water pressure generation. As discussed in Section 8.3.4 for

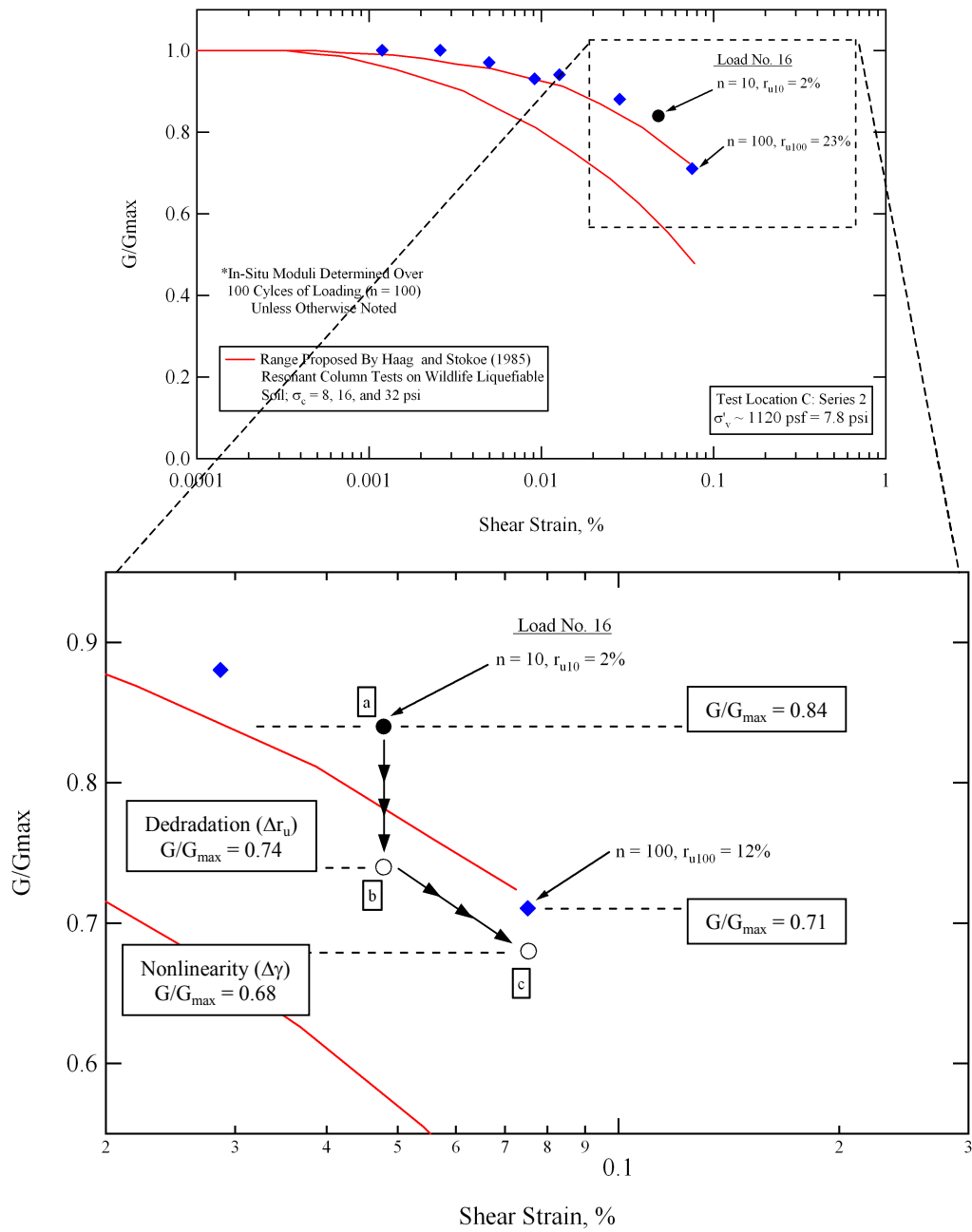


Figure 8-50 Illustration of the process used to try to predict the 100-cycle normalized shear modulus value obtained during loading stage No.16 from the 10-cycle normalized shear modulus value obtained during loading stage No. 16.

Series 1, Equation 8-1 is used for this purpose. In Figure 8-45, the 10-cycle G/G_{\max} value (0.84) is considered as G_o , and is marked by point (a). During loading stage No. 16, a pore pressure ratio of 23% was induced in the soil after 100 cycles of loading (i.e. the effective stress was reduced by 23%). Therefore, according to Equation 8-1, G_o should be multiplied by a factor of 0.88 to obtain an estimate for G_d . In Figure 8-50, G_d is marked by point (b), which has a G/G_{\max} value equal to 0.74. This reduction in shear modulus accounts for the theoretical degradation due to pore water pressure generation after 100 loading cycles. There is also a difference in the induced shear strain between the 10-cycle G/G_{\max} and 100-cycle G/G_{\max} moduli. As a result, the nonlinearity in the soil shear modulus between these points must also be accounted for. The nonlinearity can be accounted for by moving between the 10-cycle shear strain value and the 100-cycle shear strain value along a route parallel to the upper-bound curve proposed by Haag and Stokoe (1985). In Figure 8-50, this route is identified as the path between point (b) and point (c). At point (c), the G/G_{\max} value is approximately 0.68. Therefore, the modulus estimated by taking into account the combined effects of nonlinearity and degradation due to excess pore pressure generation is just slightly less than the actual 100-cycle G/G_{\max} value of 0.71.

This same process can be repeated for other stage No. 16 loading cycles using the pore pressure ratio, shear strain, and shear modulus values provided in Tables 8-10 and 8-12. The loading stage No. 16 20-, 50- and 100-cycle measured G/G_{\max} values and predicted G/G_{\max} values (after taking into account the combined effects of degradation and nonlinearity) are given in Table 8-13. The

Table 8-13 Measure G/G_{\max} values and predicted G/G_{\max} values obtained from taking into account the combined effects of modulus degradation and nonlinearity after 20, 50 and 100 cycles of loading during stage No. 16 of staged loading Series 2 at Test Location C, Wildlife Liquefaction Array

| Staged Loading Series 2, Test Location C, Wildlife Liquefaction Array | | | | |
|---|--|--|---|---|
| Number of Cycles | Loading Stage No. 16; 10-cycle $G/G_{\max} = 0.84$ | | | |
| | Measured G/G_{\max} | Predicted G/G_{\max} After Degradation | Predicted G/G_{\max} After Nonlinearity | Final Difference in G/G_{\max} Predicted - Measured |
| 20 | 0.82 | 0.82 | 0.80 | -0.02 |
| 50 | 0.78 | 0.79 | 0.75 | -0.03 |
| 100 | 0.71 | 0.74 | 0.68 | -0.03 |

differences between the measured and predicted values are also given. In general, the G/G_{\max} values predicted from the 10-cycle G/G_{\max} values by taking into account the combined effects of degradation and nonlinearity are slightly less than the measured G/G_{\max} values. However, even after 100 cycles of loading, the predicted G/G_{\max} value is only 0.03 (absolute) less than the measured G/G_{\max} value.

8.4.5 Link Between u - and G -log γ - N Relationships; Loading Series 2

The pore pressure generation characteristics and the nonlinear shear modulus behavior of a liquefiable soil deposit are inseparably linked. Therefore, it is beneficial to view these two types of data in the same figure. The pore pressure generation curves and normalized nonlinear soil shear modulus values obtained during Series 2 staged dynamic loading at Test Location C are presented together in Figure 8-51. The shear modulus of the soil exhibits nonlinearity once

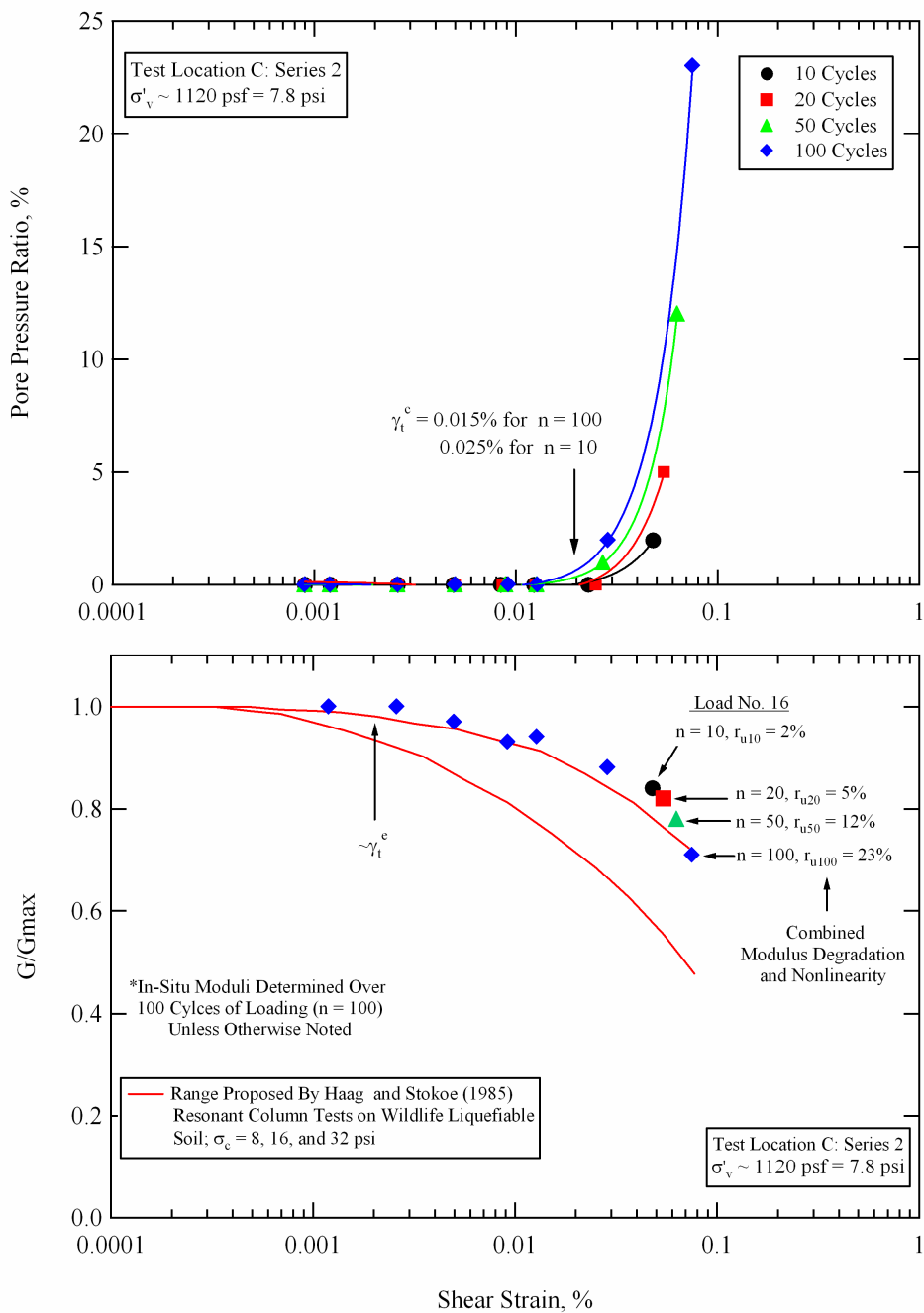


Figure 8-51 Pore pressure generation curves and nonlinear soil shear modulus values obtained during Series 2 staged dynamic loading at Test Location C, Wildlife Liquefaction Array (WLA).

shear strains greater than the elastic threshold shear strain (γ_i^e) have been induced in the soil deposit. The upper-bound curve by Haag and Stokoe (1985) indicate that the elastic threshold shear strain is close to 0.002%. The in-situ results indicate an elastic threshold shear strain slightly greater than this. The soil does not generate excess pore water pressure until shear strains greater than the cyclic threshold shear strain (γ_i^c) have been induced in the soil. The in-situ pore pressure generation curves indicate that the cyclic threshold shear strain (γ_i^c) depends on the number of cyclic shear strain cycles (n) and ranges from 0.015% for n = 100 to 0.025% for n = 10. For the in-situ results shown in Figure 8-51, noticeable shear modulus degradation due to pore pressure generation did not occur until pore pressure of a least 5% were generated at the center of the instrumented soil mass. As discussed previously, the shear moduli from loading stage No. 15 did not show any noticeable degradation with increasing numbers of loading cycles even though the pore pressure ratio at the center of the array had reached a value of 2% by the end of 100 cycles of loading.

8.5 GENERAL COMPARISON OF RESULTS FOR SERIES 1 AND SERIES 2

Two in-situ dynamic liquefaction test staged loading series were conducted at Test Location C at the Wildlife Liquefaction Array. The first staged loading series (Series 1) was conducted in the afternoon of August 17, 2005. The second staged loading series (Series 2) was conducted in the morning of August 18, 2005. Both staged loading series consisted of eight dynamic loads which started in the low-strain range and sequentially progressed until significant shear strains were induced in the instrumented soil mass. The pore pressure generation

curves and normalized nonlinear shear moduli obtained from Series 1 and Series 2 are compared in Figure 8-52. The cyclic threshold shear strain (γ_i^e) depends on the number of cyclic shear strain cycles (n). The cyclic threshold strain calculated from the data collected during Series 1 ranges from 0.01% for n = 100 to 0.02% for n = 10. The cyclic threshold strain calculated from the data collected during Series 2 ranges from 0.015% for n = 100 to 0.025% for n = 10. For a given shear strain level and number of loading cycles, the pore pressure generation curves obtained during Series 1 yield slightly higher pore pressure ratios. However, the difference is relatively minor. It seems likely that the seismic straining applied during Series 1 stiffened the soil response slightly and also densified localized areas slightly, thus requiring a slightly larger shear strain to develop equivalent pore pressure ratios during Series 2. The moduli obtained from test Series 2 indicate a slightly more linear modulus response than those obtained from test Series 1. This trend agrees well with the hypothesis that the seismic straining applied during Series 1 may have stiffened the soil response.

The in-situ nonlinear soil shear moduli obtained from both test series tend to lie closer to the upper-bound of the range in modulus reduction curves obtained from resonant column tests performed on liquefiable soil from the Wildlife Site (Haag and Stokoe, 1985). These resonant column tests were performed using confining pressures of 8, 16, and 32 psi (221 kPa). The upper-bound curve in the range of results likely came from tests performed at the higher confining pressures. Therefore, it appears that the in-situ soil (estimated to have a vertical

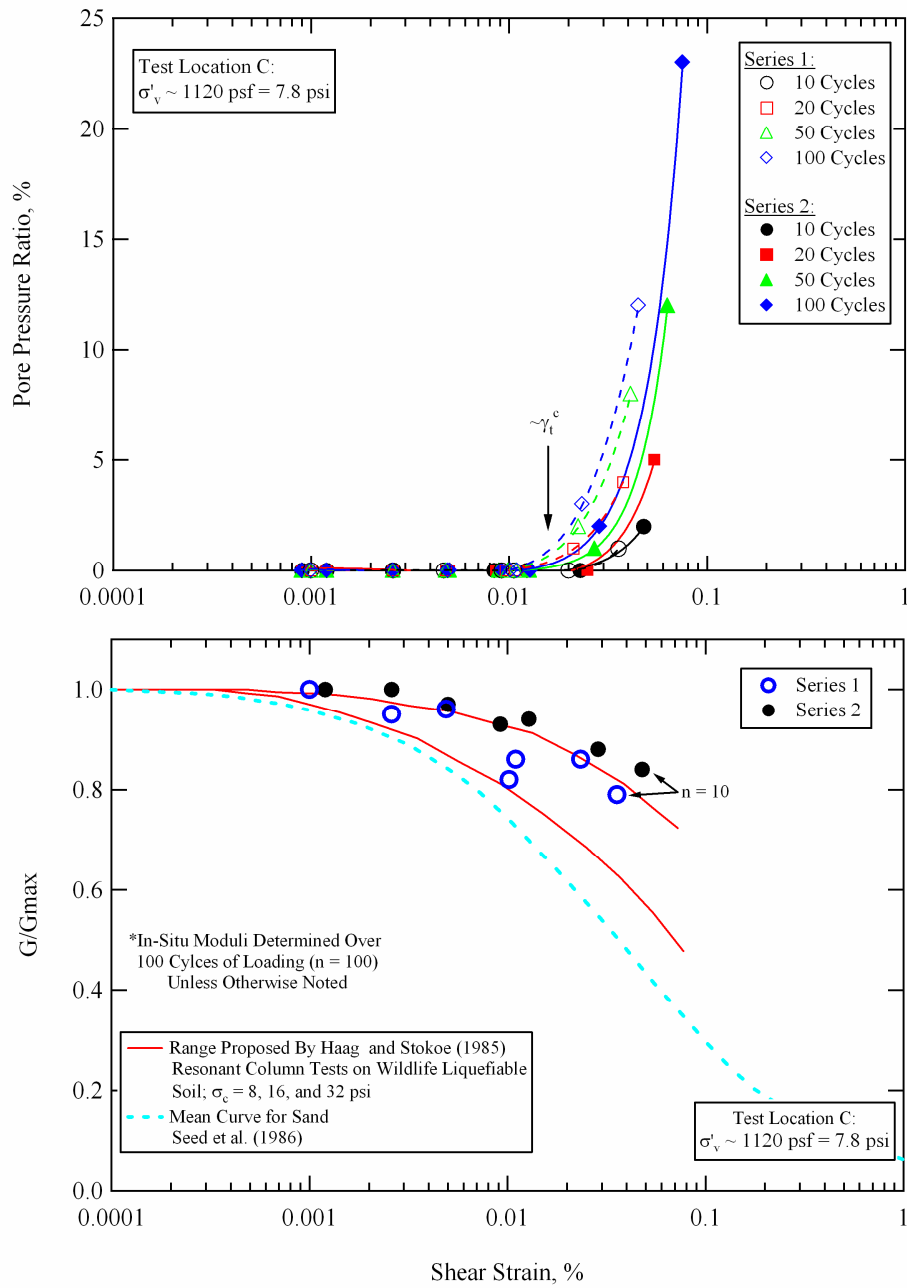


Figure 8-52 Comparison of the pore pressure generation curves and nonlinear soil shear modulus values obtained during Series 1 and Series 2 staged dynamic loading at Test Location C, Wildlife Liquefaction Array (WLA).

effective stress of approximately 7.8 psi (54 kPa) over the depth range tested) behaves more linearly than the soil tested in the laboratory at equivalent confining pressures.

8.6 SUMMARY

The in-situ liquefaction sensor array at Test Location C was installed on August 16, 2005. The sensor array was installed under the dirt access road between the 1982 (old) WLA Site and the 2004 (new) WLA Site, very close to CPT 47. The liquefaction sensors were placed within the approximate depth range of 11- to 13-ft (3.4- to 4.0-m). Two staged loading series were conducted at Test Location C. The first staged loading series (Series 1) was conducted in the afternoon of August 17, 2005. The second staged loading series (Series 2) was conducted in the morning of August 18, 2005. Both staged loading series consisted of eight loading stages, which started in the low-strain range and sequentially progressed until significant shear strains were induced in the instrumented soil mass. Shear strains induced at the center of the liquefaction sensor array during staged loading ranged from approximately 0.0009% to approximately 0.07%. Pore pressure generation curves and nonlinear soil shear modulus behavior were evaluated from the data collected during each staged loading series. The results from both test series agree very well.

The pore pressure generation curves indicate that the cyclic threshold shear strain (γ_t^e) depends on the number of cyclic shear strain cycles (n). The cyclic threshold strain calculated from the data collected during Series 1 ranges from 0.01% for n = 100 to 0.02% for n = 10. The cyclic threshold strain

calculated from the data collected during Series 2 ranges from 0.015% for $n = 100$ to 0.025% for $n = 10$. A maximum pore pressure ratio of 23% was induced at the center of the liquefaction sensor array in Series 2. The pore pressure generation curves determined at this location generally agree quite well with Dobry's pore pressure generation model that was developed for Wildlife liquefiable soil (Vucetic and Dobry, 1986). However, the in-situ test results from Series 2 exhibit slightly less pore pressure generation at a given shear strain level and number of loading cycles than predicted by Dobry's model.

The nonlinear soil shear moduli obtained from both staged loading series agree very well with the upper-bound of the range in modulus reduction curves determined from resonant column tests performed on liquefiable soil material from the Wildlife Site (Haag and Stokoe, 1985). However, the in-situ moduli measured during Series 2 are slightly more linear the upper-bound range. Once pore pressures greater than 4 to 5% were induced at the center of the liquefaction sensor array, the in-situ soil shear modulus was observed to decay due to combined effects of nonlinearity and degradation due to pore water pressure generation.

Chapter 9

In-Situ Liquefaction Test Results: Test Location B, WLA

9.1 INTRODUCTION

Three separate in-situ dynamic liquefaction tests were conducted at the Wildlife Liquefaction Array (WLA) between August 8 and August 19, 2005. The general locations of these tests are shown in Figure 7-19. In this chapter, the pore pressure generation curves that were obtained at Test Location B are presented and discussed. These results were not as complete or as easy to interpret as the results measured at Test Location C. Therefore, they are presented after the results obtained at Test Location C (Chapter 8).

9.2 TEST B: ARRAY LOCATION AND PRE-DYNAMIC LOADING INFORMATION

The in-situ liquefaction sensor array at Test Location B was installed on August 12, 2005. The approximate location of the array is shown in Figure 9-1. The sensor array was installed just outside the circular array of pore water pressure transducers that were placed at the 1982 (old) WLA Site by USGS personnel (Bennett et al., 1984; see Section 7.3.1). The center point of the liquefaction sensor array was positioned at radial distances of approximately 9.0 ft (2.7 m) and 22.9 ft (7.0 m) from Pg5 and CPT 6Cg, respectively. These locations are marked in the field, and were also surveyed by Proctor (2004) relative to several benchmarks at the site. The results from this survey can be found at

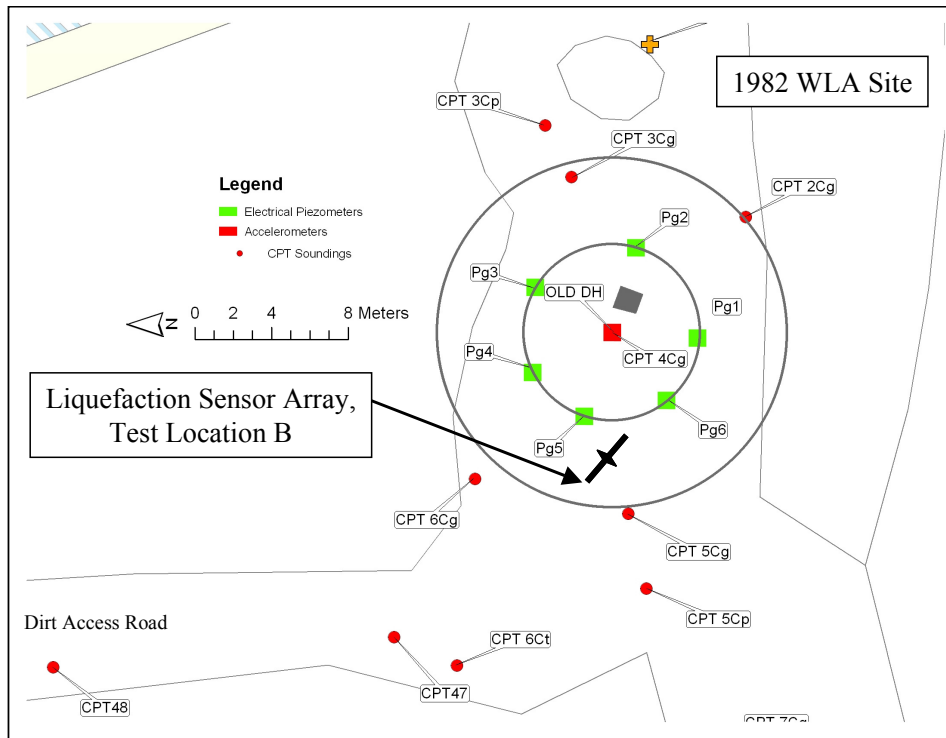


Figure 9-1 Approximate location of the in-situ liquefaction sensor array installed at Test Location B, Wildlife Liquefaction Array (WLA) (after <http://nees.ucsb.edu>).

<http://nees.ucsb.edu>. This information should be sufficient to relocate the position of the array if necessary.

The linear array at Test Location B extended in the northwest-southeast direction. The sensors were installed according to the procedure detailed in Section 5.2. A picture of an installed liquefaction sensor array, as viewed from the ground surface, is shown in Figure 9-2. As discussed in Section 5.2, the numbers next to each liquefaction sensor do not represent the order in which they were installed, but rather the positions of the sensors in the embedded trapezoidal array. A cross-sectional schematic of the sensor array is shown in Figure 9-3.

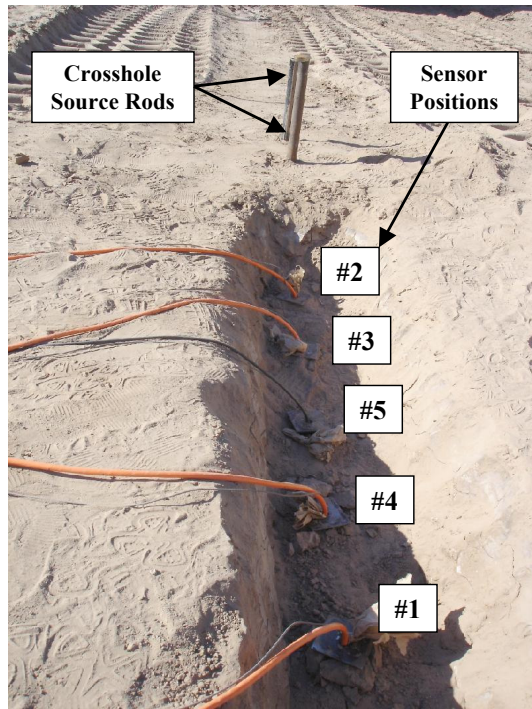


Figure 9-2 Picture of a liquefaction sensor array as seen from the ground surface.

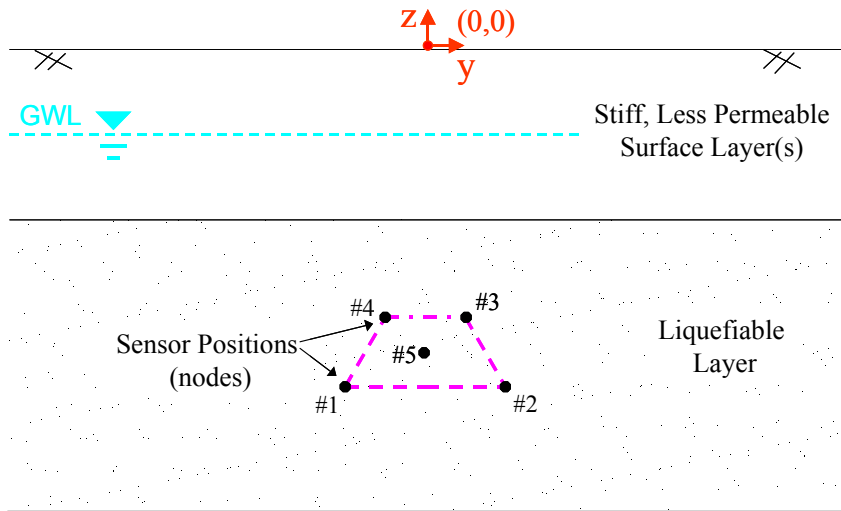


Figure 9-3 Cross-sectional schematic of an embedded liquefaction sensor array.

the sensor positions may be considered as nodes of a single quadrilateral finite element. The specific sensors that were installed in each of the nodal positions at Test Location B are listed in Table 9-1. Sensor positions No. 1 through No. 4 were occupied by liquefaction sensors containing a 3D-MEMS accelerometer and a miniature pore water pressure transducer (PPT), while sensor position No. 5 was occupied by the Druck PDCR 35/D pressure transducer. The individual calibration factors for the sensors occupying each nodal position are given in Section 4.2.

Table 9-1 also details the relative positions of each sensor in the form of y- and z-coordinates. These coordinates are referenced from a point on the ground surface directly above sensor position No. 5 (see Figure 9-3). The y-coordinate represents the horizontal, in-line distance from the center of the array, while the z-coordinate represents the vertical distance below the ground surface (depth). There is no need to provide an x-coordinate for the sensor locations because they were all installed within the same in-line plane (i.e. $x = 0$). As can be seen, the liquefaction sensors occupying positions No. 1 and No. 2 were installed roughly 2.0-ft (0.6-m) on either side of the array centerline at a depth just less than 13.0-ft (4.0-m) below the ground surface, while the liquefaction sensors occupying positions No. 3 and No. 4 were installed roughly 1.0-ft (0.3-m) on either side of the array centerline at a depth just less than 11.0-ft (3.4-m) below the ground surface. The PDCR 35/D sensor was placed at the center of the array (position No. 5) at a depth of approximately 12.0-ft (3.7-m) below the ground surface.

Table 9-1 Coordinates and tilt angles for the sensors installed in the liquefaction sensor array at Test Location B, Wildlife Liquefaction Array (WLA)

| Sensor Position (Node #) | Sensor Designation | y-coordinate (ft) | z-coordinate (ft) | Tilt Angle (degrees) | |
|-----------------------------|-----------------------|----------------------|----------------------|----------------------|--------|
| | | | | x-axis | y-axis |
| #1 | Liquefaction Sensor 1 | -1.96 | -12.93 | -1.0 | -0.6 |
| #2 | Liquefaction Sensor 5 | 2.02 | -12.98 | -2.0 | 0.0 |
| #3 | Liquefaction Sensor 6 | 1.06 | -10.98 | -2.9 | 1.0 |
| #4 | Liquefaction Sensor 9 | -0.94 | -10.99 | 0.8 | -1.1 |
| #5 | Druck PDCR 35/D PPT | 0.00 | -12.03 | NA | NA |

The sensor coordinates presented in Table 9-1 are based on measurements made from the ground surface. The accuracy of these measurements is contingent on the ability to install the sensors from the ground surface with minimal deviation (tilt). The tilt of the liquefaction sensors can be monitored via the 3D-MEMS accelerometer installed in each of them (see Section 4.2.1). Tilt about both the x- and y-axes can be sensed. The tilt angles obtained from the MEMS accelerometer in each liquefaction sensor are provided in Table 9-1. These angles were obtained from measurements taken after the sensors had reached their final locations. The tilt angles about the x- and y-axes are generally less than two degrees off vertical, indicating that the sensors were installed with minimal deviation. The PDCR 35/D sensor does not contain a MEMS accelerometer and hence does not have the ability of monitoring tilt. However, it is assumed that its deviation would be similar to the deviations experienced by the liquefaction sensors, as they are all installed in the same manner.

The position of the liquefaction sensor array, relative to the generalized soil profile at the site, is shown in Figure 9-4. The uppermost soil layer is an 8.2-ft (2.5-m) thick silt to clayey-silt bed that overlies a 14.1-ft (4.3-m) thick silty-sand layer. Beneath these floodplain deposits is a stiff 17.1-ft (5.2-m) thick clay to silty-clay layer (Bennett et al., 1984). The top of the array is approximately 3 ft (0.9 m) below the top of the liquefiable silty-sand layer. Bennett et al. (1984) originally partitioned the liquefiable silty-sand layer into an upper and lower unit, with the division between the units occurring at a depth of approximately 11.5 ft (3.5 m). Several researchers who conducted resonant column tests, cyclic triaxial tests, and cyclic simple shear tests on soil from the Wildlife Site in the 1980's also followed this notation (Haag and Stokoe, 1984; Vucetic and Dobry, 1986). The liquefaction sensor array is located partially in the upper liquefiable layer and partially in the lower liquefiable soil layer. As mentioned in Section 7.6, the upper-layer has an average fines content of 49% and an average clay-size particle content of 12%, while the lower-layer has an average fines content of 27% and an average clay-size particle content of 9%. However, the transition from the lower-layer to the upper-layer is very subtle, with fines contents generally increasing from the bottom to the top of the liquefiable soil layer. If the grain size characteristics from various researchers (see Chapter 7) obtained only from soil samples within the depth range of the liquefaction sensor array are averaged, the fines and clay-size (5 μm) particle contents are equal to 33% and 10%, respectively.

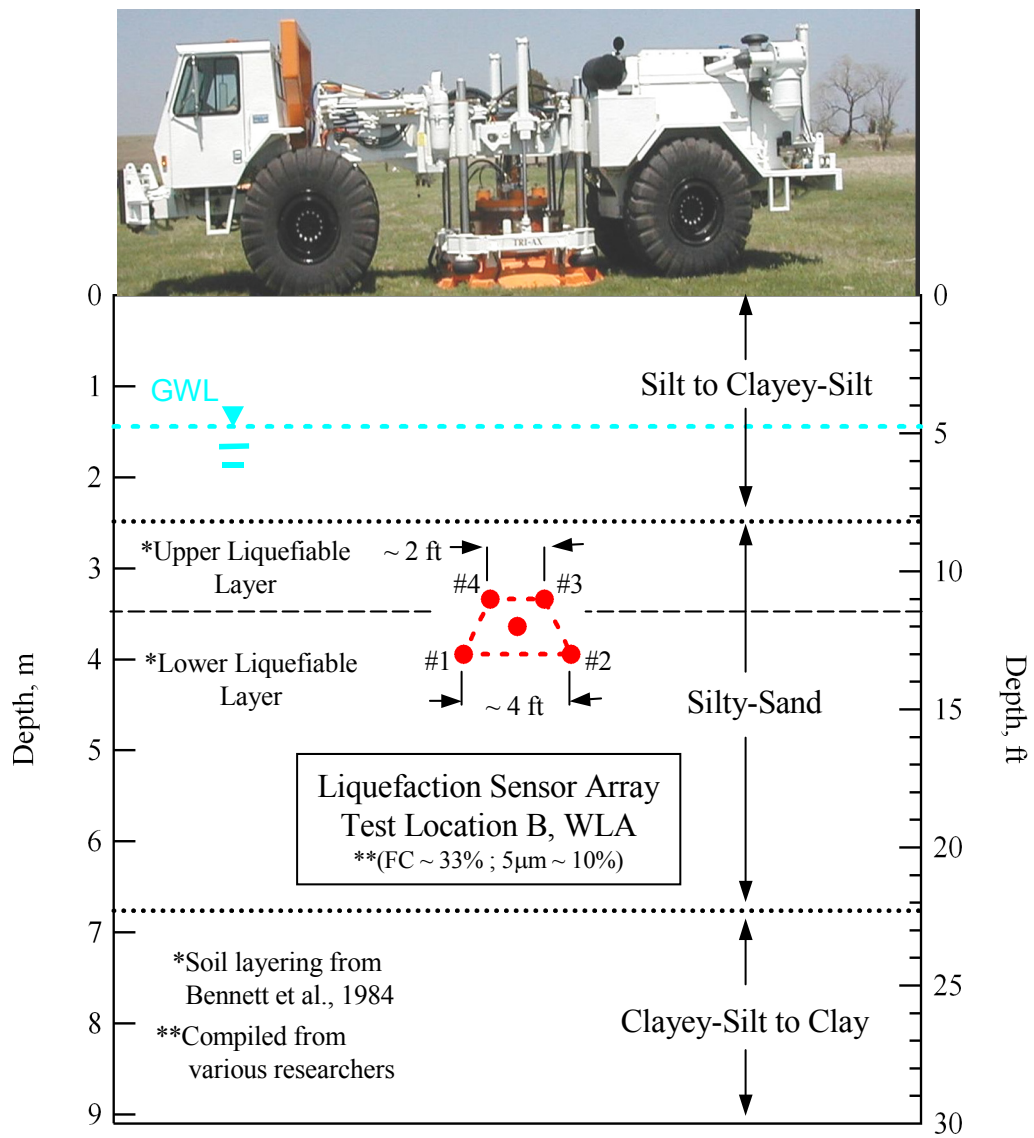


Figure 9-4 Position of the liquefaction sensor array at Test Location B, shown with respect to the general soil layering at the Wildlife Site as proposed by Bennett et al. (1984).

More recently, researchers have primarily referred to the liquefiable soil layer as a single unit (Youd and Holzer, 1994; Zeghal and Elgamal, 1994). Additionally, resonant column tests performed by Haag and Stokoe (1985) indicate that the nonlinear soil behavior of specimens from the lower liquefiable layer fall within the range of the nonlinear soil behavior of specimens from the upper liquefiable soil layer (see Figure 7-8). Similarly, Vucetic and Dobry (1986) found that the pore pressure generation data obtained from strain controlled cyclic laboratory tests on specimens from the upper and lower liquefiable soil layers could be fit with a single model (see Section 7.3.1.3). Therefore, it seems that in terms of dynamic response, the upper and lower liquefiable layers are very similar.

The approximate depth of the ground water level (GWL) at the time of testing is also shown in Figure 9-4. The GWL was evaluated from measurements taken in a standpipe and from readings obtained with the PDCR 35/D pressure transducer, located at the center of the array. The standpipe was located approximately 10 ft (3 m) away, and two separate readings taken between August 13 and August 15 placed the GWL between 4.7 and 5.1 ft (1.43 and 1.55 m) below the ground surface. More than 30 measurements made with the PDCR 35/D transducer over the same time period consistently placed the static GWL between 4.8 and 5.1 ft (1.46 and 1.55 m) below the ground surface. These similar readings show the stability and accuracy of the PDCR 35/D pressure transducer.

The liquefaction sensor array at Test Location B was installed near CPT 5Cg. The soil layering in the immediate vicinity of the liquefaction sensor array

can be verified by examining the tip resistance (q_c) and friction ratio (F_r) values obtained from CPT 5Cg. The liquefiable soil layer boundaries proposed by Bennett et al. (1984), and the depth range (approximately 11- to 13-ft or 3.4- to 4.0-m) of the in-situ liquefaction sensor array, are plotted with the tip resistance and friction ratio values from CPT 5Cg in Figure 9-5. In general, the liquefiable soil layer is marked by relatively large values of CPT tip resistance and relatively small values of CPT friction ratio compared to the layer above it. The location of the liquefiable soil layer proposed by Bennett et al (1984) was determined from site investigations performed in the vicinity of the 1982 (old) WLA Site. In fact, CPT 5Cg was one of the CPT soundings that they used to illustrate the generalized soil layering at the site (see Figure 7-2).

It is important to know the initial vertical effective stresses at the sensor locations so that excess pore pressure ratios (r_u) induced in the instrumented soil mass during dynamic loading can be calculated from the recorded excess pore water pressure data (i.e. $r_u = \Delta u / \sigma_v'$, where Δu is excess pore water pressure and σ_v' is initial vertical effective stress). The effective overburden pressures can readily be calculated knowing the depth of each sensor, the location of the GWL, and the unit weight of the soil ($\gamma \sim 120$ pcf or ~ 19.0 kN/m³). The effective overburden pressures calculated at the approximate depth of each sensor are listed in Table 9-2. These values were calculated with the static GWL located approximately 4.8-ft (1.4-m) below the ground surface.

As discussed in Section 5.2, when estimating the vertical effective stress at each sensor location, the increase in stress caused by the static hold-down force of

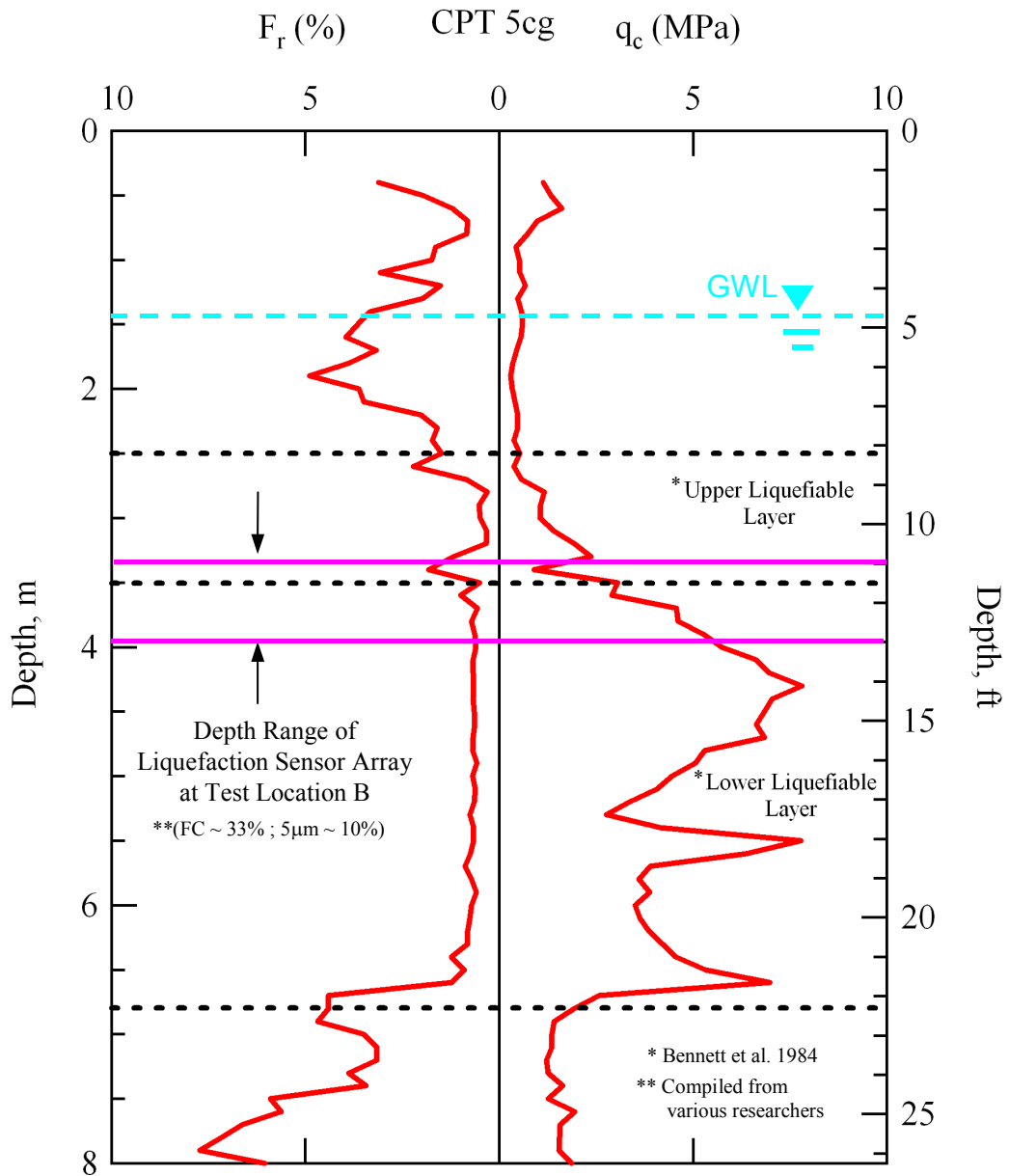


Figure 9-5 Depth range of the liquefaction sensor array at Test Location B, shown with respect to the tip resistance (q_c) and friction ratio (F_r) values obtained from CPT 5Cg and the upper and lower liquefiable soil layers proposed by Bennett et al. (1984) (raw CPT data from <http://nees.ucsb.edu>).

Table 9-2 Estimates for the effective overburden stress, increase in vertical stress due to the vibroseis base plate load, and total vertical effective stress at the approximate depth of each sensor in the liquefaction sensor array at Test Location B, Wildlife Liquefaction Array (WLA)

| Sensor Position (Node #) | Approximate Depth (ft) | Effective Overburden Stress (psf) ¹ | Increase in Stress Due to Vibroseis Base Plate Load (psf) ² | | Initial Effective Vertical Stress (psf) |
|--------------------------|------------------------|--|--|--------------------------|---|
| | | | Boussinesq | Westergaard ³ | |
| #1 | 13 | 1045 | 112 | 116 | 1160 |
| #2 | 13 | 1045 | 112 | 116 | 1160 |
| #3 | 11 | 930 | 149 | 149 | 1080 |
| #4 | 11 | 930 | 149 | 149 | 1080 |
| #5 | 12 | 990 | 128 | 131 | 1120 |

- Notes: 1. Calculated using $\gamma = 120$ pcf and GWL at 4.8 ft below ground surface
 2. Calculated beneath center of base plate with a uniform surface pressure = 800 psf
 3. Calculated with Poisson's Ratio = 0.3

the vibroseis base plate must also be taken into account. The uniform surface pressure (assuming the base plate to be rigid) applied by the base plate during testing was approximately 800 psf (38 kPa). The change in vertical stress beneath the center of the base plate at the depth of each sensor was calculated using both Boussinesq's and Westergaard's elastic stress distribution solutions (Coduto, 1994). Estimates for the changes in vertical stress obtained from calculating Boussinesq's and Westergaard's solutions at the depth of each sensor are given in Table 9-2. As can be seen, both of these solutions give very similar results. The initial vertical effective stress at each sensor depth was calculated by superimposing the change in vertical stress caused by the applied surface load of the vibroseis base plate onto the preexisting effective overburden pressure. Table 9-2 details the estimates obtained for the initial vertical effective stress at each

sensor depth. These values were used to normalize the excess pore water pressures recorded during dynamic loading to obtain excess pore pressure ratios.

As discussed in Section 6.4, readings obtained from all five pressure transducers (4 miniature PPT's located in the liquefaction sensors placed at each corner node and the larger PDCR 35/D pressure transducer located at the center of the array) were used to calculate r_u values for each stage of the in-situ liquefaction tests. However, the r_u values used to construct the pore pressure generation curves for each site were obtained solely from the PDCR 35/D transducer located at the center of the array.

9.2.1 Crosshole Test Results

As discussed in Section 5.2, crosshole seismic tests are conducted between sensors at the same depth, both before and after dynamic loading, to verify saturation and determine how the small-strain shear stiffness of the liquefiable soil was affected by the liquefaction testing. A cross-sectional schematic showing the liquefaction sensor array, the crosshole source rods, and the base plate of T-Rex is shown in Figure 9-6. At Test Location B, source rods A and B were placed in-line with the sensor array at distances of approximately 0.75 ft (0.23 m) and 1.75 ft (0.53 m) from the edge of the base plate of T-Rex, respectively. Crosshole source rod B was inserted so that its tip was located at the same elevation as sensors No. 1 and No. 2 (approximately 13-ft or 4.0-m deep), while crosshole source rod A was inserted so that its tip was located at the same elevation as sensors No. 3 and No. 4 (approximately 11-ft or 3.4-m deep). Crosshole tests were performed by vertically impacting the top of one of the

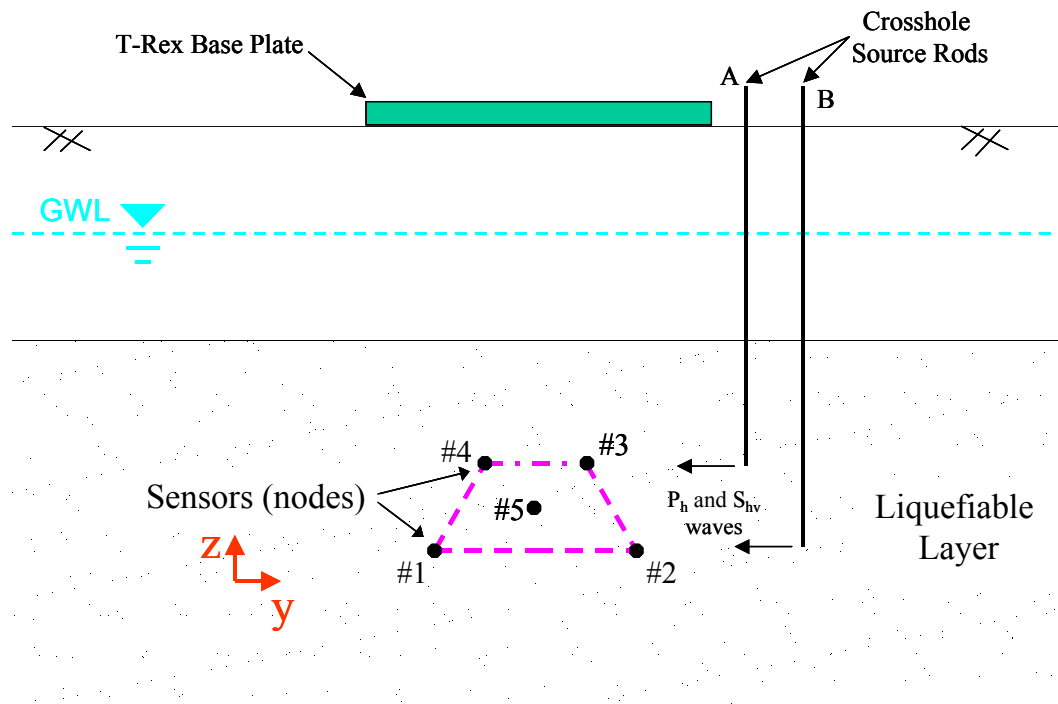
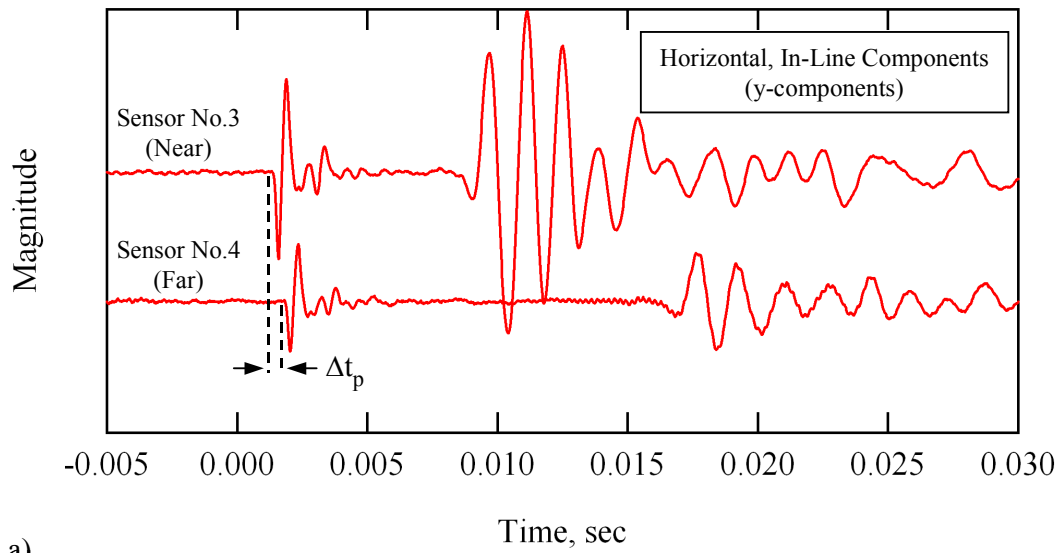


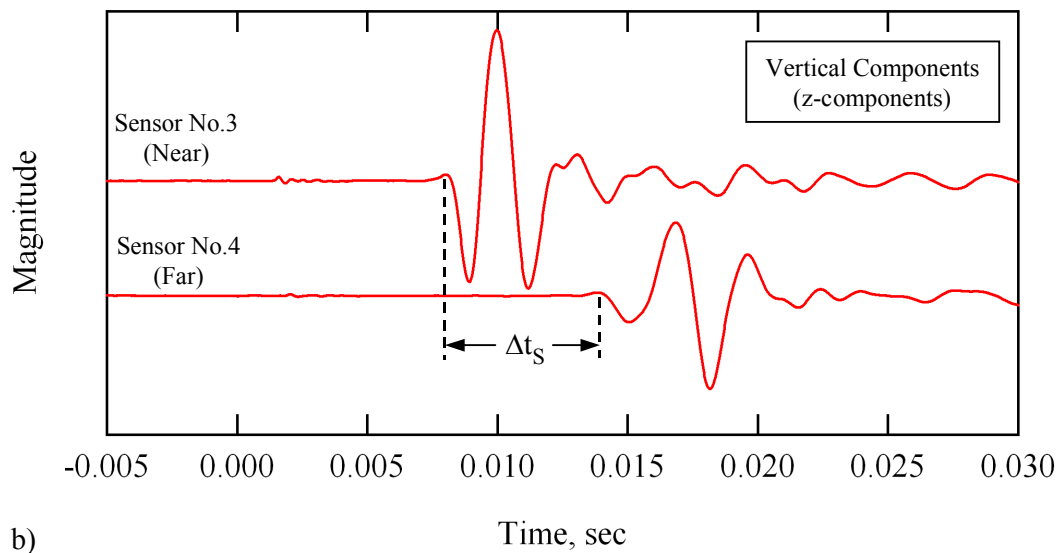
Figure 9-6 Cross-sectional schematic of the liquefaction sensor array, crosshole source rods, and the base plate of T-Rex at Test Location B.

source rods while simultaneously recording the vibration-sensing outputs of the two sensors located at the same depth as the tip of the rod. The horizontal, in-line component (y-component) of the 3D-MEMS accelerometer in each sensor was used to sense horizontally propagating compression wave (P_h -wave) arrivals, while the vertical component (z-component) was used to sense horizontally propagating, vertically polarized shear wave (S_{hv} -wave) arrivals.

Interval wave travel times between the near and far sensors were used to calculate wave velocities. Figure 9-7 shows an example of typical records that were collected from performing crosshole tests at Location B. These particular waveforms were recorded by sensors No. 3 and No. 4. Figure 9-7a shows the



a)



b)

Figure 9-7 Crosshole waveforms recorded by the: a) horizontal, in-line components (P_h -waves identified on), and b) vertical components (S_{hv} -waves identified on) of sensors No. 3 (near) and No. 4 (far) at Test Location B.

waveforms that were sensed by the horizontal, in-line components (y-components) of these sensors. The P_h -wave arrivals are identified as the first seismic energy to reach each sensor. The P_h -wave velocity (V_p) of the material between the sensors is equal to the horizontal distance between them (2.0 ft or 0.6 m; see Table 9-1) divided by the P_h -wave interval travel time (Δt_p). Figure 9-7b shows the waveforms that were sensed by the vertical components (z-components) of sensors No. 3 and No. 4. Given a downward impact at the source rod, and knowing the polarity of the sensors, the S_{hv} -wave arrivals are identified as the first major downward departure in the records. The S_{hv} -wave velocity ($V_{s,hv}$) of the material between the sensors is equal to the horizontal distance between them divided by the S_{hv} -wave interval travel time (Δt_s). As a side note, the S_{hv} -wave arrivals can be seen on the y-component records and the P_h -wave arrivals can be seen on the z-component records. However, the wave arrival times are most accurately determined by using the proper sensing components as noted above.

The P_h -wave and S_{hv} -wave velocities obtained from performing crosshole tests at Location B are provided in Table 9-3. Crosshole tests were performed three separate times throughout the course of in-situ liquefaction testing at Location B. The first set of crosshole tests was performed prior to bringing T-Rex into position over the top of the liquefaction sensor array. This set of tests was conducted to provide baseline velocities for the soil prior to application of the base plate hold-down force and subsequent staged dynamic loading. The second set of crosshole tests was performed after the full, static base plate hold-down

Table 9-3 Results from three separate sets of Crosshole tests performed between the top (sensors No. 3 and No. 4) and bottom (sensors No. 2 and No. 1) sensor pairs in the liquefaction sensor array at Test Location B, Wildlife Liquefaction Array (WLA)

| Date | Time | Condition | No. 3 to No. 4 ~ 11-ft Deep | | No. 2 to No. 1 ~ 13-ft Deep | |
|-----------|----------|--|--------------------------------|----------------------|--------------------------------|----------------------|
| | | | V _{S,hv} (fps) | V _p (fps) | V _{S,hv} (fps) | V _p (fps) |
| 8/13/2005 | 10:10 AM | Initial Baseline Readings: Prior to Static Hold-Down Force | 330 | 4450 | 430 | 5220 |
| 8/13/2005 | 11:15 AM | After Static Hold-Down Force, Prior to Series 1 Dynamic Loading | 335 | 4450 | 430 | 5220 |
| 8/15/2005 | 8:31 AM | Prior to Series 2 Dynamic Loading | 300 | 4450 | 410 | 5220 |

force of T-Rex had been applied to the soil (approximately 45000 lb or 200 kN; see Section 5.3), but prior to any dynamic loading. After the first two sets of crosshole measurements had been performed, the first series of staged dynamic loading was conducted at Location B (discussed in Section 9.3). Then, the soil was allowed to recover for approximately 44 hours, and a second series of dynamic loading was conducted (discussed in Section 9.4). The third set of crosshole measurements was performed immediately before the second series of staged dynamic loading.

The baseline crosshole test results listed in Table 9-3 show that the V_p values between the bottom sensor pair (sensors No. 2 and No. 1; approximately 13-ft or 4-m deep) in the array are slightly greater than 5000 fps (1500 m/s). As discussed in Section 2.3.1, fully saturated soils have P-wave velocities of

approximately 5000 fps (i.e. the velocity of a compression wave traveling through water). The V_p values between the top sensor pair (sensors No. 3 and No. 4; approximately 11-ft or 3.3-m deep) are nearly 4500 fps (1370 m/s). The top sensors would have to be separated by approximately 3 in. (8 cm) more to obtain V_p values of 5000 fps. It is unlikely that the distance between the sensors could be off by that much, considering that the bottom sensor pair in the array at this location, and the top and bottom sensor pairs in the array at Test Location C (see Section 8.2.1) all indicated V_p values of more than 5000 fps using the distances measured at the ground surface. While not greater than 5000 fps, this value indicates a material that is very close to complete saturation. Laboratory test results from Valle-Molina (2006) indicate that a V_p value of 4500 fps equates to a B value of approximately 0.92 and a saturation level greater than 99.9%. Laboratory test results from Ishihara et al. (2001) indicate that a V_p value of 4500 fps equates to a B value of approximately 0.9. The baseline crosshole results listed in Table 9-3 show that the $V_{S,hv}$ between the top sensors in the array was approximately 330 fps (100 m/s) and the $V_{S,hv}$ between the bottom sensors in the array was approximately 430 fps (131 m/s).

The crosshole test results listed in Table 9-3 show that the $V_{S,hv}$ between the top and bottom sensor pairs were not substantially affected by the application of the base plate hold-down force. This lack of change is not surprising as the increase in vertical stress at the sensor locations due to the base plate hold-down force was only estimated to be between 10 to 15% of the initial effective overburden stress (see Table 9-2). Since the shear wave velocity of soil

theoretically changes according to the quarter-power of the change in effective stress, it is expected that the velocities would have only increased between 2 to 4%. Results from the third set of crosshole tests indicate that the $V_{S,hv}$ values between both pairs of sensors were reduced by 20 to 30 fps (6 to 9 m/s), indicating that the first series of dynamic loading, and subsequent pore pressure generation, had a softening effect on the soil in the region of the liquefaction sensor array.

9.3 TEST B: STAGED DYNAMIC LOADING SERIES 1

The in-situ liquefaction sensor array at Test Location B was installed on August 12, 2005. The sensor installation process required a full day to complete. The pore water pressure transducer (PPT) in each sensor was powered overnight using a 12-volt battery and a DC-to-DC converter to help ensure that the static PPT outputs remained as steady as possible during testing the following day (as discussed in Section 4.3.2). The first series (Series 1) of staged dynamic loading began in the afternoon of August 13.

9.3.1 Loading Stages in Series 1

In Series 1, eleven separate dynamic loading stages were applied to the instrumented soil mass. Only the information recorded during eight of these loads was used to develop the pore pressure generation curves in the data reduction process. The other three loads all occurred at low strain levels and were duplicates of dynamic loads used in the data reduction process. They were not used in the data reduction because one of the PPT's was accidentally not

connected to the data recording system at the time of recording. The dynamic shear loads were applied by driving T-Rex in the horizontal, in-line direction. Just as done at all test locations, an external function generator was used to control the frequency, number of cycles, and drive voltage amplitude supplied to T-Rex. Details of the Series 1 staged dynamic loading sequence are provided in Table 9-4. The first three dynamic loads were applied at a frequency of 20 Hz. The last five dynamic loads were applied at a frequency of 10 Hz. All of the loads had a duration of 100 cycles, except Load No. 11, which had a duration of 200 cycles. Previous tests conducted at Test Location A (discussed in Chapter 10) had shown that higher peak shear strains could be induced in the soil deposit at a frequency of 10 Hz than at a frequency of 20 Hz. However, T-Rex has more harmonic distortion when operating at 10 Hz than at 20 Hz. As discussed in Section 6.5, harmonic distortion in the ground motion signals recorded during testing complicates the evaluation of the nonlinear soil shear modulus. Therefore, tests were conducted at 20 Hz with the goal of being able to more accurately resolve the nonlinear soil shear modulus behavior of the soil, and at 10 Hz to generate shear strains as large as possible within the instrumented soil mass. However, to avoid loading the soil beyond its cyclic threshold strain (γ_t^e), the 20-Hz loads were only carried to the point where a minute amount of excess pore water pressure was generated at the center of the liquefaction sensor array (i.e. $r_u < 1\%$). At this point, the loading frequency was decreased to 10 Hz, the drive amplitude was dropped back down to a low level, and staged dynamic loading was begun again.

Table 9-4 Details of the Series 1 staged dynamic loading sequence conducted at Test Location B, Wildlife Liquefaction Array (WLA)

| Time on 8/13/2005 | Dynamic Load Number | Function Generator Drive Signal | | | Approximate Ground Force (lb) |
|----------------------|------------------------|---------------------------------|---------------------|----------------------|-------------------------------------|
| | | Frequency (Hz) | Number of Cycles | Amplitude (volts) | |
| 11:23 AM | 1 | 20 | 100 | 0.4 | 2000 |
| 12:08 PM | 5 | 20 | 100 | 0.8 | 5000 |
| 12:13 PM | 6 | 20 | 100 | 1.5 | 10000 |
| 12:24 PM | 7 | 10 | 100 | 0.4 | 2000 |
| 12:29 PM | 8 | 10 | 100 | 0.8 | 5000 |
| 12:35 PM | 9 | 10 | 100 | 1.5 | 15000 |
| 12:42 PM | 10 | 10 | 100 | 2.5 | 20000 |
| 12:58 PM | 11 | 10 | 200 | 5 | 30000 |

Shear strains (γ) induced in the instrumented soil mass were calculated at the center of the liquefaction sensor array for every stage of dynamic loading using the 4-node, isoparametric finite element formulation presented in Section 6.3. The pore pressure ratios (r_u) at each sensor location were obtained by dividing the measured residual pore water pressure, obtained from processing the raw pore pressure transducer (PPT) records according to the procedure outlined in Section 6.4, by the total vertical effective stress at each sensor location (see Table 9-2). The r_u values used to construct the pore pressure generation curves for each site were obtained solely from the PDCR 35/D transducer located at the center of the array (Sensor No.5). The r_u values obtained from the miniature PPT's (Sensors No. 1 – No. 4) were only used in a qualitative sense to observe how the pore pressure generation varied within the instrumented soil mass.

The nonlinear shear modulus of the soil within the liquefaction sensor array could not accurately be resolved at this location due to harmonic distortion and small amounts of noise in some of the raw accelerometer records. These problems made it extremely difficult to obtain precise values for the time lags between sensors. For example, assuming a shear wave velocity for the soil of 400 fps (122 m/s) and a vertical distance between sensors of 2.0 ft (0.6 m), a sampling rate of 8192 samples per second yields approximately 40 digitized points between wave arrival times. If one were to be off by 4 data points (0.0005 seconds) in determining the time lag between sensors, the estimated shear wave velocity would be off by approximately 10%. This would alter the estimated shear modulus by approximately 20%. Frequency-domain filtering and time-domain integration were experimented with in an attempt to reduce the influence of harmonic distortion and noise in the raw accelerometer records and isolate the driving frequency. While these efforts made the records look much cleaner, the time lags between sensors were adversely altered. In general, the raw accelerometer records recorded at this location were not clean enough to accurately resolve the in-situ soil shear modulus.

9.3.2. Response of the Deposit During Loading Series 1

9.3.2.1 Loading Stage No. 1

The force applied at the ground surface by T-Rex, the shear strain induced at the center of the liquefaction sensor array, and the pore pressure ratios generated at each PPT location during loading stage No. 1 of staged loading

Series 1 are shown in Figure 9-8. The ground force during loading stage No. 1 was less than 2000 lb (8.9 kN) throughout the 100 cycles of 20-Hz loading. This load induced fairly uniform cyclic shear strains at the center of the liquefaction sensor array of approximately 0.0009%. These shear strains did not trigger the generation of any excess pore water pressure in the instrumented soil mass, as indicated by the fact that the pore pressure ratios at each sensor location remained equal to zero.

Tabulated values for the pore pressure ratios and average shear strains (averaged over the given number of loading cycles) induced in the soil during loading stage No. 1 of staged loading Series 1 are provided in Table 9-5. These values are provided for different numbers of total loading cycles for all of the loading stages applied during staged loading Series 1.

9.3.2.2 Loading Stage No. 5

The force applied at the ground surface by T-Rex, the shear strain induced at the center of the liquefaction sensor array, and the pore pressure ratios generated at each PPT location during loading stage No. 5 of staged loading Series 1 are shown in Figure 9-9. The ground force during loading stage No. 5 was slightly less than 5000 lb (22.2 kN) throughout the 100 cycles of 20-Hz loading. This load induced fairly uniform cyclic shear strains at the center of the liquefaction sensor array of approximately 0.0037% (see Table 9-5 for strain values averaged over various numbers of loading cycles). These shear strains did not trigger the generation of any excess pore water pressure in the instrumented

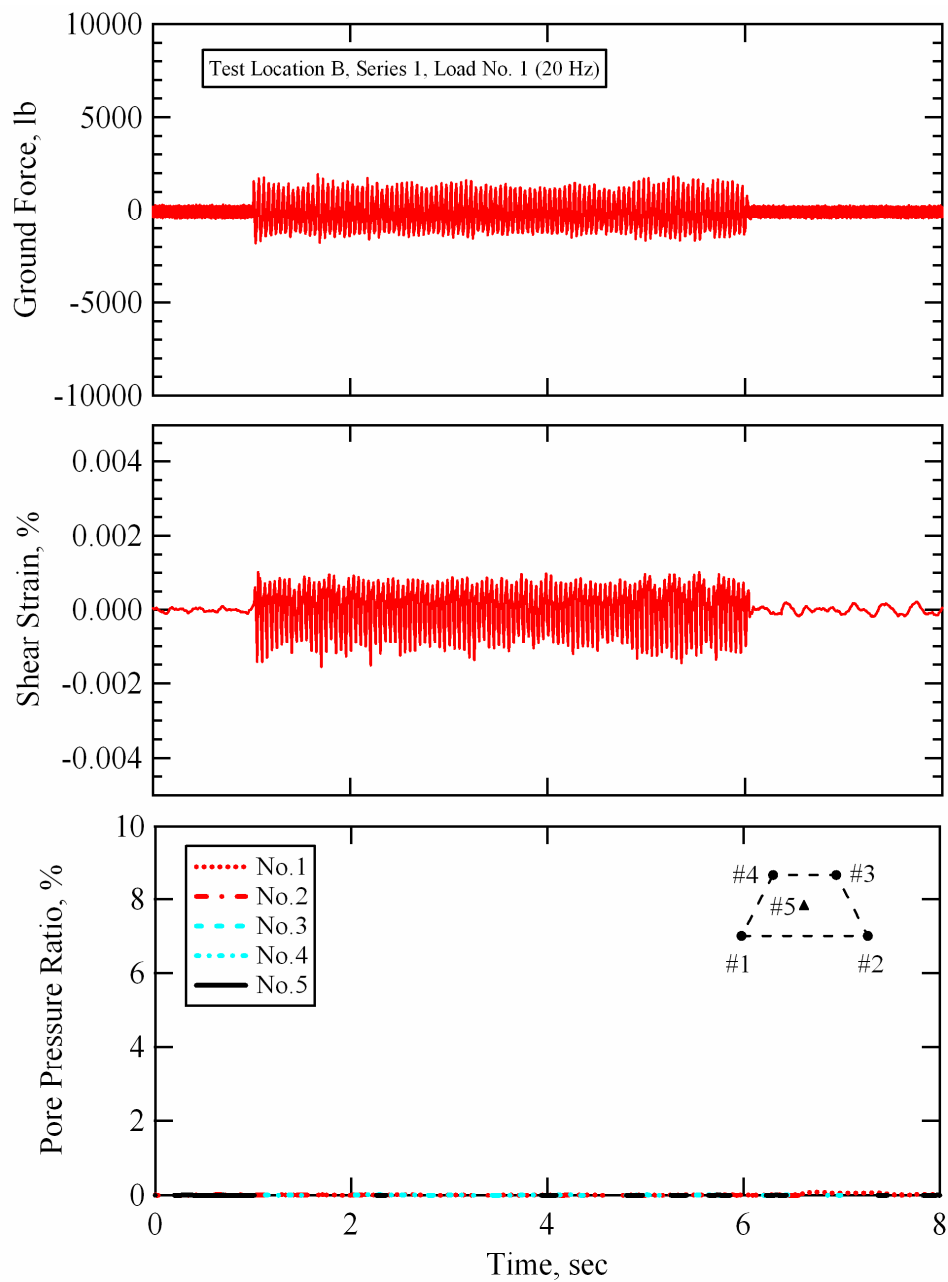


Figure 9-8 Force applied at the ground surface by T-Rex, shear strain induced at the center of the instrumented soil mass, and pore pressure ratios generated at each sensor location during Series 1, loading stage No. 1; Test Location B, Wildlife Liquefaction Array.

Table 9-5 Pore pressure ratios and average shear strains at the center of the liquefaction sensor array for different numbers of loading cycles; Series 1, Test Location B, Wildlife Liquefaction Array

| Number of Cycles | γ or r_u | Pore Pressure Ratio ¹ (r_u) and Average Shear Strain ² (γ) Values, % | | | | | | | |
|------------------|-------------------|---|--------|--------|--------|--------|--------|--------|--------|
| | | Series 1: Staged Load Number | | | | | | | |
| | | No. 1 | No. 5 | No. 6 | No. 7 | No. 8 | No. 9 | No. 10 | No. 11 |
| 10 | γ | 0.0009 | 0.0037 | 0.0085 | 0.0008 | 0.0025 | 0.0088 | 0.0196 | 0.0360 |
| | r_u | 0 | 0 | 0 | 0 | 0 | 0 | 0 | 3 |
| 20 | γ | 0.0010 | 0.0037 | 0.0085 | 0.0008 | 0.0025 | 0.0092 | 0.0204 | 0.0388 |
| | r_u | 0 | 0 | 0 | 0 | 0 | 0 | 1 | 7 |
| 30 | γ | 0.0009 | 0.0037 | 0.0085 | 0.0007 | 0.0025 | 0.0095 | 0.0211 | 0.0411 |
| | r_u | 0 | 0 | 0 | 0 | 0 | 0 | 2 | 11 |
| 40 | γ | 0.0009 | 0.0037 | 0.0085 | 0.0007 | 0.0025 | 0.0096 | 0.0217 | 0.0433 |
| | r_u | 0 | 0 | 0 | 0 | 0 | 0 | 2 | 14 |
| 50 | γ | 0.0009 | 0.0037 | 0.0085 | 0.0007 | 0.0025 | 0.0098 | 0.0220 | 0.0453 |
| | r_u | 0 | 0 | 0 | 0 | 0 | 0 | 3 | 19 |
| 60 | γ | 0.0009 | 0.0037 | 0.0085 | 0.0007 | 0.0025 | 0.0099 | 0.0223 | 0.0471 |
| | r_u | 0 | 0 | 0 | 0 | 0 | 0 | 3 | 22 |
| 70 | γ | 0.0009 | 0.0037 | 0.0085 | 0.0007 | 0.0025 | 0.0100 | 0.0225 | 0.0489 |
| | r_u | 0 | 0 | 0 | 0 | 0 | 0 | 3 | 26 |
| 80 | γ | 0.0009 | 0.0037 | 0.0085 | 0.0007 | 0.0025 | 0.0100 | 0.0227 | 0.0505 |
| | r_u | 0 | 0 | 0 | 0 | 0 | 0 | 3 | 30 |
| 90 | γ | 0.0009 | 0.0037 | 0.0085 | 0.0007 | 0.0025 | 0.0101 | 0.0229 | 0.0517 |
| | r_u | 0 | 0 | 0 | 0 | 0 | 0 | 4 | 33 |
| 100 | γ | 0.0009 | 0.0037 | 0.0085 | 0.0007 | 0.0025 | 0.0102 | 0.0230 | 0.0513 |
| | r_u | 0 | 0 | 0 | 0 | 0 | 0 | 4 | 35 |
| 150 | γ | - | - | - | - | - | - | - | * |
| | r_u | - | - | - | - | - | - | - | 39 |
| 200 | γ | - | - | - | - | - | - | - | * |
| | r_u | - | - | - | - | - | - | - | 40 |

- Notes: 1. r_u from the PDCR 35/D pressure transducer at the center of the array after the given number of loading cycles
2. γ calculated at the center of the array and averaged over the given number of loading cycles
* γ could not accurately be calculated after 100 cycles of loading

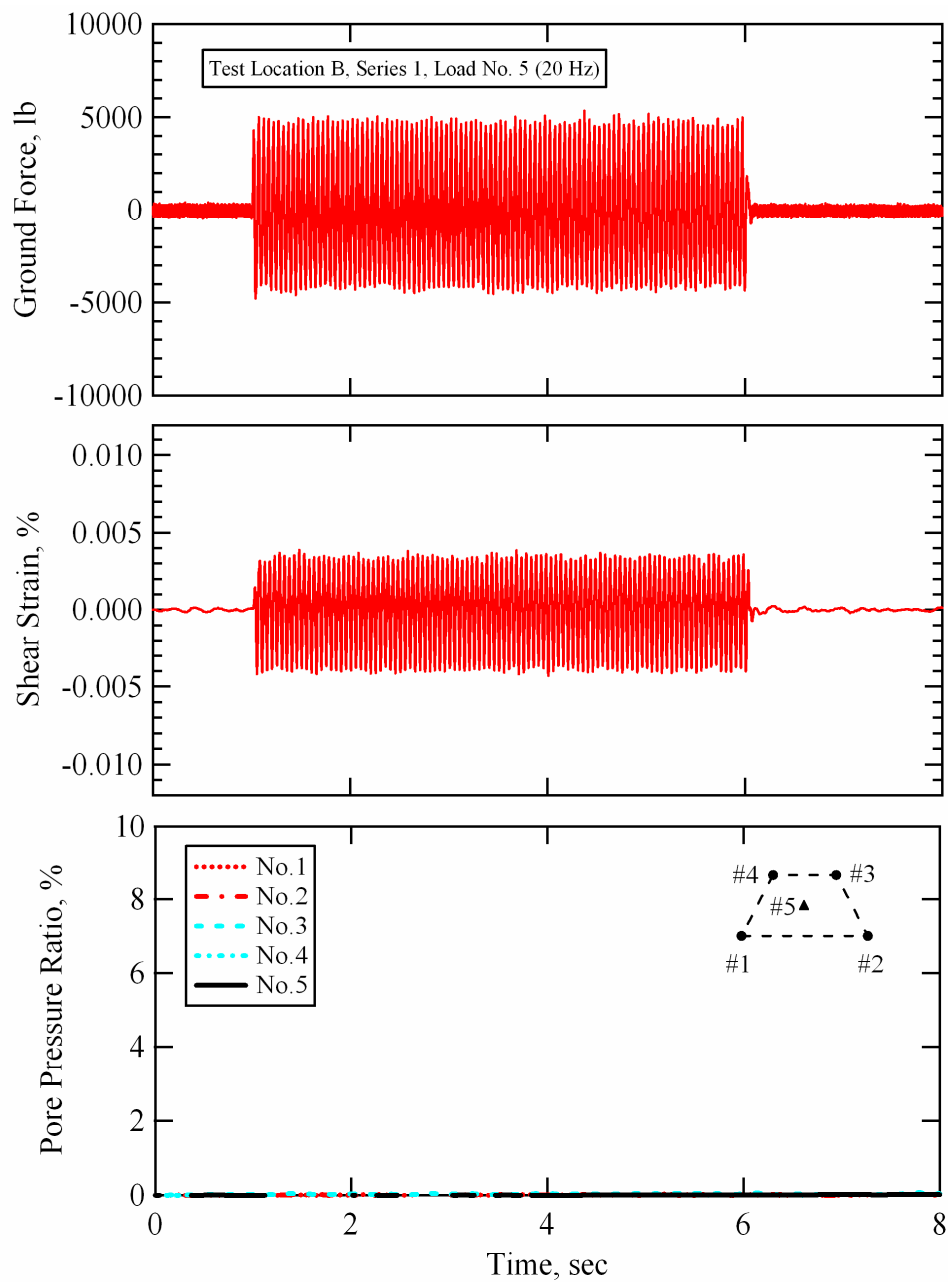


Figure 9-9 Force applied at the ground surface by T-Rex, shear strain induced at the center of the instrumented soil mass, and pore pressure ratios generated at each sensor location during Series 1, dynamic Load No. 5; Test Location B, Wildlife Liquefaction Array.

soil mass, as indicated by the fact that the pore pressure ratios at each sensor location remained equal to zero.

9.3.2.3 Loading Stage No. 6

The force applied at the ground surface by T-Rex, the shear strain induced at the center of the liquefaction sensor array, and the pore pressure ratios generated at each PPT location during loading stage No. 6 of staged loading Series 1 are shown in Figure 9-10. The ground force during loading stage No. 6 was slightly less than 10000 lb (44.5 kN) throughout the 100 cycles of 20-Hz loading. This load induced fairly uniform cyclic shear strains at the center of the liquefaction sensor array of approximately 0.0085% (see Table 9-5 for strain values averaged over various numbers of loading cycles). A minute amount of excess pore water pressure was generated in the instrumented soil mass during this test. However, none of the sensors indicated pore pressure ratios greater than 0.5%. At this point, testing was halted for approximately 10 minutes (see Table 9-5) while the pore pressures within the array were allowed to dissipate back to their static values (as monitored by the PDCR 35/D transducer). The actual time required for the pressure to return to its static condition was substantially less than the allotted time. After loading stage No. 6, the loading frequency was decreased to 10 Hz, the drive amplitude was dropped back down to a low level, and staged dynamic loading began again.

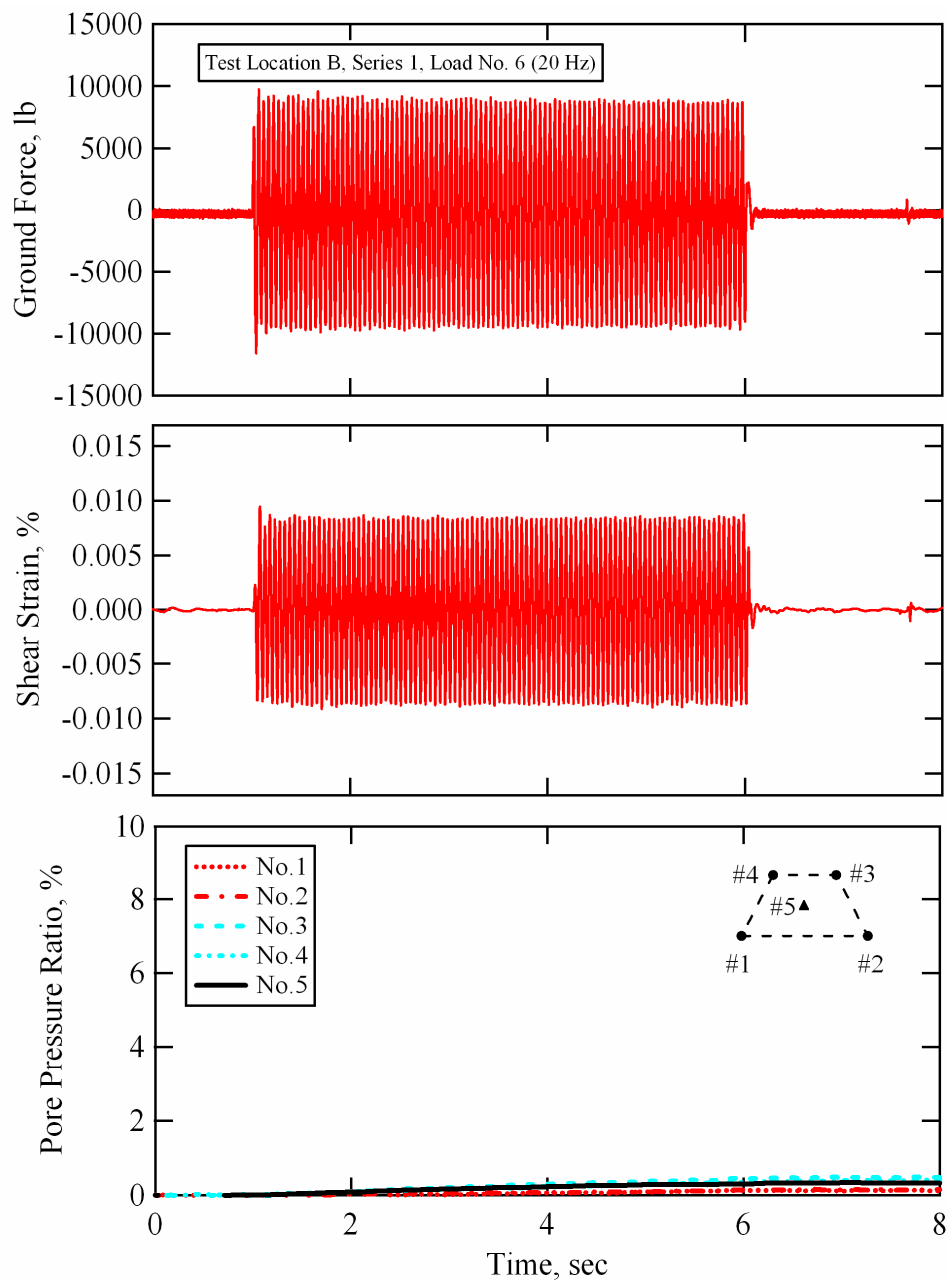


Figure 9-10 Force applied at the ground surface by T-Rex, shear strain induced at the center of the instrumented soil mass, and pore pressure ratios generated at each sensor location during Series 1, loading stage No. 6; Test Location B, Wildlife Liquefaction Array.

9.3.2.4 Loading Stage No. 7

The force applied at the ground surface by T-Rex, the shear strain induced at the center of the liquefaction sensor array, and the pore pressure ratios generated at each PPT location during loading stage No. 7 of staged loading Series 1 are shown in Figure 9-11. The ground force during loading stage No. 7 was slightly less than 2000 lb (8.9 kN) throughout the 100 cycles of 10-Hz loading. This load induced fairly uniform cyclic shear strains at the center of the liquefaction sensor array of approximately 0.0007% (see Table 9-5 for strain values averaged over various numbers of loading cycles). These shear strains did not trigger the generation of any excess pore water pressure in the instrumented soil mass, as indicated by the fact that the pore pressure ratios at each sensor location remained equal to zero.

9.3.2.5 Loading Stage No. 8

The force applied at the ground surface by T-Rex, the shear strain induced at the center of the liquefaction sensor array, and the pore pressure ratios generated at each PPT location during loading stage No. 8 of staged loading Series 1 are shown in Figure 9-12. The ground force during loading stage No. 8 was slightly less than 5000 lb (22.2 kN) throughout the 100 cycles of 10-Hz loading. This load induced fairly uniform cyclic shear strains at the center of the liquefaction sensor array of approximately 0.0025% (see Table 9-5 for strain values averaged over various numbers of loading cycles). These shear strains did not trigger the generation of any excess pore water pressure in the instrumented

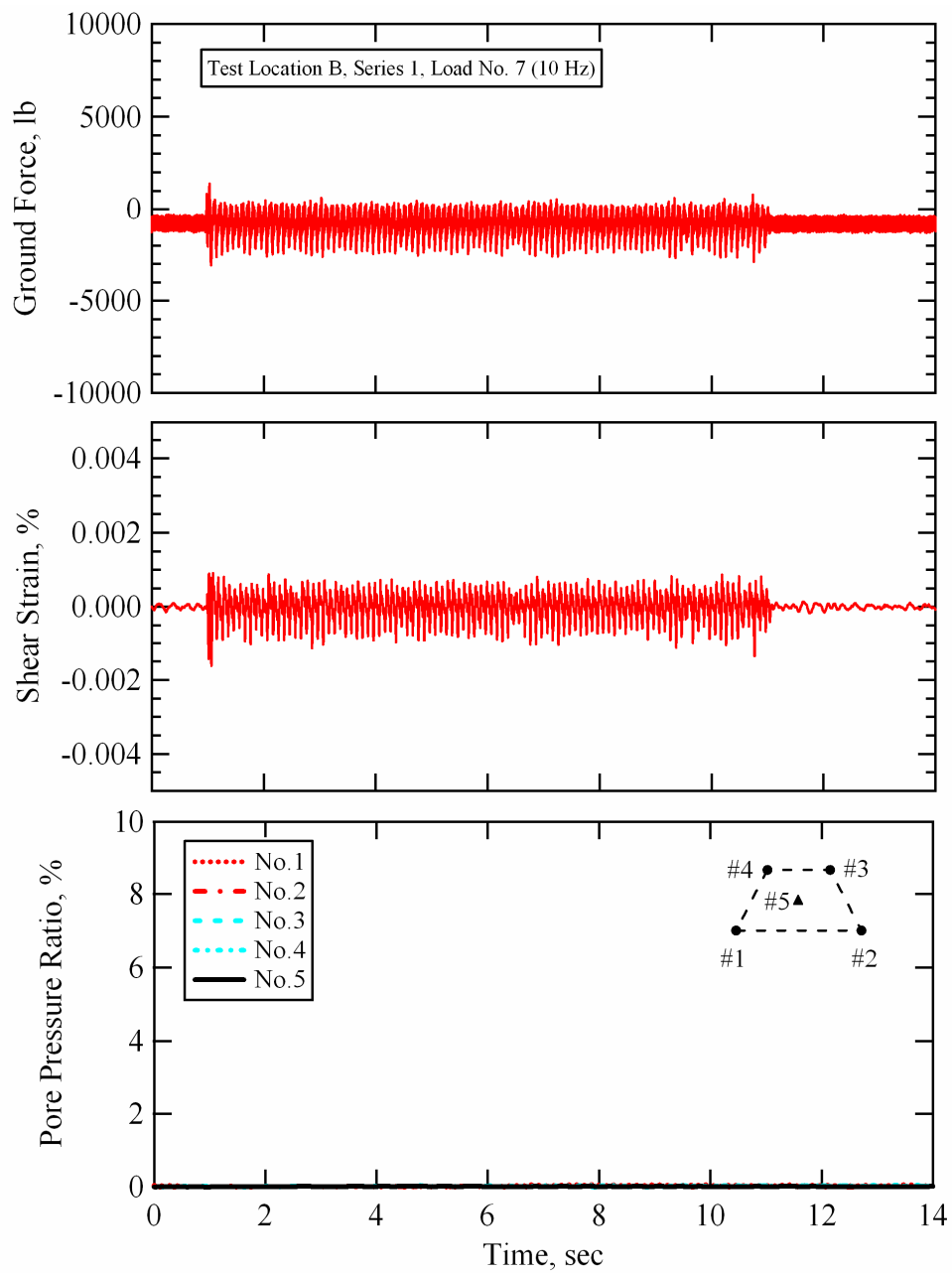


Figure 9-11 Force applied at the ground surface by T-Rex, shear strain induced at the center of the instrumented soil mass, and pore pressure ratios generated at each sensor location during Series 1, loading stage No. 7; Test Location B, Wildlife Liquefaction Array.

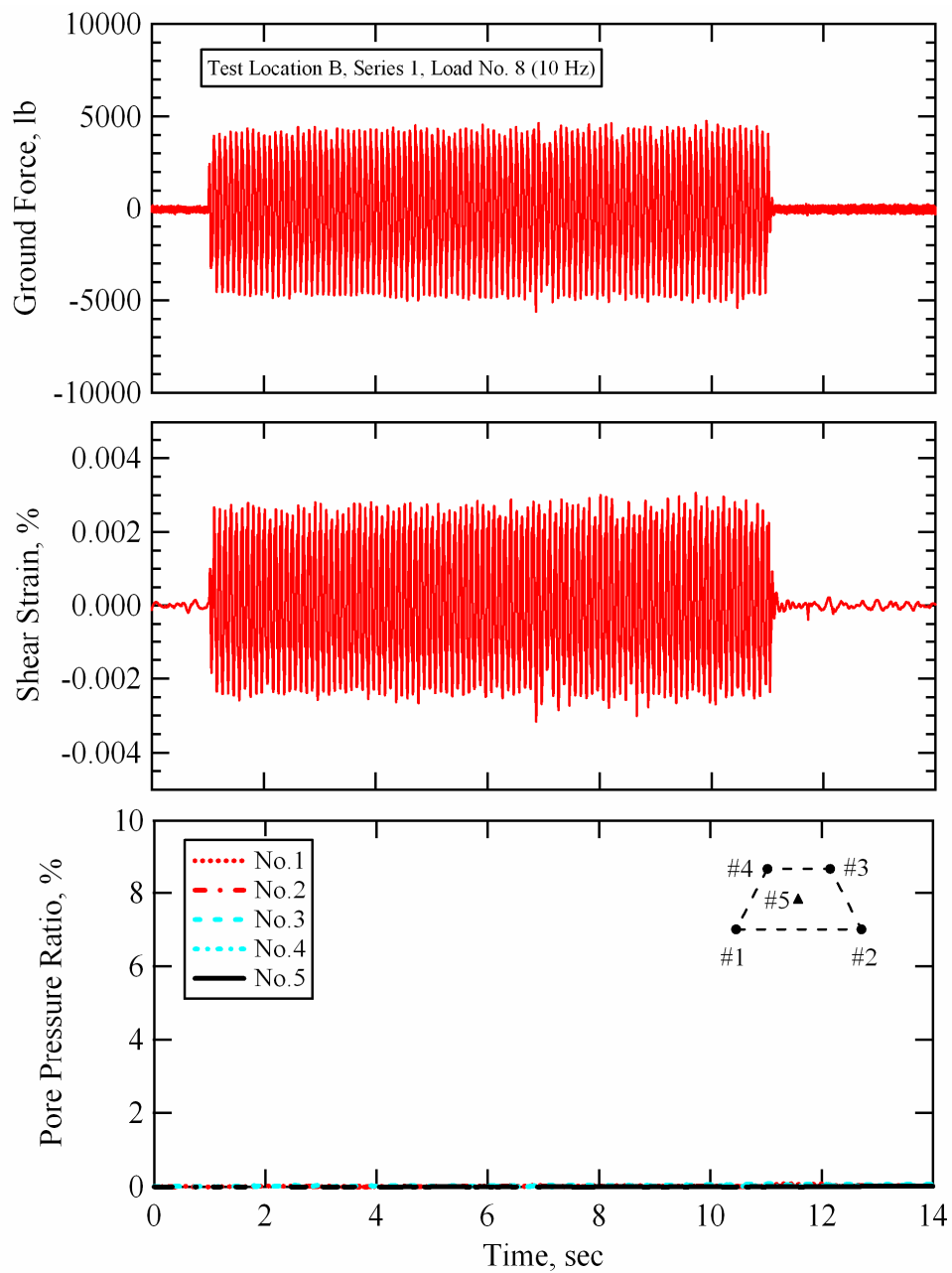


Figure 9-12 Force applied at the ground surface by T-Rex, shear strain induced at the center of the instrumented soil mass, and pore pressure ratios generated at each sensor location during Series 1, loading stage No. 8; Test Location B, Wildlife Liquefaction Array.

soil mass, as indicated by the fact that the pore pressure ratios at each sensor location remained equal to zero.

9.3.2.6 Loading Stage No. 9

The force applied at the ground surface by T-Rex, the shear strain induced at the center of the liquefaction sensor array, and the pore pressure ratios generated at each PPT location during loading stage No. 9 of staged loading Series 1 are shown in Figure 9-13. The ground force during loading stage No. 9 was slightly less than 15000 lb (66.7 kN) throughout the 100 cycles of 10-Hz loading. This load induced fairly uniform cyclic shear strains at the center of the liquefaction sensor array of approximately 0.001% (see Table 9-5 for strain values averaged over various numbers of loading cycles). These shear strains did not trigger the generation of any excess pore water pressure in the instrumented soil mass, as indicated by the fact that the pore pressure ratios at each sensor location remained essentially equal to zero.

9.3.2.7 Loading Stage No. 10

The force applied at the ground surface by T-Rex, the shear strain induced at the center of the liquefaction sensor array, and the pore pressure ratios generated at each PPT location during loading stage No. 10 of staged loading Series 1 are shown in Figure 9-14. The ground force during loading stage No. 10 was slightly larger than 20000 lb (88.9 kN) throughout the 100 cycles of 10-Hz loading. The shear strain time history is not quite as uniform as the ones presented for the earlier dynamic loads in this series. The average shear strain

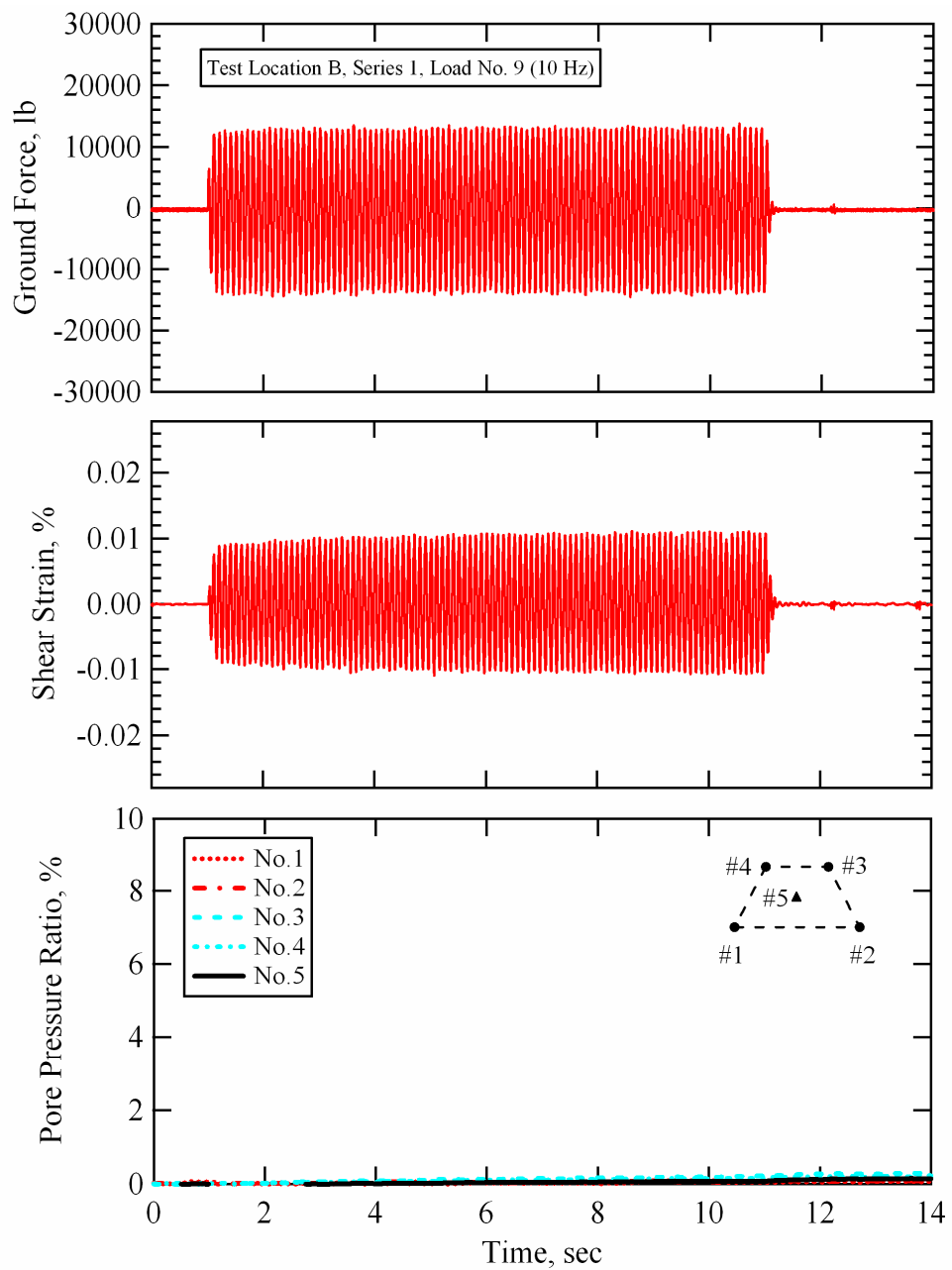


Figure 9-13 Force applied at the ground surface by T-Rex, shear strain induced at the center of the instrumented soil mass, and pore pressure ratios generated at each sensor location during Series 1, loading stage No. 9; Test Location B, Wildlife Liquefaction Array.

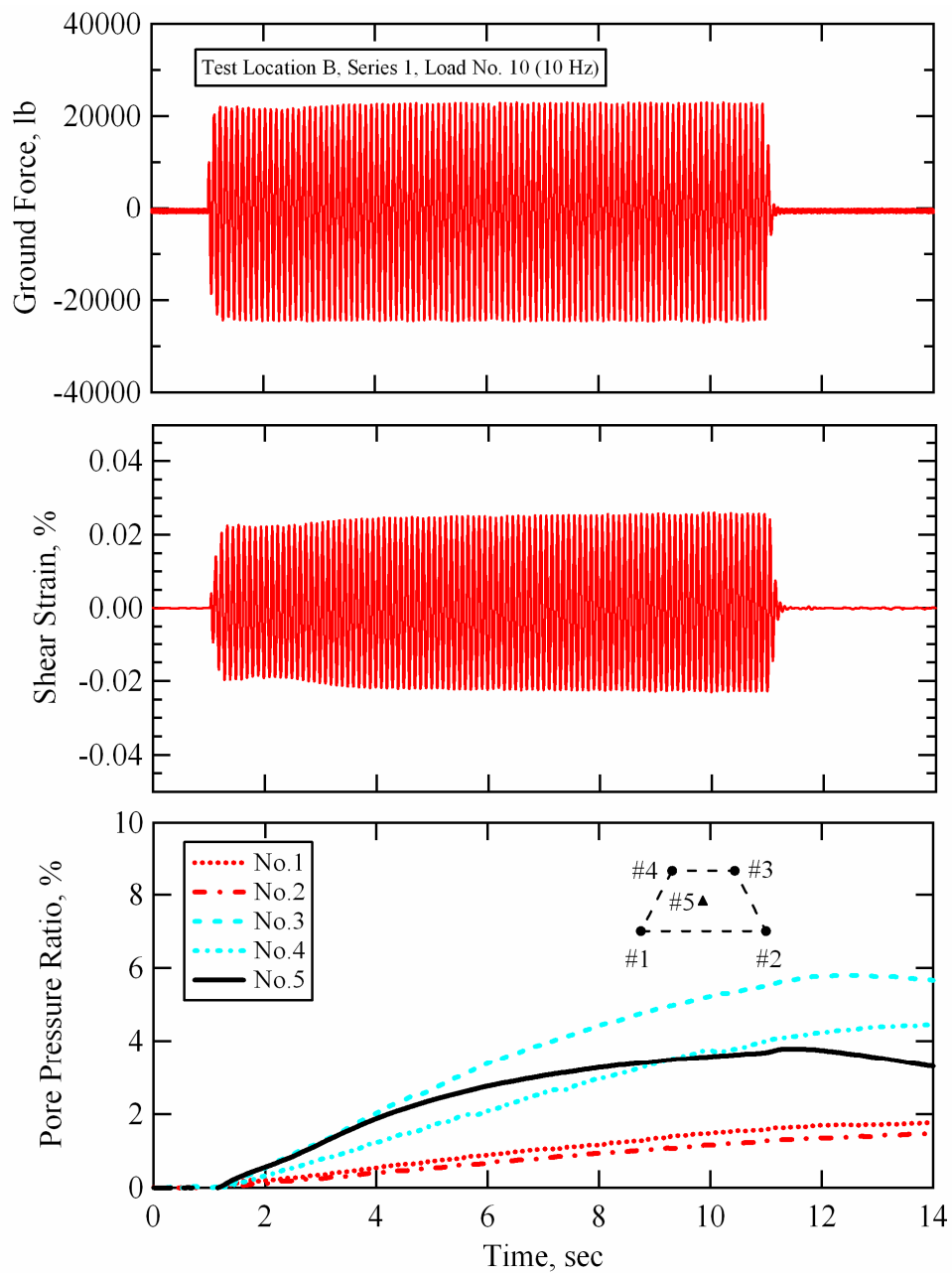


Figure 9-14 Force applied at the ground surface by T-Rex, shear strain induced at the center of the instrumented soil mass, and pore pressure ratios generated at each sensor location during Series 1, loading stage No. 10; Test Location B, Wildlife Liquefaction Array.

over the first 10 cycles of loading is 0.0196%, while the average shear strain over the first 100 cycles of loading is 0.023% (see Table 9-5).

The two deeper sensors (No. 1 and No. 2) in the array recorded nearly identical pressures that leveled off at the end of shaking. Both of these sensors indicated pore pressure ratios of just less than 2% at the end of 100 cycles of loading. The PDCR 35/D transducer (Sensor No. 5) recorded pressures that steadily increased throughout dynamic loading, reached a peak at a pore pressure ratio of approximately 4% at the end of shaking, and then began to dissipate. The two shallower sensors (No. 3 and No. 4) recorded different magnitudes of pressure. Sensor No. 4 sensed excess pore pressures very similar in magnitude to those sensed by Sensor No. 5. However, the pressures did not decay as rapidly at the end of shaking on Sensor No. 4. Sensor No. 3 sensed higher excess pore pressures that began to dissipate not long after the end of shaking. These different pore pressure responses show the variability of the material even over a relatively small area. Pore pressure data was recorded for approximately 60 seconds during loading stage No. 10. Figure 9-15 shows the pore pressure ratios measured at each sensor location with a time scale of 60 seconds. Despite recording different magnitudes of excess pore pressure during loading, the pore pressures recorded by Sensors No. 3 and No. 4 come into equilibrium approximately five seconds after the end of loading. Once again, this evidence shows that during dynamic loading pressure redistribution is minimal, even over relatively close distances. The pore pressure ratios at all sensor locations had dropped below 2% after 50 seconds had passed from the end of loading.

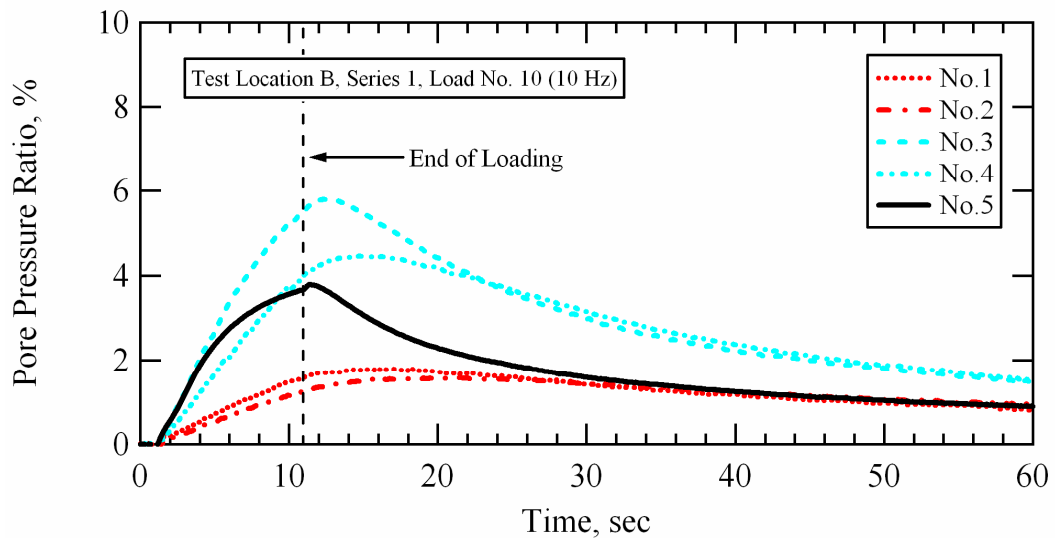


Figure 9-15 Pore pressure ratios generated at each sensor location during Series 1, loading stage No. 10; Test Location B, Wildlife Liquefaction Array.

As mentioned previously, the r_u values used to construct the pore pressure generation curves for the site were obtained solely from the PDCR 35/D transducer located at the center of the array (Sensor No. 5). The averaged shear strain values and pore pressure ratios calculated at the center of the liquefaction sensor array for dynamic Load No. 10 are presented in Table 9-5 as a function of various numbers of loading cycles. After Load No. 10, testing was halted for approximately 10 minutes (see Table 9-4) while the excess pore water pressure within the array was allowed to dissipate back to static conditions (as monitored by the PDCR 35/D transducer).

9.3.2.8 Loading Stage No. 11

During loading stage No. 11, T-Rex was driven at its maximum output (in shear mode) for 200 cycles of 10 Hz loading. The force applied at the ground surface, the shear strain induced at the center of the liquefaction sensor array, and the pore pressure ratios generated at each PPT location during loading stage No. 11 are shown in Figure 9-16. Even though the test ran for 200 cycles (20 sec), to be consistent with the other test results, only the first 100 cycles (10 sec) of loading were used in the pore pressure generation curve data reduction process. The ground force during loading stage No. 11 was not as consistent as the ground force records from previous Series 1 dynamic loads. The ground force started out close to 30000 lb (133.4 kN). However, it decayed to approximately 25000 lb (111 kN) in approximately 80 cycles of loading. It is likely that the soil around the base plate softened to the point where it could not offer enough resistance to keep the ground force at a consistently elevated level. When the soil softens, the base plate will try to move further (laterally) in an attempt to keep the ground force up, but its displacement is limited.

The shear strain time history shown in Figure 9-16 is highly irregular. During approximately the first 90 cycles of loading there is a steady increase in shear strain with increasing number of loading cycles. The average shear strain over the first 10 cycles of loading is 0.036%, while the average shear strain over the first 90 cycles of loading is 0.0517% (0.0513% over the first 100 cycles; see Table 9-5). After approximately the first 90 cycles of loading, the shear strain decays dramatically over a short number of loading cycles and eventually levels

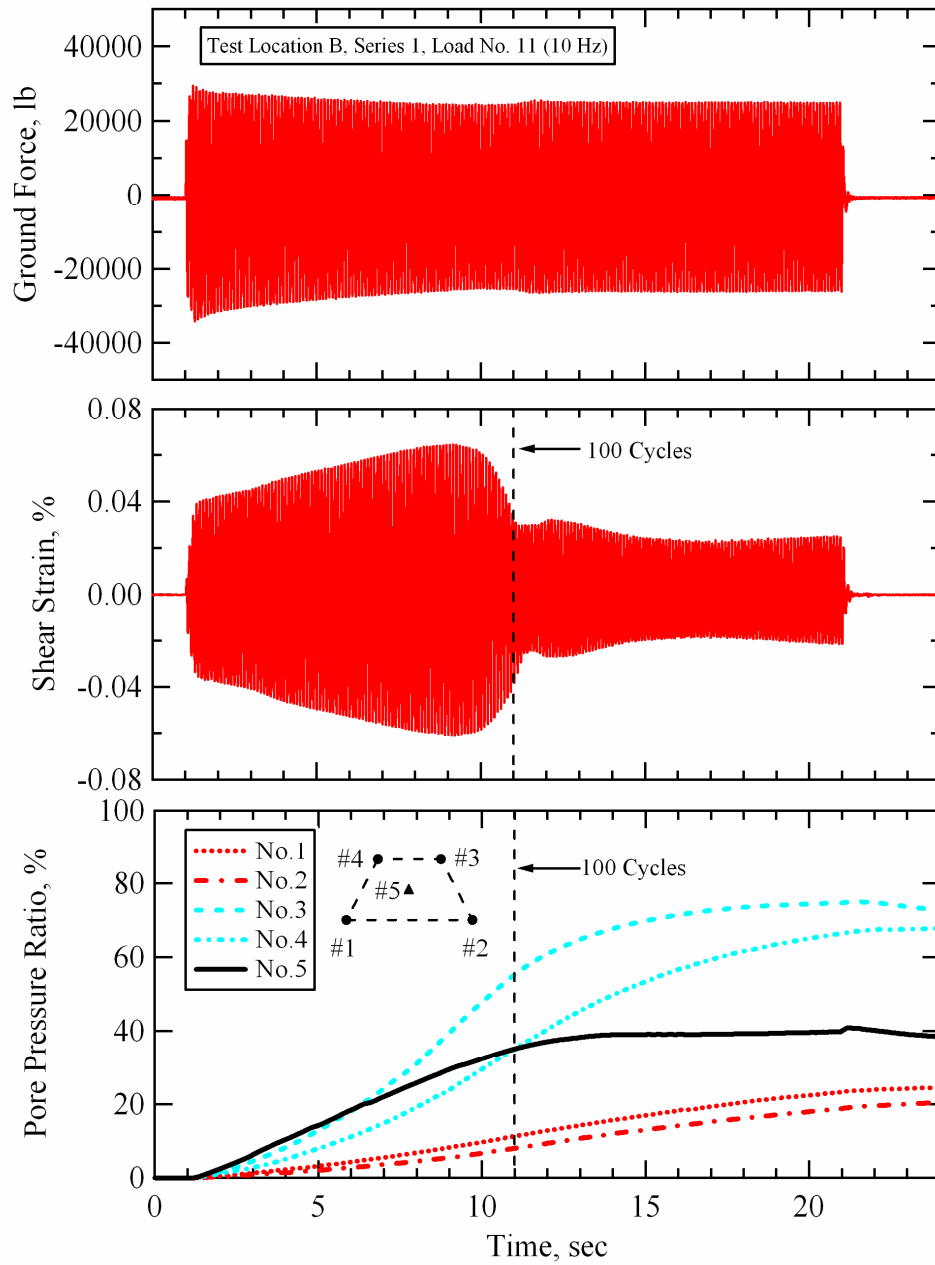


Figure 9-16 Force applied at the ground surface by T-Rex, shear strain induced at the center of the instrumented soil mass, and pore pressure ratios generated at each sensor location during Series 1, loading stage No. 11; Test Location B, Wildlife Liquefaction Array.

out at approximately 0.025%. The excess pore water pressure at Sensor No. 5 increases steadily until the shear strains at the center of the array decay. After 100 cycles of loading the pore pressure ratio is approximately 35%. Once the shear strains begin to decay and after about 120 cycles of loading, the pore water pressure remains essentially constant ($r_u \sim 40\%$) until the end of loading, after which, the pressure begins to dissipate slightly. Unlike the behavior recorded by Sensor No. 5, the pore water pressures recorded by the other PPT's continue to build throughout the duration of shaking. The sensors at the top of the array (Sensors No. 3 and No. 4) ultimately measured excess pore water pressures equivalent to pore pressure ratios of approximately 65% to 75%. The sensors at the bottom of the array (Sensors No. 1 and No. 2) measured excess pore water pressures equivalent to a pore pressure ratio of approximately 20%. Pore pressure data was recorded for approximately 120 seconds during loading stage No. 11. Figure 9-17 shows the pore pressure ratios measured at each sensor location with a time scale of 120 seconds. The pore pressures recorded by all sensors begin dissipating soon after the end of loading. Despite recording different magnitudes of excess pore pressure during loading, the pore pressures recorded by Sensors No. 3 and No. 4 come into equilibrium approximately ten seconds after the end of loading. The pore pressure ratio at Sensors No. 3 and No. 4 had decayed to approximately 30% after 100 seconds had passed from the end of loading. The pore pressure ratios at all other sensor locations had dropped below 20% after this same time period.

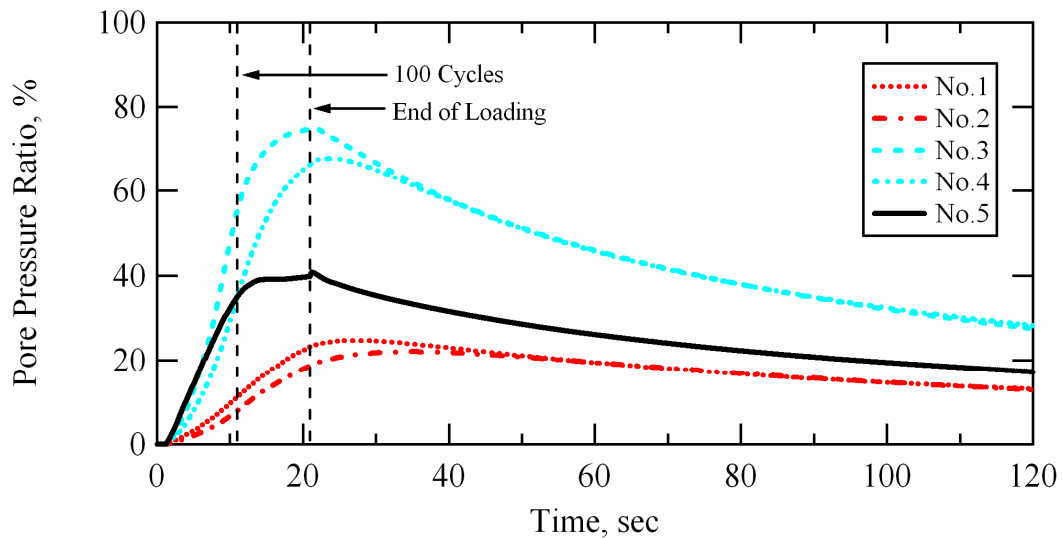


Figure 9-17 Pore pressure ratios generated at each sensor location during Series 1, loading stage No. 11; Test Location B, Wildlife Liquefaction Array.

Despite the irregular shear strain behavior in the instrumented soil mass during the last 100 cycles of loading of loading stage No. 11 (see Figure 9-16), the first 100 cycles of loading show similar behavior to that demonstrated in prior staged loads. An examination of the horizontal, in-line component (y-component) particle displacement time histories recorded at each liquefaction sensor location show that the displacements measured at each sensor location were fairly uniform over the first half of dynamic loading (see Figure 9-18). However, all sensors experienced a reduction in the particle displacement amplitudes they recorded after approximately the first 90 cycles of loading. Because this reduction happened to all sensors simultaneously, it is believed that the approximately 2.5-ft (0.8-m) thick layer of liquefiable soil above the liquefaction sensor array may

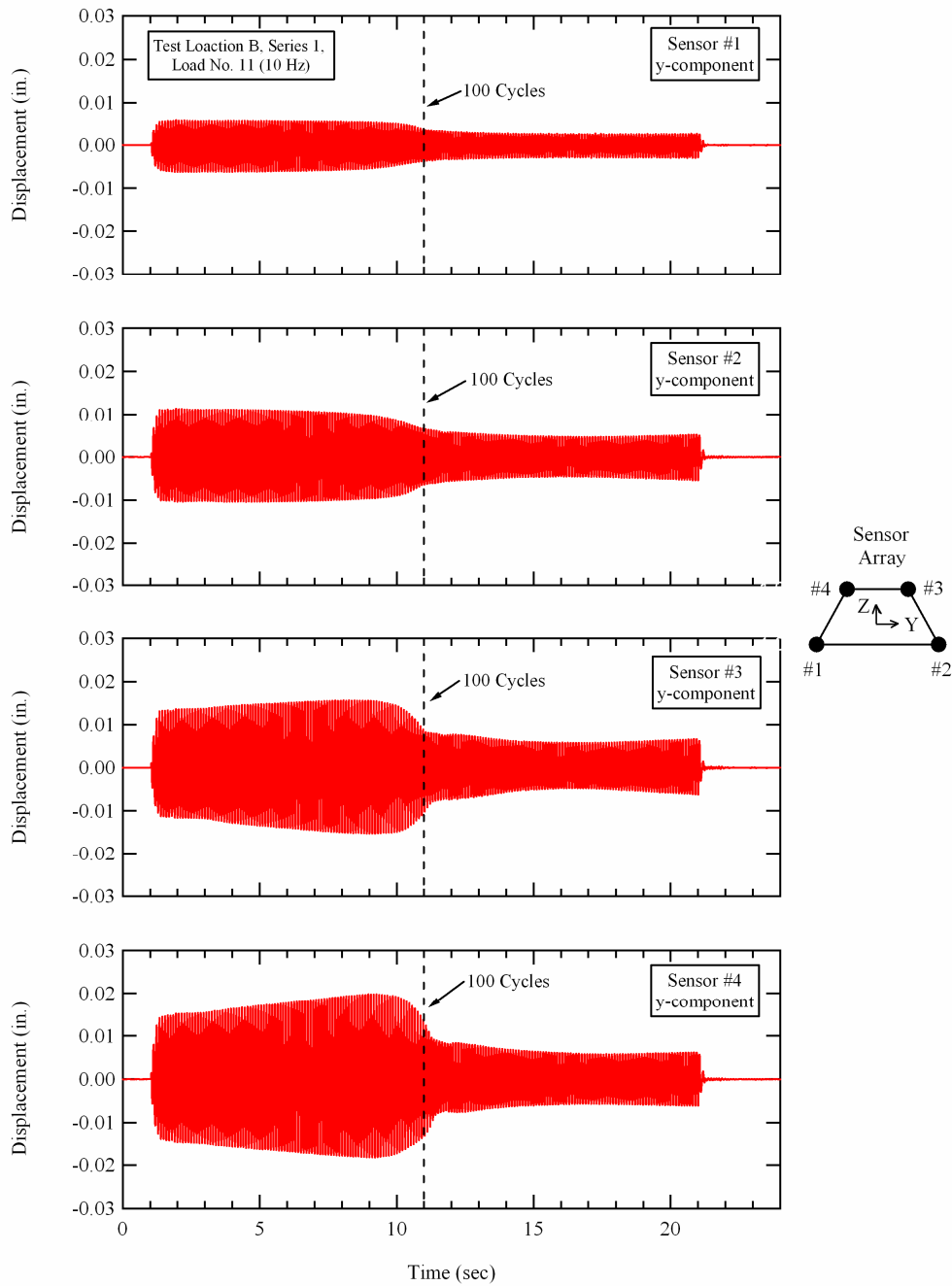


Figure 9-18 Horizontal, in-line component (y-component) particle displacements recorded at each of the liquefaction sensor location during Series 1, dynamic Load No. 11; Test Location B, Wildlife Liquefaction Array.

have experienced very high pore pressure generation, thus inhibiting the transfer of load through the softened zone and into the instrumented soil mass. This predicted response shows why it would be desirable to have three or four layers of liquefaction sensors compared with the two layers employed currently (see Figure 9-6).

9.3.3 Pore Pressure Generation Curves; Loading Series 1

Pore pressure generation curves for this series of testing can readily be constructed from the data presented in Table 9-5 using any of the given numbers of loading cycles. Figure 9-19 shows the pore pressure generation curves for 10, 20, 50, and 100 cycles of loading determined at Test Location C during staged dynamic loading Series 1. The cyclic threshold shear strain (γ_t^e) depends on the number of cyclic shear strain cycles (n) and ranges from approximately 0.01% for n = 100 to 0.02% for n = 10. Multiple data points between 0.0007% and 0.01% confirm the lack of excess pore pressure generation below γ_t^e . As expected, the data show that for a given cyclic shear strain above γ_t^e , higher pore pressures are generated with increasing numbers of loading cycles.

Figure 9-20 compares the in-situ pore pressure generation curves determined for Test Location B during dynamic loading Series 1 with Dobry's pore pressure generation model for liquefiable soils from the Wildlife Site (Vucetic and Dobry, 1986). As discussed in Section 7.3.1.3, Dobry's model for Wildlife liquefiable soils was developed from cyclic laboratory test results. A cyclic threshold shear strain of 0.02% was assumed for the model (based on experience gained from previous laboratory tests) because the laboratory tests

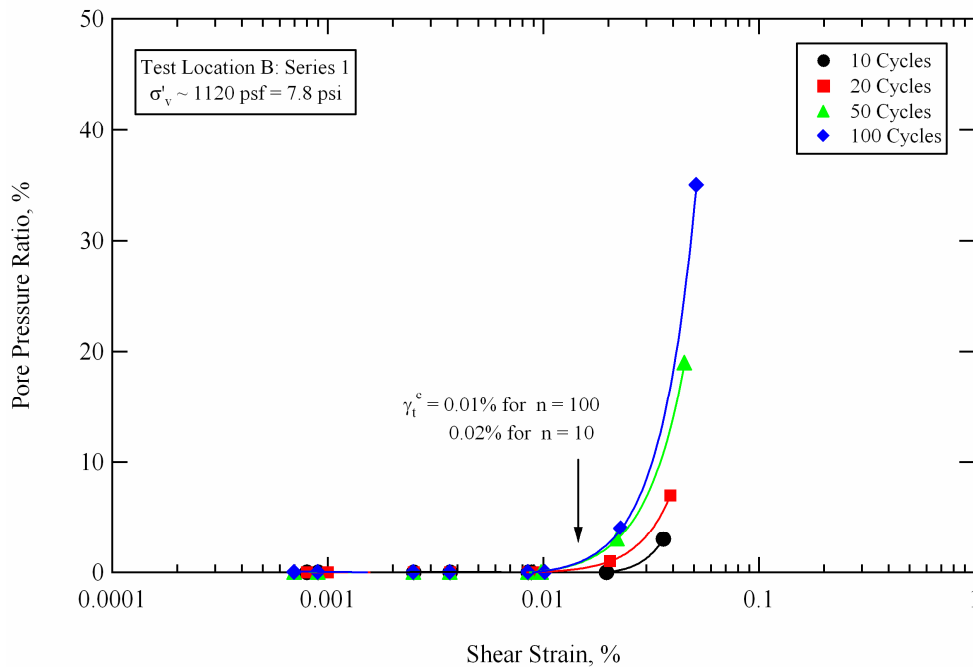


Figure 9-19 Pore pressure generation curves obtained from in-situ liquefaction tests conducted during staged dynamic loading Series 1 at Test Location B, Wildlife Liquefaction Array.

conducted in the study were not performed at shear strains that were low enough to actually determine the cyclic threshold shear strain. This cyclic threshold shear strain was assumed to be the same for any given number of loading cycles. The cyclic tests used to develop the model for Wildlife soils employed up to 30 cycles of strain-controlled loading. The assumed cyclic threshold value is equivalent to the $n = 10$ cyclic threshold shear strain determined from in-situ liquefaction tests conducted during staged loading Series 1. In Figure 9-20, Dobry's pore pressure generation model is shown for 10 loading cycles ($n = 10$) and for 100 loading cycles ($n = 100$), as calculated using Equation 7-1. The in-situ test results indicate a slightly lower threshold shear strain for 20, 50 and 100 cycles of loading.

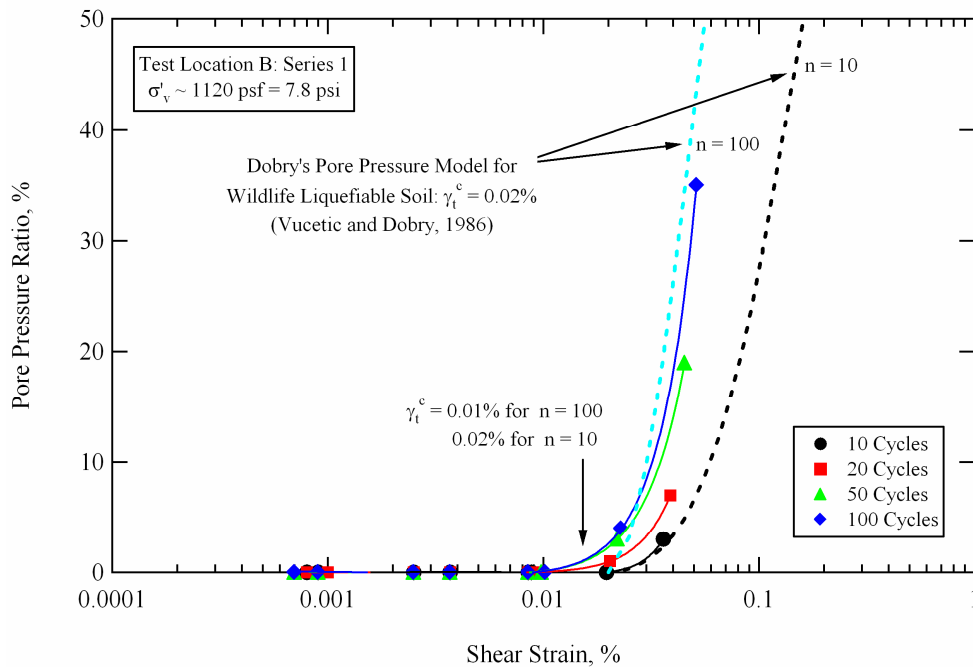


Figure 9-20 Comparison between Dobry’s pore pressure generation model (Vucetic and Dobry, 1986) and pore pressure generation curves obtained from in-situ liquefaction tests conducted during staged dynamic loading Series 1 at Test Location B, Wildlife Liquefaction Array.

However, the trend in pore pressure generation for the in-situ results is nearly identical to the trend in pore pressure generation predicted by Dobry’s model. Because the pore pressure ratios induced at the center of the liquefaction sensor array during Series 1 tests were less than 40%, the pore pressure generation curves presented in Figures 9-19 and 9-20 are shown with a maximum pore pressure ratio scale of 50%. For perspective purposes, Figure 9-21 presents the pore pressure generation curves with a maximum pore pressure ratio scale of 100%.

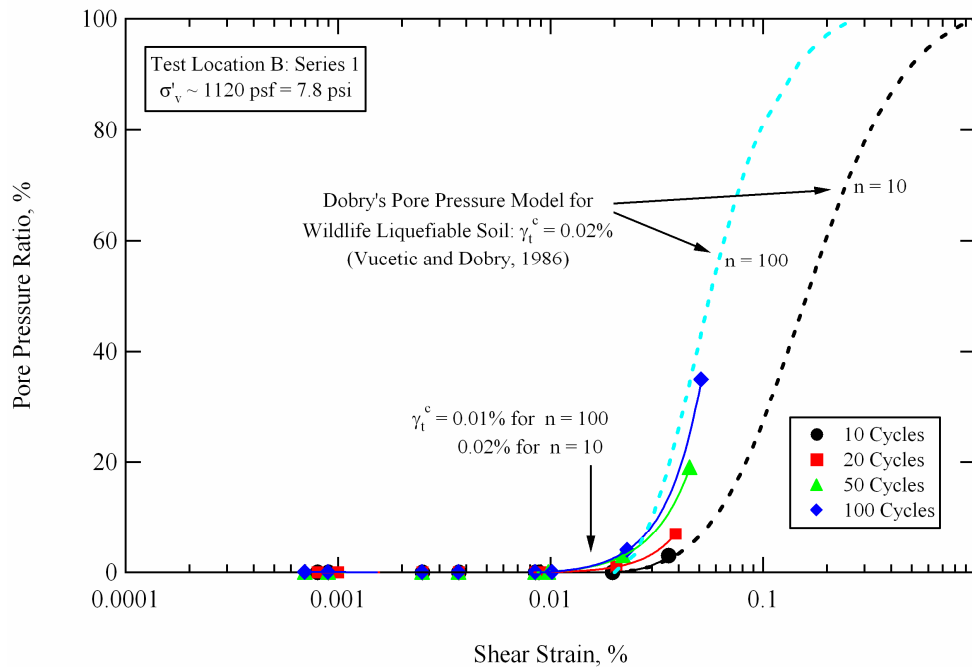


Figure 9-21 Full pore pressure ratio scale comparison between Dobry's pore pressure generation model (Vucetic and Dobry, 1986) and pore pressure generation curves obtained from in-situ liquefaction tests conducted during staged dynamic loading Series 1 at Test Location B, Wildlife Liquefaction Array.

For reasons discussed in Sections 8.3.3 and 8.3.4, it is believed that redistribution and dissipation of excess pore water pressure has little effect on the measured pore pressure response during the course of dynamic in-situ liquefaction tests.

9.4 TEST B: STAGED DYNAMIC LOADING SERIES 2

The in-situ liquefaction sensor array at Test Location B was installed on August 12, 2005. The first series (Series 1) of staged dynamic loading was conducted on the afternoon of August 13, and lasted approximately 1 hour and 45

minutes. In-situ liquefaction testing was then stopped for approximately 1.5 days. The pore water pressure transducer (PPT) in each sensor was powered during this break using a 12-volt battery and a DC-to-DC converter to help ensure that the static PPT outputs remained as steady as possible during subsequent testing (as discussed in Section 4.3.2). The second series (Series 2) of staged dynamic loading began in the morning of August 15.

9.4.1 Loading Stages in Series 2

During Series 2, eight separate dynamic loads were applied to the instrumented soil mass. The dynamic shear loads were applied by driving T-Rex in the horizontal, in-line direction, just as done in all previous tests. Details of the Series 2 staged dynamic loading sequence are provided in Table 9-6. The first three dynamic loading stages were applied at a frequency of 20 Hz. The last five dynamic loading stages were applied at a frequency of 10 Hz. All of the loads had a duration of 100 cycles, except Load No. 19, which had a duration of 200 cycles. Previous tests conducted at Test Location A (discussed in Chapter 10) had shown that higher peak shear strains could be induced in the soil deposit at a frequency of 10 Hz than at a frequency of 20 Hz. However, T-Rex has more harmonic distortion when operating at 10 Hz than at 20 Hz, as discussed in Section 6.5. As before, the tests were conducted at 20 Hz in the hopes of being able to more accurately resolve the nonlinear soil shear modulus behavior, and at 10 Hz to generate shear strains as large as possible within the instrumented soil mass. However, to avoid loading the soil beyond its cyclic threshold strain (γ_r^e), the 20-Hz loads were only carried to the point where a minute amount of excess

Table 9-6 Details of the Series 2 staged dynamic loading sequence conducted at Test Location B, Wildlife Liquefaction Array (WLA)

| Time on 8/15/2005 | Dynamic Load Number | Function Generator Drive Signal | | | Approximate Ground Force (lb) |
|----------------------|------------------------|---------------------------------|---------------------|----------------------|-------------------------------------|
| | | Frequency (Hz) | Number of Cycles | Amplitude (volts) | |
| 8:45 AM | 12 | 20 | 100 | 0.4 | 2000 |
| 8:49 AM | 13 | 20 | 100 | 0.8 | 5000 |
| 8:54 AM | 14 | 20 | 100 | 1.5 | 10000 |
| 9:04 AM | 15 | 10 | 100 | 0.4 | 2000 |
| 9:09 AM | 16 | 10 | 100 | 0.8 | 5000 |
| 9:32 AM | 17 | 10 | 100 | 1.5 | 15000 |
| 9:40 AM | 18 | 10 | 100 | 2.5 | 20000 |
| 10:05 AM | 19 | 10 | 200 | 5 | 25000 |

pore water pressure was generated at the center of the liquefaction sensor array (i.e. $r_u < 1\%$). At this point, the loading frequency was decreased to 10 Hz, the drive amplitude was dropped back down to a low level, and staged dynamic loading began again.

Shear strains (γ) induced in the instrumented soil mass were calculated at the center of the liquefaction sensor array for every stage of dynamic loading using the 4-node, isoparametric finite element formulation presented in Section 6.3. Shear strains were averaged over various numbers of loading cycles according to the procedure detailed in Section 8.3.1.

The pore pressure ratios (r_u) at each sensor location were obtained by dividing the measured residual pore water pressure, obtained from processing the raw pore pressure transducer (PPT) records according to the procedure outlined in

Section 6.4, by the total vertical effective stress at each sensor location (see Table 9-2). The r_u values used to construct the pore pressure generation curves for each site were obtained solely from the PDCR 35/D transducer located at the center of the array (Sensor No.5). The r_u values obtained from the miniature PPT's (Sensors No. 1 – No. 4) were only used in a qualitative sense to observe how the pore pressure generation varied within the instrumented soil mass.

As discussed in Section 9.3.1, the nonlinear shear modulus of the soil within the liquefaction sensor array could not accurately be resolved at this location due to harmonic distortion and small amounts of noise in some of the raw accelerometer records. These problems made it extremely difficult to obtain precise values for the time lags between sensors.

9.4.2 Response of the Deposit During Loading Series 1

9.4.2.1 Loading Stage No. 12

The force applied at the ground surface by T-Rex, the shear strain induced at the center of the liquefaction sensor array, and the pore pressure ratios generated at each PPT location during loading stage No. 12 of staged loading Series 2 are shown in Figure 9-22. The ground force during loading stage No. 12 was less than 2000 lb (8.9 kN) throughout the 100 cycles of 20-Hz loading. This load induced fairly uniform cyclic shear strains at the center of the liquefaction sensor array of approximately 0.0015%. These shear strains did not trigger the generation of any excess pore water pressure in the instrumented soil mass, as

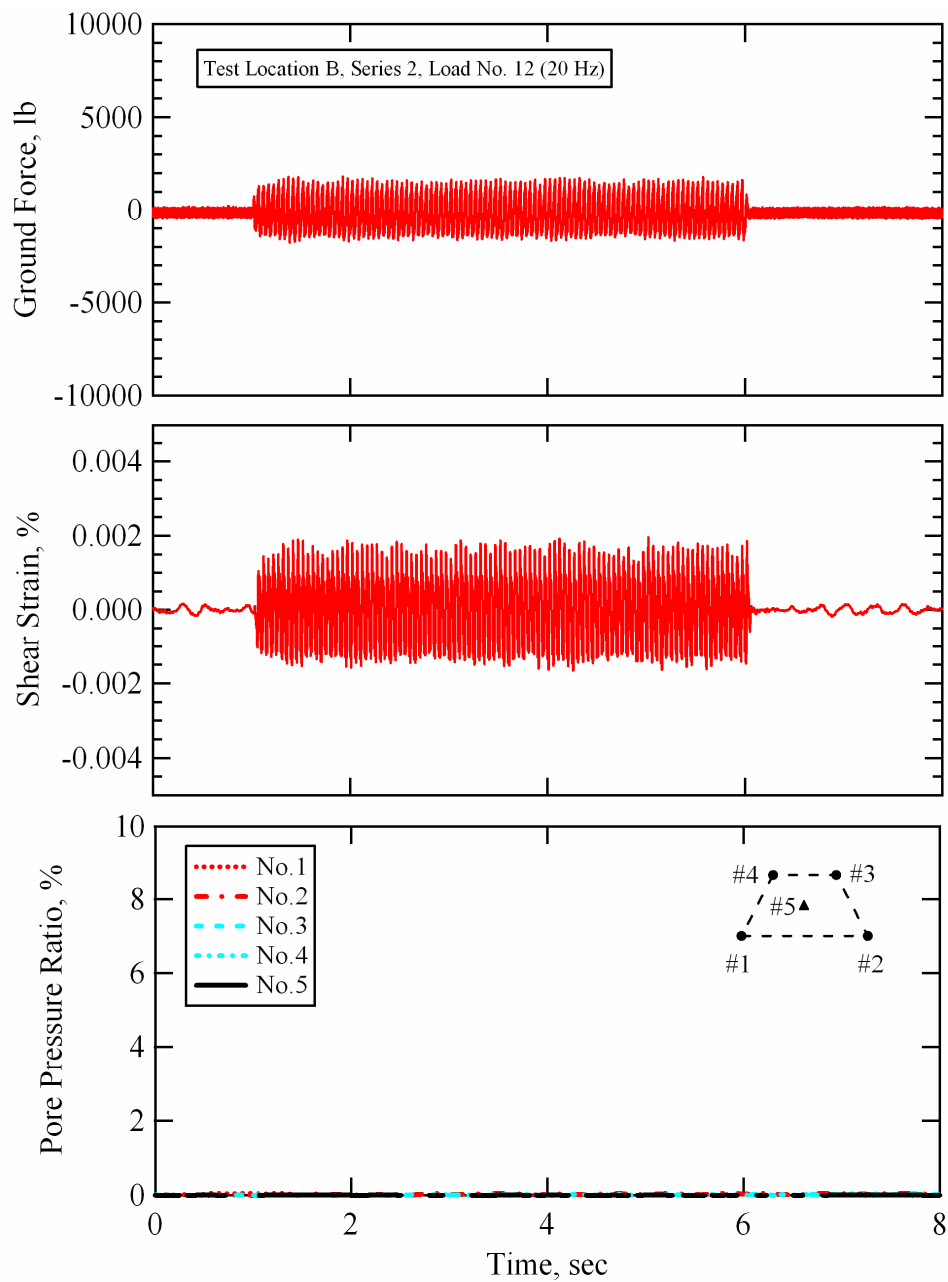


Figure 9-22 Force applied at the ground surface by T-Rex, shear strain induced at the center of the instrumented soil mass, and pore pressure ratios generated at each sensor location during Series 2, dynamic Load No. 12; Test Location B, Wildlife Liquefaction Array.

indicated by the fact that the pore pressure ratios at each sensor location remained equal to zero.

Tabulated values for the pore pressure ratios and average shear strains (averaged over the given number of loading cycles) induced in the soil during loading stage No. 1 of staged loading Series 2 are provided in Table 9-7. These values are provided for different numbers of total loading cycles for all of the loading stages applied during staged loading Series 2.

9.4.2.2 Loading Stage No. 13

The force applied at the ground surface by T-Rex, the shear strain induced at the center of the liquefaction sensor array, and the pore pressure ratios generated at each PPT location during dynamic Load No. 13 of staged loading Series 2 are shown in Figure 9-23. The ground force during loading stage No. 13 was slightly less than 5000 lb (22.2 kN) throughout the 100 cycles of 20-Hz loading. This load induced fairly uniform cyclic shear strains at the center of the liquefaction sensor array of approximately 0.0053% (see Table 9-7 for strain values averaged over various numbers of loading cycles). A minute amount of excess pore water pressure was generated in the instrumented soil mass during this test. However, none of the sensors indicated pore pressure ratios greater than 0.25%.

9.4.2.3 Loading Stage No. 14

The force applied at the ground surface by T-Rex, the shear strain induced at the center of the liquefaction sensor array, and the pore pressure ratios

Table 9-7 Pore pressure ratios and average shear strains at the center of the liquefaction sensor array for different numbers of loading cycles; Series 2, Test Location B, Wildlife Liquefaction Array

| Number of Cycles | γ or r_u | Pore Pressure Ratio ¹ (r_u) and Average Shear Strain ² (γ) Values, % | | | | | | | |
|------------------|-------------------|---|--------|--------|--------|--------|--------|--------|--------|
| | | Series 2: Staged Load Number | | | | | | | |
| | | No. 12 | No. 13 | No. 14 | No. 15 | No. 16 | No. 17 | No. 18 | No. 19 |
| 10 | γ | 0.0015 | 0.0053 | 0.0129 | 0.0013 | 0.0037 | 0.0113 | 0.0297 | 0.0493 |
| | r_u | 0 | 0 | 0 | 0 | 0 | 0 | 2 | 3 |
| 20 | γ | 0.0015 | 0.0053 | 0.0130 | 0.0013 | 0.0038 | 0.0116 | 0.0327 | 0.0426 |
| | r_u | 0 | 0 | 0 | 0 | 0 | 0 | 3 | 8 |
| 30 | γ | 0.0015 | 0.0053 | 0.0130 | 0.0013 | 0.0038 | 0.0119 | 0.0336 | 0.0386 |
| | r_u | 0 | 0 | 0 | 0 | 0 | 0 | 4 | 12 |
| 40 | γ | 0.0015 | 0.0053 | 0.0130 | 0.0013 | 0.0038 | 0.0120 | 0.0329 | 0.0363 |
| | r_u | 0 | 0 | 0 | 0 | 0 | 0 | 6 | 14 |
| 50 | γ | 0.0015 | 0.0053 | 0.0130 | 0.0013 | 0.0038 | 0.0120 | 0.0315 | 0.0350 |
| | r_u | 0 | 0 | 0 | 0 | 0 | 0 | 8 | 16 |
| 60 | γ | 0.0015 | 0.0053 | 0.0130 | 0.0013 | 0.0038 | 0.0121 | 0.0302 | 0.0341 |
| | r_u | 0 | 0 | 0 | 0 | 0 | 0 | 10 | 18 |
| 70 | γ | 0.0015 | 0.0053 | 0.0130 | 0.0013 | 0.0038 | 0.0122 | 0.0292 | 0.0335 |
| | r_u | 0 | 0 | 1 | 0 | 0 | 0 | 12 | 19 |
| 80 | γ | 0.0015 | 0.0053 | 0.0130 | 0.0013 | 0.0038 | 0.0122 | 0.0285 | 0.0331 |
| | r_u | 0 | 0 | 1 | 0 | 0 | 0 | 13 | 19 |
| 90 | γ | 0.0015 | 0.0053 | 0.0130 | 0.0013 | 0.0038 | 0.0122 | 0.0279 | 0.0328 |
| | r_u | 0 | 0 | 1 | 0 | 0 | 0 | 14 | 20 |
| 100 | γ | 0.0015 | 0.0053 | 0.0130 | 0.0013 | 0.0038 | 0.0123 | 0.0274 | 0.0324 |
| | r_u | 0 | 0 | 2 | 0 | 0 | 0 | 15 | 20 |
| 150 | γ | - | - | - | - | - | - | - | 0.0306 |
| | r_u | - | - | - | - | - | - | - | 20 |
| 200 | γ | - | - | - | - | - | - | - | 0.0299 |
| | r_u | - | - | - | - | - | - | - | 21 |

- Notes: 1. r_u from the PDCR 35/D pressure transducer at the center of the array after the given number of loading cycles
2. γ calculated at the center of the array and averaged over the given number of loading cycles

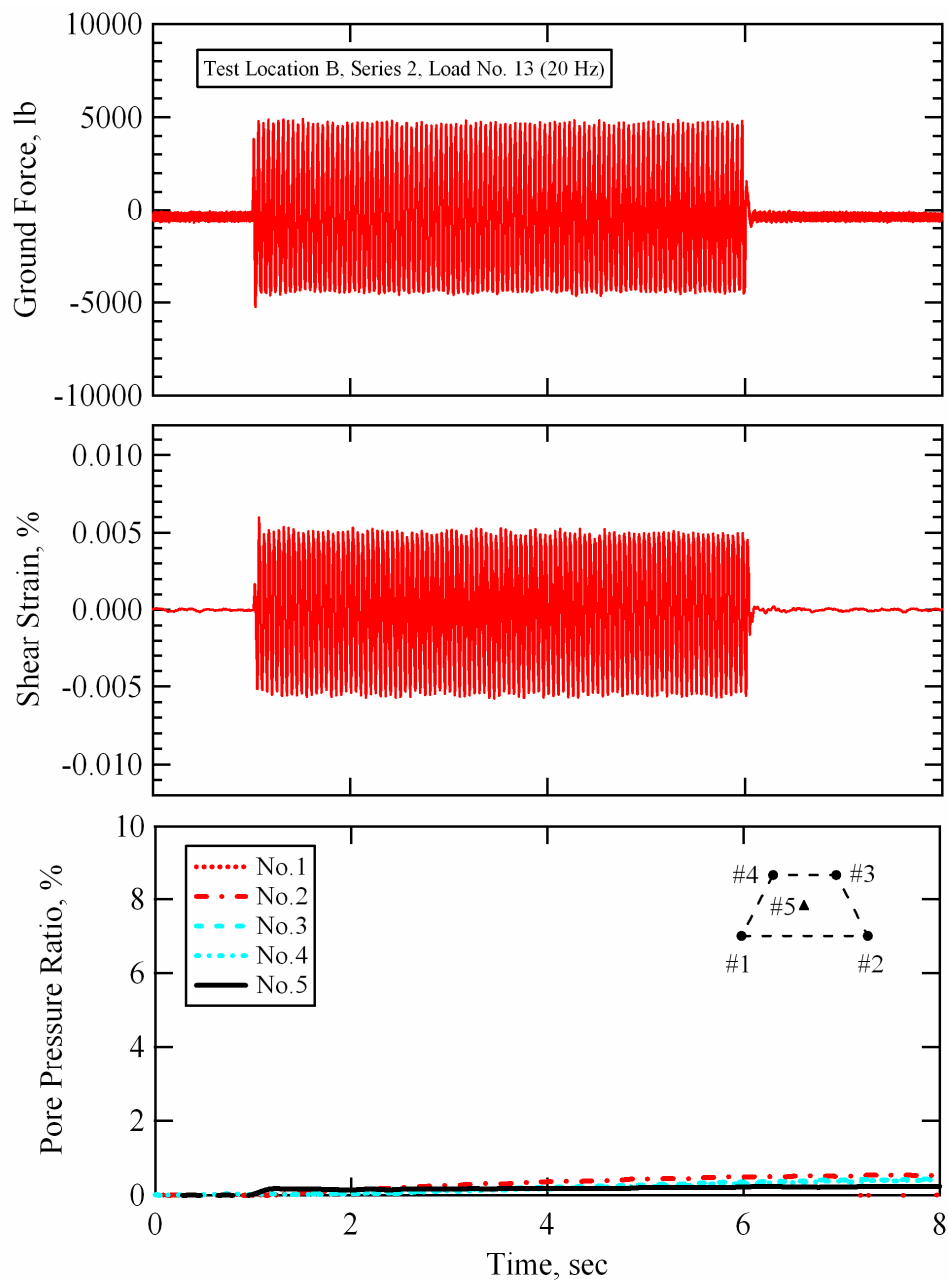


Figure 9-23 Force applied at the ground surface by T-Rex, shear strain induced at the center of the instrumented soil mass, and pore pressure ratios generated at each sensor location during Series 2, loading stage No. 13; Test Location B, Wildlife Liquefaction Array.

generated at each PPT location during loading stage No. 14 of staged loading Series 2 are shown in Figure 9-24. The ground force during loading stage No. 14 was approximately 10000 lb (44.5 kN) throughout the 100 cycles of 20-Hz loading. This load induced fairly uniform cyclic shear strains at the center of the liquefaction sensor array of approximately 0.013% (see Table 9-7 for strain values averaged over various numbers of loading cycles). Load No. 14 generated excess pore water pressures at all locations within the instrumented soil mass during shaking. The two bottom sensors in the array (Sensors No. 1 and No. 2) detected pore pressure ratios of less than 1% at the end of shaking. The two top sensors in the array (Sensors No. 3 and No. 4) detected pore pressure ratios between 3% and 5% at the end of shaking. Sensor No. 5 detected a pore pressure ratio of approximately 2% at the end of shaking. It is interesting to note that the excess pore pressures at all locations within the array continued to build slightly after the end of shaking. It is unknown what caused the bump in the pressures recorded by Sensor No. 5. However, keeping in mind the scale of the plot, this is a truly minor amount of pressure. At this point in the staged loading sequence, testing was halted for approximately 10 minutes (see Table 9-7) while the excess pore pressures within the array were allowed to dissipate back to their static values (as monitored by the PDCR 35/D transducer). The actual time required for the pressure to return to its static condition was substantially less than the allotted time. After dynamic Load No. 14, the loading frequency was decreased to 10 Hz, the drive amplitude was dropped back down to a low level, and staged dynamic loading began again.

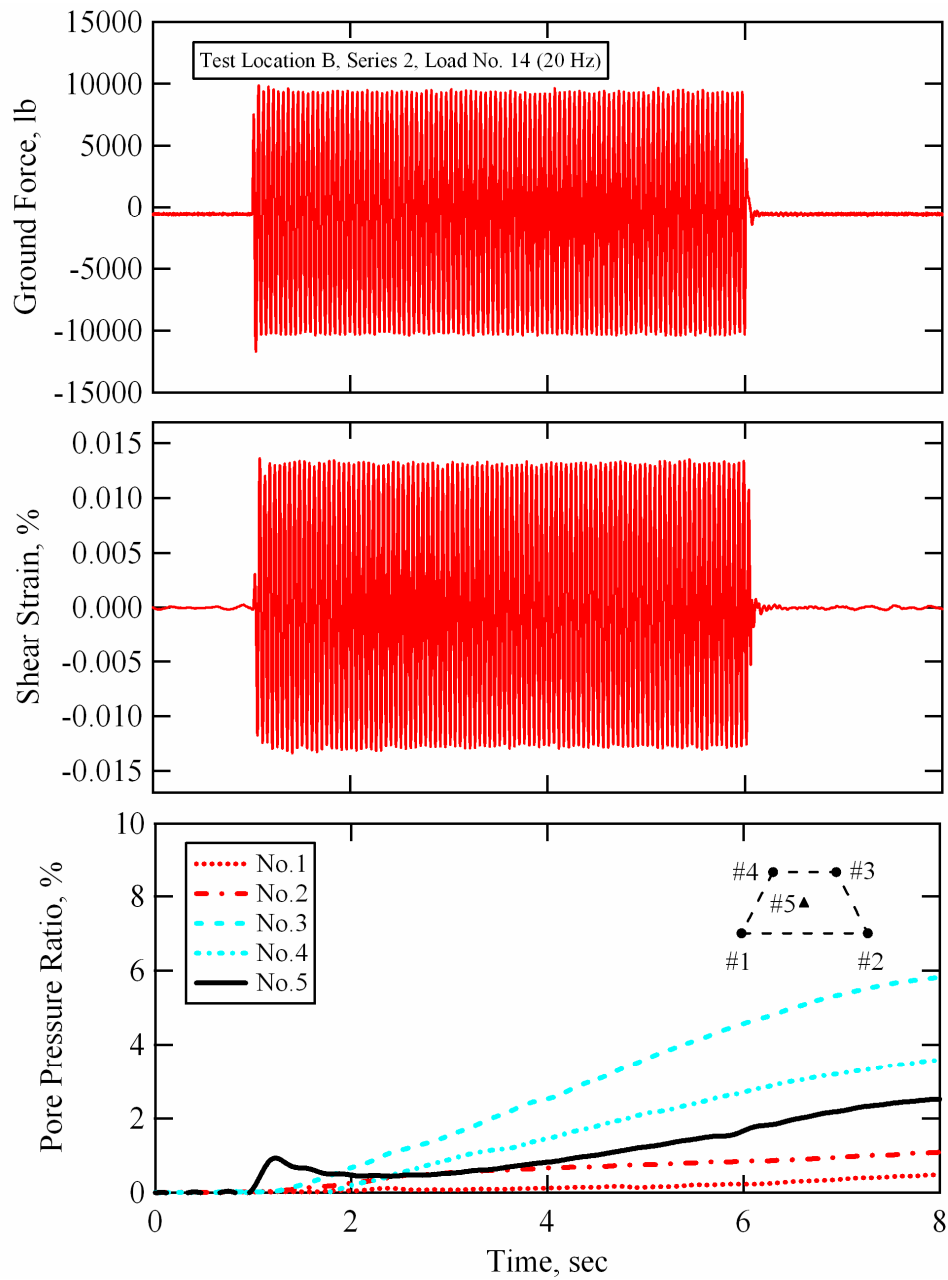


Figure 9-24 Force applied at the ground surface by T-Rex, shear strain induced at the center of the instrumented soil mass, and pore pressure ratios generated at each sensor location during Series 2, loading stage No. 14; Test Location B, Wildlife Liquefaction Array.

9.4.2.4 Loading Stage No. 15

The force applied at the ground surface by T-Rex, the shear strain induced at the center of the liquefaction sensor array, and the pore pressure ratios generated at each PPT location during loading stage No. 15 of staged loading Series 2 are shown in Figure 9-25. The ground force during loading stage No. 15 was generally less than 2000 lb (8.9 kN) throughout the 100 cycles of 10-Hz loading. This load induced fairly uniform cyclic shear strains at the center of the liquefaction sensor array of approximately 0.0013% (see Table 9-7 for strain values averaged over various numbers of loading cycles). These shear strains did not trigger the generation of any excess pore water pressure in the instrumented soil mass, as indicated by the fact that the pore pressure ratios at each sensor location remained equal to zero.

9.4.2.5 Loading Stage No. 16

The force applied at the ground surface by T-Rex, the shear strain induced at the center of the liquefaction sensor array, and the pore pressure ratios generated at each PPT location during loading stage No. 16 of staged loading Series 2 are shown in Figure 9-26. The ground force during loading stage No. 16 was approximately 5000 lb (22.2 kN) throughout the 100 cycles of 10-Hz loading. This load induced fairly uniform cyclic shear strains at the center of the liquefaction sensor array of approximately 0.0038% (see Table 9-7 for strain values averaged over various numbers of loading cycles). These shear strains did not trigger the generation of any excess pore water pressure in the instrumented

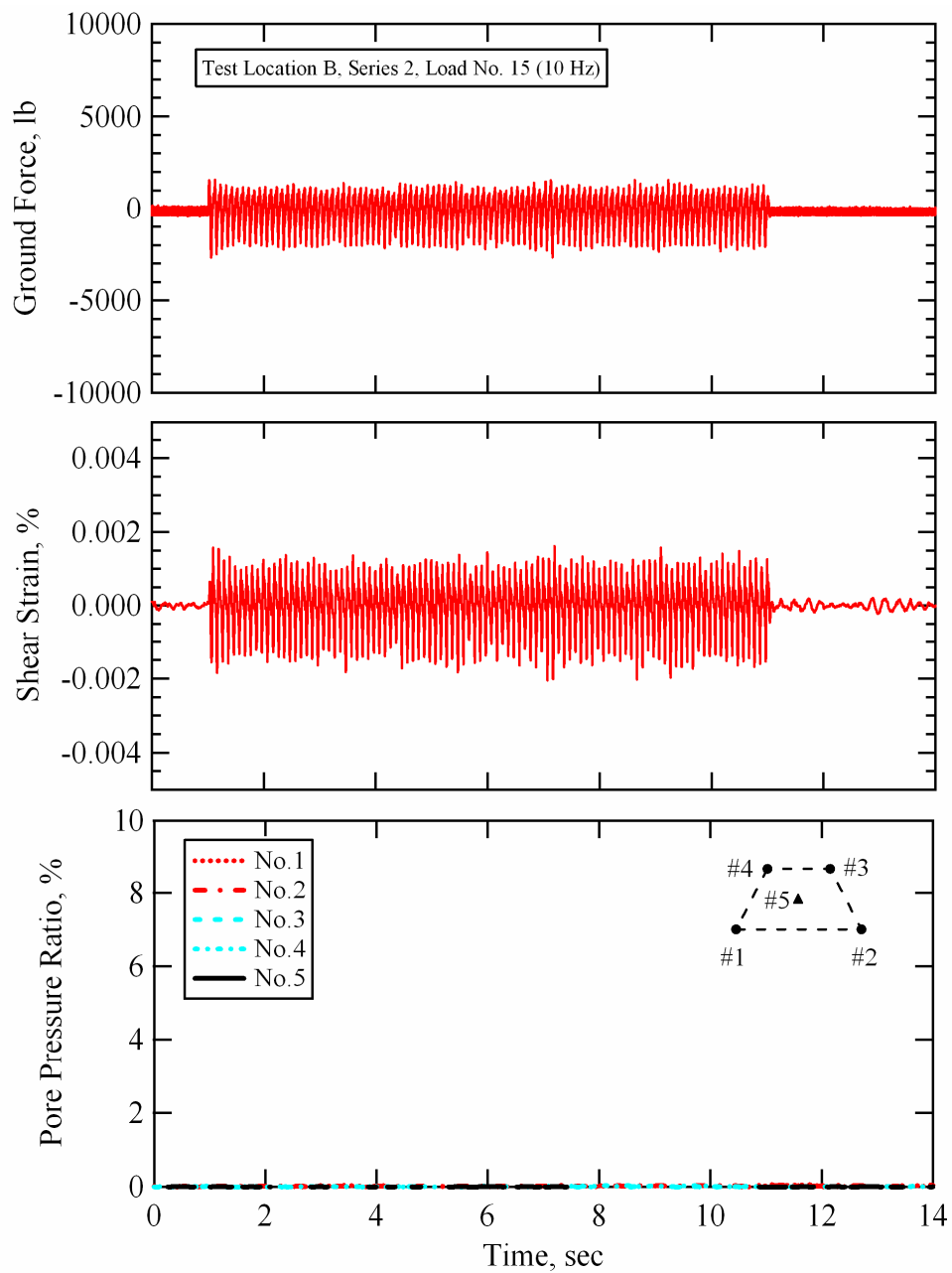


Figure 9-25 Force applied at the ground surface by T-Rex, shear strain induced at the center of the instrumented soil mass, and pore pressure ratios generated at each sensor location during Series 2, loading stage No. 15; Test Location B, Wildlife Liquefaction Array.

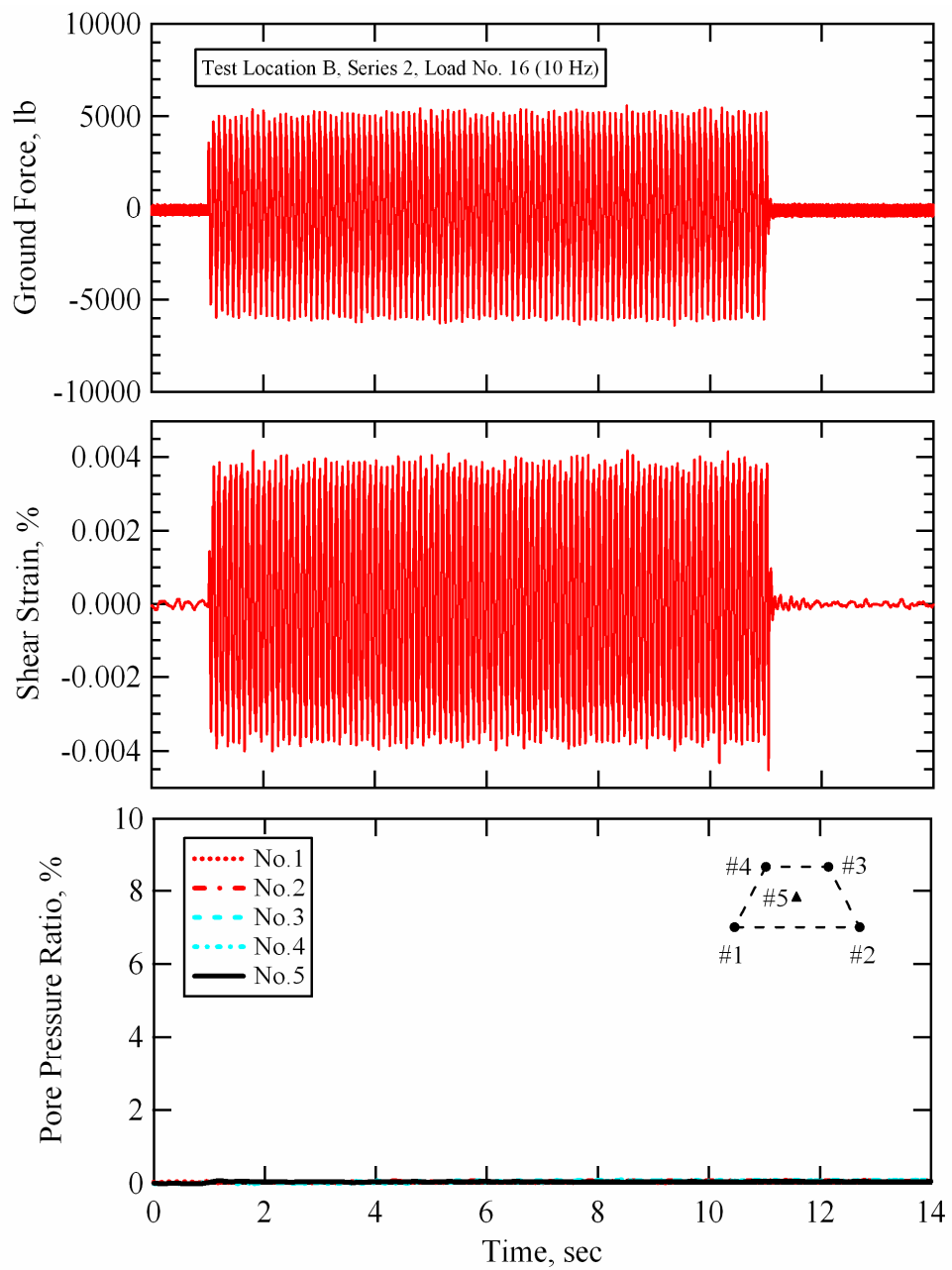


Figure 9-26 Force applied at the ground surface by T-Rex, shear strain induced at the center of the instrumented soil mass, and pore pressure ratios generated at each sensor location during Series 2, loading stage No. 16; Test Location B, Wildlife Liquefaction Array.

soil mass, as indicated by the fact that the pore pressure ratios at each sensor location remained equal to zero.

9.4.2.6 Loading Stage No. 17

The force applied at the ground surface by T-Rex, the shear strain induced at the center of the liquefaction sensor array, and the pore pressure ratios generated at each PPT location during loading stage No. 17 of staged loading Series 2 are shown in Figure 9-27. The ground force during loading stage No. 17 was slightly less than 15000 lb (66.7 kN) throughout the 100 cycles of 10-Hz loading. This load induced fairly uniform cyclic shear strains at the center of the liquefaction sensor array of approximately 0.012% (see Table 9-7 for strain values averaged over various numbers of loading cycles). A minute amount of excess pore water pressure was generated in the instrumented soil mass during this test. However, none of the sensors indicated pore pressure ratios greater than 1%.

9.4.2.7 Loading Stage No. 18

The force applied at the ground surface by T-Rex, the shear strain induced at the center of the liquefaction sensor array, and the pore pressure ratios generated at each PPT location during loading stage No. 18 of staged loading Series 2 are shown in Figure 9-28. The ground force during loading stage No. 18 was not as consistent as the ground force records from previous Series 2 dynamic loads. The ground force started at approximately 23000 lb (102.3 kN). However, it decayed to approximately 18000 lb (80.1 kN) after 40 cycles of loading. It is

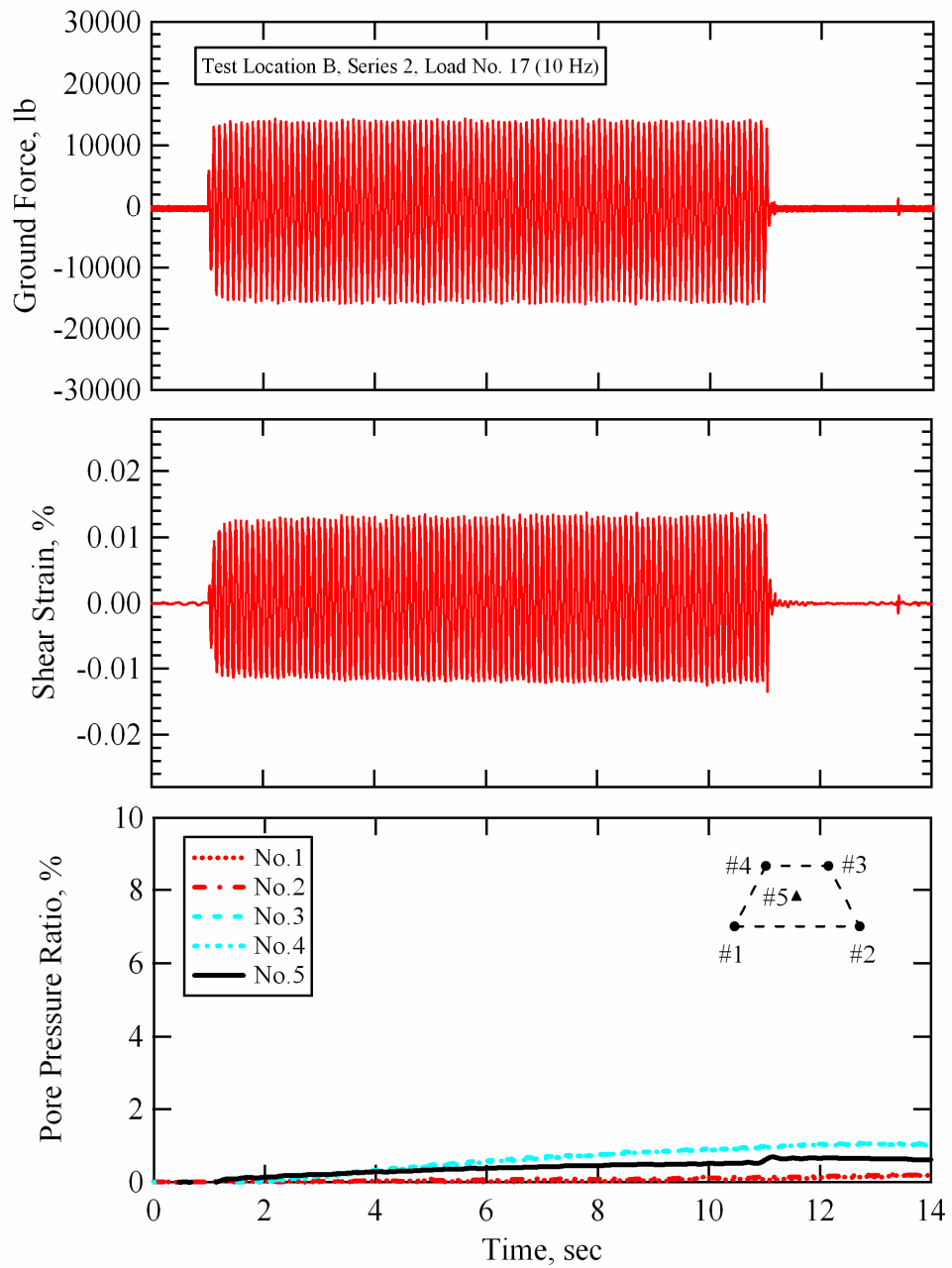


Figure 9-27 Force applied at the ground surface by T-Rex, shear strain induced at the center of the instrumented soil mass, and pore pressure ratios generated at each sensor location during Series 2, loading stage No. 17; Test Location B, Wildlife Liquefaction Array.

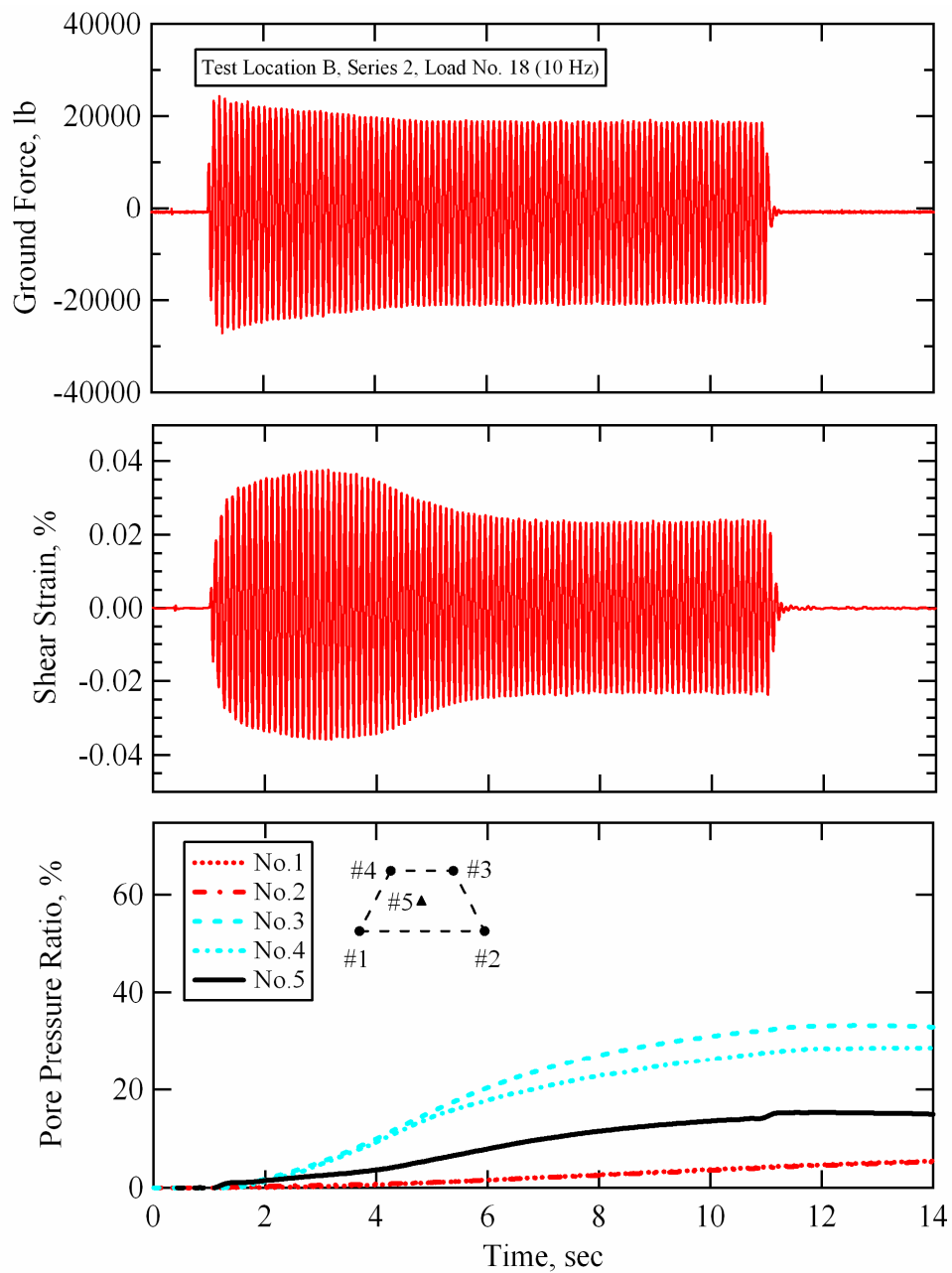


Figure 9-28 Force applied at the ground surface by T-Rex, shear strain induced at the center of the instrumented soil mass, and pore pressure ratios generated at each sensor location during Series 2, loading stage No. 18; Test Location B, Wildlife Liquefaction Array.

likely that the soil around the base plate softened to the point where it could not offer enough resistance to keep the ground force at a consistently elevated level.

The shear strain time history shown in Figure 9-28 is irregular. The average shear strain over the first 40 cycles of loading is 0.0329%. The shear strain quickly decays between 30 and 50 loading cycles. After 50 loading cycles, the shear strains remain very consistent throughout the remaining 50 cycles of loading. The average shear strain over 100 cycles is 0.0274:

The two deeper sensors (No. 1 and No. 2) in the array recorded nearly identical pressures that gradually increased throughout shaking. Both of these sensors indicated pore pressure ratios of approximately 5% at the end of 100 cycles of loading. The PDCR 35/D transducer (Sensor No. 5) recorded pressures that steadily increased throughout dynamic loading, reached a peak at a pore pressure ratio of approximately 15% at the end of shaking, and then slowly began to dissipate. The two shallower sensors (No. 3 and No. 4) recorded fairly similar pressures that peaked at a pore pressure ratio of approximately 30% at the end of loading. Pore pressure data was recorded for approximately 60 seconds during loading stage No. 18. Figure 9-29 shows the pore pressure ratios measured at each sensor location with a time scale of 60 seconds. The pressures recorded by the two shallower sensors and Sensor No. 5 began dissipating soon after the end of loading. However, the pressures recorded by the two deeper sensors continued to gradually increase for approximately 10 seconds after the end of shaking. The pore pressure ratio at Sensors No. 3 and No. 4 had decayed to approximately 15%

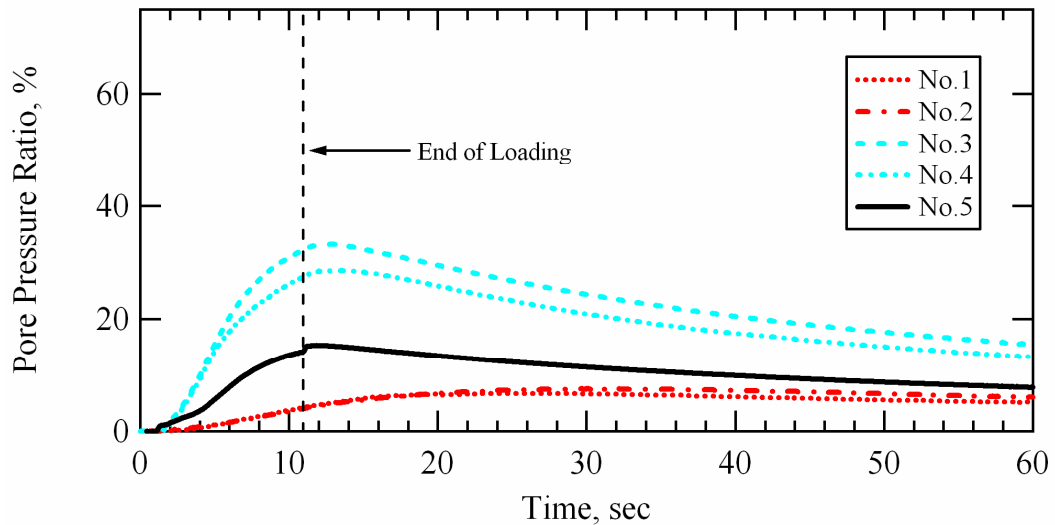


Figure 9-29 Pore pressure ratios generated at each sensor location during Series 2, loading stage No. 18; Test Location B, Wildlife Liquefaction Array.

after 50 seconds had passed from the end of loading. The pore pressure ratios at all other sensor locations had dropped below 10% after this same time period.

As mentioned previously, the r_u values used to construct the pore pressure generation curves for the site were obtained solely from the PDCR 35/D transducer located at the center of the array (Sensor No. 5). The averaged shear strain values and pore pressure ratios calculated at the center of the liquefaction sensor array for dynamic Load No. 18 are presented in Table 9-7 as a function of various numbers of loading cycles.

The horizontal, in-line component (y-component) particle displacement time histories recorded at each liquefaction sensor during loading stage No. 18 are shown in Figure 9-30. All of the sensors recorded a reduction in particle

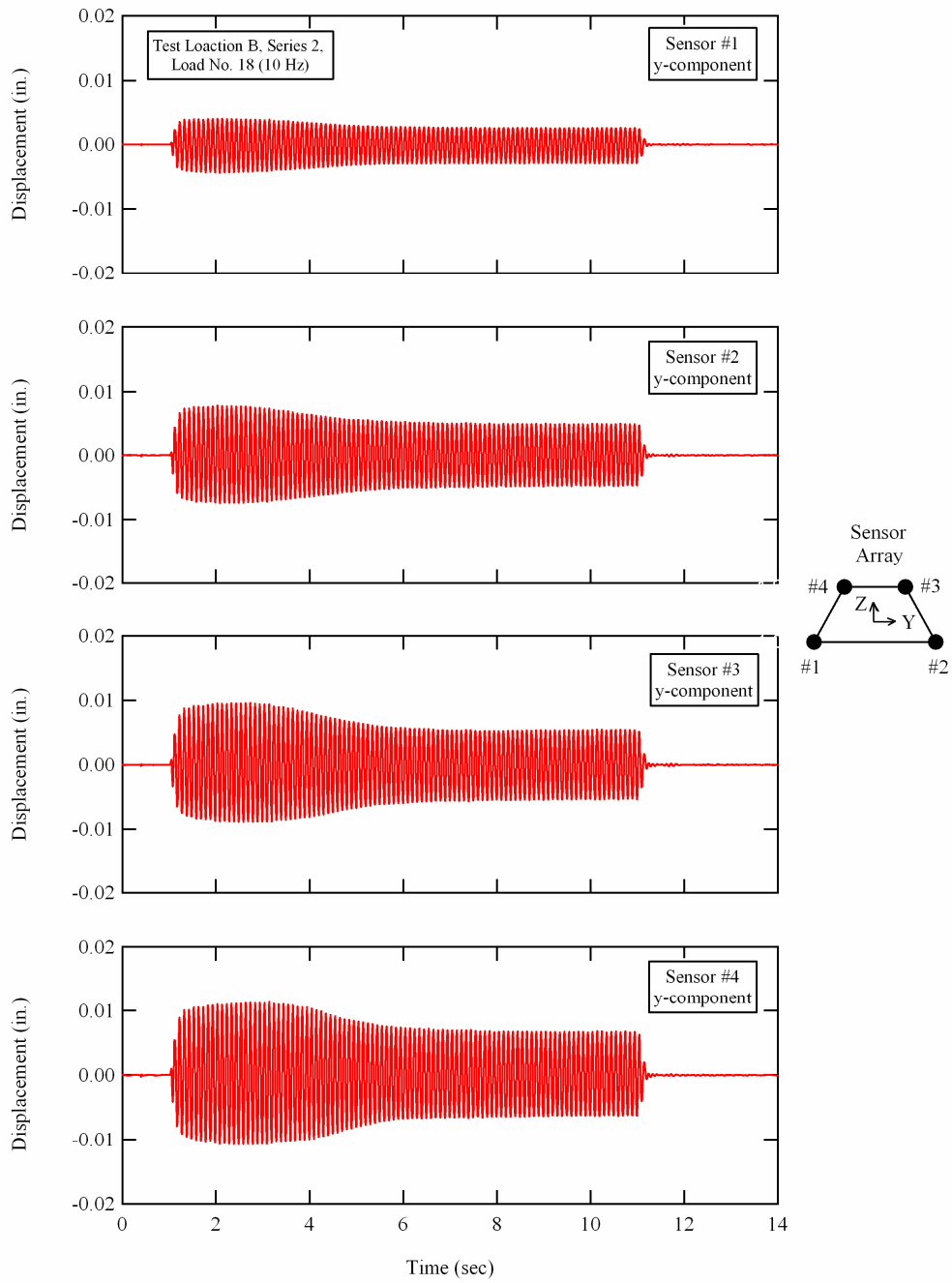


Figure 9-30 Horizontal, in-line component (y-component) particle displacements recorded at each of the liquefaction sensor locations during Series 2, loading stage No. 18; Test Location B, Wildlife Liquefaction Array.

displacement amplitude between 30 to 50 cycles of loading. The ground force is also decaying in this interval (see Figure 9-28). The drop in particle displacements, and hence shear strain, was likely caused partially by a decreasing ground force and partially by softening of the soil above the liquefaction sensor array, thus inhibiting the transfer of load through the softened zone and into the instrumented soil mass.

9.4.2.8 Loading Stage No. 19

The excess pore pressures generated during loading stage No. 18 were allowed to dissipate before applying the last staged load of Series 2. During loading stage No. 19, T-Rex was driven at its maximum output (in shear mode) for 200 cycles of 10-Hz loading. The force applied at the ground surface, the shear strain induced at the center of the liquefaction sensor array, and the pore pressure ratios generated at each PPT location during loading stage No. 19 are shown in Figure 9-31. The ground force during Load No. 19 was slightly irregular, once again having a tendency to decrease throughout loading. The ground force had a few peaks in the early loading cycles that were approximately 30000 lb (133.4 kN). However, the ground force generally trended from approximately 25000 lb (111 kN) down to about 22000 lb (97.8 kN) over the duration of shaking. It is likely that the soil around the base plate softened to the point where it could not offer enough resistance to keep the ground force at a consistently elevated level.

The shear strain time history shown in Figure 9-31 is highly irregular over approximately the first 30 cycles. However, after this point, the shear strain

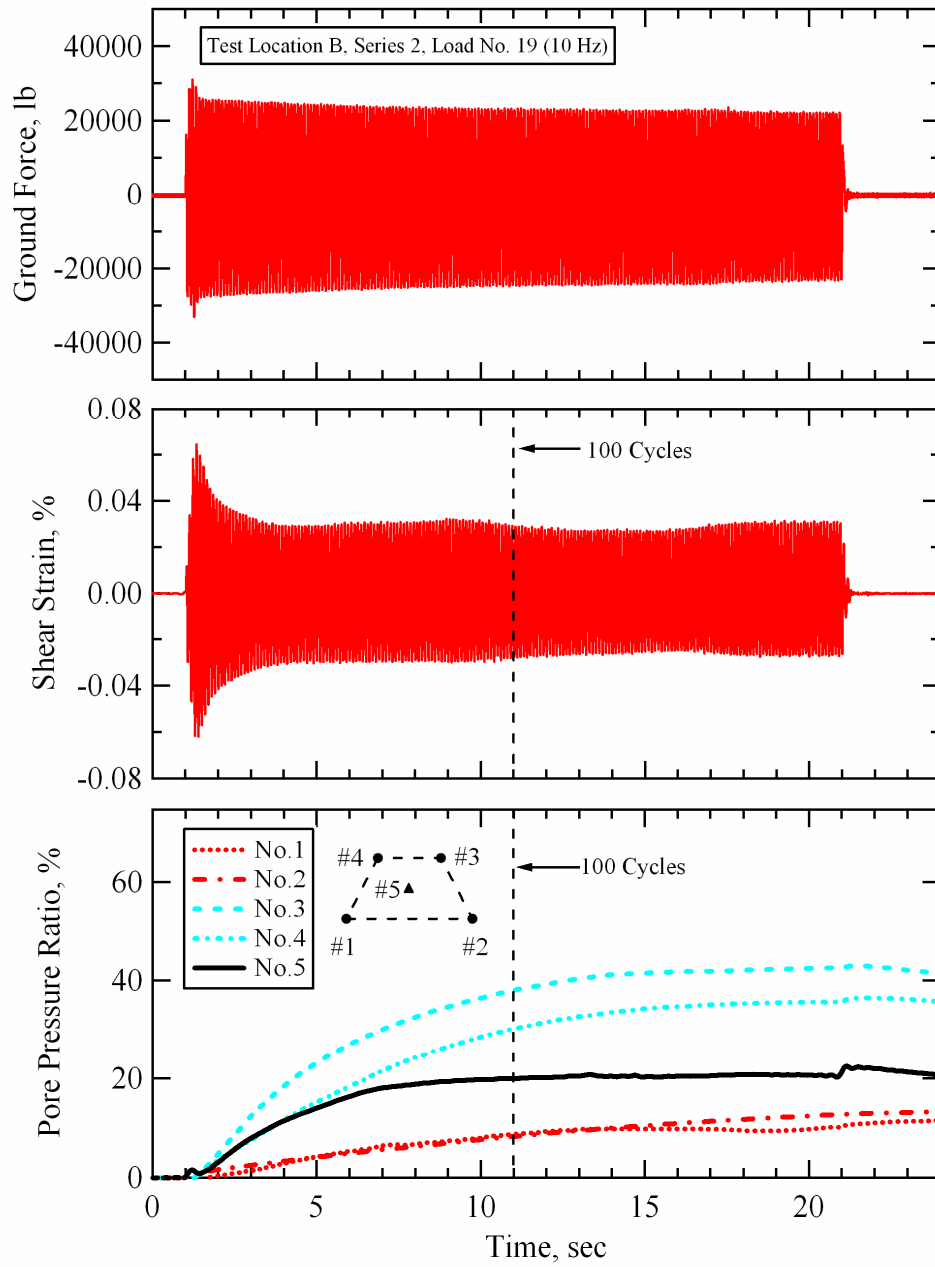


Figure 9-31 Force applied at the ground surface by T-Rex, shear strain induced at the center of the instrumented soil mass, and pore pressure ratios generated at each sensor location during Series 2, loading stage No. 19; Test Location B, Wildlife Liquefaction Array.

remains fairly consistent. The average shear strain over the first 10 cycles of loading is 0.0493%. The average shear strain over the first 100 cycles of loading is 0.0324%. The excess pore water pressure at Sensor No. 5 increased steadily through approximately the first 60 cycles of loading, and then peaked at a pore pressure ratio close to 20%. After 60 cycles of loading the pore pressure ratio remains essentially constant until loading stops, after which, the pressure begins to dissipate. Unlike the behavior recorded by Sensor No. 5, the pore water pressures recorded by the other PPT's continue to build through approximately the first 100 cycles of loading. After this point, they also remain fairly consistent throughout the duration of shaking. The sensors at the top of the array (Sensors No. 3 and No. 4) ultimately measured excess pore water pressures equivalent to pore pressure ratios of approximately 35% to 40%. The sensors at the bottom of the array (Sensors No. 1 and No. 2) measured excess pore water pressures equivalent to a pore pressure ratio of approximately 15%. Pore pressure data was recorded for approximately 120 seconds during loading stage No. 19. Figure 9-32 shows the pore pressure ratios measured at each sensor location with a time scale of 120 seconds. The pressures recorded by all of the sensors begin dissipating soon after the end of loading. The pore pressure ratio at Sensors No. 3 and No. 4 had decayed to approximately 15% after 100 seconds had passed from the end of loading. The pore pressure ratios at all other sensor locations had dropped below 10% after this same time period.

The horizontal, in-line component (y-component) particle displacement time histories recorded at each liquefaction sensor during loading stage No. 19 are

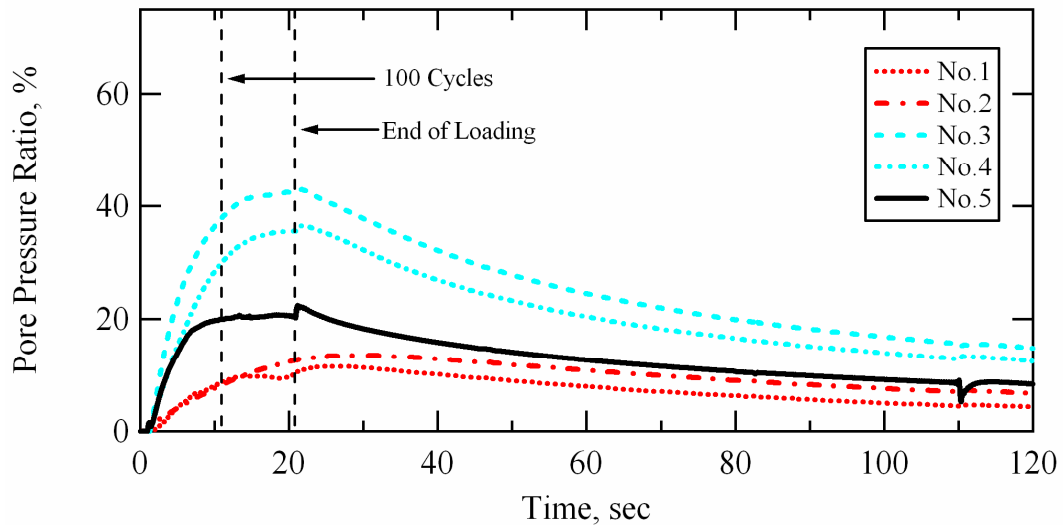


Figure 9-32 Pore pressure ratios generated at each sensor location during Series 2, loading stage No. 19; Test Location B, Wildlife Liquefaction Array.

shown in Figure 9-33. All of the sensors recorded a reduction in particle displacement amplitude early in loading. The ground force is also decaying in a similar manner over the same number of loading cycles (see Figure 9-31). The drop in particle displacements, and hence shear strain, was likely caused partially by a decreasing ground force and partially by softening of the soil above the liquefaction sensor array, thus inhibiting the transfer of load through the softened zone and into the instrumented soil mass.

9.4.3 Pore Pressure Generation Curves; Loading Series 2

Pore pressure generation curves for this series of testing can readily be constructed from the data presented in Table 9-7 using any of the given numbers of loading cycles. Figure 9-34 shows the pore pressure generation curves for 10,

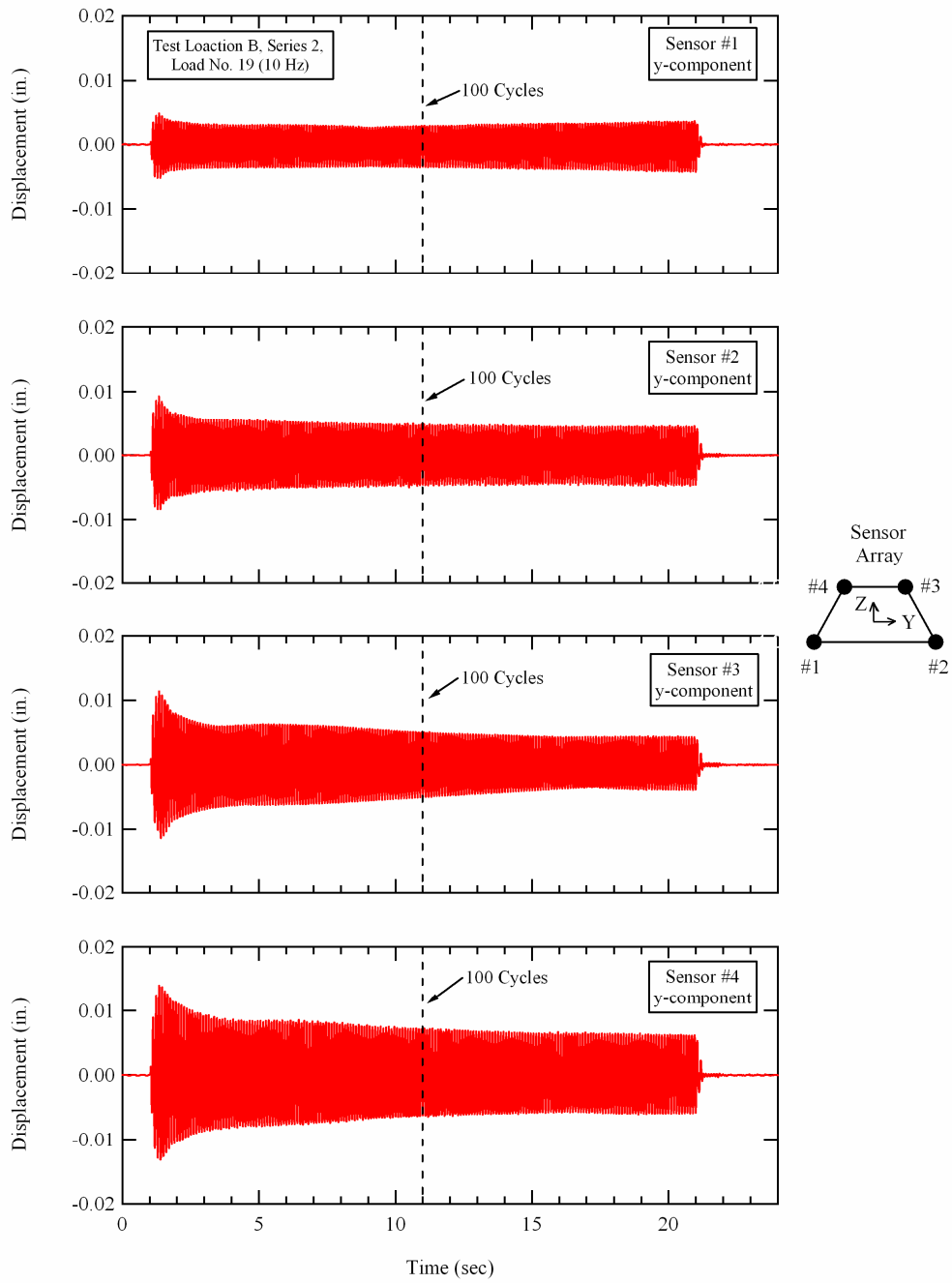


Figure 9-33 Horizontal, in-line component (y-component) particle displacements recorded at each of the liquefaction sensor locations during Series 2, loading stage No. 19; Test Location B, Wildlife Liquefaction Array.

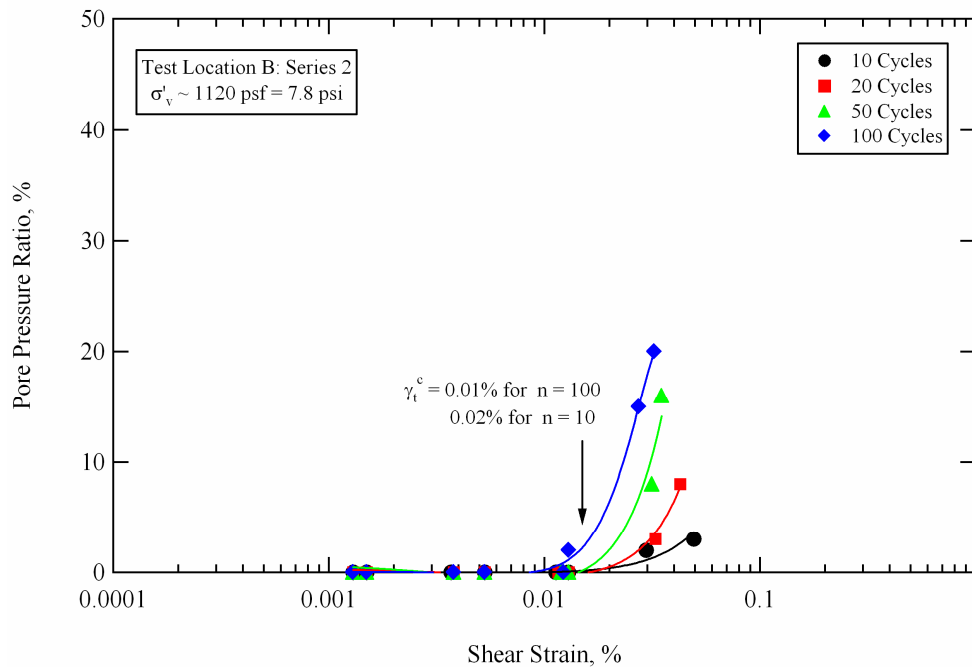


Figure 9-34 Pore pressure generation curves obtained from in-situ liquefaction tests conducted during staged dynamic loading Series 2 at Test Location B, Wildlife Liquefaction Array.

20, 50, and 100 cycles of loading determined at Test Location C during staged dynamic loading Series 2. The cyclic threshold shear strain (γ_t^e) depends on the number of cyclic shear strain cycles (n) and ranges from approximately 0.01% for $n = 100$ to 0.02% for $n = 10$. Multiple data points between 0.001% and 0.01% confirm the lack of excess pore pressure generation below γ_t^e . In general, the pore pressure data from this loading series were more difficult to fit, and follow a less consistent trend, than the data from Series 1. The odd shaped strain time histories during Loads No. 18 and No. 19 (see Figures 9-28 and 9-31, respectively) followed by the retardation of pore pressure generation measured at Sensor No. 5 early in the loading stages are likely to blame for this behavior.

Figure 9-35 compares the in-situ pore pressure generation curves determined for Test Location B during dynamic loading Series 1 with Dobry's pore pressure generation model for liquefiable soils from the Wildlife Site (Vucetic and Dobry, 1986). As discussed in Section 7.3.1.3, Dobry's model for Wildlife liquefiable soils was developed from cyclic laboratory test results. A cyclic threshold shear strain of 0.02% was assumed for the model (based on experience gained from previous laboratory tests) because the laboratory tests conducted in the study were not performed at shear strains that were low enough to actually determine the cyclic threshold shear strain. This cyclic threshold shear strain was assumed to be the same for any given number of loading cycles. The cyclic tests used to develop the model for Wildlife soils employed up to 30 cycles of strain-controlled loading. The assumed cyclic threshold value is equivalent to the $n = 10$ cyclic threshold shear strain determined from in-situ liquefaction tests conducted during staged loading Series 2. In Figure 9-35, Dobry's pore pressure generation model is shown for 10 loading cycles ($n = 10$) and for 100 loading cycles ($n = 100$), as calculated using Equation 7-1. The in-situ test results agree fairly well with the range predicted by Dobry's model. However, the 50- and 100-cycle results from this staged loading series indicate slightly higher pore pressure generation for a given shear strain level and number of cycles than the model predicts. Because the pore pressure ratios induced at the center of the liquefaction sensor array during Series 2 tests were less than 20%, the pore pressure generation curves presented in Figures 9-34 and 9-35 are shown with a

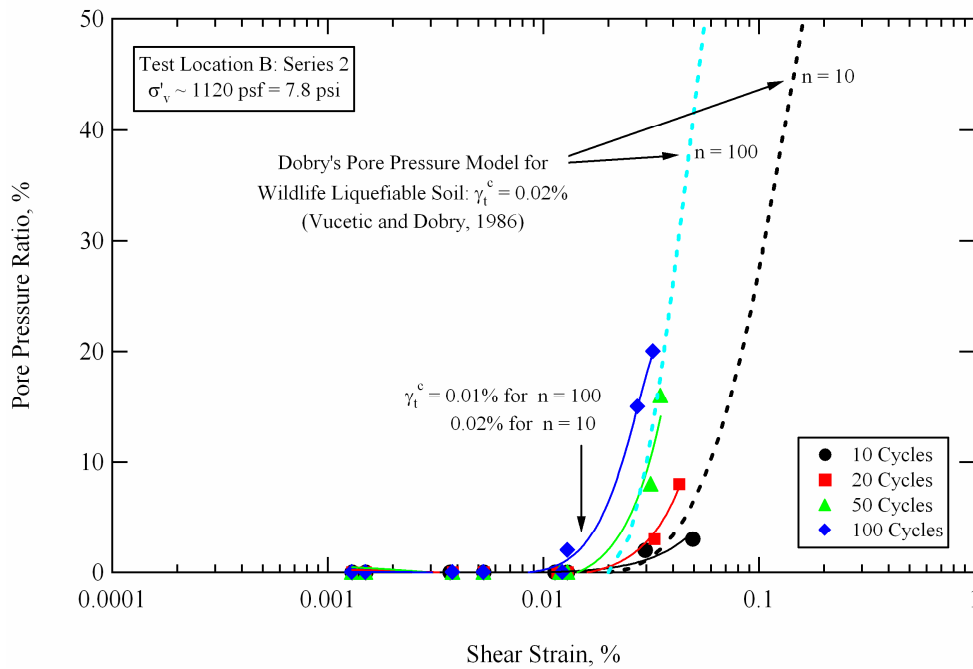


Figure 9-35 Comparison between Dobry's pore pressure generation model (Vucetic and Dobry, 1986) and pore pressure generation curves obtained from in-situ liquefaction tests conducted during staged dynamic loading Series 2 at Test Location B, Wildlife Liquefaction Array.

maximum pore pressure ratio scale of 50%. For perspective purposes, Figure 9-36 presents the pore pressure generation curves with a maximum pore pressure ratio scale of 100%.

For reasons discussed in Sections 8.3.3 and 8.3.4, it is believed that redistribution and dissipation of excess pore water pressure has little affect on the measured pore pressure response during the course of dynamic in-situ liquefaction tests.

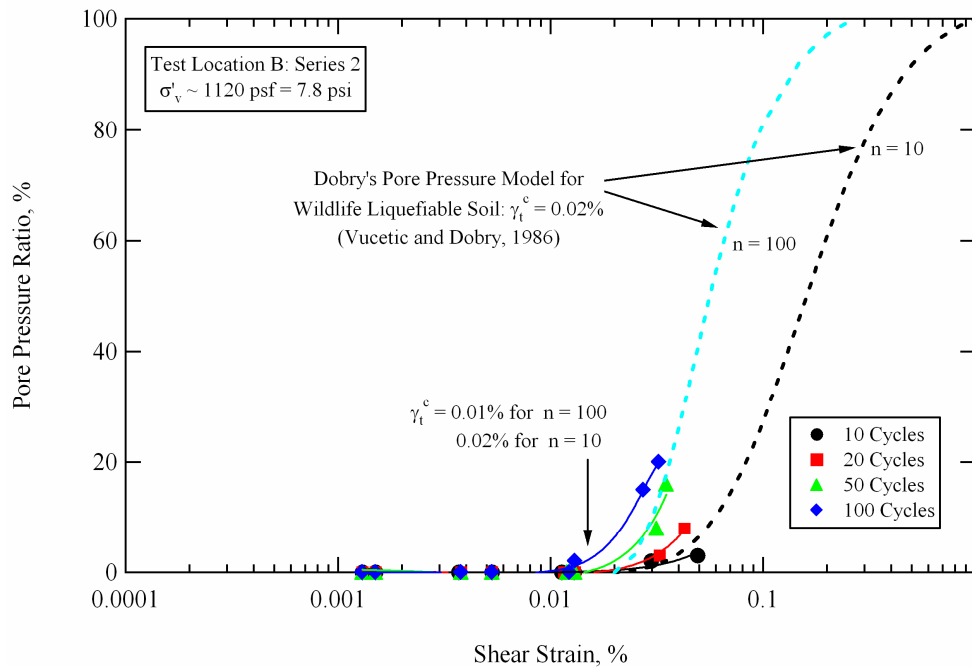


Figure 9-36 Full pore pressure ratio scale comparison between Dobry's pore pressure generation model (Vucetic and Dobry, 1986) and pore pressure generation curves obtained from in-situ liquefaction tests conducted during staged dynamic loading Series 2 at Test Location B, Wildlife Liquefaction Array.

9.5 GENERAL COMPARISON OF RESULTS FOR SERIES 1 AND SERIES 2

Two in-situ dynamic liquefaction test staged loading series were conducted at Test Location B at the Wildlife Liquefaction Array. The first staged loading series (Series 1) was conducted in the afternoon of August 13, 2005. The second staged loading series (Series 2) was conducted in the morning of August 15, 2005. Both loading series consisted of eight stages which started in the low-strain range and sequentially progressed until significant shear strains were induced in the instrumented soil mass. The pore pressure generation curves

obtained from Series 1 and Series 2 are compared in Figure 9-37. Shear strains induced at the center of the liquefaction sensor array during these staged loading series ranged from approximately 0.0007% to approximately 0.05%. The pore pressure generation curves obtained from both test series indicate that the cyclic threshold shear strain (γ_t^e) depends on the number of cyclic shear strain cycles (n) and ranges from approximately 0.01% for n = 100 to 0.02% for n = 10. The 20-cycle and 50-cycle curves from both test series are nearly identical to each other. The 100 cycle curves are slightly different, with the curve obtained during Series 2 yielding slightly higher pore pressure ratios for a given shear strain. Maximum pore pressure ratios of 35 and 20% were induced at the center of the liquefaction sensor array during Series 1 and Series 2, respectively.

9.6 SUMMARY

The in-situ liquefaction sensor array at Test Location B was installed on August 12, 2005. The instrumentation was installed just outside of the circular array of pore water pressure transducers that were placed at the 1982 (old) WLA Site by USGS personnel (Bennett et al., 1984). The liquefaction sensors were placed within the approximate depth range of 11- to 13-ft (3.4- to 4.0-m). Two staged loading series were conducted at Test Location B. The first staged loading series (Series 1) was conducted in the afternoon of August 13, 2005. The second staged loading series (Series 2) was conducted in the morning of August 15, 2005. Both staged loading series consisted of eight dynamic loads, which started in the low-strain range and sequentially progressed until significant shear strains were induced in the instrumented soil mass. Shear strains induced at the center of the

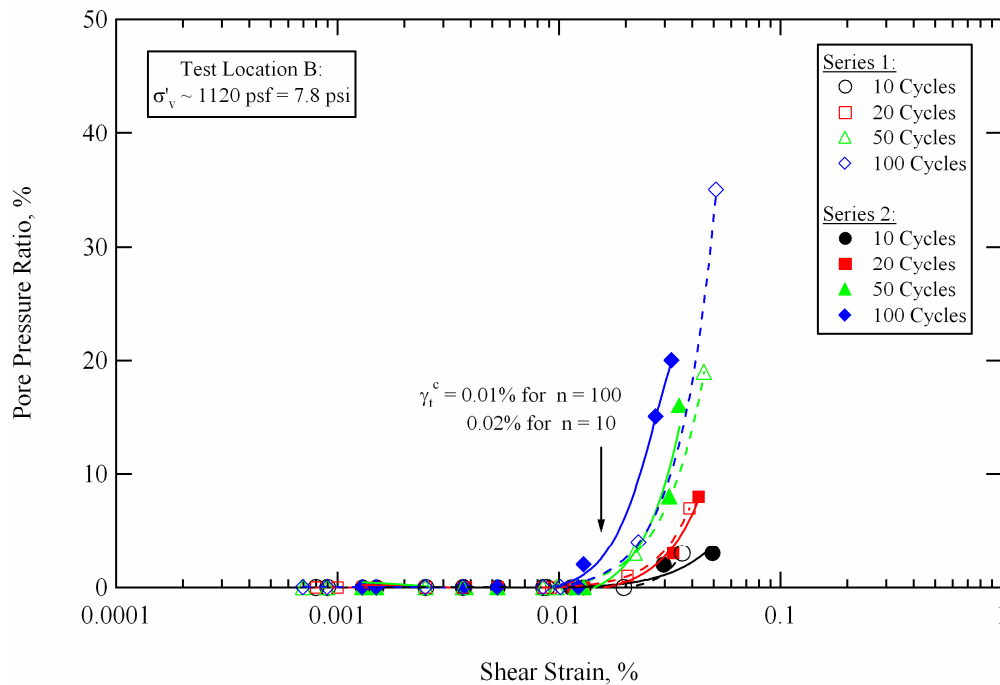


Figure 9-37 Comparison of the pore pressure generation curves obtained during Series 1 and Series 2 staged dynamic loading at Test Location B, Wildlife Liquefaction Array (WLA).

liquefaction sensor array during these staged loading series ranged from approximately 0.0007% to approximately 0.05%. Pore pressure generation curves were evaluated from the data collected during each staged loading series. The results from both test series agree very well. The pore pressure generation curves obtained from both test series indicate that the cyclic threshold shear strain (γ_t^c) depends on the number of cyclic shear strain cycles (n) and ranges from approximately 0.01% for $n = 100$ to 0.02% for $n = 10$. These curves also agree quite well with Dobry's pore pressure generation model that was developed for liquefiable soils from the Wildlife Site (Vucetic and Dobry, 1986). Maximum

pore pressure ratios of 35 and 20% were induced at the center of the liquefaction sensor array during Series 1 and Series 2, respectively.

The nonlinear soil shear modulus for the soil within the liquefaction sensor array could not accurately be resolved at this location due to harmonic distortion and small amounts of noise in some of the raw accelerometer records. These problems made it extremely difficult to obtain precise values for the time lags between sensors.

Chapter 10

In-Situ Liquefaction Test Results: Test Location A, WLA

10.1 INTRODUCTION

Three separate in-situ dynamic liquefaction tests were conducted at the Wildlife Liquefaction Array (WLA) between August 8 and August 19, 2005. The general locations of these tests are shown in Figure 7-19. In this chapter, the in-situ pore pressure generation data that was obtained at Test Location A are presented and discussed. Despite the fact that Test Location A was the first of the three locations where in-situ liquefaction tests were conducted at the WLA, the results obtained from Test Location A are presented last in this dissertation. The pore pressure generation behavior measured at Test Location A is quite different from the pore pressure generation behavior measured at Test Locations B and C. In general the pore pressure generation data collected at Test Location A indicates a higher threshold shear strain and significantly lower pore pressure ratios than expected for a given shear strain amplitude.

10.2 TEST A: ARRAY LOCATION AND PRE-DYNAMIC LOADING INFORMATION

The in-situ liquefaction sensor array at Test Location A was installed on August 9, 2005. The approximate location of the array is shown in Figure 10-1. The sensor array was installed at the 2004 (new) WLA Site (<http://nees.ucsb.edu>) close to CPT 43. The center point of the liquefaction sensor array was positioned at radial distances of approximately 15.0 ft (4.6 m) and 43.9 ft (13.4 m) from

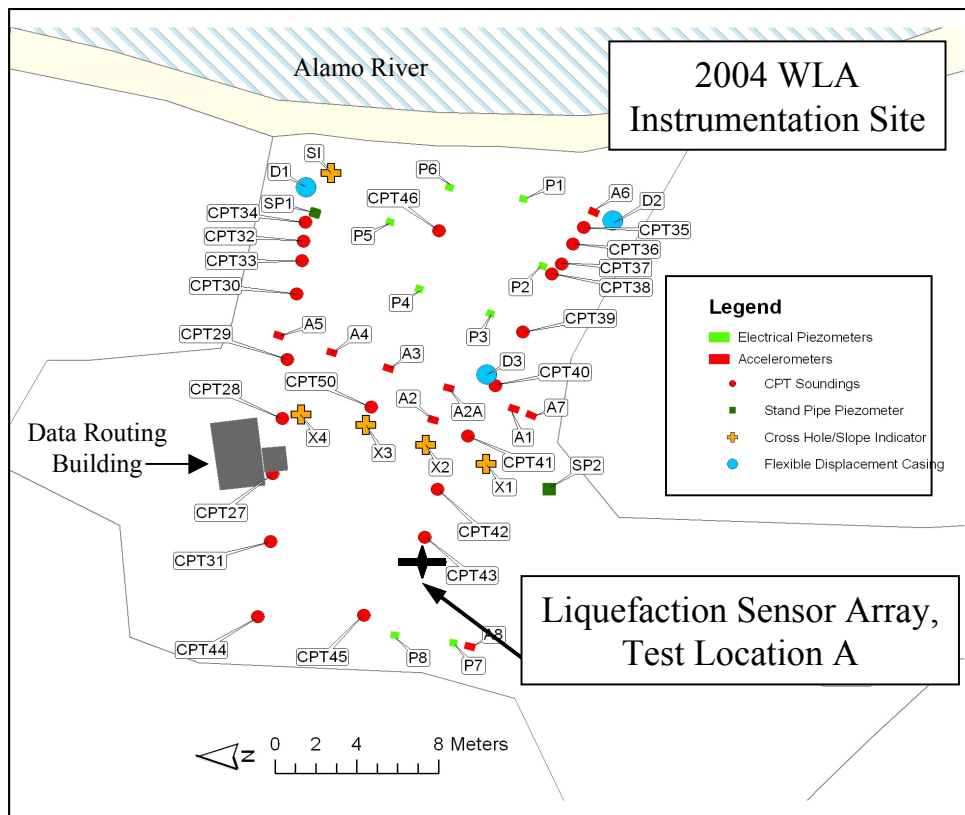


Figure 10-1 Approximate location of the in-situ liquefaction sensor array installed at Test Location A, Wildlife Liquefaction Array (WLA) (after <http://nees.ucsb.edu>).

BM2A and SBM6, respectively. These benchmarks are marked in the field, and were also surveyed by Proctor (2004). The results from this survey can be found at <http://nees.ucsb.edu>. This information should be sufficient to relocate the position of the array if necessary.

The linear array at Test Location A extended in the north-south direction. The sensors were installed according to the procedure detailed in Section 5.2. A picture of an installed liquefaction sensor array, as viewed from the ground surface, is shown in Figure 10-2. As discussed in Section 5.2, the numbers next

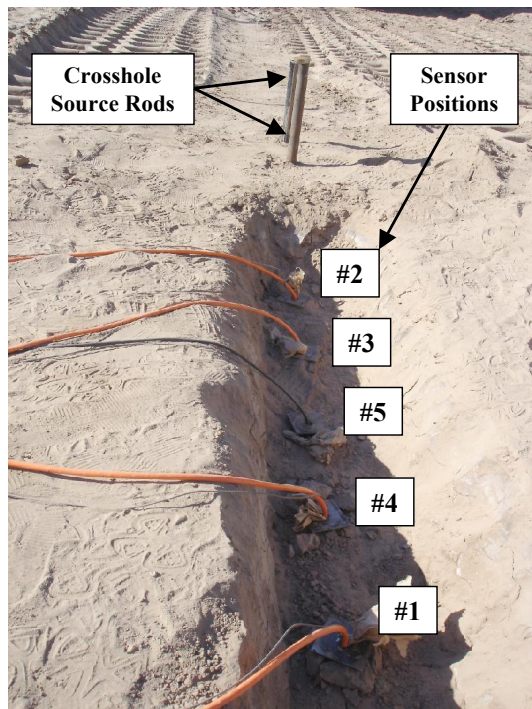


Figure 10-2 Picture of a liquefaction sensor array as seen from the ground surface.

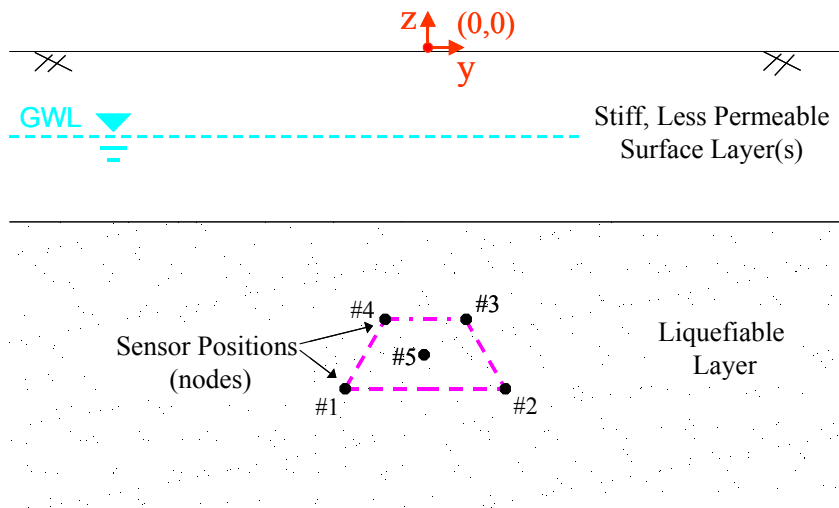


Figure 10-3 Cross-sectional schematic of an embedded liquefaction sensor array.

to each liquefaction sensor do not represent the order in which they were installed, but rather the positions of the sensors in an embedded trapezoidal array. A cross-sectional schematic of the sensor array, as viewed from below the ground surface, is shown in Figure 10-3. The sensor positions may be considered as nodes of a single quadrilateral finite element. The specific sensors that were installed in each of the nodal positions at Test Location A are listed in Table 10-1. Sensor positions No. 1 through No. 4 were occupied by liquefaction sensors containing a 3D-MEMS accelerometer and a miniature pore water pressure transducer (PPT), while sensor position No. 5 was occupied by the Druck PDCR 35/D pressure transducer. The individual calibration factors for the sensors occupying each nodal position are given in Section 4.2.

Table 10-1 also details the relative positions of each sensor in the form of y- and z-coordinates. These coordinates are referenced from a point on the ground surface directly above sensor position No. 5 (refer to Figure 10-3). The y-coordinate represents the horizontal, in-line distance from the center of the array, while the z-coordinate represents the vertical distance below the ground surface (depth). There is no need to provide an x-coordinate for the sensor locations because they were all installed within the same in-line plane (i.e. $x = 0$). As indicated, the liquefaction sensors occupying positions No. 1 and No. 2 were installed roughly 2.0-ft (0.6-m) on either side of the array centerline at a depth of approximately 12-ft (3.6-m) below the ground surface, while the liquefaction sensors occupying positions No. 3 and No. 4 were installed roughly 1.0-ft (0.3-m) on either side of the array centerline at a depth of approximately 10.0-ft (3.0-m)

Table 10-1 Coordinates and tilt angles for the sensors installed in the liquefaction sensor array at Test Location A, Wildlife Liquefaction Array (WLA)

| Sensor Position (Node #) | Sensor Designation | y-coordinate (ft) | z-coordinate (ft) | Tilt Angle (degrees) | |
|-----------------------------|-----------------------|----------------------|----------------------|----------------------|--------|
| | | | | x-axis | y-axis |
| #1 | Liquefaction Sensor 1 | -2.00 | -11.92 | -1.1 | 1.3 |
| #2 | Liquefaction Sensor 5 | 1.96 | -12.02 | -1.0 | -0.1 |
| #3 | Liquefaction Sensor 8 | 1.04 | -9.97 | -0.3 | 0.1 |
| #4 | Liquefaction Sensor 9 | 1.00 | -10.00 | 0.4 | -1.0 |
| #5 | Druck PDCR 35/D PPT | 0.00 | -10.94 | NA | NA |

below the ground surface. The PDCR 35/D sensor was placed at the center of the array (position No. 5) at a depth of approximately 11.0-ft (3.3-m) below the ground surface.

The sensor coordinates presented in Table 10-1 are based on measurements made from the ground surface. The accuracy of these measurements is contingent on the ability to install the sensors from the ground surface with minimal deviation (tilt). The tilt of the liquefaction sensors can be monitored via the 3D-MEMS accelerometer installed in each of them (see Section 4.2.1). Tilt about both the x- and y-axes can be sensed. The tilt angles obtained from the MEMS accelerometer in each liquefaction sensor are provided in Table 10-1. These angles were obtained from measurements taken after the sensors had reached their final locations. The tilt angles about the x- and y-axes are generally less than 1.5 degrees off of vertical, indicating that the sensors were installed with minimal deviation. The PDCR 35/D sensor does not contain a MEMS

accelerometer and hence does not have the ability of monitoring tilt. However, it is assumed that its deviation would be similar to the deviations experienced by the liquefaction sensors, as they are all installed in the same manner.

The position of the liquefaction sensor array, relative to the generalized soil profile at the site, is shown in Figure 10-4. The uppermost soil layer is an 8.2-ft (2.5-m) thick silt to clayey-silt bed that overlies a 14.1-ft (4.3-m) thick silty-sand layer. Beneath these floodplain deposits is a stiff 17.1-ft (5.2-m) thick clay to silty-clay layer (Bennett et al., 1984). The top of the array is approximately 2 ft (0.9 m) below the top of the liquefiable silty-sand layer. Bennett et al. (1984) originally partitioned the liquefiable silty-sand layer into an upper and lower unit, with the division between the units occurring at a depth of approximately 11.5 ft (3.5 m). Several researchers who conducted resonant column tests, cyclic triaxial tests, and cyclic simple shear tests on soil from the Wildlife Site in the 1980's also followed this notation (Haag and Stokoe, 1984; Vucetic and Dobry, 1986). The liquefaction sensor array is located partially in the upper liquefiable layer and partially in the lower liquefiable soil layer. As mentioned in Section 7.6, the upper-layer has an average fines content of 49% and an average clay-size particle content of 12%, while the lower-layer has an average fines content of 27% and an average clay-size particle content of 9%. However, the transition from the lower-layer to the upper-layer is very subtle, with fines contents generally increasing from the bottom to the top of the liquefiable soil layer. If the grain size characteristics from various researchers (see Chapter 7) obtained only from soil samples within the depth range of the liquefaction sensor array are averaged, the

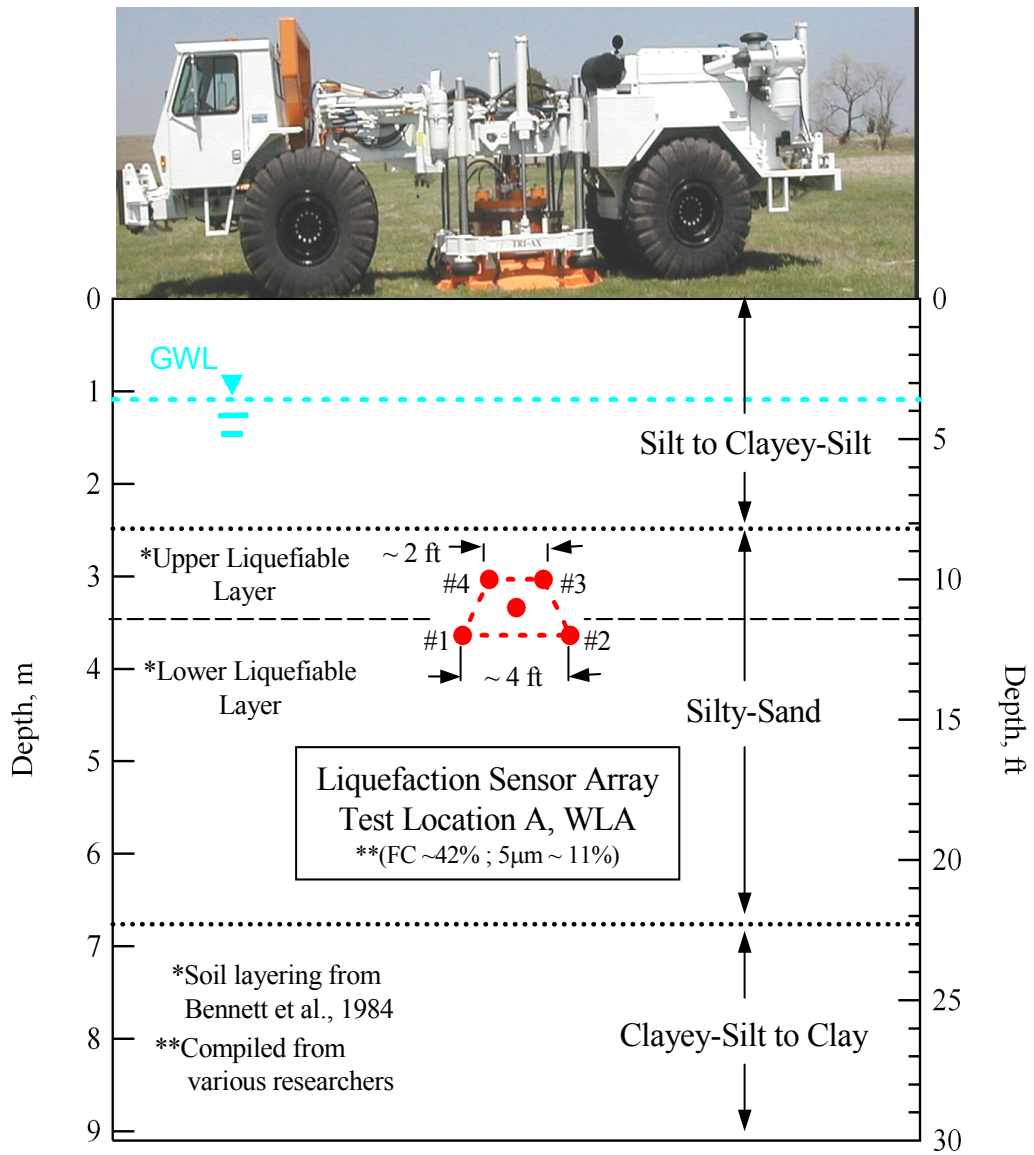


Figure 10-4 Position of the liquefaction sensor array at Test Location A, shown with respect to the general soil layering at the Wildlife Site as proposed by Bennett et al. (1984).

finer and clay-size ($5\ \mu\text{m}$) particle contents are equal to 42% and 11%, respectively

The approximate depth of the ground water level (GWL) at the time of testing is also shown in Figure 10-4. The GWL was evaluated from measurements taken in a standpipe and from readings obtained with the PDCR 35/D pressure transducer, located at the center of the array. The standpipe was located approximately 40 ft (12 m) away, and four separate readings taken between August 10 and August 11 placed the GWL between 3.2 and 4.0 ft (1.0 and 1.2 m) below the ground surface. More than 30 measurements made with the PDCR 35/D transducer over the same time period consistently placed the static GWL between 3.4 and 4.0 ft (1.0 and 1.2 m) below the ground surface. The water table was somewhat in a state of flux at this time due to a rainstorm in the area that had caused the Alamo River to rise substantially. The good agreement between the standpipe readings and the pressure transducer measurements demonstrate the stability and accuracy of the PDCR 35/D pressure transducer.

The liquefaction sensor array at Test Location A was installed near CPT 43. The soil layering in the immediate vicinity of the liquefaction sensor array can be verified by examining the tip resistance (q_c) and friction ratio (F_r) values obtained from CPT 43. The liquefiable soil layer boundaries proposed by Bennett et al. (1984), and the depth range (approximately 10- to 12-ft or 3.0- to 3.6-m) of the in-situ liquefaction sensor array, are plotted with the tip resistance and friction ratio values from CPT 43 in Figure 10-5. In general, the liquefiable soil layer is marked by relatively large values of CPT tip resistance and relatively small values

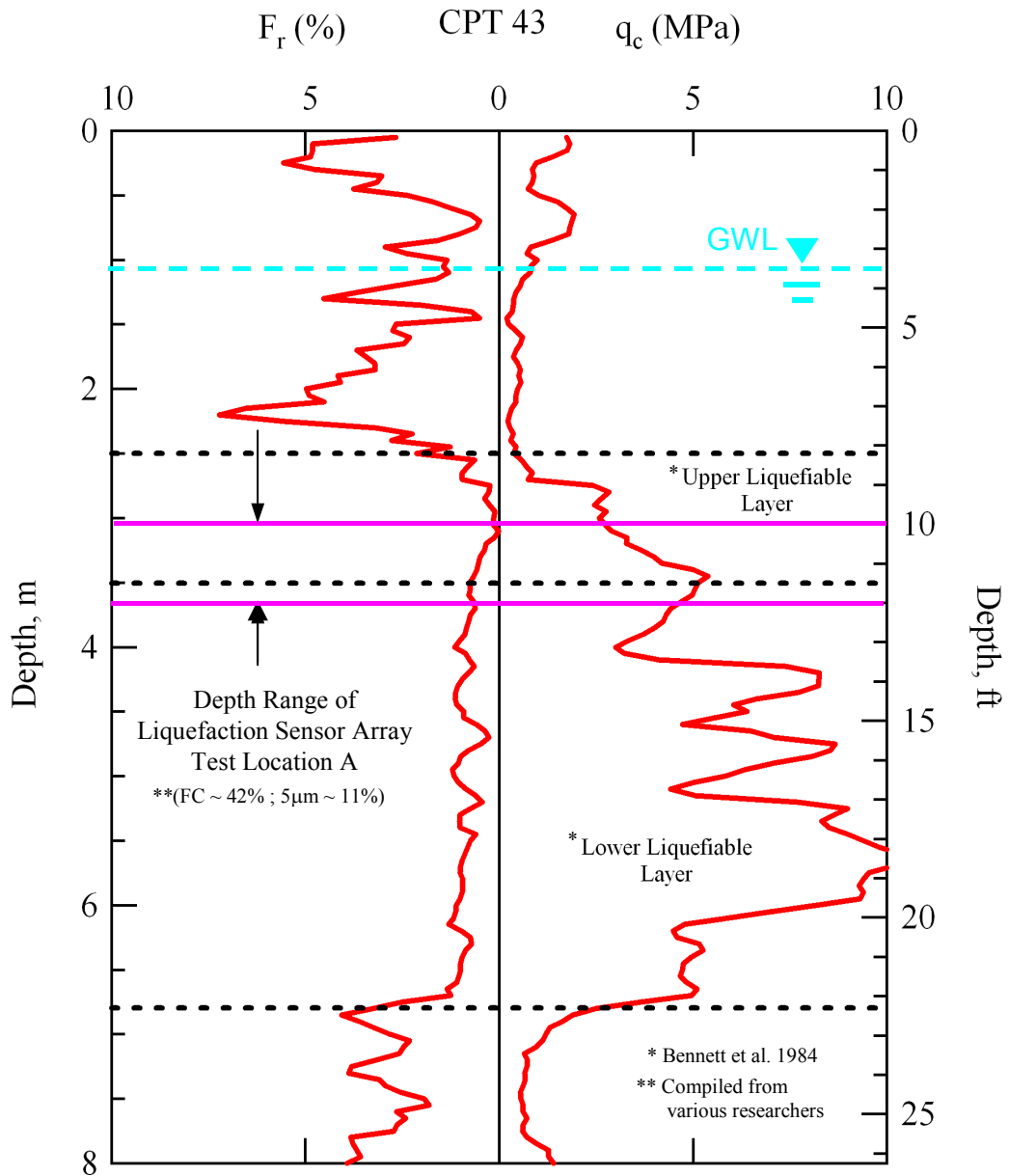


Figure 10-5 Depth range of the liquefaction sensor array at Test Location A, shown with respect to the tip resistance (q_c) and friction ratio (F_r) values obtained from CPT 43 and the upper and lower liquefiable soil layers proposed by Bennett et al. (1984) (raw CPT data from <http://nees.ucsb.edu>).

of CPT friction ratio in comparison to the layer above it. As discussed in Section 7.5, the liquefiable soil layer determined by Bennett et al. (1984) at the 1982 (old) WLA instrumentation site is a very good approximation for the liquefiable soil layer at Test Location A (near the 2004 WLA instrumentation site).

It is important to know the initial vertical effective stress at the sensor locations so that excess pore pressure ratios (r_u) induced in the instrumented soil mass during dynamic loading can be calculated from the recorded excess pore water pressure data (i.e. $r_u = \Delta u / \sigma_v'$, where Δu is excess pore water pressure and σ_v' is initial vertical effective stress). The effective overburden pressures can readily be calculated knowing the depth of each sensor, the location of the GWL, and the unit weight of the soil ($\gamma \sim 120$ pcf or ~ 19.0 kN/m³). The effective overburden pressures calculated at the approximate depth of each sensor are listed in Table 10-2. These values were calculated with the static GWL located approximately 3.5-ft (1.1-m) below the ground surface.

As discussed in Section 5.2, when estimating the vertical effective stress at each sensor location, the increase in stress caused by the static hold-down force of the vibroseis base plate must also be taken into account. The uniform surface pressure (assuming the base plate to be rigid) applied by the base plate during testing was approximately 800 psf (38 kPa). The change in vertical stress beneath the center of the base plate at the depth of each sensor was calculated using both Boussinesq's and Westergaard's elastic stress distribution solutions (Coduto, 1994). Estimates for the changes in vertical stress obtained from calculating

Table 10-2 Estimates for the effective overburden stress, increase in vertical stress due to the vibroseis base plate load, and total vertical effective stress at the approximate depth of each sensor in the liquefaction sensor array at Test Location B, Wildlife Liquefaction Array (WLA)

| Sensor Position (Node #) | Approximate Depth (ft) | Effective Overburden Stress (psf) ¹ | Increase in Stress Due to Vibroseis Base Plate Load (psf) ² | | Initial Effective Vertical Stress (psf) |
|--------------------------|------------------------|--|--|--------------------------|---|
| | | | Boussinesq | Westergaard ³ | |
| #1 | 12 | 910 | 128 | 131 | 1040 |
| #2 | 12 | 910 | 128 | 131 | 1040 |
| #3 | 10 | 795 | 174 | 171 | 965 |
| #4 | 10 | 795 | 174 | 171 | 965 |
| #5 | 11 | 850 | 149 | 149 | 1000 |

Notes: 1. Calculated using $\gamma = 120$ pcf and GWL at 3.5 ft below ground surface
 2. Calculated beneath center of base plate with a uniform surface pressure = 800 psf
 3. Calculated with Poisson's Ratio = 0.3

Boussinesq's and Westergaard's solutions at the depth of each sensor are provided in Table 10-2. As can be seen, both solutions give very similar results. The initial vertical effective stress at each sensor depth was calculated by superimposing the change in vertical stress caused by the applied surface load of the vibroseis base plate onto the preexisting effective overburden pressure. Table 10-2 details the estimates obtained for the initial vertical effective stress at each sensor depth. These values were used to normalize the excess pore water pressures recorded during dynamic loading to obtain excess pore pressure ratios.

As discussed in Section 6.4, readings obtained from all five pressure transducers (4 miniature PPT's located in the liquefaction sensors placed at each corner node and the larger PDCR 35/D pressure transducer located at the center of the array) were used to calculate r_u values for each stage of the in-situ liquefaction

tests. However, the r_u values used to construct the pore pressure generation curves for each site were obtained solely from the PDCR 35/D transducer located at the center of the array.

10.2.1 Crosshole Test Results

As discussed in Section 5.2, crosshole seismic tests are conducted between sensors at the same depth, both before and after dynamic loading, to study and estimate the degree of saturation and to determine how the small-strain shear stiffness of the liquefiable soil was affected by the liquefaction testing. A cross-sectional schematic showing the liquefaction sensor array, the crosshole source rods, and the base plate of T-Rex is shown in Figure 10-6. At Test Location A, source rods A and B were placed in-line with the sensor array at distances of approximately 0.75 ft (0.23 m) and 1.75 ft (0.53 m) from the edge of the base plate of T-Rex, respectively. Crosshole source rod A (13-ft or 4.0-m long) was inserted so that its tip was located at the same elevation as sensors No. 1 and No. 2 (approximately 12-ft or 3.6-m deep), while crosshole source rod B (10-ft or 3.0-m long) was inserted so that its tip was located at the same elevation as sensors No. 3 and No. 4 (approximately 10-ft or 3.0-m deep). Crosshole tests were performed by vertically impacting the top of one of the source rods with a hammer while simultaneously recording the vibration-sensing outputs of the two sensors located at the same depth as the tip of the rod. The horizontal, in-line component (y-component) of the 3D-MEMS accelerometer in each sensor was used to sense horizontally propagating compression wave (P_h -wave) arrivals,

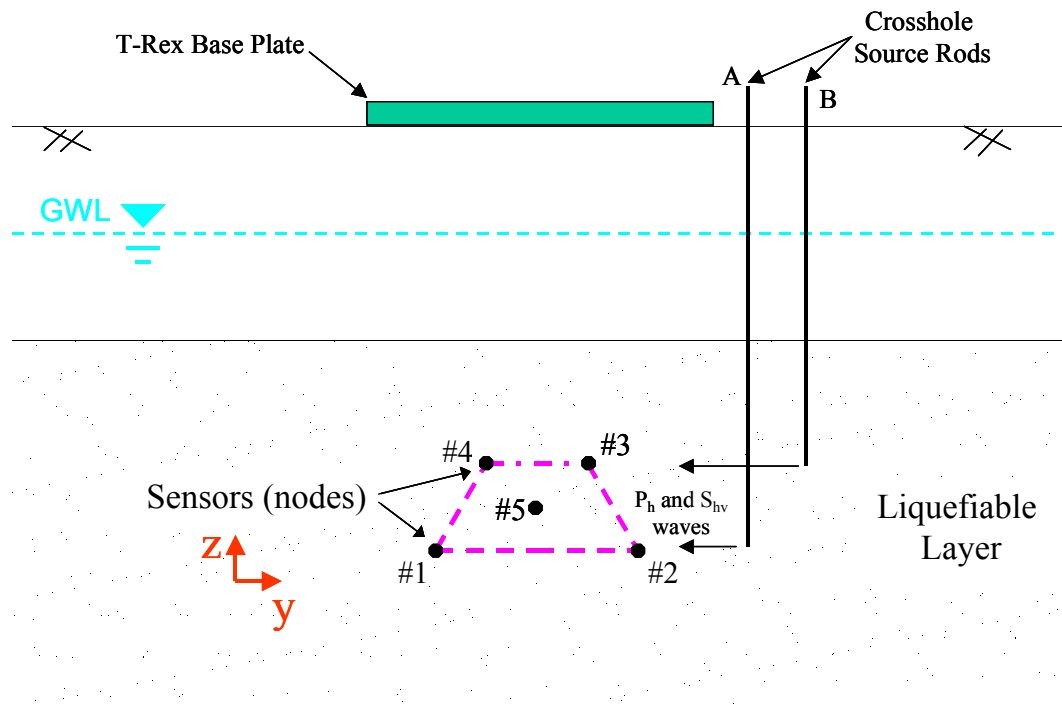


Figure 10-6 Cross-sectional schematic of the liquefaction sensor array, crosshole source rods, and the base plate of T-Rex at Test Location A.

while the vertical component (z-component) was used to sense horizontally propagating, vertically polarized shear wave (S_{hv} -wave) arrivals.

Crosshole tests were performed three separate times throughout the course of in-situ liquefaction testing at Location A. The first set of crosshole tests was performed prior to bringing T-Rex into position over the top of the liquefaction sensor array. This set of tests was conducted to provide baseline velocities for the soil prior to application of the base plate hold-down force and subsequent staged dynamic loading. The second set of crosshole tests was performed after the full, static base plate hold-down force of T-Rex had been applied to the soil (approximately 45000 lb or 200 kN; see Section 5.3), but prior to any dynamic

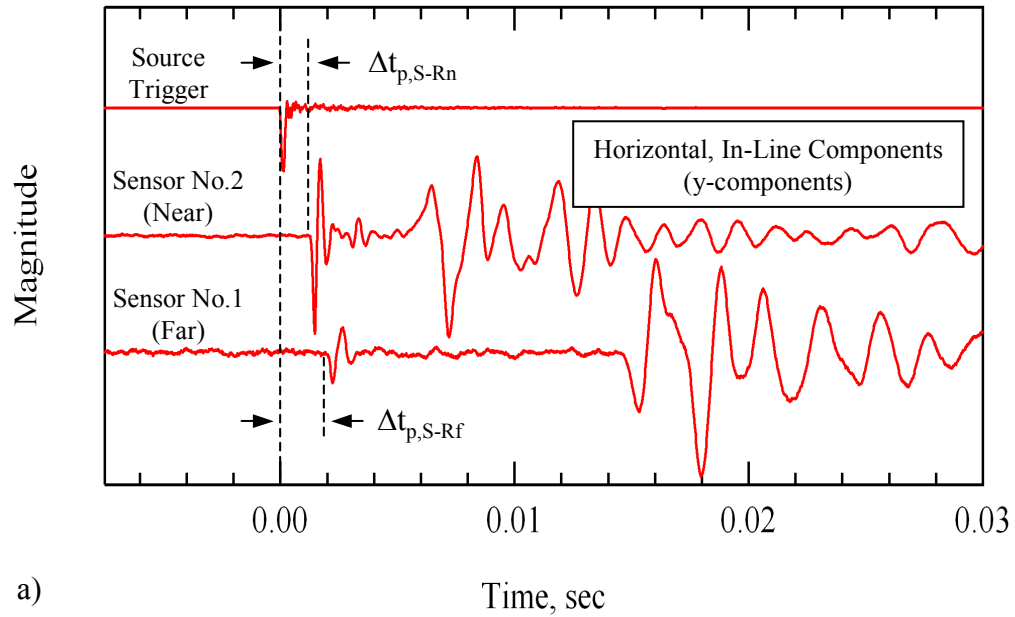
loading. After the first two sets of crosshole measurements had been performed, the first series of staged dynamic loading was conducted at Location A (discussed in Section 10.3). Then, the soil was allowed to recover for approximately 18 hours and a second series of staged dynamic loading was conducted (discussed in Section 10.4). The third set of crosshole measurements was performed immediately before the second series of staged dynamic loading.

Interval wave travel times between the near and far sensors were used to calculate crosshole wave velocities at Test Locations C and B (see Sections 8.2.1 and 9.2.1, respectively). This method is the preferred method for obtaining crosshole wave velocities. However, some of the wave arrivals (particularly P_h -wave arrivals) at Test Location A were hard to identify on the records obtained from Sensor No. 4 (the far sensor at approximately 10-ft deep). Therefore, it was necessary to use the direct travel time between the source rod and the near sensor (Sensor No. 3) to calculate velocities at this depth. The hammer used to impact the top of the crosshole source rod is instrumented with an accelerometer that establishes the time of initiation of energy at the top of the rod (zero-time). To obtain the actual time that the wave is traveling through the soil, the rod calibration time (t_r ; i.e. the time it takes the wave to travel down the source rod) must be subtracted from the measured time difference between the source accelerometer trigger at the ground surface and the wave arrival at the desired sensor. The rod calibration time was obtained from calibrations performed on various lengths of rod in the Soil Dynamics Laboratory at UT, and was found to

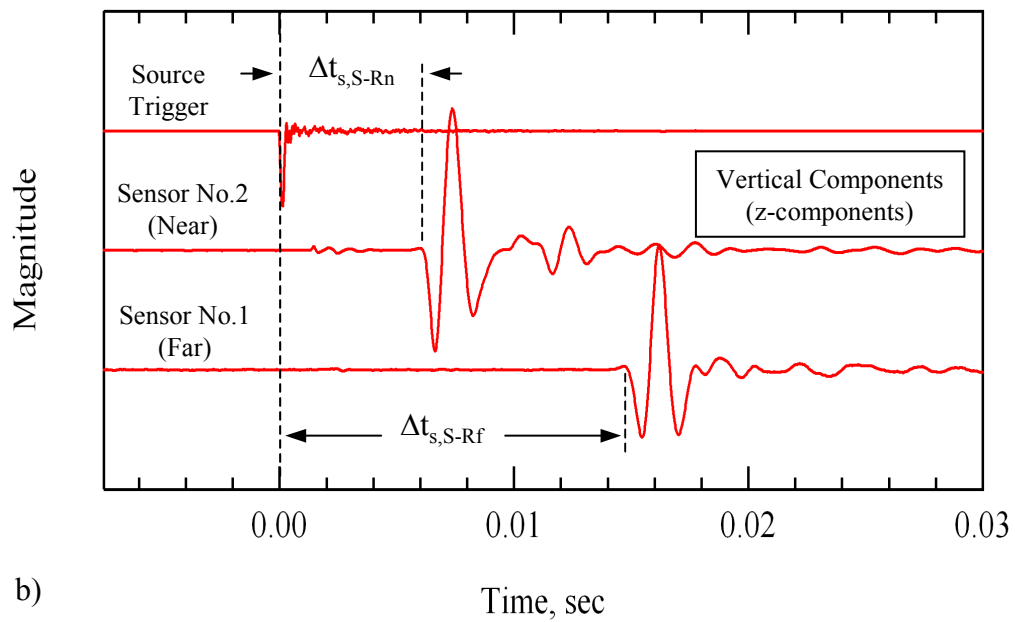
be 0.00006 sec/ft (0.0002 sec/m) or equivalently, 16665 fps (5080 m/sec). As expected, this value is approximately equivalent to the unconstrained compression wave velocity (V_c) of steel.

If wave arrivals can be identified on both receivers at the same depth, it is possible to obtain three estimates of the desired wave velocity. The three wave velocities are typically noted as: (1) the source-to-near receiver velocity, (2) the source-to-far receiver velocity, and (3) the near receiver-to-far receiver velocity (interval velocity). Ideally, all three of these estimates would yield the same velocity. However, in some cases the velocities are not equivalent. This can be caused by a material that has variable stiffness between measuring points, refracted waves, improper calibration time, or improper estimated distances between the source and receivers. As discussed above, the interval wave velocity is preferred because it is not necessary to subtract any calibration factors from the measured time difference to obtain a velocity. Additionally, in the case of the dynamic in-situ liquefaction test, the velocities obtained from interval travel times represent the velocity of only the material inside the array, and not the material between the source rod and the receiver. Because it was necessary to obtain some of the wave velocities at the top pair of sensors using direct travel times, it was also decided to be consistent and obtain direct wave velocities and interval wave velocities at the both the top and bottom pairs of sensors at Test Location A.

Figure 10-7 shows an example of typical records that were collected from performing crosshole tests between the deeper pair of sensors (Sensor No. 2 and Sensor No. 1) at Test Location A. Figure 10-7a shows the waveforms that were



a)



b)

Figure 10-7 Typical crosshole waveforms recorded by the: a) horizontal, in-line components (P-waves identified on), and b) vertical components (S_{hv} -waves identified on) of sensors No. 2 (near) and No. 1 (far) at Test Location A, Wildlife Liquefaction Array (WLA).

sensed by the horizontal, in-line components (y-components) of these sensors. The P_h-wave arrivals are identified as the first seismic energy to reach each sensor. The interval P_h-wave velocity (V_p) of the material between the sensors is equal to the horizontal distance between them (3.96 ft or 1.2 m; see Table 10-1) divided by the P_h-wave interval travel time (Δt_p). The P_h-wave interval travel time is equal to the source-to-far receiver P_h-wave travel time ($\Delta t_{p,S-Rf}$) minus the source-to-near-receiver P_h-wave travel time ($\Delta t_{p,S-Rn}$). The source-to-near receiver P_h-wave velocity is equal to the horizontal distance between source rod A and Sensor No. 2 (2.5 ft or 0.8 m) divided by the source-to-near receiver P_h-wave travel time minus the rod calibration time ($\Delta t_{p,S-Rn} - t_r$). The source-to-far receiver P_h-wave velocity is equal to the horizontal distance between source rod A and Sensor No. 1 (6.46 ft or 2.0 m) divided by the source-to-far receiver P_h-wave travel time minus the rod calibration time ($\Delta t_{p,S-Rf} - t_r$).

The interval, source-to-near receiver (Sensor No. 2) and source-to-far receiver (Sensor No. 1) P_h-wave velocities obtained from performing crosshole tests between the bottom pair of sensors at Test Location A are provided in Table 10-3. The baseline crosshole test results listed in Table 10-3 show that V_p between the bottom sensors in the array was just over 5000 fps (1500 m/sec). As discussed in Section 2.3.1, fully saturated soil has a P-wave velocity of approximately 5000 fps (i.e. the velocity of a compression wave traveling through water). The source-to-Sensor No. 2 and the source-to-Sensor No. 1 velocities are for all intents and purposes equal to the interval P_h-wave velocity obtained between Sensors No. 2 and No. 1. These results indicate that the material at

Table 10-3 P_h-wave velocity results from three separate sets of crosshole tests performed between the bottom sensor pair (sensors No. 2 and No. 1) in the liquefaction sensor array at Test Location A, Wildlife Liquefaction Array (WLA)

| Date | Time | Condition | P _h -Wave Velocities, V _p (fps) | | |
|-----------|----------|--|---|-----------|-----------|
| | | | Sensors No. 2 (near) and No. 1 (far) | | |
| | | | Approximately 12 ft Deep | | |
| | | | No. 2 - No. 1 | S - No. 2 | S - No. 1 |
| 8/10/2005 | 11:00 AM | Initial Baseline Readings: Prior to Static Hold-Down Force | 5070 | 5010 | 4910 |
| 8/10/2005 | 11:50 AM | After Static Hold-Down Force, Prior to Series 1 Dynamic Loading | 5070 | 5085 | 5110 |
| 8/11/2005 | 10:30 AM | Prior to Series 2 Dynamic Loading | 5070 | 5010 | 4910 |

approximately 12 ft (3.6 m) deep is uniformly saturated and that the estimated distances between the source rod and receivers are accurate. The P_h-wave velocities remain essentially unchanged after application of the base plate hold-down force and after the first series of dynamic loading. This is expected, as the P-wave velocity in a saturated, soft soil measures the compression stiffness of water. Therefore, the P-wave velocity should remain constant as long as the saturation level of the soil does not change.

Figure 10-7b shows an example of typical waveforms that were sensed by the vertical components (z-components) of sensors No. 2 and No. 1. Given a downward impact at the source rod, and knowing the polarity of the sensors, the S_{hv}-wave arrivals are identified as the first major downward departure in the records. The interval S_{hv}-wave velocity (V_{S,hv}), the source-to-near receiver S_{hv}-

wave velocity, and the source-to-far receiver S_{hv} -wave velocity are determined in a similar manner to that noted above for the P_h -wave velocities. However, in this case, the source-to-near receiver S_{hv} -wave travel time ($\Delta t_{s,S-Rn}$) and the source-to-far receiver S_{hv} -wave travel time ($\Delta t_{s,S-Rf}$) are used.

The interval, source-to-near receiver (Sensor No. 2) and source-to-far receiver (Sensor No. 1) S_{hv} -wave velocities obtained from performing crosshole tests between the bottom sensor pair at Test Location A are provided in Table 10-4. The baseline crosshole test results listed in Table 10-4 show that $V_{S,hv}$ between the bottom sensors in the array was 450 fps (137 m/sec). The source-to-Sensor No. 2 and the source-to-Sensor No. 1 velocities were 455 fps (139 m/sec) and 460 fps (140 m/sec), respectively. These velocities are very similar and the differences between them (i.e. less than 2%) are within the limits of accuracy of this test. These results indicate that the material at approximately 12 ft (3.6 m) deep has a fairly uniform shear stiffness and that the estimated distances between the source rod and receivers are accurate. The crosshole test results listed in Table 10-4 show that $V_{S,hv}$ between the bottom sensor pair increased only slightly (approximately 5 fps or 1.5 m/sec) after the application of the base plate hold-down force. This change is not surprising as the increase in vertical stress at the sensor locations due to the base plate hold-down force was only estimated to be approximately 15% of the initial effective overburden stress (see Table 10-2). Since the shear wave velocity of soil theoretically changes according to the quarter-power of the change in effective stress, it is expected that the velocities would have only increased by about 3%. Results from the third set of crosshole

Table 10-4 Shear wave velocity results from three separate sets of crosshole tests performed between the bottom sensor pair (sensors No. 2 and No. 1) in the liquefaction sensor array at Test Location A, Wildlife Liquefaction Array (WLA)

| Date | Time | Condition | Shear Wave Velocities, $V_{S,hv}$ (fps) | | |
|-----------|----------|--|---|-----------|-----------|
| | | | Sensors No. 2 (near) and No. 1 (far) | | |
| | | | Approximately 12 ft Deep | | |
| | | | No. 2 - No. 1 | S - No. 2 | S - No. 1 |
| 8/10/2005 | 11:00 AM | Initial Baseline Readings: Prior to Static Hold-Down Force | 450 | 455 | 460 |
| 8/10/2005 | 11:50 AM | After Static Hold-Down Force, Prior to Series 1 Dynamic Loading | 455 | 460 | 470 |
| 8/11/2005 | 10:30 AM | Prior to Series 2 Dynamic Loading | 410 | 400 | 390 |

tests indicate that $V_{S,hv}$ between the bottom pair of sensors was reduced by approximately 50 fps (15 m/s) after the first series of staged dynamic loading.

Figure 10-8 shows an example of typical records that were collected from performing crosshole tests between the shallower pair of sensors (Sensor No. 3 and Sensor No. 4) at Test Location A. Figure 10-8a shows the waveforms that were sensed by the horizontal, in-line components (y-components) of these sensors. The P_h -wave arrivals are identified as the first seismic energy to reach each sensor. However, the P_h -wave arrivals could not be identified on the waveforms recorded by Sensor No. 4. Therefore, only the source-to-near receiver (Sensor No. 3) P_h -wave velocity could be calculated. The source-to-near receiver P_h -wave velocity is equal to the horizontal distance between source rod B and

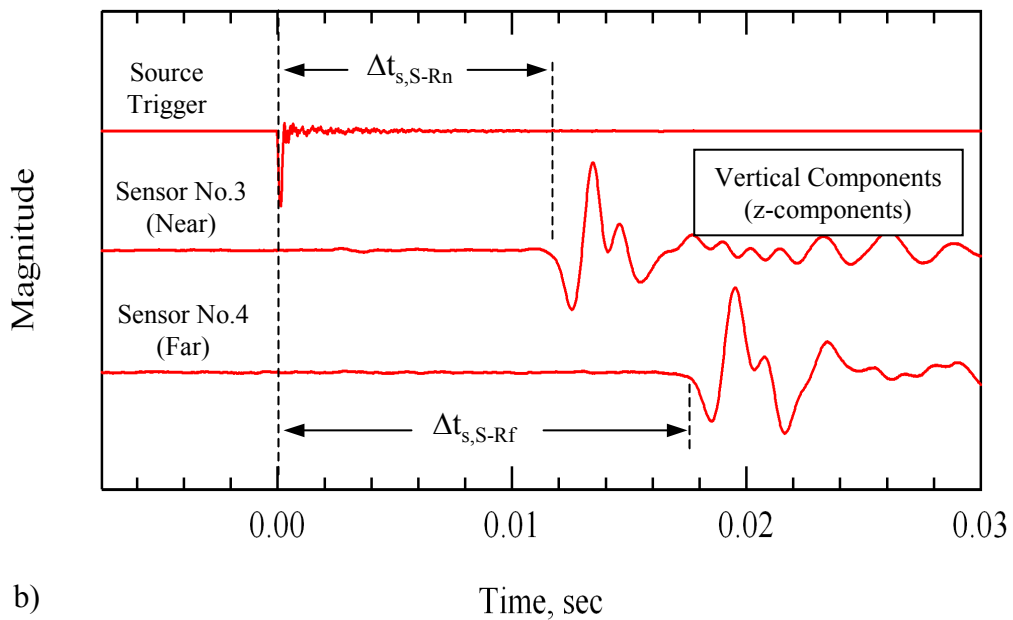
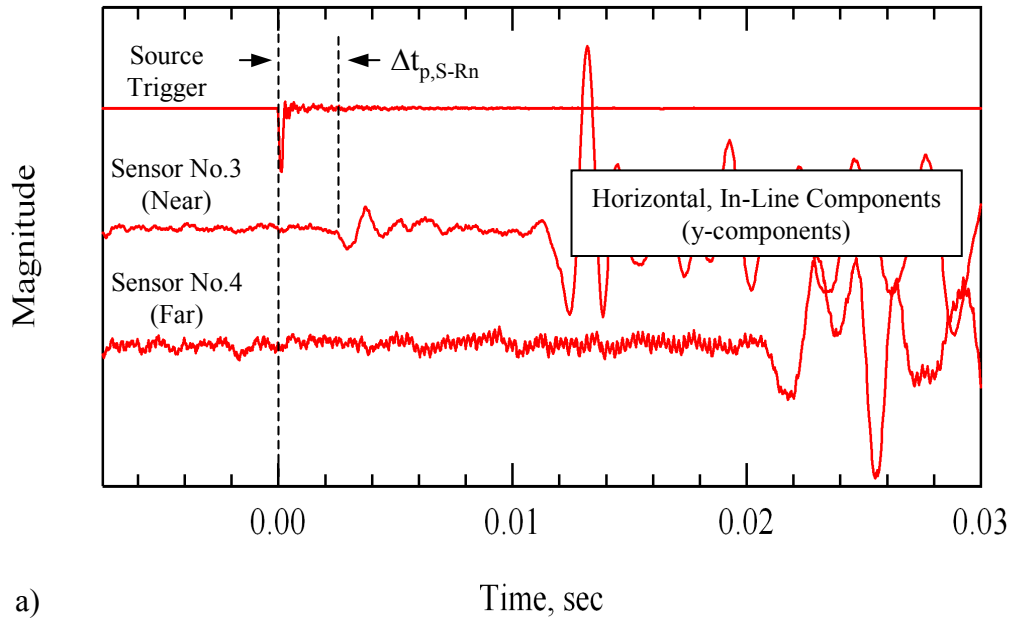


Figure 10-8 Typical crosshole waveforms recorded by the: a) horizontal, in-line components (P-waves identified on), and b) vertical components (S_{hv} -waves identified on) of sensors No. 3 (near) and No. 4 (far) at Test Location A, Wildlife Liquefaction Array (WLA).

Sensor No. 3 (4.42 ft or 1.3 m) divided by the source-to-near receiver P_h -wave travel time minus the rod calibration time ($\Delta t_{p,S-Rn} - t_r$).

The source-to-near receiver (Sensor No. 3) P_h -wave velocities obtained from performing crosshole tests between the top pair of sensors at Test Location A are provided in Table 10-5. The baseline crosshole test results listed in Table 10-5 show that V_p between source rod B and Sensor No. 3 was 2300 fps (700 m/sec), indicating that the material at this depth was not fully saturated. This is likely the reason why the P_h -wave arrival could not be identified on Sensor No. 4. If the soil is saturated the P-wave arrivals are typically very strong and are characterized by a relatively high frequency content (see Figure 10-7a, Figure 9-7a, and Figure 8-7a). Laboratory test results from Valle-Molina (2006) indicate that a V_p value of 2300 fps equates to a B value of approximately 0.72 and a saturation level of approximately 99.8%. Laboratory test results from Ishihara et al. (2001) indicate that a V_p value of 2300 fps equates to a B value of approximately 0.6 and a saturation level of approximately 99.3%. The P_h -wave velocities remain essentially unchanged after application of the base plate hold-down force and after the first series of dynamic loading. Even though the material is not fully saturated, its compression stiffness is still primarily controlled by the compression stiffness of water. Therefore, it is expected that the P-wave velocity should remain constant as long as the saturation level of the soil does not change.

Figure 10-8b shows an example of typical waveforms that were sensed by the vertical components (z-components) of sensors No. 3 and No. 4. Given a

Table 10-5 P_h-wave velocity results from three separate sets of crosshole tests performed between the top sensor pair (sensors No. 3 and No. 4) in the liquefaction sensor array at Test Location A, Wildlife Liquefaction Array (WLA)

| Date | Time | Condition | P _h -wave Velocities, V _p (fps) | | |
|-----------|----------|--|---|-----------|-----------|
| | | | Sensors No. 3 (near) and No. 4 (far) | | |
| | | | Approximately 10 ft Deep | | |
| | | | No. 3 - No. 4 | S - No. 3 | S - No. 4 |
| 8/10/2005 | 11:00 AM | Initial Baseline Readings: Prior to Static Hold-Down Force | * | 2300 | * |
| 8/10/2005 | 11:50 AM | After Static Hold-Down Force, Prior to Series 1 Dynamic Loading | * | 2300 | * |
| 8/11/2005 | 10:30 AM | Prior to Series 2 Dynamic Loading | * | 2325 | * |

Notes: * P-wave arrival could not be identified on Sensor No. 4

downward impact at the source rod, and knowing the polarity of the sensors, the S_{hv}-wave arrivals are identified as the first major downward departure in the records. The interval S_{hv}-wave velocity (V_{S,hv}), the source-to-near receiver S_{hv}-wave velocity, and the source-to-far receiver S_{hv}-wave velocity are determined in a similar manner to that noted above for the S_{hv}-wave velocities calculated between the deeper pair of liquefaction sensors. However, the S_{hv}-wave arrival could not be accurately identified on the waveform recorded by Sensor No. 4 during the third set of crosshole tests. Therefore, only the source-to-near receiver S_{hv}-wave velocity could be determined.

The interval, source-to-near receiver (Sensor No. 3), and source-to-far receiver (Sensor No. 4) S_{hv}-wave velocities obtained from performing crosshole

tests between the top sensor pair at Test Location A are provided in Table 10-6. The baseline crosshole test results listed in Table 10-6 show that $V_{S,hv}$ between the top sensors in the array was 340 fps (104 m/sec). The source-to-Sensor No. 3 and the source-to-Sensor No. 4 velocities were 400 fps (122 m/sec) and 380 fps (116 m/sec), respectively. These $V_{S,hv}$ values are more variable than the those determined between the bottom pair of sensors (see Table 10-4) at Test Location A. It is unlikely that these differences were caused by errors in the estimated distances between the source rod and the receivers because all of the sensors were installed in a similar manner and all of the sensors showed similar tilt angles after installation (see Table 10-1). There is also no evidence of refracted waves in the waveforms, and if refraction were influencing the results, the interval velocity would likely be the highest velocity and not the lowest velocity. Additionally, the source rod calibration factor has already been shown to produce uniform velocities between the deeper sensors. Therefore, the differences in these $V_{S,hv}$ values must be attributed to varying material stiffness between the source rod and receivers at this depth. In fact, if a locally stiffer portion of soil was located between source rod B and Sensor No. 3, the source-to-Sensor No. 3 velocity would be highest, followed by the source-to-Sensor No. 4 velocity. The interval velocity would not sense this material at all so it would indicate the lowest velocity. That is precisely the pattern that is shown in Table 10-6. The interval $V_{S,hv}$ values are considered to be most representative of the soil near the top of the liquefaction sensor array.

Table 10-6 Shear wave velocity results from three separate sets of crosshole tests performed between the top sensor pair (sensors No. 3 and No. 4) in the liquefaction sensor array at Test Location A, Wildlife Liquefaction Array (WLA)

| Date | Time | Condition | Shear Wave Velocities, $V_{S,hv}$ (fps) | | |
|-----------|----------|--|---|-----------|-----------|
| | | | Sensors No. 3 (near) and No. 4 (far) | | |
| | | | Approximately 10 ft Deep | | |
| | | | No. 3 - No. 4 | S - No. 3 | S - No. 4 |
| 8/10/2005 | 11:00 AM | Initial Baseline Readings: Prior to Static Hold-Down Force | 340 | 400 | 380 |
| 8/10/2005 | 11:50 AM | After Static Hold-Down Force, Prior to Series 1 Dynamic Loading | 350 | 405 | 385 |
| 8/11/2005 | 10:30 AM | Prior to Series 2 Dynamic Loading | * | 380 | * |

Notes: * S-wave arrival could not be identified on Sensor No. 4

The crosshole test results listed in Table 10-6 show that $V_{S,hv}$ between the top sensor pair increased only slightly (approximately 10 fps or 3 m/sec) after the application of the base plate hold-down force. This is not surprising as the increase in vertical stress at the sensor locations due to the base plate hold-down force was only estimated to be approximately 20% of the initial effective overburden stress (see Table 10-2). Since the shear wave velocity of soil theoretically changes according to the quarter-power of the change in effective stress, it is expected that the velocities would have only increased by about 5%. The S_{hv} -wave arrival could not accurately be identified on Sensor No. 4 during the third set of crosshole tests. Therefore, it was only possible to obtain an estimate

for the source-to-Sensor No. 3 S_{hv} -wave velocity. This velocity was reduced by approximately 25 fps (8 m/s) after the first series of staged dynamic loading.

10.2.1.1 P-Wave Velocity Profile at Test Location A

The crosshole tests performed with the liquefaction sensor array at Test Location A indicated that the material at a depth of approximately 12-ft (3.6-m) was saturated, while the material at a depth of approximately 10-ft (3-m) was not fully saturated. Because of this variability in saturation level, and the odd pore pressure generation response measured at this test location (discussed in Sections 10.3 and 10.4), it was desired to obtain a P-wave velocity profile in the vicinity of Test Location A. Therefore, a separate set of crosshole tests was performed near Test Location A on August 19, 2005. The location of sensor and source rod used to perform these tests, relative to where the Test Location A liquefaction sensor array had been installed, is shown in Figure 10-9. The measurements were performed using a single liquefaction sensor and a single crosshole source rod. The sensor was pushed into the ground approximately 6 ft (1.8 m) south of the centerline of the original liquefaction sensor array. The source rod was inserted approximately 2.9-ft (0.9-m) south of this sensor. The liquefaction sensor was pushed into the ground using the hydraulic ram on the back of T-Rex, while the crosshole source rod was driven into the ground using a fencepost-pounder.

P_h -wave velocity measurements were made at 0.5-ft (0.15-m) increments from a depth of 3.5-ft (1.1-m) to a depth of 12-ft (3.6-m) below the ground surface in this survey. Direct travel time measurements between the source rod and the sensor were used to obtain P_h -wave travel times through the soil between

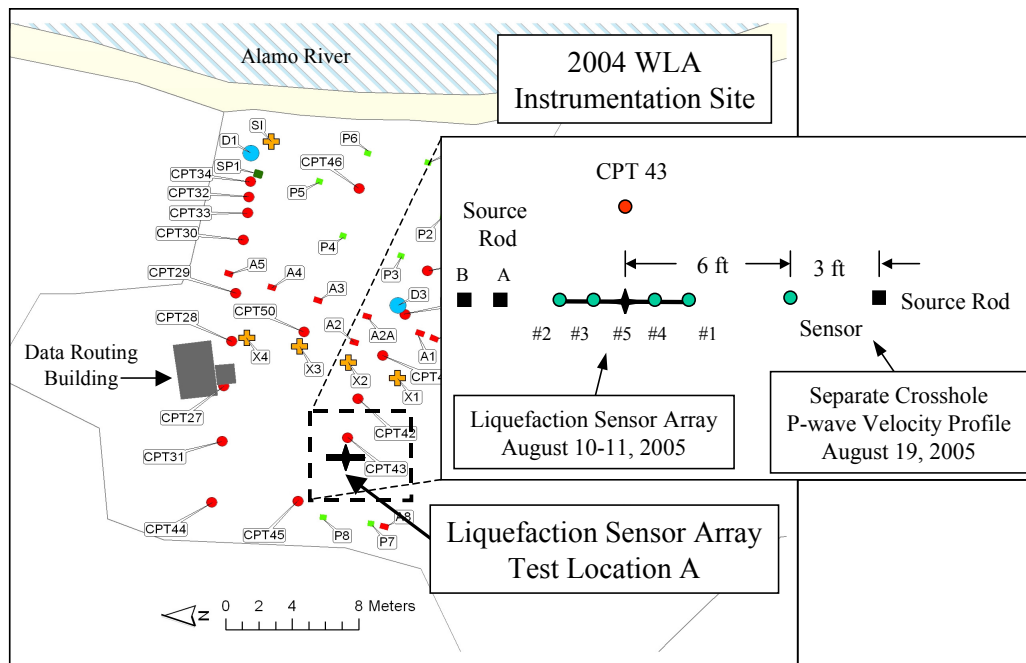


Figure 10-9 Relative locations of the liquefaction sensor array at Test Location A and the area where a separate crosshole P-wave velocity survey was conducted; Wildlife Liquefaction Array (WLA) (after <http://nees.ucsb.edu>).

the rod and sensor. The waveforms collected from the horizontal, in-line component of the liquefaction sensor during this process are shown in a waterfall plot in Figure 10-10. The P_h -wave arrivals are indicated on each record. It is interesting to observe the change in the frequency content of the P_h -wave arrival as the depth below the ground surface increases. In general, a sharp, high-frequency P_h -wave arrival indicates a material that is saturated or nearly saturated.

The P_h -wave velocity profile obtained from this set of crosshole tests is shown in Figure 10-11. The generalized soil profile at the site (Bennett et al., 1984; Youd and Holzer, 1994) and the location of the water table on the day of

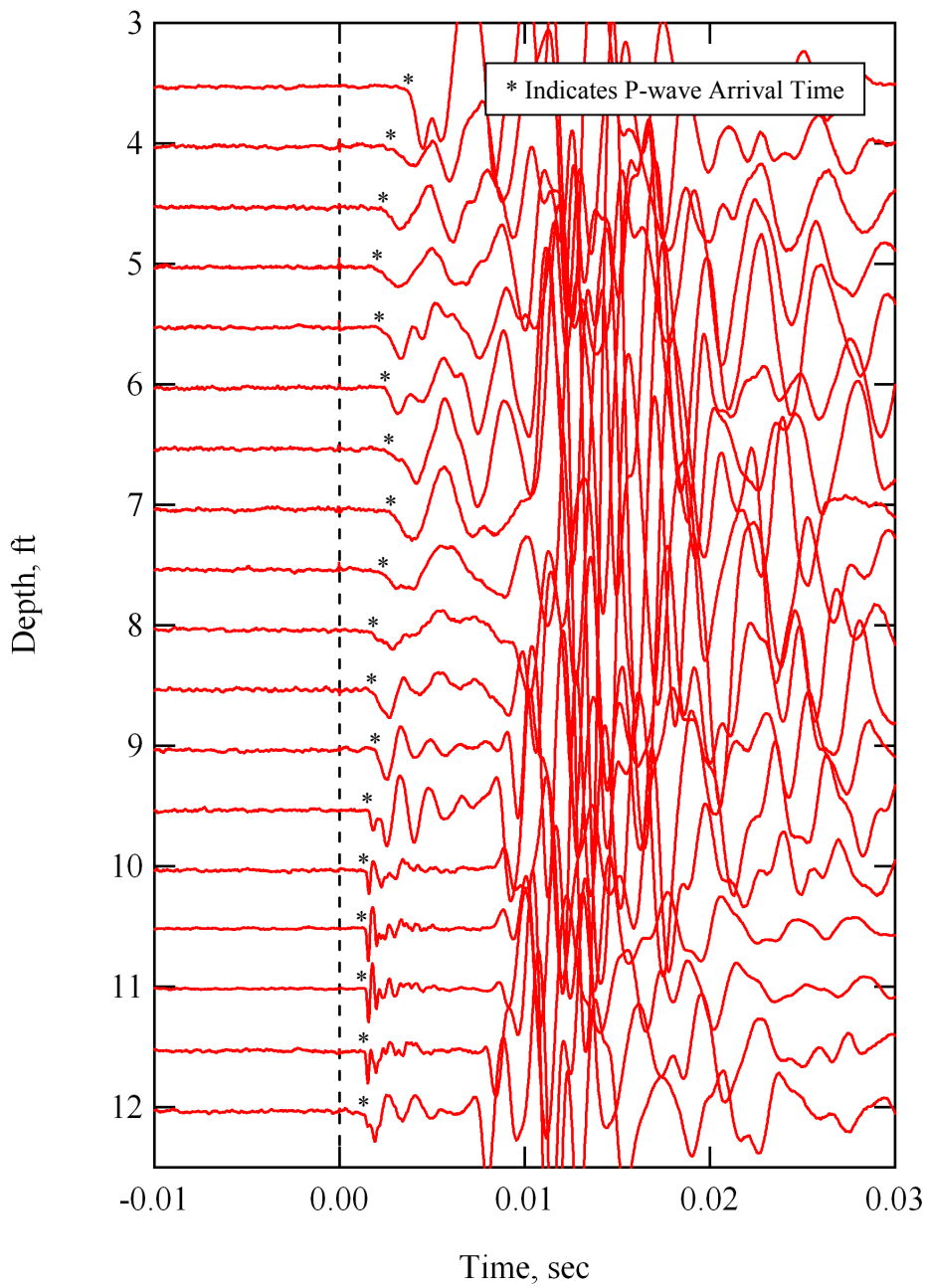


Figure 10-10 Waterfall plot of waveforms recorded by the horizontal, in-line component (P_h -waves identified on) of a sensor during crosshole tests conducted approximately 6 ft south of the liquefaction sensor array at Test Location A, Wildlife Liquefaction Array (WLA).

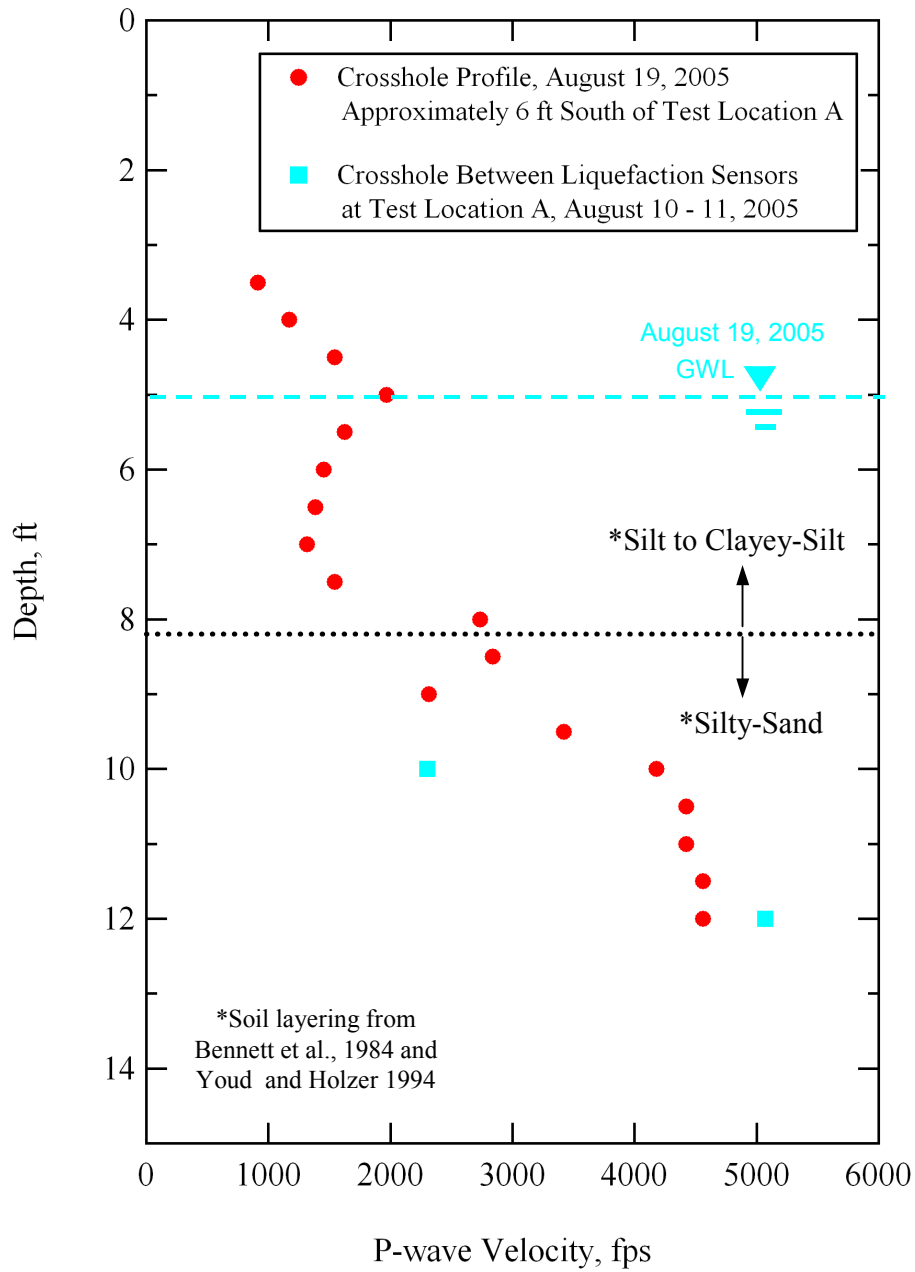


Figure 10-11 P_h -wave velocities obtained from crosshole tests between sensors in the liquefaction sensor array (August 10-11, 2005) and from a separate set of crosshole tests (August 19, 2005) conducted approximately 6 ft south of the liquefaction sensor array at Test Location A, Wildlife Liquefaction Array (WLA).

testing are also shown. The P_h -wave velocities in the top clayey-silt layer are generally less than 1500 fps (460 m/sec), despite the fact that the ground water level (GWL) is located at a depth of approximately 5 ft (1.5 m) below the ground surface. The water table at the site is controlled by the Alamo River and fluctuates up and down slightly. However, it is typically found at a depth of approximately 4 ft (1.2 m) (Holzer et al., 1989). It is interesting that the P_h -wave velocities increase substantially at a depth of approximately 8 ft (2.4 m). This depth is very close to the top boundary of the liquefiable soil layer. P_h -wave velocities in the liquefiable silty-sand layer range between 2300 fps (700 m/sec) and 3500 fps (1065 m/sec) down to a depth of approximately 10 ft (3 m). P_h -wave velocities of 2300 fps and 3500 fps correspond to B values of approximately 0.72 and 0.82, respectively, according Valle-Molina (2006), and approximately 0.6 and 0.78, respectively, according to Ishihara et al. (2001). Both of these velocities yield saturation levels that are greater than 99.8%. The P_h -wave velocity of the silty-sand between 10 ft (3 m) and 12 ft (3.6 m) varies between approximately 4200 fps (1280 m/sec) and 4600 (1400 m/sec), indicating B values of 0.9 or greater and a saturation level of 99.9%. The P_h -wave velocities obtain from this set of crosshole tests are provided in Table 10-7.

The P_h -wave velocities obtained from crosshole tests using the liquefaction sensor array at Test Location A are shown by the solid square symbols in Figure 10-11. The crosshole results performed using the liquefaction array sensors indicated a P_h -wave velocity of approximately 2300 fps (700 m/s) at a depth of 10 ft (3 m) and a P_h -wave velocity of approximately 5050 fps (1540

Table 10-7 P_h-wave velocities obtained from crosshole tests conducted approximately 6 ft south of the liquefaction sensor array at Test Location A, Wildlife Liquefaction Array (WLA)

| Depth (ft) | P _h -wave Velocity (fps) |
|------------|-------------------------------------|
| 3.5 | 915 |
| 4.0 | 1170 |
| 4.5 | 1540 |
| 5.0 | 1965 |
| 5.5 | 1625 |
| 6.0 | 1450 |
| 6.5 | 1390 |
| 7.0 | 1315 |
| 7.5 | 1540 |
| 8.0 | 2735 |
| 8.5 | 2840 |
| 9.0 | 2315 |
| 9.5 | 3420 |
| 10.0 | 4180 |
| 10.5 | 4420 |
| 11.0 | 4420 |
| 11.5 | 4560 |
| 12.0 | 4560 |

m/sec) at a depth of 12 ft (3.6 m). The P_h-wave velocities from the separate crosshole profile indicate a higher P_h-wave velocity at a depth of 10 ft, and a slightly lower P_h-wave velocity at a depth of 12 ft. However, the P_h-wave velocity profile shows the variability in the saturation level of the silty-sand within the top several feet of the layer. It is not unreasonable that the saturation

level of the material is varying with depth and location. This separate P-wave velocity profile confirmed the suspicion that at this location, the liquefiable soil layer is not fully saturated over the top several feet of the layer. This lack of saturation in the upper portion of the layer influenced the dynamic pore pressure generation characteristics of the soil as shown below.

10.3 TEST A: STAGED DYNAMIC LOADING SERIES 1

The in-situ liquefaction sensor array at Test Location A was installed on August 9, 2005. The sensor installation process required a full day to complete. The pore water pressure transducer (PPT) in each sensor was powered overnight using a 12-volt battery and a DC-to-DC converter to help ensure that the static PPT outputs remained as steady as possible during testing the following day (as discussed in Section 4.3.2). The first series (Series 1) of staged dynamic loading began in the afternoon of August 10.

10.3.1 Loading Stages in Series 1

In Series 1, seventeen separate staged dynamic loads were applied to the instrumented soil mass. Only the information recorded during fourteen of these staged loads was used to develop the pore pressure generation curves in the data reduction process. The other three loading stages all occurred at low strain levels and were duplicates of dynamic loads used in the data reduction process. The dynamic shear loads were applied by driving T-Rex in the horizontal, in-line direction. As discussed previously, external function generator was used to control the frequency, number of cycles, and drive voltage amplitude supplied to

T-Rex. Details of the Series 1 staged dynamic loading sequence are provided in Table 10-8. The first three loading stages were applied in the form of 10 cycles of a 10-Hz sinusoidal wave. The next eight loading stages were applied in the form of 20 cycles of a 20-Hz sinusoidal wave. The following two loading stages were applied in the form of a 20-Hz sinusoidal wave with durations of 60 and 100 cycles, respectively. The final load was applied in the form of 100 cycles of a 10-Hz sinusoidal wave. This loading series is not as structured as the ones employed during in-situ liquefaction testing at Test Locations C and B (discussed in Chapters 8 and 9, respectively). The difference results from knowledge gained at Test Location A, which was the first site where in-situ liquefaction tests were conducted and the optimal staged loading sequence was being studied. In general, it was found that higher peak shear strains could be induced in the soil deposit at a frequency of 10 Hz than at a frequency of 20 Hz. However, T-Rex has more harmonic distortion when operating at 10 Hz than at 20 Hz. As discussed in Section 6.5, harmonic distortion in the ground motion signals recorded during testing complicates the evaluation of the nonlinear soil shear modulus. Therefore, tests were conducted at 20 Hz with the goal of being able to more accurately resolve the nonlinear shear modulus behavior of the soil, and at 10 Hz to generate shear strains as large as possible within the instrumented soil mass.

Shear strains (γ) induced in the instrumented soil mass were calculated at the center of the liquefaction sensor array for every stage of dynamic loading using the 4-node, isoparametric finite element formulation presented in Section

Table 10-8 Details of the Series 1 staged dynamic loading sequence conducted at Test Location A, Wildlife Liquefaction Array (WLA)

| Time on 8/10/2005 | Dynamic Load Number | Function Generator Drive Signal | | | Approximate Ground Force (lb) |
|----------------------|------------------------|---------------------------------|---------------------|----------------------|-------------------------------------|
| | | Frequency (Hz) | Number of Cycles | Amplitude (volts) | |
| 12:19 PM | 1 | 10 | 10 | 0.2 | 1000 |
| 12:25 PM | 2 | 10 | 10 | 0.4 | 2000 |
| 12:35 PM | 4 | 10 | 10 | 0.8 | 5000 |
| 12:56 PM | 6 | 20 | 20 | 1.5 | 10000 |
| 1:14 PM | 7 | 20 | 20 | 0.8 | 5000 |
| 1:18 PM | 8 | 20 | 20 | 0.4 | 2000 |
| 1:22 PM | 9 | 20 | 20 | 0.2 | 1000 |
| 1:40 PM | 11 | 20 | 20 | 2.0 | 10000 |
| 2:06 PM | 12 | 20 | 20 | 2.5 | 12000 |
| 2:25 PM | 13 | 20 | 20 | 3.0 | 15000 |
| 2:56 PM | 14 | 20 | 20 | 3.5 | 15000 |
| 3:12 PM | 15 | 20 | 60 | 4.0 | 15000 |
| 3:27 PM | 16 | 20 | 100 | 5.0 | 18000 |
| 3:44 PM | 17 | 10 | 100 | 5.0 | 25000 |

6.3. Shear strains were averaged over various numbers of loading cycles according to the procedure detailed in Section 8.3.1.

The pore pressure ratios (r_u) at each sensor location were obtained by dividing the measured residual pore water pressure, obtained from processing the raw pore pressure transducer (PPT) records according to the procedure outlined in Section 6.4, by the total vertical effective stress at each sensor location (see Table 10-2). The r_u values used to construct the pore pressure generation curves for

each site were obtained solely from the PDCR 35/D transducer located at the center of the array (Sensor No.5). The r_u values obtained from the miniature PPT's (Sensors No. 1 – No. 4) were only used in a qualitative sense to observe how the pore pressure generation varied within the instrumented soil mass. The miniature PPT in Sensor No. 3 was accidentally connected to the wrong data acquisition channel during tests conducted at Test Location A. It was believed that the PPT had been damaged somehow and therefore the problem was not resolved until testing began at Test Location B. Therefore, there no pore water pressure data was recorded at the location of Sensor No. 3.

The nonlinear shear modulus of the soil within the liquefaction sensor array at Test Location A could not accurately be resolved due to harmonic distortion and small amounts of noise in some of the raw accelerometer records. The challenges regarding accurate determination of the nonlinear shear modulus during liquefaction testing are discussed in Section 9.3.1 in regards to Test Location B.

10.3.2 Response of the Deposit During Loading Series 1

During discussion of the results obtain from in-situ dynamic liquefaction tests conducted at Test Locations C and B (discussed in Chapters 8 and 9, respectively), the ground force, shear strain, and pore pressure ratio time histories were presented in graphical form for every one of the staged loads applied during testing. Most of the loads applied to the soil at Test Location A during Series 1 did not generate excess pore pressures within the instrumented soil mass. Additionally, many of the loads were conducted at such low driving levels that

very minimal shear strains were induced at the center of the liquefaction sensor array. Therefore, to avoid a lot of repetition, only a representative number of the ground force, shear strain, and pore pressure ratio time histories are presented in graphical form below. However, tabulated values for the pore pressure ratios and average shear strains (averaged over the given number of loading cycles) induced in the soil during each dynamic load of staged loading Series 1 are provided in Tables 10-9 and 10-10.

10.3.2.1 Loading Stage No. 4

The force applied at the ground surface by T-Rex, the shear strain induced at the center of the liquefaction sensor array, and the pore pressure ratios generated at each PPT location during loading stage No. 4 of staged loading Series 1 are shown in Figure 10-12. The ground force during loading stage No. 4 was approximately 5000 lb (22.2 kN) throughout the 10 cycles of 10-Hz loading. This load induced fairly uniform cyclic shear strains at the center of the liquefaction sensor array of approximately 0.0003%. These shear strains did not trigger the generation of any excess pore water pressure in the instrumented soil mass, as indicated by the fact that the pore pressure ratios at each sensor location remained equal to zero.

10.3.2.2 Loading Stage No. 6

The force applied at the ground surface by T-Rex, the shear strain induced at the center of the liquefaction sensor array, and the pore pressure ratios generated at each PPT location during loading stage No. 6 of staged loading

Table 10-9 Pore pressure ratios and average shear strains at the center of the liquefaction sensor array for different numbers of loading cycles; Series 1, loading stages No. 1 through No. 11, Test Location A, Wildlife Liquefaction Array

| Number of Cycles | γ or r_u | Pore Pressure Ratio ¹ (r_u) and Average Shear Strain ² (γ) Values, % | | | | | | | |
|------------------------|-------------------------|---|--------|--------|--------|--------|--------|--------|--------|
| | | Series 1: Staged Load Number | | | | | | | |
| | | No. 1 | No. 2 | No. 4 | No. 6 | No. 7 | No. 8 | No. 9 | No. 11 |
| 10 | γ | 0.0003 | 0.0011 | 0.0031 | 0.0122 | 0.0049 | 0.0014 | 0.0004 | 0.0187 |
| | r_u | 0 | 0 | 0 | 0 | 0 | 0 | 0 | 0 |
| 20 | γ | - | - | - | 0.0124 | 0.0050 | 0.0014 | 0.0004 | 0.0189 |
| | r_u | - | - | - | 0 | 0 | 0 | 0 | 0 |

- Notes: - Load not applied for the given number of cycles
 1. r_u from the PDCR 35/D pressure transducer at the center of the array after the given number of loading cycles
 2. γ calculated at the center of the array and averaged over the given number of cycles

Series 1 are shown in Figure 10-13. The ground force during loading stage No. 6 was slightly less than 10000 lb (44.5 kN) throughout the 20 cycles of 20-Hz loading. This load induced fairly uniform cyclic shear strains at the center of the liquefaction sensor array of approximately 0.0124% (see Table 10-9 for strain values averaged over various numbers of loading cycles). These shear strains did not trigger the generation of any excess pore water pressure in the instrumented soil mass, as indicated by the fact that the pore pressure ratios at each sensor location remained equal to zero.

10.3.2.3 Loading Stage No. 11

The force applied at the ground surface by T-Rex, the shear strain induced at the center of the liquefaction sensor array, and the pore pressure ratios

Table 10-10 Pore pressure ratios and average shear strains at the center of the liquefaction sensor array for different numbers of loading cycles; Series 1, loading stages No. 12 through Load No. 17, Test Location A, Wildlife Liquefaction Array

| Number of Cycles | γ or r_u | Pore Pressure Ratio ¹ (r_u) and Average Shear Strain ² (γ) Values, % | | | | | |
|------------------|-------------------|---|--------|--------|--------|--------|--------|
| | | Series 1: Staged Load Number | | | | | |
| | | No. 12 | No. 13 | No. 14 | No. 15 | No. 16 | No. 17 |
| 10 | γ | 0.0246 | 0.0301 | 0.0348 | 0.0384 | 0.0444 | 0.0602 |
| | r_u | 0 | 0 | 0 | 0 | 0 | 0 |
| 20 | γ | 0.0249 | 0.0305 | 0.0352 | 0.0391 | 0.0452 | 0.0719 |
| | r_u | 0 | 0 | 0 | 0 | 0 | 1 |
| 30 | γ | - | - | - | 0.0394 | 0.0455 | 0.0829 |
| | r_u | - | - | - | 0 | 0 | 2 |
| 40 | γ | - | - | - | 0.0396 | 0.0457 | 0.0967 |
| | r_u | - | - | - | 0 | 0 | 3 |
| 50 | γ | - | - | - | 0.0398 | 0.0459 | 0.1168 |
| | r_u | - | - | - | 0 | 0 | 5 |
| 60 | γ | - | - | - | 0.0399 | 0.0461 | * |
| | r_u | - | - | - | 0 | 1 | 7 |
| 70 | γ | - | - | - | - | 0.0462 | * |
| | r_u | - | - | - | - | 1 | 9 |
| 80 | γ | - | - | - | - | 0.0463 | * |
| | r_u | - | - | - | - | 1 | 11 |
| 90 | γ | - | - | - | - | 0.0465 | * |
| | r_u | - | - | - | - | 1 | 13 |
| 100 | γ | - | - | - | - | 0.0466 | * |
| | r_u | - | - | - | - | 1 | 15 |

Notes: - Load not applied for the given number of cycles

* Shear strain could not be evaluated due to significant signal clipping after 50 cycles in raw records

1. r_u from the PDCR 35/D pressure transducer at the center of the array after the given number of loading cycles

2. γ calculated at the center of the array and averaged over the given number of cycles

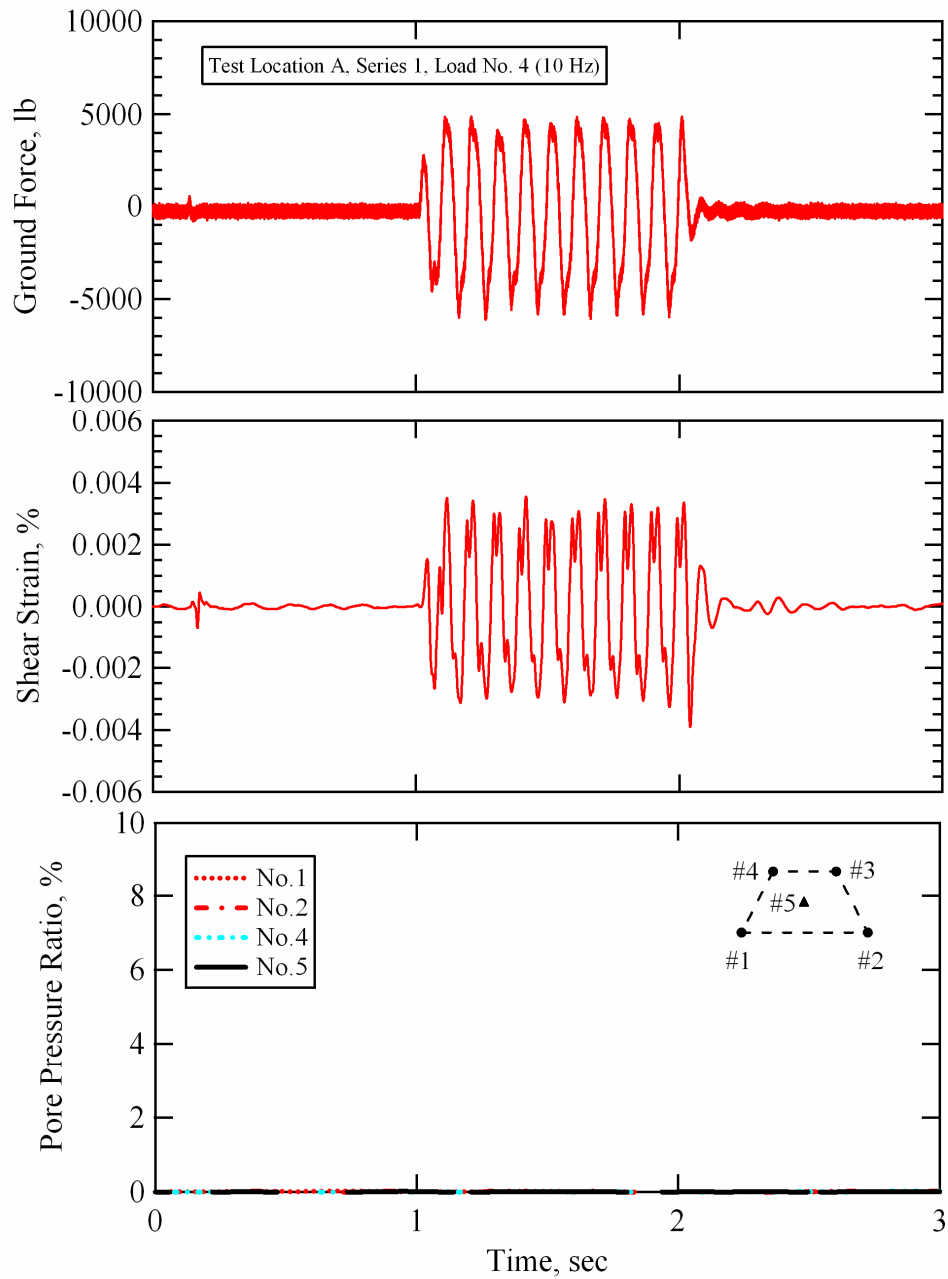


Figure 10-12 Force applied at the ground surface by T-Rex, shear strain induced at the center of the instrumented soil mass, and pore pressure ratios generated at each sensor location during Series 1, loading stage No. 4; Test Location A, Wildlife Liquefaction Array.

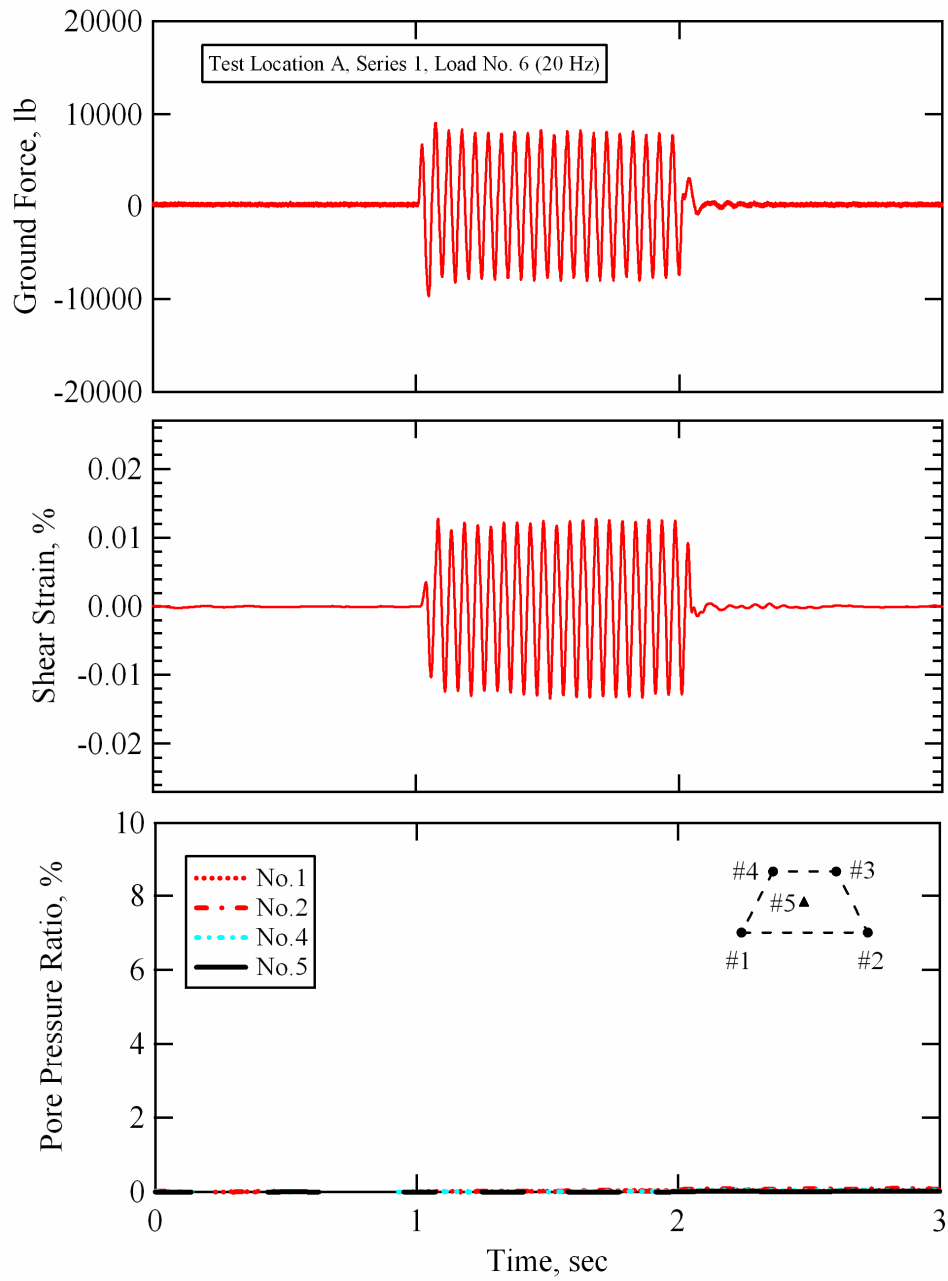


Figure 10-13 Force applied at the ground surface by T-Rex, shear strain induced at the center of the instrumented soil mass, and pore pressure ratios generated at each sensor location during Series 1, loading stage No. 6; Test Location A, Wildlife Liquefaction Array.

generated at each PPT location during loading stage No. 11 of staged loading Series 1 are shown in Figure 10-14. The ground force during loading stage No. 11 was slightly greater than 10000 lb (44.5 kN) throughout the 20 cycles of 20-Hz loading. This load induced fairly uniform cyclic shear strains at the center of the liquefaction sensor array of approximately 0.0187% (see Table 10-9 for strain values averaged over various numbers of loading cycles). These shear strains did not trigger the generation of any excess pore water pressure in the instrumented soil mass, as indicated by the fact that the pore pressure ratios at each sensor location remained equal to zero.

10.3.2.4 Loading Stage No. 15

The force applied at the ground surface by T-Rex, the shear strain induced at the center of the liquefaction sensor array, and the pore pressure ratios generated at each PPT location during loading stage No. 15 of staged loading Series 1 are shown in Figure 10-15. The ground force during loading stage No. 15 was approximately 15000 lb (66.7 kN) throughout the 60 cycles of 20 Hz loading. This load induced fairly uniform cyclic shear strains at the center of the liquefaction sensor array of approximately 0.0399% (see Table 10-10 for strain values averaged over various numbers of loading cycles). These shear strains triggered the generation of minimal excess pore water pressures within the instrumented soil mass. At the end of shaking, the pore water pressure recorded by Sensor No.4 had built to a pore pressure ratio of approximately 1%. The excess pore water pressures recorded by the other PPT's all indicated pore pressure ratios of less than 0.5% at the end of shaking. The PPT record from

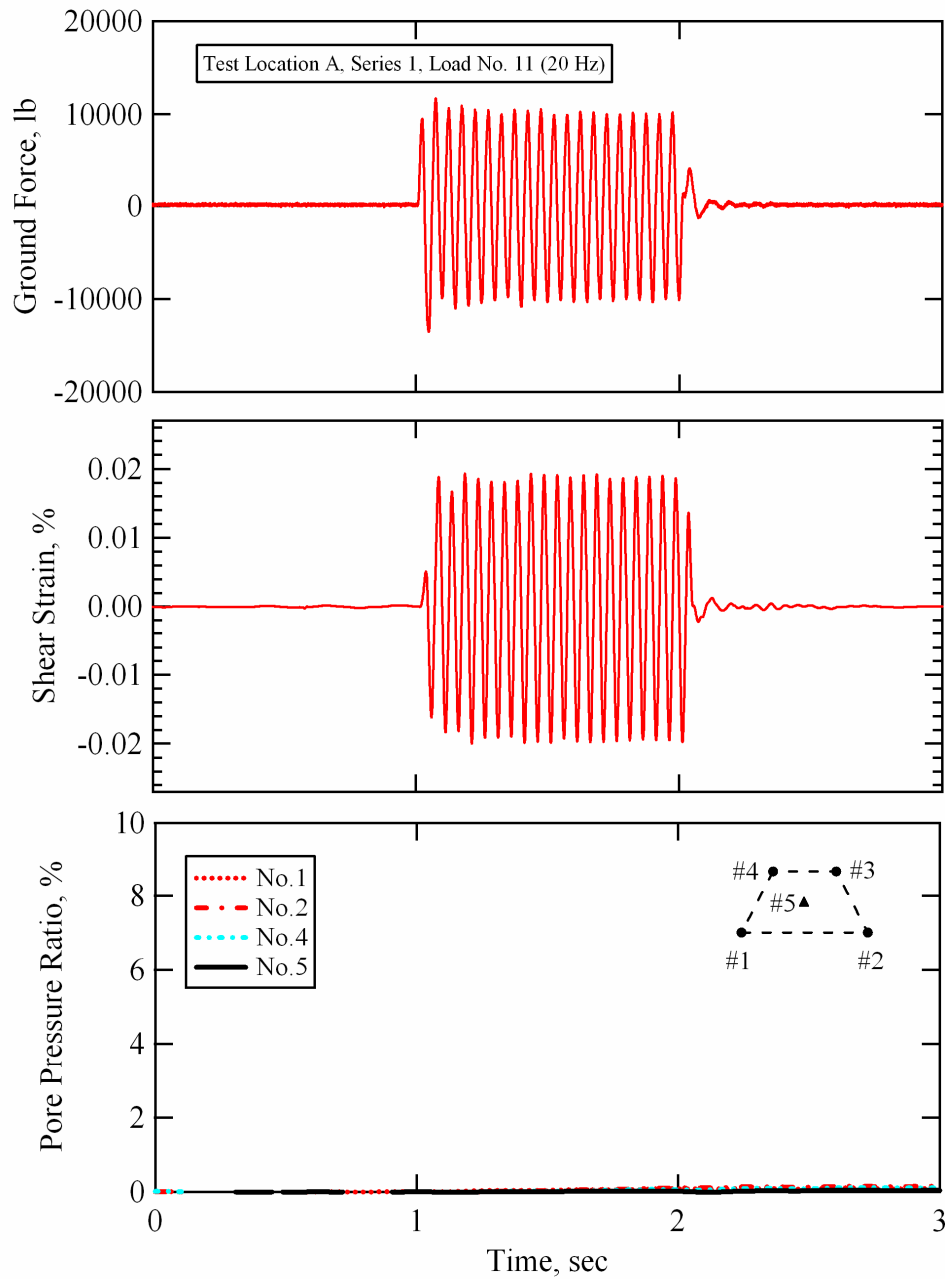


Figure 10-14 Force applied at the ground surface by T-Rex, shear strain induced at the center of the instrumented soil mass, and pore pressure ratios generated at each sensor location during Series 1, loading stage No. 11; Test Location A, Wildlife Liquefaction Array.

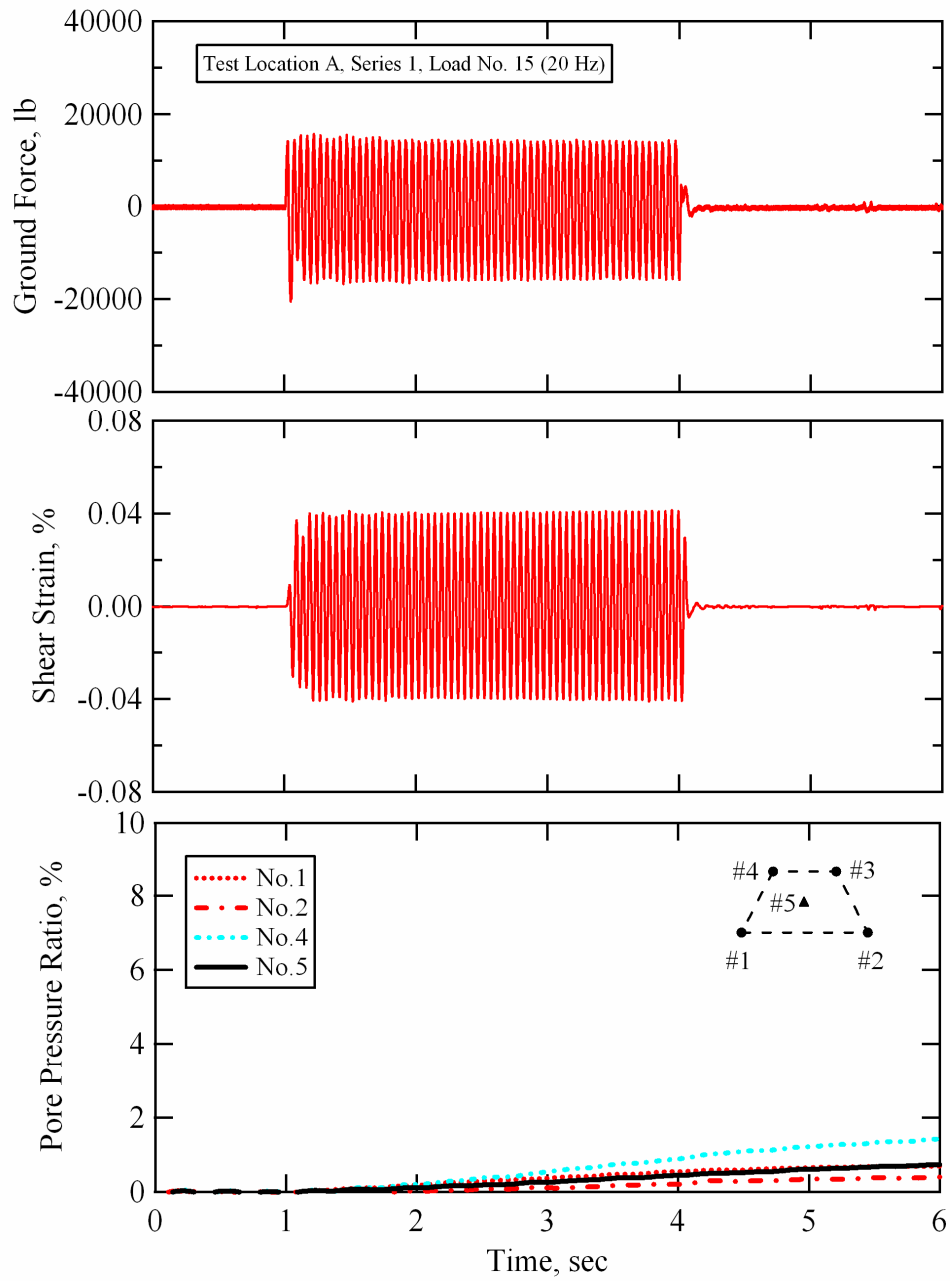


Figure 10-15 Force applied at the ground surface by T-Rex, shear strain induced at the center of the instrumented soil mass, and pore pressure ratios generated at each sensor location during Series 1, loading stage No. 15; Test Location A, Wildlife Liquefaction Array.

Sensor No. 4 showed that the pore water pressure at this location continued to increase slightly for several seconds after the end of shaking. After loading stage No. 15, testing was halted for approximately 15 minutes (see Table 10-8) while the excess pore water pressure within the array was allowed to dissipate back to static conditions (as monitored by the PDCR 35/D transducer).

10.3.2.5 Loading Stage No. 16

The force applied at the ground surface by T-Rex, the shear strain induced at the center of the liquefaction sensor array, and the pore pressure ratios generated at each PPT location during loading stage No. 16 of staged loading Series 1 are shown in Figure 10-16. The ground force during loading stage No. 16 was approximately 18000 lb (80.1 kN) throughout the 100 cycles of 20-Hz loading. This load induced fairly uniform cyclic shear strains at the center of the liquefaction sensor array of approximately 0.0466% (see Table 10-10 for strain values averaged over various numbers of loading cycles). These shear strains triggered the generation of minimal excess pore water pressures within the instrumented soil mass. At the end of shaking, the pore water pressure recorded by Sensor No.4 had built to a pore pressure ratio of approximately 2%. The excess pore water pressures recorded by the other PPT's all indicated pore pressure ratios of less than 1% at the end of shaking. Pore pressure data was recorded for approximately 30 seconds during loading stage No. 16. Figure 10-17 shows the pore pressure ratios measured at each sensor location with a time scale of 30 seconds. The pore water pressures recorded by all of the sensors continued to rise slightly for approximately five seconds after the end of loading and only

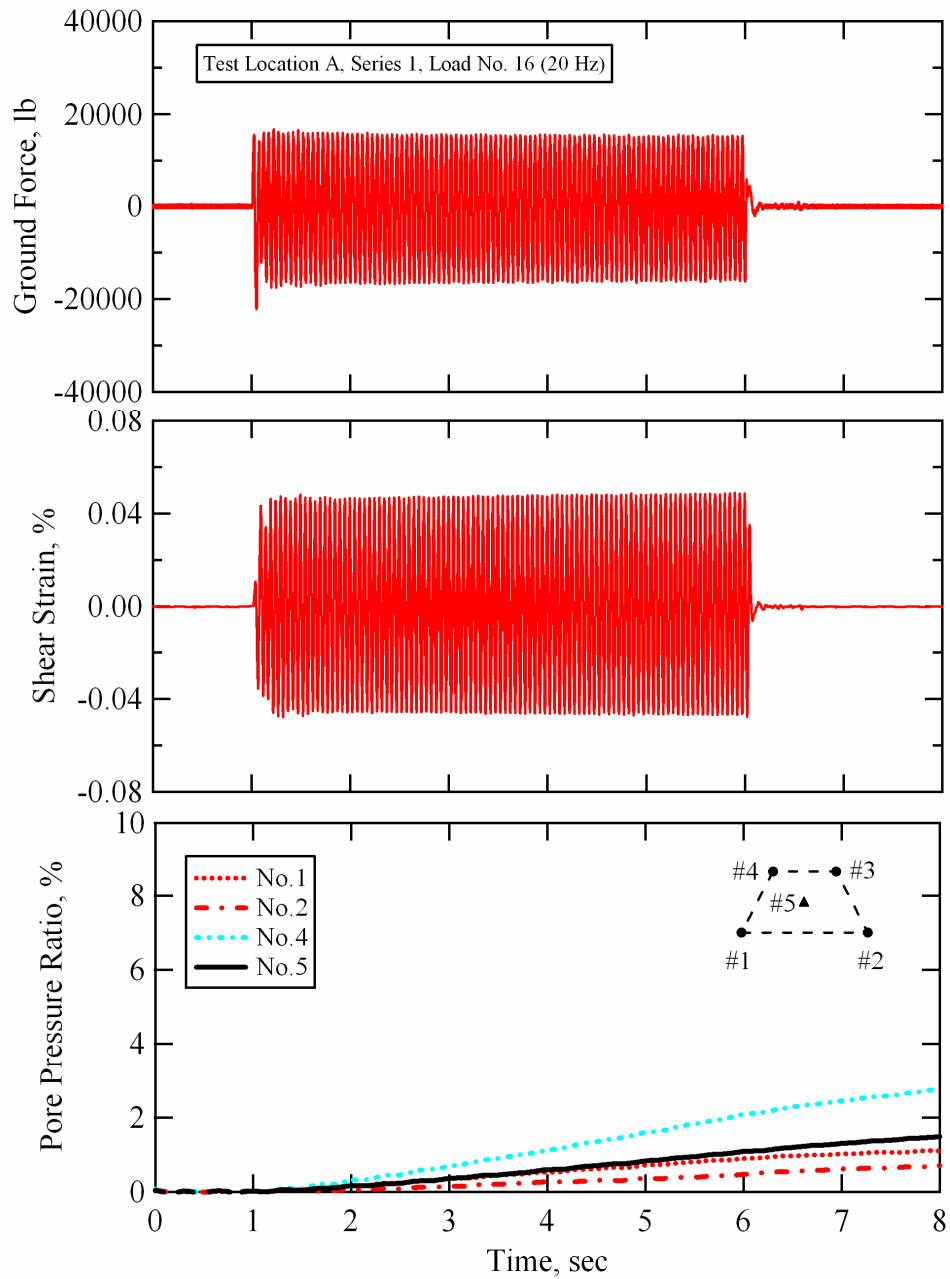


Figure 10-16 Force applied at the ground surface by T-Rex, shear strain induced at the center of the instrumented soil mass, and pore pressure ratios generated at each sensor location during Series 1, loading stage No. 16; Test Location A, Wildlife Liquefaction Array.

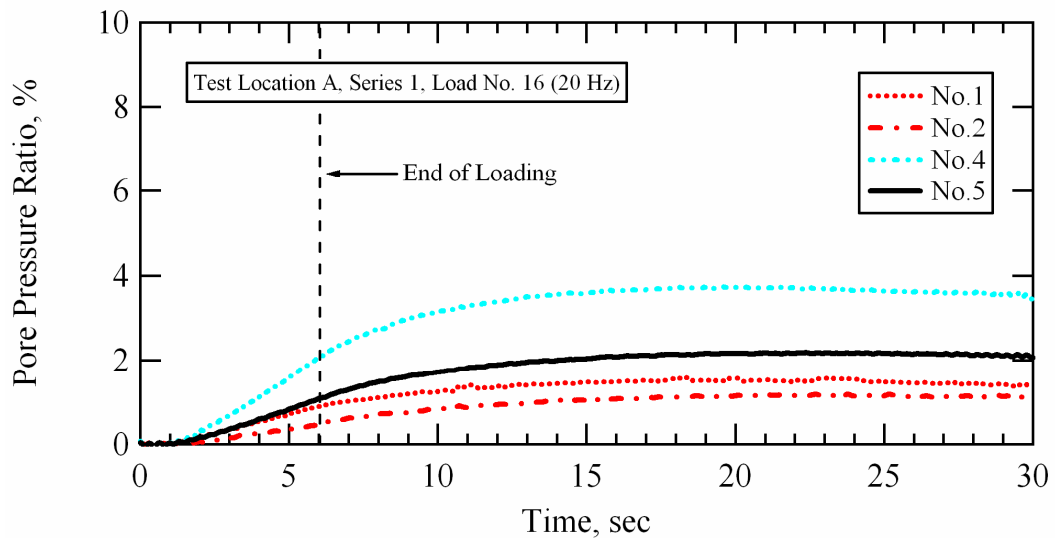


Figure 10-17 Pore pressure ratios generated at each sensor location during Series 1, loading stage No. 16; Test Location A, Wildlife Liquefaction Array.

showed minimal signs of dissipation toward the end of the recorded time period. This pore pressure behavior is different than that recorded at Test Locations C and B (discussed in Chapters 8 and 9, respectively) and is addressed in greater detail in the following section (Section 10.3.2.6). After loading stage No. 16, testing was halted for approximately 15 minutes (see Table 10-8) while the excess pore water pressure within the array was allowed to dissipate back to static conditions (as monitored by the PDCR 35/D transducer).

10.3.2.6 Loading Stage No. 17

The force applied at the ground surface by T-Rex, the shear strain induced at the center of the liquefaction sensor array, and the pore pressure ratios generated at each PPT location during loading stage No. 17 of staged loading

Series 1 are shown in Figure 10-18. The ground force during loading stage No. 17 was not as consistent over the 100 cycles of 10-Hz loading as the ground force records from previous Series 1 dynamic loads. The ground force started out close to 30000 lb (133.4 kN). However, it gradually decayed to approximately 25000 lb (111 kN). It is likely that the soil around the base plate softened to the point where it could not offer enough resistance to keep the ground force at a consistently elevated level.

The shear strain time history shown in Figure 10-18 is irregular. During approximately the first 50 cycles of loading there is a steady increase in shear strain with increasing number of loading cycles. The average shear strain over the first 10 cycles of loading is 0.0602%, while the average shear strain over the first 50 cycles of loading is 0.1168% (see Table 10-10 for strain values averaged over various numbers of loading cycles). After approximately the first 50 cycles of loading, the shear strain increases dramatically over a short number of loading cycles. This behavior was unexpected, and the digitizing range on the dynamic signal analyzer was not set high enough to record the high amplitude signals sensed by the horizontal, in-line components (y-components) of Sensors No. 3 and No. 4. As a result, these signals were substantially clipped after 50 cycles of loading. Therefore, the shear strains calculated after 50 cycles of loading are unreliable. The magnitude of the error is unknown but the shear strains calculated after 50 cycles of loading are a lower bound.

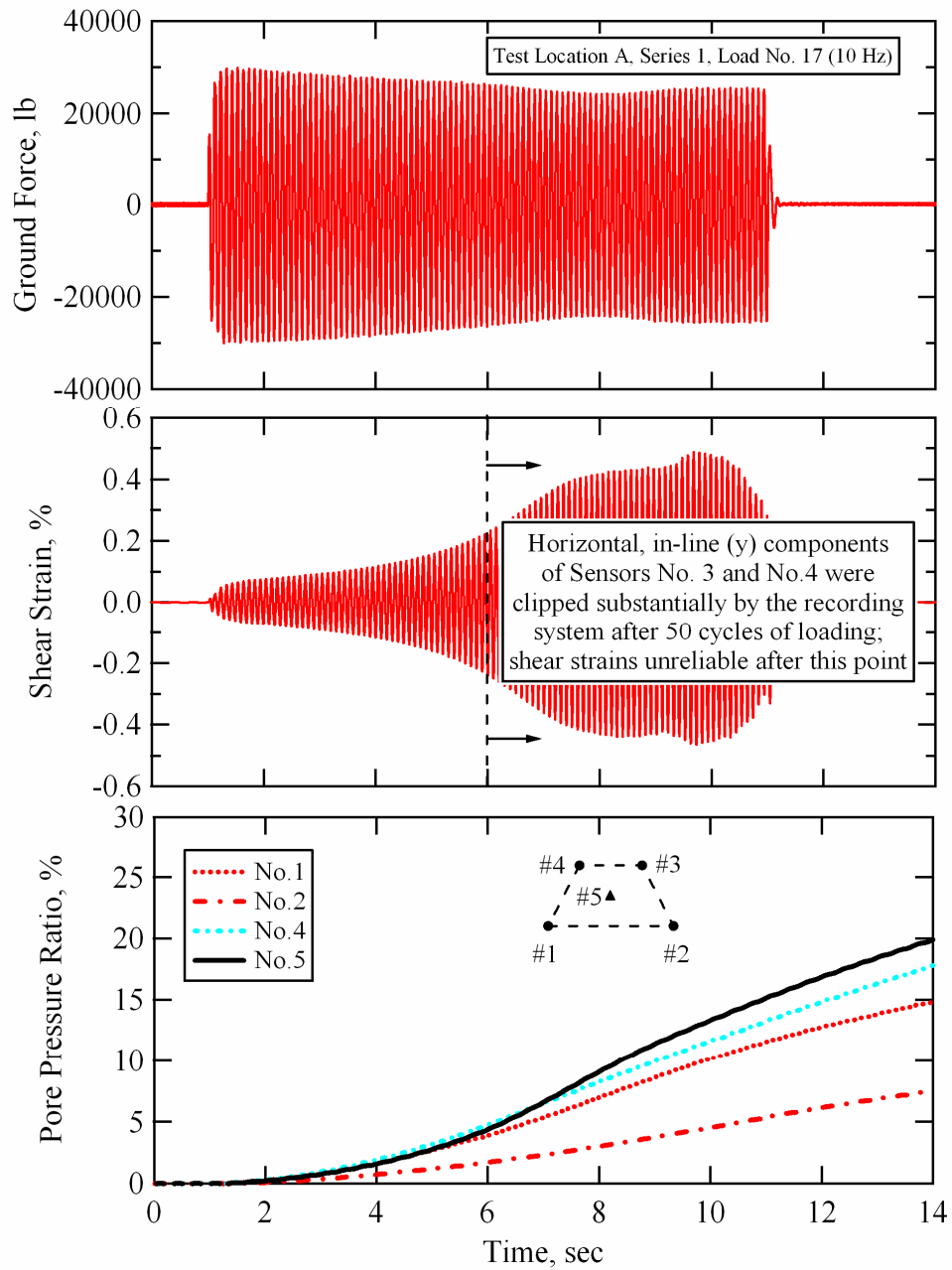


Figure 10-18 Force applied at the ground surface by T-Rex, shear strain induced at the center of the instrumented soil mass, and pore pressure ratios generated at each sensor location during Series 1, loading stage No. 17; Test Location A, Wildlife Liquefaction Array.

The excess pore water pressures recorded by all sensors continue to build after the end of shaking. This same tendency was also recorded during loading stage No. 16. It is obvious that excess pore water pressures generated outside the bounds of the liquefaction sensor array (either horizontally or vertically) during dynamic loading are dissipating and causing the pore pressures within the array to continue to rise after shaking. As the shallower silty-sand material near this location has already been shown to be slightly unsaturated (see Section 10.2.1.1), it is possible that pore water pressures generated deeper in the layer, where the soil is fully saturated, are dissipating upward. This would cause an increase in the pore water pressures recorded by the sensors in the array after shaking had ceased. The PDCR 35/D transducer at the center of the array (Sensor No. 5) sensed higher pore water pressures than the transducer in Sensor No. 4. This trend is opposite to that recorded during Loads No. 15 and No. 16, where the pore pressure recorded by Sensor No. 4 (the shallower sensor) was always greater than that recorded by the deeper sensors in the array. However, the excess pore pressures generated in these loads were much smaller than those generated in Load No. 17, and the pore pressure recorded by Sensor No. 5 does not exceed that recorded by Sensor No. 4 until midway through dynamic loading. The variable pore pressure response within the array cannot fully be explained. However, it does indicate that even within the relatively small sensor array, the pore pressure generation behavior of the material is quite variable.

Pore pressure data was recorded for approximately 30 seconds during loading stage No. 17. Figure 10-19 shows the pore pressure ratios measured at

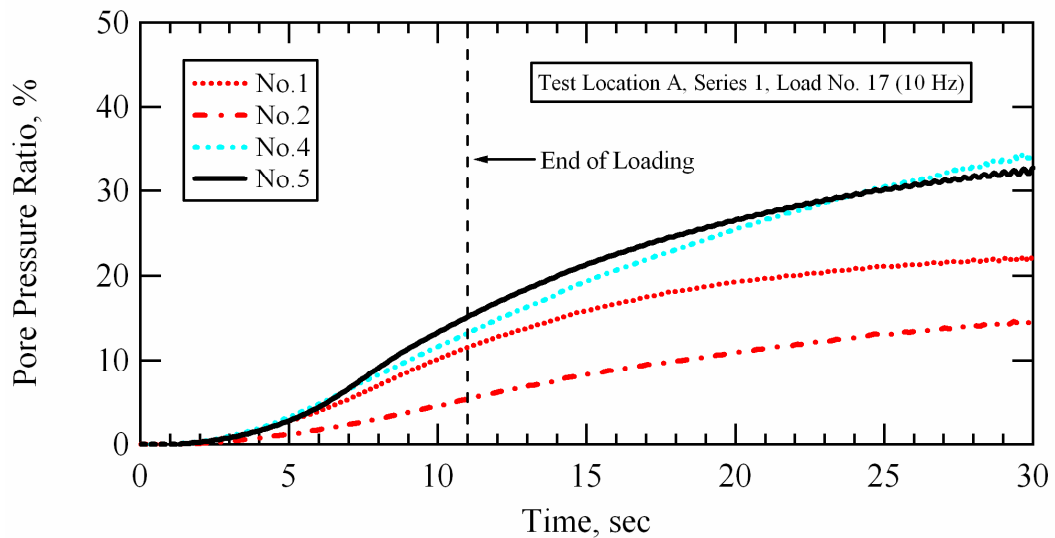


Figure 10-19 Pore pressure ratios generated at each sensor location during Series 1, loading stage No. 17; Test Location A, Wildlife Liquefaction Array.

each sensor location with a time scale of 30 seconds. The pore water pressures recorded by all of the sensors continued to rise throughout the entire recorded time period. The shear strains generated in loading stage No. 17 were substantially greater than the shear strains generated in the instrumented soil mass during in-situ liquefaction tests conducted at Test Locations B and C. It is believed that larger shear strains were not developed during tests conducted at Test Locations B and C because the liquefiable material (several feet thick) above the sensor arrays generated significant excess pore pressures and softened to the point that energy could not be transmitted through to the instrumented soil mass below. At Test Location A, it appears that larger shear strains were developed in the array because significant excess pore water pressures were not being

developed in the upper portion of the liquefiable soil material (because it was not fully saturated). Therefore, larger shear strains were induced at greater depths within the liquefiable layer at Test Location A than at Test Locations B and C. These shear strains likely generated significant excess pore pressures in the material at depth that was fully saturated. As stated above, it is believed that the continuous rise in pore pressure that was recorded by all sensors for at least 20 seconds after the end of loading stage No. 17 was caused by excess pressures generated deeper in the layer dissipating upward through the soil column.

10.3.3 Pore Pressure Generation Curves; Loading Series 1

Pore pressure generation curves for this series of testing can readily be constructed from the data presented in Table 10-9 and 10-10 using any of the given numbers of loading cycles. Figure 10-20 shows the pore pressure generation curves for 10, 20, 50, and 100 cycles of loading determined at Test Location A during staged dynamic loading Series 1. Excess pore pressures generated at the center of the array after 10 cycles of loading ($n = 10$) were not large enough to develop a pore pressure ratio greater than 1% during any of the staged loads. There is only one data point for 100 loading cycles because the 100-cycle shear strain could not be evaluated for loading stage No. 17 due to clipping of the raw data as noted in Section 10.3.2.6. The cyclic threshold shear strain (γ_i^e) for $n = 20$ cycles is approximately 0.06%. Multiple data points between 0.00031% and 0.05% confirm the lack of excess pore pressure generation below γ_i^e .

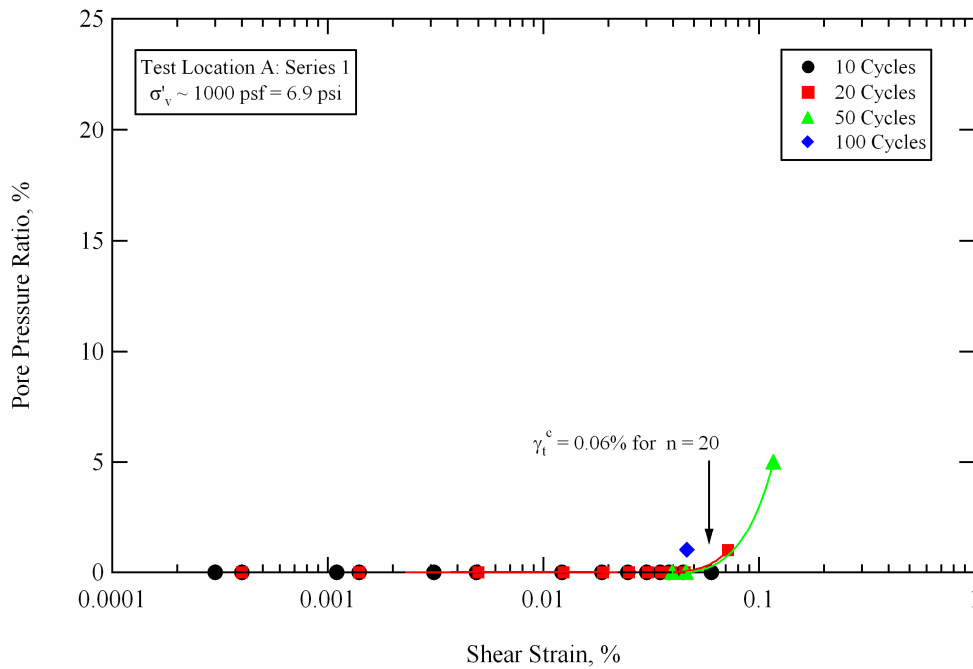


Figure 10-20 Pore pressure generation curves obtained from in-situ liquefaction tests conducted during staged dynamic loading Series 1 at Test Location A, Wildlife Liquefaction Array.

In Figure 10-21, the in-situ pore pressure generation data determined for Test Location A during dynamic loading Series 1 are compared with Dobry's pore pressure generation model for liquefiable soils from the Wildlife Site (Vucetic and Dobry, 1986). As discussed in Section 7.3.1.3, Dobry's model for Wildlife liquefiable soils was developed from cyclic laboratory test results. A cyclic threshold shear strain of 0.02% was assumed for the model (based on experience gained from previous laboratory tests) because the laboratory tests conducted in the study were not performed at shear strains that were low enough to actually determine the cyclic threshold shear strain. This cyclic threshold shear strain was assumed to be the same for any given number of loading cycles. The cyclic tests

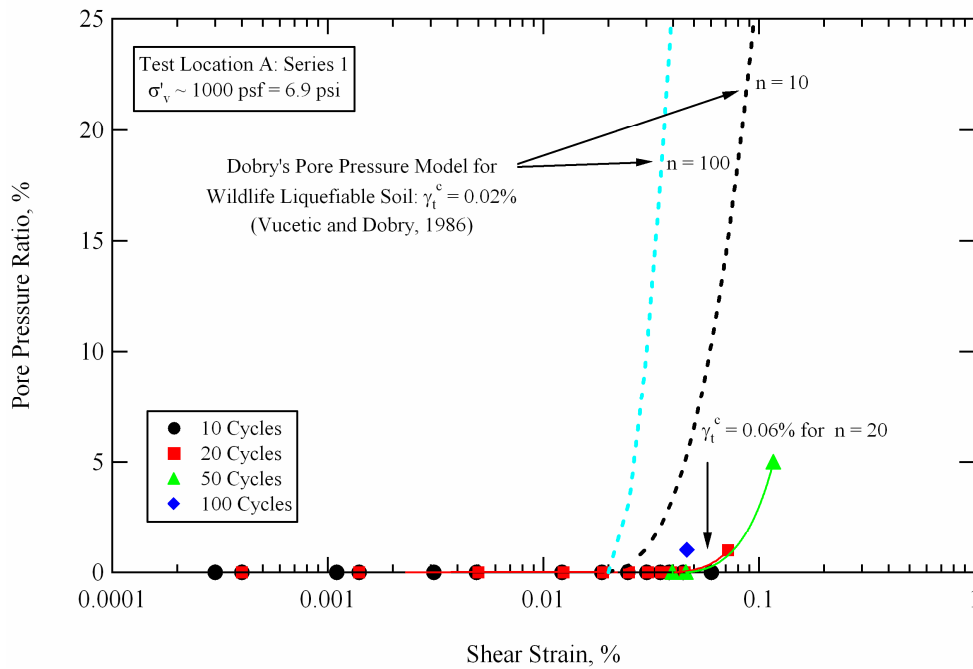


Figure 10-21 Comparison between Dobry's pore pressure generation model (Vucetic and Dobry, 1986) and pore pressure generation curves obtained from in-situ liquefaction tests conducted during staged dynamic loading Series 1 at Test Location A, Wildlife Liquefaction Array.

used to develop the model for Wildlife soils employed up to 30 cycles of strain-controlled loading. The cyclic threshold shear strain assumed in Dobry's model was very similar to the value determined from in-situ liquefaction tests conducted at Test Locations C and B (discussed in Chapters 8 and 9, respectively). However, the in-situ threshold shear strain determined during Series 1 at Test Location A is substantially greater than this value.

In Figure 10-21, Dobry's pore pressure generation model is shown for 10 loading cycles ($n = 10$) and for 100 loading cycles ($n = 100$), as calculated using Equation 7-1. The in-situ test results at this location do not agree well with the

range predicted by Dobry's model. It is hypothesized that the lower saturation level of the soil deposit in the vicinity of Test Location A retarded the generation of excess pore water pressure. Because the pore pressure ratios induced at the center of the liquefaction sensor array during Series 1 tests were less than 5%, the pore pressure generation curves presented in Figures 10-20 and 10-21 are shown with a maximum pore pressure ratio scale of 25%. For perspective purposes, Figure 10-22 presents the pore pressure generation curves with a maximum pore pressure ratio scale of 100%.

It has been shown that the upper portion (approximately the top 2 ft or 0.6 m) of the liquefiable soil deposit at this location was not saturated at the time of field testing. This lack of saturation certainly restricts and influences the development of pore pressures within the soil mass. Indeed, the equivalent B values (based on P-wave velocity measurements) for the upper portion of the silty-sand layer ranged between 0.6 and 0.82 (see Section 10.2.1.1). During laboratory tests conducted for liquefaction studies, pore pressure generation is always measured on a specimen that has a high B value (i.e. close to 1.0). If the soil in the field is not fully saturated, laboratory tests performed on fully saturated specimens will yield unrealistically high pore pressure ratios for a given induced shear strain. That appears to be the reason why Dobry's model does not agree with the in-situ pore pressure generation characteristics measured at Test Location A during dynamic loading Series 1.

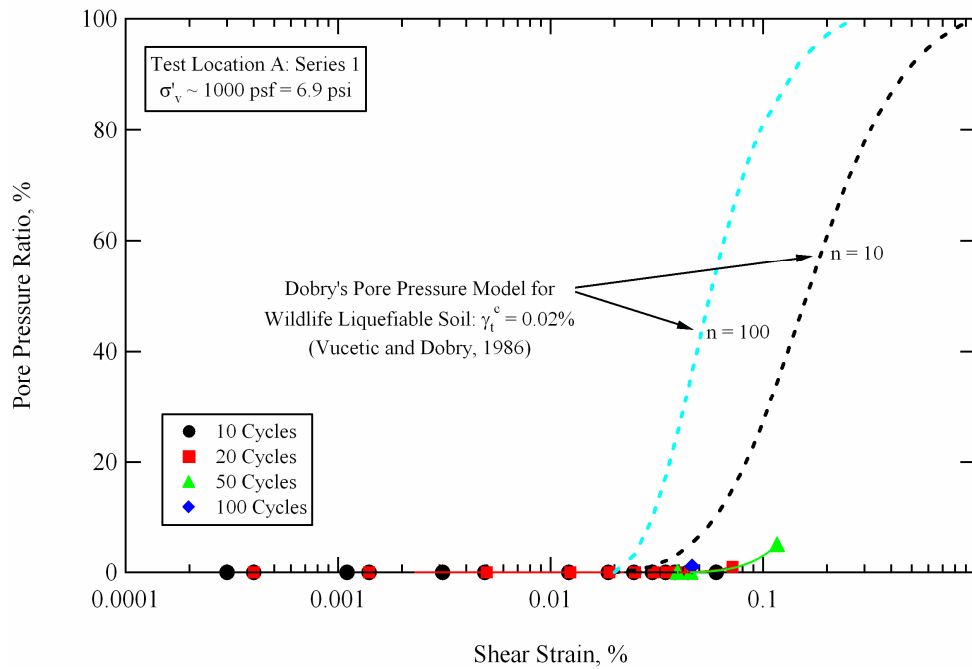


Figure 10-22 Full pore pressure ratio scale comparison between Dobry's pore pressure generation model (Vucetic and Dobry, 1986) and pore pressure generation curves obtained from in-situ liquefaction tests conducted during staged dynamic loading Series 1 at Test Location A, Wildlife Liquefaction Array.

10.4 TEST A: STAGED DYNAMIC LOADING SERIES 2

The in-situ liquefaction sensor array at Test Location A was installed on August 9, 2005. The first series (Series 1) of staged dynamic loading was conducted on the afternoon of August 10, and lasted approximately 3 hours and 30 minutes. In-situ liquefaction testing was then stopped for approximately 18 hours. The pore water pressure transducer (PPT) in each sensor was powered during this break using a 12-volt battery and a DC-to-DC converter to help ensure that the static PPT outputs remained as steady as possible during testing the

following day (as discussed in Section 4.3.2). The second series (Series 2) of staged dynamic loading began in the morning of August 11.

10.4.1 Loading Stages in Series 2

In Series 2, ten separate dynamic loading stages were applied to the instrumented soil mass. Only the information recorded during nine of these loads was used to develop the pore pressure generation curves in the data reduction process. The other load was conducted at a low strain level, at which previous 10- and 20-Hz tests had already been conducted. The dynamic shear loads were applied by driving T-Rex in the horizontal, in-line direction. An external function generator was used to control the frequency, number of cycles, and drive voltage amplitude supplied to T-Rex. All of the loads were conducted at frequencies of 10 or 20 Hz and had durations of 100 cycles. Details of the Series 2 staged dynamic loading sequence are provided in Table 10-11. This loading series is more structured than the one used during Series 1 dynamic loading and is very similar to those carried out at Test Locations C and B (discussed in Chapters 8 and 9, respectively).

10.4.2 Response of the Deposit During Loading Series 1

A representative sample of the ground force, shear strain, and pore pressure ratio time histories obtained from the staged loads applied during Series 2 at Test Location A are presented in graphical form below. The tabulated values for the pore pressure ratios and average shear strains (averaged over the given

Table 10-11 Details of the Series 2 staged dynamic loading sequence conducted at Test Location A, Wildlife Liquefaction Array (WLA)

| Time on 8/11/2005 | Dynamic Load Number | Function Generator Drive Signal | | | Approximate Ground Force (lb) |
|----------------------|------------------------|---------------------------------|---------------------|----------------------|-------------------------------------|
| | | Frequency (Hz) | Number of Cycles | Amplitude (volts) | |
| 10:46 AM | 23 | 20 | 100 | 0.4 | 2000 |
| 10:51 AM | 24 | 20 | 100 | 0.8 | 5000 |
| 10:57 AM | 25 | 20 | 100 | 1.5 | 10000 |
| 11:07 AM | 26 | 10 | 100 | 1.5 | 15000 |
| 11:18 AM | 27 | 10 | 100 | 2.5 | 20000 |
| 11:33 AM | 28 | 20 | 100 | 2.5 | 15000 |
| 11:54 AM | 30 | 10 | 100 | 3.25 | 25000 |
| 12:14 PM | 31 | 10 | 100 | 4.0 | 25000 |
| 12:28 PM | 32 | 10 | 100 | 5.0 | 25000 |

number of loading cycles) induced in the soil during each loading stage of staged loading Series 2 are provided in Table 10-12.

10.4.2.1 Loading Stage No. 23

The force applied at the ground surface by T-Rex, the shear strain induced at the center of the liquefaction sensor array, and the pore pressure ratios generated at each PPT location during loading stage No. 23 of staged loading Series 1 are shown in Figure 10-23. The ground force during loading stage No. 23 was approximately 2000 lb (8.9 kN) throughout the 100 cycles of 20-Hz loading. This load induced fairly uniform cyclic shear strains at the center of the liquefaction sensor array of approximately 0.0023%. These shear strains did not

Table 10-12 Pore pressure ratios and average shear strains at the center of the liquefaction sensor array for different numbers of loading cycles; Series 2, Test Location A, Wildlife Liquefaction Array (WLA)

| Number of Cycles | γ or r_u | Pore Pressure Ratio ¹ (r_u) and Average Shear Strain ² (γ) Values, % | | | | | | | | |
|------------------|-------------------|---|--------|--------|--------|--------|--------|--------|--------|--------|
| | | Series 2: Staged Load Number | | | | | | | | |
| | | No. 23 | No. 24 | No. 25 | No. 26 | No. 27 | No. 28 | No. 30 | No. 31 | No. 32 |
| 10 | γ | 0.0023 | 0.0097 | 0.0278 | 0.0180 | 0.0735 | 0.0466 | 0.1181 | 0.1311 | 0.1268 |
| | r_u | 0 | 0 | 0 | 0 | 0 | 0 | 0 | 0 | 0 |
| 20 | γ | 0.0023 | 0.0097 | 0.0254 | 0.0189 | 0.0994 | 0.0468 | 0.1396 | 0.1444 | 0.1375 |
| | r_u | 0 | 0 | 0 | 0 | 0 | 0 | 1 | 1 | 0 |
| 30 | γ | 0.0023 | 0.0098 | 0.0235 | 0.0193 | 0.1207 | 0.0456 | 0.1505 | 0.1492 | 0.1414 |
| | r_u | 0 | 0 | 0 | 0 | 1 | 0 | 1 | 1 | 1 |
| 40 | γ | 0.0023 | 0.0098 | 0.0225 | 0.0196 | 0.1397 | 0.0442 | 0.1575 | 0.1516 | 0.1433 |
| | r_u | 0 | 0 | 0 | 0 | 1 | 0 | 2 | 1 | 1 |
| 50 | γ | 0.0023 | 0.0098 | 0.0219 | 0.0198 | 0.1567 | 0.0427 | 0.1622 | 0.1528 | 0.1443 |
| | r_u | 0 | 0 | 0 | 0 | 2 | 0 | 2 | 2 | 1 |
| 60 | γ | 0.0023 | 0.0098 | 0.0215 | 0.0199 | 0.1723 | 0.0412 | 0.1654 | 0.1535 | 0.1449 |
| | r_u | 0 | 0 | 0 | 0 | 2 | 0 | 3 | 2 | 2 |
| 70 | γ | 0.0023 | 0.0098 | 0.0211 | 0.0201 | 0.1866 | 0.0397 | 0.1676 | 0.1537 | 0.1450 |
| | r_u | 0 | 0 | 0 | 0 | 3 | 0 | 3 | 3 | 2 |
| 80 | γ | 0.0023 | 0.0098 | 0.0209 | 0.0202 | 0.1997 | 0.0383 | 0.1687 | 0.1536 | 0.1450 |
| | r_u | 0 | 0 | 0 | 0 | 4 | 1 | 4 | 3 | 3 |
| 90 | γ | 0.0023 | 0.0098 | 0.0207 | 0.0204 | 0.2112 | 0.0370 | 0.1693 | 0.1533 | 0.1448 |
| | r_u | 0 | 0 | 0 | 0 | 4 | 1 | 4 | 3 | 3 |
| 100 | γ | 0.0023 | 0.0098 | 0.0205 | 0.0205 | 0.2211 | 0.0357 | 0.1695 | 0.1527 | 0.1445 |
| | r_u | 0 | 0 | 0 | 0 | 5 | 1 | 5 | 4 | 3 |

Notes: 1. r_u from the PDCR 35/D pressure transducer at the center of the array after the given number of loading cycles
2. γ calculated at the center of the array and averaged over the given number of cycles

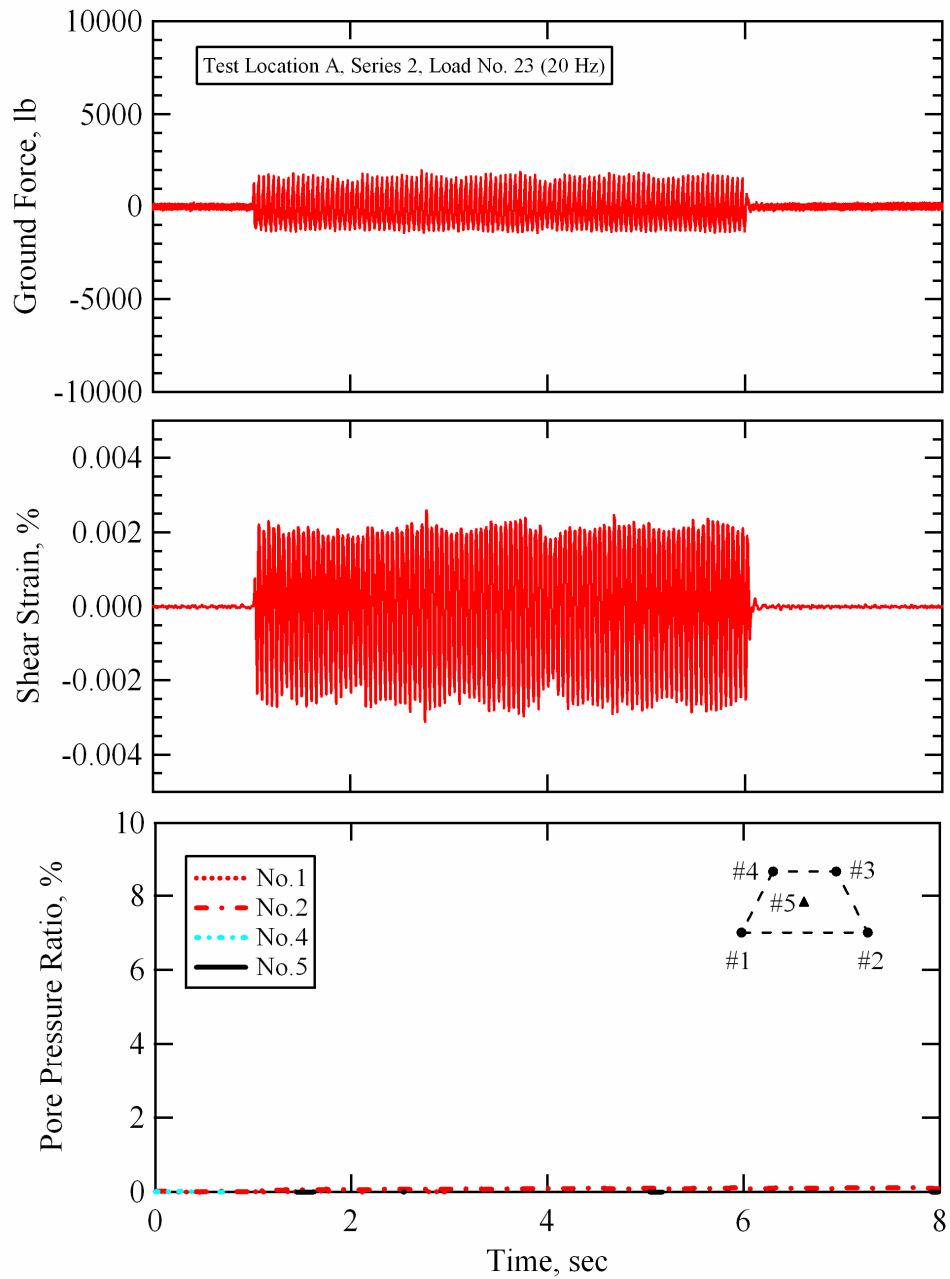


Figure 10-23 Force applied at the ground surface by T-Rex, shear strain induced at the center of the instrumented soil mass, and pore pressure ratios generated at each sensor location during Series 2, loading stage No. 23; Test Location A, Wildlife Liquefaction Array.

trigger the generation of any excess pore water pressure in the instrumented soil mass, as indicated by the fact that the pore pressure ratios at each sensor location remained equal to zero.

10.4.2.2 Loading Stage No. 24

The force applied at the ground surface by T-Rex, the shear strain induced at the center of the liquefaction sensor array, and the pore pressure ratios generated at each PPT location during loading stage No. 24 of staged loading Series 2 are shown in Figure 10-24. The ground force during loading stage No. 24 was slightly less than 5000 lb (22.2 kN) throughout the 100 cycles of 20-Hz loading. This load induced fairly uniform cyclic shear strains at the center of the liquefaction sensor array of approximately 0.0098% (see Table 10-12 for strain values averaged over various numbers of loading cycles). These shear strains triggered the generation of minute amounts of excess pore water pressures ($r_u < 0.25\%$) near Sensors No. 4 and No. 2. However, no detectable excess pore water pressure was generated at the center of the array.

10.4.2.3 Loading Stage No. 26

The force applied at the ground surface by T-Rex, the shear strain induced at the center of the liquefaction sensor array, and the pore pressure ratios generated at each PPT location during loading stage No. 26 of staged loading Series 2 are shown in Figure 10-25. The ground force during loading stage No. 26 was slightly less than 15000 lb (66.7 kN) throughout the 100 cycles of 10-Hz loading. This load induced fairly uniform cyclic shear strains at the center of the

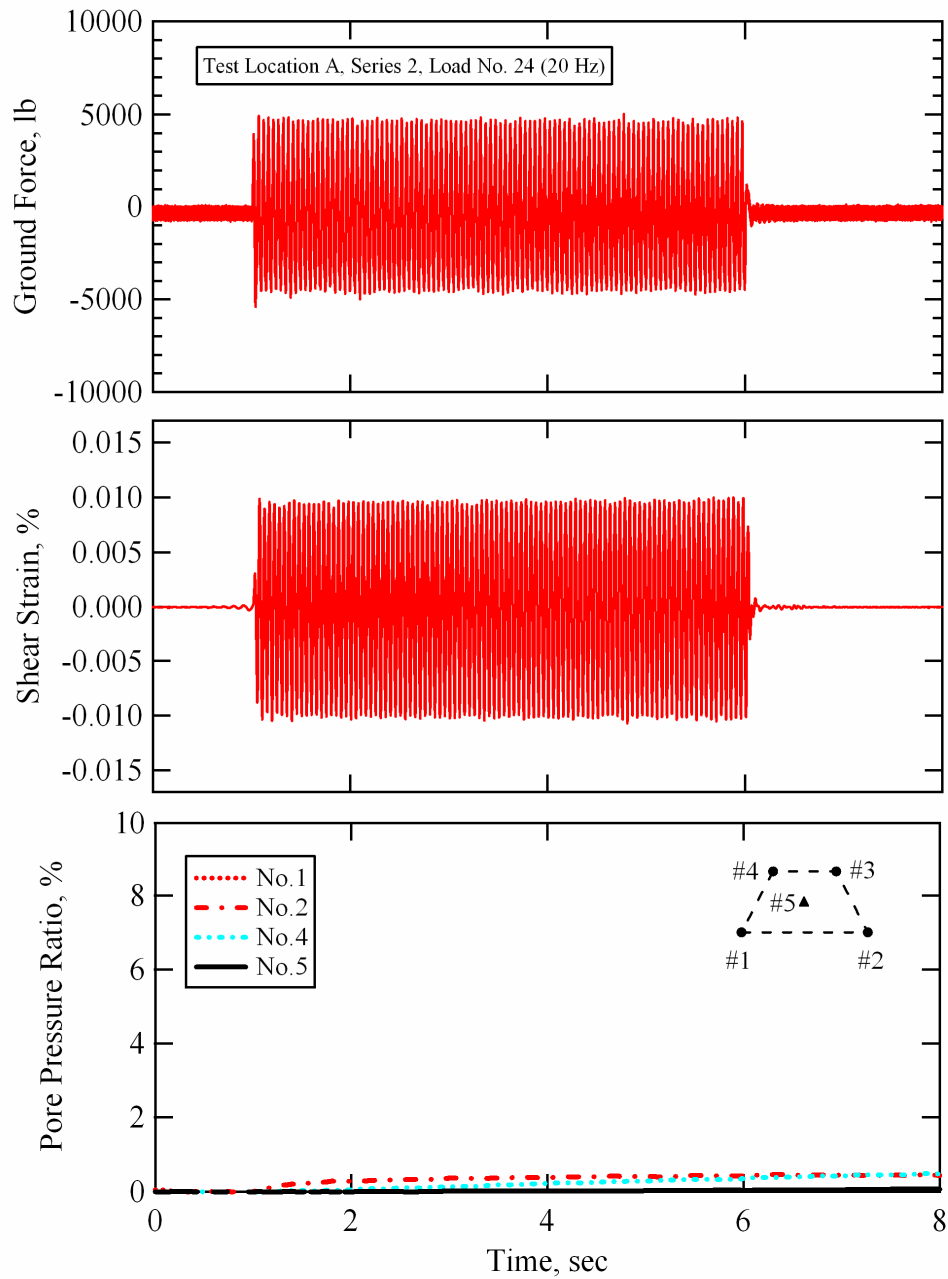


Figure 10-24 Force applied at the ground surface by T-Rex, shear strain induced at the center of the instrumented soil mass, and pore pressure ratios generated at each sensor location during Series 2, loading stage No. 24; Test Location A, Wildlife Liquefaction Array.

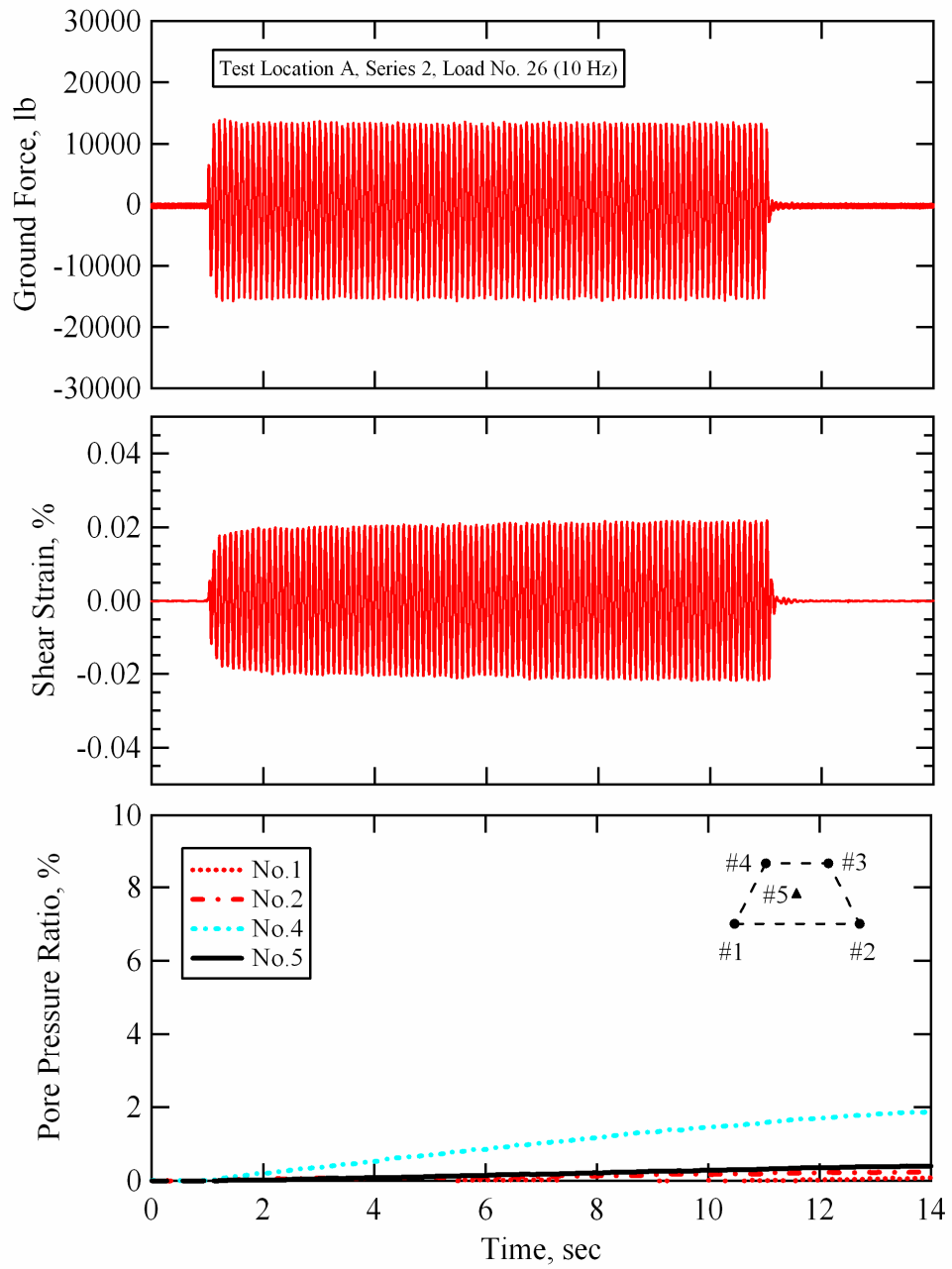


Figure 10-25 Force applied at the ground surface by T-Rex, shear strain induced at the center of the instrumented soil mass, and pore pressure ratios generated at each sensor location during Series 2, loading stage No. 26; Test Location A, Wildlife Liquefaction Array.

liquefaction sensor array of approximately 0.0205% (see Table 10-12 for strain values averaged over various numbers of loading cycles). These shear strains triggered the generation of minimal excess pore water pressures within the array. Sensor No. 4 recorded pressures equal to a pore pressure ratio of less than 2% at the end of shaking. Once again, the pore pressure recorded by this transducer continued to increase after the end of shaking. All of the other transducers recorded excess pore pressures less than an equivalent pore pressure ratio of 0.5%.

10.4.2.4 Loading Stage No. 27

The force applied at the ground surface by T-Rex, the shear strain induced at the center of the liquefaction sensor array, and the pore pressure ratios generated at each PPT location during loading stage No. 27 of staged loading Series 2 are shown in Figure 10-26. The ground force during loading stage No. 27 was not as consistent over the 100 cycles of 10-Hz loading as the ground force records from previous Series 2 dynamic loads. The ground force started at approximately 25000 lb (111.2 kN). However, it quickly decayed to approximately 20000 lb (88.9 kN). It is likely that the soil around the base plate softened to the point where it could not offer enough resistance to keep the ground force at a consistently elevated level.

The shear strain time history shown in Figure 10-26 consistently increases in magnitude throughout the duration of loading. The average shear strain over the first 10 cycles of loading is 0.0735%, while the average shear strain over 100

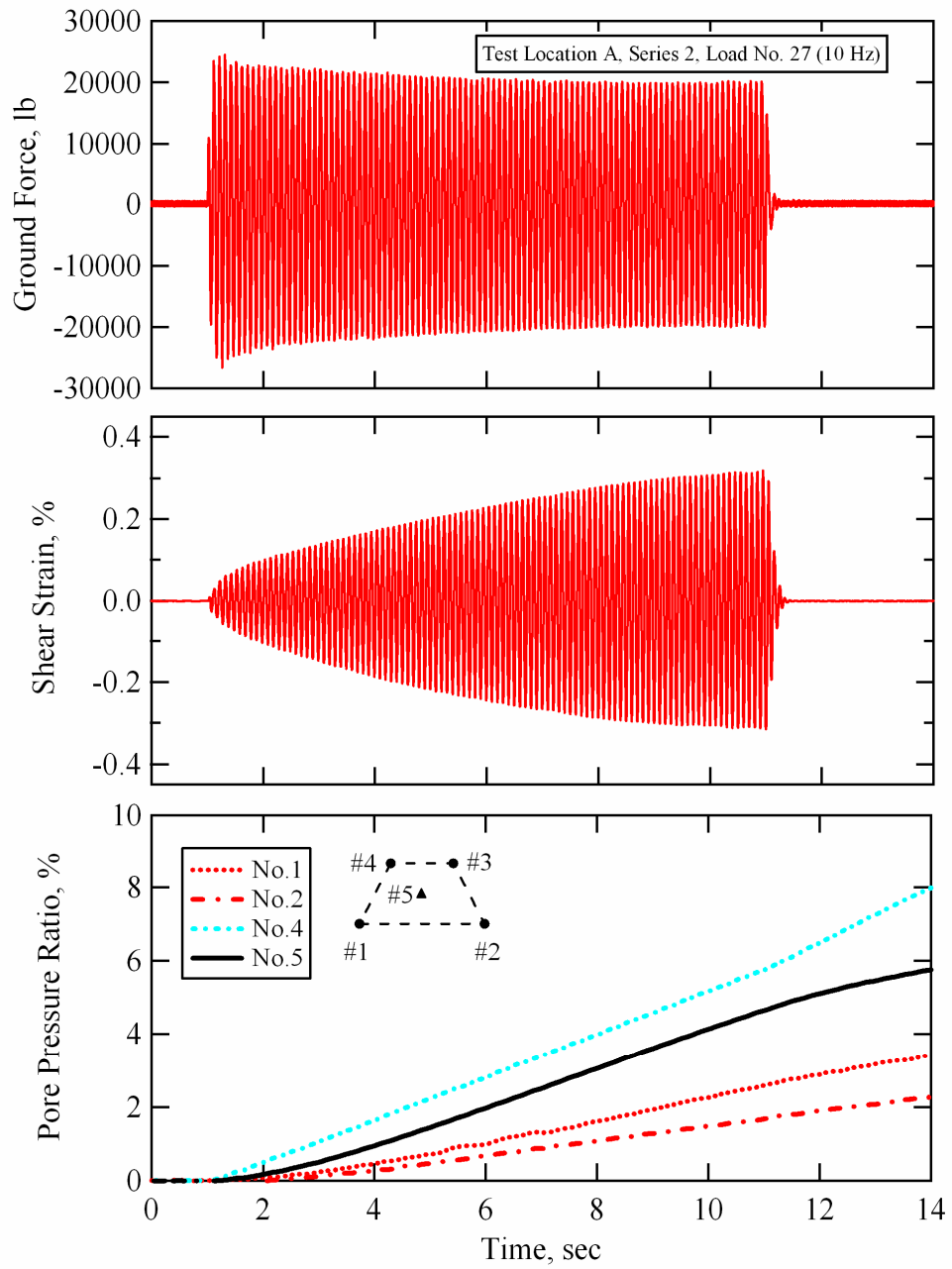


Figure 10-26 Force applied at the ground surface by T-Rex, shear strain induced at the center of the instrumented soil mass, and pore pressure ratios generated at each sensor location during Series 2, loading stage No. 27; Test Location A, Wildlife Liquefaction Array.

cycles of loading is 0.2211% (see Table 10-12). Peak shear strains of more than 0.3% were induced at the center of the array near the end of shaking.

The pore pressures recorded by all sensors continue to build after the end of loading. As stated in Section 10.3.2.6, it is believed that this continuous rise in pressure is caused by excess pore pressures generated deeper in the layer dissipating upward through the soil column. It is also likely that the partially unsaturated soil near the top of the liquefiable soil layer is retarding the pore pressure response within the instrumented soil mass. Indeed, considering the magnitude of the induced shear strains, the excess pore water pressures generated at the end of shaking are substantially less than would normally be predicted. The pore pressure ratio at the center of the array (Sensor No. 5) is only about 5% at the end of dynamic loading. As mentioned previously, the r_u values used to construct the pore pressure generation curves for the site were obtained solely from the PDCR 35/D transducer located at the center of the array.

Pore pressure data was recorded for approximately 60 seconds during loading stage No. 27. Figure 10-27 shows the pore pressure ratios measured at each sensor location with a time scale of 60 seconds. The pore water pressures recorded by all of the sensors continued to rise for extended periods of time after the end of dynamic loading. This pore pressure response is similar to that recorded during loading stage No. 17 in Series 1 (see Section 10.3.2.6).

The horizontal, in-line component (y-component) particle displacement time histories recorded at each liquefaction sensor during loading stage No. 27 are shown in Figure 10-28. It is clear that the shape of the shear strain time history

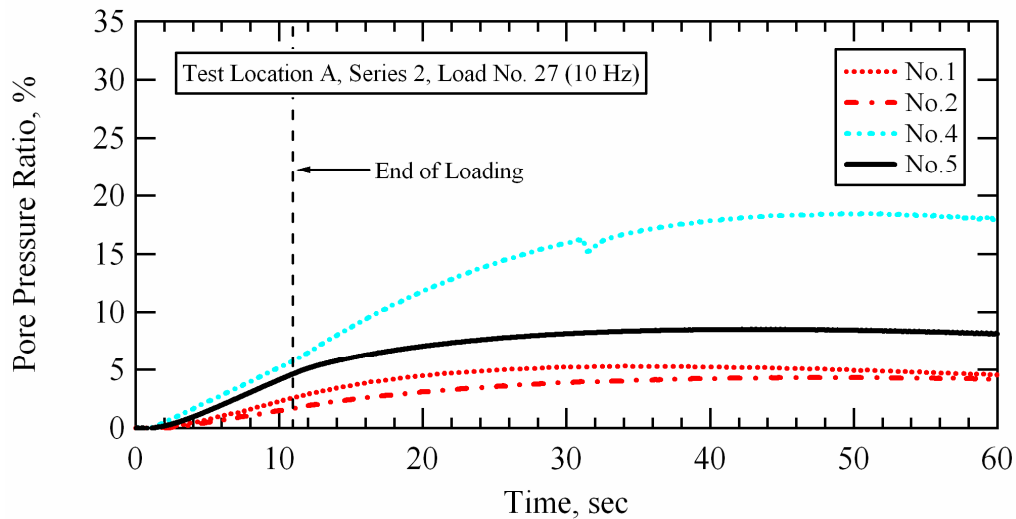


Figure 10-27 Pore pressure ratios generated at each sensor location during Series 2, loading stage No. 27; Test Location A, Wildlife Liquefaction Array.

shown in Figure 10-26 is driven by the particle displacements of the two shallower sensors (Sensors No. 3 and No. 4). The particle displacements recorded by the two deeper sensors actually remain quite constant throughout the duration of loading.

10.4.2.5 Loading Stage No. 30

The force applied at the ground surface by T-Rex, the shear strain induced at the center of the liquefaction sensor array, and the pore pressure ratios generated at each PPT location during loading stage No. 30 are shown in Figure 10-29. The ground force during loading stage No. 30 started at approximately 28000 lb (124.5 kN) and decayed to approximately 22000 lb (97.9 kN). Despite the irregularity of the ground force, the shear strain time history is

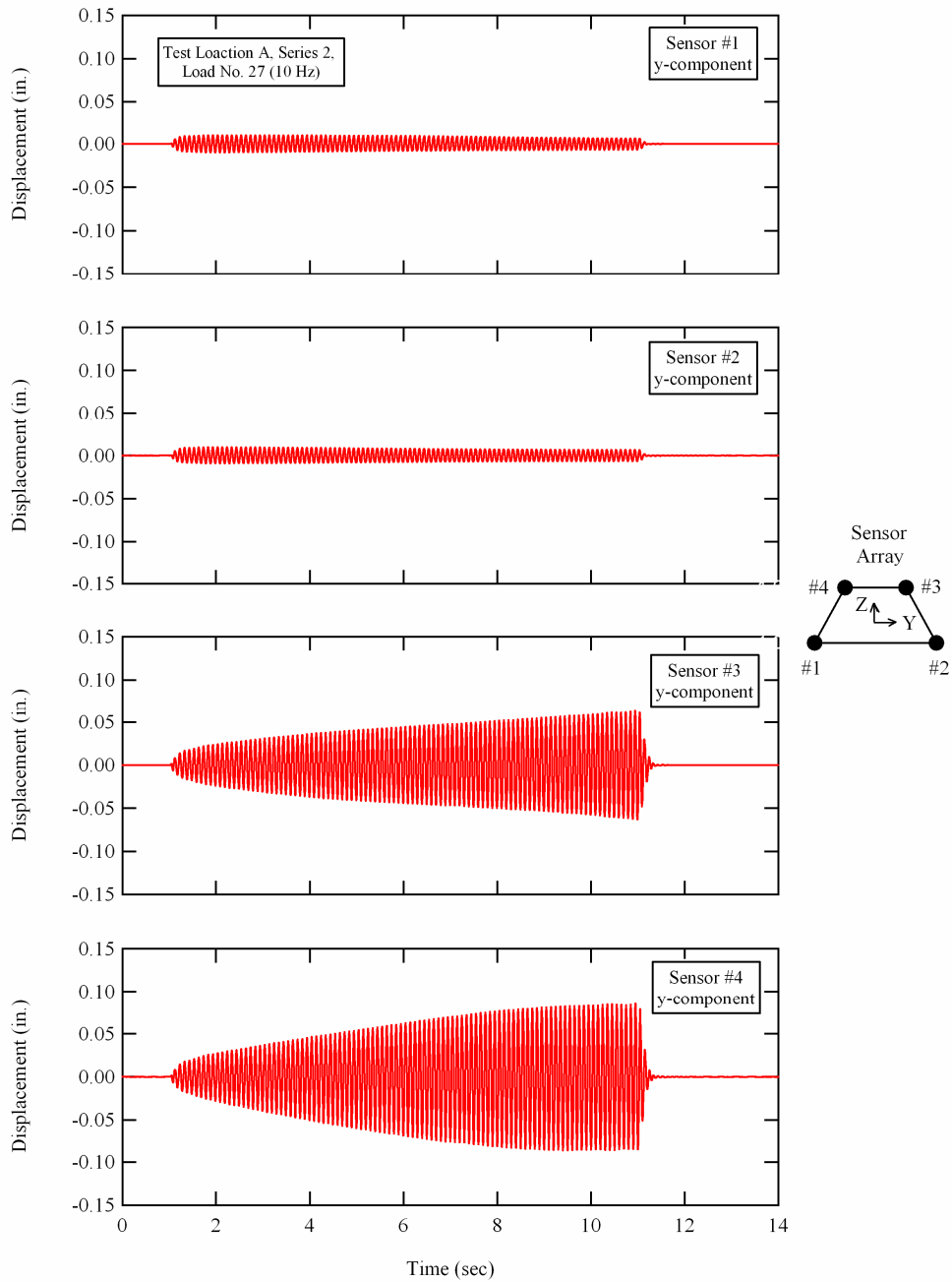


Figure 10-28 Horizontal, in-line component (y-component) particle displacements recorded at each of the liquefaction sensor locations during Series 2, loading stage No. 27; Test Location B, Wildlife Liquefaction Array.

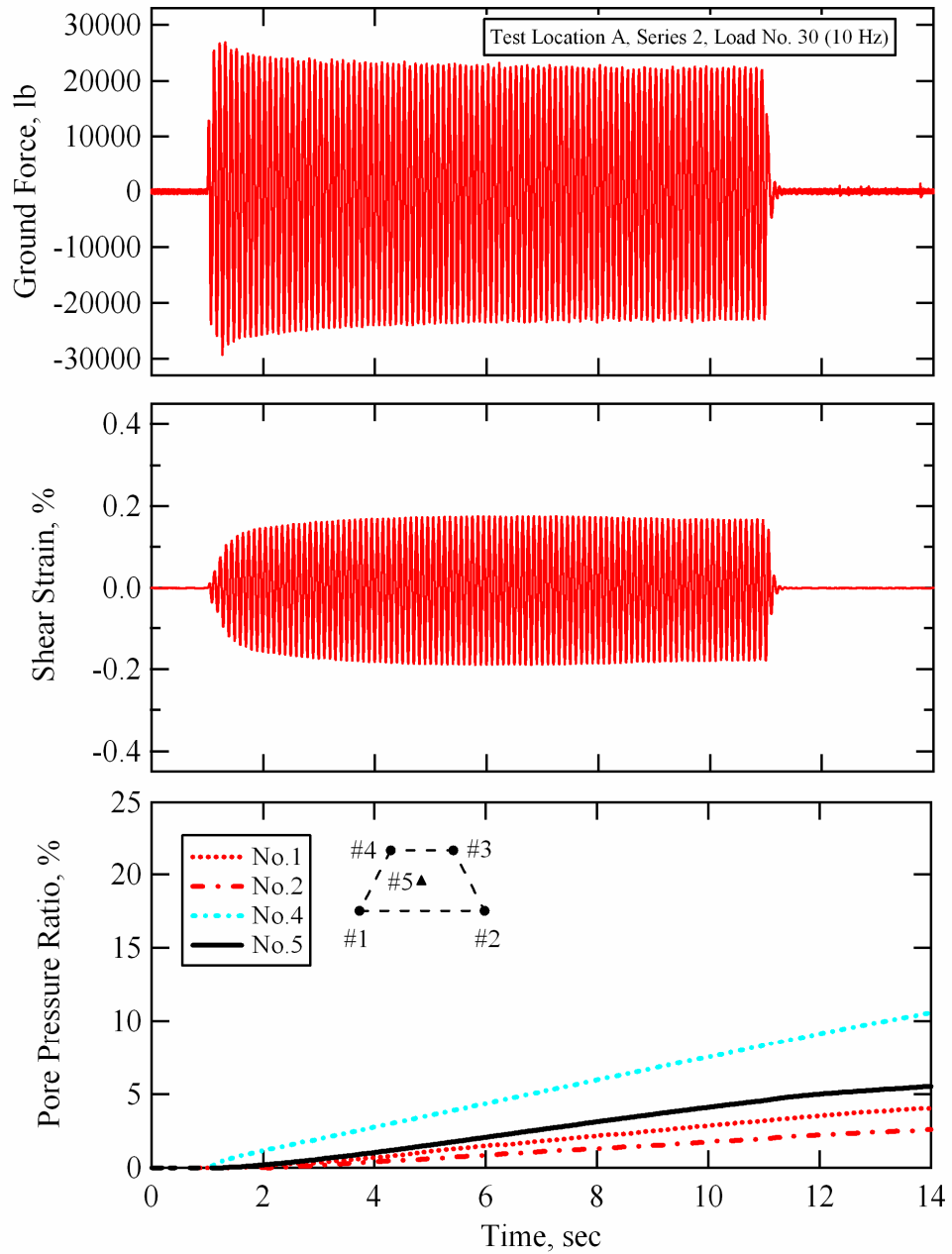


Figure 10-29 Force applied at the ground surface by T-Rex, shear strain induced at the center of the instrumented soil mass, and pore pressure ratios generated at each sensor location during Series 2, loading stage No. 30; Test Location A, Wildlife Liquefaction Array.

fairly consistent. The average shear strain induced at the center of the array over 100 cycles of loading is 0.1695% (see Table 10-12 for strain values averaged over various numbers of loading cycles). Once again, the pore pressures recorded by all sensors continue to build after the end of loading. The pore pressure ratio at the center of the array (Sensor No. 5) is only about 5% at the end of dynamic loading. Pore pressure data was recorded for approximately 60 seconds during loading stage No. 30. Figure 10-30 shows the pore pressure ratios measured at each sensor location with a time scale of 60 seconds. This pore pressure response is similar to that recorded during loading stage No. 17 in Series 1 (see Section 10.3.2.6) and loading stage No. 27 in Series 2 (see Section 10.4.2.4).

10.4.2.5 Loading Stages No. 31 and No. 32

During dynamic Loads No. 31 and 32, the drive amplitude sent to the truck was constantly increased. However, the ground force did not significantly increase. In fact, the shear strains and pore pressure ratios induced during Loads No. 27 and No. 30 were larger than the subsequent loads with higher drive amplitudes. As a result, the ground force, shear strain, and pore pressure ratio time histories obtained from Loads No. 31 and 32 are not presented in graphical form herein. However, tabulated values of pore pressure ratio and average shear strain (averaged over the given number of loading cycles) induced in the soil during each of these loads are provided in Table 10-12.

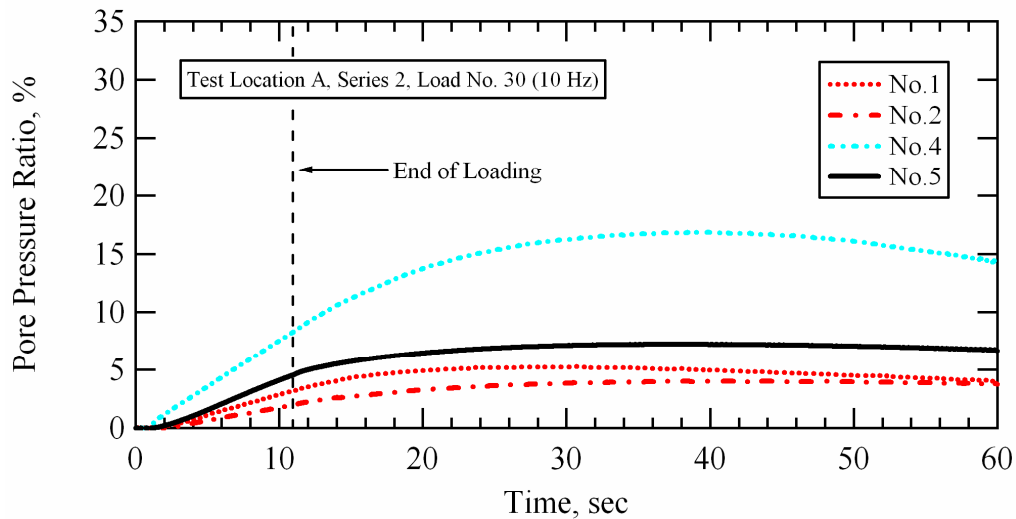


Figure 10-30 Pore pressure ratios generated at each sensor location during Series 2, loading stage No. 30; Test Location A, Wildlife Liquefaction Array.

10.4.3 Pore Pressure Generation Curves; Loading Series 2

Pore pressure generation curves for this series of testing can readily be constructed from the data presented in Table 10-12 using any of the given numbers of loading cycles. Figure 10-31 shows the pore pressure generation curves for 10, 20, 50, and 100 cycles of loading determined at Test Location A during staged dynamic loading Series 2. Excess pore pressures generated at the center of the array after 10 cycles of loading ($n = 10$) were not large enough to develop a pore pressure ratio greater than 1% during any of the staged loads. One of the 100-cycle data points indicates a pore pressure ratio of 1% at a shear strain of 0.035%. However, this point does not agree well with the other 100-cycle data points and does not agree well with the threshold shear strain indicated by all of

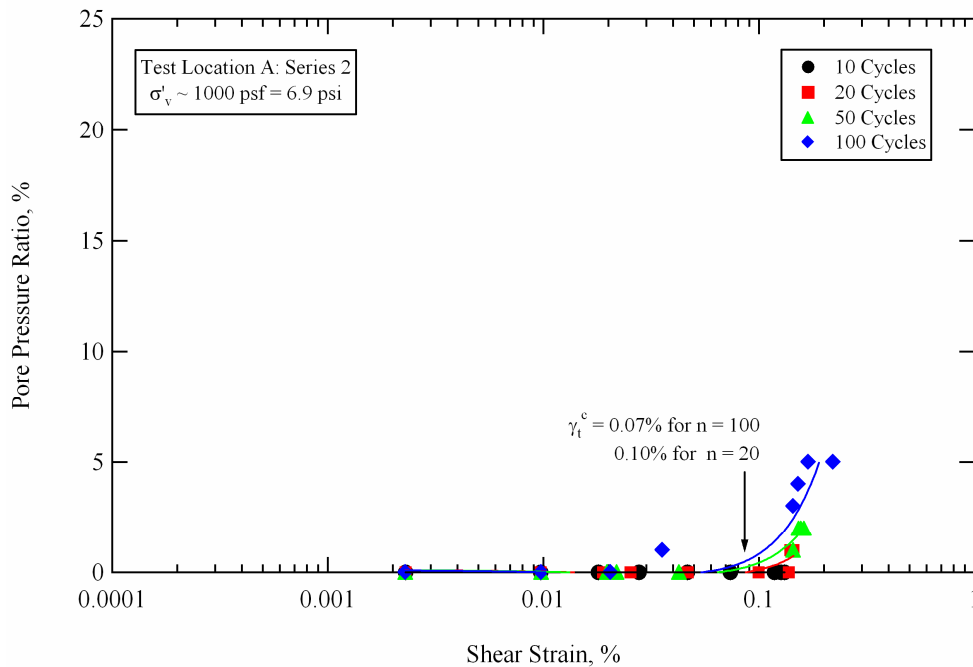


Figure 10-31 Pore pressure generation curves obtained from in-situ liquefaction tests conducted during staged dynamic loading Series 1 at Test Location A, Wildlife Liquefaction Array.

the other 20- and 50-cycle data points. Therefore, this point is considered to be unrepresentative and was ignored in the pore pressure generation curve that was fit to the 100-cycle data. The cyclic threshold shear strain (γ_t^e) for $n = 100$ cycles is approximately 0.7%. The cyclic threshold shear strain (γ_t^e) for $n = 20$ cycles is approximately 0.1%. Numerous data points between 0.003% and 0.07% confirm the lack of excess pore pressure generation below γ_t^e .

In Figure 10-32, the in-situ pore pressure generation data determined for Test Location A during dynamic loading Series 1 are compared with Dobry's pore pressure generation model for liquefiable soils from the Wildlife Site (Vucetic and Dobry, 1986). As discussed in Section 7.3.1.3, Dobry's model for Wildlife

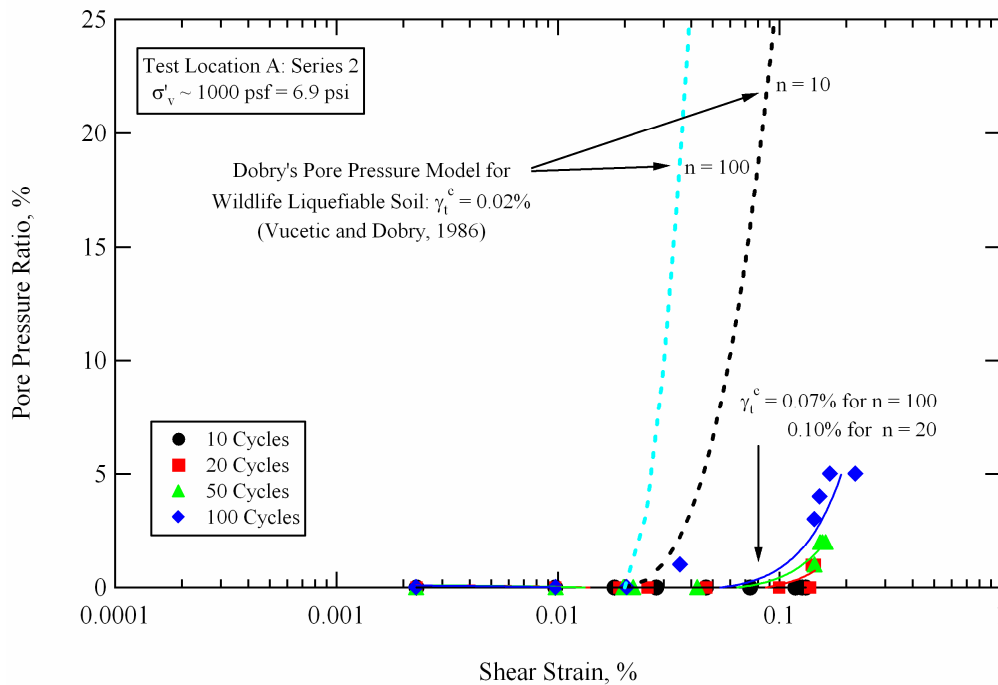


Figure 10-32 Comparison between Dobry's pore pressure generation model (Vucetic and Dobry, 1986) and pore pressure generation curves obtained from in-situ liquefaction tests conducted during staged dynamic loading Series 2 at Test Location A, Wildlife Liquefaction Array.

liquefiable soils was developed from cyclic laboratory test results. A cyclic threshold shear strain of 0.02% was assumed for the model (based on experience gained from previous laboratory tests) because the laboratory tests conducted in the study were not performed at shear strains that were low enough to actually determine the cyclic threshold shear strain. This cyclic threshold shear strain was assumed to be the same for any given number of loading cycles. The cyclic tests used to develop the model for Wildlife soils employed up to 30 cycles of strain-controlled loading. The cyclic threshold shear strain assumed in Dobry's model

was very similar to the value determined from in-situ liquefaction tests conducted at Test Locations C and B (discussed in Chapters 8 and 9, respectively). However, the in-situ threshold shear strains determined during Series 2 at Test Location A are substantially greater than this value.

The in-situ results at Test Location A do not agree well with the range predicted by Dobry's model. However, the in-situ data from Series 1 and Series 2 both indicate similar behavior (see Section 10.5). It is hypothesized that the lower saturation level of the upper-portion of the soil deposit in the vicinity of Test Location A retarded the generation of excess pore water pressure. Because the pore pressure ratios induced at the center of the liquefaction sensor array during Series 2 tests were less than 5%, the pore pressure generation curves presented in Figures 10-31 and 10-32 are shown with a maximum pore pressure ratio scale of 25%. For perspective purposes, Figure 10-33 presents the pore pressure generation curves with a maximum pore pressure ratio scale of 100%.

10.5 GENERAL COMPARISON OF RESULTS FOR SERIES 1 AND SERIES 2

Two in-situ dynamic liquefaction test staged loading series were conducted at Test Location A at the Wildlife Liquefaction Array. The first staged loading series (Series 1) was conducted in the afternoon of August 10, 2005. The second staged loading series (Series 2) was conducted in the morning of August 11, 2005. Both staged loading series started in the low-strain range and sequentially progressed until significant shear strains were induced in the instrumented soil mass. The pore pressure generation curves obtained from Series 1 and Series 2 are compared in Figure 10-34. Shear strains induced at the center

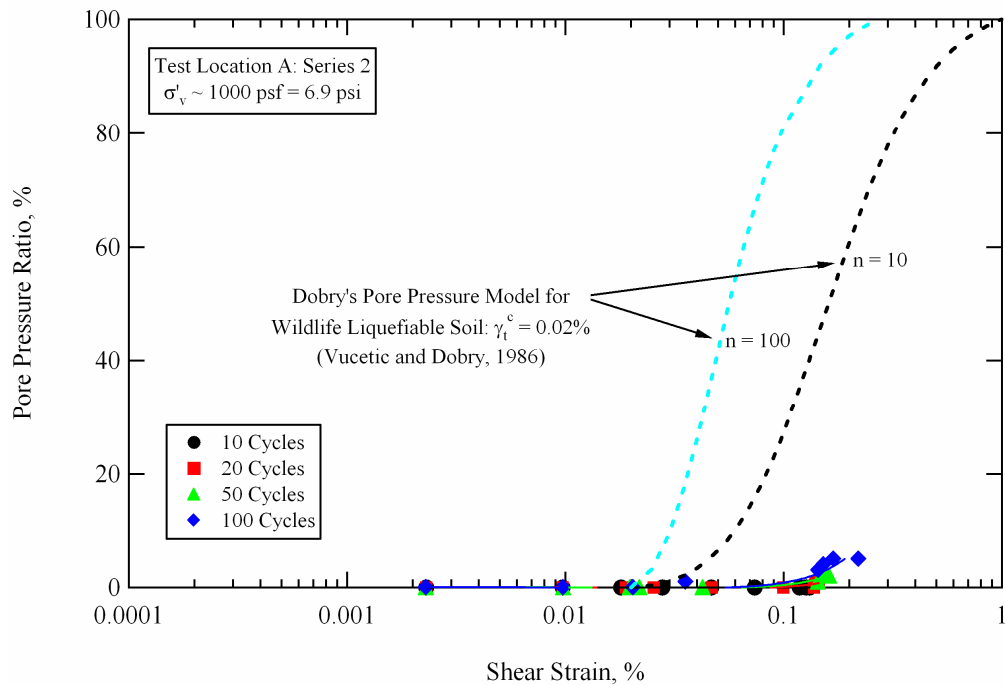


Figure 10-33 Full pore pressure ratio scale comparison between Dobry's pore pressure generation model (Vucetic and Dobry, 1986) and pore pressure generation curves obtained from in-situ liquefaction tests conducted during staged dynamic loading Series 2 at Test Location A, Wildlife Liquefaction Array.

of the liquefaction sensor array during these staged loading series ranged from approximately 0.0003% to 0.22%. The 20- and 50-cycle curves determined from Series 1 indicate a lower threshold shear strain ($\gamma_i^e = 0.06\%$) than the 20- and 50-cycle curves determined from Series 2 ($\gamma_i^e = 0.1\%$). Neither series of tests indicated any pore pressure generation for 10 cycles of loading. Despite inducing shear strains greater than 0.2% in the instrumented soil mass, the maximum excess pore pressures generated at the center of the liquefaction sensor array were only equivalent to a pore pressure ratio of 5%. It is hypothesized that the lower

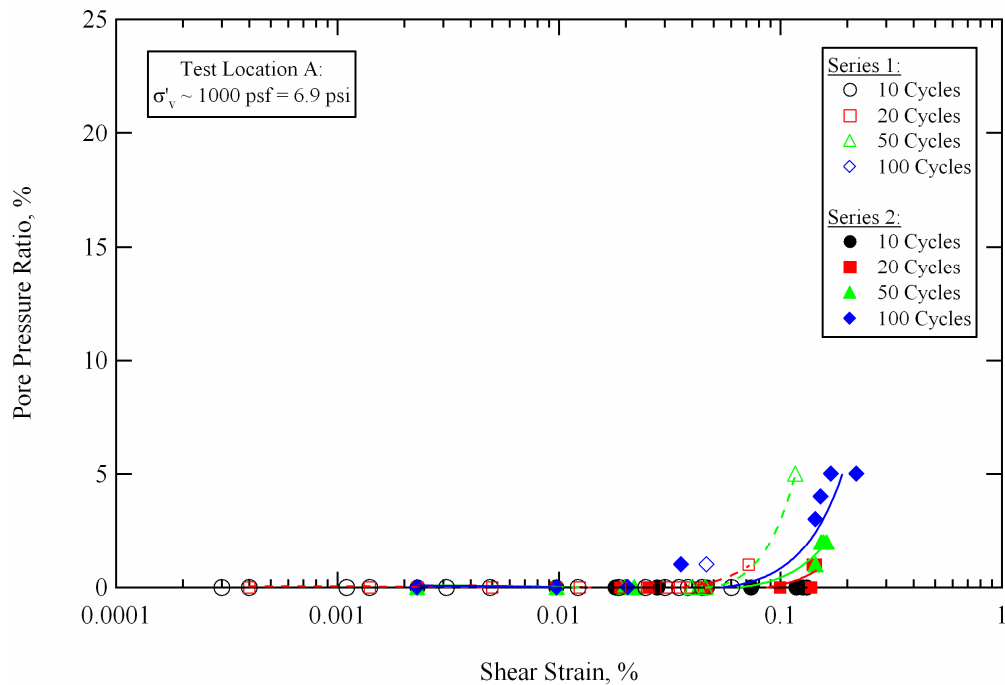


Figure 10-34 Comparison of the pore pressure generation curves obtained during Series 1 and Series 2 staged dynamic loading at Test Location A, Wildlife Liquefaction Array (WLA).

saturation level of the upper-portion of the soil deposit in the vicinity of Test Location A retarded the generation of excess pore water pressure within the instrumented soil mass.

10.6 SUMMARY

The in-situ liquefaction sensor array at Test Location A was installed on August 9, 2005. The instrumentation was installed near CPT 43 at the 2004 NEES (new) WLA Site (<http://nees.ucsb.edu>). The liquefaction sensors were placed within the approximate depth range of 10- to 12-ft (3- to 3.6-m). Two staged loading series were conducted at Test Location A. The first staged loading

series (Series 1) was conducted in the afternoon of August 10, 2005. The second staged loading series (Series 2) was conducted in the morning of August 11, 2005. Both staged loading series consisted of 10- and 20-Hz dynamic loads, which started in the low-strain range and sequentially progressed until significant shear strains were induced in the instrumented soil mass. Shear strains induced at the center of the liquefaction sensor array during these staged loading series ranged from approximately 0.0003% to approximately 0.22%. Pore pressure generation curves were evaluated from the data collected during each staged loading series. The results from these test series do not agree well with the in-situ pore pressure generation curves determined at the other WLA test locations (i.e. Test Locations C and B as discussed in Chapters 8 and 9, respectively) or the theoretical pore pressure generation model developed by Vucetic and Dobry (1986) for WLA liquefiable soils. The cyclic threshold shear strain (γ_t^e) at Test Location A was found to vary between test series. In Series 1, the cyclic threshold shear strain for $n = 20$ cycles was approximately 0.06%. In Series 2, the cyclic threshold shear strain for $n = 20$ cycles was approximately 0.1%. Despite inducing shear strains greater than 0.2% in the instrumented soil mass, a maximum pore pressure ratio of only 5% was induced at the center of the liquefaction sensor array.

Crosshole tests performed between the top pair of sensors (approximately 10 ft or 3 m deep) in the array at Test Location A indicated that the soil was not fully saturated. The measured P-wave velocity was approximately 2300 fps (700 m/sec), which corresponds to a B value of between 0.6 and 0.72 (Ishihara et al., 2001; Valle-Molina, 2006). However, P-wave velocities measured between the

bottom pair of sensors indicated a saturated material (i.e. $V_p > 5000$ fps). A separate set of crosshole tests conducted more than a week later at a location approximately 6 ft (1.8 m) south of where the liquefaction sensor array was installed confirmed that the silty-sand material between the depths of approximately 8 to 10 ft (2.4 to 3 m) was not fully saturated. It is hypothesized that the lower saturation level of the upper-portion of the soil deposit in the vicinity of Test Location A retarded the generation of excess pore water pressure during dynamic loading.

The nonlinear soil shear modulus for the soil within the liquefaction sensor array could not accurately be resolved at this location due to harmonic distortion and small amounts of noise in some of the raw accelerometer records. These problems made it extremely difficult to obtain precise values for the time lags between sensors.

Chapter 11

Comparison of Pore Pressure Generation Results: Test Locations A, B and C; WLA

11.1 INTRODUCTION

Three separate in-situ dynamic liquefaction tests were conducted at the Wildlife Liquefaction Array (WLA) between August 8 and August 19, 2005. The three locations where these tests were conducted are designated as Test Location A, Test Location B, and Test Location C. In this chapter, the pore pressure generation curves that were determined from performing in-situ liquefaction tests at each location are compared and discussed.

11.2 COMPARISON OF IN-SITU PORE PRESSURE GENERATION RESULTS

Three separate in-situ dynamic liquefaction tests were conducted at the Wildlife Liquefaction Array (WLA) between August 8 and August 19, 2005. The three locations where these tests were conducted are designated as Test Location A, Test Location B, and Test Location C. The general locations of these test sites are shown in Figure 11-1. Test Location A is at the 2004 NEES (new) WLA Site (<http://nees.ucsb.edu>), close to CPT 43 (see Figure 10-1). The liquefaction sensor array at Test Location A was installed in the depth range of 10 to 12 ft (3.0 to 3.6 m). Test Location B is at the 1982 (old) WLA Site, just outside of the circular array of pore water pressure transducers (see Figure 9-1) that were placed by USGS personnel following the 1981 Westmorland earthquake (Bennett et al.,

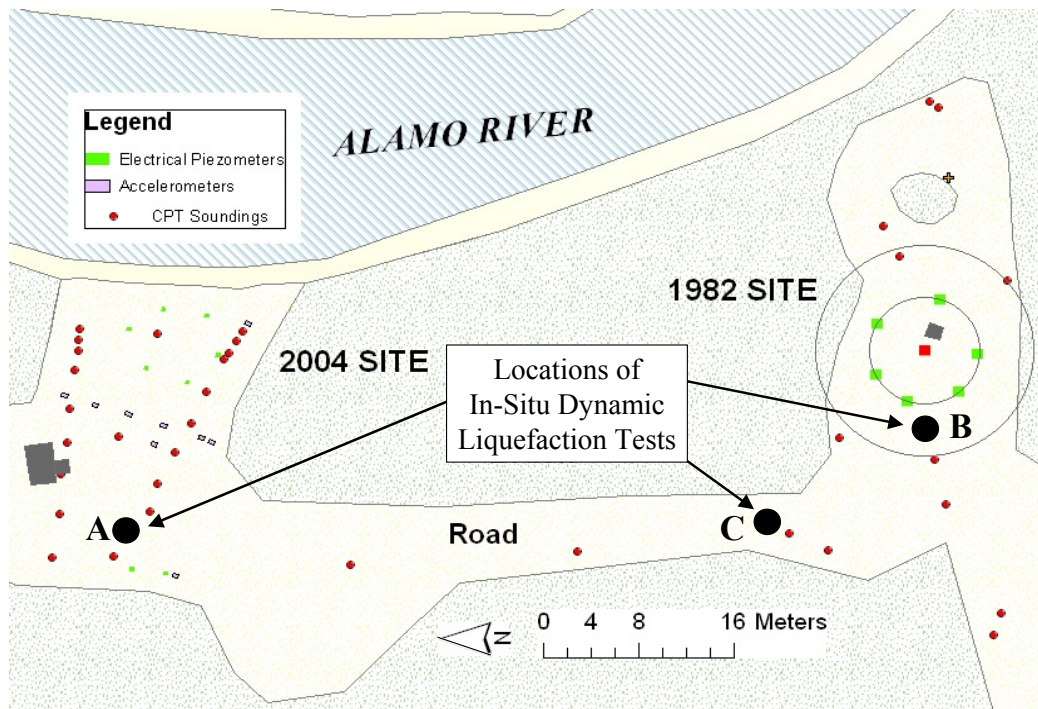


Figure 11-1 Approximate locations of the three in-situ dynamic liquefaction tests that were carried out at the Wildlife Liquefaction Array (WLA) (after <http://nees.ucsb.edu>).

1984; see Section 7.3.1). The liquefaction sensor array at Test Location B was installed in the depth range of 11 to 13 ft (3.3 to 4.0 m). Test Location C is on the dirt access road between the 1982 WLA Site and the 2004 WLA Site, close to CPT 47 (see Figure 8-1). The liquefaction sensor array at Test Location C was installed in the depth range of 11 to 13 ft (3.3 to 4.0 m).

Two staged dynamic loading series were conducted at each test location. The first staged loading series (Series 1) was conducted the day after sensor installation. Following Series 1, the soil was allowed to rest for at least 18 hours before applying the second staged loading series (Series 2). Each staged loading

series consisted of 10- and 20-Hz dynamic loads, which started in the low-strain range and sequentially progressed until significant shear strains were induced in the instrumented soil mass, resulting in pore water pressure generation. The purpose of this section is to compare the pore pressure generation response measured at each test location during each staged loading series.

11.2.1 Pore Pressure Responses During Series 1 at Each Test Location

The 10-, 20-, 50- and 100-cycle pore pressure generation curves obtained from staged loading Series 1 in-situ liquefaction tests conducted at Test Locations A, B and C are shown in Figure 11-2. Note that in this figure, the pore pressure response at Test Location C is presented in the top graph, while the pore pressure response at Test Location A is presented in the bottom graph. The pore pressure generation responses measured during Series 1 at Test Locations C and B are very similar. The cyclic threshold shear strain (γ_t^e) depends on the number of loading cycles (n) and ranges from approximately 0.01% for n = 100 to 0.02% for n = 10. The pore pressure generation response at Test Location A is very different. Excess pore pressures generated at the center of the array after 10 cycles of loading (n = 10) were not large enough to develop a pore pressure ratio greater than 1% during any of the staged loads. There is only one data point for 100 loading cycles (see Section 10.3.3), so it is not realistic to pick a 100-cycle cyclic threshold shear strain. The cyclic threshold shear strain for n = 20 cycles is approximately 0.06%.

The 10-, 20-, 50- and 100-cycle in-situ pore pressure generation curves obtained from staged loading Series 1 at Test Locations A, B and C are compared

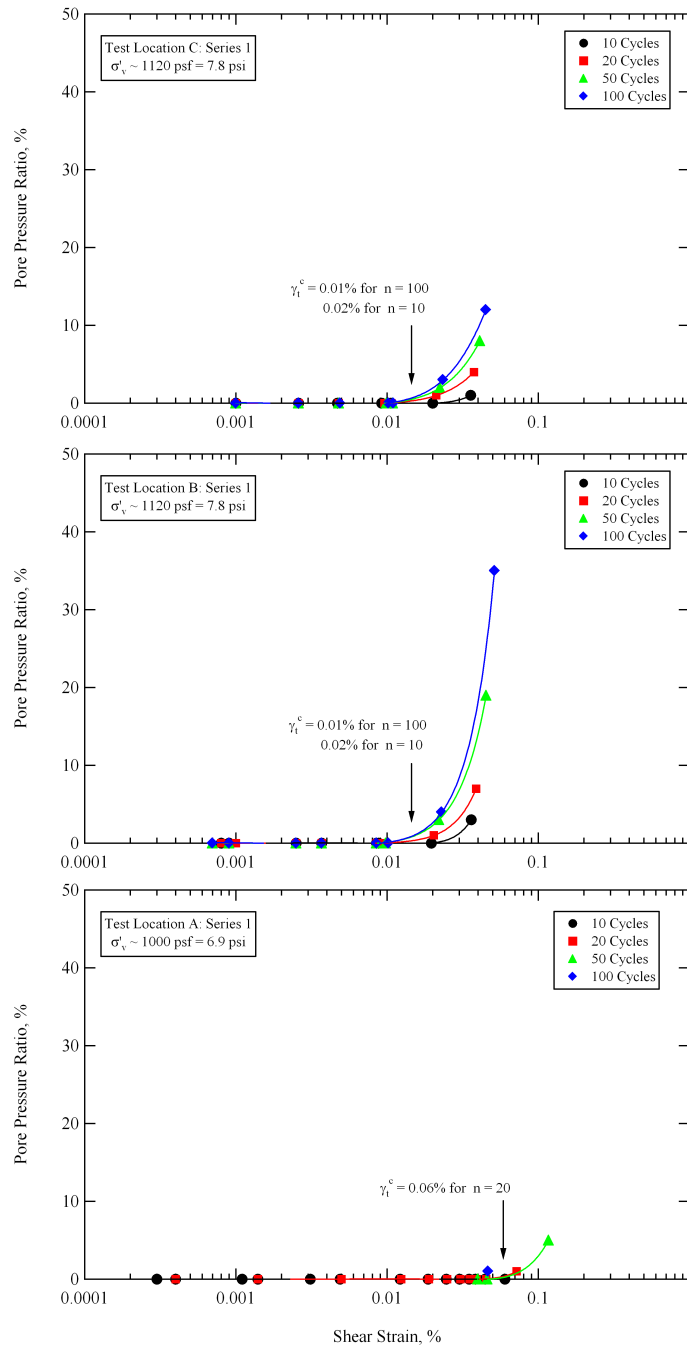


Figure 11-2 Comparison of the pore pressure generation curves obtained from staged loading Series 1 in-situ liquefaction tests at Test Locations C, B and A, Wildlife Liquefaction Array (WLA).

with Dobry's pore pressure generation model for liquefiable soils from the Wildlife Site (Vucetic and Dobry, 1986) in Figure 11-3. As discussed in Section 7.3.1.3, Dobry's model for Wildlife liquefiable soils was developed from cyclic laboratory test results. A cyclic threshold shear strain of 0.02% was assumed for the model (based on experience gained from previous laboratory tests) because the laboratory tests conducted in the study were not performed at shear strains that were low enough to actually determine the cyclic threshold shear strain. This cyclic threshold shear strain was assumed to be the same for any given number of loading cycles. The cyclic tests used to develop the model for Wildlife soils employed up to 30 cycles of strain-controlled loading. The assumed cyclic threshold value is equivalent to the $n = 10$ cyclic threshold shear strain determined from in-situ liquefaction tests conducted during staged loading Series 1 at Test Locations C and B. However, the $n = 20$ cyclic threshold shear strain at Test Location A is 0.06% and the $n = 10$ cyclic threshold shear strain could not be identified because excess pore pressures were not generated during 10 cycles of loading at this location.

The trends in pore pressure generation for the Series 1 in-situ results at Test Location B are nearly identical to the trends in pore pressure generation predicted by Dobry's model, despite the fact that the $n = 100$ cycle threshold shear strain is slightly less than the assumed model value. The Series 1 in-situ results obtained at Test Location C generally fall within the range predicted by Dobry's model. However, for a given shear strain level and number of loading cycles the in-situ pore pressure generation curves yield slightly lower pore

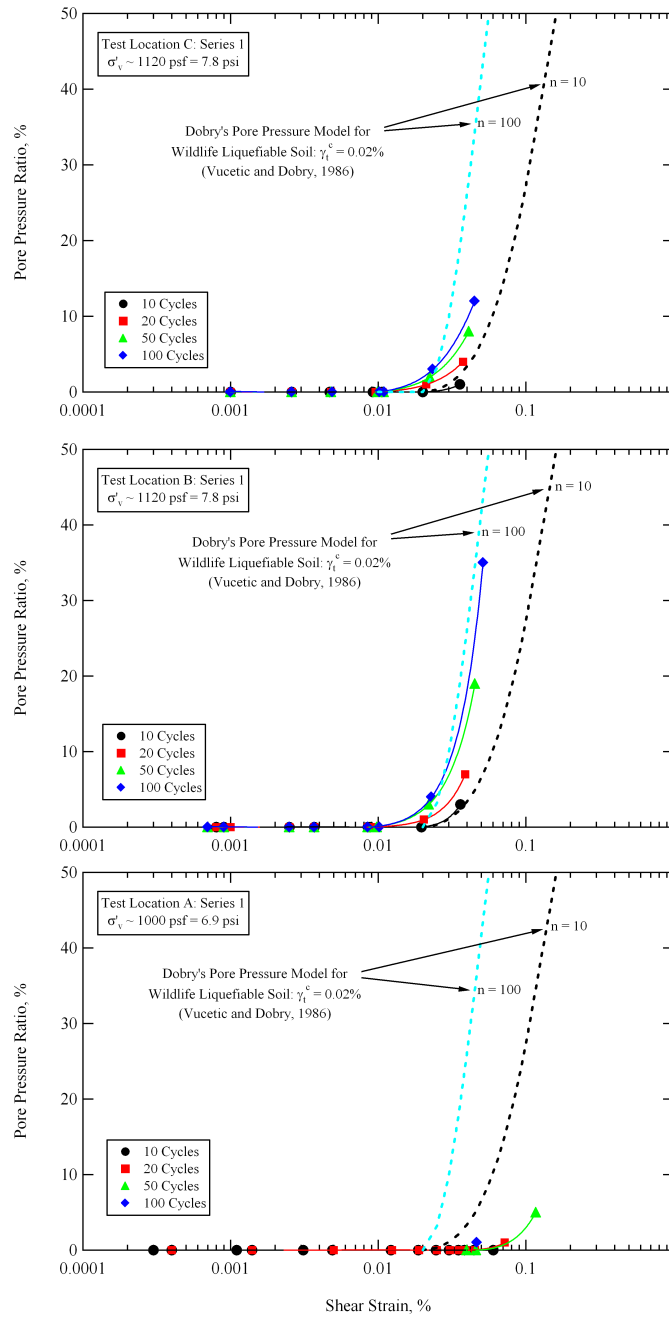


Figure 11-3 Comparison between Dobry's pore pressure generation model (Vucetic and Dobry, 1986) and the pore pressure generation curves obtained from staged loading Series 1 in-situ liquefaction tests at Test Locations C, B and A, Wildlife Liquefaction Array.

pressure ratios. The Series 1 in-situ test results obtained at Test Location A do not resemble Dobry's model and indicate minimal pore pressure generation at significant levels of induced shear strain.

11.2.2 Pore Pressure Responses During Series 2 at Each Test Location

The 10-, 20-, 50- and 100-cycle pore pressure generation curves obtained from staged loading Series 2 in-situ liquefaction tests conducted at Test Locations A, B and C are shown in Figure 11-4. Note that in this figure, the pore pressure response at Test Location C is presented in the top graph, while the pore pressure response at Test Location A is presented in the bottom graph. The pore pressure generation responses measured during Series 2 at Test Locations C and B are similar. The results from Test Location C indicate that the cyclic threshold shear strain (γ_t^e) ranges from approximately 0.015% for $n = 100$ to 0.025% for $n = 10$. These values are slightly greater than the cyclic threshold shear strains determined at Test Location C during staged loading Series 1 (see Sections 11.2.1 and 8.5), indicating that the deposit was likely densified somewhat by the first series of dynamic loading. The results from Test Location B indicate that the cyclic threshold shear strain ranges from approximately 0.01% for $n = 100$ to 0.02% for $n = 10$. These values are identical to the cyclic threshold shear strains determined at Test Location B during staged loading Series 1 (see Sections 11.2.1 and 9.5). Once again, the pore pressure generation response at Test Location A is very different than that at Test Locations C and B. Excess pore pressures generated at the center of the array after 10 cycles of loading ($n = 10$) were not large enough to develop a pore pressure ratio greater than 1% during any of the staged loads. The

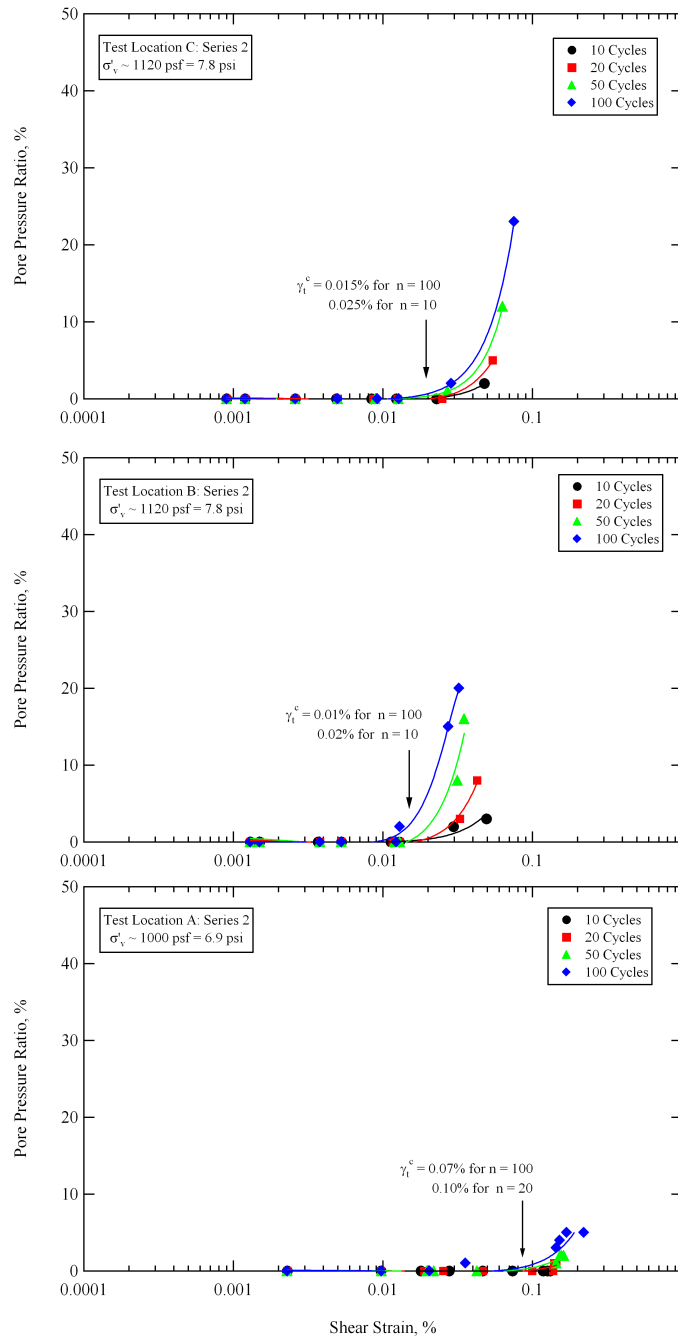


Figure 11-4 Comparison of the pore pressure generation curves obtained from staged loading Series 2 in-situ liquefaction tests at Test Locations C, B and A, Wildlife Liquefaction Array (WLA).

cyclic threshold shear strain ranges from approximately 0.07% for $n = 100$ to 0.1% for $n = 20$. These values are slightly greater than the cyclic threshold shear strains determined at Test Location A during staged loading Series 1 (see Sections 11.2.1 and 10.5), indicating that the deposit may have been densified somewhat by the first series of dynamic loading.

The 10-, 20-, 50- and 100-cycle in-situ pore pressure generation curves obtained from staged loading Series 2 at Test Locations A, B and C are compared with Dobry's pore pressure generation model for liquefiable soils from the Wildlife Site (Vucetic and Dobry, 1986) in Figure 11-5. The cyclic threshold shear strain value assumed in the model (0.02%) is close to the $n = 10$ cyclic threshold shear strain determined at Test Location C during Series 2 (0.025%) and equivalent to the $n = 10$ cyclic threshold shear strain determined at Test Location B during Series 2. The cyclic threshold shear strains at Test Location A are significantly larger.

The Series 2 in-situ results obtained at Test Location C indicate slightly lower pore pressure ratios for a given shear strain level and number of loading cycles than Dobry's model. However, the differences are fairly minor. The trends in pore pressure generation for the Series 2 in-situ results at Test Location B generally fall within the range predicted by Dobry's model, with the exception of the 100-cycle curve, which indicates higher pore pressure ratios for a given shear strain level and number of loading cycles. The Series 2 in-situ test results obtained at Test Location A do not resemble Dobry's model and indicate minimal pore pressure generation at significant levels of induced shear strain.

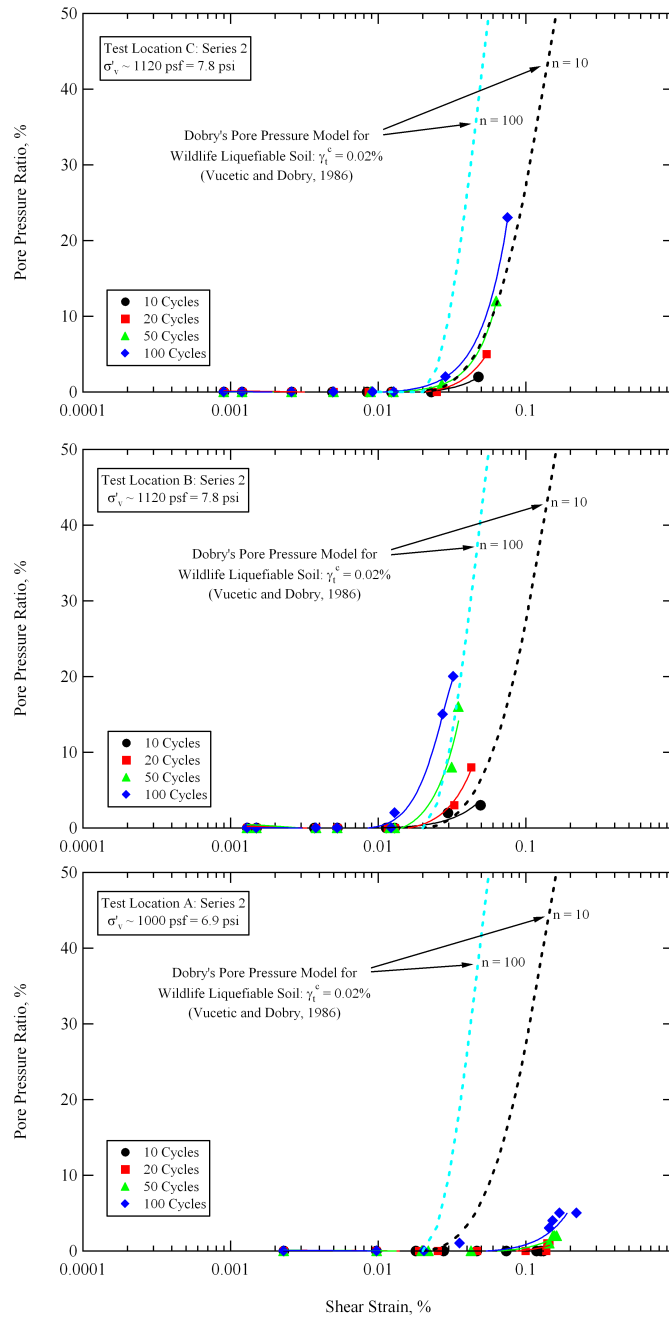


Figure 11-5 Comparison between Dobry's pore pressure generation model (Vucetic and Dobry, 1986) and the pore pressure generation curves obtained from staged loading Series 2 in-situ liquefaction tests at Test Locations C, B and A, Wildlife Liquefaction Array.

11.2.3 Generalized Pore Pressure Responses at Each Test Location

In general, the pore pressure generation curves determined at Test Locations B and C are very similar and agree well with a pore pressure generation model developed for the liquefiable Wildlife Site soils (Vucetic and Dobry, 1986). However, the in-situ pore pressure generation curves determined at Test Location A are quite different from those determined at Test Locations B and C. The pore pressure generation data collected at Test Location A show: (1) higher threshold shear strains, and (2) significantly lower pore pressure ratios for various numbers of loading cycles than expected at a given shear strain amplitude. It is hypothesized that the lower saturation level of the upper-portion of the liquefiable soil deposit in the vicinity of Test Location A (as discussed in Section 10.2.1.1) retarded the generation of excess pore water pressure at this location. Evidence to support this hypothesis is presented below.

11.3 GENERAL SITE COMPARISON

The liquefaction sensor arrays at all three test locations were installed in precisely the same manner. The procedures used to saturate and install the sensors are discussed in Chapter 5. It is therefore unlikely that the sensor saturation or installation procedures had anything to do with the atypical pore pressure generation response measured at Test Location A. Additionally, the pore water pressure transducers were calibrated before and after conducting tests at each location and were found have consistent results in all instances (see Section 4.2.2). The staged dynamic loads were also carried out in a similar manner at all three test locations. Thus, the different pore pressure generation responses

between Test Locations B and C (typical) and Test Location A (atypical) must be attributed to local site conditions.

The in-situ liquefaction sensor arrays at Test Locations B and C were installed in the depth range of 11 to 13 ft (3.3 to 4.0 m), while the sensor array at Test Location A was installed in the depth range of 10 to 12 ft (3.0 to 3.6 m). The positions of the liquefaction sensor arrays, relative to the generalized soil profile at the site, are shown in Figure 11-6. The uppermost soil layer is an 8.2-ft (2.5-m) thick silt to clayey-silt bed that overlies a 14.1-ft (4.3-m) thick silty-sand layer. Beneath these floodplain deposits is a stiff, 17.1-ft (5.2-m) thick clay to silty-clay layer (Bennett et al., 1984).

11.3.1 Fines Contents at Each Test Location

The top of the liquefaction sensor array at Test Location A was approximately 2 ft (0.6 m) below the top of the liquefiable silty-sand layer. The top of the liquefaction sensor arrays at Test Locations B and C were approximately 3 ft (0.9 m) below the top of the liquefiable silty-sand layer. It has already been shown that the 1982 WLA Site and the 2004 WLA Site have nearly identical soil profiles (see Section 7.6). The fines content of the liquefiable silty-sand (SM) generally increases from the bottom to the top of the layer. Soil particle size data collected from various researchers (see Chapter 7) who conducted laboratory tests on soils from both the 1982 and 2004 WLA Sites indicates that the soil in the depth range of 10 – 12 ft (Test Location A) has average fines contents and clay-sized ($5\ \mu\text{m}$) particle contents of 42% and 11%, respectively. The same data set indicates that the soil in the depth range of 11 –

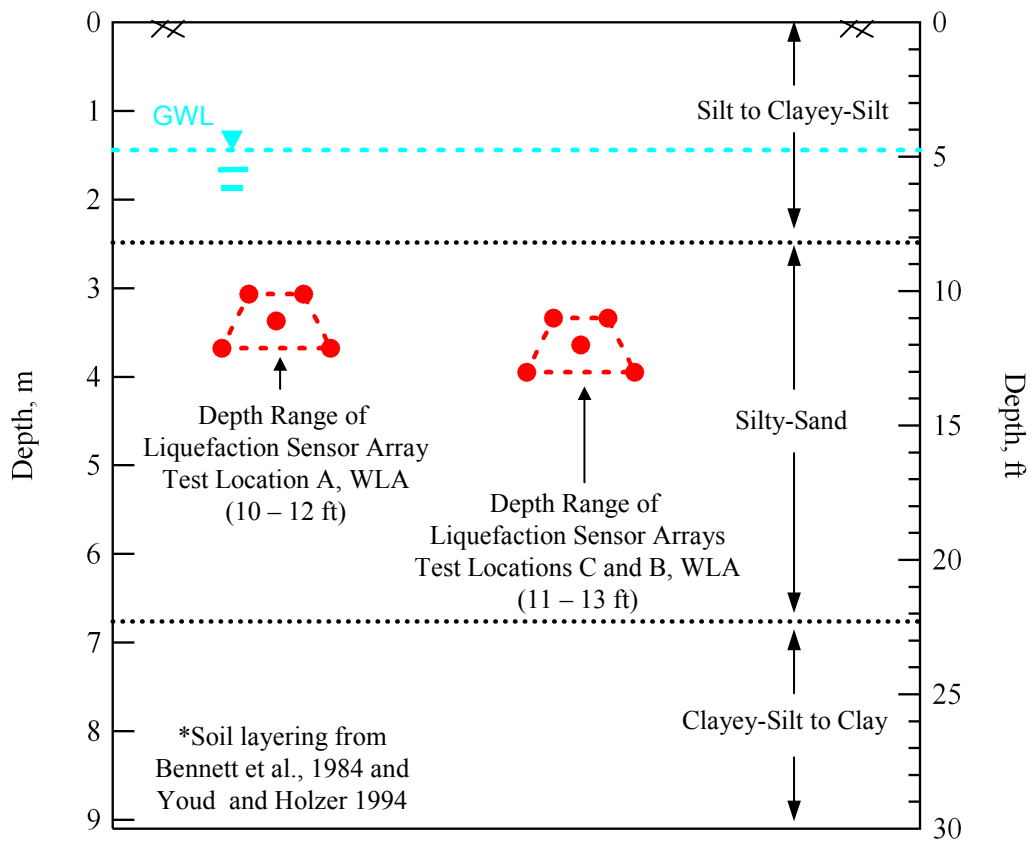


Figure 11-6 Depth ranges of the liquefaction sensor arrays at Test Locations A, B and C, shown with respect to the general soil layering at the Wildlife Site, as proposed by Bennett et al. (1984).

13 ft (Test Locations B and C) has average fines contents and clay-sized ($5 \mu\text{m}$) particle contents of 33% and 10%, respectively. None of these fines were found to be plastic in nature. These minor differences in fines content cannot be the reason for the drastic difference in pore pressure generation behavior between Test Location A and Test Locations B and C.

11.3.2 CPT Sounding at Each Test Location

The liquefaction sensor arrays at each test location were purposely placed near CPT soundings that had previously been conducted at the site. Test Location A was positioned close to CPT 43, Test Location B was positioned close to CPT 5Cg, and Test Location C was positioned close to CPT 47. The CPT tip resistance (q_c) and friction ratio (F_r) values for each of these three soundings are plotted together in Figure 11-7. The boundaries of the liquefiable soil layer proposed by Bennett et al. (1984) and the depth range containing all three liquefaction sensor arrays (10 to 13 ft or 3.0 to 4.0 m) are also identified in this figure. In general, the liquefiable soil layer is marked by relatively large values of CPT tip resistance and relatively small values of CPT friction ratio in comparison to the layer above it. The CPT soundings at all three locations are very similar. CPT 43 (near Test Location A) indicates somewhat higher tip resistances than the other two soundings in the depth range of 10 to 12 ft (3.0 to 3.6 m). However, these differences are minor, as the tip resistances from all three soundings are generally less than 104 ksf (5 MPa) in this depth range. These three CPT soundings indicate that the soil in the depth range and vicinity of each liquefaction sensor array is very similar.

Proctor (2004) performed liquefaction analyses using the simplified CPT procedure (Youd et al., 2001) for all of the CPT soundings at both the 1982 WLA Site and the 2004 WLA Site. For a moment magnitude 6.5 earthquake and a peak ground surface acceleration of 0.3 g, the results from Proctor (2004) indicate that the average factors of safety against liquefaction in the depth range of 10 to 13 ft

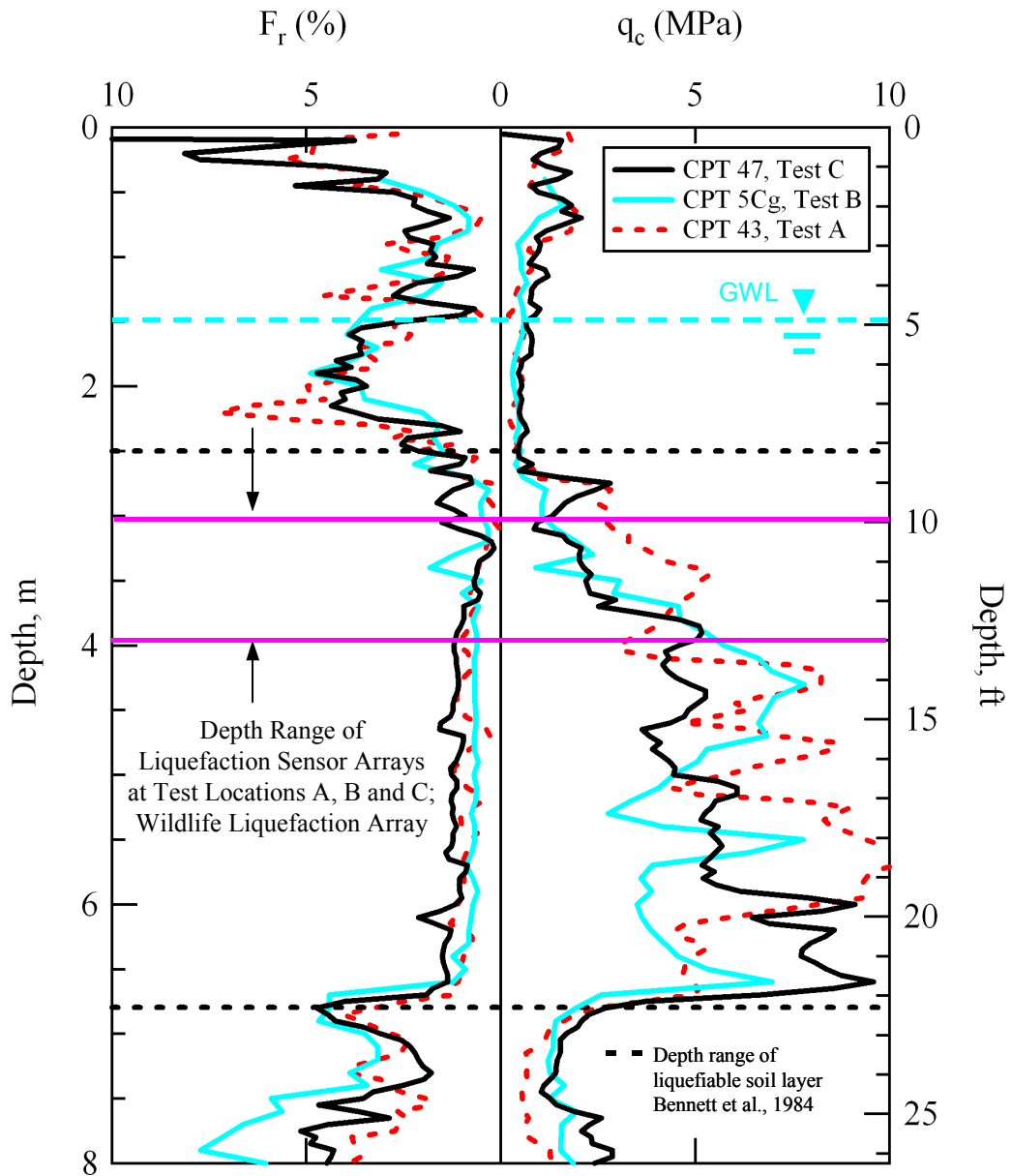


Figure 11-7 Depth range of the liquefaction sensor arrays at Test Locations A, B and C, shown with respect to the tip resistance (q_c) and friction ratio (F_r) values obtained from the closest CPT sounding at each test location, and the upper and lower liquefiable soil layers proposed by Bennett et al. (1984) (raw CPT data from <http://nees.ucsb.edu>).

(3.0 to 4.0 m) for CPT 47, CPT 5Cg and CPT 43 are 0.57, 0.58 and 0.63, respectively. Furthermore, Proctor (2004) found that in general, the soil between the depths of 8.2 ft (2.5 m) and 23.0 ft (7.0 m) is predicted as susceptible to liquefaction.

11.3.3 Crosshole Results at Each Test Location

Crosshole seismic tests were conducted between liquefaction sensors at each test location to verify saturation (P-wave velocity measurements) and determine the small-strain shear stiffness (shear wave velocity measurements) of the liquefiable soil. Details regarding the crosshole tests conducted at Test Locations A, B and C are found in Sections 10.2.1, 9.2.1 and 8.2.1, respectively. The baseline shear wave and P-wave velocities obtained at each test location are shown in Figure 11-8. Crosshole measurements were made between each pair of liquefaction sensors at the same depth in the array. Therefore, in Figure 11-8, velocities are shown at the top and bottom of the depth range covered by each liquefaction sensor array. The crosshole shear wave velocities indicate that the velocity of the soil between the shallower pair of sensors is generally 50 to 100 fps (15 to 30 m/sec) less than the velocity of the soil between the deeper pair of sensors at each test location. The trend of increasing shear wave velocity with depth over the depth range of the liquefaction sensor arrays is in agreement with the trend of increasing CPT tip resistance with depth over the same depth range. The shear wave velocities at Test Location A fall within the same range as the shear wave velocities at Test Locations B and C, indicating that the small-strain shear stiffness of the soil at all three locations is very similar.

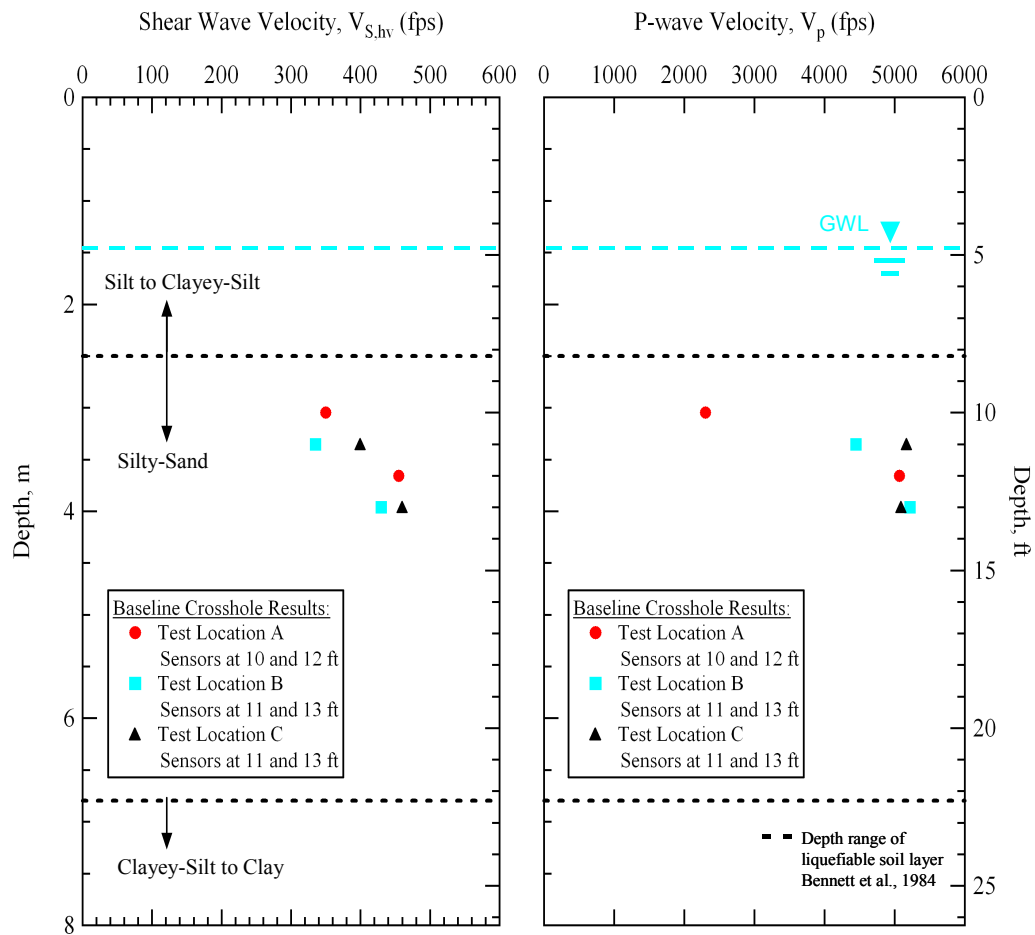


Figure 11-8 Comparison between shear wave and P-wave velocities obtained from performing crosshole tests between in-situ liquefaction sensors in the arrays installed at Test Locations A, B and C, Wildlife Liquefaction Array (WLA).

The raw shear wave velocities shown in Figure 11-8 range between approximately 350 and 450 fps (107 and 137 m/sec). These velocities equate to stress-corrected shear wave velocities (V_{s1}) of approximately 425 and 525 fps (130 and 160 m/sec), respectively (Andrus and Stokoe, 2000). Stress-corrected shear wave velocities in this range indicate that any cyclic stress ratio greater than

approximately 0.1 would be expected to liquefy the material given a moment magnitude 7.5 earthquake (see Figure 2-4). If a moment magnitude 6.5 earthquake and a peak ground surface acceleration of 0.3 g is assumed (similar to what Proctor (2004) used for the CPT analyses noted in Section 11.3.2), according to the simplified shear wave velocity procedure (Andrus and Stokoe, 2000) the average factor of safety against liquefaction in the depth range of 10 to 13 ft (3.0 to 4.0 m) is approximately 0.5.

The P-wave velocities between the deeper sensors at Test Locations A and B, and the deeper and shallower sensors at Test Location C, are greater than 5000 fps (1500 m/sec). As discussed in Section 2.3.1, fully saturated soil is generally considered to have a P-wave velocity of approximately 5000 fps. The P-wave velocity between the top sensors at Test Location B is approximately 4500 fps (1370 m/sec). While not greater than 5000 fps, this value indicates a material that is very close to complete saturation. Laboratory test results from Valle-Molina (2006) indicate that a V_p value of 4500 fps equates to a B value of approximately 0.92 and a saturation level greater than 99.9%. Laboratory test results from Ishihara et al. (2001) indicate that a V_p value of 4500 fps equates to a B value of approximately 0.9. The P-wave velocity of the soil in the shallower depth range (10 ft or 3 m) at Test Location A is equal to 2300 fps (700 m/sec). Laboratory test results from Valle-Molina (2006) indicate that a V_p value of 2300 fps equates to a B value of approximately 0.72 and a saturation level of approximately 99.8%. Laboratory test results from Ishihara et al. (2001) indicate that a V_p value of 2300

fps equates to a B value of approximately 0.6 and a saturation level of approximately 99.3%.

A separate set of crosshole tests were performed near Test Location A more than a week after the dynamic liquefaction tests had been completed and the sensors had been removed from the ground (as discussed in Section 10.2.1.1). The tests were conducted at a location approximately 6 ft (1.8 m) south of where the liquefaction sensor array was installed. P-wave velocity measurements were made between the depths of 3.5 to 12 ft (1.1 to 4.0 m) at 0.5 ft (0.15 m) increments. P-wave velocities in the liquefiable silty-sand layer ranged between 2300 fps (700 m/sec) and 3500 fps (1065 m/sec) between the depth range of approximately 8 to 10 ft (2.4 to 3.0 m). P-wave velocities of 2300 fps and 3500 fps correspond to B values of approximately 0.72 and 0.82, respectively, according to Valle-Molina (2006), and approximately 0.6 and 0.78, respectively, according to Ishihara et al. (2001). The P-wave velocity of the silty-sand between 10 ft (3 m) and 12 ft (3.6 m) varied between approximately 4200 fps (1280 m/sec) and 4600 (1400 m/sec), indicating B values of 0.9 or greater and a saturation level of 99.9%. This separate set of crosshole tests confirmed that the silty-sand material between the depths of approximately 8 to 10 ft (2.4 to 3 m) in the vicinity of Test Location A was not fully saturated.

Separate crosshole tests were not conducted at Test Locations B and C to determine at P-wave velocity profile near each test location. Therefore, it cannot be said for certain that the silty-sand material at shallower depths than the sensor arrays at these two test locations was fully saturated. However, the P-wave

velocities obtained between the liquefaction sensors at these locations indicated the material was either fully saturated, or very close to being saturated (> 99.9%). Additionally, the pore pressure generation responses measured at both of these locations were consistent with each other, and also in-line with the behavior measured in laboratory tests on fully saturated specimens. The pore pressure generation behavior recorded at Test Location A is uncharacteristic of a fully saturated material, and no other differences between the three test locations can be identified. Therefore, it is hypothesized that the lower saturation level of the upper-portion of the liquefiable soil deposit in the vicinity of Test Location A retarded the generation of excess pore water pressure during testing. These findings emphasize the importance of making P-wave velocity measurements in potentially liquefiable soil deposits to verify their saturation.

11.4 SUMMARY

Three separate in-situ dynamic liquefaction tests were conducted at the Wildlife Liquefaction Array (WLA) between August 8 and August 19, 2005. The three locations where these tests were conducted are referred to as Test Location A, Test Location B, and Test Location C. In this chapter, the pore pressure generation curves that were obtained from performing in-situ liquefaction tests at each location were compared and discussed. In overall terms, the pore pressure generation curves obtained at Test Locations B and C are very similar and generally agree well with a pore pressure generation model developed for liquefiable soils from the Wildlife Site (Vucetic and Dobry, 1986).

The pore pressure generation curves obtained at Test Location A do not agree well with the in-situ curves obtained at Test Locations B and C. In general, the pore pressure generation data collected at Test Location A indicates higher threshold shear strains and significantly lower pore pressure ratios than expected for a given number of cycles at a given shear strain amplitude. The liquefaction sensor arrays at all three test locations were installed in precisely the same manner. It is therefore unlikely that the sensor saturation or installation procedures had anything to do with the varied pore pressure generation response measured at Test Location A. The staged dynamic loads were also carried out in a similar manner at all three test locations. Thus, the different pore pressure generation responses between Test Locations B and C (typical) and Test Location A (atypical) must be attributed to local site conditions.

The soil layering, fines contents, and shear wave velocities at each test location are very similar. However, crosshole P-wave velocity measurements at Test Location A indicate that the soil in the depth range of the upper two sensors in the array (approximately 10 ft or 3 m) was not saturated during testing. It is hypothesized that the odd pore pressure generation behavior at Test Location A was caused by partially saturated soil in the upper-portion of the liquefiable silty-sand layer. These findings emphasize the importance of making P-wave velocity measurements in potentially liquefiable soil deposits to verify their saturation.

Chapter 12

Summary, Conclusions, Recommendations and Future Work

12.1 SUMMARY

Earthquake-induced soil liquefaction can cause untold amounts of damage. Diverse problems include differential settlements and bearing capacity failures of buildings, movements and failures of earth dams, lateral spreads and landslides, and floatation of buried pipes and tanks (Dobry et al., 1982). Since all of these failures result in the loss of money, and potentially lives, predicting the risk of earthquake-induced soil liquefaction is one of the most important tasks with which a geotechnical engineer is faced when working in seismically active regions.

The state of the practice for evaluating the susceptibility of soil deposits to liquefaction is centered around simplified procedures based either on direct measurements of pore pressure generation in cyclic laboratory tests (Dobry et al., 1982) or indirect empirical correlations derived from various in-situ tests (Youd et al., 2001). Unfortunately, these procedures have disadvantages related to their indirect nature when empiricism is used, and sample disturbance when laboratory testing is involved (discussed in Chapter 2). A much more robust approach to the problem of evaluating liquefaction susceptibility would involve directly measuring the pore pressure generation characteristics of the soil in situ.

During an earthquake, the generation of excess pore water pressure in a soil mass is a direct function of the level of cyclic shear strain induced in the soil (Dobry et al., 1982; Vucetic and Dobry, 1986). Therefore, the ability to evaluate the potential of a soil to strain, and hence build up excess pore pressure, is of great importance. However, at this time, no active field test methods are available to the earthquake engineering profession that can be used to determine directly the liquefaction resistance (i.e. excess pore pressure generation as a function of induced cyclic shear strain) of soil deposits in situ. A few passive in-situ measurements of both dynamic response and pore pressure generation have been reported (Ishihara et al., 1981; Ishihara et al., 1989; Shen et al., 1991; Holzer et al., 1989; Youd and Holzer, 1994). In these studies classified as passive measurements, instrumentation was installed and researchers waited for an earthquake to load the site. Surface and downhole accelerometers were used to monitor the ground response and pressure transducers were utilized to measure pore water pressure generation. Although these measurements are the ultimate field investigation of liquefaction, they have several key limitations. These limitations include: (1) the unknown recurrence of earthquakes (hence, potentially decades of waiting), (2) durability of the sensors after long waiting periods, (3) the limited amount of sensing points in the liquefiable layer, resulting in a lack of resolution both vertically and globally across the site, and (4) the inability to perform parametric studies. Hence, the need to develop a direct, active, field test method to evaluate liquefaction resistance.

12.1.1 Development of a Direct In-Situ Liquefaction Test

This dissertation has presented work conducted by researchers from the University of Texas at Austin (UT) aimed toward the development and implementation of a new in-situ liquefaction testing technique. This technique is an active method that may be used to directly evaluate the liquefaction resistance of soils in place. The test is based on the premise of dynamically loading a native soil deposit in a manner similar to an earthquake while simultaneously measuring its response with embedded instrumentation (see Figure 8-4). Dynamic loading is performed via a large, truck-mounted hydraulic shaker (vibroiseis) that is used to excite the ground surface and generate stress waves of varying amplitudes within an instrumented portion of the soil mass. The embedded sensors consist of instrumentation to measure the coupled response of soil particle motion and pore water pressure generation.

Work on this new in-situ liquefaction test is currently in its second stage of development. In the first stage, liquefaction of a large-scale, reconstituted, test specimen was successfully accomplished in the field (Chang, 2002; Rathje et al., 2004). Building on the success of the first-generation testing, it was desired to advance the technique to a second-generation level by enabling testing of native soil deposits at greater depths using vertically propagating shear waves to strain the soil (discussed in Chapter 3). The development of the second-generation testing equipment (discussed in Chapter 4), field testing technique (discussed in Chapter 5) and data analysis procedures (discussed in Chapter 6) have been presented in this dissertation.

12.2 CONCLUSIONS

The validity of this new test method has been demonstrated in this research. The validation was accomplished by conducting field experiments at the Wildlife Liquefaction Array (WLA) in Imperial Valley, California. The WLA has been intensely studied over the past 25 years (Bennett et al., 1984; Bierschwale and Stokoe, 1984; Hagg and Stokoe, 1985; Vucetic and Dobry, 1986; Youd and Bartlett, 1988; Holzer et al., 1989; Dobry et al., 1992; Youd and Holzer, 1994; Zeghal and Elgamal, 1994). It has also recently been designated as a Network for Earthquake Engineering Simulation (NEES) site for the study of soil liquefaction (<http://nees.ucsb.edu>). The extensive site characterization, the documented occurrence of earthquake-induced soil liquefaction at the site twice in the 1980's (1981, $M_w = 5.9$ Westmorland earthquake; and 1987, $M_w = 6.6$ Superstition Hills earthquake) and the likelihood for re-liquefaction of the site during subsequent earthquakes made the WLA an ideal location for verifying the proposed in-situ dynamic liquefaction test method (discussed in Chapter 7).

12.2.1 In-Situ Test Results

In-situ liquefaction tests were carried out at three separate locations at the WLA. These test locations are referred to as Test Location A, Test Location B and Test Location C. The sites are named in the order of testing with Test Location A tested first. At Test Location C, the last site to be tested and the site with the most complete data set, in-situ liquefaction tests were successful at measuring excess pore water pressure generation and nonlinear shear modulus behavior in the WLA native silty-sand deposit as a function of induced cyclic

shear strain and number of loading cycles. These results are compared to pore pressure generation curves and nonlinear shear modulus curves previously developed for WLA soils from laboratory testing methods (discussed in Chapter 8). At Test Locations B and A (discussed in Chapters 9 and 10, respectively), in-situ liquefaction tests were successful at measuring excess pore water pressure generation in the native silty-sand deposits as a function of induced cyclic shear strain and number of loading cycles. These results are compared to pore pressure generation curves previously developed for WLA soils from laboratory testing methods. The nonlinear shear modulus behavior of the soil within the liquefaction sensor arrays at Test Locations A and B could not accurately be resolved due to harmonic distortion and small amounts of noise in some of the raw accelerometer records. It is believed that testing at higher frequencies would help resolve this problem (see Section 12.2).

12.2.1.1 Pore Water Pressure Generation

The in-situ pore pressure generation curves obtained at Test Locations B and C are very similar and generally agree well with a pore pressure generation model developed for liquefiable Wildlife Site soils (Vucetic and Dobry, 1986). The test results from both sites indicate a cyclic threshold shear strain for the soil of approximately 0.02%. The threshold shear strain was found to be slightly dependent on the number of loading cycles, with larger numbers of loading cycles inducing pore pressure generation at smaller shear strains. The pore pressure generation response measured at Test Location A does not agree well with the in-situ curves obtained at Test Locations B and C (discussed in Chapter 11). In

general the pore pressure generation data collected at Test Location A indicates a higher threshold shear strain and significantly lower pore pressure ratios than expected for a given shear strain amplitude and number of loading cycles.

The liquefaction sensor arrays at all three test locations were installed in precisely the same manner. It is therefore unlikely that the sensor saturation or installation process had anything to do with the varied pore pressure generation response measured at Test Location A. The staged dynamic loads were also carried out in a similar manner at all three test locations. Thus, the different pore pressure generation responses between Test Locations B and C (typical) and Test Location A (atypical) must be attributed to local site conditions. The soil layering, fines contents, and shear wave velocities at each test location are very similar. However, crosshole P-wave velocity measurements at Test Location A (discussed in Section 10.2.1) indicate that the soil in the depth range of the upper two sensors (approximately 10 ft or 3 m) was not saturated during testing. It is hypothesized that the odd pore pressure generation behavior at Test Location A was caused by partially saturated soil in the upper-portion of the liquefiable silty-sand layer. These findings emphasize the importance of making P-wave velocity measurements in potentially liquefiable soil deposits to verify their saturation.

12.2.1.2 Nonlinear Shear Modulus

As noted above, the nonlinear shear modulus behavior of the silty-sand was successfully measured at Test Location C. The in-situ nonlinear shear modulus behavior was found to generally agree well with an upper-bound range of modulus reduction curves determined from resonant column tests on

liquefiable soil from the Wildlife Site (Haag and Stokoe, 1985). However, these resonant column tests were conducted at higher mean confining pressures than the in-situ tests. It therefore appears, that the in-situ shear modulus behavior is more linear than predicted from laboratory tests on specimens at equivalent confining pressures. Shear modulus reduction due to the combined effects of nonlinearity and degradation due to pore water pressure generation were observed in the in-situ moduli once the cyclic threshold strain of the soil deposit was exceeded and pore pressure ratios of approximately 5% were induced at the center of the liquefaction sensor array. Minimal modulus degradation was observed at pore pressure ratios less than 5%.

12.2.2 Summary of Significant Accomplishments

As a result of this research, several significant, new accomplishments were made. First, a new in-situ liquefaction sensor was designed and constructed that couples the ability to measure dynamic soil particle motions and pore water pressures (see Section 4.2). The sensor is lightweight and compact. It can be pushed into position from the ground surface, decoupled from the push-rods, and extracted from the ground at the end of testing. The sensor design can be duplicated and/or improved by other researchers if needed. Second, a field testing technique for conducting in-situ liquefaction tests has been established (see Chapter 5). The field testing technique includes a sensor installation procedure (including an optimum array configuration), an effective staged dynamic loading sequence, and a sensor extraction procedure. Third, data analysis techniques for calculating induced cyclic shear strains, excess pore water pressure ratios, and

nonlinear shear moduli within the instrumented soil mass during in-situ liquefaction tests have been developed and refined (see Chapter 6).

These new developments enabled, for the first time, pore pressure generation measurements as a function of induced cyclic shear strain and number of loading cycles in native soil deposits using an active test method. These measurements allowed for in-situ determination of the cyclic threshold shear strains of native soil deposits, as well as the tendency for pore pressure generation once shear strains greater than the cyclic threshold shear strain had been induced in the instrumented soil mass. Also, for the first time, the in-situ nonlinear shear modulus behavior of a liquefiable soil deposit was quantified in terms of induced shear strain magnitude and number of loading cycles using an active test method. These measurements indicated that no noticeable shear modulus degradation due to increased number of loading cycles and pore water pressure generation occurred in the soil until a pore pressure ratio of approximately 5% had been generated. It therefore seems reasonable, that a cyclic threshold shear strain of engineering significance for liquefaction studies should be established as the shear strain level that induces a pore pressure ratio of 5%, rather than 0%. This definition will also allow different cyclic threshold shear strains to be established for different numbers of loading cycles.

The importance of making compression wave velocity (V_p) measurements during in-situ liquefaction studies has also been demonstrated. V_p measurements can be used to establish the degree of saturation at potential liquefaction test sites. It has been shown that the in-situ degree of saturation has a strong influence on

both the cyclic threshold shear strain and the subsequent magnitude of excess pore water pressure generation (see Chapter 11). Pore pressure generation in native soils with saturation levels (estimated from V_p measurements) of less than 99.8% may be retarded substantially.

These accomplishments, including the successful in-situ measurement of excess pore water pressure generation and nonlinear shear modulus behavior in native soil deposits as a function of induced cyclic shear strain and number of loading cycles, represent a large step forward in the ability to accurately evaluate the susceptibility of a soil deposit to earthquake-induced liquefaction.

12.3 RECOMMENDATIONS

Recommendations regarding various aspects of the in-situ dynamic liquefaction test are presented below. The comments are generally presented in a similar order to the chapter-by-chapter organization of this dissertation.

12.3.1 In-Situ Liquefaction Sensors

Chapter 4 of this dissertation should be consulted for details regarding some of the points discussed below.

The liquefaction sensors designed and built for this research are composed of a sealed, miniature pore water pressure transducer (PPT) and a three-component (3D) Micro-Electrical Mechanical Systems (MEMS) accelerometer. The liquefaction sensors performed very well during in-situ testing. However, as discussed below, some modifications to the sensors may be desirable.

12.3.1.1 Pore Pressure Transducers (PPT's)

The miniature PPT's are used to monitor the dynamic response of the pore water at the same location where dynamic soil particle motions are recorded with the MEMS accelerometers. However, accurate static water pressure readings can not be made with the miniature PPT's due to problems associated with static drift and shifting zero offset values when the transducers are re-powered. Therefore, a larger, more stable Druck model PDCR 35/D pore pressure transducer was inserted at the center of the liquefaction sensor array and used as a reference standard for both static and dynamic pressure readings.

The PDCR 35/D performed extremely well during field testing. The static pressure measurements made with it were nearly identical to ground water level readings obtained from standpipes. This accuracy allowed the excess pore water pressures generated during testing to be tracked to ensure that they had dissipated prior to continuing staged dynamic loading. Additionally, dynamic calibrations on the PDCR 35/D indicate a more stable dynamic response than the miniature PPT's installed in the individual liquefaction sensors. As a result, the miniature PPT's in each liquefaction sensor were only used in a qualitative sense to observe the general variation of excess pore water pressure generation within the instrumented soil mass.

Data collected from the miniature PPT's during field testing indicated a much larger variation in pore pressure response than expected for measurements recorded over such a small region. This information is valuable. However, the cost-benefit of installing a miniature PPT in each liquefaction sensor will need to

be addressed for future testing needs. The Entran model EPX VO2 miniature PPT's cost approximately \$450 a piece. The Druck model PDCR 35/D costs approximately \$650. It may be more beneficial to not include miniature PPT's in future liquefaction sensors, but rather purchase several more PDCR 35/D's and install them at various locations outside the extent of the base plate loading area. This arrangement would help to accurately quantify the pore pressure generation on a larger scale. As discussed previously, to an unknown extent, the pore pressures being generated over a finite loaded area during in-situ liquefaction tests are simultaneously redistributing inside of, and dissipating away from, the loaded area. It is not currently known how large an area is being influenced by dynamic loading. Placing several other PDCR 35/D's within and outside of the loading area would lend insight into the problem of simultaneous pore pressure generation and dissipation.

12.3.1.2 MEMS Accelerometers

The MEMS accelerometer that was ultimately selected for use in the in-situ liquefaction sensors is a Silicon Designs model 2430-002. MEMS accelerometers were chosen for the vibration-sensing component of the liquefaction sensor because of: (1) their compact size, (2) their high output at low frequencies of vibration, (3) their ability to track tilt of the sensor as it is pushed into place, and (4) their ability to monitor any tilt of the sensor that might occur during liquefaction testing. The MEMS accelerometers performed very well during dynamic in-situ liquefaction field testing. Their ability to track tilt of the sensors proved very useful. Incremental tilt readings were not made during

sensor installation due to practical considerations with the sensor saturation and installations process (see Section 4.2.1.1). However, tilt readings taken once the sensors reached their final positions during field testing generally showed that the sensors had been installed with less than two degrees of tilt (often times with less than one degree of tilt). This information assured that the sensors had deviated very little during installation and that the distances between sensors measured at the ground surface were representative of the distances between sensors at depth. Additional readings taken following significant pore pressure generation during dynamic testing indicated changes in the tilt of the sensors of only a few tenths of a degree. This information could not have been gathered from other vibration-sensing devices.

Even though the MEMS accelerometers worked well, they are fairly sensitive devices that may not hold up to extended use in tough field testing conditions. They are fairly susceptible to damage caused by electrostatic discharge (ESD) and general over-voltage supply. During field testing, the potential for ESD and over-voltage supply is enhanced because the electrical leads are constantly being handled, connected, and disconnected from the power supply and signal recording equipment. The 2430 MEMS accelerometers are substantially less susceptible to these problems than some other models because they include on-board voltage regulation and an internal voltage reference. Despite this protection, two out of the ten MEMS accelerometers installed inside the current set of liquefaction sensors have experienced problems since their calibration and installation.

The x-component of MEMS accelerometer No. 0664 (installed in liquefaction sensor No. 7; see Table 4-1) has an intermittent problem where it tends to constantly output its full range voltage. If the sensor is tapped on, the component may begin to function properly again, however this does not always produce the desired effect in a timely manner. Additionally, the sensors cannot be tapped on once they are installed in the ground. All three vibration-sensing components of MEMS accelerometer No. 0647 (installed in liquefaction sensor No. 2; see Table 4-1) are completely “fried”. The manufacturer attributes this failure to ESD, which, of course, they accept no responsibility for. These failures, combined with the failures of many of the model 2422 MEMS accelerometers installed in the ten original (out of commission) liquefaction sensors mentioned in Section 4.2.1, have caused serious reflection on the practicality of using MEMS accelerometers in field testing situations. Additionally, 3D-MEMS accelerometers are not cheap. The model 2430’s cost approximately \$1250 a piece. Once again, the cost-benefit of installing MEMS accelerometers in future liquefactions sensors needs to be considered.

Geophones are really the only other option for liquefaction sensor vibration-sensing components. However, without getting into too much detail, geophones with a small enough size to be installed in liquefaction sensors have relatively low outputs at the desired testing frequencies. Additionally, they do not have the ability to provide any information about tilt of the sensor, which is very important anytime sensors are being pushed into position from the ground surface.

12.3.2 In-Situ Liquefaction Test Procedure

Chapter 5 of this dissertation should be consulted for details regarding some of the points discussed below.

The generalized in-situ liquefaction test procedure may be subdivided into three basic categories. The categories are: (1) sensor installation, (2) staged dynamic loading, and (3) sensor extraction. During field testing, the sensor installation and extraction processes went smoothly. However, they are by far the most time consuming portions of the test procedure. It takes approximately one full day to install the liquefaction sensor array and associated crosshole source rods, and approximately one-half of a day to remove the instrumentation from the ground after testing. A complete staged dynamic loading series can be conducted in less than two hours. Improvements to the sensor installation and extraction processes would be greatly beneficial.

12.3.2.1 Sensor Installation and Extraction

The sensor installation and extraction procedures are, by nature, time consuming processes. Installation of the sensors could be expedited slightly by reducing the number of times push rods have to be slipped on and off the sensor cables. Prior to field testing, a slotted section of push rod was constructed to help minimize this problem. However, it was found that the slotted rod (approximately 1.2 ft or 0.36 m long) was not long enough to be used in several applications. A slotted rod least 2.5 ft (0.8 m) in length should be constructed. This would speed sensor installation up slightly. It would also be beneficial if several more 1- and 2-ft (0.3- and 0.6-m) regular rod sections were constructed.

The sensors were extracted from the ground relatively smoothly. After the sensors and rods were removed, it was found that the rubber gasket placed inside the push rod to retard the upward flow of water during excess pore pressure generation performed well. The rod section below the gasket was compacted with liquefiable soil material, while the rod section above the gasket was clean. Ideally, the rubber gasket should be placed as close to the bottom of the rod as possible. Originally, the gasket was design to fit directly above where the aluminum top piece of the liquefaction sensor couples to the push rod. However, when the design of the top piece was changed to allow the wire rope to be removed from the sensor, the gasket no longer would fit in this location. Therefore, it had to be placed at the top of the first section of push rod. Additional time could be devoted to figuring out a way to place the gasket close to the liquefaction sensor.

12.3.2.2 Staged Dynamic Loading

The staged dynamic loading sequence used during field testing worked well. As discussed in previous sections, higher frequencies of vibration (i.e. greater than 20 Hz) should be experimented with in an effort to more accurately resolve the nonlinear soil shear modulus. Harmonic distortion in the recorded ground motions at lower frequencies complicated this procedure greatly. Testing at higher frequencies will have at least two beneficial effects: (1) the output of T-Rex should have less harmonic distortion at higher frequencies, and (2) the shorter wavelengths associated with higher frequencies will reduce the possibility of near-field effects influencing the measured shear wave velocity during dynamic

loading. Tests can be conducted at higher frequencies until a small amount of pore pressure has been generated as the center of the array. At this point, it will likely be necessary to lower the loading frequency to induce maximum shear strains in the deposit. Additionally, the base plate of T-Rex should be horizontally impacted with a sledgehammer (in a manner similar to downhole testing) to obtain a good reference for the small strain, vertically propagating, horizontally polarized shear wave velocity prior to any staged dynamic loading. This was discussed prior to field testing but was not performed. Of course, the proper protective attachment to the base plate would be required so that the hammer blows would not damage it.

12.3.3 Data Analysis Procedures

Chapter 6 of this dissertation should be consulted for details regarding some of the points discussed below.

The raw data recorded during an in-situ dynamic liquefaction test consists of acceleration and pore water pressure time histories generated at each sensor location. The processed data desired from an in-situ dynamic liquefaction test are: (1) induced cyclic shear strain, (2) excess pore water pressure ratio as a function of induced cyclic shear strain and number of loading cycles, and (3) nonlinear shear modulus of the soil as a function of induced cyclic shear strain and change in pore water pressure. Determination of the excess pore water pressure ratio is a relatively straightforward process. Ideas have already been discussed about how improvements to the determination of the nonlinear soil shear modulus procedure can be made. Several aspects related to the evaluation

of the shear strain induced in the soil under the current testing configuration are discussed below.

12.3.3.1 Shear Strain Evaluation

The 4-node, isoparametric finite element strain computation method was the only method used to calculate shear strains for the dynamic in-situ liquefaction test results provided in this dissertation. However, the data collected during in-situ liquefaction tests allow shear strains induced in the instrumented portion of the soil to be calculated in several different ways. Various displacement-based (DB) and wave propagation-based (WB) strain evaluation methods were experimented with to calculate shear strains induced in the instrumented soil mass. These shear strain computation methods were investigated in hopes of determining an accurate method for calculating shear strains that would require less instrumentation to be installed. However, it was determined that shear strain evaluation methods that did not include contributions from vertical particle motions (caused by base plate rocking) tended to under predict the induced shear strains (see Section 6.3.1.3). Therefore, at least four in-situ liquefaction sensors that are capable of sensing vertical and horizontal vibrations need to be installed in an array to accurately evaluate shear strains induced in the soil under the current test configuration. The contribution of the out-of-plane particle motions to shear strains induced in the instrumented soil mass were also considered. It is believed that these contributions are minor (see Section 6.3.1.3).

12.4 FUTURE WORK

The validity of the proposed dynamic in-situ liquefaction test has been demonstrated by conducting field experiments at the Wildlife Liquefaction Array (WLA) in Imperial Valley, California. The tests were successful at measuring: (1) excess pore water pressure generation, and (2) nonlinear shear modulus behavior in the native silty-sand deposits as a function of induced cyclic shear strain and number of loading cycles. To the writers knowledge, this is the first time that pore pressure generation curves and nonlinear shear modulus reduction curves have been simultaneously developed from active in-situ tests.

To further investigate soil saturation and its affect on the measured pore pressure generation response at Test Location A, it would be desirable to determine the lateral extent of the zone of unsaturated material by conducting additional crosshole tests at the WLA site. A set of cased boreholes exist at the 2004 WLA Site (close to Test Location A) where crosshole tests could be performed using a traditional source and receivers. An attempt to conduct crosshole tests in these boreholes was made on the first day of field work at the site in August 2005. However, due to equipment complications, these tests could not be conducted. These boreholes are approximately 15 to 20 ft away from Test Location A, and are close to the majority of the permanently installed pore water pressure transducers at the 2004 site. It would be beneficial to perform crosshole tests in these boreholes to investigate the saturation profile near the permanent instrumentation. This work needs to be done before a future earthquake so that the data can be used to help accurately analyze the soil response recorded by the

permanent pore water pressure transducers and other instrumentation installed at the site.

12.4.1 Potential Applications

The in-situ liquefaction tests conducted at the Wildlife Liquefaction Array were the first of their kind. In-situ liquefaction tests of this nature show great potential and will ultimately have many practical applications. This test method will most certainly be used to directly evaluate the coupled pore pressure response and nonlinear soil behavior of many different types of liquefiable soils under their in-situ conditions (state of stress, saturation level, density, etc...). It will be possible to perform in-situ evaluations on soils with different fines contents, geologic ages, plasticities, and particle sizes (i.e. gravels). The test will be especially useful in evaluating the liquefaction potential of “borderline” sites (i.e. sites that are close to the empirical liquefaction triggering lines using current simplified liquefaction evaluation procedures). Parametric studies to evaluate factors affecting soil liquefaction and the effectiveness of various ground improvement techniques will also be performed with this method. It will also prove useful for evaluating model input parameters for soil liquefaction and general site response analysis programs, as well as for generating data sets to refine and validate current numerical models for predicting pore pressure generation and soil softening due to the combined affects of modulus nonlinearity and degradation. These accomplishments will lead the profession to deformation-based liquefaction analysis. The ability to make in-situ measurements of the pore pressure generation characteristics and nonlinear shear modulus behavior of soils

at the desired time and place provides geotechnical engineers with a powerful new tool for directly evaluating the susceptibility of a soil deposit to earthquake-induced liquefaction.

References

- Andrus, D.R. and Stokoe, K. H., II (2000), "Liquefaction Resistance of Soils from Shear-Wave Velocity," ASCE, *Journal of Geotechnical and Geoenvironmental Engineering*, Vol. 126, No. 11, pp 1015-1025.
- Bartholomew, H.A.J. (2004), "Geotechnical Logs and Data from Permanently Instrumented Sites (GVDA and WLA) Included in the Network for Earthquake Engineering Simulation (NEES) Laboratories," *Masters Project Report*, Brigham Young University, Provo, Utah.
- Bathe, K. -J. (1996) *Finite Element Procedures*, Prentice-Hall, Inc., NJ, 1037 pp.
- Bennett, M.J., McLaughlin, P.V., Sarmiento, J.S. and Youd, T.L. (1984), *Geotechnical Investigation of Liquefaction Sites, Imperial Valley, California, Open File Report 84-252*, Department of the Interior, U.S. Geological Survey, Menlo Park, California.
- Bierschwale, J.G. and Stokoe, K.H., II (1984), *Analytical Evaluation of Liquefaction Potential of Sands Subjected to the 1981 Westmorland Earthquake*, Geotechnical Engineering Report GR 84-15, University of Texas, Austin.
- Chang, W.J. (2002), *Development of an In-Situ Dynamic Liquefaction Test*, Ph.D. Dissertation, The University of Texas at Austin.
- Chaney, R. (1978), "Saturation Effects on the Cyclic Strength of Sands," *Earthquake Engineering and Soil Dynamics*, Vol. 1, pp. 342-358.
- Charlie, W.A., Jacobs, P.J. and Doehring, D.O. (1992), "Blast-Induced Liquefaction of an Alluvial Sand Deposit," *Geotechnical Testing Journal*, Vol. 15, No. 1, pp.14-23.
- Coduto, D.P. (1994), *Foundation Design; Principles and Practices*, Prentice-Hall, Inc., NJ, 796 pp.
- Cook, R.D., Malkus, D.S. and Plesha, M.E. (1989), *Concepts and Applications of Finite Element Analysis, 3rd Edition*, John Wiley and Sons, New York, NY.

- Cox, B.R. (2001), *Shear Wave Velocity Profiles at Sites Liquefied by the 1999 Kocaeli, Turkey Earthquake*, M.S. Thesis, Utah State University, Logan, Utah. 274 p.
- De Alba, P., Chan, C.K. and Seed, H.B. (1975), "Determination of Soil Liquefaction Characteristics by Large-Scale Laboratory Tests," *Report EERC 75-14*, Earthquake Engineering Center, University of California, Berkeley.
- Dobry, R., Ladd, R.S., Yokel, F.Y., Chung, R.M. and Powell, D. (1982), *Prediction of Pore Water Pressure Buildup and Liquefaction of Sands During Earthquakes by the Cyclic Strain Method*, National Bureau of Standards Building Science Series 138, July, 168 p.
- Dobry, R., Elgamal, A.-W., Baziar, M. and Vucetic, M. (1989), "Pore Pressure and Acceleration Response of Wildlife Site During the 1987 Earthquake," *2nd U.S. – Japan Workshop on Soil Liquefaction*, T.D. O'Rourke and M. Hamada, eds. NECEER Report No. 89-0032, Buffalo, N.Y., pp. 145-160.
- Dobry, R., Baziar, M.H., O'Rourke, T.D., Roth, B.L. and Youd, T.L. (1992), "Liquefaction and Ground Failure in the Imperial Valley, Southern California During the 1979, 1981 and 1987 Earthquakes," *Case Studies of Liquefaction and Lifeline Performance During Past Earthquakes*, Vol. 2, Edited by T. O'Rourke and M. Hamada, Feb., Technical Report NCEER-92-0002
- Dunncliff, J. (1988), *Geotechnical Instrumentation for Monitoring Field Performance*, John Wiley & Sons, Inc., New York, 577 pp.
- EERI (2000), "The Izmit (Kocaeli), Turkey Earthquake of August 17, 1999," *Earthquake Spectrum Supplement A*, Vol. 16. No. 4.
- EERI (2001), "The Chi-Chi, Taiwan Earthquake of September 21, 1999," *Earthquake Spectrum Supplement A*, Vol. 17. No. 1.
- Finn, W.D.L., Lee, K.W. and Martin, G.R. (1977), "An Effective Stress Model for Liquefaction," *Journal of the Geotechnical Engineering Division*, ASCE, GT6, pp. 517-533.

- Gohl, W.B., Howie, J.A. and Rea, C. E. (2001), "Use of Controlled Detonation of Explosives for Liquefaction Testing," *Proceedings, 4th Int. Conf. on Recent Advances in Geotechnical Earthquake Geotechnical Engineering and Soil Dynamics a Symposium in Honor of Professor W. D. Liam Finn*, Paper No. 9.13, San Diego, CA, USA, March 26-31.
- Haag, E.D. and Stokoe, K.H., II (1985), *Laboratory Investigation of Static and Dynamic Properties of Sandy Soils Subjected to the 1981 Westmorland Earthquake*, Research Report GR85-11, Geotechnical Engineering Center, University of Texas, Austin.
- Hardin, B. O. (1978), "The Nature of Stress-Strain Behavior of Soil", *Proc. ASCE Specialty Conference on Earthquake Engineering and Soil Dynamics*, ASCE, New York, N.Y., 3-90.
- Holzer, T. L., Youd, T. L. and Hanks, T. C. (1989), "Dynamics of Liquefaction During the Superstition Hills Earthquake (M=6.5) of November 24,1987," *Science*, 244, April 7: 56-59.
- Hushmand, B., Scott, R.F. and Crouse, C.B. (1992) "In-Situ Calibration of USGS Transducers at Wildlife Liquefaction Site, California, USA," *Proc. 10th World Conference on Earthquake Engineering*, A.A. Balkema Publishers, Rotterdam, Netherlands, pp. 1263 – 1268.
- Ishihara, K., Shimizu, K. and Yamada, Y. (1981), "Pore Water Pressure Measured in Sand Deposits During an Earthquake," *Soils and Foundations*, 2(4): 85-100.
- Ishihara, K., Muroi, T. and Towhata, I. (1989), "In-Situ Pore Water Pressure and Ground Motions During the 1987 Chiba-Toho-Oki Earthquake," *Soils and Foundations*, 29(4): 75-90.
- Ishihara, K., Tsuchiya, H., Huang, Y. and Kamada, K. (2001), "Recent Studies on Liquefaction Resistance of Sand - Effect of Saturation," *Proceedings, 4th Int. Conf. on Recent Advances in Geotechnical Earthquake Engineering and Soil Dynamics a Symposium in Honor of Professor W. D. Liam Finn*, Keynote Lecture, San Diego, CA, USA, March 26-31.
- Keane, C.M. and Prevost, J.H. (1989), "An Analysis of Earthquake Data Observed at the Wildlife Liquefaction Array Site, Imperial Valley Country, California," *Proceedings, Second U.S. – Japan Workshop on Liquefaction, Large Ground Deformation, and their Effects on Lifeline Facilities*, Niagara Falls, New York, pp. 176-192.

- Kramer, L. S. (1996), *Geotechnical Earthquake Engineering*, Prentice-Hall, Inc., NJ, 653 pp.
- Ladd, R.S. (1982), *Geotechnical Laboratory Testing Program for Study and Evaluation of Liquefaction Ground Failure Using Stress and Strain Approaches, Heber Road Site, Oct. 15, 1979 Imperial Valley Earthquake*, Volumes I to III, Woodward Clyde Consultants, Eastern Region, Clifton, New Jersey.
- Lee, K.W. and Finn, W.D.L. (1978), *DESRA-2: Dynamic Effective Stress Response Analysis of Soil Deposits with Energy Transmitting Boundary Including Assessment of Liquefaction Potential*, Faculty of Applied Science, University of British Columbia, Vancouver, Canada.
- Moss, R.E.S., Collins, B.D. and Whang, D.H. (2005), "Retesting of Liquefaction /Nonliquefaction Case Histories in the Imperial Valley," *Earthquake Spectra*, Vol. 21, No. 1, Feb.
- Peck, R.B. (1979), "Liquefaction Potential: Science Versus Practice," *Journal of the Geotechnical Engineering Division*, ASCE, Vol. 105, No. GT3, March, pp. 393-398.
- Prevost, J.H. (1985), "A Simple Plasticity Theory for Cohesionless Frictional Soils," *International Journal of Soil Dynamics and Earthquake Engineering*, Vol. 4, No. 1, pp. 9-17.
- Prevost, J.H. (1988), *DYNAID: A Computer Program for Nonlinear Seismic Site Response Analysis*, Report No. NCEER-88-xxx, Dept. of Civil Engineering and Operations Research, Princeton University.
- Proctor, J.S. (2004), "Maps, Stratigraphy and Liquefaction Resistance for the WLA and GVDA NEES Sites," *Masters Project Report*, Brigham Young University, Provo, Utah.
- Rathje, E.M., Chang, W.J. and Stokoe, K.H., II (2005), "Development of an In Situ Dynamic Liquefaction Test," *ASTM Geotechnical Testing Journal*, Vol. 28, No. 1, pp. 50-60.
- Rathje, E.M., Chang, W.-J., Stokoe, K.H., II and Cox, B.R. (2004), "Evaluation of Ground Strain from In Situ Dynamic Testing," Paper No. 3099, *13th World Conference on Earthquake Engineering*, Vancouver, Canada, August.

- Richart, F. E., Hall, J. R. and Woods, R. D. (1970), *Vibration of Soils and Foundations*. Prentice-Hall, Inc., New Jersey.
- Robertson, P.K., Woeller, D.J. and Finn, W.D.L. (1992), “Seismic Cone Penetration Test for Evaluating Liquefaction Potential Under Cyclic Loading,” *Canadian Geotechnical Journal*, Vol. 29, pp. 686-695.
- Robertson, P.K. and Fear, C.E. (1996), “Soil Liquefaction and its Evaluation Based on SPT and CPT,” *Proceedings, NCEER Workshop on Evaluation of Liquefaction Resistance*, Jan. 4-5, Salt Lake City, Utah.
- Robertson, P.K. and Wride, C.E. (1998), “Evaluating Cyclic Liquefaction Potential Using the Cone Penetration Test,” *Canadian Geotechnical Journal*, Ottawa, Vol. 35, No. 3, pp. 442-459.
- Seed, H.B., Martin, P.P. and Lysmer, J. (1975), “The Generation and Dissipation of Pore Water Pressures During Soil Liquefaction,” *Report EERC 75-26*, Earthquake Engineering Center, University of California, Berkeley.
- Seed, H.B. (1979), “Soil Liquefaction and Cyclic Mobility Evaluation for Level Ground During Earthquakes,” *Journal of the Geotechnical Engineering Division*, ASCE, Vol. 105, No. GT2, February, pp. 201-255.
- Seed, H.B. and Idriss, I.M. (1967), “Analysis of Soil Liquefaction: Niiagata Earthquake,” *Journal of the Soil Mechanics and Foundations Division*, ASCE, Vol. 93, No. SM3, Proceedings Paper 5233, May, pp. 83-108.
- Seed, H.B. and Idriss, I.M. (1970), “Soil Modulus and Damping Factors for Dynamic Response Analysis,” *Rep. No. EERC 70-10*, Earthquake Engrg. Res. Ctr., Univ. of California at Berkeley, Calif.
- Seed, H.B. and Idriss, I.M. (1971), “Simplified Procedure for Evaluating Soil Liquefaction Potential,” *Journal of the Soil Mechanics and Foundations Division*, ASCE, Vol. 97, No. SM9, September, pp. 1249-1274.
- Seed, H.B. and Idriss, I.M. (1982), *Ground Motion and Soil Liquefaction During Earthquakes*, Earthquake Engineering Research Institute, Berkeley, California, 134 p.
- Seed, H.B., Idriss, I.M. and Arango, I. (1983), “Evaluation of Liquefaction Potential Using Field Performance Data,” *Journal of the Geotechnical Engineering Division*, ASCE, Vol. 109, No. GT3, March, pp. 458-482.

- Seed, H.B., Tokimatsu, K., Harder, L.F. and Chung, R.M. (1985), "Influence of SPT Procedures in Soil Liquefaction Resistance Evaluations," *Journal of Geotechnical Engineering*, ASCE, Vol. 111, No. 12, pp. 1425-1445.
- Seed, H.B., Wong, R.T., Idriss, I.M. and Tokimatsu, K. (1986), "Moduli and Damping Factors for Dynamic Analyses of Cohesionless Soils," *Journal of Geotechnical Engineering*, ASCE, 112(11), 1016-1032.
- Sharp, R.V. (1982), "Variable Rates of Later Quaternary Strike-Slip on San Jacinto Fault Zone, Southern California," *Journal of Geophysical Research*, 86(B3), 1754-1762.
- Shen, C.K., Wang, Z. and Li, X.S. (1991), "Pore Pressure Response During the 1986 Lotung Earthquake," *Proceedings, 2nd Int. Conf. on Recent Advances in Geotech. Earthquake Engrg. and Soil Dynamics*, S. Prakash, ed., National Science Foundation, Washington, D.C: 557-563
- Stokoe, K.H. II and Nazarian, S. (1985), "Use of Raleigh Waves in Liquefaction Studies," *Proceedings, Measurement and Use of Shear Wave Velocity for Evaluating Dynamic Soil Properties*, GED, ASCE, Denver, Colorado.
- Stokoe, K.H. II, Rosenblad, B.L., Bay, J.A., Redpath, B., Diehl, J.G., Steller, R.A., Wong, I.G., Thomas, P.A. and Luebbers, M. (2003), "Comparison of Vs Profiles from Three Seismic Methods at Yucca Mountain," *SARA 2003, 12th Panamerican Conference of Soil Mechanics and Geotechnical Engineering*, Cambridge, MA, 22-26 June.
- Stokoe K.H. II, Rathje, E.M. and Cox, B.R. (2004), "Using Large Hydraulic Shakers to Induce Liquefaction in the Field," *International Conference on Cyclic Behavior of Soils and Liquefaction Phenomena*, Bochum, Germany, March 31– April 2.
- Valle-Molina, C. (2006), *Measurements of Vp and Vs in Dry, Unsaturated and Saturated Sand Specimens with Piezoelectric Transducers*, Ph.D. Dissertation, The University of Texas, Austin, Texas. 387 p.
- Vucetic, M. and Dobry, R. (1986), "Pore Pressure Build Up and Liquefaction at Level Sandy Sites During Earthquakes," *Research Report*, Department of Civil Engineering, Rensselaer Polytechnic Institute, Troy, New York.
- Youd, T.L., and Wiczorek, G.F. (1984), "Liquefaction During the 1981 and Previous Earthquakes Near Westmorland, California," *USGS Open-File Report*, United States Geological Survey.

- Youd, T.L. and Bartlett, S.F. (1988), "U.S. Case Histories of Liquefaction-Induced Ground Failure," *Proceedings, First Japan-U.S. Workshop on Liquefaction, Large Ground Deformation, and Their Effects on Lifeline Facilities*, Tokyo, Japan, pp. 22-31.
- Youd, T.L. and Holzer, T.L. (1994), "Piezometer Performance at Wildlife Liquefaction Site, California," *Journal of the Geotechnical Engineering Division*, ASCE, 120(GT6): 975-995.
- Youd, T.L., Idriss, I.M., Andrus, R.D., Arango, I., Castro, G., Christian, J.T., Dobry, R., Finn, W.D.L., Harder, F.L., Jr., Hynes, M.E., Ishihara, K., Koester, J.P., Liao, S.S.C., Marcuson, W.F., III, Martin, G.R., Mitchell, J.K., Moriwaki, Y., Power, M.S., Robertson, P.K., Seed, R.B., and Stokoe, K.H., II (2001), "Liquefaction Resistance of Soils: Summary Report from the 1996 NCEER and 1998 NCEER/NSF Workshops on Evaluation of Liquefaction Resistance of Soils," *ASCE Journal of Geotechnical and Geoenvironmental Engineering*, Vol. 127, No. 10, pp. 817-833.
- Youd, T.L., Steidel, J.H. and Nigbor, R.L. (2004a), "Lessons Learned and Need for Instrumented Liquefaction Sites," *Soil Dynamics and Earthquake Engineering*, Vol. 24, No. 9-10, pp. 639-646.
- Youd, T.L., Bartholomew, H.A.J. and Proctor, J.S. (2004b), "Geotechnical Logs and Data From Permanently Instrumented Field Sites: Garner Valley Downhole Array (GVDA) and Wildlife Liquefaction Array (WLA)," *Unpublished Report (CD)*, Department of Civil and Environmental Engineering, Brigham Young University, Provo, Utah.
- Zeghal, M. and Elgamal, A.-W. (1994), "Analysis of Site Liquefaction Using Earthquake Records," *Journal of the Geotechnical Engineering Division*, ASCE, Vol. 120, No. 6, pp. 996-1017.
- Zeghal, M., Elgamal, A.-W., Tang, H.T. and Stepp, J. C. (1995), "Lotung Downhole Array. II: Evaluation of Soil Nonlinear Properties," *Journal of the Geotechnical Engineering Division*, ASCE, Vol. 121, No. 4, pp. 363-378.

Vita

Brady Ray Cox was born in Provo, Utah on August 30th, 1976. He is the second of three children born to Clayton M. and Jerri Lynn Cox. Brady was raised in Helper, Utah and graduated from Carbon High School in Price, Utah in 1994. He received his A.S. degree in June 1995 from the College of Eastern Utah in Price, Utah. Brady lived in London, England between August 1995 and August 1997 where he served as a volunteer missionary for The Church of Jesus Christ of Latter-day Saints. He married Audrey Steele on December 20th, 1997. They currently have two daughters, Kayla and Savannah. Brady received his B.S. and M.S. degrees in Civil Engineering in May 2000 and August 2001, respectively, from Utah State University in Logan, Utah. In August 2001, he enrolled at The University of Texas at Austin to pursue a PhD in Civil Engineering.

Permanent address: 4488 North U.S. Hwy #6, Helper, Utah 84526

This dissertation was typed by Brady Ray Cox.